80th Birth Anniversary of Boris Ieremievich Verkin(1919–1990)

Fiz. Nizk. Temp. **25**, (August–September 1999)

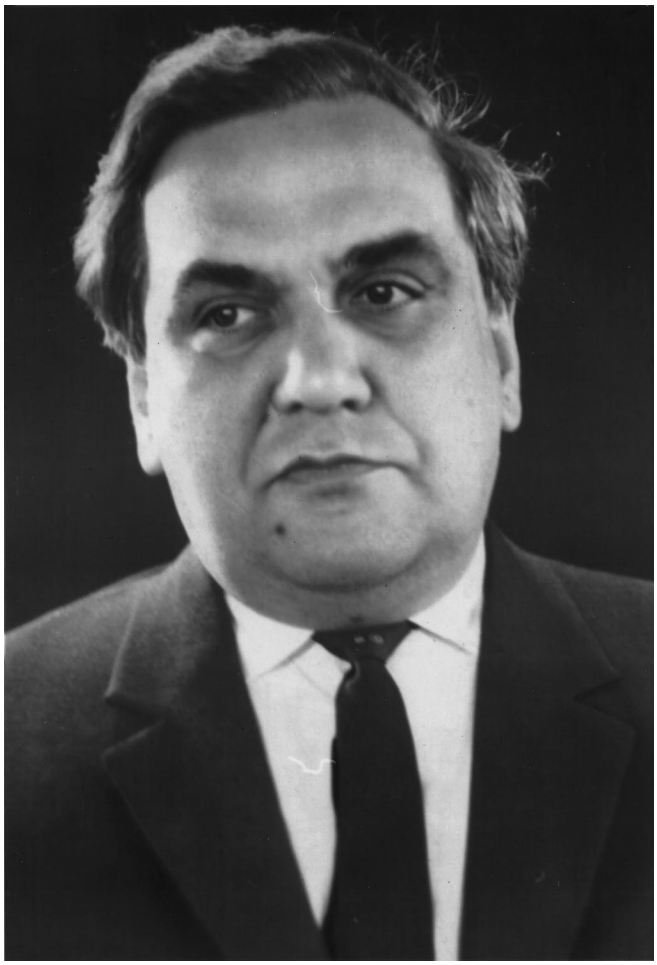

The 80th birth anniversary of late Boris Ieremievich Verkin, Member of the Ukrainian Academy of Sciences, leading scientist and organizer falls on August 6, 1999.

A connoisseur and appraiser of various arts, he was himself endowed with the great gift of creation. Together with his irrepressible spirit and energy, Boris Ieremievich devoted this gift to the service of science. In addition to his own remarkable scientific publications, he made a significant contribution to science by paving the way for others to attain the heights of their scientific career. His lifetime ambition was realized in the organization of a unique creative workshop called the Institute for Low Temperature Physics and Engineering. Physicists and mathematicians, biologists and doctors, designers and production engineers have been working hand-in-hand for many years, supporting and enriching one another at this science- and-engineering complex with their intellect, philosophy, experience, and the warmth of friendly relations. To carry out such a large-scale operation, it was necessary to find an extraordinary personality devoted utterly to the cause of learning, who could start from a scratch, deprived of all kinds of government authority but having a clear idea of the aims, the strength of conviction and charm. He had no axe to grind for his personal ends, and did it only for Science and service to the Motherland. This is the reason behind the tremendous response and encouragement he received for his efforts.

The Institute is proud to be named after its founder who, in addition, was its Director for many years. He was the brain, soul and heart of the Institute which served as the starting point for other scientific establishments. The members of its staff are known and acknowledged in the world of science. The instruments and equipment produced

 © 1999 American Institute of Physics

at the Institute are being used in quest and acquisition of knowledge, production activity, food and health industry. They were also exploited successfully in terrestrial and space applications, and were deployed for exploration of other planets. The contribution made by B. I. Verkin in these efforts can be hardly overestimated. His colleagues and pupils are proud of having been his contemporaries and enthusiasts in a common cause.

It is about a decade since Academician Verkin left for heavenly abode. His legacy includes unique Institute, a large number of pupils, the journal ''Low Temperature Physics'' which he founded, hundreds of scientific publications, monographs, handbooks, and inventions. He continues to be a shining example of selfless and altruistic service of the Motherland for new generations of creators who will certainly be called for by the country after the passage of present hard times.

I. V. Svechkarev

This jubilee publication of the journal consists of two issues and is devoted to the 80th Birth Anniversary of B. I. Verkin, founder and permanent Chief Editor of the journal ''Low Temperature Physics.'' Most of the articles have been contributed by close associates and pupils of Boris Ieremievich, but even they fail to give a complete picture of the diversities of his scientific interests. The de Haas–van Alphen effect played a significant role both in the physics of metals and in the life of B. I. Verkin who carried out pioneering investigations of this effect. The current trends of this effect in its application to superconductors have been highlighted in the journal in the works of leading scientists.

The Editorial Board of the journal is deeply indebted to the authors who sent their papers for inclusion in the Jubilee issue, and apologizes for its inability to include all of them in this issue. The articles not included here will be published in the next issue with appropriate dedication.

Editorial Board

De Haas–van Alphen oscillation in both the normal and superconducting mixed states of $NbSe_2$, $CeRu_2$, URu_2Si_2, and UPd_2Al_3 (Review Article)

Y. Inada

*Graduate School of Science, Osaka University, Toyonaka, Osaka 560-0043, Japan**

Y. Ōnuki

*Graduate School of Sciences, Osaka University, Toyonaka, Osaka 560-0043, Japan; Advanced Science Research Center, Japan Atomic Energy Research Institute, Tokai, Ibaraki 319-1195, Japan***

(Submitted March 22, 1999)
Fiz. Nizk. Temp. **25**, 775–795 (August–September 1999)

The de Haas–van Alphen (dHvA) oscillation was observed clearly in both the normal and superconducting mixed states in $NbSe_2$, $CeRu_2$, URu_2Si_2, and UPd_2Al_3. The dHvA frequency, which is proportional to the extremal cross-sectional area of the Fermi surface, does not change in magnitude between the normal and mixed states. For the *f*-electron superconductors, the cyclotron effective mass is found to be reduced and the corresponding Dingle temperature or scattering rate of the conduction electron increases in the mixed state. An anisotropic energy gap with a line node for URu_2Si_2 and UPd_2Al_3 is discussed from the angular dependence of the dHvA amplitude in the mixed state. © *1999 American Institute of Physics.* [S1063-777X(99)00208-X]

1. INTRODUCTION

Under a strong magnetic field the orbital motion of a conduction electron is quantized and forms Landau levels. The de Haas–van Alphen (dHvA) effect, which is caused when the Landau levels cross the Fermi energy by increasing the magnetic field, is a powerful method for determining the topology of the Fermi surface, the cyclotron effective mass m_c^* and the scattering lifetime τ of the conduction electron. This phenomenon was studied in the strongly correlated electron systems of the rare earth and uranium compounds, or so-called heavy fermion compounds.[1] In fact, the heavy mass of about $100\,m_0$ (m_0 is the rest mass of an electron) was detected by the dHvA effect in $CeRu_2Si_2$[2] and UPt_3.[3,4] The heavy fermion state is based on the hybridization effect between the conduction electrons with a wide energy band and the almost localized *f*-electrons. Especially, the Kondo effect is a basic phenomenon in the cerium and uranium compounds.

The many-body Kondo bound state is understood as follows. For the simplest case of no orbital degeneracy, the localized spin $\uparrow(l)$ is compensated by the conduction electron spin polarization $\downarrow(c)$. Consequently the singlet state $\{\uparrow(l)\downarrow(c)+\downarrow(l)\uparrow(c)\}$ is formed with the binding energy k_BT_K relative to the magnetic state. Here, the Kondo temperature T_K is the single energy scale in the simple Kondo problem. In other words, disappearance of the localized moment is thought to be due to the formation of a spin-compensating cloud of the conduction electrons around the impurity moment.

The Kondo effect occurs independently at each cerium site even in a lattice system of the cerium compound such as $CeCu_6$.[1] The ground-state properties of the Kondo lattice system are interesting with respect to magnetism. The electrical resistivity ρ follows a Fermi-liquid nature of $\rho=\rho_0+AT^2$. The $\sqrt{A}$ value is extremely large, which correlates with an enhanced Pauli susceptibility $\chi\simeq\chi_0$ and a large electronic specific heat coefficient γ. In other words, the magnetic specific heat of the *f*-electrons is changed into the electronic specific heat γT at low temperatures.

The dHvA effect was studied to clarify the heavy fermion state, as mentioned above. To our surprise, the dHvA oscillation was observed even in the superconducting mixed state of type II superconductors. The first measurement in the mixed state was done by Graebner and Robbins for a layered compound $NbSe_2$ by means of a magnetothermal technique.[5] Onuki *et al.* confirmed this oscillation by the measurement of the standard field modulation *ac* susceptibility.[6,7]

Figure 1 shows the typical dHvA oscillation in both the normal and mixed states for $NbSe_2$. $NbSe_2$ is a conventional superconductor with a hexagonal structure. A transition temperature T_c is 7.2 K and the upper critical field H_{c2} is highly anisotropic; about 45 kOe for the field along the [0001] direction and 145 kOe for the field perpendicular to [0001]. In Fig. 1 the field is tilted by 18° from $[10\bar{1}0]$ to [0001], where H_{c2} is about 100 kOe. One dHvA oscillation with a frequency of 1.5×10^6 Oe is clearly observed even in the mixed state. The dHvA frequency, Dingle temperature and cyclotron mass did not obviously change between the normal and mixed states,[6,7] although, it was reported that only the Dingle temperature slightly increases with decreasing the field below H_{c2}.[8]

Recently we have clearly observed the dHvA oscillation in *f*-electron superconductors $CeRu_2$,[9,10] URu_2Si_2[11] and UPd_2Al_3[12] in both the normal and superconducting mixed states. Till now, the dHvA oscillation in the mixed state has been observed for several compounds such as V_3Si,

 © 1999 American Institute of Physics

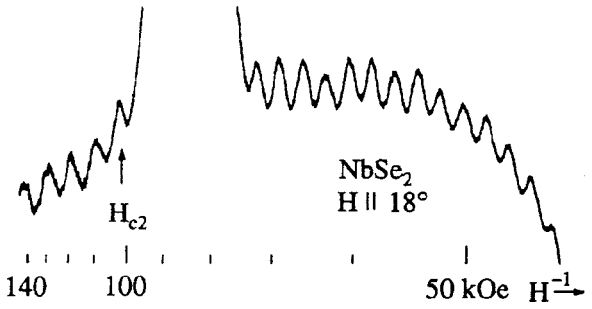

FIG. 1. De Haas–van Alphen oscillation in $NbSe_2$.

Nb_3Sn,[8,13] YNi_2B_2C[14–16] as well as $NbSe_2$, $CeRu_2$, URu_2Si_2[17] and UPd_2Al_3 mentioned above.

The most important issue for heavy fermion superconductors such as UPt_3, URu_2Si_2 and UPd_2Al_3 is that superconductivity is realized in the antiferromagnetic state.[18] The superconducting properties such as the specific heat and the spin-lattice relaxation rate do not follow the exponential dependence of $e^{-\Delta\ {}^{k}B^{T}}$ which is expected from the BCS theory, but obey the power law of T^n. Here, Δ is the superconducting energy gap and n is an integer. These results are based on the fact that quasiparticles with heavy masses of $10-100\,m_0$ are of an *f*-electron character, as mentioned above, which originates from the strong Coulomb repulsion between the *f*-electrons. These quasiparticles condense into Cooper pairs.

When we compare the phonon-mediated attractive interaction to the strong repulsive interaction among the *f*-electrons, it is theoretically difficult for the former interaction to overcome the latter. To avoid a large overlap of the wave functions of the paired particles, the heavy fermion system would rather choose an anisotropic channel, like a *p*-wave spin triplet or a *d*-wave spin singlet state to form Cooper pairs. In fact, the heavy fermion superconductor exhibits antiferromagnetic ordering as mentioned above. Recent neutron scattering experiments clearly indicated evidence for a close relationship between superconductivity and magnetic excitation in UPd_2Al_3.[19,20] A magnetic excitation gap, which appears in the inelastic neutron profile below T_c, corresponds to the superconducting order parameter.

Figure 2 shows a schematic view of the superconducting order parameter with the *s*-, *p*- and *d*-wave pairing. The order parameter $\mathbf{\Psi(r)}$ with even parity (*s*- and *d*-wave) is symmetric with respect to $\mathbf{r}$, where one electron with the up-spin state of the Cooper-pair is simply considered to be located at the center of $\mathbf{\Psi(r)}$, $\mathbf{r}=0$ and the other electron with the down-spin state is located at $\mathbf{r}$. The width of $\Psi(\mathbf{r})$ with respect to $\mathbf{r}$ is called the coherence length ξ, as shown in Fig. 2a. UPd_2Al_3 is considered to be a *d*-wave superconductor from the NMR experiments, which is applied to the case in Fig. 2c.[21,22] On the other hand, $\Psi(\mathbf{r})$ with odd parity (*p*-wave) is not symmetric with respect to $\mathbf{r}$, where the parallel spin state is shown in Fig. 2b. From the NMR and magnetization experiments,[23,24] UPt_3 is considered to possess odd parity in symmetry. Parity in URu_2Si_2 is not clear because almost all of the NMR-Knight shift was due to the orbital part, while the contribution of the spin part of the conduction electron was not detected.[25]

The dHvA voltage $V_{\rm osc}$ is obtained by the method of 2ω detection of the field modulation;[1]

$$V_{\rm osc}=A\sin\left(2\pi\frac{F}{H}+\varphi\right), \tag{1}$$

$$A\propto J_2(x)TH^{-1/2}\left|\frac{\partial^2 S}{\partial k_H^2}\right|^{-1/2}\frac{\exp(-\alpha m_c^* T_D/H)}{\sinh(\alpha m_c^* T/H)}\times\cos\left(\frac{1}{2}\pi g\frac{m_c^*}{m_0}\right),$$

$$x=2\pi\frac{Fh}{H^2},\quad \alpha=\frac{2\pi^2 c k_B}{e\hbar},$$

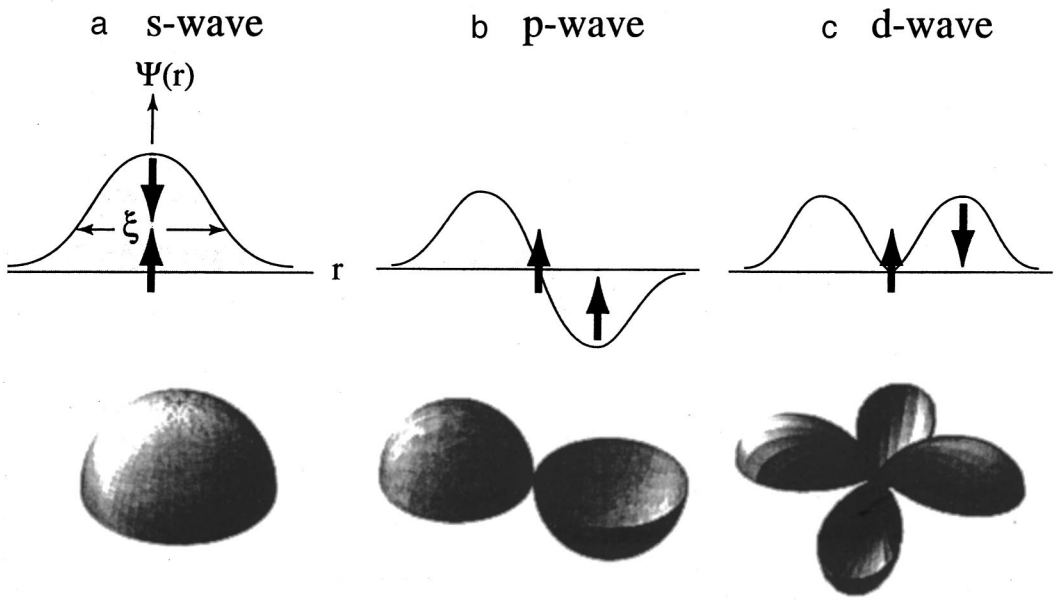

FIG. 2. Schematic view of the superconducting order parameter with the *s*-, *p*- and *d*-wave pairing.

where $J_2(x)$ is the Bessel function, which depends on the dHvA frequency F, the modulation field h and the magnetic field strength H. The dHvA frequency $F[=(c\hbar/2\pi e)S_F]$ is proportional to the extremal (maximum or minimum) cross-sectional area S_F of the Fermi surface. The quantity $|\partial^2 S/\partial k_H^2|^{-1/2}$ is the inverse square root of the curvature factor $\partial^2 S/\partial k_H^2$, where the rapid change of the cross-sectional area around the extremal cross-sectional area along the field direction diminishes the dHvA amplitude for this extremal area. We can determine the cyclotron mass m_c^* from the temperature dependence of the dHvA amplitude A, namely, from the slope of a plot of $\ln A[1-\exp(-2\alpha m_c^* T/H)]/T$ vs T at constant H and h by using a method of successive approximations, and we can obtain the Dingle temperature T_D $[=(\hbar/2\pi k_B)\tau^{-1}]$ or the scattering lifetime τ from the field dependence of the amplitude, namely, from the slope of a plot of $\ln[AH^{1/2}\sinh(\alpha m_c^* T/H)/J_2(x)]$ vs H^{-1} at constant temperature. Here, g is the g-factor of the conduction electron, which is 2 for the free electron.

The dHvA oscillation is detected when the highfield condition is satisfied; $\omega_c\tau/2\pi>1$, and the spacing between the Landau levels is larger than the thermal broadening k_BT; $\hbar\omega_c>k_BT$. If the magnetic field H is 100 kOe and the carrier possesses a cyclotron mass of $10\,m_0$, the following conditions for the temperature and the scattering lifetime are required: $T<1.3\,\mathrm{K}$ and $\tau>3.6\times10^{-11}\,\mathrm{s}$ or $T_D<0.03\,\mathrm{K}$. A temperature of 0.4 K can be attained in the ^{3}He-cryostat and much lower temperatures are also obtainable in a dilution refrigerator. The typical Dingle temperature of a high-quality sample in the f-electron system is about 0.1 K, and thus fields higher than 100 kOe are necessary to detect the dHvA amplitude of the heavy conduction electron.

We have continued growing high-quality single crystals of f-electron superconductors such as $CeRu_2$, URu_2Si_2 and UPd_2Al_3, and extended our investigations on the dHvA experiments. The dHvA oscillation for these compounds has been observed in both the normal and superconducting mixed states. The field dependence of the cyclotron mass and the Dingle temperature in the mixed state is clarified in this paper. An anisotropic energy gap with a line node is also discussed on the basis of the angular dependence of the dHvA amplitude in the mixed state.

2. THEORETICAL

Maki,[26] Wasserman and Springford,[27] Dukan and Tešanović[28] Vavilov and Mineev[29] and Gor'kov and Schrieffer[30] have discussed theoretically the dHvA oscillation in the mixed state on the basis of the quasiparticles in magnetic fields. They claim that the dHvA frequency is unchanged from the normal state, but the amplitude is reduced by an additional quasiparticle scattering rate or the Dingle temperature, depending on the field and temperature. These characteristic features have been confirmed by the results of experiments for those compounds mentioned above.

For example, we have confirmed for $CeRu_2$, URu_2Si_2 and UPd_2Al_3 that the dHvA frequency is unchanged and the following simple relation holds between the Dingle temperature in the mixed state $\tilde{T}_D$ and the one in the normal state T_D: $\tilde{T}_D = T_D + \Delta T_D$, where ΔT_D is the additional Dingle temperature in the mixed state.[10] Moreover, the mass is found to decrease with decreasing field below H_{c2}. No report on the change of the mass has been done for the other superconductors. The change in the mass might be found in the highly correlated electron systems because $CeRu_2$, URu_2Si_2 and UPd_2Al_3 are f-electron superconductors with large effective masses. Experimentally, the dHvA oscillation in the mixed state can be most likely detected for any superconductor if its upper critical field H_{c2} is large enough, for example, more than about 30 kOe, and the single crystalline sample is of high quality. We shall explain briefly the reason why the dHvA oscillation is observed in the mixed state, considering a conventional superconductor of $CeRu_2$ with a cubic structure.

When the field is applied in a normal-state metal, the quasi-continuum momentum energy of the conduction electrons with up- and down-spin states is changed into the discrete energy levels, the so-called Landau levels. The dHvA oscillation is caused when the Landau levels cross the Fermi energy by increasing the field. Two scenarios might exist to explain the dHvA effect in the mixed state, where the dHvA oscillation is caused either by quasiparticles or by the Cooper-pair electrons. It is not certain whether each electron in the Cooper-pair could be quantized in energy by fields, while remaining the Cooper-pair with $(k,\uparrow)$ and $(-k,\downarrow)$ at 0 K. On the other hand, the de-paired electrons due to magnetic fields, namely, the quasiparticles could be quantized into Landau levels as in the usual normal-state metal. We shall discuss the latter case.[10]

There exist three reduction factors in the dHvA oscillation. One is an inhomogeneous field due to vortices. The second is the electron scattering at the boundary between the normal region and the superconducting one, called the Andreev reflection. The last is the field dependence of the carrier concentration of the quasiparticles.

We shall examine the mixed state based on the Ginzburg–Landau (GL) theory. The order parameter $\boldsymbol{\Psi}(\mathbf{r})$ and the microscopic magnetic field $\mathbf{h}(\mathbf{r})=\nabla\times\mathbf{A}(\mathbf{r})$ in the mixed state are determined by solving the GL equations for $\boldsymbol{\Psi}(\mathbf{r})$ and $\mathbf{A}(\mathbf{r})$.[31] We rewrite the GL equations in terms of $\psi(\mathbf{r})=|\boldsymbol{\Psi}(\mathbf{r})|$ and $h(\mathbf{r})$ as

$$-\xi^2\nabla^2\psi(\mathbf{r})+\frac{\lambda^2}{2\dot{H}_c^2}\left(\frac{\nabla h(\mathbf{r})}{\psi^2(\mathbf{r})}\right)^2\psi(\mathbf{r})-\psi(\mathbf{r})+\psi^3(\mathbf{r})=0, \tag{2}$$

$$-\lambda^2\nabla\cdot\left(\frac{\nabla h(\mathbf{r})}{\psi^2(\mathbf{r})}\right)+h(\mathbf{r})=\Phi_0\sum_n\delta(\mathbf{r}-\mathbf{r}_n), \tag{3}$$

where $\mathbf{r}_n$ is the position of the vortex center, H_c is the thermodynamic critical field, Φ_0 is the fluxoid, ξ is the coherence length, λ is the penetration depth. Applying the boundary condition $\psi(\mathbf{r}_n)=0$ at the vortex center and the periodic boundary condition at the boundary of the unit cell of the vortex lattice, we solve Eqs. (2) and (3) numerically for $\kappa=\lambda/\xi=25$, self-consistently by the relaxation method and considering $CeRu_2$.

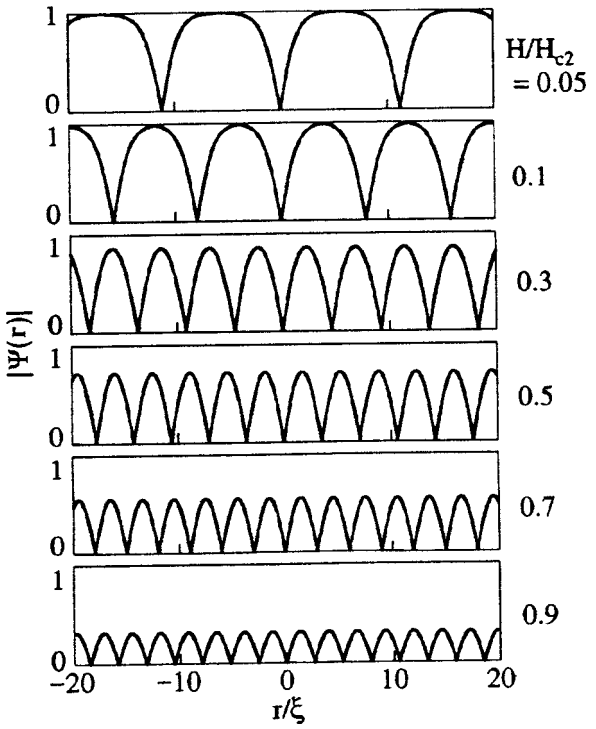

FIG. 3. Spatial dependence of the order parameter $|\Psi(\mathbf{r})|$ at several fields.

We show in Fig. 3 the spatial dependence of the order parameter $\psi(\mathbf{r})$ or $|\Psi(\mathbf{r})|$, where ξ is the coherence length of 79 Å. At a low field of $H/H_{c2}=0.1$, the vortices are separated enough and the order parameter between vortices is near to unity. On the other hand, at a high field of $H/H_{c2}=0.7$, vortices are numerous and the order parameter decreases almost by half. In the latter high field condition, the quasiparticles could circulate the cyclotron orbits in real space. Figure 4 shows a schematic Abrikosov lattice of the vortices and the cyclotron orbits at $H/H_{c2}=0.7$. Each vortex with a diameter of $2\xi(=158\,\text{Å})$ is separated by 255 Å at $H/H_{c2}=0.7$. The corresponding cyclotron orbits in real space are illustrated for branches $\varepsilon_{1,2,3}$, δ and α with diameters of 1720, 3950 and 9440 Å, respectively, for $CeRu_2$.

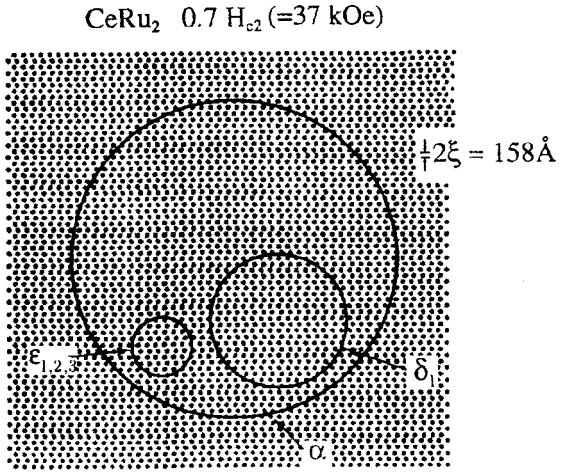

FIG. 4. Schematic Abrikosov lattice of the vortices and the cyclotron orbits at $H/H_{c2}=0.7$ in $CeRu_2$.

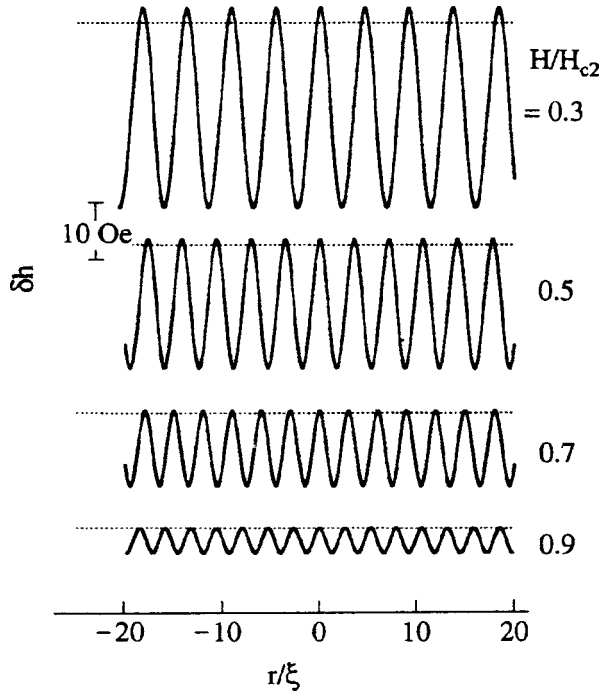

FIG. 5. Spatial variation of the magnetic field in $CeRu_2$.

The quasiparticles have to tunnel into the superconducting region in order to complete the cyclotron motion, which is prevented by the so-called Andreev reflection at a low field of $H/H_{c2}=0.1$. The high field condition, for example, $H/H_{c2}>0.1$ is necessary to complete the cyclotron motion, as mentioned above. Experimentally, the lowest fields to detect the dHvA oscillation in the mixed state are $0.6\,H_{c2}$ for V_3Si,[8] $0.2\,H_{c2}$ for YNi_2B_2C,[14] $0.4\,H_{c2}$ for branch $\varepsilon_{1,2,3}$ for $CeRu_2$,[10] $0.4\,H_{c2}$ for URu_2Si_2[11] and $0.7\,H_{c2}$ for UPd_2Al_3.[12]

Next we discuss inhomogeneity of the magnetic field $\delta h(\mathbf{r})$ defined by $\delta h(\mathbf{r})=h(\mathbf{r})-H$. Figure 5 shows the spatial inhomogeneity of the magnetic field in the superconductor at $H/H_{c2}=0.3$, 0.5, 0.7 and 0.9. Inhomogeneous fields at $H/H_{c2}=0.3$, 0.5, 0.7 and 0.9 are 35, 23, 13 and 4 Oe, respectively. The field H is shown by a horizontal dotted line in Fig. 5.

We note that a field interval for one cycle of the dHvA oscillation is 1880 Oe for branch ε, 340 Oe for δ and 60 Oe for α at $H=0.7\,H_{c2}(=37\,\text{kOe})$. If this inhomogeneous field is directly related to the dHvA oscillation, the oscillation of branch α will be reduced in amplitude. This inhomogeneous field might not reduce the dHvA amplitude directly if the vortices formed a regular lattice.

An additional effective scattering rate in the mixed state $\delta\tau^{-1}$ is estimated by the uncertainty principle of $\delta\tau^{-1}\approx v_F\delta k_F$, where δk_F is variation in radius of the orbit cutting the same flux and v_F is Fermi velocity.[13] The area of the cyclotron orbit A is changed into $A+\delta A$ by the inhomogeneity of the field δh:

$$A+\delta A=\pi\left(\frac{m^*v_Fc}{e(H+\delta h)}\right)^2=\pi\left(\frac{m^*v_Fc}{eH}\right)^2-2\pi\left(\frac{m^*v_Fc}{eH}\right)^2\frac{\delta h}{H}=\pi r^2-2\pi r^2\frac{\delta h}{H},\qquad(4)$$

where r is the radius of the cyclotron orbit. By using $\delta A = 2\pi r\,\delta r$, we can get the following relation:

$$\frac{2\pi r^2 \delta h}{H} = 2\pi r\,\delta r \quad \text{or} \quad \delta r = r\frac{\delta h}{H}. \tag{5}$$

Therefore, the final relation is obtained from Eq. (5).

$$\delta k_F = \left(\frac{eH}{c\hbar}\right)\delta r \approx \frac{re\,\delta h}{c\hbar}. \tag{6}$$

From the calculated values of δh mentioned above and Eq. (6), $\delta\tau^{-1}$ for $H/H_{c2}=0.7$ is estimated to be of the order of $10^8\ \mathrm{s}^{-1}$ for branches α, δ_1 and $\varepsilon_{1,2,3}$. This value corresponds to a small value of δT_D, being of the order of 10^{-2} K. Inhomogeneity in the field is thus a minor reduction factor.

Using Maki's theory [26], we shall explain the change in the Dingle temperature and the mass in the mixed state. The Dingle temperature in the mixed state $\tilde{T}_D$ was given as the imaginary part of the self-energy for the quasiparticles in the mixed state close to H_{c2}:

$$\tilde{T}_D = T_D + \Delta T_D, \tag{7}$$

$$\Delta T_D = \frac{\Delta^2(H,T)}{\sqrt{\pi}k_B\alpha}, \tag{8}$$

$$\alpha = v_F\sqrt{2e\hbar H/c}, \tag{9}$$

$$\Delta^2(H,T) = \Delta^2(T)(1-H/H_{c2}), \tag{10}$$

where T_D is the Dingle temperature in the normal state, ΔT_D is an additional one, v_F is Fermi velocity which is given as $\sqrt{2e\hbar F/c}/m_c^*$, and $\Delta(T)$ is the temperature-dependent BCS energy gap in zero field.

The effective mass of the quasiparticles in the mixed state $\tilde{m}_c^*$ was not given theoretically by Maki. We have calculated it by using the following formula:[32]

$$\tilde{m}_c^* = m_c^*\left[\frac{1-\partial\Sigma_R(\xi,\omega)/\partial\omega}{1+\partial\Sigma_R(\xi,\omega)/\partial\xi}\right]_{\xi=0,\omega=0}, \tag{11}$$

where $\Sigma_R(\xi,\omega)$ is the real part of the self-energy for the quasiparticles in the mixed state, and ξ and m_c^* are the quasiparticle's energy measured relative to the Fermi energy and the effective mass in the normal state, respectively. The energy ω is also measured relative to the Fermi energy and therefore $\omega=0$ corresponds to the Fermi energy. Using the self-energy derived by Brandt *et al.*,[33]

$$\Sigma(\xi,\omega) = \Delta^2(H,T)\int_{-\infty}^{\infty}\frac{du}{\sqrt{\pi}}\frac{\mathrm{e}^{-u^2}}{\omega+i\delta+\xi-\alpha u}, \tag{12}$$

we obtain the cyclotron effective mass in the mixed state $\tilde{m}_c^*$ as

$$\tilde{m}_c^* = m_c^*\frac{1-2(\Delta(H,T)/\alpha)^2}{1+2(\Delta(H,T)/\alpha)^2} \simeq m_c^*\frac{1}{1+4(\Delta(H,T)/\alpha)^2}. \tag{13}$$

A Maki's theory is based on a mixed state self-energy calculated by Brandt *et al.*[33] They clarified the spatially averaged density of states of type II superconductors in fields. Figure 6 shows the energy dependence of the density of states $D_s(\omega)$ in the pure limit, which was calculated by Brandt *et al.* As mentioned above, the energy at $\omega=0$ corresponds to the Fermi energy. $D_s(\omega)$ in the energy range of $\omega/\Delta_0=0$ to 1 is zero at zero field but increases with increasing the field, reaching an ω-independent value of D_0 at H_{c2}.

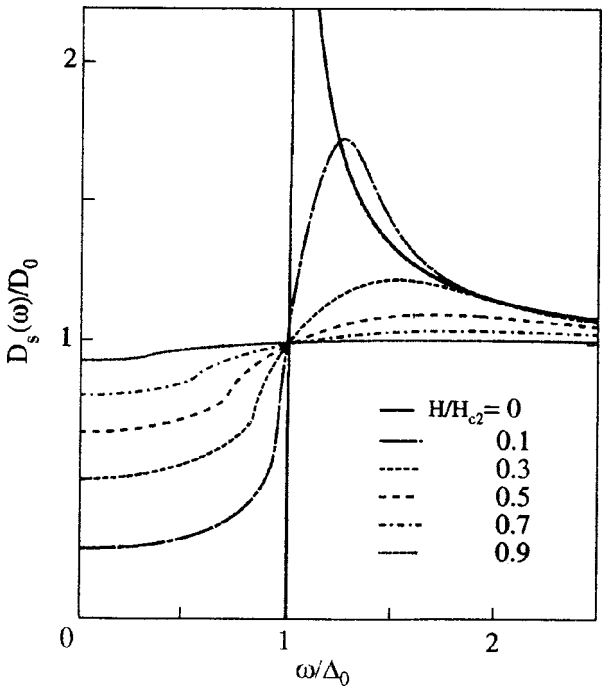

FIG. 6. Energy dependence of the density of states $D_s(\omega)/D_0$ in the pure limit.

The density of states is found to vary from the ''gapless'' state to the BCS type as the angle θ changes from $\pi/2$ to zero. Figure 7 shows the field dependence of the density of states at the Fermi energy ($\omega=0$) in the mixed state for several angles. Here, the angle θ is the polar angle of the quasiparticle momentum p with respect to the direction of

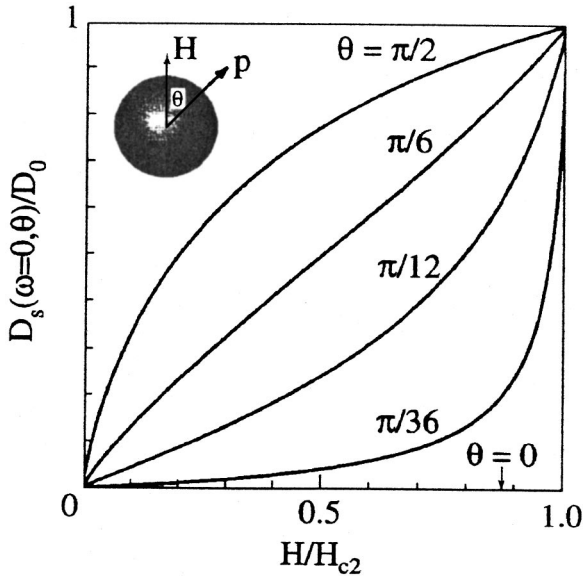

FIG. 7. Field dependence of the density of states in the mixed state for several polar angles.

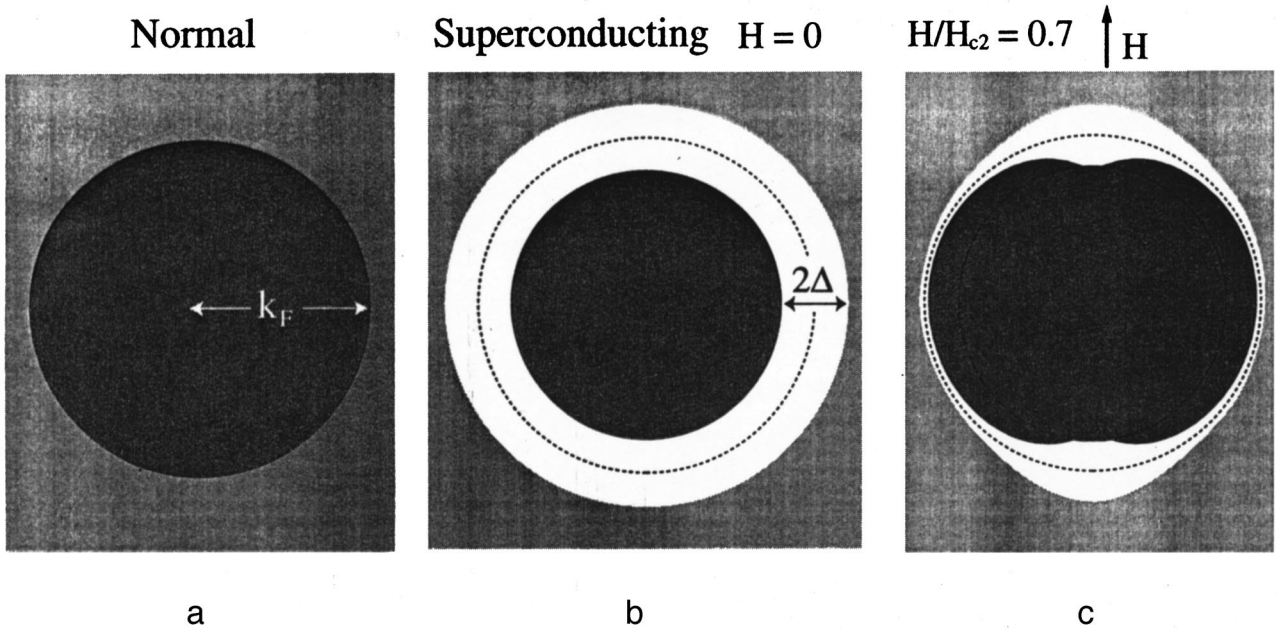

FIG. 8. Schematic superconducting energy gap in $H/H_{c2}=0$ and 0.7.

the magnetic field, as shown in an inset of Fig. 7. The Maki's theory corresponds to the $\theta=\pi/2$ case because α in Eq. (9) is changed into $\alpha=v_F \sin\theta\sqrt{2e\hbar H/c}$ for the angle θ. $D_s(\omega)$ in Fig. 6 is also the total density of states, namely, an average over the angle θ of 0 to $\pi/2$.

$D_s(\omega=0,\theta)$ in fields possesses a finite value for any angle except $\theta=0$, corresponding to the gapless state mentioned above. In particular, $D_s(\omega=0,\theta=\pi/2)/D_0$ is 0.85 at $0.7\,H_{c2}$ or 37 kOe in $CeRu_2$. The angle $\theta=\pi/2$ corresponds to a maximum area of the spherical Fermi surface S_F in the dHvA oscillation, as schematically shown in Fig. 8. This is the reason why the dHvA oscillation can be detected in the mixed state.

Finally, we discuss the local density of states. The local density of states for the quasiparticles propagating in the direction of $\mathbf{v}_F=v_F(\sin\theta\cos\varphi,\sin\theta\sin\varphi,\cos\theta)$, where φ is the azimuthal angle in the plane perpendicular to the magnetic, field, is calculated by the formula

$$D_s(\mathbf{r};\theta,\varphi;\omega)=-\frac{1}{\pi}D_0\sum_i \int_{-\infty}^{\infty} d\xi_p \,\mathrm{Im}[G_\omega(\mathbf{p},\mathbf{K}_i)]e^{i\mathbf{K}_i\mathbf{r}}, \tag{14}$$

where $G_\omega(\mathbf{p},\mathbf{K}_i)$ are the quasiparticle Green's functions calculated from the Gor'kov equation and $\mathbf{K}_i$ are the reciprocal lattice vectors of the vortex lattice. Assuming the Abrikosov solution for the order parameter, we can solve the Gor'kov equation numerically for $G_\omega(\mathbf{p},\mathbf{K}_i)$.

The density of states averaged, over r, θ and φ may be calculated by using the Green's function with $\mathbf{K}=0$ alone, as done by Brandt *et al.* However, in order to calculate the spatial variation of the density of states in the mixed state, it is crucial to incorporate Green's functions with $\mathbf{K}\neq 0$. Thus we take into account the reciprocal lattice vectors of $\mathbf{K}_0=0$ and 60 vectors $(\mathbf{K}_1,\ldots,\mathbf{K}_{60})$ surrounding $\mathbf{K}_0$ and calculate the Green's functions with the $\mathbf{K}_1$'s.

In relation with the dHvA effect, we are interested in the quasiparticles propagating in the plane perpendicular to $\mathbf{H}(\theta=\pi/2)$, particularly along the line connecting the neighboring vortices where the direction of the line is chosen to be $\varphi=0$. In Fig. 9 we show the local density of states at the Fermi level $D_s(\mathbf{r};\pi,0;0)$ for $H/H_{c2}=0.5$, 0.7 and 0.9. The

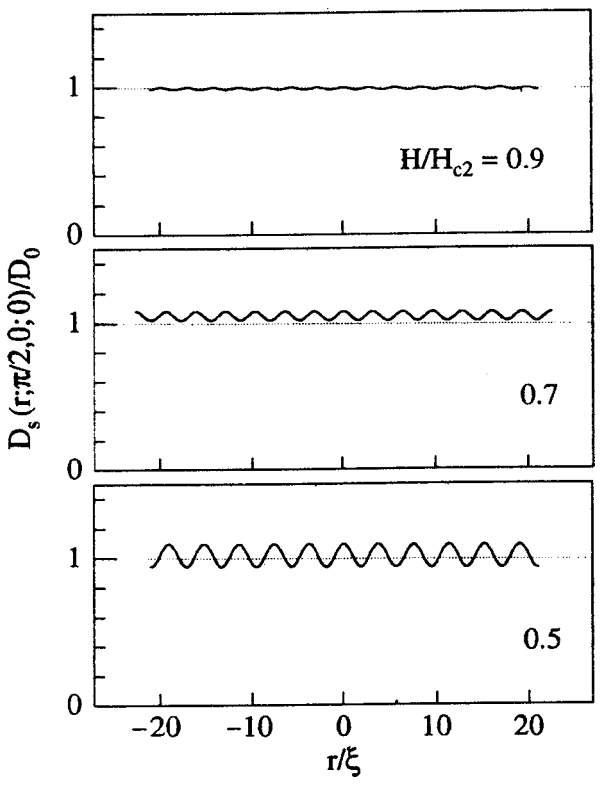

FIG. 9. Local density of states for the quasiparticles along the direction connecting the neighboring vortices.

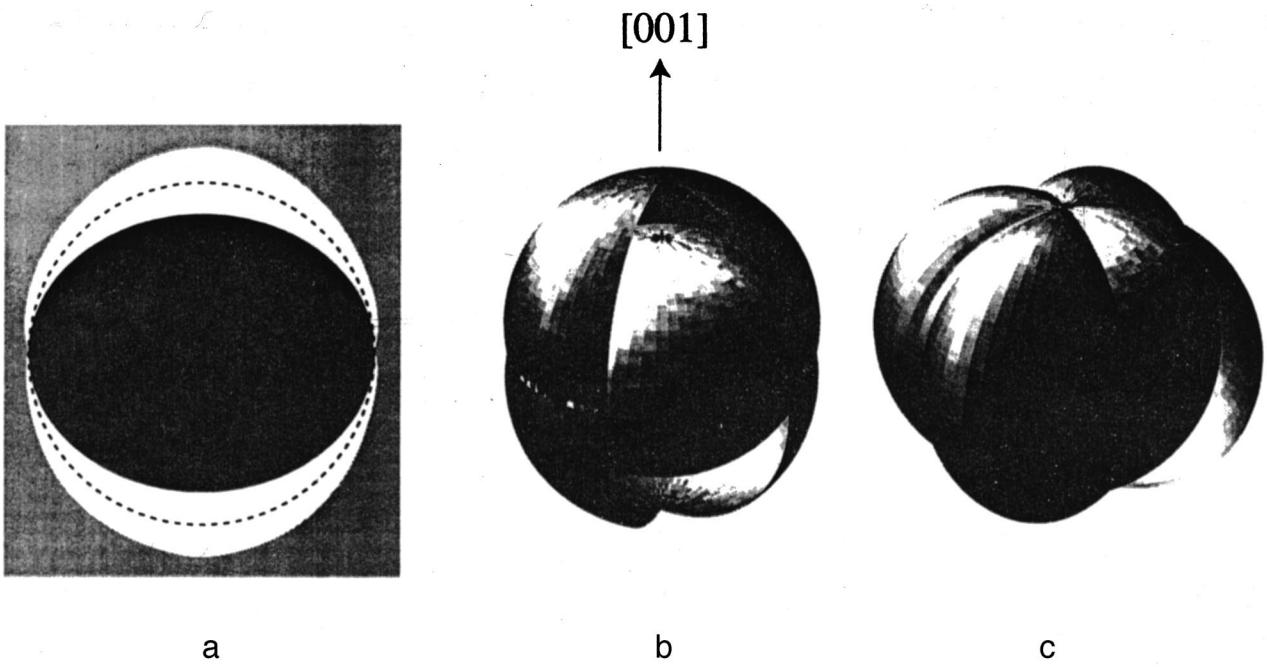

FIG. 10. Schematic superconducting energy gap with a nodal line (a) and (b). The nodal line exists along the equator (a) in the cross-section of (b). In (c), there exist two nodal line crossing poles.

densities of states for $H/H_{c2}=0.5$, 0.7 and 0.9 are close to the value in the normal state and their modulation is rather small. Unexpectedly, in the intermediate fields of $H/H_{c2}=0.5$ and 0.7, the density of states is enhanced comparing to that at 0 K in the normal state, indicating the suppression of $D_s(\mathbf{r};\pi/2,\varphi;0)$ in other directions. This enhancement persists down to $\sim 0.2H_{c2}$. This is the reason why the dHvA effect is observed even at low fields of $0.2H_{c2}$ as in YNi_2B_2C.

As mentioned in Sec. 1, the NMR and specific heat experiments predict the anisotropic energy gap with a nodal line in uranium-based heavy fermion superconductors such as URu_2Si_2 and UPd_2Al_3. They are unconventional superconductors. Figure 10 shows an energy gap with a nodal line of a so-called polar type. As mentioned above, S_F is the extremal area of cross-section of the Fermi surface by planes perpendicular to the field direction. If S_F corresponds to the maximum cross-section with the nodal line (polar type) shown in Fig. 10a and 10b, it is not easy to distinguish experimentally the nodal line in the anisotropic energy gap from the gapless state based on the pair-breaking by applying the magnetic fields. In this case, it is necessary to deviate S_F from the cross-section with the nodal line by tilting the field direction. It is thus a challenging study to detect the nodal line in the anisotropic energy gap for URu_2Si_2 and UPd_2Al_3 via the dHvA oscillation in the mixed state.

3. EXPERIMENTAL RESULTS AND DISCUSSION

3.1. $CeRu_2$

A single crystals of $CeRu_2$ with the cubic Laves-phase structure was grown by the Czochralski method in a tetra-arc furnace. Figure 11 shows the crystal structure of $CeRu_2$. An as-grown ingot of 3–4 mm in diameter and 60 mm in length was annealed at 700–800 °C under vacuum of 10^{-10} Torr by means of the electro-transport method. Figure 12 shows the temperature dependence of the electrical resistivity. The residual resistivity ρ_0 was estimated as 0.6 $\mu\Omega\cdot$cm by using a Fermi-liquid formula $\rho=\rho_0+AT^2$ and the residual

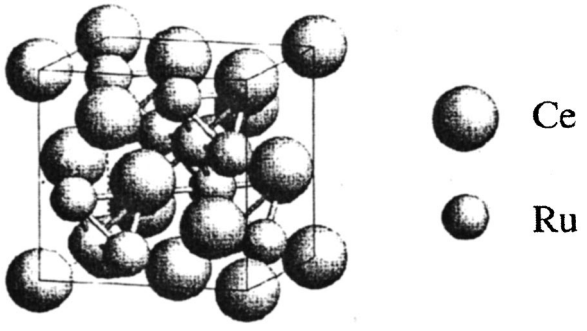

FIG. 11. Crystal structure of $CeRu_2$.

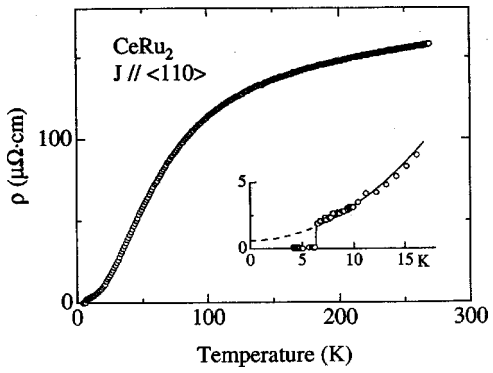

FIG. 12. Electrical resistivity of $CeRu_2$.

TABLE I. Superconducting properties of $CeRu_2$, URu_2Si_2 and UPd_2Al_3.

		T_c, K	H_{c2}, kOe	H_c, kOe	H_{c1}, kOe	ξ, Å	λ, Å	κ
$CeRu_2$		6.2	52.3	1.49	0.175	79.3	1980	25
URu_2Si_2	$H\|\|[100]$	1.3–1.5	130	0.8	0.033	64	4600	70
	$H\|\|[001]$		30					
UPd_2Al_3	$H\|\|[0001]$	2	37	0.49	0.1	85	4000	47
	$H\|\|[11\bar{2}0]$		32					

resistivity ratio ρ_{RT}/ρ_0 was 270, indicating a high-quality sample. Superconductivity occurred below $T_c = 6.4$ K.

$CeRu_2$ is a conventional type II-superconductor because the coherence peak at T_c is clearly observed in the NMR experiment,[34] and the spin-lattice relaxation rate in NMR and the specific heat follow an exponential law in the temperature dependence.[35] The superconducting properties are summarized in Table I. Values of the upper critical field at 0 K $H_{c2}(0)$, thermodynamic critical field $H_c(0)$ and lower critical field $H_{c1}(0)$ shown in Table I have been determined directly from the specific heat and magnetization experiments.[35] The other physical values are estimated from the conventional relations $H_{c2} = \Phi_0/2\pi\xi^2$, $\kappa = \lambda/\xi$ and $H_{c2} = \kappa\sqrt{2}H_c$.

Figure 13a shows the dHvA oscillation for the field along ⟨111⟩ at 0.47 K. The dHvA oscillation is observed in both the normal and superconducting mixed states; although it is not observed near H_{c2} of about 50 kOe because of the so-called peak effect.[36] The fast Fourier transform (FFT) spectra in Fig. 13b indicate that for two branches, denoted by $\varepsilon_{1,2,3}$ and δ_1, the detected dHvA frequencies are the same between the normal and mixed states. The similar dHvA oscillations are obtained for any field direction. For example, branch α is observed for the field along ⟨100⟩ in both the normal and mixed states.

Figure 14 shows the angular dependence of the dHvA frequency. The data denoted by large circles indicate clear and large signals, while those denoted by small circles do not indicate harmonics or sums and differences of the fundamental dHvA frequencies but signals of small amplitudes. Thin solid lines are guidelines, while thick solid lines show the corresponding result of band calculations. Figure 15 indicates the Fermi surfaces based on the relativistic linear augmented-plane-wave (RLAPW) calculations under the assumption that $4f$ electrons are itinerant. The dHvA data are in good agreement with the result of band calculations.

Next we have determined the cyclotron mass m_c^* from the temperature dependence of the dHvA amplitude, namely from a so-called mass plot. We show in Table II the dHvA

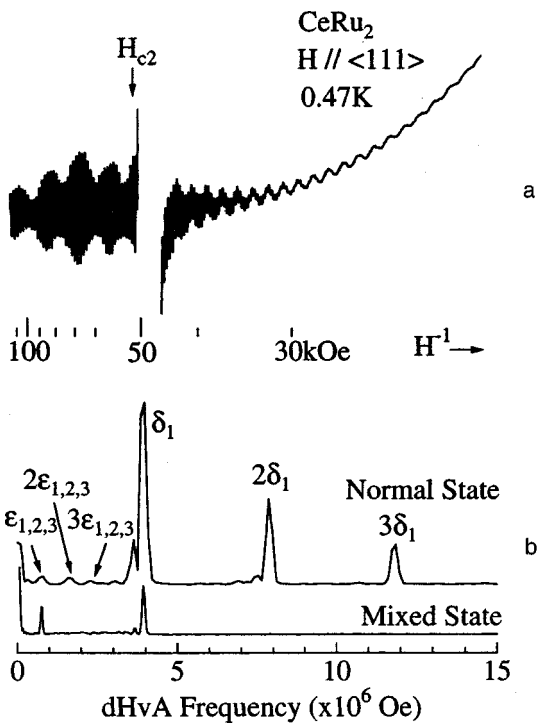

FIG. 13. Typical dHvA oscillation of $CeRu_2$ (a) and the corresponding FFT spectra in both the normal and superconducting mixed states (b)

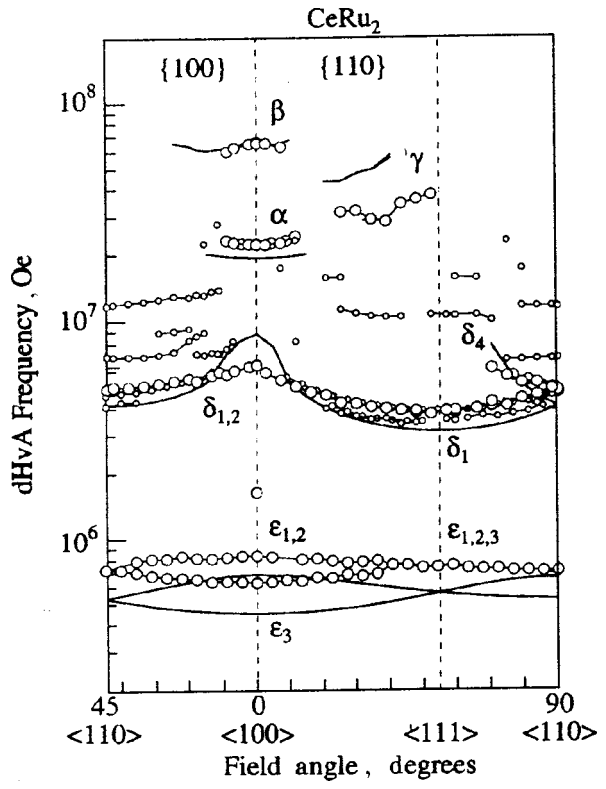

FIG. 14. Angular dependence of dHvA branches in $CeRu_2$. The data shown with large circles possess large magnitudes in FFT spectra, while those shown with small circles indicate small ones. Thin solid lines are guidelines, while thick solid lines are the result of band calculations.

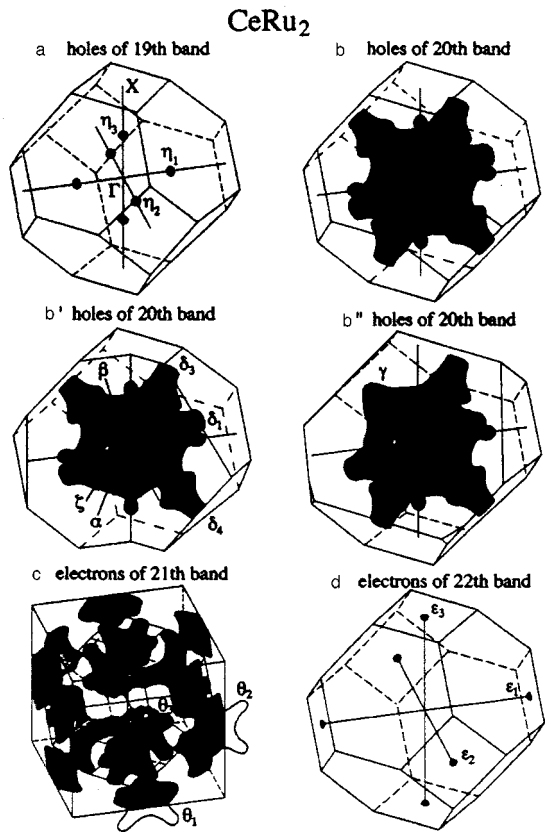

FIG. 15. Fermi surfaces of 19th band-hole, 20th band-hole, 21st band-electron and 22nd band-electron in $CeRu_2$.

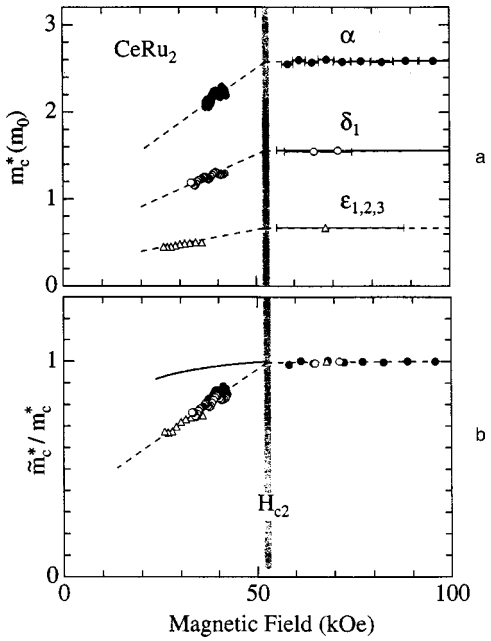

FIG. 16. Field dependence of the cyclotron mass for three branches: m_c^* (a) and $\tilde{m}_c^*/m_c^*$ (b) in $CeRu_2$.

frequency and the corresponding mass for the typical field directions in the normal state.

We have also determined the cyclotron mass by six cycles of the dHvA oscillation in the mixed state. The field dependence of the cyclotron mass for branches α, δ_1 and $\varepsilon_{1,2,3}$ is shown in Fig. 16a. The cyclotron mass gradually decreases below H_{c2}. It is interesting that the ratio of the cyclotron mass in the mixed state $\tilde{m}_c^*$ to that in the normal state m_c^* shows a similar field dependence in the mixed state for three branches, as shown in Fig. 16b. Here the solid line indicates the theoretical curve of Eq. (13), where $2\Delta(T=0)/k_BT_c=3.7$ and Fermi velocity $v_F=9.1\times10^6$ cm/s are used in calculations for the branch $\varepsilon_{1,2,3}$. The value of $2\Delta(T=0)/k_BT_c=3.7$ was obtained from the specific heat measurement for the same sample.[35] The theoretical curve is highly different from the experimental data.

A similar field dependence is also observed for the Dingle temperature T_D. T_D in the normal state has been determined from the field dependence of the dHvA amplitude at constant temperatures of 0.5 K and 30 mK, namely, from a so-called Dingle plot. Figure 17a shows the field dependence of the Dingle temperature for three branches. The difference $\Delta T_D=\tilde{T}_D-T_D$ between the Dingle temperature $\tilde{T}_D$ in the mixed state and the Dingle temperature T_D in the normal state is also shown in Fig. 17b. Here we note that the ''Dingle plot'' to determine T_D is not valid for the present dHvA oscillation in the mixed state because both m_c^* and T_D depend on the field in the mixed state. We have determined the Dingle temperature so as to fit the dHvA amplitude following the Lifshitz–Kosevich formula under the assumption that the cyclotron mass in the mixed state decreases linearly with decreasing the field as shown in Fig. 16a. As shown in

TABLE II. The de Haas–van Alphen frequency and the corresponding cyclotron mass for the typical field direction in $CeRu_2$. The angle of 42° means the field direction tilted by 42° from ⟨100⟩ to ⟨110⟩ in ⟨110⟩.

	Experimental					Theoretical		
	Branch	F, 10^6 Oe	m_c^*, m_0	T_D, K	l, Å	Band	F, 10^6 Oe	m_b, m_0
$H\|\|\langle100\rangle$	β	65.8	7.61			20	64.6	0.22
	α	22.6	2.64	0.57	2450	20	19.7	0.76
	$\delta_{1,2}$	6.38	4.39			20	6.38	1.97
	$\varepsilon_{1,2}$	0.84	0.71			22	0.69	0.31
	ε_3	0.63	0.55			22	0.46	0.20
⟨111⟩	δ_1	3.97	1.56	0.5	1980	20	3.16	0.50
	$\varepsilon_{1,2,3}$	0.75	0.61	0.45	2450	22	0.57	0.26
⟨110⟩	$\delta_{1,2}$	4.60	1.90			20	4.13	0.68
42°	γ	36.8	8.20			20	58.3	4.30

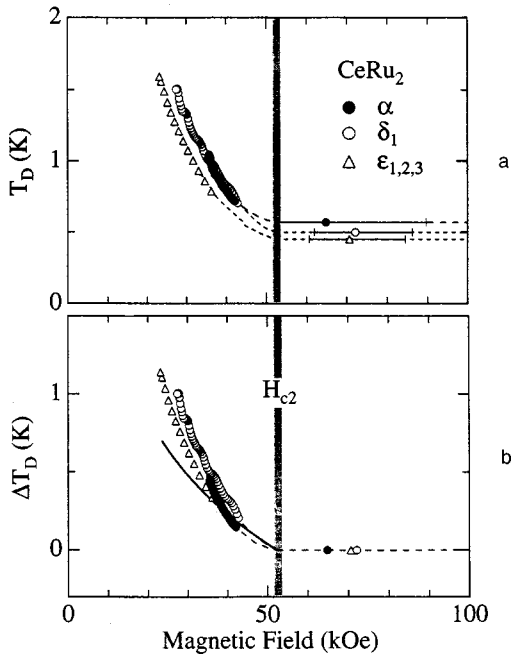

FIG. 17. Field dependence of the Dingle temperature for three branches: T_D (a) and ΔT_D (b) in $CeRu_2$.

Fig. 17b. ΔT_D increases with decreasing the field below H_{c2}.

We have measured the sample dependence of the Dingle temperature to study the additional damping term in the mixed state for branch $\varepsilon_{1,2,3}$, as shown in Fig. 18. Five samples of different quality were used in the experiments. The Dingle temperature in the mixed state $\tilde{T}_D$ depended on the magnetic field. A following simple relation holds between the Dingle temperature in the mixed state $\tilde{T}_D$ and that in the normal T_D; $\tilde{T}_D = T_D + \Delta T_D$, where ΔT_D is an additional Dingle temperature in the mixed state. That is, the value of ΔT_D shows approximately the similar field dependence for five samples. The solid lines in Figs. 17b and 18b represent the theoretical result of Eq. (7) for branch $\varepsilon_{1,2,3}$. The theoretical curve is approximately consistent with the experimental one.

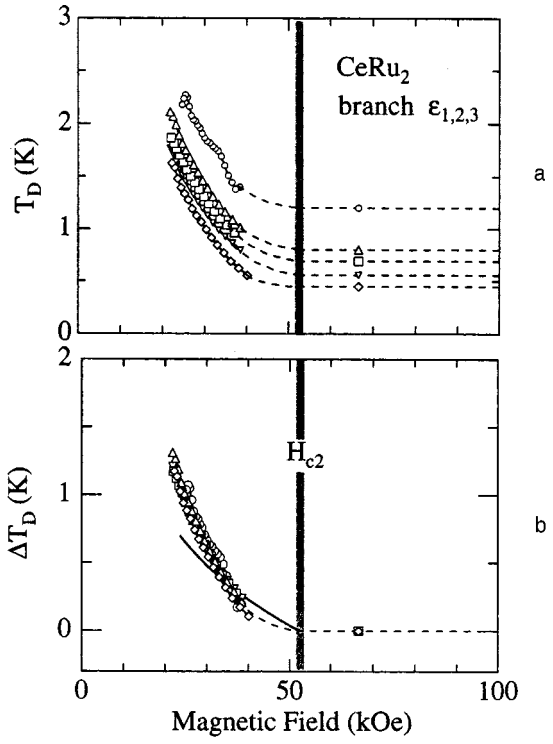

FIG. 18. Field dependence of the Dingle temperature for branch $\varepsilon_{1,2,3}$ in five different samples of $CeRu_2$; T_D (a) and ΔT_D (b).

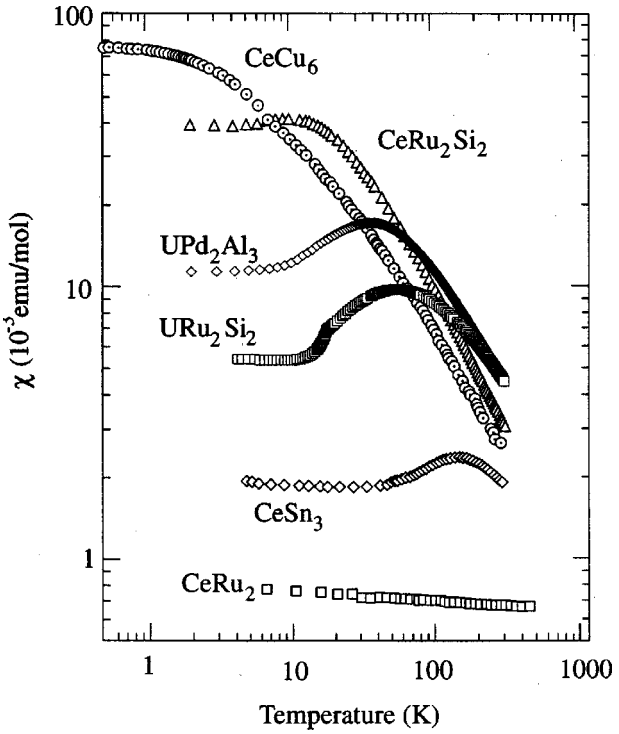

FIG. 19. Temperature dependence of the magnetic susceptibility for Ce and U compounds.

3.2. URu_2Si_2

Among the uranium intermetallic compounds, URu_2Si_2 and UPd_2Al_3 are fascinating magnetic superconductors. They are classified as the heavy fermion compounds. Quasiparticles with a heavy mass of $10-100\,m_0$ are of an *f*-electron character, condensing into Cooper pairs. Superconductivity is realized in the antiferromagnetic state. The ordered state in URu_2Si_2 is, however, anomalous because of an unusually small moment of $0.03\,\mu_B$/U.[37] On the other hand, UPd_2Al_3 has a relatively large moment of $0.85\,\mu_B$/U.[38]

In the Ce-based heavy fermion compound such as $CeRu_2Si_2$, the magnetic susceptibility χ increases with decreasing the temperature, following the Curie-Weiss law with the effective moment of Ce^{3+}, and possesses a maximum at a characteristic temperature $T_{\chi\,\max}$. The magnetic susceptibility becomes thus constant at lower temperatures, indicating enhanced Pauli paramagnetism, as shown in Fig. 19. This large susceptibility is correlated with the large mass. The temperature $T_{\chi\,\max}$ approximately corresponds to the Kondo temperature T_K.

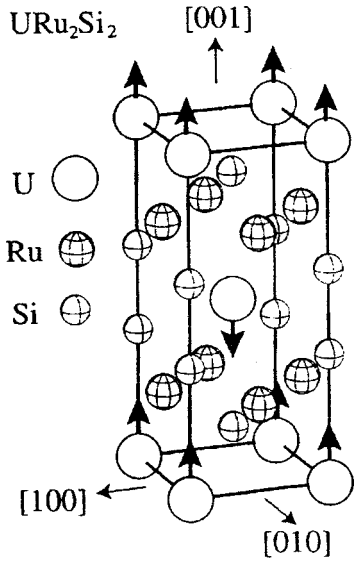

FIG. 20. Crystal structure of URu_2Si_2. Arrows show the directions of the antiferromagnetic moments.

A similar behavior is observed in URu_2Si_2 and UPd_2Al_3. The susceptibility for the field along [001] in URu_2Si_2 and for $[11\bar{2}0]$ in UPd_2Al_3 increases with decreasing the temperature, following the Curie–Weiss law, and has a maximum at $T_{\chi\,\max}\simeq 55$ K in URu_2Si_2 and 35 K in UPd_2Al_3. At lower temperatures both compounds order antiferromagnetically.

Figure 20 shows the tetragonal crystal structure of URu_2Si_2, where arrows indicate the directions of the antiferromagnetic moments. The phase diagrams is shown in Fig. 21. The metamagnetic transition occurs at about 400 kOe. This transition with three steps is sharp when observed below the Néel temperature $T_N=17.5$ K, and become broad above T_N, changing into one step in the metamagnetic transition. The transition field slightly increases with increasing the temperature.[39] A temperature dependence of the Néel temperature in the magnetic field is also shown by a dotted line in Fig. 21.[40] This phase boundary is not directly related

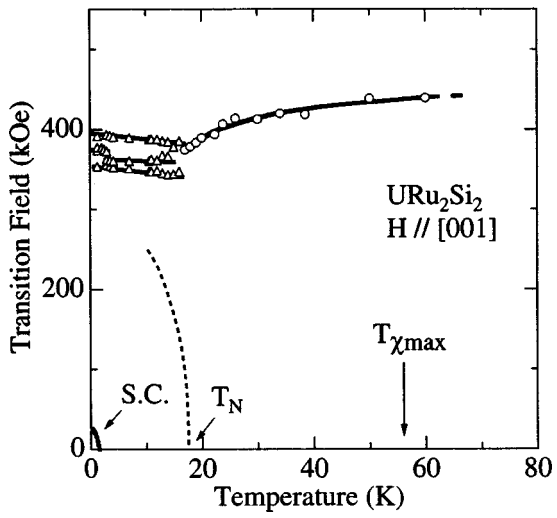

FIG. 21. Phase diagram of URu_2Si_2.

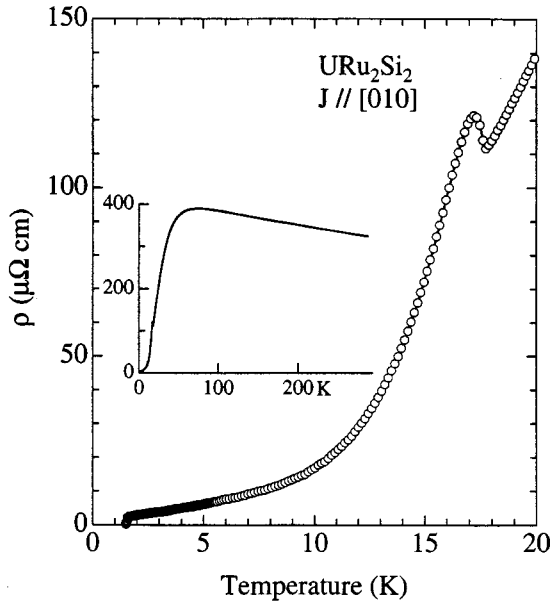

FIG. 22. Temperature dependence of the electrical resistivity in URu_2Si_2. The inset shows the overall behavior of the resistivity.

to the observed metamagnetic transition, although the metamagnetic transition itself is closely related to the antiferromagnetic ordering. In the phase diagram, S.C. denotes the superconducting state.

Transport, thermal and magnetic data indicate that this magnetic order below 17.5 K opens a gap on a large part of the Fermi surface. The corresponding electronic specific heat coefficient γ is changed from 110 to 64 mJ/(K$^2\cdot$mol) through this transition, indicating that about 40% of the Fermi surface is removed after this transition.[41] Superconductivity occurs below the critical temperature $T_c=1.4$ K in the antiferromagnetic state. $H_{c2}(0)$ at 0 K is highly anisotropic, being about 130 kOe for the field along [100] (*a*-axis) and about 30 kOe for [001] (*c*-axis).[42,43] Below T_c the specific heat and the spin-lattice relaxation rate follow T^2- and T^3-dependences, respectively.[43,44] These results claim a line node in the superconducting energy gap. Superconducting properties are summarized in Table I.[43,45]

A single crystal of URu_2Si_2 was grown by the Czochralski method in a tetra-arc furnace. The starting material of U was purified by the electro-transport method in high vacuum of 10^{-10} Torr. See the details in Ref. 46. An ingot of 3–4 mm in diameter and 80 mm in length was purified again by the electro-transport method in high vacuum of $1-10^{-11}$ Torr, for one week.

First we show in Fig. 22 the temperature dependence of the electrical resistivity in the current J along the [010] direction. The resistivity has a peak at about 17 K, which corresponds to the Néel temperature, and decreases steeply with decreasing the temperature. The overall behavior of the temperature dependence of the resistivity is shown in an inset of Fig. 22. The resistivity increases with decreasing the temperature and shows a characteristic peak around 70 K, similar as that in heavy fermion compounds $CeCu_2Si_2$ and $CeCu_6$.[47]

As shown in Fig. 22, the resistivity become zero below

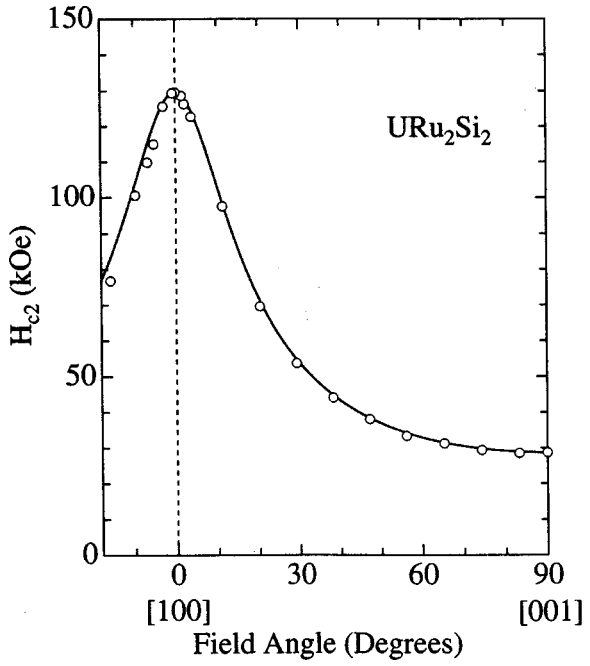

FIG. 23. Angular dependence of H_{c2} at 40 mK in URu_2Si_2.

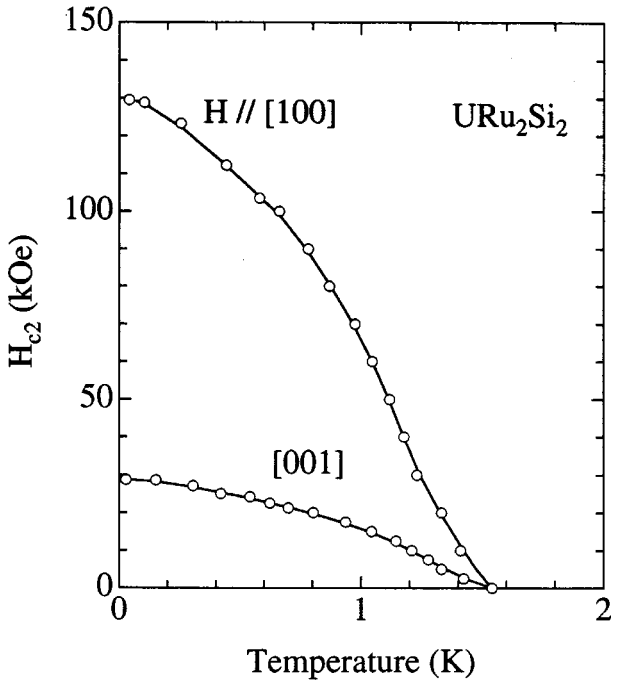

FIG. 24. Temperature dependence of H_{c2} for fields along [100] and [001] in URu_2Si_2.

1.5 K. The residual resistivity extrapolated to 0 K, ρ_0 and the residual resistivity ratio (RRR), ρ_{RT}/ρ_0 are 1.27 $\mu\Omega\cdot$cm and 255, respectively. This sample is, as far as we know, the best sample.

Next we have determined the upper critical field H_{c2} from the electrical resistivity data in the magnetic field. Figure 23 shows the angular dependence of the upper critical field at 40 mK. The solid line is a theoretical curve based on the formula:[43]

$$H_{c2}(\theta)=\frac{H_{c2}(H\|[100])}{(\cos^2\theta+\kappa^2\sin^2\theta)^{1/2}}, \tag{15}$$

where $H_{c2}(H\|[100])$ is 130 kOe and κ $[=H_{c2}(H\|[100])/H_{c2}(H\|[001])]=4.5$. H_{c2} is highly anisotropic, which is due to the paramagnetic effect, reflecting the anisotropic magnetic susceptibility. We also show in Fig. 24 the temperature dependence of H_{c2} for fields along [100] and [001]. These data are almost the same as the previous results.[43]

We show in Fig. 25 the typical dHvA oscillation in both the normal and mixed states and the corresponding FFT spectra for a tilt angle $\theta=8.1°$ in the field range from 40 to 150 kOe at 35 mK. The magnetic field direction was tilted by θ from [100] to [001]. One dHvA branch named α is clearly observed in both the normal and mixed states. In other directions, another branches named β and γ are detected in the normal state, although their amplitudes are small.

Figure 26 shows the angular dependence of the dHvA frequency F. Branch α is almost constant as a function of the field tilt angle θ, indicating that the Fermi surface is spherical. In the (001) plane, branch α is four-fold split. The reason of this splitting is not clear. The Fermi surface might be corrugated, possessing maxima and minima in cross-section.

Branches β and γ are not observed in the whole field angle. According to the previous report by Keller *et al.*,[48] similar branches have been observed. Branches β and γ were also observed by Keller *et al.* at some field angles in the (001) and (010) planes. From these dHvA and also the magnetoresistance results,[11] we conclude that three branches represent closed Fermi surfaces.

When we compare the dHvA result with the result of band calculations in an itinerant $5f$-band model shown in Fig. 27, branches α, β and γ might correspond to the band 17-hole, 19-electron centered at X and 20-electron Fermi surfaces, respectively, in magnitude, although γ is different from the theoretical one in the angular dependence. These Fermi surface are small in volume. Much larger Fermi sur-

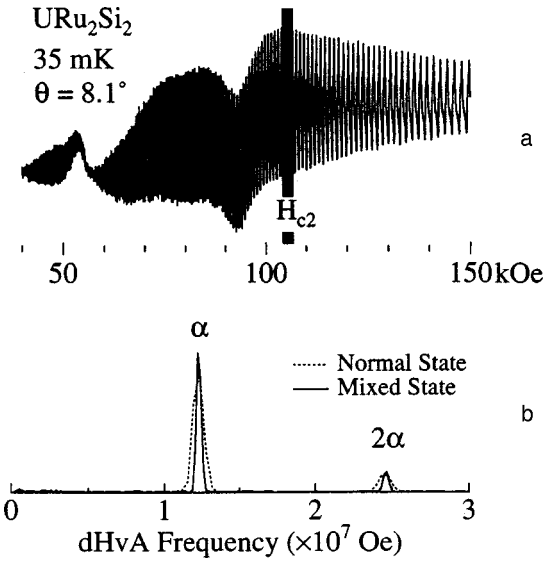

FIG. 25. DHvA oscillation and the corresponding FFT spectrum for a tilt angle $\theta=8.1°$ in URu_2Si_2.

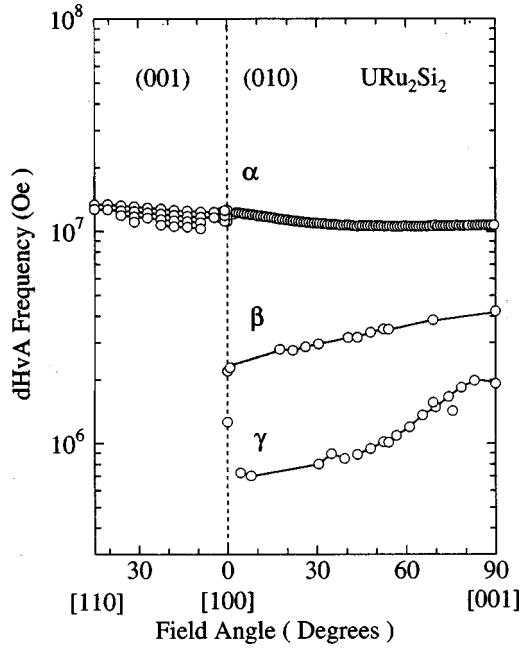

FIG. 26. Angular dependence of the dHvA frequency in URu_2Si_2.

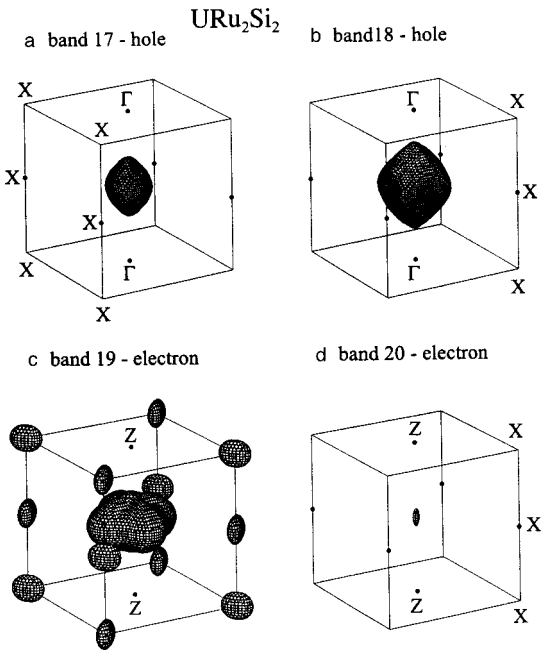

FIG. 27. Fermi surfaces for URu_2Si_2 in the paramagnetic state. The band 17-hole centered at the Z point (a), the band 18-hole at the Z point (b), the band 19-electrons at the Γ and X points (c) and the band 20-electron at the Γ point (d).

faces of bands 18-hole and 19-electron have not been observed experimentally. If we assume that these larger Fermi surfaces disappear completely below the ordering temperature, this change of the Fermi surface is inconsistent with the reduction of the electronic specific heat coefficient.[41] There should exist other remaining Fermi surfaces not observed in our experiment because URu_2Si_2 is a compensated metal with equal numbers of electrons and holes from the result of the magnetoresistance, and then the hole Fermi surface of branch α does not compensate with the electron Fermi surfaces of branches β and γ in volume.

Next, we have determined the cyclotron mass from the temperature dependence of the dHvA amplitude, and the Dingle temperature from the field dependence of the dHvA amplitude for the field along [001]. All branches are heavy. The cyclotron masses are $13\,m_0$ for branch α, $25\,m_0$ for β and $8.2\,m_0$ for γ. It is surprising that a small Fermi surface of branch β possesses such a large cyclotron mass. The Dingle temperature is small, 0.035 K for branch α, 0.045 K for β and 0.11 K for γ, indicating a high-quality sample. We have determined the mean free path l from the relation of $S_F=\pi k_F^2$, $\hbar k_F=m_c^* v_F$ and $l=v_F\tau$, where v_F is Fermi velocity and k_F is half of the caliper dimension of the Fermi surface. The l-value is large. 5500 Å for branch α, 1400 Å for β and 1200 Å for γ. These values are by one order larger than the coherence length ξ, indicating that superconductivity is close to the pure limit. These Fermi surface properties are summarized in Table III.

We show in Fig. 28a the typical dHvA oscillation for the field along [001]. H_{c2} is about 29 kOe. The dHvA oscillation named α is observed in the mixed state down to about 20 kOe. Figure 28b shows the field dependence of the cyclotron mass. We determined the mass from the temperature dependence of the dHvA amplitude over seven cycles of the oscillation. The cyclotron mass is constant above H_{c2}, but decreases gradually with decreasing the field below H_{c2}. The mass is not correctly determined in the field range from 25 to 28 kOe because this is a region of the so-called peak effect.

A similar field dependence is also observed for the Dingle temperature T_D, as shown in Fig. 28c. T_D was determined directly from the dHvA amplitude by using the mass in Fig. 28b. The Dingle temperature in the mixed state increases with decreasing field below H_{c2}. Solid lines in

TABLE III. The de Haas–van Alphen frequency F, the cyclotron effective mass m_c^*, the band mass m_b. the Dingle temperature T_D and the mean free path l in URu_2Si_2.

	Experimental					Theoretical	
$H\|\|[001]$	F, 10^6 Oe	m_c^*, m_0	T_D, K	l, Å		F, 10^6 Oe	m_b, m_0
α	10.5	13	0.035	5500	band 17 (Z)	18.5	1.62
					band 18 (Z)	36.8	2.72
					band 19 (Γ)	62.9	8.02
β	4.2	25	0.045	1400	band 19 (X)	4.6	3.20
γ	1.9	8.2	0.11	1200	band 20 (Γ)	0.3	0.25

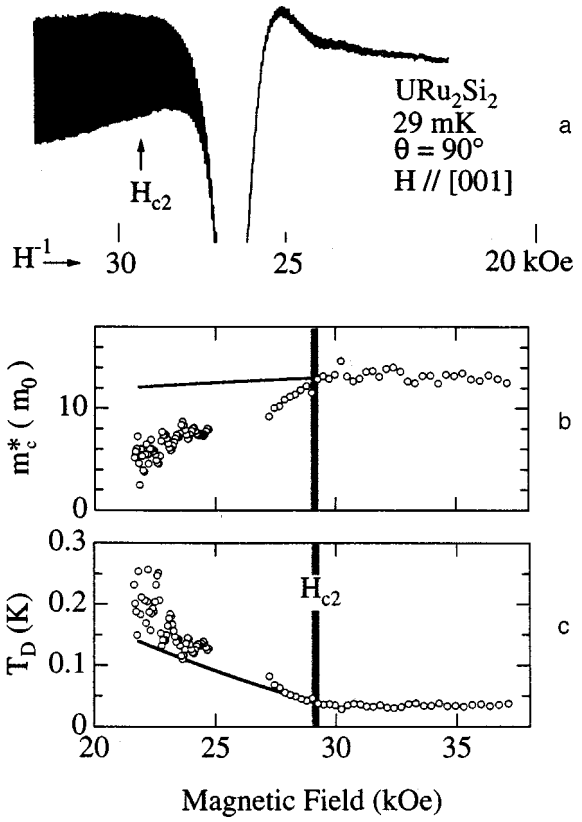

FIG. 28. DHvA oscillation at 29 mK for [001] (a), field dependences of the cyclotron mass (b) and the Dingle temperature (c) in URu_2Si_2.

Fig. 28b and 28c are theoretical curves of Eqs. (13) and (7) for branch α, where a BCS relation of $2\Delta/k_BT_c=3.54$ and $v_F=1.6\times10^6$ cm/s were used in calculations. The theoretical curve for T_D is approximately consistent with the experimental one, while the theoretical field dependence of the mass is highly different from the experimental one, as in $CeRu_2$.

An interesting point in URu_2Si_2 is an anisotropic energy gap because the existence of the line node is clear from the specific heat[43] and the nuclear spin-lattice relaxation rate[44] experiments. It was discussed theoretically that the superconducting gap disappears as a line node on the Fermi surface, for momenta perpendicular to the antiferromagnetic wave vector parallel to the [001] direction, as shown in Fig. 10a and 10b.[49] We have tried to determine the position of the line node on the Fermi surface via the dHvA experiment.

Figure 29 shows the dHvA oscillation for several field directions. The tilt angle θ is the field angle from [100] to [001], as defined above. No appreciable change of the dHvA oscillation has been found for any field, when the field is tilted from [001] to [100].

In Fig. 30 the angular dependences of the dHvA amplitudes in both the normal and mixed states are represented by circles and squares, respectively. Effective fields are 46.9 kOe in the normal state and 23.7 kOe ($\simeq0.8H_{c2}$) in the mixed state. The amplitude reduction for several field angles is due to the zero spin-splitting. This is reflected even in the mixed state. This result shows clearly that it is difficult to distinguish experimentally the nodal line in the anisotropic energy gap from the gapless state based on the pair-breaking

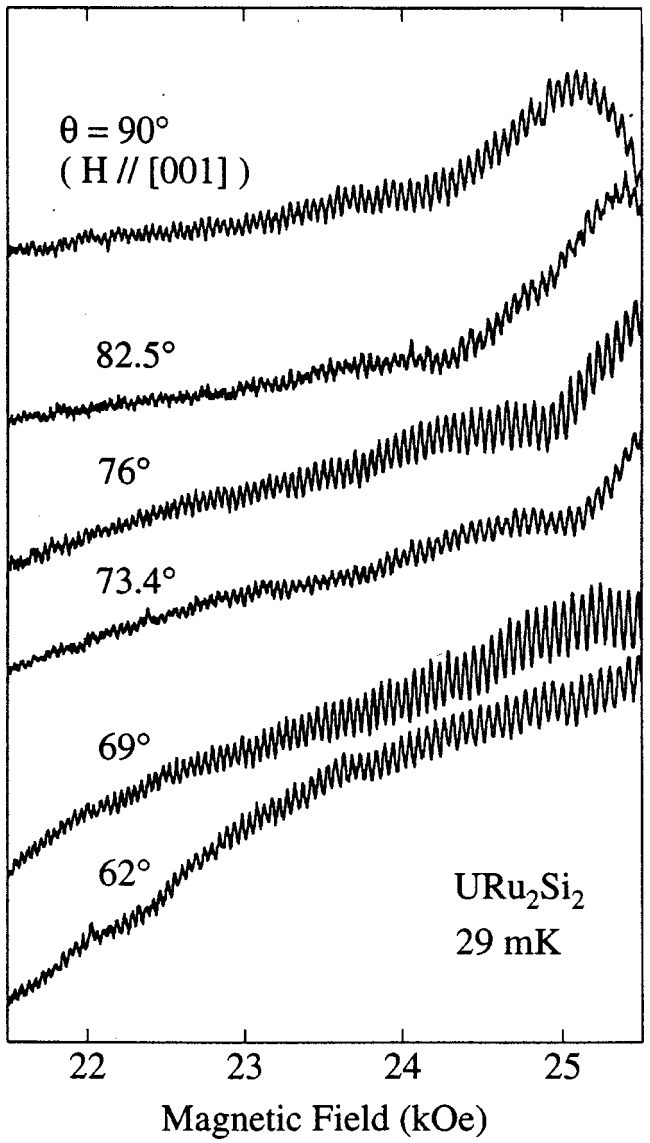

FIG. 29. DHvA oscillations for several tilt angles in the (010) plane for URu_2Si_2.

in the magnetic field. The former effect schematically shown in Fig. 10a and 10b is compared to the latter one in Fig. 8c. If the dHvA oscillation is found in the mixed state far below H_{c2}, the former should be distinguished from the latter.

The dHvA oscillation is observed in fields down to 30–40 kOe in the (001) plane. No appreciable change of the dHvA oscillation for any field direction in the (001) plane was found. This result also implies that a line node, as shown in Fig. 10c, does not exist and/or it is difficult to distinguish experimentally the line node with the gapless state, as in the (010) plane.

3.3. UPd_2Al_3

UPd_2Al_3 with the hexagonal structure is also a fascinating magnetic superconductor.[50] Superconductivity with the transition temperature $T_c\simeq2$ K is realized in the antiferromagnetic state with the Néel temperature $T_N=14$ K. Neutron scattering measurements revealed that the magnetic moments of $0.85\,\mu_B$/U are ferromagnetically oriented along the

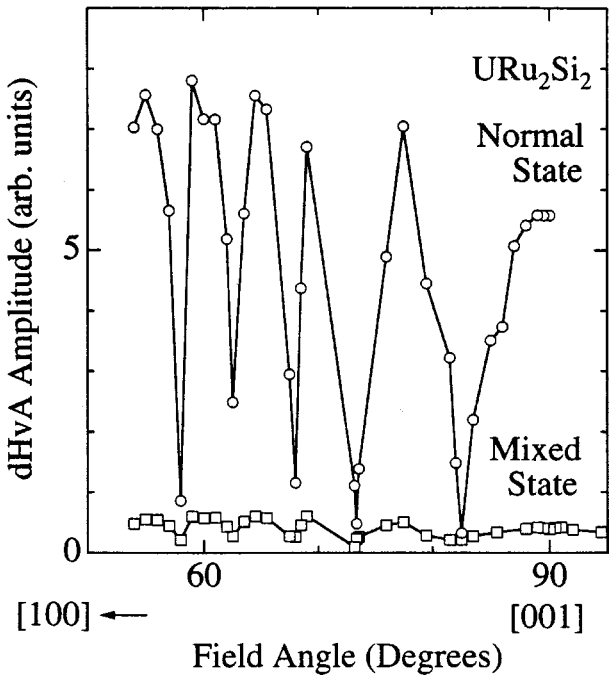

FIG. 30. Angular dependence of the dHvA amplitude in both the normal and mixed states for branch α in URu_2Si_2.

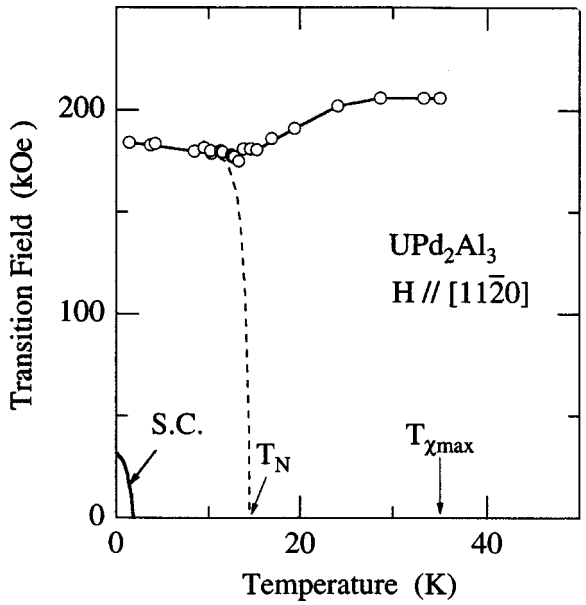

FIG. 32. Phase diagram of UPd_2Al_3.

$[11\bar{2}0]$ direction but are coupled antiferromagnetically along the [0001] direction with the wave vector $Q=(0,0,0.5)$,[38] as shown in Fig. 31. Superconducting properties are summarized in Table I.

The high-field magnetization indicates a sharp metamagnetic transition at about 180 kOe below $T_N=14$ K. It becomes, however, broad above T_N. This metamagnetic transition occurs for the field parallel to the basal plane, indicating a XY-type in character, which is compared to an Ising type along [001] in URu_2Si_2.

Figure 32 shows the phase diagram. The metamagnetic transition is found above T_N, up to the characteristic temperature, $T_{\chi\,\max}=35$ K. This means that this transition is not related to the antiferromagnetic ordering but to a change of the $5f$-electron character as in URu_2Si_2. We note that the ordered state, which is shown by a dotted line in Fig. 32, is closely related to the sharpness of the metamagnetic transition. In the phase diagram, S.C. denotes the superconducting state.

Figure 33 shows the temperature dependence of the elec-

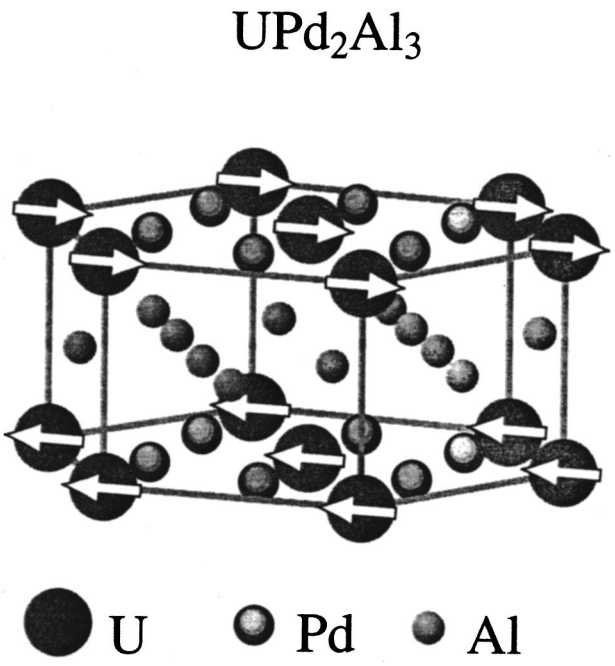

FIG. 31. Crystal structure of UPd_2Al_3. Arrows indicate the directions of the antiferromagnetic moments.

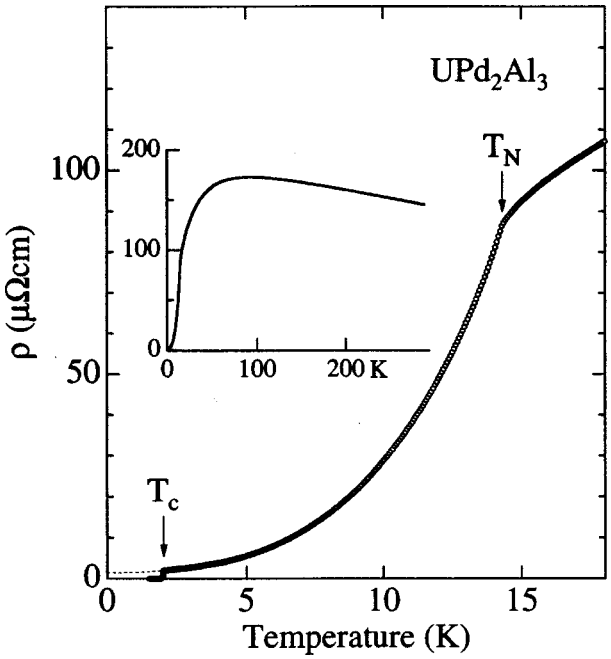

FIG. 33. Temperature dependence of the electrical resistivity of UPd_2Al_3. The inset shows the resistivity from room temperature to 1.5 K.

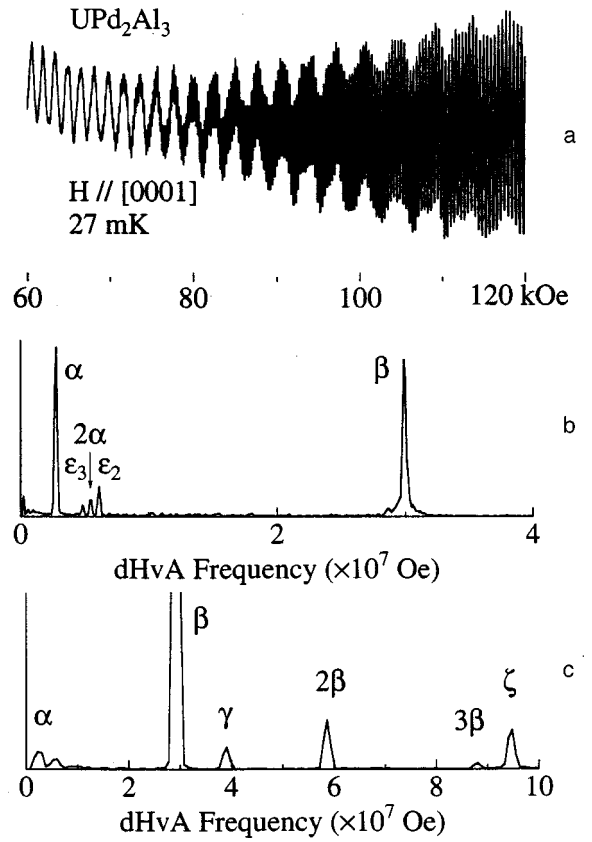

FIG. 34. DHvA oscillation and the corresponding FFT spectra for the field along [0001] in UPd_2Al_3.

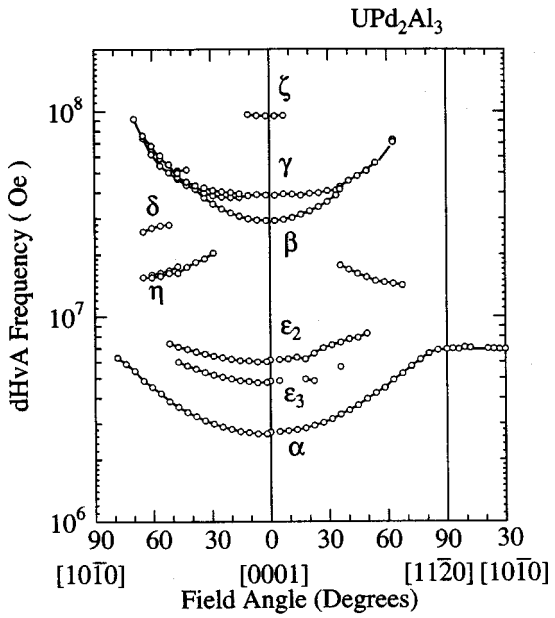

FIG. 35. Angular dependence of the dHvA frequency in UPd_2Al_3.

trical resistivity ρ. Overall features are the same as the previously reported ones.[50] As seen in an inset of Fig. 33, we observed a Kondo-like logarithmic-temperature dependence from room temperature to about 100 K, a sharp decrease below $T_N = 14$ K and finally a superconducting transition at $T_c = 1.9$ K. The residual resistivity extrapolated to 0 K, ρ_0, as shown by a dotted line in Fig. 33, and the residual resistivity ratio ρ_{RT}/ρ_0 are 1.40 $\mu\Omega\cdot$cm and 104, respectively. These are the best values as far as we know. The present single crystal was grown by the Czochralski method in a tetra-arc furnace, as described in Ref. 51 in detail.

Figure 34 shows the typical dHvA oscillation and the corresponding FFT spectrum for the magnetic field along the [0001] direction. Magnetic fields used in the FFT spectra are in the ranges from 60 to 120 kOe in Fig. 34b and from 138 to 169 kOe in Fig. 34c. Figure 35 shows the angular dependence of the dHvA frequency.

Almost all of the branches labeled α, β, γ, δ and ε_3 are the same as the previous dHvA results obtained by Inada *et al.*[52] According to the previous result of band calculations,[53,54] where $5f$ electrons were treated as itinerant electrons and brought about the antiferromagnetic moment of $0.85\,\mu_B$/U, branches ε_2, ε_3, δ and ζ are due to a band·69&70-hole Fermi surface called ''party hat,'' branches β and γ correspond to the maximum and minimum cross-sectional areas of a band 71&72-electron Fermi surface called ''column,'' branch α is due to an ellipsoidal band 71&72-electron Fermi surface called ''cigar'' and branch η is due to a band 73&74-electron Fermi surface named ''egg,'' as shown in Fig. 36. In the hexagonal symmetry, branches ε_2 and ε_3 have the same cross-section, but they have different cross-sections, reflecting the magnetic moment oriented along $[11\bar{2}0]$.[53,54]

We have determined the values of the cyclotron mass and the Dingle temperature, as shown in Table IV. These values are almost the same as the previous results.[52] We note that branch ζ has a large mass of $65\,m_0$. This is the largest mass in UPd_2Al_3. The masses in the range from 6 to $65\,m_0$ in Table IV are consistent with a large γ-value of 145 mJ/(K$^2\cdot$mol).[50] T_D of 0.20 K is small, reflecting a high-quality sample. Therefore, the mean free path is longer than 1000 Å.

As shown in Fig. 37a, the dHvA oscillation is clearly observed in both the normal and mixed states. The dHvA oscillation, which is observed up to the upper critical field $H_{c2}(=39$ kOe) with decreasing field, is due to branch α. This branch is still seen in the mixed state at fields down to about 25 kOe. The dHvA oscillation is not observed in the field range from 39 to 31 kOe, which is due to the peak effect, as discussed before.[51] The dHvA frequency of 2.64×10^6 Oe for branch α is the same between the normal and mixed states. We have determined the cyclotron mass m_c^* from the temperature dependence of the dHvA amplitude over six cycles of the dHvA oscillation. As shown in Fig. 37b, the mass decreases gradually with decreasing the field below H_{c2}. The cyclotron mass at 24 kOe ($=0.62\,H_{c2}$) is $3.8\,m_0$, which is compared to the mass of $5.6\,m_0$ in the normal state.

A similar field dependence is also observed for the Dingle temperature T_D, as shown in Fig. 37c. The Dingle temperature in the mixed state increases steeply with decreasing field below H_{c2}. The solid line in Fig 37c is a theoretical curve of Eq. (7) for branch α, where the BCS relation of $2\Delta\,k_BT_c = 3.54$ and Fermi velocity $v_F = 1.86$

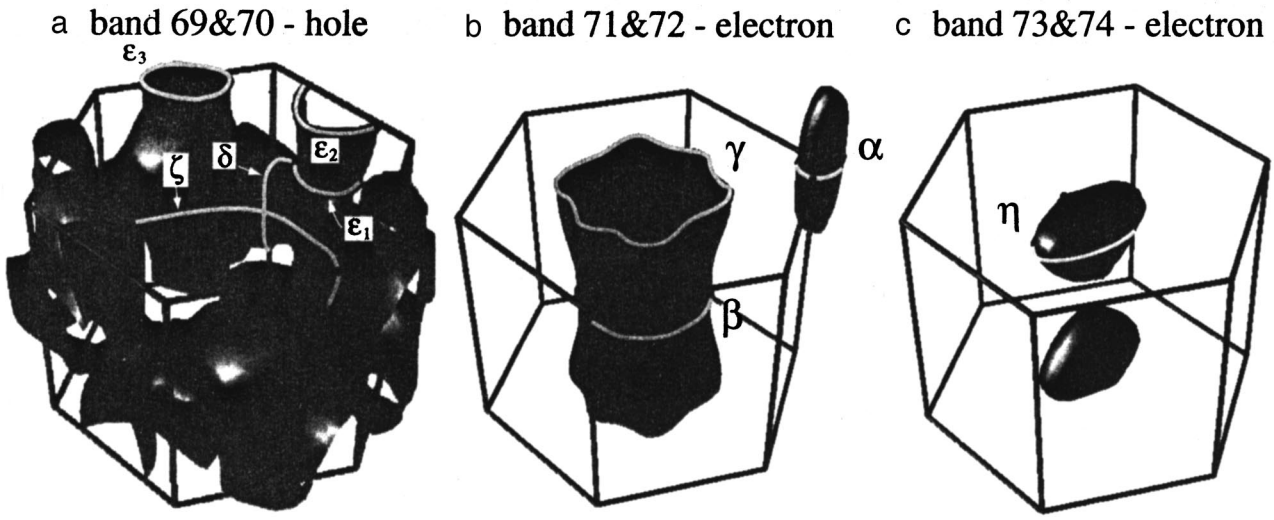

FIG. 36. Band 69&70-hole (a), band 71&72-electron (b) and band 73&74-electron Fermi surfaces (c) of UPd_2Al_3, cited from Ref. 54.

$\times 10^6$ cm s are used in calculations. The Dingle temperature in the mixed state in Fig. 37c is slightly smaller than the theoretical curve. On the other hand, the cyclotron mass is reduced compared to the theoretical one, as shown in Fig. 37b. The mass reduction was not found in other non-*f* compounds. It was found only for $CeRu_2$, URu_2Si_2 and now for UPd_2Al_3.

As mentioned above, S_F is the extremal cross-sectional area of the Fermi surface by planes perpendicular to the field direction. If S_F corresponds to the maximum cross-section with the line node, it is not easy to distinguish the line node in the anisotropic energy gap from the gapless state in magnetic fields, as in URu_2Si_2. We have also studied the angular dependence of the dHvA oscillation, as shown in Fig. 38. Here, the field angle θ is a tilt angle from [0001] to $[10\bar{1}0]$. The angular dependence of the dHvA amplitude is also shown in both the normal and mixed states. The dHvA amplitudes were obtained from the FFT spectra in the field range from 55.5 to 62.5 kOe in the normal state and from 25.0 to 26.5 kOe in the mixed state. The Fermi surface of branch α is approximately of an ellipsoid of revolution, as shown in Fig. 36, following $S_F(\theta)=6.94\times 10^6/(\sin^2\theta+(2.6)^2\cos^2\theta)^{t/2}$ Oe. The cyclotron mass in the normal state also shows the same angular dependence; $m_c^*(\theta)=14.3/(\sin^2\theta+(2.6)^2\cos^2\theta)^{1/2}m_0$.

On the other hand, the Dingle temperature in the normal state is nearly angle-independent up to $\theta=30°$; $T_D=0.21$ K. By using these data, we can calculate the dHvA amplitude at 25.7 kOe ($\simeq 0.65\,H_{c2}$) which is an effective field in the field range from 25.0 to 26.5 kOe. Thus, the dotted line in Fig. 38 is the curve obtained at 25.7 kOe under the assumption that values of the cyclotron mass and the Dingle temperature in the normal state are unchanged in the mixed state. The dHvA amplitude data at 25.7 kOe, shown by squares in Fig. 38, are reduced roughly by one half, compared to the dotted line. If we fit the result calculated for $\theta=0°$ ($H\|[0001]$) to the dHvA amplitude for $\theta=0°$ in the mixed state, the dotted line is changed into a thick solid line. This solid line is in good agreement with the dHvA data in the mixed state. This result implies that a line node in the anisotropic energy gap, shown in Fig. 10a and 10b, does not exist and/or it is difficult to distinguish experimentally the line node in the anisotropic energy gap from the gapless state based on pair-breaking by applying a magnetic field. If the dHvA oscillation is found in the mixed state far below H_{c2}, the line node should be distinguished from the gapless state in fields. That is, the dHvA data are expected to deviate from the thick solid line or to reduce steeply with increasing the tilt angle.

TABLE IV. The de Haas–van Alphen frequency F, the cyclotron effective mass m_c^*, the Dingle temperature T_D and the mean free path l in UPd_2Al_3. The theoretical frequency in the paramagnetic state is cited from Ref. 53.

	Experimental				Theoretical	
$H\|[0001]$	F, 10^7 Oe	m_c^*, m_0	T_D, K	l Å		F, 10^7 Oe
ζ	9.45	65	0.10	1190	band 69 & 70 (Γ)	8.87
γ	4.06	33	0.28	540	band 71 & 72 (A)	3.82
β	3.06	19	0.15	1550	band 71 & 72 (Γ)	3.07
ε_2	0.61				band 69 & 70 (L)	1.50
ε_3	0.48					
α	0.26	5.7	0.20	1200	band 71 & 72 (H)	0.30

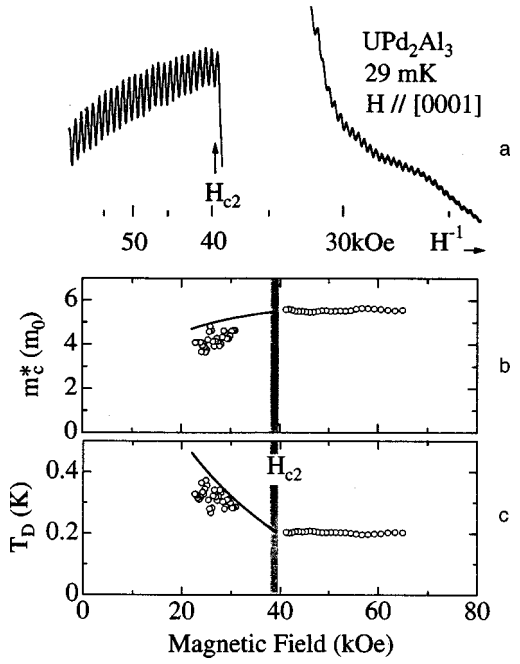

FIG. 37. DHvA oscillation at 29 mK for [0001] (a), field dependences of the cyclotron mass (b) and the Dingle temperature (c) in UPd_2Al_3.

4. CONCLUDING REMARKS

We have succeeded in growing high-quality single crystals of $NbSe_2$, $CeRu_2$, URu_2Si_2 and UPd_2Al_3 and observed the dHvA oscillation in both the normal and superconducting mixed states. Our experimental results can be summarized as follows:

1) The dHvA oscillation, which is observed near H_{c2} in the normal state, is also observed in the mixed state.

2) The dHvA frequency in the normal state remains unchanged in the mixed state.

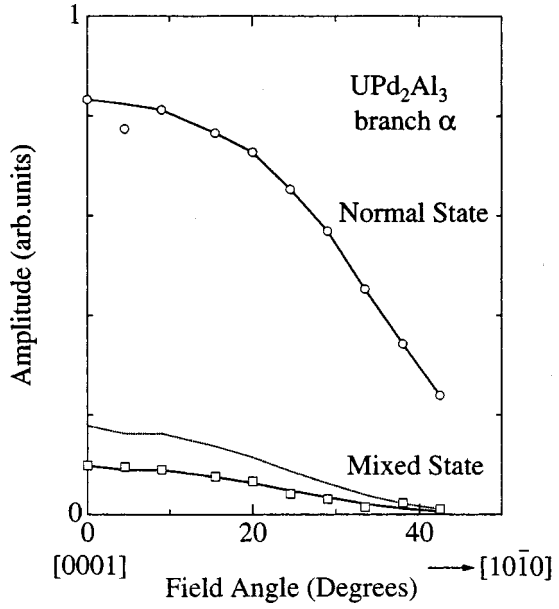

FIG. 38. Angular dependence of the dHvA amplitude in UPd_2Al_3.

3) The cyclotron mass in the mixed state decreases in magnitude with decreasing the field. This is found only in the f electron system, not observed in $NbSe_2$ and the other non-f electron superconductors. This can not be explained by Maki's theory based on the density of states in magnetic fields after Brandt *et al.*

4) The corresponding Dingle temperature is enhanced with increasing the field below H_{c2}. This is approximately explained by the Maki's theory.

5) We searched for the anisotropic energy gap from the angular dependence of the dHvA oscillation in the mixed state. From the present result, it was difficult to distinguish the line node in the anisotropic gap from the gapless state based on the pair-breaking in magnetic fields.

We suppose that the origin of the mass reduction below H_{c2} is related to the correlation effect between the quasiparticles.[55] In heavy fermion compounds, the magnetic part of the specific heat is changed into the electronic specific heat at low temperatures. For example, the $4f$-levels of the Ce ion are generally split into three doublets at high temperatures because the $4f$-electrons in the Ce compounds are almost localized in nature, following the Curie–Weiss law. At low temperatures, the magnetic entropy of the ground-state doublet in the $4f$-levels or the magnetic specific heat C_m is changed into the electronic specific heat γT via the many-body Kondo effect as follows:

$$R \ln 2 = \int_0^{T_K} \frac{C_m}{T} dT, \tag{16}$$

$$C_m = \gamma T. \tag{17}$$

The γ-value can be obtained as

$$\gamma = \frac{R \ln 2}{T_K} \simeq \frac{10^4}{T_K} mJ/(K^2 \cdot \mathrm{mol}). \tag{18}$$

In fact, the γ-value in $CeCu_6$ is 1600 mJ/(K^2·mol) for $T_K = 5$ K.[47,56]

The magnetic susceptibility in URu_2Si_2 and UPd_2Al_3 increases with decreasing the temperature, following the Curie-Weiss law, and has a maximum at the characteristic temperature $T_{\chi\,\max}$. $T_{\chi\,\max}$ for URu_2Si_2 and UPd_2Al_3 approximately corresponds to the Kondo temperature T_K for $CeRu_2Si_2$ and $CeCu_6$ where almost localized $4f$-electrons become itinerant below T_K, forming the heavy fermion state with an extremely large γ-value.

All energy bands in $CeRu_2$, URu_2Si_2 and UPd_2Al_3 contain the f-electron component and have flat dispersion, bringing about relatively large band masses. Nevertheless, the cyclotron effective masses are considerably larger than the corresponding band masses, as shown in Tables II–IV. The mass enhancement is not included in the conventional band calculations. It is caused by spin fluctuations, where the freedom of the charge transfer of the f-electrons appears in the form of the f-itinerant band, but the freedom of spin fluctuations of the same f-electrons reveals an unusual magnetic ordering, especially in URu_2Si_2 and enhances the effective mass as in the many-body effect for $CeCu_6$ and $CeRu_2Si_2$. In the mixed state, the number of quasiparticles, which are produced on the basis of the pair-breaking in the magnetic

fields, decreases with decreasing the field below H_{c2}. This might influence the correlation effect between the quasiparticles, most likely bringing about the mass reduction below H_{c2}.

We are very grateful to K. Maki, S. Koh, K. Mivake and J. Kübler for a helpful discussion and to M. Hedo, H. Ohkuni, K. Sugiyama, R. Settai, T. Honma, Y. Haga, E. Yamamoto, M. Higuchi, H. Yamagami, S. Takahashi, T. Yanagisawa and A. Hasegawa for collaborated studies. This work was supported by the Grant-in-Aid for COE Research (10CE2004) of the Ministry of Education, Science, Sports and Culture.

*E-mail: inaka@phys.sci.osaca-u.ac.jp
**E-mail: onuki@phys.sci.osaca-u.ac.jp

[1] Y. Ōnuki and A. Hasegawa, Handbook on the Physics and Chemistry of Rare Earths, Vol. 20, K. A. Gschneidner, Jr. and L. Eyring (Eds.), Elsevier, Amsterdam (1995). p. 1.
[2] H. Aoki, S. Uji, A. K. Albessard, and Y. Ōnuki, Phys. Rev. Lett. **71**, 2110 (1993).
[3] L. Taillefer and G. G. Lonzarich, Phys. Rev. Lett. **60**, 1570 (1988).
[4] N. Kimura, T. Komatsubara, D. Aoki, Y. Onuki, Y. Haga, E. Yamamoto, H. Aoki, and H. Harima, J. Phys. Soc. Jpn. **67**, 2185 (1998).
[5] J. E. Graebner and M. Robbins, Phys. Rev. Lett. **36**, 422 (1976).
[6] Y. Onuki, I. Umehara, T. Ebihara, N. Nagai, and K. Takita, J. Phys. Soc. Jpn. **61**, 692 (1992).
[7] Y. Onuki, I. Umehara, T. Ebihara, A. K. Albessard, K. Satoh, K. Takita, H. Aoki, S. Uji, and T. Shimizu, Physica B **186–188**, 1050 (1993).
[8] R. Corcoran, N. Harrison, C. J. Haworth, S. M. Havden, P. Meeson, M. Springford, and P. J. van der Wel, Physica B **206–207**, 534 (1995).
[9] M. Hedo, Y. Inada, T. Ishida, E. Yamamoto, Y. Haga, Y. Onuki, M. Higuchi, and A. Hasegawa, J. Phys. Soc. Jpn. **64**, 4535 (1995).
[10] M. Hedo, Y. Inada, K. Sakurai, E. Yamamoto, Y. Haga, Y. Onuki, S. Takahashi, M. Higuchi, T. Maehira, and A. Hasegawa, Philos. Mag. A **B77**, 975 (1998).
[11] H. Ohkuni, T. Ishida, Y. Inada, Y. Haga, E. Yamamoto, Y. Ōnuki, and S. Takahashi, J. Phys. Soc. Jpn. **66**, 48 (1997).
[12] Y. Haga, Y. Inada, K. Sakurai, Y. Tokiwa, E. Yamamoto, T. Honma, and Y. Onuki, J. Phys. Soc. Jpn. **68**, 339 (1999).
[13] T. J. B. M. Janssen, C. Haworth, S. M. Havden, P. Meeson, M. Springford, and A. Wasserman, Phys. Rev. B **57**, 11698 (1998).
[14] T. Terashima, H. Takeya, S. Uji, K. Kadowaki, and H. Aoki, Solid State Commun. **96**, 459 (1995).
[15] M. Heinecke and K. Winzer, Z. Phys. **B98**, 147 (1995).
[16] G. Goll, M. Heinecke, A. G. M. Jansen, W. Joss, L. Nguyen, E. Steep, K. Winzer, and P. Wyder, Phys. Rev. B **53**, 8871 (1996).
[17] C. Bergemann, S. R. Jullian, G. J. McMullan, B. K. Howard, G. G. Lonzarich, P. Lejay, J. P. Brison, and J. Flouquet, Physica B **230–232**, 348 (1997).
[18] M. Sigrist and K. Ueda, Rev. Mod. Phys. **63**, 239 (1991).
[19] N. Sato, N. Aso, G. H. Lander, B. Roessli, T. Komatsubara, and Y. Endoh, J. Phys. Soc. Jpn. **66**, 1884 (1997).
[20] N. Metoki, Y. Haga, Y. Koike, and Y. Ōnuki, Phys. Rev. Lett. **80**, 5417 (1998).
[21] M. Kyogaku, Y. Kitaoka, K. Asayama, C. Geibel, C. Schank, and F. Steglich, J. Phys. Soc. Jpn. **61**, 2660 (1992).
[22] K. Matsuda, Y. Kohori, and T. Kohara, Phys. Rev. B **55**, 15223 (1997).
[23] H. Tou, Y. Kitaoka, K. Asayama, N. Kimura, Y. Onuki, E. Yamamoto, and K. Maezawa, Phys. Rev. Lett. **77**, 1374 (1996); Phys. Rev. Lett. **80**, 3129 (1998).
[24] K. Tenya, M. Ikeda, T. Sakakibara, E. Yamamoto, K. Maczawa, N. Kimura, R. Settai, and Y. Onuki, Phys. Rev. Lett. **77**, 3193 (1996).
[25] K. Matsuda, Y. Kohon, and T. Kohara, J. Phys. Soc. Jpn. **65**, 679 (1996).
[26] K. Maki, Phys. Rev. B **44**, 2861 (1991).
[27] A. Wasserman and M. Springford, Physica B **194–196**, 1801 (1994).
[28] S. Dukan and Z. Tesanović, Phys. Rev. Lett. **74**, 2311 (1995).
[29] M. G. Vavilov and Y. P. Mineev, Zh. Eksp. Teor. Fiz. **112**, 1873 (1997) [JETP **85**, 1024 (1997)].
[30] L. P. Gor'kov and J. R. Schrieffer, Phys. Rev. Lett. **80**, 3360 (1998).
[31] M. Tinkham, *Introduction to Superconductivity*, McGraw-Hill, New York (1975), p. 111.
[32] G. D. Mahan, *Many-Particle Physics*, Plenum Press, New York (1981).
[33] U. Brandt, W. Pesch, and L. Tewordt, Z. Phys. **201**, 209 (1967).
[34] K. Ishida, H. Mukuda, Y. Kitaoka, K. Asayama, and Y. Ōnuki, Z. Naturforsch., A: Phys. Sci. **51a**, 793 (1996).
[35] M. Hedo, Y. Inada, E. Yamamoto, Y. Haga, Y. Ōnuki, Y. Aoki, T. D. Matsuda, H. Sato, and S. Takahashi, J. Phys. Soc. Jpn. **67**, 272 (1998).
[36] M. Hedo, Y. Kobayashi, Y. Inada, E. Yamamoto, Y. Haga, J. Suzuki, N. Metoki, Y. Onuki, H. Sugawara, H. Sato, K. Tenya, T. Tayama, H. Amitsuka, and T. Sakakibara, J. Phys. Soc. Jpn. **67**, 3561 (1998).
[37] C. Broholm, J. K. Kjems, W. L. Buyers, P. Matthews, T. T. M. Palstra, A. A. Menovsky, and J. A. Mydosh, Phys. Rev. Lett. **58**, 1467 (1987).
[38] A. Krimmel, P. Fischer, B. Roessli, H. Maletta, C. Geibel, C. Schank, A. Grauel, A. Loidl and F. Steglich, Z. Phys. B **86**, 161 (1992).
[39] K. Sugivama, M. Nakashima, H. Ohkuni, K. Oda, K. Kindo, N. K. Sato, N. Kimura, T. Komatsubara, E. Yamamoto, Y. Haga, T. Honma, R. Settai, and Y. Onuki, *Physics of Strongly Correlated Electron Systems*, T. Komatsubara, H. Fujii, Y. Onuki, and H. Shiba (Eds.), Jpn. J. Appl. Phys., Suppl. **11**, 18 (1999).
[40] S. A. Mentink, T. E. Mason, S. Süllow, G. J. Nieuwenhuys, A. A. Menovsky, and J. A. Mydosh, Phys. Rev. B **53**, R6014 (1996).
[41] M. B. Maple, J. W. Chen, Y. Dalichaouch, T. Kohara, C. Rossel, and M. S. Torikachvn, Phys. Rev. Lett. **56**, 185 (1986).
[42] W. K. Kwok, L. E. DeLong, G. W. Crabtree, and D. G. Hinks, Phys. Rev. B **41**, 11649 (1990).
[43] J. P. Brison, N. Keller, P. Lejay, A. Huxley, L. Schmidt, A. Buzdin, N. R. Bernhoeft, I. Mineev, A. N. Stepanov, J. Flouquet, D. Jaccard, S. R. Julian, and G. G. Lonzarich, Physica B **199–200**, 70 (1994).
[44] K. Matsuda, Y. Kohori, and T. Kohara, J. Phys. Soc. Jpn. **65**, 679 (1996).
[45] S. Wüchner, N. Keller, J. L. Tholence, and J. Floquet, Solid State Commun. **85**, 355 (1993).
[46] Y. Haga, T. Honma, E. Yamamoto, H. Ohkuni, Y. Ōnuki, M. Ito, and N. Kimura, Jpn. J. Appl. Phys., Part 1 **37**, 3604 (1998).
[47] Y. Onuki and T. Komatsubara, J. Magn. Magn. Mater. **63–64**, 281 (1987).
[48] N. Keller, S. A. J. Wiegers, J. A. A. J. Berenboom, A. de Visser, A. A. Menovsky, and J. J. M. Franse, J. Magn. Magn. Mater. **177–181**, 298 (1998).
[49] J. P. Brison, P. Lejay, A. Buzdin, and J. Flouquet, Physica C **229**, 79 (1994).
[50] C. Geibel, C. Schank, S. Thies, H. Kitazawa, C. D. Bredl, A. Böhm, M. Rau, A. Grauel, R. Caspary, R. Heltrich, U. Ahlheim, G. Weber, and F. Steglich, Z. Phys. B **84**, 1 (1991).
[51] Y. Haga, E. Yamamoto, Y. Inada, D. Aoki, K. Tenya, M. Ikeda, T. Sakakibara, and Y. Onuki, J. Phys. Soc. Jpn. **65**, 3646 (1996).
[52] Y. Inada, A. Ishiguro, J. Kimura, N. Sato, A. Sawada, T. Komatsubara, and H. Yamagami, Physica B **206–207**, 33 (1995).
[53] L. M. Sandratskii, J. Kübler, P. Zahn, and I. Mertig, Phys. Rev. B **50**, 15834 (1994).
[54] K. Knöpfle, A. Mavromaras, L. M. Sandratskii, and J. Kübler, J. Phys.: Condens. Matter **8**, 901 (1996).
[55] S. Koh, Phys. Rev. B **51**, 11669 (1995).
[56] K. Satoh, T. Fujita, Y. Maeno, Y. Onuki, and T. Komatsubara, J. Phys. Soc. Jpn. **58**, 1012 (1989).

This article was published in English in the original Russian journal. It was edited by R. T. Beyer.

QUANTUM LIQUIDS AND QUANTUM CRYSTALS

Growth and dissolution kinetics of ^{3}He inclusions in phase-separated ^{3}He–^{4}He solid mixtures

A. N. Gan'shin, V. N. Grigor'ev, V. A. Maĭdanov, N. F. Omelaenko, A. A. Penzev, E. Ya. Rudavskiĭ, A. S. Rybalko, and Yu. A. Tokar

*B. Verkin Institute for Low Temperature Physics and Engineering, National Academy of Sciences of the Ukraine, 310164 Kharkov, Ukraine**)

(Submitted March 1, 1999)
Fiz. Nizk. Temp. **25**, 796–814 (August–September 1999)

Comprehensive experimental results on growth, dissolution, and melting kinetics of solid inclusions of ^{3}He formed as a result of phase separation of solid mixtures of ^{3}He in ^{4}He are described. A new method developed for obtaining high- quality crystals by cycling the temperature of a solid mixture within the separation region makes it possible to obtain reproducible values of time constants for growth and dissolution of inclusions. Precise measurements of pressure in the crystal at constant volume are used for obtaining data on effective mass diffusion of ^{3}He atoms in the crystal. It is shown that quantum diffusion is strongly suppressed at low temperatures due to elastic fields induced near the boundaries of inclusions. Abnormally rapid transport of matter of the threshold type is observed during dissolution of inclusions. The observed effects can be explained qualitatively in the proposed model of multistage dissolution of ^{3}He inclusions. The data on the variation of pressure as a result of melting and crystallization of ^{3}He inclusions are also obtained. It is proposed that a part of ^{3}He remains in the liquid phase after crystallization. © *1999 American Institute of Physics.*
[S1063-777X(99)00308-4]

1. INTRODUCTION

Solid ^{3}He–^{4}He mixtures are systems in which quantum effects are manifested in macroscopic properties. Such manifestations include isotopic phase separation of mixtures, which was observed for the first time by Edwards *et al.*[1] and was an important stage in the study of quantum crystals. Among other things, these investigations stimulated the development of the theory of quantum diffusion by Andreev and Lifshits.[2] In this phenomenon, peculiarities distinguishing quantum crystals from other solids are manifested most clearly. It was proved[2] that impurities and point defects in quantum crystals at low temperatures must be transformed into a sort of quasiparticles (impuritons and defectons) that can move almost freely over the entire volume in a certain energy band. The mobility of such quasiparticles is limited by their mutual collisions as well as by collisions with other quasiparticles or defects in the crystal. This leads to temperature and concentration dependences of the diffusion coefficients that are quite unusual for solids. The diffusion coefficient D in perfect crystals at comparatively high temperatures and low impurity concentrations, for which collisions of impurities with phonons are the main mechanism of scattering, increases with decreasing T according to the law $D \propto T^{-9}$. In the region of low temperatures and/or higher concentrations, the interaction between impurities becomes decisive, and the diffusion coefficients becomes independent of temperature and varies in inverse proportion to the concentration. Subsequent theoretical investigations confirmed the correctness of the basic concepts developed in the theory[2] and made it possible to derive analytic relations, while the NMR experiments made simultaneously on ^{3}He impurities in the hcp phase of ^{4}He revealed main regularities predicted by the theory and some peculiarities of spin diffusion in the bcc phase of ^{3}He–^{4}He mixtures (see, for example, Refs. 3 and 4).

Since the kinetics of phase transformations in solids are closely related to diffusion, it is natural to expect that an analysis of phase separation of solid mixtures of helium isotopes will provide additional information on diffusion effects in quantum crystals. Such expectations are justified the more so since diffusion processes occurring during phase separation have a number of peculiarities which are not observed in self-diffusion studied by the NMR method in solid helium.

(1) Since phase separation in ^{3}He–^{4}He mixtures occurs at low temperatures, we can disregard the interaction of ^{3}He with phonons even for very low concentrations and take into account only the interaction of impuritons with one another and with imperfections in the crystal.
(2) Diffusion takes place for finite concentration gradients, and leveling out of concentrations is described by the mutual diffusion coefficient to which collisions between impuritons contribute only due to probable U-processes.

 © 1999 American Institute of Physics

At the same time, the self-diffusion coefficient measured by the NMR method takes into account all types of collisions.

(3) The molar volume of the concentrated phase formed as a result of phase separation of dilute solutions of ^{3}He is much larger than that of the initial solution. This gives rise to inhomogeneities and stressed state of the crystal so that diffusion of impurities occurs in the field of elastic forces.

(4) Nonuniformity of potential also leads to a difference between energy levels of impuritons at adjacent crystal lattice sites; if such a mismatching in energy levels becomes comparable to the width of the energy band of an impuriton, this reduces significantly the tunneling probability, and hence the diffusion coefficient.

(5) In some cases, phase separation in the crystal can give rise to additional defects that can also affect diffusion processes significantly.

These peculiarities enrich considerably the pattern of mass transfer and render the study of phase separation kinetics very promising. On the other hand, however, the results of analysis of the phase-separation kinetics of ^{3}He–^{4}He mixtures could not be systematized in any way for a long time in view of the difficulties encountered in this case (see, for example, Refs. 5–7), and attempts to establish correlation with the data on quantum diffusion led to contradictory results. For example, Iwasa and Suzuki[5] concluded that mass transport during phase separation cannot be described by laws of quantum diffusion, while Shvarts *et al.*[8] observed a qualitative agreement between analogous results.

In such a situation, systematic analysis of the phase-separation kinetic for solid mixtures is required to clarify the influence of various factors on the type of mass transport. In the present paper, we describe the results of experiments made by the method of pressure measurements in the sample during cooling and heating in the region of two-phase state. Special attention is paid to comparison of the obtained parameters of mass transport with the results of quantum diffusion measurements. Preliminary results of these experiments were reported in Refs. 9–12.

Phase separation of an isotope mixture is a first-order phase transition in which first derivatives of thermodynamic potential such as volume or pressure are known to experience jumps. The excess volume V_E emerging during the formation of a mixture with concentration x for helium isotopes was determined by Mullin:[13]

$$V_E = 0.4x(1-x)[\mathrm{cm}^3/\mathrm{mole}]. \tag{1}$$

The correctness of this expression was confirmed in many experiments. If phase separation occurs at constant volume, the corresponding change in pressure

$$P_E = \frac{V_E}{V\beta}, \tag{2}$$

takes place, where V and β are the molar volume and compressibility of the mixture.

For low concentrations, the value of P_E is proportional to concentration to a fairly high degree of accuracy, and the measurement of pressure can be used for unambiguous determination of the change in concentration. Using the known value of β for pure ^{4}He to estimate the sensitivity of such a method, we obtain

$$|\Delta P| \approx 10^6 |\Delta x| [Pa]. \tag{3}$$

This relation shows that pressure measurements ensure sufficiently high sensitivity for concentration measurements during phase separation of helium isotopes. The high sensitivity of the method and available reliable pressure gauges for the milikelvin temperature range have determined the choice of experimental technique used by us here.

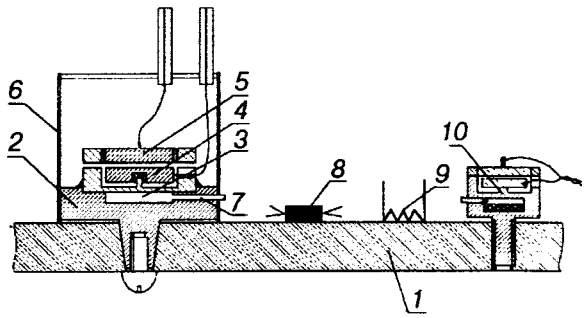

FIG. 1. Schematic diagram of measuring cell: copper plate of mixing chamber (*1*), casing (*2*), sample chamber (*3*), movable electrode of capacitive pressure gauge (*4*), fixed electrode (*5*), rf screen (*6*), filling capillary (*7*), resistance thermometer (*8*), heater (*9*), ^{3}He melting curve thermometer (*10*).

2. MEASURING CELL AND SAMPLES

The cell for experiments on the kinetics of phase transitions in solid mixtures of helium isotopes involving precise measurements of pressure at ultralow temperatures must ensure above all reliable cooling of the sample with a short thermal relaxation time (as compared to the characteristic time of the phase transition). Besides, the cell geometry must be chosen so that inhomogeneities appearing during sample crystallization are minimized. We must also ensure a high resolution of the detector of pressure variation in the crystal. Taking into account all these requirements, we developed the construction of the experimental cell which is shown schematically in Fig. 1. The cell is in fact a *Straty*-Adams capacitive gauge fixed directly to the plate of the dilution chamber with the help of a conic junction. The efficiency of such a junction was investigated earlier.[14] The diameter of the inner cavity in which solid helium samples were grown was 9 mm and its height 1.5 mm. The cell was not supplied with a heat exchanger made of fritted silver powder, since a low- porosity medium strongly changes the type of phase transitions in solid mixtures of helium as compared to open geometry (see, for example, Ref. 15).

According to calculations, the time of stabilization of thermal equilibrium associated with the thermal conductivity of the crystal was ~1 s for solid helium in such a geometry at $T = 100-200$ mK. The thermal relaxation time determined by the Kapitsa resistance between the helium crystal and the casing of the cell proved to be much longer. For the chosen

constructions of the cell, this time was estimated by us as 25–50 s in the entire temperature range in which measurements were made.

The kinetics of phase transition was studied on the basis of precise measurements of pressure in the sample, which was recorded with the help of a General Radio capacitive bridge 1615-A. The pressure resolution was higher than 8 Pa for all the samples. A crystallization thermometer was mounted on the plate of the dilution chamber close to the experimental cell (see Fig. 1). Using a digital (commercial) capacity gauge E7-8, we could obtain temperature resolution of 0.3 mK. The temperature was determined from the pressure corresponding to melting of ^{3}He using the polynomial proposed by Schuster *et al.*[16]. Several resistance thermometers calibrated with the help of the crystallization thermometer were also mounted on the plate of the dilution chamber. The resistance was recorded by using an ac bridge R 441 as well as a specially developed a.c. digital bridge with a power lower than 10^{-15} W liberated in a resistance thermometer.[17] Temperature was stabilized by a heater mounted on the dilution chamber plate having a feedback with the digital resistance gauge. All measurements of temperature and pressure in the sample were automatic.

We studied the mixtures obtained as a result of decomposition of the initial mixture with the ^{3}He concentration $x_0 \approx 2.05\%$ in the gaseous phase, and crystalline samples were grown using the capillary blocking technique. When solid samples of helium isotope mixtures were crystallized, the temperature was elevated, and the annealing of the crystals was carried out for two days at a temperature close to the melting point. The sample quality was controlled by the reproducibility of pressure after several cooling–heating cycles in the one-phase region.[18] We studied several different crystals in the pressure range 31.7–36 bar corresponding to molar volume 20.54–20.27 cm^3/mole. Measurements were made in the temperature range 40–700 mK.

3. EXPERIMENTAL TECHNIQUE

In our experiments, we mainly studied the kinetics of two processes:

(1) the growth of a new phase containing almost pure ^{3}He and formed as a result of phase separation of ^{3}He–^{4}He solid mixture upon cooling in the phase-separation region, and
(2) dissolution of formed solid inclusions of ^{3}He upon heating of the two-phase mixture.

In addition, we studied the kinetic of melting of ^{3}He solid inclusions for some crystals. It should be noted that, in the pressure range used by us here, the initial mixture and the dilute phase have hcp lattices, while the concentrated phase is characterized by a bcc lattice.

The growth of the new phase during phase separation of ^{3}He–^{4}He solid mixtures was studied during step-wise cooling of the samples as well as during single cooling from different temperatures to the same final temperature. Figure 2a gives the schematic diagram of experiments with a step-wise cooling of the samples. The change in temperature in one step was usually 10–15 mK. After each cooling, the sample temperature was stabilized with continuous recording of pressure. The next cooling was carried out after the two-phase crystal attained equilibrium, and so on.

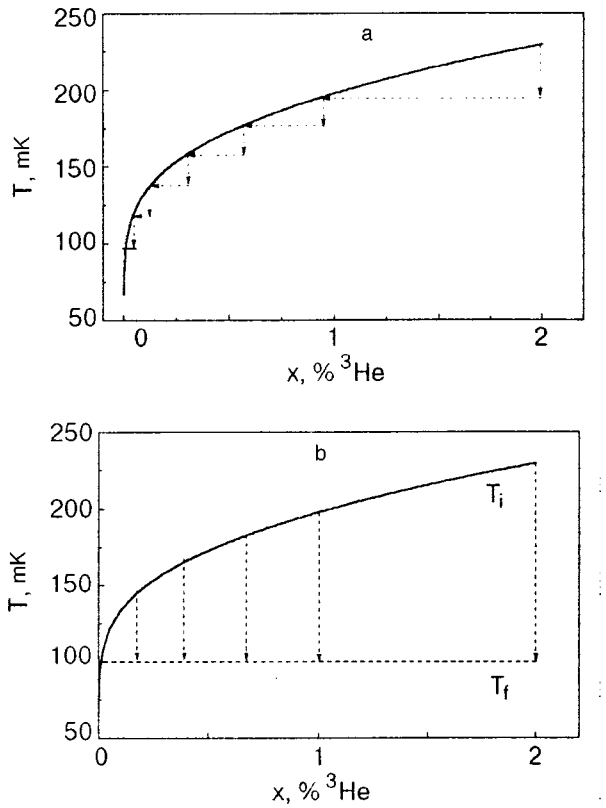

FIG. 2. Diagram illustrating the experiment on the growth of new phase inclusions: step—wise cooling (a) and single cooling (b). The solid curve corresponds to equilibrium phase separation.

The schematic diagram of experiments in which samples were cooled from different initial temperatures T_i to the same final temperature T_f is presented in Fig. 2b. The samples were cooled from the equilibrium state in different steps $\Delta T = T_i - T_f$. After the stabilization of T_f, the change in pressure reflecting the kinetics of the growth of the new phase was also recorded.

Figure 3 shows typical time dependences of pressure variation during cooling of a two-phase sample by different steps ΔT. Experiments proved that the decrease in temperature causes an increase in pressure in the crystal which is correctly described by the exponential dependence

$$P = P_f - (P_f - P_i)\exp(-t/\tau), \tag{4}$$

in the entire range of variation of ΔT from 5 to 130 mK, where τ is the characteristic time determining the kinetics of phase separation of ^{3}He–^{4}He solid mixtures after cooling by ΔT, P_i the initial pressure in the sample, and P_f the final equilibrium pressure for the given temperature.

Dissolution of solid ^{3}He inclusions in a two-phase crystal was also studied during step-wise heating of the samples as well as during rapid heating from the same initial temperature T_i to different final temperatures T_f. A schematic diagram of such experiments is shown in Figs. 4a and 4b. In

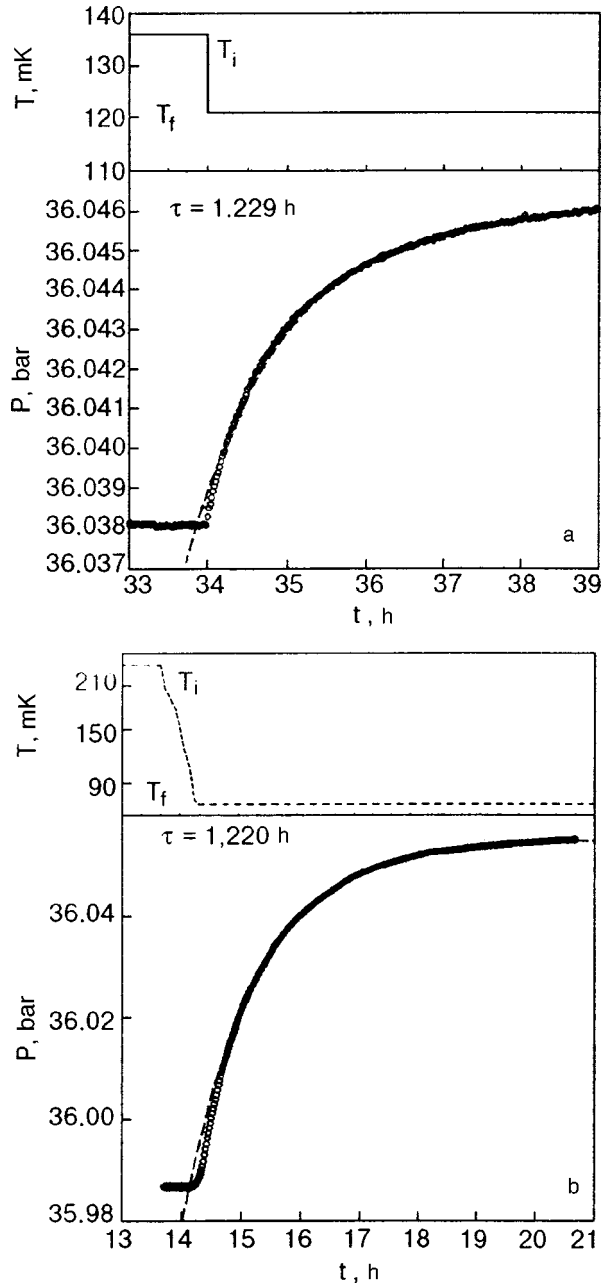

FIG. 3. Thermogram and corresponding kinetics of pressure variation during cooling of a two-phase crystal: $T_i = 136$ mK, $T_f = 121$ mK (a); $T_i = 230$ mK, $T_f = 103$ mK (b).

the case of step-wise heating [Fig. 4(a)], the samples were heated in a small step of 10–15 mK; then the temperature was stabilized, and the kinetics of pressure drop in the sample as a result of an increase in the ^{3}He concentration in the dilute phase with partially dissolved solid inclusions was studied. After the $P(t)$ dependence attained saturation (equilibrium pressure), the temperature was again elevated, and so on.

Figure 4b shows a schematic diagram of experiments with rapid heating of the samples from the same initial temperature to different final temperatures. The temperature increment $\Delta T = T_f - T_i$ varied in this case from 5 to 690 mK. After each heating and temperature stabilization, pressure relaxation in the sample was measured. Before the next measurement, the samples were cooled to the initial temperature, and the next temperature step was made. The heating time was ~1 s.

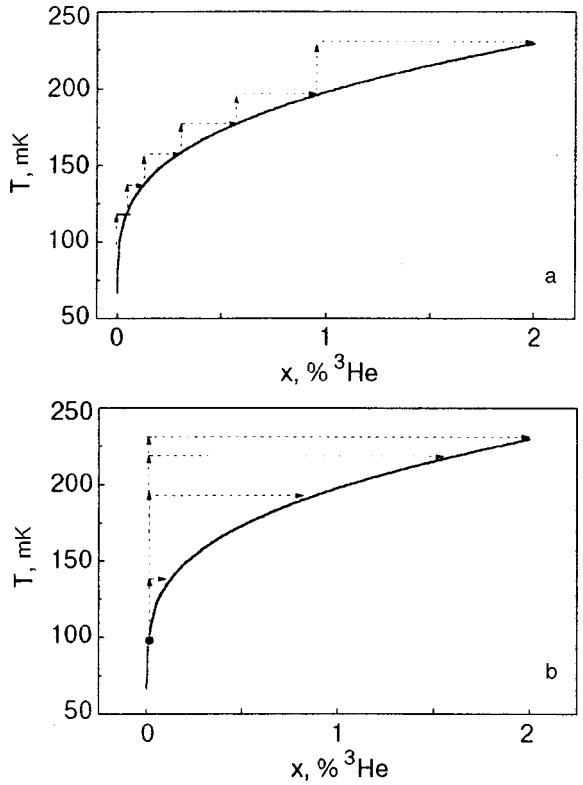

FIG. 4. Diagram illustrating the experiment on dissolution of new phase inclusions for a step-wise heating of a two-phase crystal (a) and rapid heating (b). The solid curve corresponds to equilibrium phase separation.

A typical $P(t)$ dependence for a step-wise heating is presented in Fig. 5 illustrating the variation of pressure as a result of slight heating of the sample. In this case, the pressure variation is also described correctly by the exponential dependence

$$P = P_f - (P_f - P_i)\exp(-t/\tau^*), \tag{5}$$

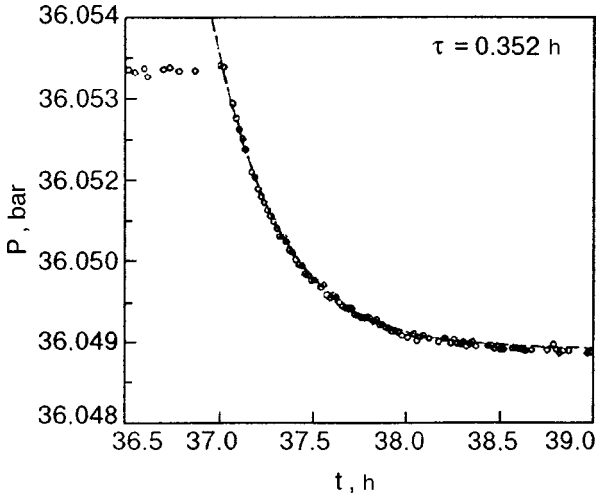

FIG. 5. Kinetics of decrease in pressure of a two-phase crystal during its slight heating ($T_i = 118$ mK, $T_f = 125$ mK). Dashed curve is the approximation by formula (5).

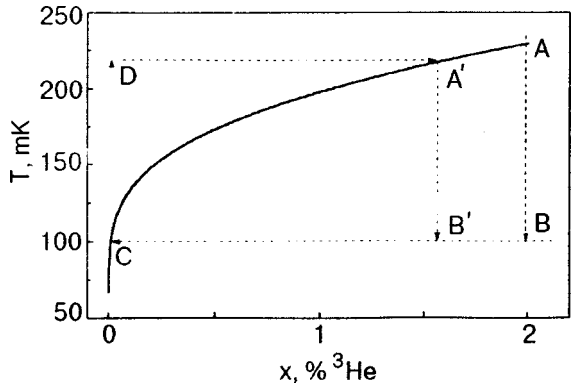

FIG. 6. Temperature cycling in samples under investigation.

where τ^* is the characteristic time determining the kinetics of dissolution of solid ^{3}He inclusions for small temperature increments, the remaining parameters being the same as in formula (4). As the value of the increment ΔT increases, the $P(t)$ dependence becomes more complicated and will be described in detail below.

4. TEMPERATURE CYCLING OF THE CRYSTALS UNDER INVESTIGATION

In order to obtain reproducible results, the samples were subjected to a special treatment before measurements, involving thermocycling at temperatures lower than the point of phase separation of ^{3}He–^{4}He solid mixtures with an initial concentration of 2%. Such a thermocycling is illustrated in Fig. 6. The solid curve corresponds to the low-temperature part of the phase diagram for separation of solid mixtures of helium isotopes. After annealing, the sample was cooled at a maximum rate ensured by the cooling capacity of the refrigerator to a temperature below the phase-separation point of the initial solution (normally to 100 mK). After sample cooling (*AB* line), the temperature was stabilized, and the solid mixture relaxed to its equilibrium state (*BC* line). This was accompanied by the formation and growth of solid ^{3}He inclusions, and concentration of ^{3}He in the matrix decreased. As the equilibrium state (*C*) was attained, the plate of the mixing chamber was heated rapidly (in 1–2 s) to a temperature close to the phase-separation point (*CD* line) and was stabilized at this temperature. Solid helium samples were heated in this case during a time of 25–50 s determined by the Kapitsa resistance. After heating the solid mixture tended to its equilibrium state (DA' line). Solid inclusions of ^{3}He were partially dissolved in this process, and the ^{3}He concentration in the matrix increased. When the equilibrium state (A') was reached, the pressure in the sample became constant, and the sample was cooled again to the same temperature ($A'B'$ line). Such a cycling of temperature ($A'B'CD$) was repeated 4–6 times for each sample. As a result of such a treatment of the samples, we obtained the following two important results.

(1) Growth and dissolution kinetics of inclusions became reproducible. The phase- separation time decreased and became constant for all the cycles starting from the third (Fig. 7). Temperature cycling also affects the dissolution kinetics of inclusions in the case of heating of a two-phase crystal.
(2) After the cooling–heating cycles were completed, the pressure in the crystal became lower than the initial pressure, indicating the improvement of the sample quality.[18] It should be noted that the decrease in pressure after the first cycle was larger than after subsequent cycles (Fig. 8). Such a process is apparently more effective for eliminating defects than traditional annealing which does not ''remove'' completely all defects in the crystal.

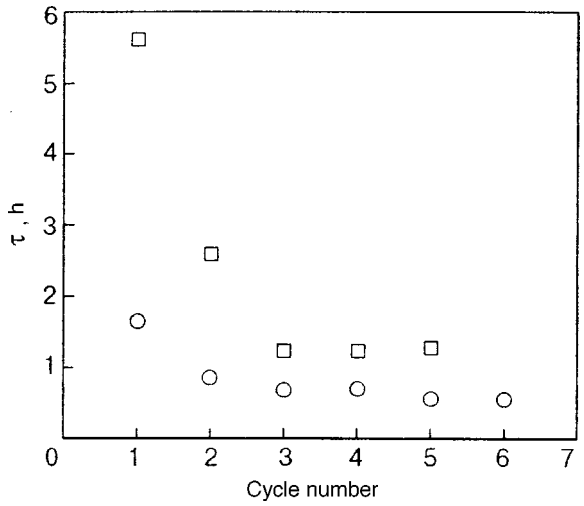

FIG. 7. Effect of temperature cycling in the range 103–230 mK on the time constant for growth of inclusions for samples with different molar volumes V, cm^3/mole: 20.27 (□) and 20.44 (○).

It should be noted that the total time of phase separation for ^{3}He–^{4}He solid mixtures is the sum of two time intervals: the time of formation of stable nuclei of the new phase and the time of growth of these nuclei due to the transport of ^{3}He atoms from the surrounding dilute mixture. Since heating to above the phase-separation temperature was not usually carried out in the experiments on growth kinetics, the number of nuclei remained unchanged; in the course of cooling or heating, the kinetics of growth or partial dissolution of a constant number of solid ^{3}He inclusions was studied, and the processes associated with nucleation were immaterial in most of

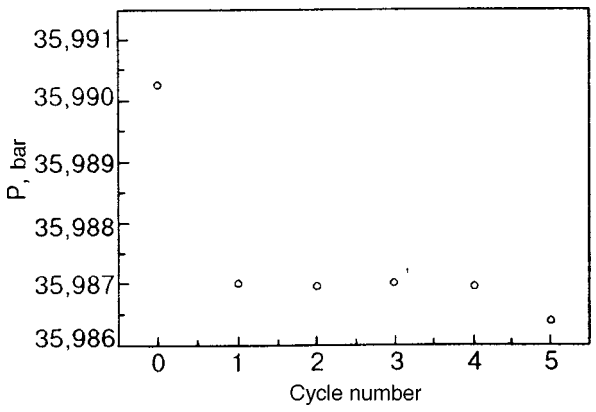

FIG. 8. Dependence of pressure after a cooling-heating cycle on the cycle number.

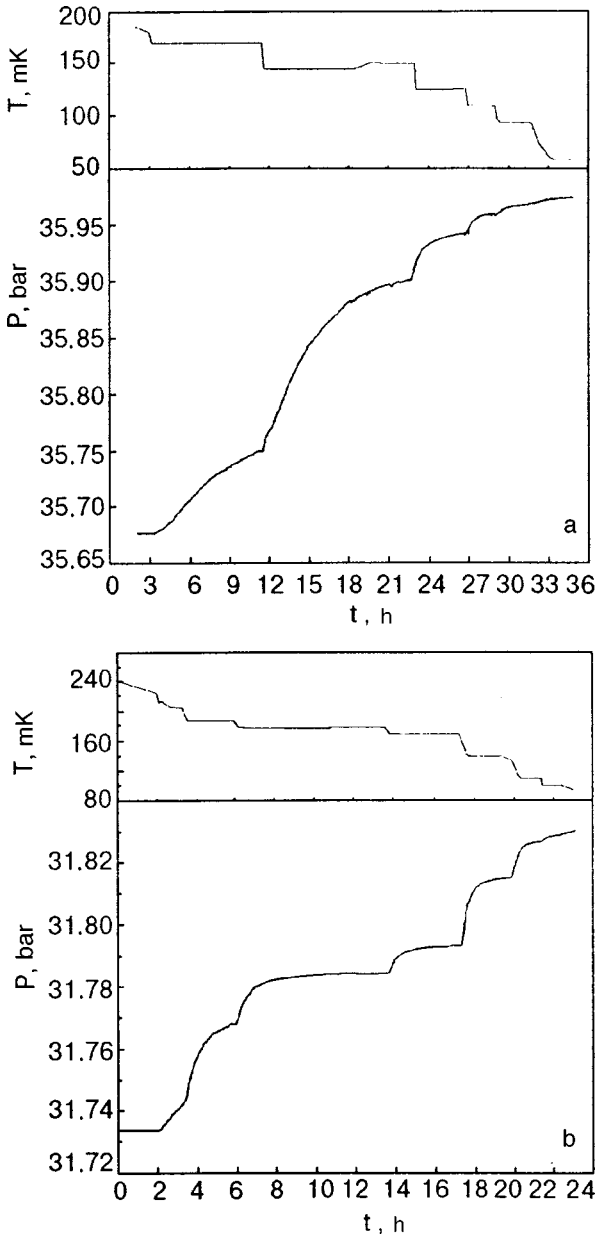

FIG. 9. Thermograms and corresponding pressure variation during stepwise cooling of samples with different molar volumes V,cm^3/mole: 20.28 (a) and 20.54 (b).

the experiments. It should be noted that the number of nuclei of the new phase at later stages of phase separation can decreases due to coalescence. According to estimates,[19] however, the time of initiation of such a process in the given case amounts to $\sim 10^7$ s, and the experimentally established fact that the value of τ remains constant during several days confirms the correctness of such an estimate.

5. GROWTH KINETICS OF ^{3}He INCLUSIONS

After the processes of stabilization of sample quality described in the previous section, we studied the kinetics of inclusion growth using a step-wise decrease in temperature. Schematic thermogram and the $P(t)$ dependences obtained in this case are presented in Fig. 9. It was mentioned above that the dependences determined within each step are successfully described by exponentials of type (4), which allowed us to determine the corresponding characteristic time τ to within a few percent. Figure 10 shows the temperature dependences of τ for three samples investigated by us. The most typical feature of the $\tau(T)$ dependence for the sample with $V=20.27$ cm^3/mole (which was investigated most thoroughly) is its clearly manifested nonmonotonicity and the presence of a well-pronounced minimum near 100 mK. A similar tendency in the behavior of τ is also observed for the sample with a molar volume of 20.28 cm^3/mole. For the larger molar volume (20.54 cm^3/mole), low-temperature measurements were not made since, according to the phase diagram, solid inclusions for the given density must melt and become liquid drops at $T<90$ mK.

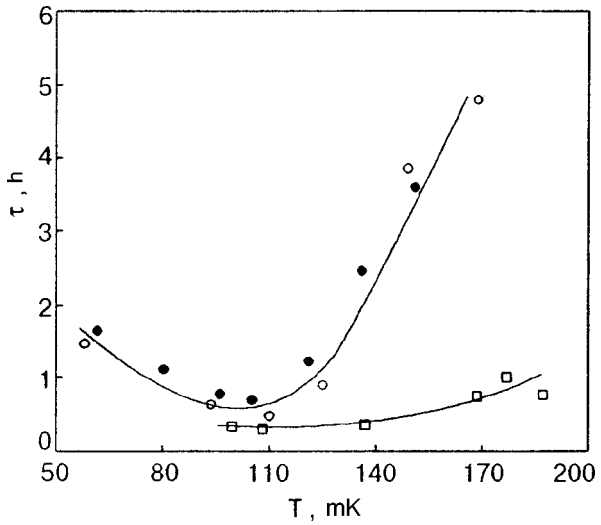

FIG. 10. Temperature dependence of characteristic time constant τ associated with the growth of inclusions for samples with different molar volumes V,cm^3/mole: 20.28 (○), 20.27 (●), and 20.54 (□).

It is natural to associate the obtained values of τ with peculiarities of diffusion under the given conditions. For this purpose, we must first of all establish a correlation between τ and the effective diffusion coefficient determining the corresponding mass transport. This will be done on the basis of a simple model which is commonly used for solving problems associated with diffusion-induced phase separation of mixtures (see, for example, Ref. 20). We shall assume that inclusions of the new phase are spheres of the same radius R_1 distributed uniformly over the sample with a separation $2R_2$

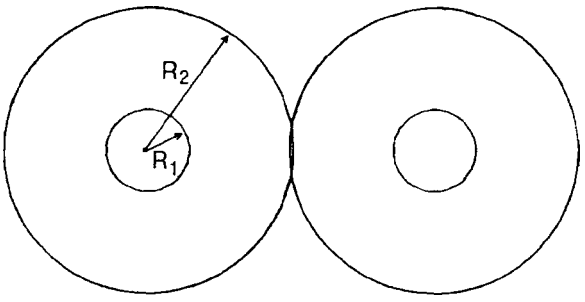

FIG. 11. Diagram illustrating the model of uniformly distributed spherical inclusions used for solving the diffusion problem.

between their centers (Fig. 11). The possibility of describing the experimental dependences $\tau(T)$ with the help of a single exponential to within the error of measurements can be regarded to a certain extent as an indication of a small spread in the values of R_1 and R_2.

In this case, the relation between τ and a certain effective diffusion coefficient D_{eff} can be determined from the solution of the conventional diffusion equation, which has the following form in spherical coordinates:

$$\frac{\partial x}{\partial t}=D_{\text{eff}}\left(\frac{\partial^2 x}{\partial r^2}+\frac{2}{r}\frac{\partial x}{\partial r}\right). \tag{6}$$

The boundary conditions for such a model can be written in the form

$$x(R_1,t)=x_f, \quad \left.\frac{\partial x}{\partial r}\right|_{r=R_2}=0, \tag{7}$$

and the initial condition is

$$x(r,0)=x_i, \tag{8}$$

where x_i is the initial concentration of the solution and x_f its concentration at the boundary of new-phase inclusions, corresponding to the phase diagram at the temperature T_f. Here we speak of the effective diffusion coefficient since it is known beforehand that the diffusion coefficient under the given conditions is a function of concentration, and strictly speaking, we must solve a nonlinear diffusion equation. However (see, for example, Ref. 21), the new phase growth rate in the case of concentration dependence of D is the same as that determined for a constant diffusion coefficient by averaging according to the law

$$D=\frac{1}{x_f-x_i}\int_{x_i}^{x_f}D(x)dx, \tag{9}$$

and the solution of Eq. (6) with the conditions (7) and (8) has the form[1)]

$$\frac{x_i-x(r,t)}{x_i-x_f}=\sum_{n=0}^{\infty}\frac{2R_1\exp(-D_{\text{eff}}\lambda_n^2 t)}{\lambda_n[R_2\sin^2\lambda_n(R_2-R_1)-R_1]}\times\frac{\sin[\lambda_n(r-R_1)]}{r}, \tag{10}$$

where λ_n are the roots of the transcendental equation

$$\tan\lambda_n(R_2-R_1)=\lambda_n R_2. \tag{11}$$

The series (10) converges quite rapidly, and we can confine our analysis to the first term for not very small t. Since the measured values of pressure increment ΔP are proportional to Δx [see (3)], a comparison of (4) and (10) leads to the following expression for the diffusion coefficient

$$D_{\text{eff}}=(\lambda^2\tau)^{-1}. \tag{12}$$

Solution (10) was obtained under the condition $R_1=\text{const}$. Lyubov[20] gives the solution of the diffusion problem obtained by taking into account the variation of the radius of inclusions during their growth, which shows that the form of time dependence does not change for large values of t, and the emerging corrections are insignificant under the given conditions. This is true especially in the case when the size of inclusion changes insignificantly at each step. The most significant refinement in the case of a considerable variation of R_1 is that the radius of an inclusion for $t=0$ is used instead of R_1 in (11).

In order to determine the value of λ from (11), we must know the values of R_1 and R_2. The results of various experiments in which the size of bcc inclusions of ^{3}He were determined are considered in Ref. 11. In all of them the value of $R_1\sim 1-2\ \mu$m. We can expect that the values of R_1 are determined by the initial concentration x_0. However, such a dependence has not been established as yet. In our opinion, the most reliable results were obtained by Kingsley *et al.*[23] who obtained the value $R_1=2.25\ \mu$m from an analysis of the observed effect of limited spin diffusion in bcc inclusions. We shall use this value for obtaining subsequent estimates. The above value of R_1 was obtained at low temperatures, when almost all of ^{3}He is contained in inclusions, i.e., corresponds to the maximum size of inclusions R_{1m}. Using the law of conservation of ^{3}He, we can estimate the size of an inclusion for an intermediate concentration of the hcp solution:

$$R_1\approx R_{1m}\left(1-\frac{x}{x_0}\right)^{1/3}, \tag{13}$$

as well as the mean distance between inclusions:

$$R_2\approx R_{1m}\left(\frac{V_0}{x_0 V}\right)^{1/3}, \tag{14}$$

where x_0 and V_0 are the concentration and molar volume of the initial mixture, and $V\approx V_3$ is the molar volume of the bcc phase being formed. In the present case, it follows from (14) that $R_2\approx 7.8\ \mu$m. The values of D_{eff} obtained from (12) for two values of molar volume used by us are shown in Fig. 12 which also contains information on quantum diffusion in mixtures of appropriate concentrations[2)] calculated by using the following relation describing diffusion of impuritons:[25]

$$D_s=\alpha\frac{a^2 J^{5/3}}{x U_0^{2/3}}\left(1-\frac{x}{x_c}\right)^n, \tag{15}$$

where α and n are constants (the remaining parameters are functions of density), a is the separation between nearest neighbors, J_{34} the exchange integral describing the exchange of ^{3}He and ^{4}He atoms in mixtures, U_0 the amplitude of interaction of ^{3}He impurities, and x_c the critical percolation concentration corresponding to the formation of a macroscopic inclusion of immobile impurities. We have used the values of parameters obtained from NMR experiments and described in Ref. 4. For each step, the values of D_s were averaged in accordance with (9).

A comparison of D_{eff} and $\overline{D_s}$ curves shows that the concentration dependences almost coincide only at high temperatures (concentrations). Choosing appropriate values of R_1 and R_2, we can attain the coincidence of absolute values also. However, this is not essential since it was noted (see Introduction) that the coefficient of mutual diffusion determining the kinetics of phase separation of mixtures can differ from the self-diffusion coefficient measured by the NMR

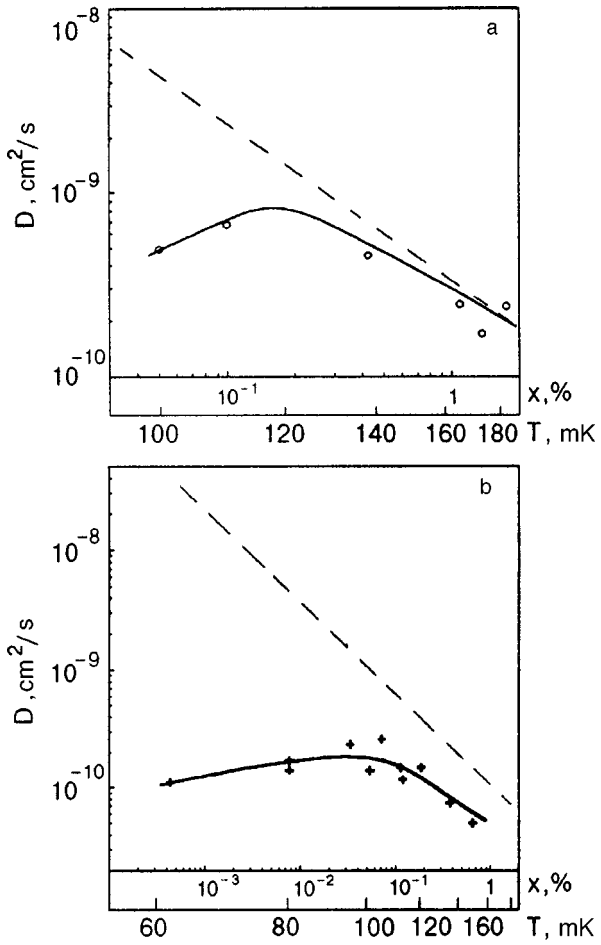

FIG. 12. Concentration (temperature) dependence of the effective diffusion coefficient corresponding to measured values of time constant τ. Dashed line corresponds to mean value of spin diffusion coefficient under relevant conditions. $V=20.54$ cm^3/mole (a) and 20.27 cm^3/mole (b).

method due to the fact that the probability of U-processes in collisions of ^{3}He impuritons can differ from unity. At lower temperatures (concentrations), the value of D_{eff} becomes much smaller than $\overline{D_s}$, and the $D_{\text{eff}}(x)$ and $\overline{D}(x)$ dependences are found to differ qualitatively: as the concentration (temperature) decreases, D_{eff} attains its maximum value and starts decreasing, while the value of $\overline{D_s}$ increases monotonically according to the law $D_s \propto x^{-1}$.

The most probable reason behind the observed difference in the behavior of D_{eff} and $\overline{D_s}$ is apparently the variation of the diffusion process by elastic fields induced in the crystal during the formation and growth of bcc inclusions with a molar volume noticeably larger than that of the initial mixture.

It is well known that the diffusive flux can be written in the form (see, for example, Ref. 20)

$$j=-\frac{Dx}{v}\left(\frac{\nabla x}{x}+\frac{\nabla U}{kT}\right), \tag{16}$$

in the presence of a gradient ∇U of the elastic potential, where v is the atomic volume and ∇x the concentration gradient.

TABLE I. Basic Parameters Characterizing the Growth of ^{3}He Inclusions during Sample Cooling from Different Temperatures to 103 mK, $P_0=33.44$ bar, $V=20.44$ cm^3/mole.

T_i, mK	x_i, %	x_f, %	τ, h	R_1 μm	$\overline{D_s}\cdot 10^9$, cm^2/s	$D_{\text{eff}}\cdot 10^{10}$, cm^2/s
154	0.36	0.021	0.498	2.18	2.48	2.15
151	0.32	0.021	0.535	2.19	2.70	1.99
128	0.11	0.021	0.455	2.23	5.58	2.27
120	0.070	0.021	0.524	2.23	7.43	1.96
113	0.044	0.021	0.457	2.24	9.70	2.24
108	0.031	0.021	0.488	2.24	1.18	2.09
108	0.031	0.021	0.593	2.24	1.18	1.72

It follows from (16) that, in the case when ∇x and ∇U have opposite signs and the first and second terms in the parentheses have comparable absolute values, the diffusion flux can decrease significantly. Since ∇U in this case emerges as a result of a natural process occurring under the action of concentration gradient, the opposite signs can be due to the Le Chatelier principle. In order to estimate the value of ∇U quantitatively, we must solve the corresponding problem in the theory of elasticity, taking into account the anisotropy of the crystal since it is well known that the forces acting between dilatation centers (in our case, ^{3}He impurities to a high degree of accuracy) in an isotropic infinite medium do not affect diffusive fluxes (see, for example, Ref. 26).

Additional information in this field can be obtained from experiments with different values of ∇x. We studied the growth kinetics of ^{3}He inclusions during cooling of a two-phase mixture from different initial temperatures T_i to the same final temperature $T_f \sim 100$ mK. Under these conditions, the second term in (16) could vary in view of the dependence of ∇U on the size of inclusions, which remained practically unchanged in the low-temperature region (see Table I). The pressure in the sample before phase separation was 33.44 bar and the molar volume was 20.44 cm^3/mole. The data ob-

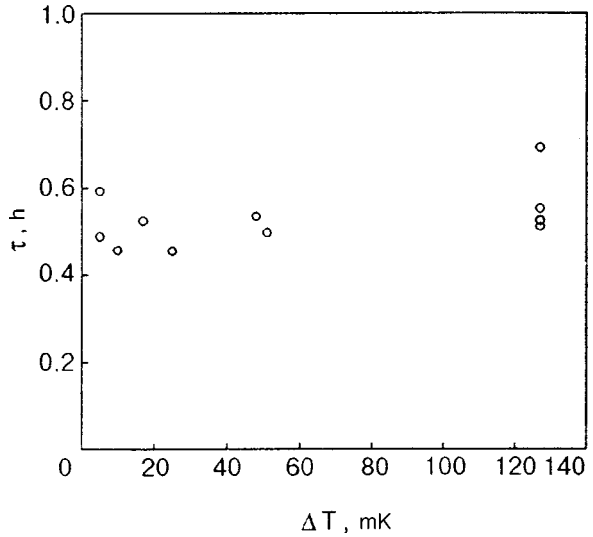

FIG. 13. Characteristic time constants of inclusion growth for different values of supersaturation during cooling from different initial temperatures to 103 mK. $V=20.44$ cm^3/mole.

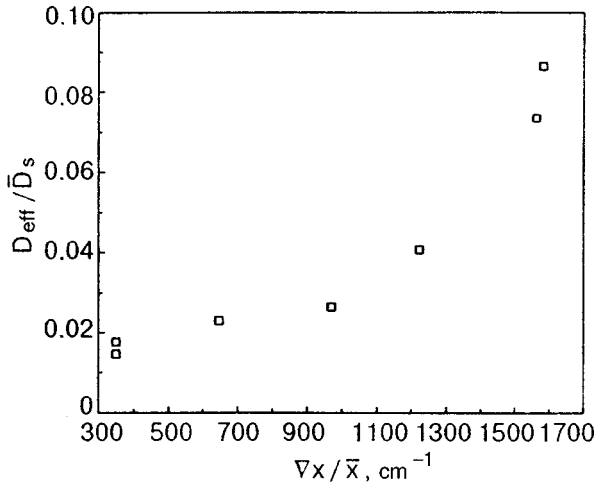

FIG. 14. Dependence of $D_{\text{eff}}/\overline{D_s}$ on the averaged concentration gradient. $V=20.44\ \text{cm}^3$/mole.

tained for τ at various values of ΔT are presented in Fig. 13. The observed independence of τ on ΔT is quite unexpected and requires the theoretical analysis mentioned above for its interpretation.

Using the procedure described above, the corresponding values of D_{eff} and $\overline{D_s}$ were determined from the obtained values of τ. Figure 14 shows the dependence of $D_{\text{eff}}/\overline{D_s}$ on the quantity $\nabla x/\overline{x}$ averaged over time and distance. The observed monotonic decrease in the value of D_{eff}/D_s with $\nabla x/\overline{x}$ can be attributed, in accordance with (16) to the increasing role of elastic forces for small concentration gradients. It was mentioned above that a considerable decrease in the diffusion coefficient must take place under the conditions when the terms in (16) having opposite signs become comparable in absolute value. Figure 14 shows that a sharp decrease in $D_{\text{eff}}/\overline{D_s}$ is observed for $\nabla x/\overline{x}\sim 10^3\ \text{cm}^{-1}$ Assuming that the second term in the parentheses of (16) has the same order of magnitude, we can estimate the difference in elastic energies ΔU for impurity atoms which are nearest neighbors in the hcp lattice as $\sim 4\cdot 10^{-6}$ K. The presence of such potential gradients under the given conditions is quite feasible and at the same time sufficient for explaining the experimentally observed difference between D_{eff} and D_s.

It should be noted that the estimated value of ΔU is much smaller that the energy band width $\Delta_3\sim 10^{-4}$ K for impuritons in a hcp mixture and hence cannot lead to a noticeable mismatching of the energy levels for impuritons and a suppression of diffusion. Consequently, a noticeable influence of elastic potential gradients on the motion of impurities due to direct action of forces must be manifested earlier than the effect of a change in the tunneling frequency under the action of this potential. On the other hand, our estimates give only the average value of the potential which is a power function of the distance, and the value of ΔU in the immediate vicinity of a bcc inclusion of ^{3}He can become as large as $\sim\Delta_3$. In this case, the tunneling frequency and the quantum diffusion coefficient determined by this quantity can decrease considerably. It should also be noted that potential gradients obviously do not exceed the elastic limit of the crystal at least even at macroscopic distances from the inclusions, which is reflected in the absence of hysteresis effects in these experiments (the opposite situation will be considered in Sec. 7).

6. PECULIARITIES OF DISSOLUTION KINETICS OF ^{3}He INCLUSIONS

Many authors investigating the kinetics of phase separation of ^{3}He–^{4}He solid mixtures noted the nonequivalence of growth and dissolution of bcc phase inclusions. In most cases, it was found that the dissolution of inclusions occurs at a higher rate than the growth,. However, no attempts have been made until recently to explain this phenomenon or even to study it systematically. In this section, we describe the results of such investigations.

The results obtained for a rapid heating of the mixture after phase separation from the same initial temperature $T_i=103$ mK to different final temperatures $T_f=108$–690 mK according to the diagram presented in Fig. 4b. The experiments were made on the sample whose average molar volume was $20.44\ \text{cm}^3$/mole. Some of the $P(t)$ dependences obtained in this case are presented in Fig. 15. It was found that the form of the dependences was determined by the value of T_f.

For a small increase in temperature, the $P(t)$ dependence can be described by a universal exponential (see Figs. 5 and 15a) as in most of our experiments and is characterized by a time constant $\tau\sim 10^3$ s. For intermediate values of T_f (127–230 mK), the $P(t)$ curve (see Fig. 15b) has two different segments: the nearly vertical segment (the corresponding time interval did not exceed the time of stabilization of thermal equilibrium) and a nearly exponential segment characterized by the time constant τ_{eff} that is almost the same as that observed for lower T_f. The value of τ_{eff} indicated in Fig. 15b is an effective quantity obtained when the smooth segment of the $P(t)$ curve is described by the single exponential, while in fact this segment of the curve can be described only by two exponential to within the experimental error. During sample heating (above the phase-separation region), complete relaxation of pressure occurs very rapidly (see Fig. 15c).

Figure 16 shows the relative pressure jump observed for intermediate value of ΔT as a function of the difference T_f-T_i. It can be seen that this dependence is of the threshold type: a finite pressure jump occurs at a certain critical value ΔT_c. It order to verify whether the obtained value of $\Delta T_c\approx 25$ mK is dominant, we made two experiments on the same sample with heating from 150 and 230 mK. The results of one of these experiments are presented in Fig. 17. These experiments did not reveal a jump-wise change in pressure, and the $P(t)$ dependence can be described by two exponentials with the corresponding values of $\tau_1\approx 85$ s and $\tau_2\approx 390$ s. Apparently, we cannot speak of the critical value of the chemical potential difference $\Delta\mu$ in the initial and final states as the reason behind the emergence of the pressure jump ΔP either since the value of $\Delta\mu$ obtained in the latest experiments (Fig. 17) is considerably higher than that obtained previously (see Fig. 15) for $\Delta T=25$ mK.

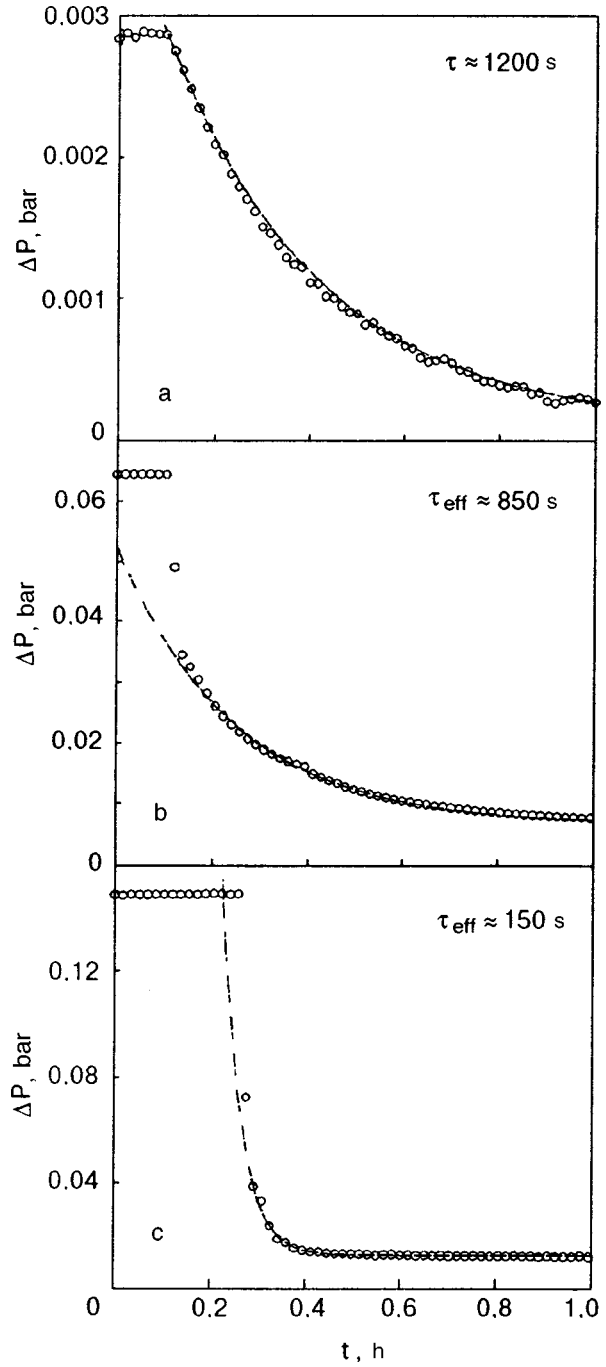

FIG. 15. Variation of pressure with time during dissolution of ^{3}He inclusions for different final temperatures T_f, mK: 110 (a), 150 (b), and 570 (c). Dashed curves correspond to approximation by formula (5) with corresponding time constants indicated on the figure.

The observed effects can be explained qualitatively on the basis of a model in which the process of dissolution of ^{3}He inclusions upon heating consists of several stages. The possibility of considerable suppression of quantum diffusion near the boundaries of inclusions under the action of elastic fields emerging due to the difference in the molar volumes of ^{3}He inclusions and the matrix noted in the previous section is also essential. Under such conditions, a rapid mass transport is possible only if, a crystal layer near the inclusion with the maximum gradient of potential is eliminated.

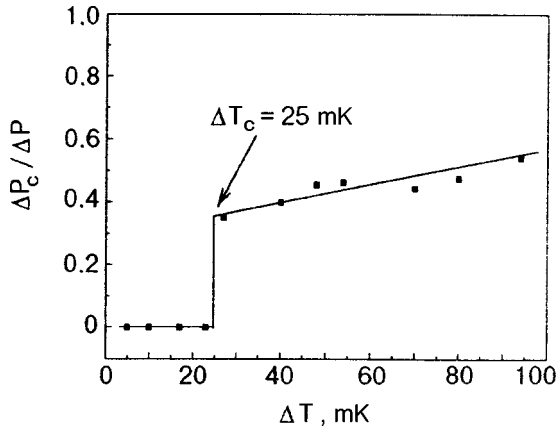

FIG. 16. Dependence of the relative pressure jump on the difference between the final and initial temperatures $\Delta T = T_f - T_i$.

This can be done at the first stage of the dissolution process [Fig. 18(a)], when ^{3}He inclusions are saturated with ^{4}He atoms following the increase in temperature and the equilibrium concentration of ^{4}He. Diffusive penetration of ^{4}He inside a ^{3}He inclusion treated as a sphere of radius R occurs during the characteristic time

$$\tau_4 = \frac{R^2}{\pi^2 D}, \tag{17}$$

where the corresponding diffusion coefficient D describes the transport of ^{4}He atoms in solid ^{3}He through random tunnel jump. According to Andreev and Lifshitz,[2] the diffusion coefficient D can be written in the form

$$D \propto J_{43} a^2, \tag{18}$$

where a is the separation between nearest neighbors and J_{43} the exchange integral characterizing the tunneling frequency for ^{4}He atoms in the ^{3}He matrix. We can expect that the value of J_{43} is close to the frequency J_{34} of tunneling of ^{3}He in the ^{4}He crystal, which was reliably established in experi-

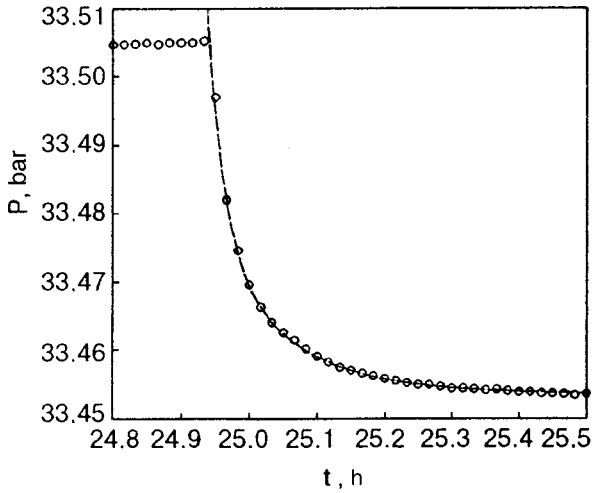

FIG. 17. Time dependence of the pressure variation during dissolution of ^{3}He inclusions during heating from $T_i = 150$ mK to $T_f = 230$ mK. Dashed curve corresponds to approximation by the formula $\Delta P(t)/(P_f - P_i) = 0.0472e^{-t/\tau_1} + 0.2619e^{-t/\tau_2}$ with $\tau_1 \approx 85$ s and $\tau_2 \approx 390$ s.

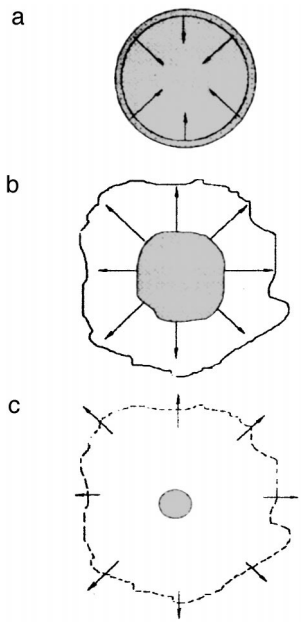

FIG. 18. Schematic diagram of the multistage model of dissolution of ^{3}He inclusions during heating: dissolution of ^{4}He from the stressed layer in the inclusion (a), ''evaporation'' of ^{3}He from inclusions (b), and diffusive dissolution of inclusions (c).

ments on quantum diffusion. Extrapolating the known values[4] of J_{34} to the molar volume typical of the inclusion with $V \approx 24\,\mathrm{cm}^3$/mole, we find that $J_{34} \approx J_{43} \approx 2\times 10^7\,\mathrm{s}^{-1}$, which gives $D \sim 10^{-8}\,\mathrm{cm}^2/\mathrm{s}$. Substituting the obtained value of D into (17) and considering that $R \approx 2\ \mu$m, we obtain $\tau_4 \sim 0.1$ s.

Thus, the first stage of dissolution is quite rapid, but the change in pressure ΔP at this stage is very small. The change in the volume of inclusions will be determined by the change Δx_4 in the ^{4}He concentration in it, which is always smaller than x_0 if the system is within the phase-separation region. The fraction of volume occupied by all inclusions corresponds to the concentration x_0, and hence the total change in the sample volume due to dissolution of ^{4}He is proportional to the product of two small quantities $\Delta x_4 x_0$, and the value of ΔP determined according to (3) is smaller than 2% of the change in pressure during phase separation (to the extent to which Δx_4 is smaller than x_0).

Nevertheless, this stage can affect the dissolution of inclusions significantly since ^{4}He atoms leaving the stressed boundary region around inclusions actually destroy it and permit the free motion of impuritons, determining the second stage of the process [see Fig. 18(b)]. The characteristic time of this stage is determined by the rate of emergence of ^{3}He atoms from an inclusion, which can be estimated in analogy with the process of evaporation of liquid, for which the number of atoms evaporating from unit surface per unit time can be written in the form (see, for example, Ref. 27)

$$\alpha \sim \theta N, \tag{19}$$

where θ is the average velocity of atoms in the vapor and N their density. As applied to our case, $\theta \propto a\Delta_3$,[2] (Δ_3 is the energy band width for ^{3}He impuritons in the hcp mixture), and the role of N is played by the density N_3 of ^{3}He atoms in the mixture, which is proportional to the concentration x:

$$N_3 = N_m x, \tag{20}$$

where N_m is the density of atoms in the mixture.

In this case, neglecting the difference in the molar volumes of the inclusion and the mixture, we can find the time of evaporation of an inclusion of radius R:

$$\tau \simeq \frac{R}{3\Delta_3 a x}, \tag{21}$$

Substituting $R \sim 10^{-4}\,\mathrm{cm}, \Delta_3 \sim 10^7\,\mathrm{s}^{-1}$, and $x = 10^{-2}\%$ into (21), we obtain $\tau \sim 1$ s, i.e., this stage is also quite rapid.

This dissolution stage is followed by the formation of a spherical layer enriched in ^{3}He around the inclusion, the thickness of this layer attaining several mean free paths λ_3 of ^{3}He impuritons in the solution. The value of λ_3 amounts to $\sim 10^2 a$ for $x_i \sim 10^{-2}\%$,[28] and hence the thickness of such layers is $\sim 10^{-5}$ cm, and their formation can ensure the experimentally observed value of ΔP_c. In view of a high probability of U-processes during collisions between impuritons, the propagation of ^{3}He over large distances must be of diffusion type [Fig. 18(c)], and the characteristic times of this third dissolution stage are of the same order of magnitude as those observed during phase-separation of ^{3}He–^{4}He solid mixtures in other situations.

The threshold effect in the proposed model always takes place when the stressed layer surrounding a ^{3}He inclusion and preventing quantum diffusion is eliminated completely after the first stage of dissolution of ^{4}He. Since the amount of ^{4}He dissolved in this case is in one-to-one correspondence with the difference in equilibrium concentrations at the final and initial temperatures, critical conditions correspond to a temperature difference ΔT_c for which the difference Δx ensures complete elimination of the stressed layer.

The difference in equilibrium concentrations of ^{4}He in an inclusion at the final temperature $T_f \approx 130$ mK corresponding to the critical pressure jump and at the initial temperature $T_i \approx 103$ mK amounts approximately to 0.2%. To ensure such a change in concentration, we must dissolve a spherical layer of thickness $\delta R \approx 0.7\times 10^{-3} R \approx 1.4 \times 10^{-7}$ cm in the inclusion. In other words, the critical value ΔT_c corresponds to dissolution of 3–4 atomic layers, which is quite a reasonable value for the thickness of a layer in which quantum diffusion of impuritons can be hampered. Moreover, the process of dissolution of ^{4}He is associated with a decrease in density, ensuring an additional removal of stresses.

The other necessary condition for observing a pressure jump is a sufficiently long mean free path of impuritons in the mixture for the initial concentration (temperature). This follows from the result of the above-mentioned experiment with a sample heated from 150 mK. At this temperature, the equilibrium concentration of ^{3}He is more than an order of magnitude higher than at 100 mK. Accordingly, the mean free path for impuritons is smaller by the same factor, and ''evaporation'' of inclusions cannot be responsible for a noticeable pressure jump. Nevertheless, this process apparently accelerates the dissolution of the inclusion significantly, thus

ensuring the effect comparable with the subsequent diffusion. As a result, the $\Delta P(t)$ dependence is the sum of two exponentials. Thus, the process of dissolution of inclusions heated from the temperature $T_i \approx 100$ mK to 125 mK$< T_f <230$ mK can be regarded as a combination of three stages: (1)Dissolution of ^{4}He in bcc ^{3}He leading to dissolution of the stressed layer around the inclusion; (2) the formation of a layer enriched by ^{3}He around the inclusion, and (3) diffusive dissolution of this layer. The first two stages take a time of the order of a few seconds, while the last stage occurs during a time $\sim 10^3$ s typical of diffusive mass transport.

For higher temperature increments corresponding to the exit beyond the phase-separation curve, the first stage of the process has no above-mentioned limitation on concentration and can ensure a noticeable change in pressure, which is reflected in experiments. In this case, the characteristic time τ is close to the time of stabilization of thermal equilibrium [see Fig. 15(c)].

In the model under consideration, the nonequivalence of growth and dissolution of inclusions noted in Ref. 9 appears as quite natural since the former process includes only the slowest stage. In this case, quantum diffusion is limited due to the formation of a stressed layer at the inclusion boundary (see above). It is appropriate to note in this connection that the absence of a sharp jump in pressure in the experiments on dissolution of inclusions illustrated by Fig. 6 in Ref. 9 is associated with a much lower rate of sample heating (as compared to that used by us here).

The multistage nature of dissolution of ^{3}He inclusions described above is manifested fully only for quite strong supersaturation and at lower initial temperatures. For small temperature increments, dissolution must occur in the conventional way, which is in fact observed in experiments carried out in accordance with the schematic diagram shown in [Fig. 4(a)], in which the kinetics of dissolution of ^{3}He inclusions was studied upon a step-wise increase in temperature. All the $P(t)$ dependences determined in this case are correctly described by exponentials (Fig. 19) with characteristic times τ^* shown in Fig. 20, where the $\tau(\overline{x})$ dependence obtained in experiments on the growth of inclusions in the sample with the same density is also plotted for comparison. It can be seen that the behavior of characteristic times of dissolution is qualitatively the same as for the growth of inclusions: a minimum also exists (although it is slightly displaced towards higher concentrations (temperatures). The values of τ^* are smaller than τ over the entire region. The relation between these quantities can be compared quantitatively only on the basis of a theoretical analysis of both processes.

Specific features of experiments on dissolution are due to the fact that diffusion occurs from the very outset in an elastic field which is formed during the growth of inclusions and which can facilitate the removal of ^{3}He impurities from the inclusion, i.e., accelerate diffusion during dissolution. However, such an acceleration is observed only if the gradient ∇U created during the growth is insufficient for a noticeable decrease in quantum diffusion due to mismatching of impuriton energy levels. Since the latter effect does not depend on the sign of ∇U, it decelerates the growth as well as

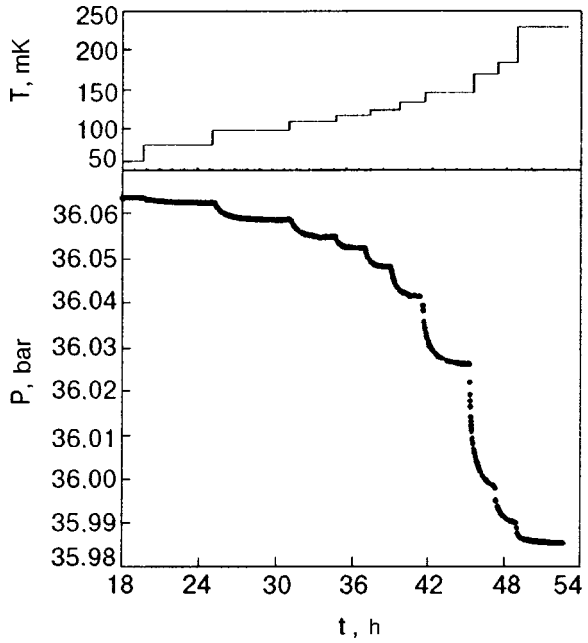

FIG. 19. Thermogram and time variation of pressure during step-wise heating of a two- phase crystal. $V = 20.27$ cm^3/mole.

dissolution of inclusions. However, the above-mentioned processes at each stage are not very clearly manifested and occur simultaneously, so that these processes can be described by a unified ''effective'' diffusion coefficient which is noticeably larger than D_{eff} for phase separation. As regards the effect of dissolution of ^{4}He in inclusions, this process gives a negligible contribution to the change in pressure in view of the small difference in concentrations at each step, the stressed layer near the boundary is gradually eliminated and disappears completely only when the concentration in the hcp mixture becomes high enough for the dissolution of ^{3}He inclusions to occur only through the diffusion mechanism.

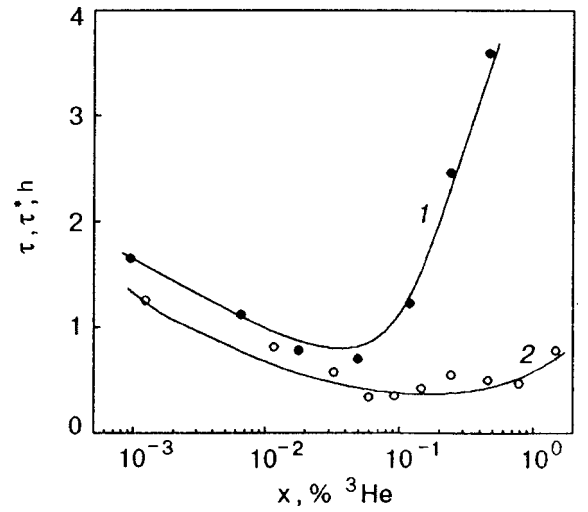

FIG. 20. Dependence of characteristic time constants τ and τ^* for growth (curve *1*) and dissolution (curve *2*) of ^{3}He inclusions on average concentration $\overline{x}$. Solid curves connect experimental points.

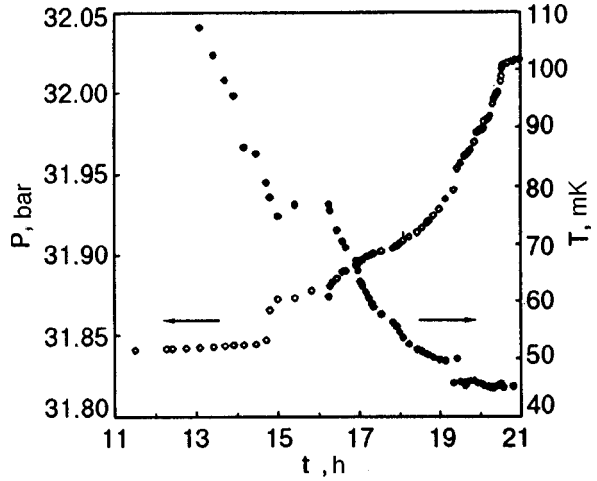

FIG. 21. Thermogram of crystal cooling and corresponding change in pressure for the sample with $V=20.54\ \mathrm{cm}^3$/mole, illustrating phase separation at 100 mK and melting of formed ^{3}He inclusions during subsequent cooling.

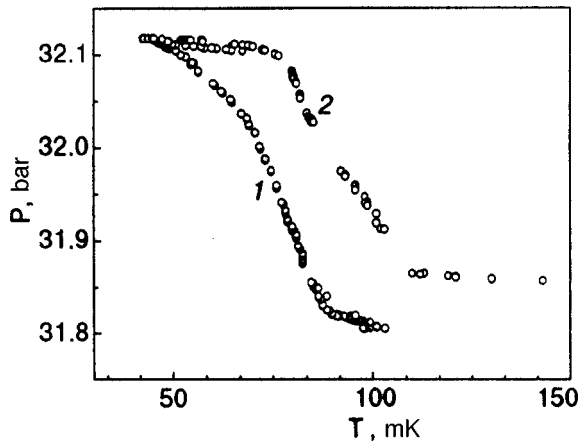

FIG. 22. Temperature dependence of pressure during melting and subsequent crystallization of ^{3}He inclusions: cooling (curve *1*) and heating (curve *2*). $V=20.54\ \mathrm{cm}^3$/mole.

The experiments described in the present section proved, on the one hand, that the type of dissolution and growth of inclusions for small step-wise variations of temperature and concentration is approximately the same, although dissolution always occurs at a higher rate. On the other hand, the dissolution time decreases abruptly for considerable changes in temperature, the dissolution apparently becomes a multistage process. The available experimental data do not contradict the proposed pattern of multistage process, although its correctness requires additional verification.

7. MELTING AND CRYSTALLIZATION OF ^{3}He INCLUSIONS

The peculiarity of the phase diagram for ^{3}He allows us to melt ^{3}He inclusions formed during phase separation of the mixture by further cooling and to crystallize them in the course of subsequent heating. It was interesting to trace the effect of these processes on the phase-separation kinetics. Such experiments were made on a sample with a molar volume of $20.54\ \mathrm{cm}^3$/mole($P_0=31.7$ bar). We measured the time dependence of pressure during cooling at a rate of $\sim$10 mK/h followed by heating. The general dependence $P(t)$ shown in (Fig. 21) has two clearly manifested segments on which the pressure increases, the first segment being associated with the phase separation of the mixture and the second with melting of ^{3}He inclusions formed. The obtained dependence is similar qualitatively to that obtained by Shrenk *et al.*[7] for a mixture with 0.9% ^{3}He at $P=32$ bar. As in most of similar experiments, phase separation of the mixture can be described by an exponential of the type (4) with $\tau \approx 1200$ s. Melting is extended in time and occurs not very smoothly apparently due to a noticeable liberation of heat during melting (it should be recalled that $dP_m/dT<0$ for ^{3}He under these conditions). After cooling to $T\approx 40$ mK, the sample was heated, which led to crystallization of ^{3}He inclusions and corresponding decrease in pressure. The temperature dependence of pressure for melting and crystallization of the sample is shown in (Fig. 22).

It is interesting to compare the amplitudes of pressure variation $\Delta P_{s(m)}$ during phase separation and melting. In both cases, the values of $\Delta P_{s(m)}$ are proportional to the change $\Delta V_{s(m)}$ in the molar volume. In the case of phase separation to quite low temperatures, $\Delta V_s \approx 0.4 x_0\ \mathrm{cm}^3$/mole in accordance with (1) for $x_f \ll x_0$, while in the case of melting $\Delta V_m \approx x_0(V_l - V_s)\ \mathrm{cm}^3$/mole, where V_l and V_s are molar volumes of the liquid and the crystal on the melting curve. Considering that $V_l - V_s \approx 1.27\ \mathrm{cm}^3$/mole at low temperatures (see, for example, Ref. 29), we obtain $\Delta V_m \approx 3\Delta V_s$. The corresponding values of ΔP must obey a similar regularity, which is in good agreement with experimental results. In our opinion, this is an indication of the fact that the sample quality remains quite good at the first stage of the experiment.

In this connection, a comparison with the results of similar experiments[28] made on a sample in silver powder is representative. It was observed[28] that the measured variation of pressure amounts to only 8% of the calculated value. In our opinion, this is an indication of a considerable inhomogeneity of the sample, which is inevitable during its crystallization in virtually closed pores. It should also be noted that the values of ΔP_m obtained in Ref. 7 under similar conditions for samples grown in free volume are higher, but still noticeably lower than the theoretical values ($\Delta P_m/\Delta P_s \approx 1$).

A number of peculiarities emerging at the next stages of the experiments under consideration are worth noting. Figure 22 presenting the temperature dependence of pressure in the sample shows that the crystallization of molten inclusions displays hysteresis effects, although the actual difference between the curves recorded during cooling and heating is apparently smaller that in Fig. 22 since the temperature laid on the ordinate axis is that of the thermometer, while the actual temperature of inclusions must be higher during cooling and lower during heating of the sample in view of the heat of transition. Crystallization of an inclusion occurs at a constant volume and is accompanied by a pressure drop in the inclusion in view of the difference in the densities of the crystal and the liquid. As a result, its density and pressure in the crystallized layer are nonuniform.

A comparison of the $P(T)$ curves recorded during cool-

ing and heating (see Fig. 22) shows that the final pressure in the sample after its crystallization is noticeably higher than the initial pressure. A similar effect was observed by Haley and Adams.[30] The most natural explanation of this fact is based on the assumption that a part of inclusion remains liquid. This is possible if the decrease in pressure of the inclusion during its crystallization is sufficient for the final pressure in it to become lower than the pressure $P_{\min}$ corresponding to the minimum on the melting curve. Apparently, a difference in pressures of the sample and in the inclusion also appears during melting which probably also occurs at a constant volume. This assumption is supported by the fact that the pressure in the sample at the end of melting at $T \sim 50$ mK is approximately lower by 0.5 atm than the value of P_m for pure ^{3}He at such a temperature, while the beginning of melting matches to the melting curve for ^{3}He. Naturally, the pressure gradient during melting must be lower since it can emerge only in the adjacent layer of the matrix in view of the uniformity of pressure in the liquid. The experimentally observed difference between the initial and final pressure in the sample is due to the fact that approximately 20% of ^{3}He remain in the liquid state. It should be noted that the pressure in the sample had increased additionally by approximately 0.015 atm after the next crystallization.

The presence of high potential gradients that can suppress diffusion completely is an inevitable consequence of nonuniformity of density and pressure in the crystallized inclusion. The absence of a noticeable change in sample pressure after crystallization upon further heating is the most graphic indication of this effect (see Fig. 22). High-quality samples heated to $T \sim 150$ mK display a very rapid drop of pressure associated with dissolution of clusters (see the previous section). Distortions caused by crystallization proved to be so significant that they could not be eliminated by homogenization of the sample at $T \sim 300$ mK for several hours carried out before the next cooling. This is not surprising since a pressure drop of several atmospheres between the inclusion and adjacent layers of the matrix having a thickness of a few micrometers, which should be observed in the proposed model, must naturally be accompanied by plastic deformation whose consequences are difficult to eliminate.

Unfortunately, no attempts were made to reduce the emerging distortions by cyclic phase- separation processes (see Sec. 2). For this reason, the pressure in the sample before the second phase separation was noticeably higher, while the pressure measured after the second melting of inclusions (which was probably also incomplete as in Refs. 7 and 30), was 0.1 atm lower than after the first melting (Fig. 23).

Thus, it was found from experiments with melting of ^{3}He inclusions that their melting is almost complete after the first cooling to a temperature below T_m, but the pressure in the cluster at the end of melting is apparently higher ($\sim$0.5 atm) than the pressure recorded by the external gauge. Crystallization of molten inclusion is accompanied by strong distortions of the crystal, as a result of which a fraction of liquid ^{3}He ($\sim$20%) is preserved even at the temperature much higher than T_m. The deceleration of dissolution of the inclusion during its subsequent heating as well as incomplete

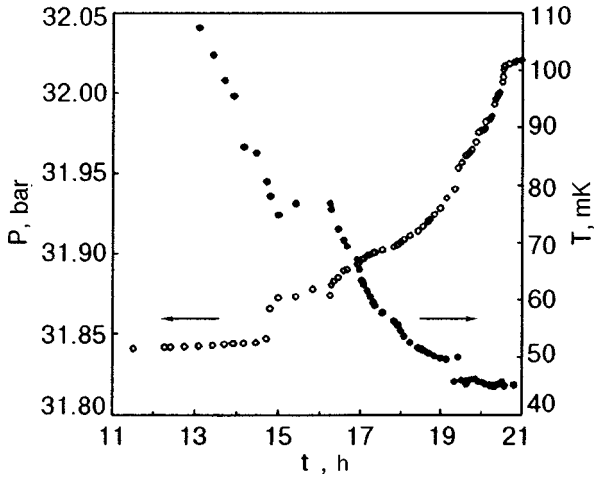

FIG. 23. Kinetics of cooling and corresponding change in pressure during repeated melting. $V = 20.54$ cm^3/mole.

melting as a result of repeated cooling are also manifestations of a strong distortion of the lattice near the inclusion boundary. Subsequent crystallization leads to an increase in the fraction of uncrystallized liquid.

The experiments described in this section confirm once again the assumption concerning a strong effect of sample inhomogeneity on mass transport. The obtained results are in qualitative agreement with the model proposed by us here.

8. CONCLUSIONS

Let us summarize the main results of this research.

(1) A new method of obtaining high-quality homogeneous samples of solid mixtures of helium isotopes is proposed and implemented. Its essential element is several cycles of growth and dissolution of bcc inclusions ^{3}He carried out in phase-separation region. Indications of the high quality of the samples obtained in this case are
   - a further decrease in the sample pressure as a result of the cycling as compared to the traditional annealing;
   - obtaining of short and reproducible characteristic time of growth and dissolution of ^{3}He inclusions, which is much shorter than in most other experiments;
   - good coincidence of the values of phase-separation temperature in the initial sample for cooling and heating (the value of ΔT does not exceed 10
   - the closeness of the observed values of pressure variation during phase separation and first melting to the theoretical values;
   - proportionality of pressure variation and the concentration of the hcp mixture on the phase-separation curve.

(2) It is shown that the characteristic time of the growth of ^{3}He inclusions has a nonmonotonic temperature dependence and increases at low temperatures. Such a behavior apparently indicates a noticeable limitation of quantum diffusion due to fields of stresses emerging in the crystal during phase separation.

(3) During the dissolution of ^{3}He inclusions, anomalously rapid mass transport is observed in the crystal under the conditions of strong deviations from equilibrium, and its threshold nature is established.
(4) A model of multistage dissolution of ^{3}He inclusions, which explains qualitatively its main peculiarities, is proposed. The model takes into account the presence of a stressed layer near the boundary of inclusion, which is formed due to the difference in the molar volumes of the two phases, and its destruction during the dissolution of ^{4}He in ^{3}He inclusions.
(5) The kinetics of melting and crystallization of ^{3}He inclusions due to temperature variation is studied. It is found that repeated crystallization of molten inclusions gives rise to a large pressure gradient near the boundary of inclusions, which suppresses quantum diffusion considerably and may lead to incomplete crystallization of inclusions.

This research was partly supported by grants QSU 082169 and QSU 082048 of the International Program on Science and Education.

*)E-mail: rudavskii@ilt.kharkov.ua
1)A similar problem was solved, for example, in Ref. 22.
2)The concentration of the mixture at the given temperature was assumed to be equal to the equilibrium concentration of the hcp mixture and was determined from the phase diagram in accordance with the results obtained by Edwards and Balibar.[24]

[1] D. O. Edvards, A. S. McWilliams, and J. G. Daunt, Phys. Lett. **1**, 218 (1962).
[2] A. F. Andreev and I. M. Lifshits, Zh. Éksp. Teor. Fiz. **56**, 2057 (1969) [Sov. Phys. JETP **29**, 1107 (1969)].
[3] Yu. Kagan, J. Low Temp. Phys. **87**, 525 (1987).
[4] V. N. Grigor'ev, Fiz. Nizk. Temp. **23**, 5 (1997) [Low Temp. Phys. **23**, 1 (1997)].
[5] I. Iwasa and H. Suzuki, in *Proceedings LT-17*, North-Holland, Amsterdam (1984).
[6] V. A. Mikheev, V. A. Maidanov, N. P. Mikhin *et al.*, Fiz. Nizk. Temp. **14**, 563 (1988) [Sov. J. Low Temp. Phys. **14**, 309 (1988)].
[7] R. Shrenk, O. Friz, Y. Fujii *et al.*, J. Low Temp. Phys. **84**, 133 (1991).
[8] V. A. Shvarts, N. P. Mikhin, E. Ya. Rudavskii *et al.*, Fiz. Nizk. Temp. **21**, 717 (1995) [Low Temp. Phys. **21**, 556 (1995)].
[9] A. N. Gan'shin, V. A. Maidanov, N. F. Omelaenko *et al.*, Fiz. Nizk. Temp. **24**, 815 (1998) [Low Temp. Phys. **24**, 611 (1998)].
[10] A. N. Gan'shin, V. A. Maidanov, N. F. Omelaenko *et al.*, Fiz. Nizk. Temp. **24**, 1117 (1998) [Low Temp. Phys. **24**, 840 (1998)].
[11] A. N. Gan'shin, V. N. Grigor'ev, V. A. Maidanov *et al.* Fiz. Nizk. Temp. **25**, 356 (1999) [Low Temp. Phys. **25**, 259 (1999)].
[12] V. A. Maidanov, Fiz. Tverd. Tela (St. Petersburg) (in press).
[13] W. J. Mullin, Phys. Rev. Lett. **20**, 254 (1968).
[14] A. S. Rybalko and M. B. Sterin, Fiz. Nizk. Temp. **22**, 1095 (1996) [Low Temp. Phys. **22**, 837 (1996)].
[15] D. N. Bittner and E. D. Adams, J. Low Temp. Phys. **97**, 519 (1994).
[16] G. Schuster, A. Hoffmann, and D. Hechtfisher, V. 19, doc. CCC/96-25 Bureau Intern. des Poids et Mesures, Comit Consulativ de Thermon trie, Sevres, France (1996).
[17] G. A. Mikhailov, in *Proceedings 14 Intern. Cryog. Eng. Conf. and Intern. Cryog. Mater. Conf.*, Kiev, Cryogenics, **32 (Suppl.),** 130 (1992).
[18] I. Iwasa and H. Suzuki, J. Low Temp. Phys. **62**, 1 (1986).
[19] I. M. Lifshits and V. V. Slezov, Zh. Éksp. Teor. Fiz. **35**, 479 (1958) [Sov. Phys. JETP **8**, 331 (1958)].
[20] B. Ya. Lyubov, *Diffusion Processes in Heterogeneous Solid Media* [in Russia], Nauka, Moscow (1981).
[21] J. Christian, *The Theory of Transformations in Metals and Alloys*, Pergamon Press, Oxford (UK) (1975).
[22] B. M. Budak, A. A. Samarskii, and A. N. Tikhonov, *A Collection of Problems in Mathematical Physics* (Pergamon Press, Oxford, 1964).
[23] S. C. J. Kingsley, V. Maidanov, J. Saunders, and B. Cowan, J. Low Temp. Phys. **113**, 7 (1998).
[24] D. O. Edwards and S. Balibar, Phys. Rev. B **39**, 4083 (1989).
[25] Yu. M. Kagan and L. A. Maksimov, Zh. Éksp. Teor. Fiz. **84**, 792 (1983) [Sov. Phys. JETP **57**, 459 (1983)].
[26] A. M. Kosevich and A. S. Kovalev, Fiz. Tverd. Tela (Leningrad) **13**, 219 (1983) [*sic*].
[27] Ya. I. Frenkel, *Kinetic Theory of Liquids* (Clarendon Press, Oxford, 1946).
[28] A. R. Allen, M. G. Richards, and J. Schratter, J. Low Temp. Phys. **47**, 289 (1982).
[29] B. N. Eselson, V. N. Grigor'ev, V. G. Ivantsov *et al.*, *Mixtures of* ^{3}He–^{4}He *Quantum Liquids* [in Russian], Nauka, Moscow (1973).
[30] R. P. Haley and E. D. Adams, J. Low Temp. Phys. **110**, 121 (1998).

Translated by R. S. Wadhwa

Spin dynamics of ^{3}He-B with dissipation for the general spin-orbital configurations

G. Kharadze and N. Suramlishvili

Andronikashvili Institute of Physics, Georgian Academy of Sciences 6 Tamarashvili st., 380077 Tbilisi, Georgia

(Submitted April 5, 1999)
Fiz. Nizk. Temp. **25**, 815–819 (August–September 1999)

The spatially homogeneous spin dynamics of the superfluid ^{3}He-B with dissipation is considered for the general spin-orbital configurations. It is demonstrated that the possibility of new coherent spin-precessing modes appears explicitly in the equations of motion describing the relaxation of the spin variables towards various attractors (resonance states) found previously as the stationary solutions and observed experimentally. © *1999 American Institute of Physics.* [S1063-777X(99)00408-9]

1. The order parameter rigidity of the superfluid phases of liquid ^{3}He gives life to a number of the long-lived excitations at the background of the Cooper pair condensate. Among them, a great importance, since the discovery of ultralow-temperature ordered states of ^{3}He, has been attributed to the investigation of the coherent spin dynamics. A crucial role here is played by a weak spin-orbital coupling stemming from the dipole-dipole interaction between nuclear magnetic moments of ^{3}He atoms. In the ordered (superfluid) states the dipole-dipole potential U_D lifts the spin-orbital degeneracy and stabilizes the appropriate equilibrium or dynamical spin-orbital configurations of ^{3}He-A and ^{3}He-B.

The spin dynamics of the superfluid phases of ^{3}He is a coupled motion of the nuclear magnetization $\mathbf{M}=g\mathbf{S}$ and the spin part of the order parameter. In the dissipationless approach a starting point is the Leggett Hamiltonian (in what follows we consider a spatially homogeneous spin dynamics)

$$\mathcal{H}_L=\frac{1}{2\chi}\mathbf{M}^2-\mathbf{M}\cdot\mathbf{H}_0+U_D=\frac{g^2}{2\chi}\mathbf{S}^2-\omega_0 S_z+U_D, \qquad (1)$$

where χ is the magnetic susceptibility, the external magnetic field $\mathbf{H}_0=-H_0\mathbf{z}$ and the Larmore frequency $\omega_0=gH_0$. The order parameter here enters through the dipole-dipole potential U_D and introduces the characteristic features of superfluid phases. Below we concentrate on the properties of the spin-precessing modes of ^{3}He-B. For the B phase

$$U_D=\frac{2}{15}\chi_B\left(\frac{\Omega_B}{g}\right)^2\left(\mathrm{Tr}\,\hat{R}-\frac{1}{2}\right)^2, \qquad (2)$$

where Ω_B is the frequency of the longitudinal NMR and the orthogonal matrix $\hat{R}$ is the B-phase order parameter describing $3D$ relative rotations of the spin and orbital degrees of freedom. Introducing the triples of Euler angles $(\alpha_S,\beta_S,\gamma_S)$ and $(\alpha_L,\beta_L,\gamma_L)$ describing $3D$ rotations in the spin and orbital spaces, respectively, it can be shown that

$$\begin{aligned}\mathrm{Tr}\,\hat{R}=&\,s_z l_z+\frac{1}{2}(1+s_z)(1+l_z)\cos(\alpha+\gamma)\\&+\frac{1}{2}(1-s_z)(1-l_z)\cos(\alpha-\gamma)\\&+\sqrt{(1-s_z^2)(1-l_z^2)}(\cos\alpha+\cos\gamma),\end{aligned} \qquad (3)$$

where $s_z=\cos\beta_S$, $l_z=\cos\beta_L$, $\alpha=\alpha_S-\alpha_L$ and $\gamma=\gamma_S-\gamma_L$.

In the strong magnetic field case ($\omega_0\gg\Omega_B$) the spin dynamics is governed by a set of the Hamiltonian equations for two pairs of the conjugate variables (S_z,α) and (S,γ) with S being the magnitude of $\mathbf{S}$. According to Eq. (1) this set of equations reads as

$$\dot{S}_z=-\frac{\partial U_D}{\partial\alpha},\quad \dot{\alpha}=-\omega_0+\frac{\partial U_D}{\partial S_z}; \qquad (4)$$

$$\dot{S}=-\frac{\partial U_D}{\partial\gamma},\quad \dot{\gamma}=(S/S_0)\omega_0+\frac{\partial U_D}{\partial S}; \qquad (5)$$

where $S_0=\chi\omega_0/g^2$ (the magnitude of equilibrium magnetization $M_0=gS_0$).

The angle α is a fast variable in the sense that $|\dot{\alpha}|\gg\Omega_B$ and the same is true for γ (except the case with $S\ll S_0$ which we do not consider here). On the other hand, the combination $\Phi=\alpha+(S_0/S)\gamma$ is a slow variable. The significance of this resonance becomes clear when considering the structure of the dipole-dipole potential U_D. Inserting Eq. (3) into Eq. (2) we conclude that

$$U_D/S_0\omega_0=\varepsilon f(s_z,l_z,\alpha,\gamma)=\varepsilon\sum_{kl} f_{kl}(s_z,l_z)e^{i(k\alpha+l\gamma)}, \qquad (6)$$

where $\varepsilon\propto(\Omega_B/\omega_0)^2$.

Assuming that $\varepsilon=1/10(\Omega_B/\omega_0)^2$, it follows from Eqs. (2) and (3) that $f_{kl}=f_{lk}=f_{-l-k}$ for the B phase and the non-zero coefficients are given as:

$$f_{00}=1+2s_z^2l_z^2+(1-s_z^2)(1-l_z^2),$$

$$f_{10}=2s_zl_z\sqrt{1-s_z^2}\sqrt{1-l_z^2},$$

 © 1999 American Institute of Physics

$$f_{20}=\frac{1}{2}(1-s_z^2)(1-l_z^2),$$

$$f_{1\pm1}=\frac{1}{3}(1\pm s_z)(1\pm l_z)(1\mp 2s_z)(1\mp 2l_z), \tag{7}$$

$$f_{1\pm2}=\frac{1}{3}(1\pm s_z)(1\pm l_z)\sqrt{1-s_z^2}\sqrt{1-l_z^2},$$

$$f_{2\pm2}=\frac{1}{12}(1\pm s_z)^2(1\pm l_z)^2.$$

It is easily verified that at $l_z=1$, which corresponds to an equilibrium orbital states of ^{3}He-B (the so called Leggett configuration), f_{kl} are nonzero only for $k=l=0,\pm1,\pm2$. This means that for an orbital state with $l_z=1$ the dipole-dipole potential depends only on the combination $\Phi=\alpha+\gamma$ and, as we have seen, it is a slow variable at $S\simeq S_0$. This well known resonance is operative even at $l_z\neq1$ because all other linear combinations of α and γ are fast variables at $S\simeq S_0$ for the strong-field case ($\varepsilon\ll1$) and they disappear on the average. The conventional spin dynamics at $S\simeq S_0$ has been explored thoroughly in the past.[1,2]

On the other hand, at $l_z\neq1$ (non-Leggett orbital configuration) an unconventional spin dynamics is also possible since a new resonance regime can develop. Indeed, an inspection of the coefficients f_{kl} shows that a new combination $\Phi=\alpha+2\gamma$ appears in the expression for U_D which turns out to be a slow variable at a special value of $S=S_0/2$ (another resonance at $S=2S_0$ is also possible). This has been noticed in Ref. 3 (for more details see Ref. 4) and the corresponding experimental investigations were undertaken recently.[5,6]

The stationary solutions for s_z, l_z and Φ corresponding to the particular coherent spin-precessing modes at the fixed resonance values of S are found by minimizing the time-averaged dipole-dipole potential $\overline{U_D}$ (the Van der Pol picture). On the other hand, in order to explore the time evolution of S starting from some initial value, and to find out the routes leading to the mentioned resonance regimes, a full description of the spin dynamics, including the dissipation effects, is necessary. In what follows a theoretical background for the analysis of the relaxation processes in the spin dynamics of ^{3}He-B will be presented. It is a direct generalization of the approach adopted in Ref. 7 and allows us to consider the case of the non-Leggett orbital configurations. It should be noted that using the computer simulation programs (like a package elaborated by A. A. Leman) the spin dynamics including the Leggett–Takagi dissipation mechanism can be explored quite efficiently. At the same time, an analytical approach has the merits of its own and gives, as we shall see, a transparent insight into the essence of the problem.

2. A standard procedure of incorporating the relaxation processes into the homogeneous spin dynamics is based on the introduction of a dissipative function

$$\mathcal{F}_d=\frac{1}{2}\kappa(\dot{\mathbf{S}}-g\mathbf{S}\times\mathbf{H}_0)^2=\frac{1}{2}\kappa\left[\frac{S^2}{S^2-S_z^2}\left(\dot{S}^2+\dot{S}_z^2-2\frac{S_z}{S}\dot{S}\dot{S}_z\right)+(S^2-S_z^2)(\dot{\alpha}+\omega_0)^2\right], \tag{8}$$

where κ will be considered as a phenomenological coefficient.[7]

During the time interval δt the energy of a dissipative system changes by

$$\delta E=-2\mathcal{F}_d\delta t=\kappa\left[\frac{S^2}{S^2-S_z^2}\left(\frac{\partial U_D}{\partial\gamma}-\frac{S_z}{S}\frac{\partial U_D}{\partial\alpha}\right)\delta S+\frac{S^2}{S^2-S_z^2}\left(\frac{\partial U_D}{\partial\alpha}-\frac{S_z}{S}\frac{\partial U_D}{\partial\gamma}\right)\delta S_z+(S^2-S_z^2)\frac{1}{\omega_0}\left(\frac{\partial U_D}{\partial S_z}\right)^2\delta\alpha\right]. \tag{9}$$

This last relation allows to pass from the Hamiltonian Eqs. (4) and (5) to a set of equations for the spin dynamics with dissipation (from now on the time is measured in units of $1/\omega_0$ and (S_z,S) in units of S_0):

$$\dot{S}_z=\varepsilon X_z,\quad \dot{\alpha}=-1+\varepsilon Y_\alpha, \tag{10}$$

$$\dot{S}=\varepsilon X_S,\quad \dot{\gamma}=S+\varepsilon Y_\alpha, \tag{11}$$

where

$$X_z(S_z,S,\alpha,\gamma|\varepsilon)=-\frac{\partial f}{\partial\alpha}+\varepsilon\kappa(S^2-S_z^2)\left(\frac{\partial f}{\partial S_z}\right)^2, \tag{12}$$

$$X_S(S_z,S,\alpha,\gamma)=-\frac{\partial f}{\partial\gamma}, \tag{13}$$

$$Y_\alpha(S_z,S,\alpha,\gamma)=\frac{\partial f}{\partial S_z}-\frac{\kappa S^2}{S^2-S_z^2}\left(\frac{\partial f}{\partial\alpha}-\frac{S_z}{S}\frac{\partial f}{\partial\gamma}\right), \tag{14}$$

$$Y_\gamma(S_z,S,\alpha,\gamma)=\frac{\partial f}{\partial S}-\frac{\kappa S^2}{S^2-S_z^2}\left(\frac{\partial f}{\partial\gamma}-\frac{S_z}{S}\frac{\partial f}{\partial\alpha}\right). \tag{15}$$

Since $\varepsilon\ll1$ a well-known procedure of separating of the slow (S_z,S) and the fast (α,γ) motions can be applied[8] to solve Eqs. (10) and (11). Although the main points are described in Ref. 7, here we show the principle steps for completeness.

Passing to the new variables $\overline{S_z}$, $\overline{S}$, $\overline{\alpha}$ and $\overline{\gamma}$ according to the prescription

$$\begin{aligned}
S_z&=\overline{S_z}+\varepsilon u_z+\varepsilon^2 v_z+\ldots,\\
S&=\overline{S}+\varepsilon u_S+\varepsilon^2 v_S+\ldots,\\
\alpha&=\overline{\alpha}+\varepsilon u_\alpha+\varepsilon^2 v_\alpha+\ldots,\\
\gamma&=\overline{\gamma}+\varepsilon u_\gamma+\varepsilon^2 v_\gamma+\ldots,
\end{aligned} \tag{16}$$

where $u_i=u_i(\overline{S_z},\overline{S},\overline{\alpha},\overline{\gamma})$ and $v_i=v_i(\overline{S_z},\overline{S},\overline{\alpha},\overline{\gamma})$, and assuming that the new variables are subject to a set of equations

$$\begin{aligned}
\dot{\overline{S_z}}&=\varepsilon A_z+\varepsilon^2 B_z+\ldots,\\
\dot{\overline{S}}&=\varepsilon A_S+\varepsilon^2 B_S+\ldots,\\
\dot{\overline{\alpha}}&=-1+\varepsilon A_\alpha+\varepsilon^2 B_\alpha+\ldots,\\
\dot{\overline{\gamma}}&=\overline{S}+\varepsilon A_\gamma+\varepsilon^2 B_\gamma+\ldots,
\end{aligned} \tag{17}$$

with $A_i=A_i(\overline{S_z},\overline{S})$ and $B_i=B_i(\overline{S_z},\overline{S})$, we arrive at the equations for yet unknown functions u_i, and v_i:

$$-\frac{\partial u_i}{\partial\overline{\alpha}}+\overline{S}\frac{\partial u_i}{\partial\overline{\gamma}}=g_i-A_i, \tag{18}$$

$$-\frac{\partial v_i}{\partial\overline{\alpha}}+\overline{S}\frac{\partial v_i}{\partial\overline{\gamma}}=h_i-B_i. \tag{19}$$

In Eq. (18), in describing the first order effects in ε, the functions g_i are given as follows:

$$\begin{aligned} g_z&=X_z(\overline{S_z},\overline{S},\overline{\alpha},\overline{\gamma}|0),\\ g_S&=X_S(\overline{S_z},\overline{S},\overline{\alpha},\overline{\gamma}),\\ g_\alpha&=Y_\alpha(\overline{S_z},\overline{S},\overline{\alpha},\overline{\gamma}),\\ g_\gamma&=X_\gamma(\overline{S_z},\overline{S},\overline{\alpha},\overline{\gamma})+u_S(\overline{S_z},\overline{S},\overline{\alpha},\overline{\gamma}). \end{aligned} \tag{20}$$

The second order effects in ε are governed by Eq. (19) and the functions h_i contain derivatives of X_i and Y_i, with respect to $\overline{S_z},\overline{S},\overline{\alpha},\overline{\gamma}$ and ε (calculated at $\varepsilon=0$). In particular

$$\begin{aligned} h_z=&\frac{\partial X_z}{\partial\overline{S_z}}u_z+\frac{\partial X_z}{\partial\overline{S}}u_S+\frac{\partial X_z}{\partial\overline{\alpha}}u_\alpha+\frac{\partial X_z}{\partial\overline{\gamma}}u_\gamma+\frac{\partial X_z}{\partial\varepsilon}u_\varepsilon\\ &-\left(A_z\frac{\partial u_z}{\partial\overline{S_z}}+A_S\frac{\partial u_z}{\partial\overline{S}}+A_\alpha\frac{\partial u_z}{\partial\overline{\alpha}}+A_\gamma\frac{\partial u_z}{\partial\overline{\gamma}}\right). \end{aligned} \tag{21}$$

The other h_i have the similar structure. According to Eqs. (12)–(15) and (6) the functions g_i are periodic in α and γ:

$$g_i=\sum_{kl}{}'\, g_{kl}^{(i)}(\overline{S_z},\overline{S})e^{i(k\overline{\alpha}+l\overline{\gamma})}, \tag{22}$$

and the bounded solutions of Eq. (18) are given as

$$\begin{aligned} u_i&=i\sum_{kl}{}'\,\frac{g_{kl}^{(i)}}{k-\overline{S}l}e^{i(k\overline{\alpha}+l\overline{\gamma})},\\ A_i&=g_{00}^{(i)}(\overline{S_z},\overline{S}), \end{aligned} \tag{23}$$

where a prime in the summation over k and l excludes the contribution of $k=l=0$. In a similar way can be found the solutions of Eq. (19).

Performing the above-mentioned procedure it can be established that

$$\begin{aligned} &A_z=A_S=0,\quad A_\alpha=\frac{\partial f_{00}}{\partial\overline{S_z}},\quad A_\gamma=\frac{\partial f_{00}}{\partial\overline{S}},\\ &B_z=h_{00}^{(z)},\quad B_S=h_{00}^{(S)}. \end{aligned} \tag{24}$$

After having calculated $h_{00}^{(S)}$ it can be shown that

$$\dot{\overline{S}}=\varepsilon^2B_S=\frac{\varepsilon^2\kappa}{1-s_z^2}\sum_{kl}\frac{l}{k-\overline{S}l}(k^2+l^2-2s_zkl)f_{kl}^2, \tag{25}$$

where only the dissipative contribution to B_S is retained. In a similar way it is concluded that

$$\begin{aligned} \dot{\overline{S_z}}=\varepsilon^2B_z=&\frac{\varepsilon^2\kappa}{1-s_z^2}\sum_{kl}\frac{k}{k-\overline{S}l}(k^2+l^2-2s_zkl)f_{kl}^2\\ &+\varepsilon^2\kappa(1-s_z^2)\sum_{kl}\left(\frac{\partial f_{kl}}{\partial s_z}\right)^2. \end{aligned} \tag{26}$$

In Ref. 7 the set of Eqs. (25) and (26) has been used to explore the dissipative processes in the superfluid A and B phases for the special orbital states, the Leggett configurations. For ^{3}He-B, which we consider here, this corresponds to $l_z=1$. At $l_z=1$ only the components with $l=k=\pm1,\pm2$ contribute to the r.h.s. of Eqs. (25) and (26) and, as mentioned in Ref. 7, irrespective of the initial conditions, $\overline{S}$ is attracted to the resonance value $\overline{S}=1$.

For a non-Leggett orbital configuration (with $l_z\neq1$) the new possibilities appear. For the general spin-orbital configurations Eq. (25) can be put in the following form:

$$\begin{aligned} \dot{\overline{S}}=&-\frac{2\varepsilon^2\kappa}{1-s_z^2}\left[\frac{1}{\overline{S}}(f_{10}^2+4f_{20}^2)+2\frac{1-s_z}{\overline{S}-1}(f_{11}^2+4f_{22}^2)\right.\\ &+\left(\frac{5-4s_z}{\overline{S}-1/2}+\frac{5-4s_z}{\overline{S}-2}\right)f_{12}^2+2\frac{1+s_z}{\overline{S}+1}(f_{1-1}^2+4f_{2-2}^2)\\ &\left.+\left(\frac{5+4s_z}{\overline{S}+1/2}+\frac{5+4s_z}{\overline{S}+2}\right)f_{1-2}^2\right]. \end{aligned} \tag{27}$$

Here (and below) $s_z=\overline{S_z}/\overline{S}$. By using Eq. (26) it can be shown that

$$\begin{aligned} \dot{\overline{S_z}}=\varepsilon^2\kappa\left\{\frac{1}{1-s_z^2}\right.&\left[2(f_{10}^2+4f_{20}^2)-4\frac{1-s_z}{\overline{S}-1}(f_{11}^2+4f_{22}^2)\right.\\ &-\left(\frac{5-4s_z}{\overline{S}-1/2}+4\frac{5-4s_z}{\overline{S}-2}\right)f_{12}^2+4\frac{1+s_z}{\overline{S}+1}(f_{1-1}^2+4f_{2-2}^2)\\ &\left.\left.+\left(\frac{5+4s_z}{\overline{S}+1/2}+4\frac{5+4s_z}{\overline{S}+2}\right)f_{1-2}^2\right]+(1-s_z^2)\sum_{kl}\left(\frac{\partial f_{kl}}{\partial s_z}\right)^2\right\}. \end{aligned} \tag{28}$$

From the set of Eqs. (27) and (28) it is seen that, along with a conventional resonance at $\overline{S}=1$, the new resonances at $\overline{S}=(1/2,2)$ intervene for the case with $f_{12}\neq0$. It should be kept in mind that, according to their derivation procedure, Eqs. (27) and (28) are applicable not too close to the mentioned resonance values of S, but the general tendencies of the various relaxation scenarios, leading to the attractors at $\overline{S}=(1,1/2,2)$, can still be established.

As an illustration of the content of Eq. (27) we shall consider a non-Leggett orbital state with $l_z=0$. One can fix this orbital configuration by applying sufficiently strong superfluid counterflow in the transverse direction with respect to the magnetic field. Such a possibility is realized, in particular, in the rotating cryostat in the vortex-free region.[9]

From Eq. (27) it is found that at $l_z=0$ and $s_z \to 1\overline{S}$ is evolving according to the equation

$$\dot{\overline{S}} = -\frac{32}{9}\varepsilon^2 \kappa \frac{(\overline{S}-S_+)(\overline{S}-S_-)}{(\overline{S}-1)(\overline{S}-1/2)(\overline{S}-2)}, \tag{29}$$

where $S_\pm = (19 \pm \sqrt{73})/16$. From Eq. (29) it is immediately concluded that $\overline{S}$ is tending to its resonance value $\overline{S}=1$ if initially $\overline{S}$ is confined to an interval $S_- < \overline{S} < S_+$. On the other hand, $\overline{S}$ is attracted to 1/2 if $\overline{S} < S_-$, and $\overline{S}$ approaches 2 for $\overline{S} > S_+$. These conclusions, although rather qualitative, contain interesting hints. More detailed analysis of the solutions of the set of Eqs. (27) and (28) will be given elsewhere.

ACKNOWLEDGMENTS

This work was supported by the Grant No. 2.16 of the Georgian Academy of Sciences.

[1] Yu. A. Bunkov, in *Progress in Low Temperature Physics*, Vol. 24, W. P. Halperia (Ed.), Elsevier Sciences (1995), p. 69.
[2] I. A. Fomin, in *Modern Problems in Condensed Matter Sciences*, Vol. 26: Helium Three, W. P. Helperin and L. P. Pitaevskii (eds.), North Holland, Amsterdam (1990), p. 610.
[3] G. Kharadze and G. Vachnadze, Pis'ma Zh. Éksp. Teor. Fiz. **56**, 474 (1992) [JETP Lett. **56**, 458 (1992)].
[4] G. Kharadze, N. Suramlishvill, and G. Vachnadze, J. Low Temp. Phys. **110**, 851 (1998).
[5] V. V. Dmitriev, I. V. Kosarev, M. Krusius, D. M. Ponarin, V. M. H. Ruutu, and G. E. Volovik, Phys. Rev. Lett. **78**, 86 (1997).
[6] V. B. Eltsov, V. V. Dmitriev, M. Krusius, J. J. Ruohio, and G. E. Volovik, J. Low Temp. Phys. **113**, 645 (1998).
[7] I. A. Fomin, Zh. Eksp. Teor. Fiz. **50**, 278 (1979) [Sov. Phys. JETP **50**, 144 (1979)].
[8] N. N. Moiseev, *Asymptotic Methods in Nonlinear Mechanics*, Nauka, Moscow, (1981) (in Russian).
[9] V. V. Dmitriev, V. B. Eltsov, M. Krusius, J. J. Ruohio, and G. E. Volovik, cond-mat/9805119 (1998).

This article was published in English in the original Russian journal. It was edited by R. T. Beyer.

SUPERCONDUCTIVITY, HIGH-TEMPERATURE SUPERCONDUCTIVITY

De Haas–van Alphen effect and superconductivity

L. P. Gor'kov

*National High Magnetic Field Laboratory, Florida State University, 1800 E. Paul Dirac Dr., Tallahassee, FL 32310; L. D. Landau Institute for Theoretical Physics, Russian Academy of Sciences, 117334 Moscow, Russia**

(Submitted March 17, 1999)
Fiz. Nizk. Temp. **25**, 820–823 (August–September 1999)

The problem of the robust de Haas–van Alphen oscillations seen experimentally in mixed superconducting state is discussed. The new threshold mechanism is suggested to explain persistence of the quantum oscillations deep in the superconducting state. © *1999 American Institute of Physics.* [S1063-777X(99)00508-3]

I am very glad to be able to provide a paper for the issue dedicated to the memory of Professor B. I. Verkin. His own contributions and his efforts to promote condensed matter research in Kharkov to new highs were, indeed, impressive and successful. Currently, the Institute for Physics and Technology at Low Temperatures (FTINT) which he had helped to organize from scratch enjoys a reputation of one of the main scientific centers in the field.

The Kharkov School is famous for its pioneering studies of normal metals' properties by various means and tools. Thus, among others, observations of quantum oscillations are the most direct assessment of electronic spectra in metals via the famous Lifshitz-Kosevich formula for the de Haas–van Alphen (dHvA) effect. Fermi surfaces (FS) of countless metals and intermetallic compounds have been determined and classified with the use of this method during the last flew decades.

It is worthwhile to emphasize that the very concept of FS is at the core of the Landau Fermi-liquid (FL) theory. With the remarkable recent progress in synthesis of new materials, many of which reveal unexpected peculiarities in their physical properties, the question arose whether the Landau FL theory remains applicable in spite of the observed complications, or electron-electron interactions, being strong enough, may breach the FL-theory. Studies of the dHvA effect would provide the most direct test of the FL-assertions.

Below we address the issue of existence of the dHvA oscillations in the superconducting state. Whatever is the mechanism of interactions causing superconductivity, the latter may usually be well understood in terms of the BCS microscopic theory. The truth is that it is far from being clear whether the BCS scheme remains applicable, say, in cuprates, heavy fermions (HF), or borocarbides, to mention a few. However, the BCS theory is based upon the FL concept. If the dHvA-effect in superconducting state in these materials (see below) could be described in frameworks of the BCS scheme, it would become an indirect proof of FL for these substances.

The dHvA effect in normal metals is nothing but the WKB phenomena. An electron possessing large momentum, $p_F \sim a^{-1}$, its levels in magnetic field are equidistant near the chemical potential, μ ($\mu \equiv E_F$, the Fermi energy):

$$E_N = \omega_c \left(N + \frac{1}{2} \right) \tag{1}$$

where ω_c, the cyclotron frequency, is the characteristic of an effective electron mass in case of some arbitrary FS. A minor variation in the field, B, such that $\Delta B/B \sim \omega_c/E_F \ll 1$, may push a level across the chemical potential causing abrupt change in levels' occupation numbers and, hence, the step-like change in magnetization. (For simplicity we consider a two-dimensional (2D) case where this mechanism becomes most transparent). In the quasiclassical approximation an electron performs a closed-orbit motion (circular orbits, in an isotropic model), which may be equally well described as the Larmor motion in real space, or as the electron motion in the momentum representation along a closed orbit encircling a FS. Equation (1) is then nothing but the result of quantization in accordance with the Bohr correspondence principle.

The dHvA effect in superconducting state is observed in the second-type superconductors when the magnetic field is gradually decreased below the upper critical field, H_{c2}. At $B < H_{c2}$, the mixed state superconductivity[1] sets in. The magnetic field in the sample remains practically homogeneous, $B = \overline{B}$, while the superconducting order parameter periodically varies in space. At $B \ll H_{c2}$ the gap structure corresponds to a lattice of vortices (intervortex distance, d, being larger than ξ_0, the coherence length which defines the vortex core size) separated by the ''bulk'' where the amplitude of the gap is saturated to a constant, Δ_B:

$$\Delta(\mathbf{r},\mathbf{p}) \simeq \Delta_B(\mathbf{p}) \exp\{i\varphi(\mathbf{r})\} \tag{2}$$

[$\Delta_B(\mathbf{p})$ depends on $\overline{B}$, although in order of magnitude it is close to the value of the gap in the absence of field].

A challenge, and a theoretical puzzle, is that the dHvA effect is observed in the well-developed superconducting state, down to $B \sim 0.2 H_{c2}$. This fact apparently contradicts our intuitive notion of the dHvA effect resulting from the

 © 1999 American Institute of Physics

mechanism of crossing the chemical potential by an energy level. Indeed, although vortex cores produce some low energy excitation, these are known to be localized inside the core. The ''bulk'' of the superconductor, at distances $r \sim d \gg \xi_0$ from the core is fully ''gapped,'' according to Eq. (2). The chemical potential being positioned in the middle of the gap, levels on the two branches of superconducting excitations (even in the presence of the field, $\overline{B}$) would never cross the chemical potential, in particular, because

$$\omega_c \ll \Delta,\ T_c\,. \tag{3}$$

Equation (3) is a strong inequality, as follows from the microscopic theory, and may be rewritten in the form

$$\frac{B}{H_{c2}(p_F \xi_0)} \ll 1. \tag{4}$$

Therefore it is commonly accepted that well below H_{c2} an effective ''Dingle'' temperature

$$T^* \sim \Delta \tag{5}$$

would result in the fast decay of the dHvA signal. Experiments[2–4] strongly contradict the above arguments.

The field range $B \sim 0.2 H_{c2}$ which has been reached experimentally in Refs. 3 and 4 presents considerable difficulties for a theoretical analysis because the vortex lines are not yet well defined ($d \gtrsim \xi_0$). However, it is natural to wonder about whether a specific and new mechanism lies behind the observed phenomenon of slow decay of the dHvA effect below H_{c2}, and whether such a mechanism may be consistent with the microscopic theory. In Refs. 5 and 7 we have chosen to address the issue in the limit of:

$$B \ll H_{c2};\ \delta_L \gg d \gg \xi_0 \tag{6}$$

to search for a new mechanism which may provide not so severe limitations on the dHvA amplitude, as is given by Eq. (5). Such mechanism does exist, indeed, and is explained below in some simple physical terms. A rigorous proof and the mathematical details can be found in Refs. 5 and 7.

At first, it is worth our while to discuss briefly a tempting guess that the persistence of the dHvA effect below H_{c2} may be caused by an unconventional symmetry of the superconducting order parameter. Once we consider a 2D case (a cylindrical FS), a natural suggestion is a ''*d*-wave'' pairing often assumed to be the ground state in high T_c cuprates. In this model the gap disappears at the four points on the Fermi surface where the electron-like and the hole-like branches for excitations merge. It turned out,[5] however, that although a level always exists in the presence of the magnetic field in the very vicinity of the chemical potential, its position is *fixed*. It is not changed by variations of the magnetic field. In other words, although the gapless ''*d*-wave'' superconductivity significantly changes the structure of levels, when compared to the ''*s*-wave'' pairing, the mechanism of crossing the chemical potential by a level at a variation of the magnetic field is again excluded.

The true mechanism which causes the dHvA oscillations in the superconducting state, at least in the limit $B \ll H_{c2}$, Eq. (6), may be called the ''threshold'' mechanism (see Refs. 6 and 7). There are two features in the superconducting energy spectrum that are responsible for its origin: an anisotropy of the superconducting order parameter, $\Delta(\mathbf{p})$, and the Doppler shift of the excitation energy by supercurrents flowing in the periodic vortex lattice, $\mathbf{v}_s(\mathbf{r})$. Consider them first in the absence of quantizing effects of the magnetic field.

If the gap, $\Delta(\mathbf{p})$, depends on the position of $\mathbf{p}$ along the Fermi surface, so that $\Delta_{\min}$ and $\Delta_{\max}$ are its minimal and maximum values, correspondingly, there are no excitations with the energy less than $\Delta_{\min}$. Excitations with an energy $\varepsilon(\mathbf{p}) > \Delta_{\max}$ may propagate freely to infinity in the real space. However, excitations with an energy such that $\Delta_{\min} < \varepsilon(\mathbf{p}) < \Delta_{\max}$ can perform an infinite motion only if the momentum lies in the proper restricted angular cone.

Recall that excitations have no definite charges in the BCS-theory. Instead, there are two branches, one ''electron-like'' and one ''hole-like.'' The meaning of these definitions is that the full electron charge is restored only far enough from the Fermi surface, while, say, the ''electron-like'' character of an excitation gradually diminishes by degrees as its energy tends to $\Delta_{\min}$.

An electron in the normal state placed in the magnetic field performs the motion along a closed orbit under the Lorentz force:

$$\dot{p} = \frac{e}{c}[\mathbf{v}_F(\mathbf{p}) \times \mathbf{B}]. \tag{7}$$

Although Eq. (7) is not applicable for excitations in a superconductor since the excitation's charge is not fixed, as explained above, it helps to explain the origin of the ''threshold'' mechanism in a qualitative way. In the absence of the magnetic field excitations (the wave packets) move along straight lines, the momentum being preserved. The magnetic field bends the trajectories. While at an energy $\Delta_{\max}$ the excitation still can perform a closed motion (along the large Larmor-like orbit, $R_L \sim v_F/\omega_c$, in the real space, or along a trajectory encircling the Fermi surface, in the momentum space), this is not true for excitations with an energy less than $\Delta_{\max}$. Changing the direction of momentum in the magnetic field brings it to the boundary of the angular cone beyond which extended motion of the wave packet is impossible. The ''electron-like'' character gets lost, and the excitation being rejected back (in the direction along FS), starts its motion as a ''hole-like'' particle. This process repeats on the other side of the allowed directions. Excitations with energies between $\Delta_{\min}$ and $\Delta_{\max}$ will form ''localized'' states. Thus, there exists the energy threshold, $\varepsilon_{\rm th} = \Delta_{\max}$, which separates the localized states and the ''extended'' states. For the latter an excitation behaves basically in the same way as ordinary electrons (except, of course, that their effective charge at $\varepsilon \gtrsim \varepsilon_{\rm th}$ is reduced from the bare electron charge and depends on energy). At the field variation the ''extended'' energy levels cross the threshold, becoming the ''localized'' ones.

The ''threshold'' effect caused by the anisotropy of the order parameter only, would lead to a significant dHvA effect even in the extreme case of Eq. (6):[5]

$$M^s_{\rm osc} \sim (\omega_c/\Delta)^{1/2} M^N_{\rm osc}\,. \tag{8}$$

However, so far we have been neglecting the contribution from the Doppler effect. The Doppler shift in energy of excitations

$$\varepsilon(\mathbf{p}) \to E(\mathbf{p}) = \varepsilon(\mathbf{p}) + \mathbf{p}\cdot\mathbf{v}_s(\mathbf{r}) \tag{9}$$

is due to the presence of the periodic supercurrents which flow even in the ''bulk,'' i.e., away from the vortex cores. The second term in (9) is smaller than the scale of the gap, $\Delta_{\min} \sim \Delta_{\max}$. Its role is two-fold. On the one side, the mechanism (9) may itself be the source of a threshold between ''localized'' and ''extended'' states. Indeed, consider a Larmor trajectory. Its radius, $R_L \sim v_F/\omega_c$, is much larger than d, the vortex lattice periodicity. Therefore, the quasiclassical packet may be thought in the first approximation as moving locally along a straight line, with some $\mathbf{p}$. Along that line $\mathbf{v}_s(\mathbf{r})$ varies but is limited in its value. Therefore, at $E < \Delta_{\max} + |\mathbf{p}\cdot\mathbf{v}_s(\mathbf{r})|_{\max}$, an excitation is bound again. Such a threshold effect exists even if the isotropic gap were chosen.[7]

Unfortunately, the mechanism (9) also plays a destructive role on the dHvA effect. To understand this, recall that the gap anisotropy had led to the threshold position exactly at $\varepsilon = \Delta_{\max}$. The term $\mathbf{p}\cdot\mathbf{v}_s(\mathbf{r})$, although being small itself in the range of fields given by Eq. (6), significantly smears out the sharpness of this threshold due to spatial distribution of the superfluid velocity, $\mathbf{v}_s(\mathbf{r})$. As a result, the amplitude of the dHvA effect given by Eq. (8), suffers a sharp decrease, becoming again exponentially small. However, the value of an effective Dingle temperature turns out to be considerably reduced compared to Eq. (5):

$$T^*_{\text{eff}} \sim \Delta(\xi_0/d) \ll \Delta. \tag{10}$$

Using other language,[5–7] the destructive effect of the Doppler shift may be interpreted as due to scattering of an electron moving along the Larmor orbit by the flux lines of the vortex lattice.

Thus, it is shown that, at least in the regime of Eq. (6), there exists a specific new mechanism of the dHvA oscillations in the developed superconducting mixed state that consists of crossing the threshold energy by levels of excitations in the magnetic field, while in the normal phase the oscillations originate from crossing the chemical potential. The regime of the magnetic field where $B \lesssim H_{c2}$ is more difficult for theoretical analysis. However, we expect that similar threshold phenomena should take place even at $d \sim \xi_0$ to explain the robustness of the dHvA effect in the superconducting state.

The work was supported by the NHMFL through NSF cooperative agreement No. DMR-9016241 and the State of Florida.

*E-mail: gorkov@magnet.fsu.edu

[1] A. A. Abrikosov, Zh. Éksp. Teor. Fiz. **32**, 1442 (1957) [Sov. Phys. JETP **5**, 1174 (1957)].
[2] R. Corcoran, N. Harrison, C. J. Haworth, S. M. Hayden, P. Messon, M. Springford, and P. J. van der Wel, Physica B **206–207**, 534 (1995).
[3] T. Terashima, C. Haworth, H. Takeya, S. Vji, H. Aoki, and K. Kadowaki, Phys. Rev. B **56**, 5120 (1997).
[4] Y. Onuki, in *Proceedings of the Conference SCES'98*, Paris (1998) (to be published).
[5] L. P. Gor'kov and J. R. Schrieffer, Phys. Rev. Lett. **36**, 3360 (1998).
[6] L. P. Gor'kov and V. Z. Kresin, Pis'ma Zh. Éksp. Teor Fiz. **67**, 934 (1998) [JETP Lett. **67**, 985 (1998)].
[7] L. P. Gor'kov and J. R. Schrieffer, Cond-Mat/9804328 (1998) (to be published).

This article was published in English in the original Russian journal. It was edited by R. T. Beyer.

Magnetic properties of conventional superconductors with columnar defects

Gregory M. Braverman

Max Planck Institute for Kernphysik-Heidelberg, Heidelberg, Germany

Sergey A. Gredeskul and Yshai Avishai

*Department of Physics, Ben Gurion University of the Negev, Beer Sheva, Israel**

(Submitted March 29, 1999)
Fiz. Nizk. Temp. **25**, 824–837 (August–September 1999)

Equilibrium vortex configuration in conventional type II superconductors containing short-range columnar defects is investigated theoretically. In the bulk superconductor near the upper critical field H_{c2} a single defect causes a strong local deformation of the vortex lattice which has C_3 or C_6 point symmetry. The vortices can collapse onto attractive defects, while in the case of repulsion the regions free of vortices appear near a defect. Increasing the applied magnetic field results in an abrupt change of the configuration of vortices related to the formation of multiquantum vortices and giving rise to reentering transitions between configurations with C_3 or C_6 symmetry. In the case of a small concentration of defects these transitions manifest themselves as jumps of magnetization and discontinuities of the magnetic susceptibility. Columnar defects also influence significantly the magnetic properties of a mesoscopic superconducting disc. They help the penetration of vortices into the sample, thereby decreasing the sample magnetization and reducing its upper critical field. Even the presence of weak defects splits a giant vortex state (usually appearing in a clean disc in the vicinity of the transition to a normal state) into a number of vortices with smaller topological charges. In a disc with a sufficient number of strong sufficently defects vortices are always placed onto defects. The presence of defects lead to the appearance of additional magnetization jumps related to the redistribution of vortices that are already present on the defects and not to the penetration of new vortices.
© *1999 American Institute of Physics.* [S1063-777X(99)00608-8]

1. INTRODUCTION

The magnetic properties of type II superconductors in mixed state or Shubnikov phase[1] are mostly determined by Abrikosov vortices penetrating into the sample.[2] A single vortex in a macroscopic superconductor with size much bigger than the penetration length $\lambda(T)$ carries the superconducting flux quantum $\phi_0=\pi\hbar c/e$. Repulsive interaction between vortices leads to formation of a triangular vortex lattice in a uniform sample. The lattice constant decreases with the increasing of a magnetic field and near the upper critical field H_{c2}; for an infinite sample it is of order $\xi(T)$ (the coherence length at temperature T). The magnetization density also decreases, and at H_{c2} it vanishes, that is, the superconductor becomes a normal state.

In a mesoscopic superconductor, with size much smaller than the penetration length, each vortex carries flux that is less than the flux quantum. In a uniform disc with size of order of a few coherence lengths in a strong field $H_{c2}<H<H_{c3}$, all the penetrated vortices are located at the disc center[3–5] forming so-called giant vortex. Penetration of the new vortices into the sample (as the applied magnetic field increases) manifests itself as a sequence of jumps on the magnetization curve. These jumps were observed experimentally[6] and have been discussed in a series of theoretical works.[4,5,7–9]

Various kinds of defects, such as dislocations, groups of point defects, twinning boundaries or regions with different superconducting properties can pin the vortices, deforming the vortex lattice and increasing the critical current. The most effective in this sense are the columnar defects appearing after the heavy ion irradiation of superconducting sample.[10] These defects serve as strong pinning centers, each of which is able to pin a single vortex as a whole. The radius of the columnar defect could be much more or less than the coherence length (long-range or short-range defects, respectively). Strong long-range columnar defects may lead to the formation of multiquantum vortices in high temperature superconductors.[11,12] Such vortices were observed experimentally on submicron artificial holes in mutlilayers Pb/Ge.[13] Columnar defects, essentially influence magnetic properties of the sample. In bulk high temperature superconductors they lead to important changes of the reversible magnetization curve.[14]

In this paper we show that short-range columnar defects strongly affect the properties of conventional type II superconductors. In a bulk superconductor near the upper critical field H_{c2} these defects cause a strong local deformation of the vortex lattice. This deformation has C_3 or C_6 point symmetry. If the vortex-defect interaction is attractive, the vortices can collapse onto defect, promoting the formation of a multiquantum vortex. Increasing the applied magnetic field results in reentering transitions between configurations with C_3 or C_6 symmetry. In the case of a small concentration

 © 1999 American Institute of Physics

of defects these transitions manifest themselves as jumps of magnetization and discontinuties of the magnetic susceptibility.

On the other hand, in a mesoscopic superconducting disc near the upper critical field H_{c3} even weak defects can destroy a giant vortex state splitting it into a number of vortices with smaller topological charges. Columnar defects should also change significantly the magnetic properties of mesoscopic superconductors. When the number of defects is of the order of the number of vortices one can expect that they will essentially suppress the magnetic response of the sample and reduce the critical field H_{c3}. If the number of defects is larger than the number of vortices and the defects are strong enough it seems plausible that all vortices could be pinned by defects. As the applied field changes the vortices can change their position on the defects. These rearrangements should lead to increasing of the number of mesoscopic jumps of the magnetization curve as compared with that of a clean sample. In the present paper we show that all these a scenarios really take place in small enough superconducting discs.

The paper is organized as follows. The rest of this section contains basic notations and description of the model. In section 2 we consider bulk superconductor with small concentration of columnar defects. The third section is devoted to the properties of mesoscopic superconducting disc containing a number of defects. In the last section the main results are summarized.

Consider a type II superconductor containing columnar defects. The sample is subject to an applied magnetic field, which is parallel to the defects. Therefore the problem becomes essentially a 2D one. Throughout the paper we use dimensionless variables, measuring magnetic field and vector potential in units of $H_{c2}=\Phi_0/2\pi\xi^2(T)$ and $\Phi_0/2\pi\xi(T)$, respectively. Any length appearing is measured in units of the temperature dependent coherence length $\xi(T)$. In these units the penetration length coincides with the Ginzburg–Landau parameter κ. Then the density of the thermodynamic potential and the order parameter are measured in units α_0^2/β and $\sqrt{-\alpha_0/\beta}$, where $\alpha_0<0$ and $\beta>0$ are the standard Ginzburg–Landau coefficients of the clean sample. In the presence of defects located at the points $\mathbf{r}_j$ ($\mathbf{r}$ being a 2D vector) the coefficient α should be modified:

$$\alpha(\mathbf{r})=\alpha_0[1-\delta\alpha(\mathbf{r})]$$

and depends on position as

$$\delta\alpha(\mathbf{r})=\sum_j \delta\alpha_1(\mathbf{r}-\mathbf{r}_j).$$

In what follows we use the simplest model

$$\delta\alpha_1(\mathbf{r})=\alpha_1\exp\left(-\frac{r^2}{2l_0^2}\right), \tag{1}$$

where l_0 is the dimensionless size of the defect. The modification term is simply related to the critical temperature change $\delta T_c(\mathbf{r})$ caused by defects:

$$\delta\alpha(\mathbf{r})=\frac{\delta T_c(\mathbf{r})}{T_c-T}, \tag{2}$$

where T_c is the critical temperature of a clean sample. Generally speaking, the third Ginzburg–Landau coefficient $\gamma(\gamma_0=1/2m)$ should also be modified as

$$\gamma(\mathbf{r})=\gamma_0[1+\delta\gamma(\mathbf{r})].$$

This modification term is described by analogous equations where α should be replaced by γ. For a fixed temperature close to the critical temperature T_c, the Ginzburg–Landau density g of the Gibbs potential[16] of such a superconductor is written as

$$g=-|\Psi|^2+\frac{1}{2}|\Psi|^4+\delta\gamma(\mathbf{r})|\mathbf{D}_-\Psi|^2+\delta\alpha(\mathbf{r})|\Psi|^2 + \kappa^2[\mathbf{b}(\mathbf{r})-\mathbf{h}]^2.$$

The gauge invariant gradient $\mathbf{D}_-$ is given by

$$\mathbf{D}_-\equiv -i\frac{\delta}{\delta\mathbf{r}}+\mathbf{a},$$

where $\mathbf{a}$ is the vector potential of the magnetic induction $\mathbf{b}(\mathbf{r})$.

2. BULK SUPERCONDUCTOR

Consider a superconductor containing columnar defects. In the linear approximation with respect to small concentration of defects the problem is effectively reduced to a single defect problem.[15] Near the upper critical field $h=1$ of a uniform bulk superconductor, the behavior of a superconductor can be derived within the lowest Landau level (LLL) approximation[17,18] by minimization of the density of the Gibbs potential

$$g_1(\mathbf{r};[\Psi])=(1-h)|\Psi|^2+\frac{1}{2}\left(1-\frac{1}{2\kappa^2}\right)|\Psi|^4 + \delta\alpha_1(\mathbf{r})|\Psi|^2+\delta\gamma_1(\mathbf{r})|\mathbf{D}_-^0\Psi|^2, \tag{3}$$

which depends only on the order parameter. Here h stands for a dimensionless external magnetic field and $\mathbf{D}_-^0$ is the gauge invariant gradient of the vector potential of the external field $\mathbf{H}$. In what follows we shall use the vector potential in the symmetric gauge.

To find the order parameter which realizes this minimum one can expand $\mathbf{\Psi}(\mathbf{r})$ in terms of Landau functions $L_m(\mathbf{r})$ of the lowest Landau level (m is the orbital momentum) substitute this expansion into Eq. (3) and find the expansion coefficients from the minimum condition.[19] Such an expansion serves as a good approximation and one can neglect the contribution of the highest Landau levels even at a field much less than upper critical field.[20,21] In the case of isotropic functions $\alpha_1(r)$ and $\gamma_1(r)$ the symmetry of the unperturbed Abrikosov lattice enables us to consider only two cases corresponding either to C_6 symmetry or to C_3 symmetry. The hexagonal symmetry corresponds to the distorted vortex lattice with one vortex placed on the defect. The trigonal one corresponds to the lattice with the defect located in the center of the vortex triangle. In the hexagonal case the trial order parameter can be written as

$$\Psi_6(\mathbf{r})=i\sum_{m=0}^{\infty}[\pi^{-1}M_6(m)+D(m)]L_m(\mathbf{r}). \tag{4}$$

Here $D(m)$ are the variational parameters which are to be found. The case when all D_m are equal to zero and only the coefficients $M_6(m)$ remain, corresponds to the order parameter $\Psi_6^A(\mathbf{r})$ which describes the Abrikosov lattice with one of the vortices located at the origin and one of the symmetry axes parallel to the x axis. The coefficients $M_6(m)$ are real and obey the selection rule[19] $m=6M+1$, $M=0,1,2,\ldots$. In the trigonal case the trial order parameter is written as

$$\Psi_3(\mathbf{r})=\sum_{m=0}^{\infty}i^{-m}[\pi^{-1}M_3(m)+D(m)]L_m(\mathbf{r}). \tag{5}$$

The case when all $D(m)$ are equal to zero, corresponds to the order parameter $\Psi_3^A(\mathbf{r})$ which describes the Abrikosov lattice whose origin coincides with the center of the vortex triangle and one of the symmetry axes is parallel to the x axis. The real coefficients $M_3(m)$ obey the selection rule $m=3M$, $M=0,1,2,\ldots$.

To obtain the lattice deformation caused by a single defect we have to find separately the extremal set of the variational parameters $D(m)$ within each of the two symmetry classes separately, and to choose the most preferable one from the two of them. Direct substitution of the test function $\mathbf{\Psi}(\mathbf{r})$ expressed in the forms (4) or (5) into the expression for the Gibbs potential density (3) and minimization with respect to the variational parameters $D(m)$ yields

$$\begin{aligned}
&\frac{2}{3^{1/4}\beta_A}\Bigg\{\sum_{l,m}\frac{(l+m)!}{2^{l+m+1}\sqrt{k!l!m!(l+m-k)!}}\\
&\times[\pi D(l)D(m)D^*(l+m-k)\\
&+M(l+m-k)D(l)D(m)]\\
&+\sum_{l,m}\frac{(k+m)!M(k-l+m)}{2^{k+m}\sqrt{k!l!m!(k-l+m)!}}D(l)D^*(m)\\
&+\sum_{l}\left[2l(k,l)D(l)+\sqrt{\frac{(k+l)!}{k!l!}}J(k+l)D^*(l)\right]\Bigg\}\\
&-D(k)+[\pi^{-1}M(k)+D(k)]\frac{\varphi^k}{(1+\varphi)^k}\\
&\times\{\alpha\varphi+\gamma\times[\varphi^2+k(1+2\varphi^2)]\}=0.
\end{aligned} \tag{6}$$

Here

$$\varphi=hl_0^2, \tag{7}$$

$\beta_a=1.1596$, α and β are properly scaled strengths of the defect:

$$\alpha=\frac{\tilde{\alpha}}{1-h},\ \gamma=\frac{\tilde{\gamma}h}{1-h}, \tag{8}$$

and

$$I(k,l)=\sum_m\frac{(l+m)!}{\sqrt{k!l!m!(l+m-k)!}}\frac{M(m)M(l+m-k)}{2^{l+m+1}\pi},$$

$$J(k)=\sum_m\left(\frac{k!}{m!(k-m)!}\right)^{1/2}\frac{M(m)M(k-m)}{2^{k+1}\pi}.$$

Equations (6) were obtained by Ovchinnikov[19] who used their linearized version for studying possible structural transitions. They are valid for both two symmetries C_6 and C_3. In each of these cases one should take into account the selection rules

$$\begin{aligned}
&M_3(m)=\delta_{m,3M}M_3(3M),\\
&M_6(m)=\delta_{m,6M+1}M_6(6M+1),\quad M=0,1,2,\ldots,
\end{aligned} \tag{9}$$

and use for $M_{3.6}$(m) their corresponding (real) values.[22] A quite natural assumption (which is verified below) is that the perturbed lattice conserves its initial symmetry. This means that the coefficients $\{D(m)\}$ obey the same selection rules that the initial coefficients $M(m)$ do. We use this assumption in our analysis below.

The qualitative information concerning the behavior of the coefficients $D(m)$ in a magnetic field can be obtained directly from Eqs. (6). Consider, for example, an attractive defect with $\alpha_1>0$ and $\gamma_1=0$. In this case, if one is not too close to the critical field $h=1$, the hexagonal symmetry should be realized and one starts from an analysis of the C_6 solutions. Due to selection rules, the first nonvanishing equation of the system (6) corresponds to the value $m=1$. This equation depends strongly on the (scaled) defect parameters α, γ and φ. But right in the next equation (which corresponds to the value $m=7$) this term is proportional to φ^7 and due to the short range nature of the defect ($\varphi\leqslant 1$) it is very small. Therefore all the higher order equations (6) with $m=13,19,\ldots$ are practically homogeneous. As a result, the solution of (6) will give nonzero coefficients $D(m)$ only for some small values of m. Thus the deformation of a vortex lattice happens mainly near the defect, at the distance of order of the Larmor radius $R_m\propto m_{\max}^{1/2}$ corresponding to the largest value of m such that $D(m_{\max})\neq 0$, while the rest of the lattice remains undistorted.

With raising of the applied magnetic field the effective coupling constants α and γ increase drastically [see Eq. (8)], while the parameter φ (7) does not undergo any visible change. This leads to increasing values of the higher coefficients $D(m)$ in the expansion (4) of the order parameter and as a result, to spreading of the deformation far from the defect. The further the growth of the magnetic field, the larger the effective coupling constants. This implies that the last term in Eq. (6) for $m=1$ becomes much larger than all preceding terms. In this case the solution is $D_6(1)=-\pi^{-1}M_6(1)$, i.e., the first expansion coefficient practically reaches its limiting value. This value completely compensates the contribution of the unperturbed Abrikosov lattice to the $m=1$ expansion coefficient in Eq. (4). In this region of fields the expansion (4) begins from $m=7$. The order parameter in the nearest vicinity of the defect becomes

$$\Psi\propto r^7e^{7i\theta}.$$

This means that the six nearest vortices have (almost) collapsed on the defect which pins the vortex containing seven flux quanta. One can see this effect in Fig. 1(a).

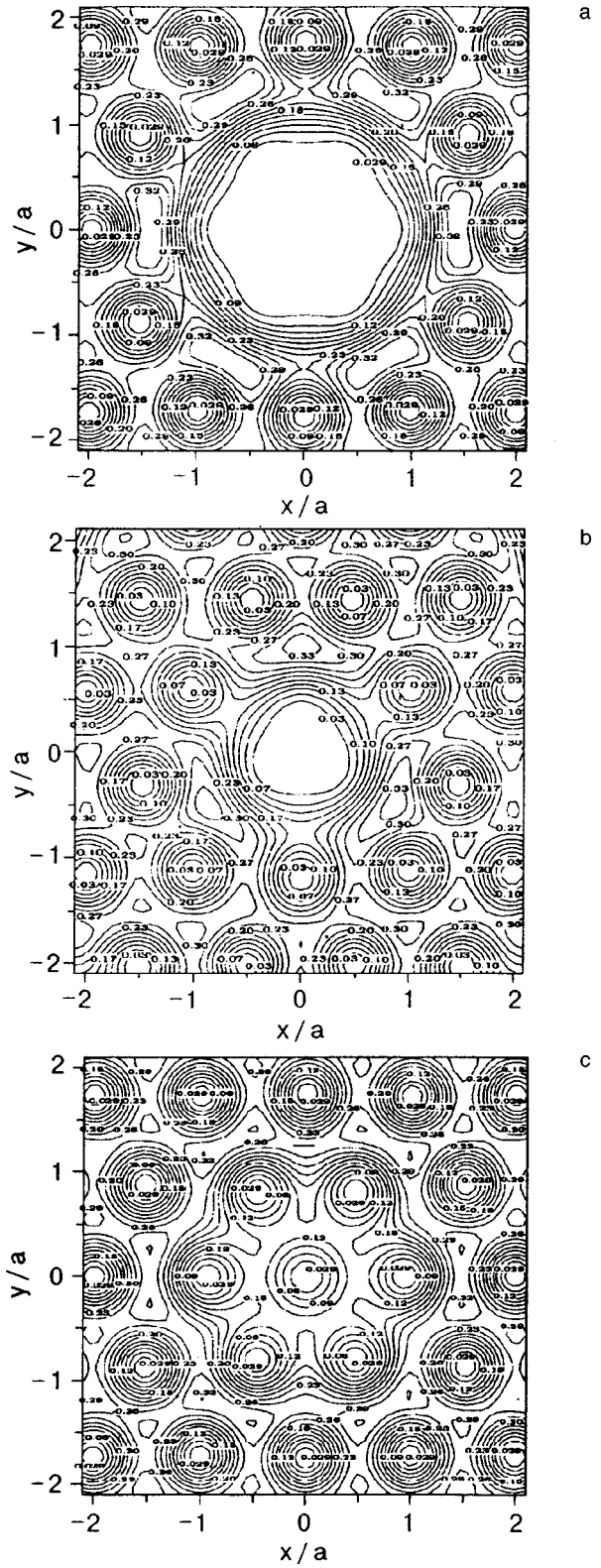

FIG. 1. The square modulus of the order parameter for $\tilde{\alpha}=0.5$, $\tilde{\gamma}=0$, $\varphi/h=0.5$ in the hexagonal case for the applied field $h\approx 0.93$. Seven vortices collapse on the defect (a) and for the applied field $h=0.85$. Attractive defect causes a comparatively weak vortex lattice deformation (b) the same in the trigonal case for the applied field $h=0.85$ and three vortices collapse on the defect (c).

With further increasing of the applied field the next coefficients $D_6(7)$, $D_6(13)$, and so on will reach their limiting compensation values $-\pi^{-1}M_6(7)$, $-\pi^{-1}M_6(13),\ldots$, and one could principally get a vortex containing thirteen, nineteen, etc., flux quanta. However, numerical calculations show that for a realistic field range (not extremely close to the upper critical field) only the first collapse can be realized.

A similar behavior of the expansion coefficients $\{D(m)\}$ takes place in the trigonal case C_3. Here in the case of attraction the coefficient $D_3(0)$ is the first one that reaches its compensation value $-\pi^{-1}M_3(0)$, which corresponds to the three vortices collapse on the defect. Such a configuration is displayed in Fig. 1(b). With increasing magnetic field one expects the appearance of six-, etc., multiquanta vortices. As in the previous case, numerical analysis shows that only the first collapse occurs in a realistic range of field.

Note that for the same set of parameters the first collapse within the trigonal symmetry occurs at a weaker field ($h\approx 0.85$) than in the hexagonal symmetry ($h\approx 0.93$). The reason is that in the C_3 symmetry seven vortices must overcome their mutual repulsion in order to fall on the defect, while in the C_3 system only three vortices collapse. For the field $h\approx 0.85$, at which, in the symmetry C_3, three vortices are already collapsed on the defect (Fig. 1b) in the C_6 symmetry, the lattice is distorted but still without any vortex collapse (Fig 1c).

Up to now we analyzed the solutions of Eqs. (6) within two symmetries C_6 and C_3 separately. Now we can choose the most preferable one from them and describe the typical vortex lattice behavior in some interval of the magnetic fields close to the upper critical field. We start from the same case of attractive defects $\alpha_1>0$ ($\gamma_1=0$) of a small concentration of defects. If the applied field is not too close to the upper critical field, then a deformation of the lattice near a single defect is small and the preferable local symmetry near each defect is C_6. The defects are occupied by vortices and the rest of the lattice is slightly deformed. With increasing of the magnetic field the deformation near defects becomes stronger (as shown in Fig. 1(c) and at some critical field h_1 the C_3 solution of Eqs. (6) corresponding to collapse of three vortices on the defect becomes preferable (see Fig. 1b). As a result, a local structural transition $C_6\rightarrow C_3$ occurs. With further increasing of the field, one deals with C_3 symmetry, three vortices occupying the defect and the deformation of the nearest part of the vortex lattice (with respect to the defect) is observed. But at some critical field h_2 the C_6 solution of Eqs. (6) corresponding to collapse of seven vortices on the defect (see Fig. 1a) becomes preferable and a local structural transition $C_3\rightarrow C_6$ occurs and so on. Thus, one has a sequence of reentering first order phase transitions $C_6\rightarrow C_3\rightarrow C_6\rightarrow\ldots$.

This qualitative analysis is supported by numerical solution of the infinite nonlinear system of Ovchinnikov equations without any simplification in the general case where $\tilde{\alpha}\neq 0$ and $\tilde{\gamma}\neq 0$. The results obtained confirm our symmetry assumption formulated above and enable us to construct a phase diagram in the (α, γ) plane for a fixed scaled size $\varphi(7)$ of a defect. Part of such diagram is given in Fig. 2. Here the two solid curves separate the regions where the local symmetry is hexagonal (C_6) or trigonal (C_3). Near the upper critical field $\varphi\propto l_0^2$ and the diagram becomes universal. For

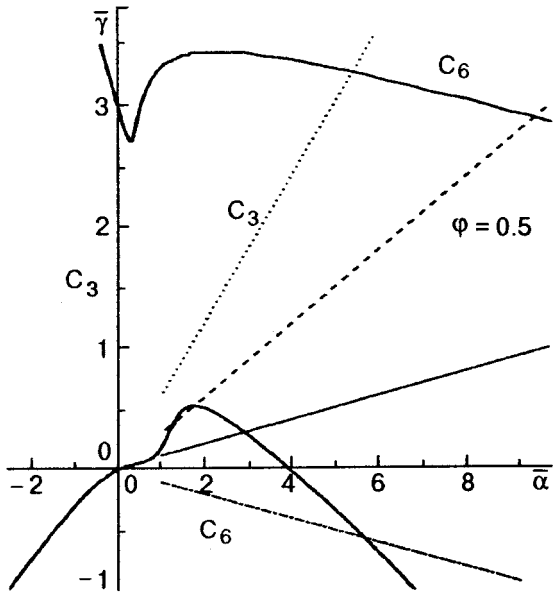

FIG. 2. Phase diagram in the (α, γ) plane of a superconductor with $\bar{\alpha} = 0.1$. The initial magnetic field is $h_0 = 0.9$. Solid ray: $\tilde{\gamma} = 0.01$. Dashed ray: $\tilde{\gamma} = 0.03$. Dotted ray: $\tilde{\gamma} = 0.06$. Dashed-dotted ray: $\tilde{\gamma} = -0.01$.

each fixed defect parameters and for each value of the magnetic field the diagram enable us to determine the preferable local symmetry of the system.

To explain how to extract this information from the phase diagram consider a sample with some fixed parameters α_1, γ_1, and l_0, and start from an initial applied field h_0. This corresponds to a starting point $(\alpha = \alpha^0, \gamma = \gamma^0)$ in the diagram of Fig. 2, where α^0 and γ^0 are determined by Eqs. (8) with $h = h_0$. Further evolution of the parameters α and γ with growth of the magnetic field is described by the equation

$$\gamma = \frac{\gamma_1}{\alpha_1}(\alpha - \alpha^0) + \gamma^0$$

and corresponds to some ray in the phase diagram, starting at the initial point (α^0, γ^0) and directed out of the origin. Four such rays are displayed in Fig. 2. For all rays the starting field is $h_0 = 0.9$ and $\alpha_1 = 0.1$. Increasing of the magnetic field leads to alternation of the effective coupling constants (8), i.e., to the motion of a starting point along the ray. This movement in its turn results in a sequence of reentering transitions from one local symmetry to another.

The most interesting case is represented by a dashed ray and corresponds to the value $\gamma_1 = 0.03$. Here even in the comparatively low field $h \approx 0.775 < h_0$ (the corresponding point of the ray is not displayed in Fig. 2) the $C_6 - C_3$ symmetry transition occurs. In both the two lattice configurations below and above the transition the lattice deformation is small. The dashed ray on the diagram starts from the field $h_0 = 0.9$ and for the first time crosses the lower solid curve at a field $h \approx 0.906$, at which the lattice undergoes the next $C_3 \rightarrow C_6$ transition. No vortex collapse still happens at this field (see Fig. 1c) because the value of $D_6(1)$ is still far from its compensating value. However two next transitions take place because of vortex collapse. The second transition to the symmetry C_3 at a field $h \approx 0.94$ happens when the coefficient $D_3(0)$ in the symmetry C_3 almost reaches its compensating value $D_3(0) = -\pi^{-1} M_3(0)$ and therefore this transition corresponds to the collapse of the three vortices at the defect (Fig. 1b). Similarly the third transition to the symmetry C_6 at a field $h \approx 0.99$ corresponds to the collapse of the seven vortices at the defect (Fig. 1a).

Note that the Figs. 1b and 1c already referred to above, present the contour plots of the square modulus of the order parameter near defect in the vicinity of the $C_6 \rightarrow C_3$ transition due to collapse of the three nearest vortices on the defect. These plots correspond to the point (≈ 4.0) on the ray coinciding with the positive α-semiaxis on the phase diagram. At this point the order parameter exhibits a small deformation in the symmetry C_6 as it is displayed in Fig. 1(c), while in the symmetry C_3 it is strongly deformed due to the collapse (see Fig. 1b).

Until now we have dealt with a single defect problem that corresponds to a linear approximation within the Gibbs potential concentration expansion. To be sure that our results are related to a macroscopic system with a small but finite concentration (dimensionless density) of defects we have to be sure that the next (second order) concentration correction to the Gibbs potential is small. To estimate this correction one has to solve the two defects problem exactly,[15] which is much more complicated. Therefore, we choose another way. Consider for simplicity an attractive case and magnetic field that is not too close to H_{c2}. Put the undistorted vortex lattice on the plane where (point) defects are distributed and shift one of the vortices nearest to each inhomogeneity to the position of that inhomogeneity. There are many similar ways to arrange the vortex lattice, but one has to choose such a way which leads to alternation of the regions where the lattice is compressed with ones where its rarefied. Finally, let us distort the regions of the lattice close to inhomogeneities according to the results obtained within single defect approximation. This latter distortion is already taken into account exactly. So one has only to estimate the additional contribution to the thermodynamic potential from the intermediate regions (between inhomogeneities) whose deformation is well described by elastic theory.

The number of extra vortices per region is of the order of unity. Therefore, the deformation tensor up to a numerical factor of order unity equals the concentration c of defects. The correction to the thermodynamic potential will be of order Cc^2, where C is the elastic modulus. But the elastic part of the deformation has an alternating behavior with a characteristic wavelength of the order of the average distance between inhomogeneities. As it was shown by Brandt,[23] all the elastic moduli are proportional to $(1-h^2)$ if this distance is much less than the penetration length divided by $(1-h)^{1/2}$. The latter inequality can be rewritten as $36\kappa c \gg 1 - h$. In the region of parameters which we are mostly interested in $c = 0.03$, $1 - h = 0.06$ and the inequality $\kappa \gg 1$ is evidently valid. This means that corresponding contribution to the thermodynamic potential is of the order of $(1-h)^2 c^2$. This is exactly the second order concentration correction which in the case $c \ll 1$ is smaller than the contribution accounted for within the linear concentration expansion.

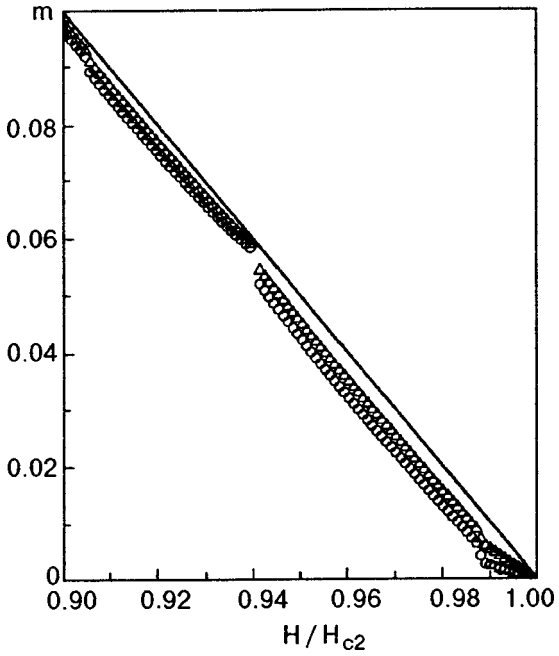

FIG. 3. Dimensionless magnetization of a superconductor with parameters $\tilde{\alpha}=0.1$; $\tilde{\gamma}=0.03$ for the concentration values $c=0.03(\Delta)$ and 0.05 (○).

Thus in the case of small concentration one can use the results obtained in the two previous sections and describe the thermodynamics of the system near the upper critical field. All the local symmetry transitions described above manifest themselves as jumps of the magnetization M or its dimensionless version

$$m \equiv -4\pi(2\kappa^2-1)\beta_A \frac{M}{H_{c2}}$$

(see Fig. 3) and as discontinuities of the magnetic susceptibility

$$\chi = \frac{\partial m}{\partial h}$$

(Fig. 4). The most pronounced jumps occur at the two transitions accompanied by vortex collapse, namely at the fields $h \approx 0.94$ and $h \approx 0.99$.

3. MESOSCOPIC DISC

Consider now a type II superconducting disc with dimensionless thickness d and radius r_0 containing columnar defects of size l_0 and subject to an applied magnetic field, which is parallel both to the defects and to the disc axis. In this section we assume that defects change only the Ginzburg–Landau coefficient α. We assume that the disc is thin and small $d \ll r_0 < \kappa$ (in all numeric calculations we use the value $r_0 = 2.6$). All the dimensions of such a disc are smaller than the penetration depth κ. Therefore as in the previous case the problem becomes essentially $2D$ one, and, moreover, it is possible to neglect the spatial variation of the magnetic induction $\mathbf{b}$ inside the disc and replace it by its average value $\langle \mathbf{b} \rangle$[5] (here and below the brackets $\langle .. \rangle$ mean averaging over the sample area). As a result one gets the following expression for the Gibbs potential per unit area:

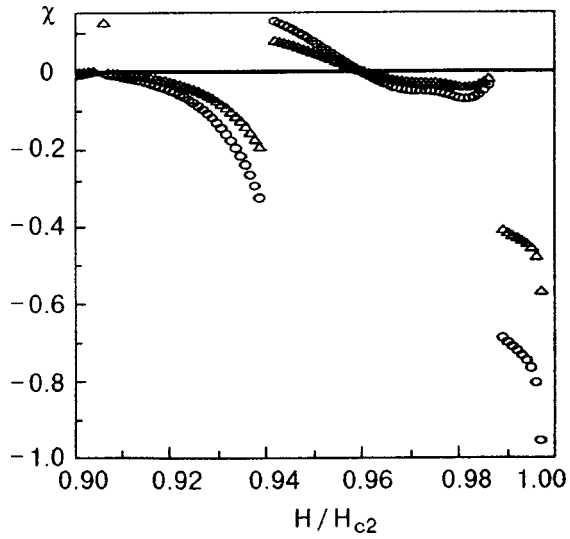

FIG. 4. Magnetic susceptibility of a superconductor with parameters $\tilde{\alpha}=0.1$; $\tilde{\gamma}=0.03$ for the concentration values $c=0.03(\Delta)$ and 0.05 (○).

$$G = \left\langle -|\Psi|^2 + \frac{1}{2}|\Psi|^4 + |\mathbf{D}_-\Psi|^2 + \delta\alpha(\mathbf{r})|\Psi|^2 \right\rangle + \kappa^2(\langle b \rangle - h)^2. \tag{10}$$

Here the vector potential entering to the expression of the gauge invariant gradient $\mathbf{D}_-$ is given by $\mathbf{a} = \langle b \rangle r\hat{\boldsymbol{\theta}}/2$.

According to the general approach of the Ginzburg-Landau theory one has to minimize the Gibbs potential density (10) with respect to the order parameter Ψ with an average induction $\langle b \rangle$ fixed and then to minimize the result once more with respect to $\langle b \rangle$. The first step results in a nonlinear differential equation with a boundary condition

$$\mathbf{D}_-\Psi|_{r=r_0} = 0, \tag{11}$$

the solution of which is rather difficult even in the absence of defects. Therefore, we use the variational procedure choosing the trial function as a linear combination of the eigenfunctions of the operator $(D_-)^2$ with the boundary condition (11). The corresponding eigenfunctions $\Delta_{n,m}$ and eigenvalues $\sigma_{n,m}$ depend on the disc radius r_0. As in the previous section m is an orbital number and n stands for the number of the Landau level which this eigenvalue belongs to when the disc radius r_0 tends to infinity. In strong enough magnetic field one can take into account only $n=0$ states and therefore the quantum number n will be omitted in what follows. Such an approximation is adequate when the strength of defects $\delta\alpha(\mathbf{r})$ is much smaller than the distance between the $n=0$ and 1 eigenvalues. Then, to describe states with a fixed number N_v of vortices the maximal orbital number or topological charge which enters the trial function should be equal to N_v. Finally, our trial function can be written as

$$\Psi = \sum_{m=0}^{N_v} C_m \exp(-im\theta)\Delta_m, \tag{12}$$

where Δ_m is given by

$$\Delta_m = \sqrt{\langle b\rangle}\exp\left(-\frac{r^2}{2}\langle b\rangle\right)\Phi\left(\frac{\langle b\rangle-\sigma_m}{2\langle b\rangle},\ m+1;\frac{r^2}{2}\langle b\rangle\right). \tag{13}$$

In Eq. (12) the expansion coefficients C_m serve as variation parameters and $\mathbf{\Phi}(a,c,x)$ in Eq. (13) is the confluent hypergeometric function.[24]

To proceed further one should substitute the trial function (12) into the expression (10) for the thermodynamic potential density and first minimize it with a respect to the expansion coefficients C_m at fixed average induction $\langle b\rangle$. As a result one obtains a system of a finite number of nonlinear equations for the coefficients C_m. This system is a finite version of the Ovchinnikov[19] Eqs. (6). However in the presence of disordered set of defects the solution of these equations is very complicated. The point is that now no selection rule (successfully used in the homogeneous case[5,19,22] can be applied. Thus the problem needs another approach.

In what follows we consider a disc that contains N_d short-range defects of range $l \ll 1$ placed at the points $\mathbf{r}_1, \mathbf{r}_2, \ldots, \mathbf{r}_{N_d}$. The number of defects N_d is assumed to be larger than the maximal possible number of vortices N_v. As we could see below a small enough clean disc can accumulate vortices only in its center. The defects attract the vortices and due to their short range can pin the latters exactly on their positions. Therefore, we consider only some special configurations of vortices such that they occupy only the positions of defects and the disc center. This choice of trial function implies the following procedure. Let us fix a defect configuration $\{\mathbf{r}_j\}$, $j=0,1,\ldots,N_d$, $\mathbf{r}_0=0$, a set of corresponding topological charges $\{p(j)\}$, an external magnetic field h and an average induction $\langle b\rangle$. Each topological charge $p(j)$ is a non negative integer and the set $\{p(j)\}$ satisfies the condition

$$\sum_{j=0}^{N_d} p(j) = N_v. \tag{14}$$

Thus our procedure accounts for the existence of multiple vortices located on the disc center or on any defect position as well. The trial function (12) has zeros only at points $\{r_j\}$ with multiplicities $p(j)$. The latter condition completely defines all coefficients $\{C_m\}$ $(m=0,1,\ldots, N_i-1)$ up to a common multiplier C_{N_v}, which we term as the order parameter amplitude. Further, we need to minimize the thermodynamic potential with respect to this amplitude and the average induction. The result has to be compared with those obtained for different total numbers of vortices and different sets of ''occupation numbers'' $\{p(j)\}$. Comparing the obtained value of the thermodynamic potential with that corresponding to a normal state one finally finds the preferable state of the disc for a fixed value of external magnetic field. Repeating this procedure for various values of the magnetic field one could describe magnetic properties of the sample in a wide range of the fields up to the upper critical field H_{c3}.

To construct the trial function (12) one should first obtain the eigenvalues $\sigma_{n,m}$ and eigenfunctions Δ_m of the operator $(\mathbf{D}_-)^2$ with boundary condition (11). This textbook problem was solved many times but we need the solution for various disc radii and various average induction values. Therefore we tabulated some needed eigenvalues $\sigma_{n,m}$ and the corresponding eigenfunctions Δ_m for various quantum numbers $n=0,1$, $m=1,2,3,4,5$ and disc radius $r_0=2.6$. The eigenvalues as functions of an average induction are shown in the Fig. 5. These results are completely consistent with, e.g., those obtained earlier in Ref. 25. One can observe that the distance between the zeroth and the first Landau levels is of the order of unity. So we can indeed neglect in expansion (12) the contributions of higher ''Landau levels'' as long as defects are not extremely strong, $\delta\alpha(\mathbf{r})<1$.

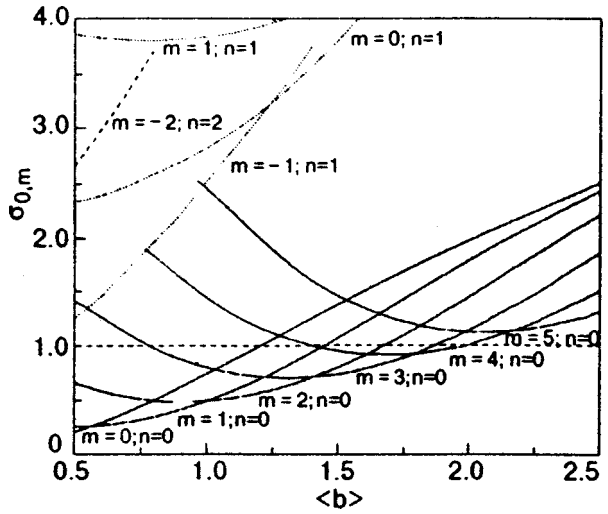

FIG. 5. Eigenvalues $\sigma_{n,m}$ for the disc of radius $r_0=2.6$ as a function of the applied field h.

The results shown in Fig. 5 help us estimate how many vortices can enter the sample. Indeed, for $\sigma=1$ the eigenvalue equation for operator $(\mathbf{D}_-)^2$ coincides with the linearized Ginzburg–Landau equation. Therefore the maximal average induction $\langle b\rangle_m$ corresponding to $\sigma_m=1$ can be treated as the upper critical field for a given orbital number m. The highest of these fields is the genuine upper critical field h_{c3} and the corresponding value of m gives the topological charge of the giant vortex usually appearing in the vicinity of the clean disc phase transition point.[3,4] In the case $r_0=2.6$ considered here the highest possible field at which superconductivity still exists is $h_{c3}=1.98$. This corresponds to the intersection point of the curve σ_4 and the dashed line $\sigma=1$. Thus a clean superconducting disc of this radius at the phase transition point can accumulate only four vortices since the curve for $n=0$, $m=5$ never reaches the line $\sigma=1$.

Substituting the test function (12) for the order parameter into the expression for the averaged Gibbs potential (10) one obtains

$$G = -\sum_{m=0}^{N_v} |C_m|^2(1-\sigma_m)I_m + \frac{\langle b\rangle}{2}\sum_{k,m,n=0}^{N_v} C_m^* C_n^* C_k C_{m+n-k} J_{m,n,k} + \langle \delta\alpha|\Psi|^2\rangle + \kappa^2[\langle b\rangle - h]^2, \tag{15}$$

where the brackets $\langle ... \rangle$ mean averaging over the sample area; $I_m \equiv \langle \Delta_m^2 \rangle$, $J_{m,n,k} \equiv \langle \Delta_m \Delta_n \Delta_k \Delta_{m+n-k} \rangle$ and $\sigma_m \equiv \sigma_{0,m}$. For the state characterized by a topological charge N_v the coefficient C_{N_v} necessarily differs from zero. We choose it as an amplitude of the order parameter and introduce new expansion coefficients D_m and new order parameter ψ:

$$\begin{cases} C_m = C_{N_v} D_m, \\ D_{N_v} = 1, \\ \Psi = C_{N_v} \psi. \end{cases} \tag{16}$$

Rewriting the thermodynamic potential (15) in terms of these new variables and varying it with respect to the amplitude C_{N_v} we obtain the following expression for its extremal value φ:

$$|\varphi|^2 = \frac{\Sigma_{m=0}^{N_v} (1-\sigma_m) I_m - \langle \delta\alpha |\psi|^2 \rangle}{\langle b \rangle \Sigma_{k,m,n=0}^{N_v} D_m^* D_n^* D_k D_{m+n-k} J_{m,n,k}}. \tag{17}$$

The expansion coefficients of the order parameter (12), (16) are completely defined by the position of vortices on the defects. Let us choose some configuration of vortices $\{\mathbf{r}_j\}$. In this set there are points occupied by a single vortex ($p(j) = 1$) and points corresponding to multiple vortices with topological charge $p(j) > 1$. Then the set of coefficients $\{D_m\} = \{\varphi^{-1} C_m\}$ can be calculated from the following system of N_v linear equations:

$$\sum_{m=0}^{N_v - 1} D_m \exp(-im\theta_j) \Delta_m^{[p(j)]}(\mathbf{r}_j) = \exp(-iN_v\theta_j) \Delta_{N_v}^{[p(j)]}(\mathbf{r}_j), \tag{18}$$

where the notation $f^{(n)}(x)$ is used for the nth derivative.

As in the previous section we choose the Gaussian form (1) for the ''defect term'' proportional to $\delta\alpha(\mathbf{r})$ in Eq. (10). In this case the ''defect term'' in (15) in the leading approximation with respect to our small parameter l_0 can be rewritten as

$$\langle \delta\alpha |\psi|^2 \rangle = 2\alpha_1 \frac{l_0^2}{r_0^2} \sum_{j=1}^{N_d} |\psi(\mathbf{r}_j)|^2. \tag{19}$$

Substituting equations (16), (17) and (19) into Eq. (15) we obtain the final expression for the averaged Gibbs potential of the disc with defects:

$$G = -\frac{\left(\Sigma_{m=0}^{N_v} \left| D_m \right|^2 [(1-\sigma_m) I_m] - 2\alpha_1 \frac{l_0^2}{r_0^2} \Sigma_{j=1}^{N_d} \left| \psi(\mathbf{r}_j) \right|^2 \right)^2}{2\langle b \rangle \Sigma_{k,m,n=0}^{N_v} D_m^* D_n^* D_k D_{m+n-k} J_{m,n,k}} + \kappa(\langle b \rangle - h)^2. \tag{20}$$

We solve the system (18) for each combination of vortices on the defects in order to find the set of expansion coefficients $\{D_m\}$ as a function of the average induction $\langle b \rangle$. The set of coefficients is then plugged into expression (20) for the Gibbs potential G at a fixed applied field h. Now we can find the average magnetic induction $\langle b \rangle$ at which the thermodynamic potential (20) has a minimal value at fixed applied field and configuration of vortices. After that we must repeat this procedure for different configurations and different values of the applied field. As a result, we obtain a number of data sets for the Gibbs potential as a function of the applied field for different configurations of vortices. Then for each value of an applied field we should choose the preferable vortex configuration which minimizes the thermodynamic potential. This enables us to obtain the disc magnetization as a function of the applied magnetic field.

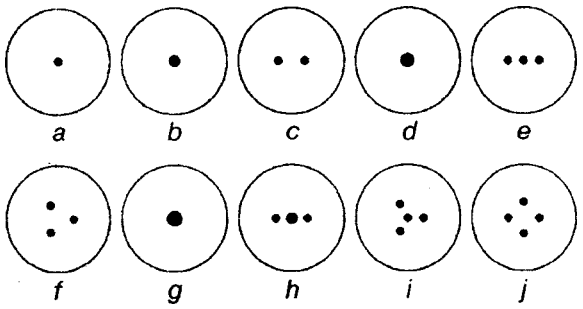

FIG. 6. Possible configurations of vortices inside clean disc of radius $r_0 = 2.6$.

Let us start from the case of a clean disc with radius $r_0 = 2.6$ and $\kappa = 3$. Although this value of κ limits the condition $\kappa \gg r_0^-$, the chosen region of applied fields enables us to neglect the spatial variation of the magnetic induction.[5] As we already showed the maximal number of vortices in such a disc equals four. Due to the sample geometry and small maximal number of vortices they can form only a number of symmetric configurations when some vortices occupy the disc center and the others are placed away from the center in such a way that they form a regular polygon. All these configurations are presented in Fig. 6. In cases *b, h; d*, and *g* the topological charge of the multiple vortex at the origin is equal to 2, 3, and 4, respectively. In cases *c, e, f, h, i, j* the shifted vortices are place at a distance ρ from the origin.

For a given vortex configuration the expansion coefficients $\{D_m\}$ can be calculated from the system of linear equations (18). For each possible vortex configuration we substitute these coefficients into the expression for the thermodynamic potential of the clean disc

$$G = -\frac{(\Sigma_{m=0}^{N_v} |D_m|^2 [(1-\sigma_m) I_m]^2}{2\langle b \rangle \Sigma_{k,m,n=0}^{N_v} D_m^* D_n^* D_k D_{m+n-k} J_{m,n,k}} + \kappa(\langle b \rangle - h)^2$$

and minimize it with respect to the average induction $\langle b \rangle$. We repeat this procedure for all configurations and for various distances of vortices from the disc center inside each configuration. Thus the problem has three variational parameters: the type of vortex configuration (Fig. 6), the distance ρ of vortices from the disc center and the average induction $\langle b \rangle$. We changed the distance ρ by step of $\delta\rho = 0.1 r_0$. Numerical calculation showed that because of the disc's small size only configurations in which $\rho = 0$ (Fig. 6a, 6b, 6d, and 6g) gain the energy. So within the calculation accuracy $\delta\rho = 0.26$ we have only a multiple vortex at the disc center with a possible topological charge $p(0) = 1,2,3,4$.

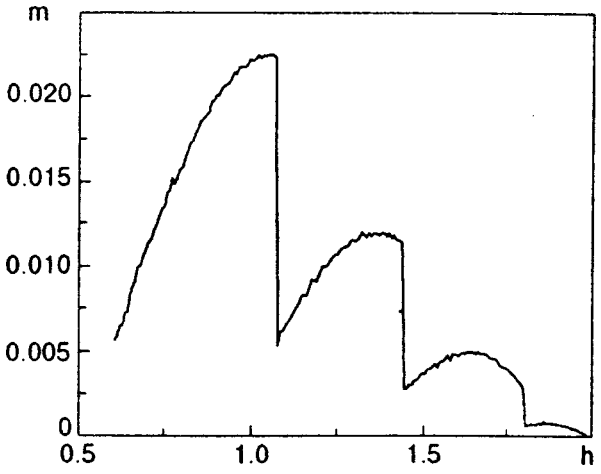

FIG. 7. Magnetization curve of a clean superconducting disc of radius $r_0=2.6$.

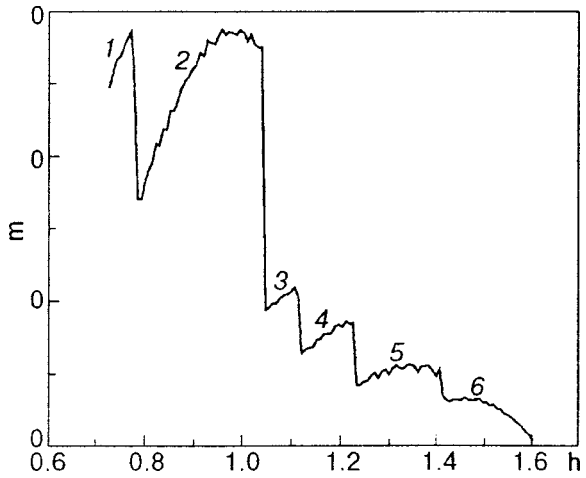

FIG. 9. Magnetization curve of the superconducting disc of radius $r_0=2.6$ and $\kappa=3$ in the presence of defects with an effective coupling constant $\tilde{\alpha}=0.3$.

The dimensionless magnetization $m=h-\langle b\rangle$ of the clean disc is presented in Fig. 7. Penetration of an additional vortex inside the sample is manifested by magnetization jump. Each branch of the curve corresponds to the one-, two-, three- and four-vortex states. This result is similar to that obtained by Palacios[5] and Deo *et al.*[7] for discs with larger radii and it will be used further.

In the case of disc with defects, one should take into account the defects configuration and minimize the Gibbs potential (20). We present below the results for a single configuration of the defects obtained with the help of a random number generator. We hope that it is rather typical (see Fig. 8). In any case the results obtained, below for this configuration enable us to demonstrate all the new features characterizing the magnetic properties of a sample with defects and to confirm all the expectations formulated above in the Introduction.

We analyze the thermodynamic properties of the disc for various values of the scaled defect strength $\tilde{\alpha}\equiv\alpha_1 l_0^2$. This constant can be easily varied experimentally by changing the sample temperature [see Eq. (2)]. To present the results more clearly we collect all configurations of vortices which will be realized for values considered for the defect strength $\tilde{\alpha}$ in Table I. The left column of the Table contains the values of the coupling constants. The upper line enumerates the vortex configurations ordered with accordance to their appearance with the growth of a magnetic field. The same numbers enumerate different regions of the magnetization curves in Fig. 9. Note that the last configuration in each line appears just before the phase transition to the normal state at the upper critical field h_{c3}. Then, each configuration is described by an ordered sequence of six numbers. The jth number is equal to the topological charge located at the point $\mathbf{r}_{j-1}$. In other words, the first number is the topological charge at the disc center, the second number is the topological charge at the first defect and so on. For example configuration {211000} corresponds to a double vortex at the disc center and two single vortices placed at the first and the second defects.

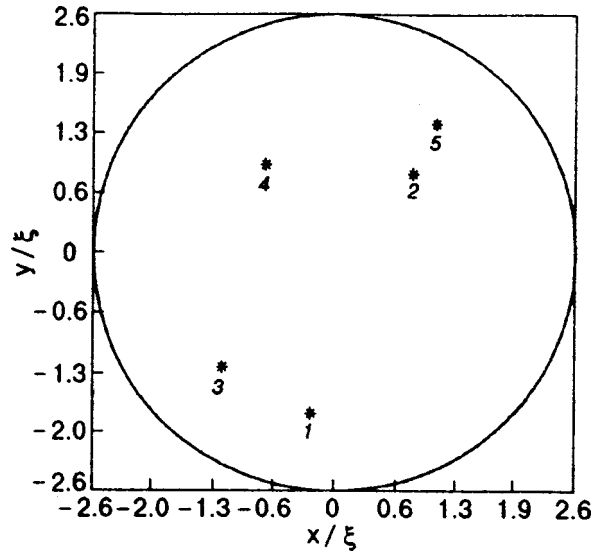

FIG. 8. Defects positions in the disc.

One can get fom the Table I that already at $\tilde{\alpha}=0.08$ near the phase transition point the four-multiple vortex at the disc center is split: three-multiple vortex remains at the center and one more vortex occupies the first defect (configuration {310000}). More complicated splitting is observed in the case $\tilde{\alpha}=0.12$ where two vortices remain at the disc center, one occupies the first defect and another one occupies the second defect (configuration {211000}). Further increasing of the coupling constant leads to the appearance of additional mesoscopic jumps related to the rearrangement of the vortices on the defects as the applied magnetic field changes. Consider the case $\tilde{\alpha}=0.16$. At small values of the applied field one gets one- and two-vortex states at the disc center. However, when the third vortex is allowed to penetrate the multiple vortex is destroyed and the vortices occupy the disc center, the second defect and the third defect (configuration {101100}). With further increase in the applied field the system turns again into the three-multiple vortex state at the disc center. So in the same sample two different vortex configurations with the same total topological charge are possible. When the fourth vortex penetrates the disc the three-multiple

TABLE I. Configurations of vortices.

$\tilde{\alpha}$	1	2	3	4	5	6
0.04	100000	200000	300000	40000	-	-
0.08	100000	200000	300000	310000	-	-
0.12	100000	200000	300000	211000	-	-
0.16	100000	200000	101100	300000	101200	211000
0.30	000101	000110	000111	001110	000130	001210

vortex state splits again into double vortex at the third defect, one vortex at the disc center and another one at the second defect (configuration {101200}). The appearance of the second vortex on the third defect is a result of a very restricted space of the trial functions. Indeed, according to Eq. (20) any defect that is already occupied by a vortex is put out of the game and one cannot gain energy adding one more vortex to the same defect. This means that in a wider variational space the configuration {101200} would be replaced by another one which would be preferable. At the same time it will necessary lead to the corresponding magnetization jump. With increase in the applied field we have a new jump of the magnetization curve, which is caused by rearrangement of the vortices into the configuration {211000} identical to that of the four vortex state in the case $\tilde{\alpha}=0.12$.

Thus one can see that the stronger defects are the greater is the tendency of vortices to occupy defects. The destruction of the giant vortex at the disc center begins near the upper critical field. Increasing the defect strength destroys the centered multiple vortices with lower multiplicity. The preferable arrangement of the vortices corresponds to the maximal reduction of the square order parameter modulus.

At strong coupling constant one expects to get states where all vortices are placed onto defects for all values of the applied field. Consider the results of studying the case $\tilde{\alpha}=0.3$. The magnetization curve of such disc is shown in Fig. 9. Penetration of vortices inside the disc with such strong defects occurs at values of the applied field smaller than that of the previously considered discs with relatively weak defects. Because of that, already at a field $h=0.6$ the disc accumulates two vortices. Their configuration is {000101} (see Fig. 10a). As the applied field increases this configuration is changed by another one {000110} with the same total topological charge. Three vortices appearing at higher fields always occupy three different defects. The corresponding configurations are {000111} and {001110}. Two configurations with total topological charge four are realized. Both contain a multiple vortex on one of the defects. The first configuration appearing in relatively low field is {000130}. Here one has three-multiple vortex on the fourth defect. The second configuration {001210} preceding the transition to the normal state at h_{c3} contains a double vortex at the third defect. Plots of the square modulus of the order parameter for these cases are shown in Figs. 10b and 10c. Thus in the case of a strong defect $\tilde{\alpha}=0.3$ considered here, the number of magnetization jumps within the same field region is twice the number of possible values of the total topological charge. We do believe that this number will increase in a disc of the same radius containing more defects.

We have already noticed that the presence of attractive defects reduces the upper critical field h_{c3} at which the Gibbs potential of the superconductor (20) becomes equal to zero (the Gibbs potential of the normal metal). Figure 9 shows that the larger the defect strength $\tilde{\alpha}$ is, the lower is the transition field. The dependence of the upper critical field on the defect strength $\tilde{\alpha}$ is shown in Fig. 11.

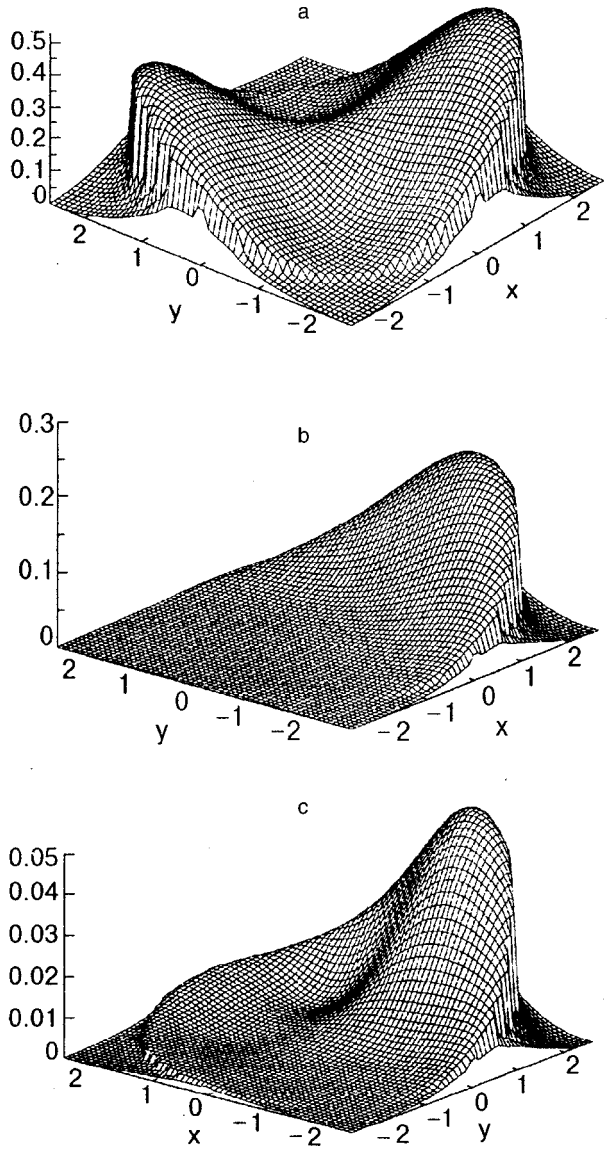

FIG. 10. Square modulus of the order parameter for $\tilde{\alpha}=0.3$ at an applied field $h=0.71$, the vortex configuration is {000101} (a), at $h=1.31$, the vortex configuration is {000130} (b), and at $h=1.55$, the vortex configuration is {001210} (c).

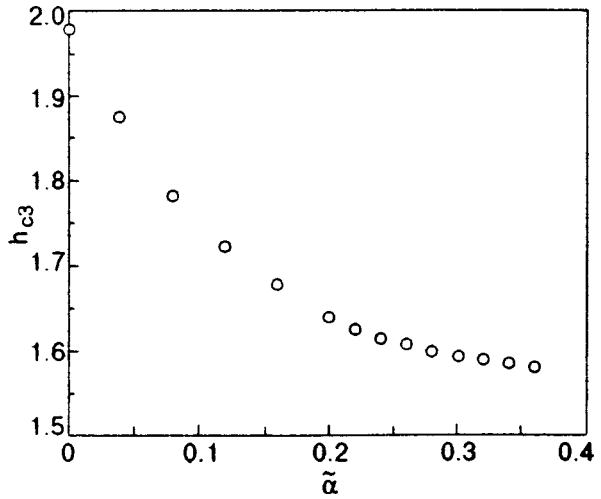

FIG. 11. The upper critical field as a function of the defect strength.

SUMMARY

We have studied the equilibrium properties of conventional type II superconductor with randomly placed identical short-range columnar defects.

The vortex lattice of the bulk superconductor with a small concentration of defects in the vicinity of the upper critical field H_{c2} undergoes a strong deformation with two possible local symmetries-hexagonal one C_6 and trigonal one C_3. The character of the deformation is determined by the vortex-defect interaction. The vortices can collapse onto attractive defects and the formation of multy-quanta vortices becomes possible. Note that formation of the multiquantum vortices was predicted earlier,[11] but in ''twice'' opposite limiting case. We deal with a short-range defect and gain an energy because of softening of the Abrikosov lattice near H_{c2}, while in[11] a very strong defect with a radius comparable with the penetration length was considered.

Increasing the external field gives rise to the reentering transitions between the two possible types of symmetry. These transitions are described by a universal phase diagram. They manifest themselves as jumps of the magnetization and peculiarities of the magnetic susceptibility. One of the way to observe these equilibrium states near H_{c2} is to cool a sample subject to a magnetic field in the normal state, below the critical temperature. Another possibility is to observe not the equilibrium state as a whole, but to visualize the local deformation of the vortex lattice near defects.

We have also studied magnetic properties of a mesoscopic superconducting disc with such defects the number of which is assumed to be larger than the maximal possible number of vortices accumulated by the disc. We obtained the magnetization curves for various strengths of defects in a wide region of the applied magnetic field. The results show that the defects help the penetration of vortices into the sample. They also reduce both the value of the magnetization and the upper critical field. Even the presence of weak defects can split the giant vortex state at the disc center (usually existing in a clean disc of small radius) into vortices with smaller topological charges. This splitting occurs in the vicinity of the upper critical field h_{c3}. Strong enough defects always pin all vortices, splitting multiple vortex states at the disc center in all field region. This leads to the appearance of additional mesoscopic jumps in the magnetization curve related not to the penetration of new vortices into the sample but to redistribution of vortices within the set of defects. The number of these jumps increases with the number of defects.

ACKNOWLEDGEMENTS

This research is supported by grants from the Israel Academy of Science ''Mesoscopic effects in type II superconductors with short-range pinning inhomogeneities'' (S.G.) and ''Center of Excellence'' (Y.A.) and by a DIP grant for German-Israel collaboration (Y.A.).

DEDICATION

This paper is dedicated to the memory of Boris Ieremievich Verkin, founder and, for thirty years, Director of the Kharkov Institute for Low Temperature Physics and Engineering where one of us (S.G.) was lucky to work almost twenty years.

*E-mail: sergeyg@bgumail.bgu.ac.il

[1] L. V. Shubnikov, V. I. Khotkevich, Yu. D. Shepelev, and Yu. N. Ryabinin, Sov. Phys. JETP **7**, 221 (1937).
[2] A. A. Abrikosov, Zh. Éksp. Teor. Fiz. **32**, 1442 (1957) [Sov. Phys. JETP **5**, 1174 (1957)].
[3] D. Saint Jams and P. G. De-Gennes, Phys. Lett. **7**, 306 (1963).
[4] V. A. Schweigert, F. M. Peeters, and P. S. Deo, Phys. Rev. Lett. **81**, 2783 (1998).
[5] J. J. Palacios, Phys. Rev. B **58**, R5948 (1998).
[6] A. K. Geim, I. V. Grigorieva, S. V. Dubonos, J. G. S. Lok, J. C. Maan, A. E. Filippov, and F. M. Peeters, Nature (London) **390**, 259 (1997).
[7] P. Singha Deo, V. A. Schweigert, F. M. Peeters, and A. K. Geim, Phys. Rev. Lett. **79**, 4653 (1997).
[8] P. Singha Deo, F. M. Peeters, and V. A. Schweigert, cond-mat/9812193 (1998).
[9] E. Akkermans and K. Mallick, cond-mat/9812275 (1998).
[10] L. Civale, A. D. Marwick, M. W. McElfresh, T. K. Worthington, A. P. Malozemoff, F. H. Holtzberg, J. R. Thompson, and M. A. Kirk, Phys. Rev. Lett. **65**, 1164 (1990); L. Civale, A. D. Marwick, T. K. Worthington, M. A. Kirk, J. R. Thompson, L. Krusin-Elbaum, Y. Sun, J. R. Clem, and F. H. Holtzberg, Phys. Rev. Lett. **67**, 648 (1991).
[11] I. B. Khalfin and B. Ya. Shapiro, Physica C **202**, 393 (1992).
[12] A. I. Buzdin, Phys. Rev. B **47**, 11416 (1993).
[13] M. Baert, V. V. Metlushko, R. Jonckheere, V. V. Moshchalkov, and Y. Bruynseraede, Phys. Rev. Lett. **74**, 3269 (1995).
[14] C. J. van der Beek, M. Konczykowski, T. W. Li, P. H. Kes, and W. Benoit, Phys. Rev. B **54**, R792 (1996).
[15] I. M. Lifshits, Nuovo Cimento 3, Suppl. 716 (1963).
[16] V. L. Ginzburg and L. D. Landau, Zh. Éksp. Teor. Fiz. **20**, 1064 (1950).
[17] E. H. Brandt, Phys. Status Solidi B **71**, 277 (1975).
[18] A. I. Larkin and Yu. N. Ovchinnikov, J. Low Temp. Phys. **34**, 409 (1978).
[19] Yu. N. Ovchinnikov, Zh. Éksp. Teor. Fiz. **82**, 2020 (1982) [Sov. Phys. JETP **55**, 1162 (1982)].
[20] E. H. Brandt, Phys. Status Solidi B **51**, 345 (1972).
[21] D. Li and B. Rosenstein, cond-mat./9902294 (1999).
[22] G. M. Braverman, S. A. Gredeskul, and Y. Avishai, Phys. Rev. B **57**, 13899 (1998).
[23] E. H. Brandt, J. Low Temp. Phys. **26**, 709,735 (1977).
[24] I. S. Gradstein and I. M. Ryzhik, Tables of Integtrals, Sums, Series and Products, Academic Press, New York (1980).
[25] R. Benoist and W. Zwerger, Z. Phys. B **103**, 377 (1997).

This article was published in English in the original Russian journal. It was edited by R. T. Beyer.

Cooper instability in the occupation dependent hopping Hamiltonians

H. Boyaci

Department of Physics, Bilkent Universilty, Ankara 06533, Turkey

I. O. Kulik

Department of Physics, Bilkent University, Ankara 06533, Turkey;
*B. Verkin Institute for Low Temperature Physics and Engineering, National Academy of Sciences of Ukraine, Lenin Ave. 47, 310164 Kharkov, Ukraine**

(Submitted April 13, 1999)
Fiz. Nizk. Temp. **25**, 838–849 (August–September 1999)

A generic Hamiltonian, which incorporates the effect of the orbital contraction on the hopping amplitude between nearest sites, is studied both analytically at the weak coupling limit and numerically at the intermediate and strong coupling regimes for a finite atomic cluster. The effect of the orbital contraction due to hole localization at atomic sites is specified with two coupling parameters V and W (multiplicative and additive contraction terms). The singularity of the vertex part of the two-particle Green's function determines the critical temperature T_c and the relaxation rate $\Gamma(T)$ of the order parameter at temperature above T_c. Unlike the case in conventional BCS superconductors, Γ has a non-zero imaginary part which may influence the fluctuation conductivity of the superconductor above T_c. We compute the ground state energy as a function of the particle number and magnetic flux through the cluster, and show the existence of the parity gap Δ appearing at the range of system parameters consistent with the appearance of the Cooper instability. Numeric calculation of the Hubbard model (with $U>0$) at arbitrary occupation does not show any sign of superconductivity in a small cluster.
© *1999 American Institute of Physics.* [S1063-777X(99)00708-2]

1. FORMULATION OF THE MODEL

High temperature superconductivity in lanthanum,[1] yttrium[2] and related copper-oxide compounds remains the subject of intensive investigation and controversy. It was suggested that the electron-phonon interaction mechanism, which is very successful in understanding conventional (''low temperature'') superconductors within the Bardeen–Cooper–Schrieffer scheme,[3] may not be adequate for high-T_c cuprates, and even the conventional Fermi liquid model of the metallic state may require reconsideration. This opens an area for investigation of mechanisms of electron-electron interaction which can be relevant in understanding the peculiarities of superconducting, as well as normal state, properties of cuprates. Specific to all of them is the existence of oxide orbitals. Band calculations[4,5] suggest that hopping between the oxygen p_x, p_y orbitals and between the copper $d_{x^2-y^2}$ orbitals may be of comparable magnitude. On the experimental side, spectroscopic studies[6,7] clearly show that the oxygen band appears in the same region of oxygen concentration in which superconductivity in cuprates is the strongest. Therefore there exists the possibility that specific features of oxide compounds may be related to oxygen-oxygen hopping, or to the interaction between the copper and the rotational p_x-p_y collective modes. If the oxygen hopping is significant, then it immediately follows that the intrinsic oxygen carriers (p_x,p_y oxygen holes) should be different from the more familiar generic *s*-orbital derived itinerant carriers. The difference is related to low atomic number of oxygen such that removing or adding of one electron to the atom induces a substantial change in the Coulomb field near the remaining ion and therefore results in a change of the effective radius of atomic orbitals near the ion. This will strongly influence the hopping amplitude between this atom and the atoms in its neighborhood. Such an ''orbital contraction'' effect represents a source of strong interaction which does not simply reduce to the Coulomb (or phonon) repulsion (or attraction) between the charge carriers. It was suggested by Hirsch and coauthors,[8–10] and by the present authors[11–14] that the occupation dependent hopping can have relevance to the appearance of superconductivity in high-temperature oxide compounds. In the present paper, we investigate the generic occupation-dependent hopping Hamiltonians with respect to peculiarities of the normal state, and to the range of existence of the superconducting state. Theoretical investigation of the Cooper instability is supplemented by numeric study of pairing and diamagnetic currents in finite atomic clusters. We study the effect of Cooper pairing between the carriers and show that at certain values and magnitudes of the appropriate coupling parameters, the system is actually superconducting. The properties of such superconducting state are in fact only slightly different from the properties of conventional (low-T_c) superconductors. Among those we so far can only mention the change in the fluctuation conductivity above or near the critical temperature T_c. Relaxation of the pairing parameter to equilibrium acquires a small real part due to the asymmetry of contraction-derived interaction between the quasi-particles above and below the Fermi energy.

 © 1999 American Institute of Physics

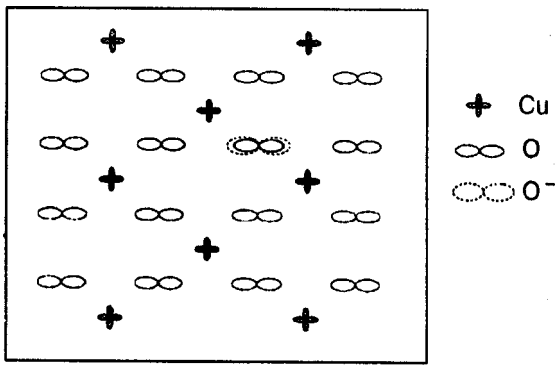

FIG. 1. Site configuration in the CuO_2 plane of cuprates. Dotted line represents the effect of orbital contraction/expansion due to the localization/delocalization of an extra hole at a specific site. The enlarged orbital attains the larger value of the hopping amplitude to the nearest sites.

Oxygen atoms in the copper-oxygen layers of the cuprates (Fig. 1) have a simple quadratic lattice. We assume that p_z orbitals of oxygen (z is the direction perpendicular to the cuprate plane) are bound to the near cuprate layers whereas carriers at the p_x, p_y orbitals may hop between the oxygen ions in the plane.

Let t_1 be the hopping amplitude of $p_x(p_y)$ and t_2 the hopping amplitude of $p_y(p_x)$ oxygen orbitals between the nearest lattice sites in the $x(y)$ direction in a square lattice with a lattice parameter a. Then the non-interacting Hamiltonian is

$$H_0=-t_1\sum_{\langle ij\rangle_x} a_i^+ a_j - t_2\sum_{\langle ij\rangle_y} a_i^+ a_j - t_1\sum_{\langle ij\rangle_y} b_i^+ b_j - t_2\sum_{\langle ij\rangle_x} b_i^+ b_j \tag{1}$$

where $a_i^+(a_i)$ is the creation (annihilation) operator for p_x and correspondingly $b_i^+(b_i)$ for p_y orbitals. The interaction Hamiltonian includes the terms

$$H_1=\sum_{\langle ij\rangle} a_i^+ a_j[Vm_im_j+W(m_i+m_j)] + \sum_{\langle ij\rangle} b_i^+ b_j[Vn_in_j+W(n_i+n_j)] \tag{2}$$

where $n_i=a_i^+a_i$; $m_i=b_i^+b_i$. This corresponds to the dependence of the hopping amplitude on the occupation numbers n_i, m_i of the form

$$(\hat{t}_{ij})_{a_i\to a_j}=\tau_0(1-m_i)(1-m_j)+\tau_1[(1-m_i)m_j + m_i(1-m_j)]+\tau_2 m_i m_j \tag{3}$$

and correspondingly $(\hat{t}_{ij})_{b_i\to b_j}$ of the same form with m_i replaced with n_i. The amplitudes τ_0, τ_1, τ_2 correspond to the transitions between the ionic configurations of oxygen:

$$\begin{aligned}&\tau_0: O_i^- + O_j^{2-}\to O_i^{2-}+O_j^-,\\ &\tau_1: O_i + O_j^{2-}\to O_i^{2-}+O_j,\\ &\tau_2; O_i + O_j^-\to O_i^-+O_j.\end{aligned} \tag{4}$$

O corresponds to the neutral oxygen ion whereas O^- to the single charged and O^{2-} to the double charged negative ions. Since oxygen atom has $1s^22p^42s^2$ configuration in its ground state, filling of the p shell to the full occupied configuration $2p^6$ is the most favorable. Amplitudes V and W relate to the parameter τ_0, τ_1, τ_2 according to

$$V=\tau_0-2\tau_1+\tau_2, \quad W=\tau_1-\tau_2. \tag{5}$$

Assuming $t_1=t_2=t$ and replacing a_i, b_i with a_i with the pseudo-spin indices $\sigma=\downarrow,\uparrow$ we write the Hamiltonian Eq. (1) in the form

$$H=-t\sum_{\langle ij\rangle\sigma} a_{i\sigma}^+ a_{j\sigma}+H_U+H_V+H_W \tag{6}$$

where

$$H_U=U\sum_i n_{i\uparrow}n_{i\downarrow}; \tag{7}$$

$$H_V=V\sum_{\langle ij\rangle\sigma} a_{i\sigma}^+ a_{j\sigma}n_{i\bar{\sigma}}n_{j,\bar{\sigma}}; \tag{8}$$

$$H_W=W\sum_{\langle ij\rangle\sigma} a_{i\sigma}^+ a_{j\sigma}(n_{i,\bar{\sigma}}+n_{j,\bar{\sigma}}) \tag{9}$$

where we also included the in-site Coulomb interaction (U) between the dissimilar orbitals at the same site. σ can also be considered as a real spin projection of electrons at the site. In that case, the pairing will originate between the spin-up and spin-down orbitals, rather than between p_x and p_y orbitals. More complex mixed spin- and orbital-pairing configurations can also be possible within the same idea of orbital contraction (or expansion) at hole localization but are not considered in this paper. The following discussion does not distinguish between the real spin and the pseudo-spin pairing. The Hamiltonian, Eq. (6), is a model one which cannot refer to the reliable values of the parameters appropriate to the oxide materials. The purpose of our study is rather to investigate the properties of superconducting transition specific to the model chosen and to find the range of the U, V, W values which may correspond to superconductivity. This will be done along the lines of the standard BCS model[15] in the weak coupling limit, U, V, $W\to 0$, and by an exact diagonalization of the Hamiltonian for a finite atomic cluster at large and intermediate coupling.

In the momentum representation, the Hamiltonian becomes $H=H_0+H_1+H_2$ with

$$H_0=\sum_{\mathbf{p}\sigma}\xi_{\mathbf{p}}a_{\mathbf{p}\sigma}^+ a_{\mathbf{p}\sigma}, \tag{10}$$

$$H_1=\frac{1}{4}\sum_{p_1p_2p_3p_4,\alpha\beta\gamma\delta} a_{\mathbf{p}_1\alpha}^+ a_{\mathbf{p}_2\beta} \times\Gamma^0_{\alpha\beta\gamma\delta}(p_1,p_2,p_3,p_4)a_{\mathbf{p}_4\delta}a_{\mathbf{p}_3\gamma} \tag{11}$$

where

$$\xi_{\mathbf{p}}=-t\sigma_{\mathbf{p}}-\mu, \quad \sigma_{\mathbf{p}}=2(\cos p_xa+\cos p_ya), \tag{12}$$

and μ is the chemical potential. $\Gamma^0_{\alpha\beta\gamma\delta}$ is the zero order vertex part, defined as

$$\Gamma^0_{\alpha\beta\gamma\delta}(p_1,p_2,p_3,p_4)=\left[U+\left(W+\frac{1}{2}\nu V\right)(\sigma_{\mathbf{p}_1}+\sigma_{\mathbf{p}_2}+\sigma_{\mathbf{p}_3}+\sigma_{\mathbf{p}_4})\right]\tau^x_{\alpha\beta}\tau^x_{\gamma\delta}(\delta_{\alpha\gamma}\delta_{\beta\delta}-\delta_{\alpha\delta}\delta_{\beta\gamma})\,\delta_{\mathbf{p}_1+\mathbf{p}_2\cdot\mathbf{p}_3+p_4} \tag{13}$$

where $\tau^x_{\alpha\beta}$ is the Pauli matrix

$$\begin{pmatrix}0 & 1\\ 1 & 0\end{pmatrix}.$$

For reasons which will be clear later, we separated H_V and put some part of it into the H_1 term, while the remaining part is included in the H_2 term, thus giving

$$H_2=V\sum_{\langle ij\rangle\sigma} a^+_{i\sigma}a_{j\sigma}(a^+_{i\bar{\sigma}}a_{i\bar{\sigma}}-\nu/2)(a^+_{j\bar{\sigma}}a_{j\bar{\sigma}}-\nu/2) \tag{14}$$

with $\nu=\langle n_i\rangle$ being the average occupation of the site.

2. THE COOPER INSTABILITY IN THE OCCUPATION-DEPENDENT HOPPING HAMILTONIANS

The Cooper instability is realized at certain temperature $T=T_c$ as a singularity in a two-particle scattering amplitude at zero total momentum. We introduce a function

$$\Gamma(p_1,p_2,\tau-\tau')=\langle T_\tau a_{\mathbf{p}_1\uparrow}(\tau)a_{-\mathbf{p}_1\downarrow}(\tau)\bar{a}_{-\mathbf{p}_2\downarrow}(\tau')\bar{a}_{\mathbf{p}_2\uparrow}(\tau')\rangle \tag{15}$$

where $\bar{a}_{\mathbf{p}\alpha}(\tau)=\exp(H\tau)a^+_{\mathbf{p}\alpha}\exp(-H\tau)$, $a_{\mathbf{p}\alpha}=\exp(H\tau)a_{\mathbf{p}\alpha}\times\exp(-H\tau)$ are the imaginary time (τ) creation and annihilation operators. At $\mathbf{p}_1=-\mathbf{p}_2$, $\mathbf{p}_3=-\mathbf{p}_4$, the kernel of $\Gamma_{\alpha\beta\gamma\delta}$ is proportional to $G^x_{\alpha\beta}\,G^x_{\gamma\delta}$ (G is the one-electron Green's function). We keep the notation $\Gamma(\mathbf{p},\mathbf{p}')$ for such a reduced Green's function specifying only momenta $\mathbf{p}=\mathbf{p}_1=-\mathbf{p}_2$ and $\mathbf{p}'=\mathbf{p}_3=-\mathbf{p}_4$. By assuming temporarily $V=0$, this Hamiltonian results in an equation for the Fourier transform $\Gamma(p,p',\Omega)$

$$\Gamma(\mathbf{p},\mathbf{p}',\Omega)=\Gamma^0(\mathbf{p},\mathbf{p}')-T\times\sum_\omega\sum_{\mathbf{k}}\Gamma^0(\mathbf{p},\mathbf{k})G_\omega(\mathbf{k})G_{-\omega+\Omega}(-\mathbf{k})\times\Gamma(\mathbf{k},\mathbf{p}',\Omega) \tag{16}$$

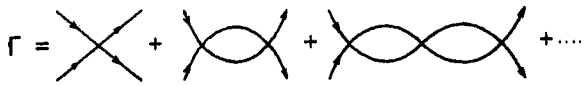

FIG. 2. Feynmann diagrams for 4-vertex interactions, U and W.

corresponding to summation of the Feynmann graphs shown in Fig. 2. In the above formulas, $\omega=(2n+1)\pi T$ and $\Omega=2\pi mT$ (n, m integers) are the discrete odd and even frequencies of the thermodynamic perturbation theory[15]. $G(\mathbf{k},\omega)$ is a one-particle Green's function in the Fourier representation

$$G(\mathbf{k},\omega)=\frac{1}{\xi_k-i\omega}. \tag{17}$$

Diagrams of Fig. 2 are singular since equal momenta of two parallel running lines bring together singularities of both Green's functions $G(\mathbf{k},\omega)$ and $G(-\mathbf{k},\omega)$.

The 6-vertex interaction, Eq. (8), is not generally considered in the theories of strongly-correlated fermionic systems. Such interaction also results in singular diagrams for $\mathbf{p}\to-\mathbf{p}$ scattering shown in Fig. 3. Since a closed loop in this figure does not carry any momentum to the vertex, it reduces to the average value of $\bar{G}$ which in turn is the average of the number operator, $\langle a^+a\rangle$. Taking such diagrams into consideration is equivalent to replacing one of the n_i's in Eq. (8) to its thermodynamical average $\nu=\langle a^+_{i\sigma}a_{i\sigma}\rangle$. Then the V term can be added to the renormalized value of W,

$$W\to W+\frac{1}{2}\nu V.$$

We shall check to what extent such an approximation may be justified by numeric analysis in Sec. 3.

Solution of Eq. (16) can be obtained by putting

$$\Gamma(\mathbf{p},\mathbf{p}',\Omega)=A(\Omega)+B_1(\Omega)\sigma_{\mathbf{p}}+B_2(\Omega)\sigma_{\mathbf{p}'}+C(\Omega)\sigma_{\mathbf{p}}\sigma_{\mathbf{p}'}. \tag{18}$$

Substituting this expression into Eq. (16) and introducing the quantities

$$S_n(\Omega)=T\sum_\omega\sum_{\mathbf{k}}\sigma^n_{\mathbf{k}}G_\omega(\mathbf{k})G_{-\omega+\Omega}(-\mathbf{k}) \tag{19}$$

we obtain a system of coupled equations for A, B_1, B_2, C

$$\begin{pmatrix}1+US_0+\tilde{W}S_1 & US_1+\tilde{W}S_2 & 0 & 0\\ \tilde{W}S_0 & 1+\tilde{W}_1 & 0 & 0\\ 0 & 0 & 1+US_0+\tilde{W}S_1 & US_1+\tilde{W}S_2\\ 0 & 0 & \tilde{W}S_0 & 1+\tilde{W}S_1\end{pmatrix}\begin{pmatrix}A\\ B_1\\ B_2\\ C\end{pmatrix}=\begin{pmatrix}U\\ \tilde{W}\\ \tilde{W}\\ 0\end{pmatrix} \tag{20}$$

where $\tilde{W}=W+(1/2)\nu V$, which are solved to give

$$A=\frac{U-\tilde{W}^2S_2}{D},$$

$$B_1=B_2=\frac{\tilde{W}(1+\tilde{W}S_1)}{D},\quad C=-\frac{\tilde{W}^2S_0}{D} \tag{21}$$

where D is a determinant

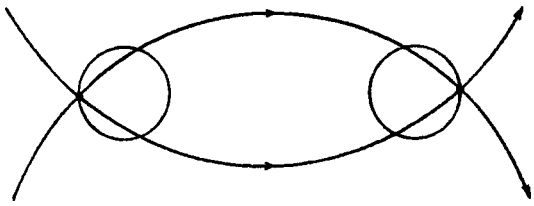

FIG. 3. Feynmann diagram for 6-vertex interaction, V.

$$D=\begin{vmatrix} 1+US_0+\tilde{W}S_1 & US_1+\tilde{W}S_2 \\ WS_0 & 1+WS_1 \end{vmatrix}. \tag{22}$$

The determinant becomes zero at some temperature which means an instability in the two-particle scattering amplitude ($\Gamma\to\infty$). This temperature is the superconducting transition temperature T_c. At T_c, Eq. (16) is singular, which means that two-particle scattering amplitude becomes infinite. Below T_c, the finite value of Γ is established by including the non-zero thermal averages (the order parameters), $\langle a_{\mathbf{p}}^{+}a_{-\mathbf{p}}^{+}\rangle$, $\langle a_{\mathbf{p}}a_{-\mathbf{p}}\rangle$. We first analyze the case of non-retarded, non-contraction interaction U, and after that will consider the effect of the occupation-dependent hopping terms, V and W.

2.1. Direct non-retarded interaction

Neglecting contraction parameters V, W, the solution of Eq. (16) reduces to

$$-\frac{1}{U}=T\sum_{\omega}\sum_{\mathbf{k}}\frac{1}{\xi_{\mathbf{k}}^2+\omega^2} \tag{23}$$

which, after the summation over the discrete frequencies, reduces to the conventional BCS equation (at negative U)

$$\frac{1}{|U|}=\sum_{\mathbf{k}}\frac{1-2n_{\mathbf{k}}}{2\xi_{\mathbf{k}}}, \tag{24}$$

with $n_{\mathbf{k}}=[\exp(\beta\xi_k)+1]^{-1}$. At finite frequency Ω, Eq. (23) reduces to

$$\ln\frac{T}{T_c}=T\sum_{\omega}\int_{-E_1}^{E_2}d\xi\frac{-i\Omega}{(\xi^2+\omega^2)(\xi+i\omega+i\Omega)} \tag{25}$$

where, for simplicity, we replaced an integration over the Brillouin zone $\int d^3k$ by the integration over the energy assuming that the density of states near the Fermi energy μ is flat. $-E_1$ and E_2 are the lower and upper limits of integration equal to $-4t-\mu$ and $4t-\mu$, respectively. Such an approximation is not very bad since most singular contributions to integral comes from the point $\xi_p=0$ where the integrand is the largest.

Above T_c, Eq. (25) determines the frequency of the order parameter relaxation.[16–18] There is a small change in this frequency compared to the BCS model in which limits of the integration $(-E_1,E_2)$ are symmetric with respect to the Fermi energy, and small in comparison to ε_F; therefore we shall briefly discuss it now.

To receive a real-time relaxation frequency, Eq. (25) needs to be analytically continued to a real frequency domain from the discrete imaginary frequencies $i\omega_n=(2n+1)\pi iT$.[15] Using the identity

$$T\sum_{\omega}\frac{1}{(\omega+i\xi_1)(\omega+i\xi_2)\ldots(\omega+i\xi_n)}$$
$$=(-i)^n\sum_{i=1}^{n}\prod_{i\neq j}\frac{n(\xi_i)}{\xi_i-\xi_j} \tag{26}$$

where $n(\xi)$ is a Fermi function $n(\xi)=[\exp(\beta\xi)+1]^{-1}$ gives

$$\ln\frac{T}{T_c}=\frac{i\Omega}{2}\int_{-E_1}^{E_2}\frac{\tanh(\xi/2T)}{\xi(2\xi+i\Omega)}d\xi \tag{27}$$

where

$$T_c=\frac{2\gamma}{\pi}\sqrt{E_1E_2}\exp\left(-\frac{1}{N(\varepsilon_F)|U|}\right),\quad \ln\gamma=C=0.577, \tag{28}$$

C is the Euler constant. Analytic continuation is now simple: we change Ω, to $i(\omega-i\delta)$, $\delta=+0$, to receive a function which will be analytic in the upper half plane of complex ω, Im $\omega>0$. The order parameter relaxation equation becomes

$$\left(\ln\frac{T}{T_c}-\frac{\omega}{4}\int_{-E_1}^{E_2}\frac{\tanh(\xi/2T)}{\xi(\xi-\omega/2+i\delta)}d\xi\right)\Delta=0. \tag{29}$$

At $\omega\ll T_c$ and $T-T_c\ll T_c$, the real and imaginary parts of Eq. (29) are easily evaluated to give

$$\left(T-T_c-\frac{\pi i\omega}{8T_c}+\omega\frac{E_1-E_2}{4E_1E_2}\right)\Delta=0. \tag{30}$$

Thus, the order parameter relaxation equation at $T>T_c$ becomes

$$(1+i\lambda)\frac{\partial\Delta}{\partial t}+\Gamma\Delta=0 \tag{31}$$

where

$$\Gamma=\frac{8}{\pi}(T-T_c),\quad \lambda=\frac{2(E_1-E_2)}{\pi E_1E_2}T_c. \tag{32}$$

In comparison to the BCS theory in which $E_1=E_2=\omega_D$ (ω_D is the Debye frequency) and therefore $\lambda=0$, we obtain a relaxation which has a non-zero ''inductive'' component, $-i\lambda\Gamma$. Typically, $E_1\sim E_2\sim\varepsilon_F$ and therefore $|\lambda|$ is a small quantity. It increases however near the low ($v\ll 1$) or near the maximal ($v\simeq 2$) occupation where E_1 or E_2 become small. Such mode of relaxation is specific to a non-retarded (non-phonon) interaction which is not symmetric near ε_F and spans over the large volume of the **k**-space rather than is restricted to a narrow energy $\omega_D\ll\varepsilon_F$ near the Fermi energy.

2.2. Occupation-dependent hopping instability and relaxation

Neglecting direct interaction, we put $U=0$ in Eq. (22) and obtain

$$-\frac{1}{\tilde{W}}=S_1(\omega)\pm\sqrt{S_0(\omega)S_2(\omega)} \tag{33}$$

where at finite frequency ω

$$S_n(\omega)=N(\varepsilon_F)T\sum_{\omega}\int_{-E_1}^{E_2}\left(\frac{\xi+\mu}{-t}\right)^n\frac{\tanh(\xi/2T)}{2\xi-\omega+i\delta}d\xi. \tag{34}$$

Putting $\omega=0$ we obtain a transition temperature T_c from Eq. (33). The equation has a solution at $\tilde{W}<0$, $\mu<0$, or at $\tilde{W}>0$, $\mu>0$ (we assume that $t>0$). The plus or minus sign is chosen to obtain the maximal value of T_c (the second solution corresponding to smaller T, then, has to be disregarded since the order parameter will be finite at $T<T_c$ and therefore Eqs. (20)–(22) do not apply). This gives us an expression for T_c

$$T_c=\frac{2\gamma}{\pi}\sqrt{E_1E_2}\exp\left[\frac{E_1-E_2}{2|\mu|t}(t-|\mu|)+\frac{E_2^2-E_1^2}{8\mu^2}\right]\times\exp\left(-\frac{t}{2|\tilde{W}|N(\varepsilon_F)}\right) \tag{35}$$

where $\mu<0$, $\tilde{W}<0$ (second exponent is dominating the first one in the weak coupling limit $\tilde{W}\to 0$). Real and imaginary parts of $S_n(\omega)$ are calculated at $\omega\ll T_c$

$$\mathrm{Im}\,S_n(\omega)\simeq-\frac{\pi\omega}{8T_c}\left(-\frac{\mu}{t}\right)^n N(\varepsilon_F). \tag{36}$$

$$\mathrm{Re}\,S_n(\omega)=\frac{\omega}{4}N(\varepsilon_F)\left(-\frac{\mu}{t}\right)^n\times\begin{cases}\dfrac{E_2-E_1}{E_1E_2}, & n=0,\\[2mm] \dfrac{E_2-E_1}{E_1E_2}+\dfrac{2}{\mu}\ln\dfrac{\gamma\sqrt{E_1E_2}}{T_c}, & n=1,\\[2mm] \dfrac{E_2-E_1}{E_1E_2}+\dfrac{E_1-E_2}{\mu^2}+\dfrac{2}{\mu}\ln\dfrac{\gamma\sqrt{E_1E_2}}{T_c}, & n=2.\end{cases} \tag{37}$$

Equation for λ is received with a value larger than the previous one [Eq. (32)]

$$\lambda\simeq\frac{T_c}{\mu}\left(3\ln\frac{2\gamma\sqrt{E_1E_2}}{\pi T_c}+\frac{2\mu(E_2-E_1)}{E_1E_2}+\frac{E_1-E_2}{2\mu}\right). \tag{38}$$

The eigenvalue equation gives the **p**-dependence of the two particle correlator $\Gamma(\mathbf{p},\mathbf{p}')=\langle a^+_{\mathbf{p}\uparrow}a^+_{-\mathbf{p}\downarrow}a_{-\mathbf{p}'\downarrow}a_{\mathbf{p}'\uparrow}\rangle$ near T_c

$$\Gamma(\mathbf{p},\mathbf{p}')=C[S_2-S_1(\sigma_{\mathbf{p}}+\sigma_{\mathbf{p}'})+S_0\sigma_{\mathbf{p}}\sigma_{\mathbf{p}'}]. \tag{39}$$

Since C diverges at T_c, this determines that the order parameter becomes macroscopic at $T<T_c$. Then, the pair creation operator, $a^+_{\mathbf{p}}a^+_{-\mathbf{p}}$, will almost be a number, i.e., we may decompose Eq. (39) into a product

$$\Delta^*_{\mathbf{p}}\Delta_{\mathbf{p}}=\langle a^+_{\mathbf{p}\uparrow}a^+_{-\mathbf{p}\downarrow}\rangle\langle a_{-\mathbf{p}'\downarrow}a_{\mathbf{p}'\uparrow}\rangle \tag{40}$$

and, to be consistent with the **p**, **p**′ dependences, by putting $\xi_{\mathbf{p}}=\xi_{\mathbf{p}'}$ we obtain

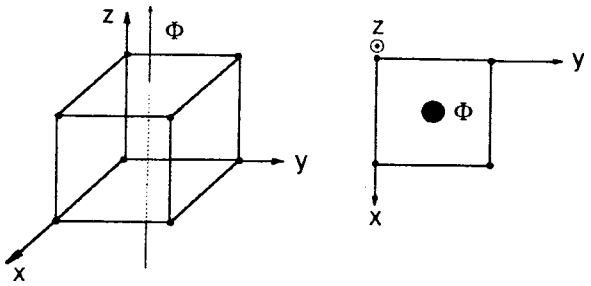

FIG. 4. Sample configuration. The flux Φ through the cube is produced by a solenoid.

$$\Delta_{\mathbf{p}}=C_1[\exp(i\theta/2)\sqrt{S_2(0)}+\exp(-i\theta/2)\sqrt{S_0(0)}]\exp(i\varphi) \tag{41}$$

where

$$\cos\theta=-S_1(0)/\sqrt{S_0(0)S_2(0)} \tag{42}$$

and φ is an overall phase which is irrelevant for a single superconductor but is important for calculating currents in multiple or weakly coupled superconductors. Therefore, the system undergoes a pairing transition at a temperature found from Eq. (35). Since the pairs are charged, the state below T_c cannot be non-superconducting.

We have not calculated the Meissner response but in the following section we present a numerical calculation of flux quantization which supports the above statement.

3. EXACT DIAGONALIZATION OF THE OCCUPATION-DEPENDENT HOPPING HAMILTONIANS IN A FINITE CLUSTER

We calculate the ground state energy of a cubic system as shown in Fig. 4. A magnetic flux Φ is produced by a solenoid passing through the cube. The corners of the cube are the lattice sites that can be occupied by electrons. With the inclusion of the magnetic flux, model Hamiltonian, Eq. 6, becomes

$$H=-t\sum_{\langle ij\rangle\sigma}a^+_{i\sigma}a_{j\sigma}\exp(i\alpha_{ij})+\mathrm{h.c.}+U\sum_i n_{i\uparrow}n_{i\downarrow}+\sum_{\langle ij\rangle\sigma}a^+_{i\sigma}a_{j\sigma}[Vn_{i\bar{\sigma}}n_{j\bar{\sigma}}+W(n_{i\bar{\sigma}}+n_{j\bar{\sigma}})]\times\exp(i\alpha_{ij})+\mathrm{h.c.} \tag{43}$$

where

$$\alpha_{ij}=(2\pi/\Phi_0)\int_{\mathbf{r}_i}^{\mathbf{r}_j}\mathbf{A}\cdot d\mathbf{l} \tag{44}$$

and $\Phi_0=hc/e$ is the magnetic flux quantum. Throughout the calculations we take $t=1$.

We start with constructing the model Hamiltonian. In the Hilbert space of one electron

$$a=\begin{pmatrix}0&1\\0&0\end{pmatrix},\quad a^+=\begin{pmatrix}0&0\\1&0\end{pmatrix}, \tag{45}$$

with a basis specified as $\psi_0=(0,1)$ for the ground state ($n=0$) and $\psi_1=(1,0)$ for the excited state ($n=1$). In case of N states, the operator of annihilation a_n takes the form

$$a_n=v^{n-1}\otimes a\otimes u^{N-n} \tag{46}$$

where u is the unit matrix and v is unitary matrix

$$u=\begin{pmatrix}1 & 0\\ 0 & 1\end{pmatrix},\quad v=\begin{pmatrix}1 & 0\\ 0 & -1\end{pmatrix} \tag{47}$$

and $\otimes$ stands for the Kronecker matrix multiplication. Explicitly, we have

$$a_1=a\otimes u\otimes u\otimes u\ldots\otimes u$$

$$a_2=v\otimes a\otimes u\otimes u\ldots\otimes u$$

$$\ldots\ldots\ldots\ldots\ldots\ldots\ldots$$

$$a_N=v\otimes v\otimes v\ldots\otimes v\otimes a$$

Thus, for example, for two states

$$a_1=\begin{pmatrix}0 & 1 & 0 & 0\\ 0 & 0 & 0 & 0\\ 0 & 0 & 0 & 1\\ 0 & 0 & 0 & 0\end{pmatrix},\quad a_2=\begin{pmatrix}0 & 0 & 1 & 0\\ 0 & 0 & 0 & -1\\ 0 & 0 & 0 & 0\\ 0 & 0 & 0 & 0\end{pmatrix}. \tag{48}$$

These matrices, which are annihilation operators, and the corresponding Hermitian conjugate matrices, which are the creation operators, satisfy the Fermi anti-commutation relation. These operators are sparse matrices with only $N/2$ nonzero elements, which are equal to ± 1. Next we solve the Schrödinger equation $H_\psi=E_\psi$. We implemented a novel algorithm for solving such sparse systems, which will be described elsewhere.

The cubic cluster within the Hubbard Hamiltonian and no external flux applied to the system was studied previously by Callaway *et al.*[19] Quantum Monte Carlo methods applicable to large systems within the Hubbard model (both attractive and repulsive), but not the occupation-dependent hopping Hamiltonians, are reviewed in a paper of Dagotto.[20]

3.1. The number parity effect

Superconductivity reveals itself in the lowering of the ground state energy as electrons get paired. Therefore the energy needs to be minimal for an even number of electrons n and will attain a larger value when n is odd. We consider a ''gap'' parameter[21]

$$\Delta_l=E_{2l+1}-\frac{1}{2}(E_{2l}+E_{2l+2}) \tag{49}$$

as a possible ''signature'' of superconductivity (where E_m corresponds to the ground state energy for m fermions). For all interaction parameters set to zero ($U=V=W=0$), no sign of pairing is observed. To check our analytic results of Sec. 2.2 and the argument following Eq. (34), we calculated Δ above and below the half-filling ($n=8$ in the case of cubic cluster). Below the half-filling chemical potential is negative ($\mu<0$) and above the half-filling it is positive ($\mu>0$). We first checked that the $W\to 0^+$, $W\to 0^-$ and $V\to 0^+$, $V\to 0^-$ calculation is consistent with an exact solution available for a non-interacting system of n electrons.

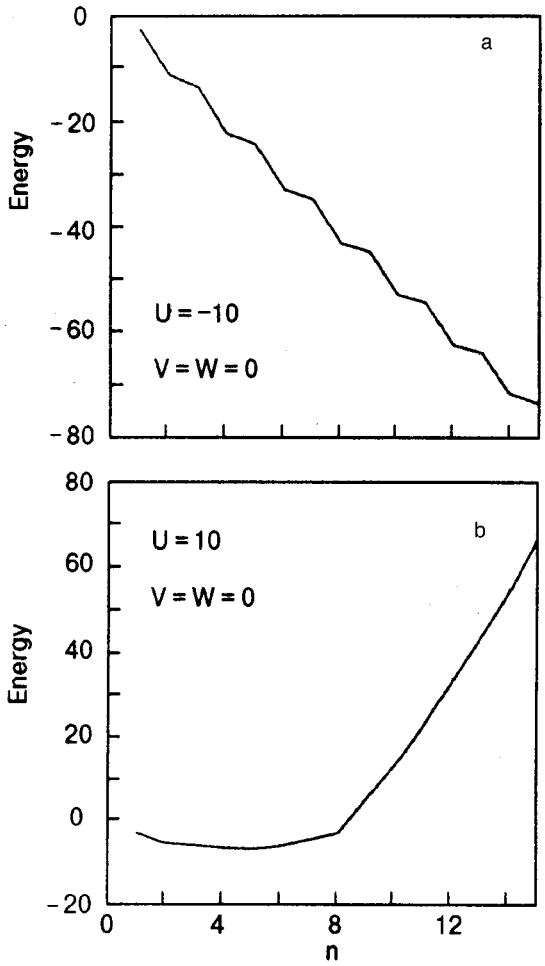

FIG. 5. Dependence of the ground state energy upon the number of particles with $U\neq 0$ and $V=W=0$. Energy, as well as U, is in units of t. (a) For $U<0$, the pairing effect is clearly seen. (b) For $U>0$, there is no pairing.

We then test our program for the case of negative-U Hubbard Hamiltonian ($U<0$, $V=0$, $W=0$) which is known to be superconducting (e.g., Refs. 22 and 23). Positive-U Hubbard model does not show any sign of superconductivity, in disagreement with some statements in the literature.[24] Our calculations cannot disprove the (possible) non-pairing mechanisms of superconductivity but these seem to be unlikely models for the problem of superconductivity in oxides which clearly shows pairing of electrons (holes) in the Josephson effect and in the Abrikosov vortices. The relation $2eV=\hbar\omega$ is justified in the first case[25] and flux quantum of a vortex is $hc/2e$ in the second,[26] both with the value of the charge equal to twice the electronic charge, e.

Figure 5 shows the dependence of the ground state energy upon the number of particles in case of negative-U and positive-U Hubbard models assuming $V=0$ and $W=0$. Such dependences are typical for any value of $|U|$. There clearly is the pairing effect when $U<0$ and there is no sign of pairing at $U>0$.

Tests for pairing in the contraction V,W-models ($V\neq 0$, $U=W=0$ and $W\neq 0$, $U'=V=0$, respectively) are shown in Figs. 6 and 7. The results are in agreement with our pertur-

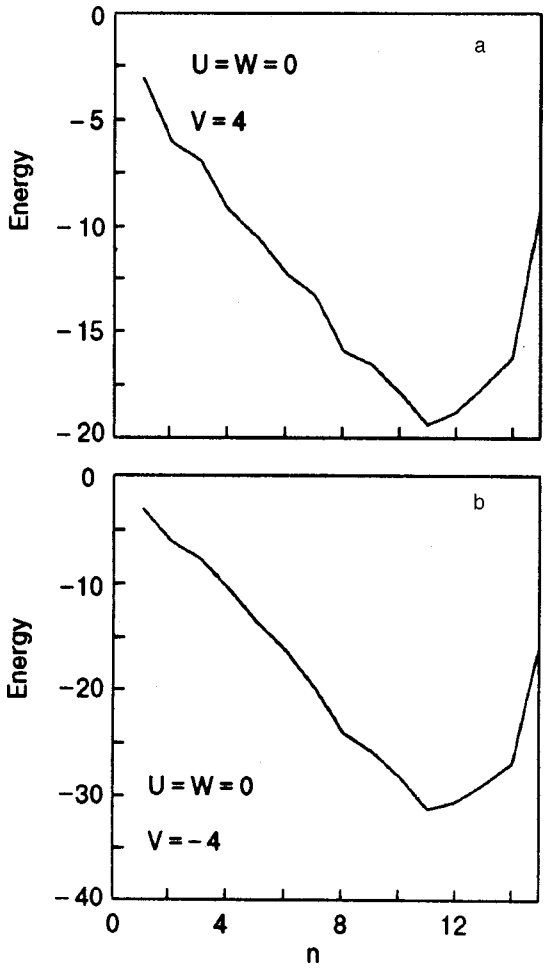

FIG. 6. Dependence of the ground state energy upon the number of particles with $V \neq 0$ and $U = W = 0$. Energy, as well as V, is in units of t. (a), (b) Both for $V > 0$ and $V < 0$, around the half-filling, there is a small pairing effect.

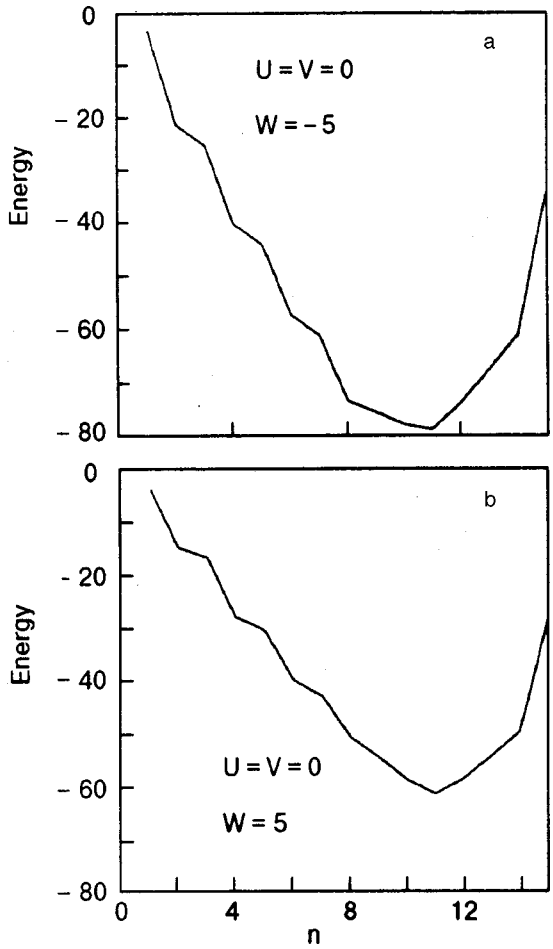

FIG. 7. Dependence of the ground state energy upon the number of particles with $W \neq 0$ and $U = V = 0$. Energy, as well as W, is in units of t. (a), (b) Both for $W > 0$ and $W < 0$, there is a more pronounced pairing effect below the half-filling.

bative calculation of Sec. 2 and with its extension for the intermediate and strong coupling limits $|V| \gtrsim t$, $|W| \gtrsim t$. Since the chemical potential is negative below the half-filling and positive above the half-filling, there is no pairing in the former case ($\tilde{W} \to 0^+$) and there is a sign of pairing in the latter case ($\tilde{W} > 0$), in accord with the value of the effective coupling constant $\tilde{W} = W + (1/2)\nu V$. Similarly, for $\tilde{W} \to 0^-$ below the half-filling there is a sign of pairing ($\Delta \neq 0$) while above the half-filling there is no pairing. These results are summarized in Table I.

For larger values of the interaction parameters, the perturbative results do not remain applicable anymore. Figure 8b shows the dependence of the parity gap Δ on the strength of the interaction. From Fig. 8, it is understood that the W interaction introduces a ''signature'' of pairing in a similar way as the negative-U interaction does. The possibility of ''contraction'' pairing has been investigated previously in the papers.[10,13]

3.2. Flux quantization

Flux quantization is another signature of superconductivity which is a consequence of the Meissner effect. We also tested for the periodicity of the energy versus flux dependence with the period $\Phi_1 = hc/2e$ as compared to the period $\Phi_0 = hc/e$ in the non-interacting system.[27,28] Unfortunately, the even harmonics of Φ_0-periodic dependence of the ground state energy (and related to it, the harmonics of the persistent current $J = -\partial E/\partial \Phi$[27,28]) may simulate the pairing in a non-superconductive system. A small-size (mesoscopic) system can mask the superconducting behavior.[20] Flux quantization in Hubbard Hamiltonians was studied formerly in Refs. 29–31.

TABLE I. Pairing effect for arbitrarily small values of V and W, computed by exact diagonalization of the Hamiltonian. The results presented here are in complete agreement with the perturbative calculations.

	$U = W = 0$		$U = V = 0$	
	$V \to 0^+$	$V \to 0^-$	$W \to 0^+$	$W \to 0^-$
below half-filling ($\mu < 0$)	$\Delta = 0$ (no pairing)	$\Delta \neq 0$ (pairing)	$\Delta = 0$ (no pairing)	$\Delta \neq 0$ (pairing)
above half-filling ($\mu > 0$)	$\Delta \neq 0$ (pairing)	$\Delta = 0$ (no pairing)	$\Delta \neq 0$ (pairing)	$\Delta = 0$ (no pairing)

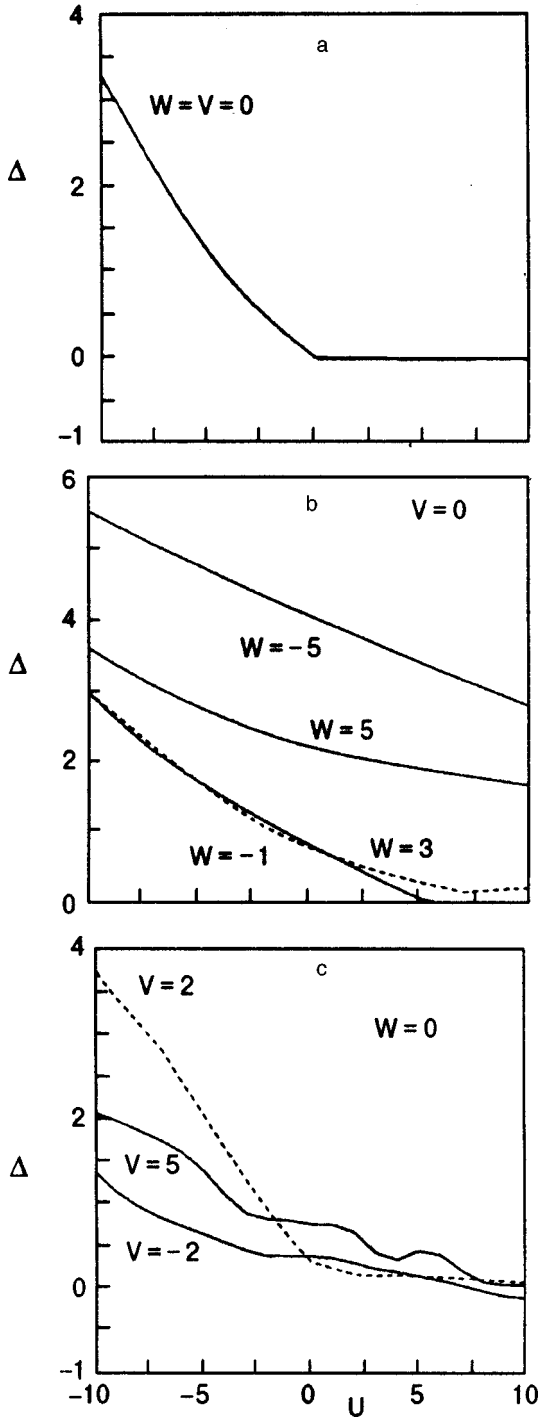

FIG. 8. Dependence of the parameter Δ upon U for various values of W and V below the half-filling. (Δ, U, V and W is in units of t).

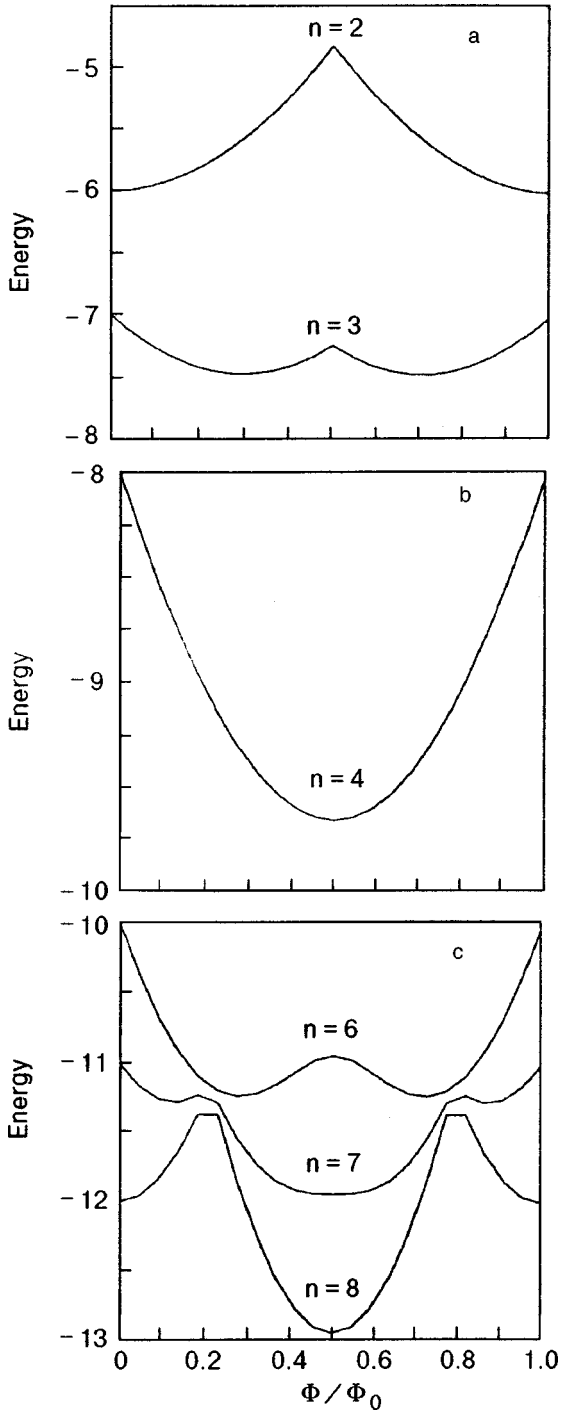

FIG. 9. Dependence of the ground state energy (in units of t) upon magnetic flux. All three interaction parameters are zero, i.e., $U=W=V=0$.

We first demonstrate the behavior of the ground state energy with respect to flux, Fig. 9. A characteristic feature of a mesoscopic system suggests that addition of one extra particle to the system changes the sign of the derivative of the ground state energy with respect to magnetic flux at $\Phi=0$. That is, depending on the parity of the number of particles and on the number of sites, system can change from paramagnetic to diamagnetic state or vice versa. But this behavior is not always observed for the cubic geometry studied. Except the sign change from $n=2$ to $n=3$ and from $n=7$ to $n=8$, no such behavior is seen. As mentioned above, however, the Φ_1-periodic component of the $E(\Phi)$ dependence begins to appear at the higher value of n (Fig. 9c). For both contraction parameters equal to zero, i.e., $W=V=0$, we observe the appearance of the $hc/2e$-periodic component for some values of U (Fig. 10). Even for positive (repulsive) values of U, it is possible to see a local minimum appearing at $\Phi=hc/2e$ (Fig. 10b). This is in agreement with the authors' previous works.[13,29] But this minimum, which does not lead to an exact periodicity of the ground state energy

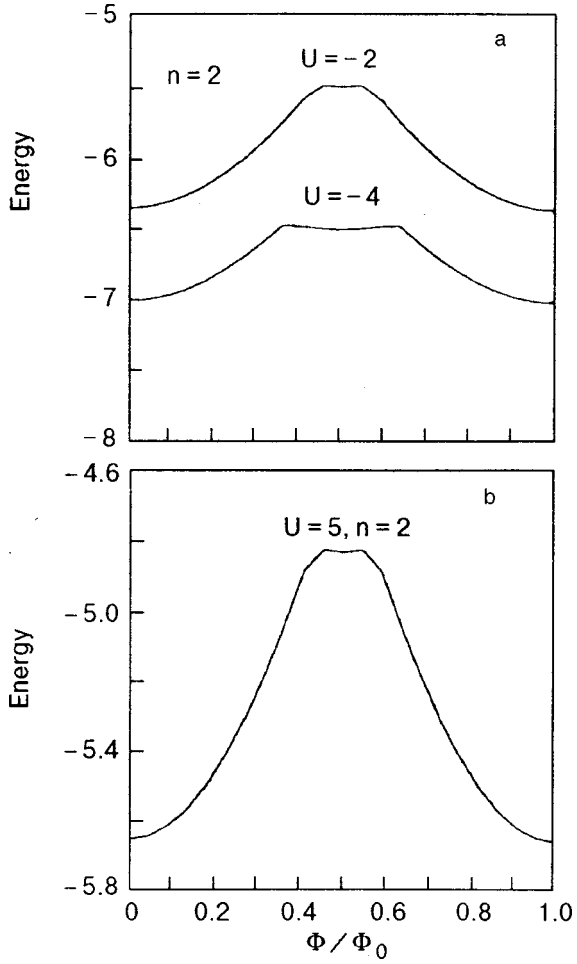

FIG. 10. Dependence of the ground state energy upon magnetic flux. Contraction parameters are both zero, i.e., $W=V=0$, only the on-site interaction parameter U is nonzero. Energy, as well as U, is in units of t.

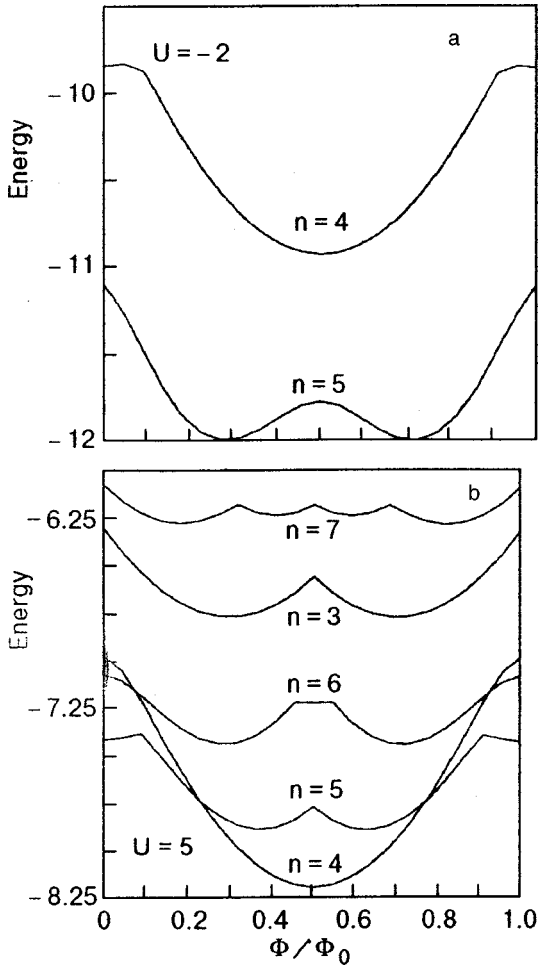

FIG. 11. Dependence of the ground state energy upon magnetic flux. Comparing (a) with Figure 9b clearly shows that the change in the parity of the number of particles for the case of negative U values introduces a sign change in the slope of $E(\Phi)$ at $\Phi=0$. Energy, as well as U, is in units of t.

with a period $\Phi_0/2$, should not be attributed to superconductivity, this is rather a characteristic behavior in mesoscopic systems.

For $U<0$ (while $W=V=0$), the expected mesoscopic behavior, that is, the change of the sign of the slope of ground state energy at $\Phi=0$, starts to reveal itself (Fig. 11). But this happens at sufficiently large absolute values of (negative) U. For other values of U, however, there is no such change.

More pronounced $hc/2e$-periodic components are observed with the introduction of non-zero interaction parameters. The role of W in the ground state energy, when both U and V are zero, is shown in Fig. 12. Meanwhile setting both U and W to zero and observing the effect of the non-zero V shows that V does not play a role as significant as the other two interaction parameters do. There is not much difference in the behavior of the ground state energy upon magnetic flux between the zero and non-zero V (for example $V=-1$) cases.

CONCLUSIONS

We studied the peculiarity of electron conduction in systems in which conduction band is derived from the atomic shells with a small number of electrons (N_e) in an atom. Such materials may include oxygen ($N_e=8$) in the oxides, carbon ($N_e=6$) in borocarbides (e.g., $LuNi_2B_2C$), hydrogen ($N_e=1$) in some metals (e.g., Pd–H). Some materials of this kind are superconductors. It was argued that the Coulomb effects within the atoms strongly influence the inter-atom wave function overlap between the atomic sites and therefore the electron hopping amplitude between the sites. The phenomenology of such conduction mechanism results in a novel addition, to the conventional solid state theory, i.e., Hamiltonians called the occupation-dependent-hopping (or contraction) Hamiltonians, specified with the two coupling parameters V, W. We then attempted a study of superconductivity in such systems within the BCS-type approach assuming Cooper pairing of electrons. The weak-coupling limit allows the determination of the range of parameters V, W values and also of the in-site Coulomb interaction U value which show the Cooper instability. The strong-coupling limit was addressed by a numeric calculation on finite clusters using a novel algorithm (of non-Lanczos type) for eigenvalues of large sparse matrices. One of the results of this

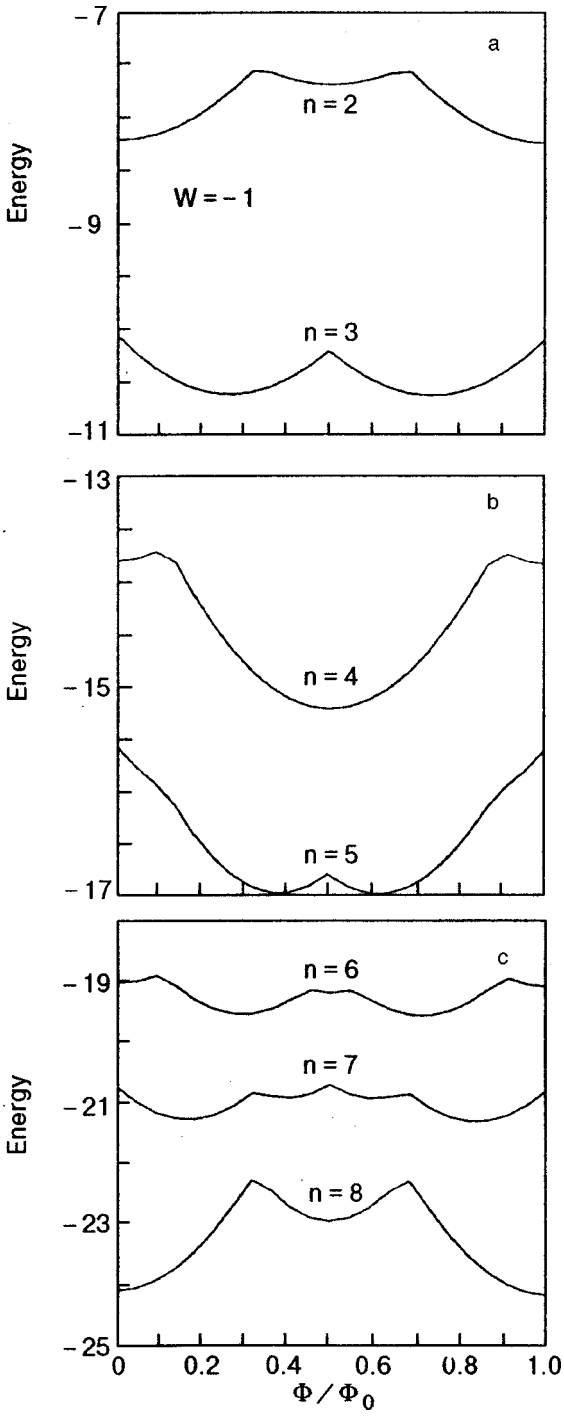

FIG. 12. Dependence of the ground state energy upon the magnetic flux. On-site interaction parameter U and one of the contraction parameters. V, are zero. All plots correspond to the non-zero interaction parameter $W=-1$. Energy, as well as W, is in units of t.

numeric calculation was that the positive-U Hubbard model, sometimes believed to be a candidate for high-T_c superconductivity, does not comply with the goal.

This work was partially supported by the Scientific and Technical Research Council of Turkey (TÜBITAK) through the BDP program.

*E-mail: kulik@fen.bilkent.edu.tr

[1] J. G. Bednorz and K. A. Muller, Z. Phys. B **64**, 189 (1986).
[2] M. K. Wu, J. R. Ashburn, C. J. Torng, P. H. Hor, R. L. Meng, L. Cao, Z. L. Huang, Y. Q. Wang, and C. W. Chu, Phys. Rev. Lett. **58**, 908 (1987).
[3] J. Bardeen, L. N. Cooper, and J. R. Schrieffer, Phys. Rev. **108**, 1175 (1957).
[4] M. S. Hybertsen, E. B. Stechel, M. Schlüter, and D. R. Jennison, Phys. Rev. B **41**, 11068 (1990).
[5] A. K. Mahan, J. A. Annett, and R. M. Martin, Phys. Rev. **108**, 1175 (1957).
[6] N. Nucker, J. Fink, J. C. Fugle, P. J. Durham, and W. M. Temmerman, Phys. Rev. B **37**, 5158 (1998).
[7] P. Kuiper, G. Kruizinaga, J. Ghijsen, M. Grioni, P. J. W. Weijs, F. M. de Groot, and G. A. Sawatsky, Phys. Rev. B **38**, 6483 (1988).
[8] J. E. Hirsch, Phys. Lett. A **134**, 451 (1989).
[9] J. E. Hirsch and F. Marsiglio, Phys. Rev. B **39**, 11515 (1989).
[10] J. E. Hirsch, Phys. Rev. B **48**, 3327 (1993); *ibid.* **48**, 9815 (1993).
[11] I. O. Kulik, Sov. Superconductivity: Phys. Chem. Tech. **2**, 201 (1989).
[12] I. O. Kulik, *Contraction Mechanism for Pairing Interaction in Oxides and Hydrides*, in *Progress in High Temperature Physics*, Vol. 25, R. Nicholsky, (Ed.), World Scientific, Singapore (1990).
[13] H. Boyaci and I. O. Kulik, Fiz. Nizk. Temp. **24**, 316 (1998) [Low Temp. Phys. **24**, 239 (1998)].
[14] I. O. Kulik, Tr. J. Phys. **20**, 627 (1996).
[15] A. A. Abrikosov, L. P. Gorkov, and I. E. Dzyaloshinsky, *Methods of Quantum Field Theory in Statistical Physics*, Dover Publications, New York (1975).
[16] E. Abrahams and T. Tsuneto, Phys. Rev. **152**, 416 (1966).
[17] L. P. Gorkov and G. M. Eliashberg, Z. Éksp. Teor. Fiz. **54**, 612 (1968) [Sov. Phys. JETP **27**, 328 (1968)].
[18] I. O. Kulik, O. Entia-Wohlman, and R. Orbach, J. Low Temp. Phys. **43**, 591 (1981).
[19] J. Callaway, D. P. Chen, and Y. Zang, Phys. Rev. **36**, 2084 (1987).
[20] E. Dagotto, Rev. Mod. Phys. **66**, 763 (1994).
[21] K. A. Matveev and A. I. Larkin, Phys. Rev. Lett. **78**, 3749 (1997).
[22] I. O. Kulik, Physica B **126**, 280 (1984); Int. J. Mod. Phys. B **1**, 851 (1988).
[23] R. Micnas, J. Ranninger, and S. Robaszklewicz, Rev. Mod. Phys. **62**, 113 (1990).
[24] C. H. Pao and N. E. Bickers, Phys. Rev. Lett. **72**, 1870 (1994); D. J. Scalapino, Phys. Rep. **250**, 329 (1995).
[25] T. J. Witt, Phys. Rev. Lett. **61**, 1423 (1988); D. Esteve, J. M. Martinis, C. Urbina, M. H. Devoret, G. Collin, P. Monod, R. Ribault, and A. Percolevski, Europhys. Lett. **3**, 1237 (1987).
[26] P. L. Gammel, D. J. Bishop, G. J. Dolan, J. R. Kwo, C. A. Murray, L. F. Schneener, and J. V. Waszczak, Phys. Rev. Lett. **59**, 2592 (1987); L. Ya. Vinnikov, L. A. Gurevich, G. A. Yemelchenko, and Yu. A. Ossipyan, Solid State Commun. **67**, 253 (1988).
[27] I. O. Kulik, Pisma Zh. Éksp. Teor. Fiz **11**, 407 (1970) [JETP Lett. **11**, 275 (1970)].
[28] M. Buttiker, Y. Imry, and R. Landauer, Phys. Lett. A **96**, 365 (1983).
[29] A. Ferretti, I. O. Kulik, and A. Larni, Phys. Rev. B **47**, 12235 (1993).
[30] R. M. Fye, M. J. Martins, and D. J. Scalapino, Phys. Rev. B **44**, 6909 (1991).
[31] A. Sudbo, C. M. Varma, T. Giamarchi, E. B. Stechel, and R. T. Scalettar, Phys. Rev. Lett. **70**, 978 (1993).

This article was published in English in the original Russian journal. It was edited by R. T. Beyer.

Superconducting and normal properties of the set of Mo/Si superlattices with variable Si layer thickness

M. Yu. Mikhaĭlov, O. I. Yuzephovich, A. S. Pokhila, Yu. V. Bomze, N. Ya. Fogel, and I. M. Dmitrenko

B. Verkin Institute for Low Temperature Physics and Engineering, National Academy of Sciences of Ukraine, 47 Lenin Ave., 310164 Kharkov, Ukraine[a]

S. A. Yulin

Kharkov State Polytechnic University, 21 Frunze St., 310002 Kharkov, Ukraine

A. S. Sidorenko and O. B. Moldovan

Institute of Applied Physics, 5 Academiei Str., 2028 Kishinev, Moldova

E. I. Buchstab

Department of Physics, Solid State Institute, Technion, 32100 Haifa, Israel
(Submitted March 15, 1999)
Fiz. Nizk. Temp. **25**, 850–856 (August–September 1999)

We report the results of the superconducting and kinetic parameter measurements (transition temperature T_c, parallel and perpendicular critical fields H_{c2}, resistivity in the normal state) on a set of Mo/Si superconducting superlattices with a constant metal layer thickness $d_{\mathrm{Mo}}=22$ Å and variable semiconducting one $d_{\mathrm{Si}}(14-44\,\text{Å})$. Our data show a monotonic dependence of all measured parameters on d_{Si}. It is found that the Josephson interlayer coupling energy depends exponentially on the spacer thickness. The data obtained allowed us to determine the characteristic electron tunneling length for amorphous silicon with high precision. It is equal to 3.9 Å. Enhancement of interlayer coupling leads to the Mo. Si multilayer transition temperature increasing, in agreement with Horovitz theory and with the experimental data on high-T_c materials. © *1999 American Institute of Physics.* [S1063-777X(99)00808-7]

INTRODUCTION

Artificial superconducting superlattices have been of enduring interest for a long time as a perfect model system for the study of layered superconductor physics. Their tunability, i.e., the possibility of changing independently and in an arbitrary way the thicknesses of the superconducting layers and nonsuperconducting interlayers (spacers) and of using a wide spectrum of constituting materials, makes artificial multilayers very attractive objects for the investigation of many fundamental properties. The dimensionality effects, the role of the intrinsic anisotropy and its influence on T_c, the thermal and quantum fluctuation effects, etc., belong to such properties. It is especially important that for these systems the fine control over the interlayer Josephson coupling strength, which has a most profound influence on the behavior of layered superconductors, may be achieved.[1,2] In spite of an obvious importance of direct investigations of Josephson coupling, such studies are very scarce because of the necessity of preparing a large set of the variable layer thickness superlattices with a big number of bilayers N, very high regularity of the layering and with extremely small ''steps'' in the spacer thickness between neighboring samples in the set. The latter circumstance is associated with the expected exponential dependence of the interlayer coupling parameter on the insulating or semiconducting spacer thickness.[1] Such a dependence, consistent with the picture of quantum-mechanical tunneling of the charge carriers through a barrier, follows from obvious physical considerations. In Ref. 1 the experimental data on the coupling parameter obtained on Nb/Ge superlattices were interpreted in such a way, although, unfortunately, the spread of the experimental data points was very large.

However, it has been found out recently that such a simple description of the interlayer coupling based on an usual tunneling mechanism is not applicable for all representatives of the S/I multilayer class (S is a superconductor, I is a semiconductor). The anomalous oscillatory behavior of the superconducting and kinetic characteristics has been discovered on Mo/Si multilayers with a constant Si layer thickness ($d_{\mathrm{Si}}=25$ Å) and variable Mo layer thickness ($d_{\mathrm{Mo}}=8-200$ Å).[3,4] The periodicity of all the oscillations was $\Delta d_{\mathrm{Mo}}=35$ Å. The most nontrivial effect among all observed phenomena is the oscillating behavior of the interlayer coupling strength at the constant thickness of the Si layers.[5] The background normal conductivity and superconducting transition temperature T_c dependencies on d_{Mo} for these samples are reasonably explained in terms of quantum interference effects in quasi-independent disordered films.[6]

In spite of obviously similar features in the oscillatory behavior on Mo/Si superlattices and on simple films of Sn and semimetals.[7–9] the explanation of the oscillations found

 © 1999 American Institute of Physics

on superlattices in terms of the usual quantum size effect [10,11] appeared to be rather doubtful because of the quite small longitudinal transport mean free path of the electrons (about several interatomic distances) in the system under study.[3] It means that in the case of the usual quantum size effect the smearing of the quantum levels connected with the charge carrier scattering on the crystal lattice imperfections may exceed the distance between the energy levels, and the oscillations have to become practically indiscernible. The results of the investigations of the T_c dependence on d_{Mo} for single molybdenum film series with silicon underlayers and overlayers did confirm these expectations: in contrast to multilayered samples, the molybdenum films have revealed a monotonic T_c increase with d_{Mo} (Ref. 12).[1)] Thus, the oscillatory behavior found is the property inherent only in the layered system.

Recently, a new type of quantum size effect in metal-semiconductor superlattices has been predicted.[13] Giant oscillations of the tunnel current and the superlattice transverse conductivity should appear if size quantization of the electron spectrum in the metal layers occurs. This effect results from a sharp dependence of the probability of electron tunneling through a semiconducting interlayer on the incidence angle of the electrons moving to the interface. Due to this fact, it is expected that the effect of the size-quantization-controlled oscillations of the transverse conductivity may result. Spikes of transverse conductivity are bound to appear when the quantized electron levels pass through the Fermi level at the thickness of metal layer d_m variation. One of the most interesting features of the theory considered is the prediction as to the possibility of observing quantum oscillations of the transverse conductivity even in the case of rather disordered systems, provided that the electrons in the metal layers undergo soft (low-angle) scattering on the imperfections. It was shown [13] that a lifetime τ_s for the size-quantized states giving the main contribution to the tunnel current is d_m/a times greater than a typical τ value determining the in-plane transport (a is the interatomic distance). This fact is due to the structure of the size-quantized spectrum in an individual metal film. While the typical distance between quantized electron terms at a given energy is of the order of $\hbar/d_m$, the distance between the neighboring terms determining the tunnel probability is of the order of $p_F(a/d_m)^{1/2}$, i.e., noticeably larger. Under low-angle scattering conditions, when the changes in the electron longitudinal momentum are rather small, the electron transitions between these latter states are hampered, and, therefore, the lifetime is significantly enhanced.

It is clear that the predicted oscillations of the tunnel probability may at least lead to interlayer Josephson coupling strength oscillations. The conspicuous correlations between the oscillations of different physical characteristics are found on Mo/Si superlattices,[3,5] and it allows one to believe that experimentally observed oscillation effects are close in its origin to the phenomenon considered theoretically.

It follows from the theory [13] that the oscillations arise at d_m variation, while the thickness of the semiconductor layer d_s influences only the oscillation amplitude. Thus, one can expect that all multilayer parameters should depend monotonically on d_s in a set of superlattices with a variable value of d_s and a fixed value of d_m.

Here we report the results of the measurements of kinetic and superconducting parameters on such a set of Mo/Si superlattices.

SAMPLE PREPARATION AND EXPERIMENTAL METHODS

The superlattices were prepared by dc-magnetron sputtering onto optical quality glass substrates kept at 100 °C. The number of bilayers in all the set of superlattices was 50. The initial pressure in the deposition chamber was no worse than 10^{-6} Torr. Argon with the pressure 3×10^{-3} Torr was used as a sputtering gas. A time of exposition of the sample holder in the zone of every source and its displacement in another zone was regulated with a precise time controller. The thicknesses of the two layers in the bilayer were determined by the deposition rates of both Mo and Si and by the time of exposition. In order to ensure the constant deposition rates, the stabilized power supplies for molybdenum and silicon sources and a precise gas admission system were used (with an accuracy to within 0.1% for both the gas pressure and the applied power). The deposition rates were 2–3 Å/s.

X-ray diffractometry was used for structural characterization of the superlattices. The low-angle diffractometry allowed us to determine the multilayer periods with the accuracy of 0.1 Å. For Mo/Si superlattices with the wavelengths exceeding 100 Å, which have been prepared under the same conditions, the number of satellites on the diffractograms was about 10. For the short-period superlattices investigated here, this number was 4–5. These data as well as the small width of satellite lines testify to the high regularity of the layering. The separation between satellites and their position confirm the layer spacing expected from fabrication process. The relative difference of the Mo layer thickness for all the samples did not exceed 0.3 Å.

The recorded $\theta-2\theta$ diffraction patterns for superlattices revealed that molybdenum layers consist of small crystallites (with the size of 25–30 Å), while silicon ones are amorphous.

The low temperature measurements were carried out in a ^{4}He cryostat equipped with a 5 T superconducting coil. The temperature was measured with a carbon-glass thermometer, calibrated against a Ge thermometer in a zero field. Temperature was controlled within 1.4–10 K with the accuracy of 1 mK. Due to a small magnetoresistance a maximum deviation of temperature was about 10 mK in a magnetic field of 5 T as compared to the temperature at zero magnetic field. The resistivity measurements were performed with an ac bridge using the conventional four-probe method. Both the T_c and the H_{c2} were defined as the midpoints of the $R(T)$ and $R(H)$ transitions.

EXPERIMENTAL RESULTS AND DISCUSSION

The typical dependencies of the resistance R on the temperature in a range 4–100 K for Mo/Si multilayers are presented in Fig. 1. A negative temperature coefficient of resistivity was observed for all samples investigated between

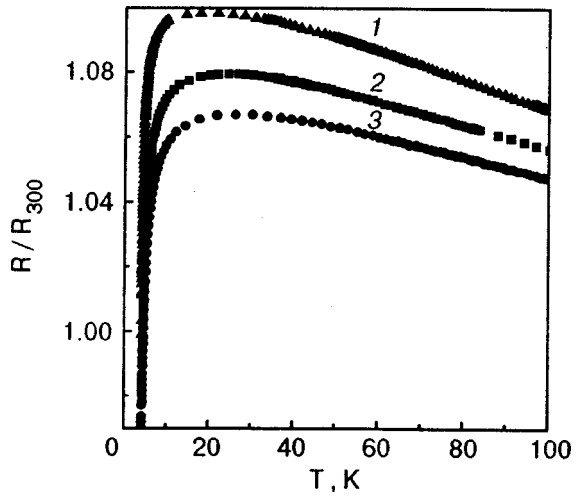

FIG. 1. The resistance ratio as a function of temperature for some of Mo/Si samples (*1*—$d_{Si}=39$ Å; *2*—$d_{Si}=43$ Å; *3*—$d_{Si}=34$ Å).

300 K and a temperature where the resistance starts to decrease due to the approach to the superconducting transition. A similar $R(T)$ behavior was previously observed on Mo/Si multilayer series with $d_{Si}=\text{const}=25$ Å and a variable d_{Mo} in the d_{Mo} range 13–90 Å.[14] Analysis of these dependencies as well as of the data on the magnetoresistance in magnetic fields perpendicular to the layers has revealed that layers quantum corrections to the conductivity are essential in the Mo/si system with disordered metal layers.[14] As the data obtained show, the same is true for the set of superlattices investigated here.

The dependence of the resistance ratio R_{300}/R_m on the thickness of silicon layer d_{Si} is shown in Fig. 2a (R_m is the maximum resistance before the superconducting transition). There is an obvious tendency towards diminishing of R_{300}/R_m with d_{Si} increase which suggests that the magnitude of the quantum interference corrections to the resistivity for the multilayers with the better separated metal layers are enhanced.

Figures 2b and 2c demonstrate the transition temperature T_c and the derivative of the perpendicular critical magnetic field $dH_{c\perp}/dT|_{T_c}$ as a function of d_{Si}. While $dH_{c\perp}/dT$ does not in practice depend on d_{Si}, T_c noticeably diminishes with d_{Si} increase. The T_c vs d_{Si} dependence shows a tendency to saturation at large d_{Si} values. Only the derivative of the parallel critical magnetic field and, correspondingly, the anisotropy parameter $\gamma=(M/m)^{1/2}=(dH_{c\parallel}/dT)/(dH_{c\perp}/dT)|_{T_c}$ exhibits a very pronounced dependence on the spacer thickness (M/m is an effective mass ratio).

In Fig. 3 the magnetic critical field dependencies on temperature are shown for the samples with different d_{Si}. For the case of a field orthogonal to the layer planes the dependencies $H_{c\perp}(T)$ are linear. Parallel critical fields $H_{c\parallel}$ for the multilayers with the smallest values of d_{Si} are also linear with temperature in all accessible range of magnetic fields. For samples with $d_{Si}\geqslant 34$ Å the change in the temperature dependence of $H_{c\parallel}$ is observed at low temperatures which points to the dimensional $3D$-$2D$ crossover. The anisotropy becomes larger with increase in the spacerthickness, and γ

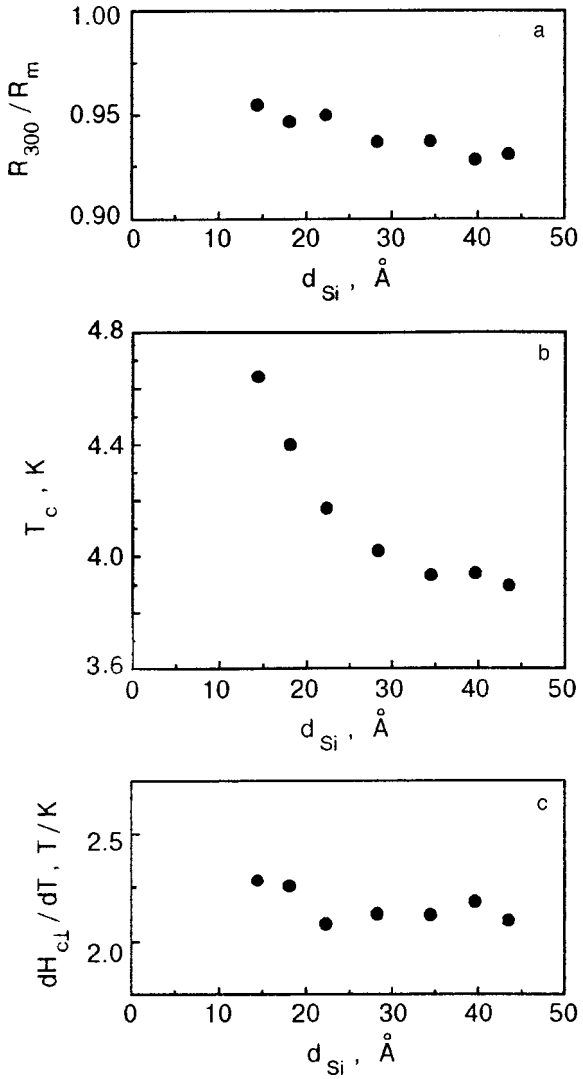

FIG. 2. The dependencies of multilayer parameters on silicon spacer thickness d_{Si}: resistance ratio R_{300}/R_m (see text) (a); transition temperature T_c (b); derivative of the perpendicular critical magnetic field $(dH_{c\perp}/dT)_{T_c}$(c).

amounts to the value of 23 at $d_{Si}=43$ Å. The anisotropy parameter γ as a function of d_{Si} is presented in Fig. 4.

The theory of the critical magnetic fields for layered systems with the Josephson coupling between the superconducting layers is highly developed.[2,15–18] Using the effective-mass model of Lawrence and Doniach,[19] which is a good approximation for the weak field range, one can estimate the Josephson coupling energy by the formula [15]

$$\eta_J=\frac{\hbar^2}{2ms^2\gamma^2}. \tag{1}$$

Here, $s=d_m+d_s$ is a superlattice period.

Using the experimental γ values (Fig. 4) one can determine the Josephson coupling parameter η_J. The coupling parameter as a function of d_{Si} is shown in Fig. 5. As follows from the experimental data, the η_J decreases exponentially with an increase in the silicon layer thickness according to the relation:

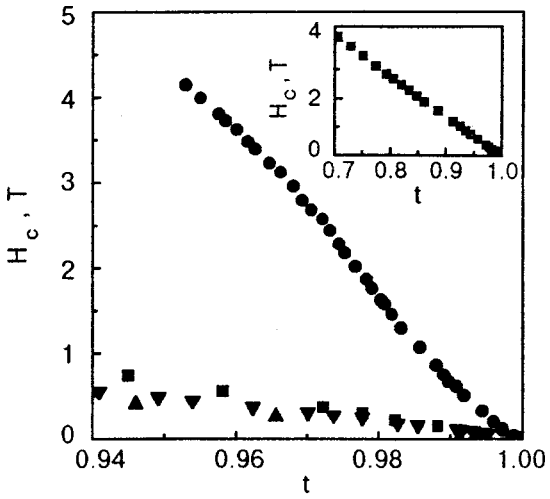

FIG. 3. Critical magnetic fields $H_{c2}(T)$ as a function of the reduced temperature $t=T/T_c$ for two Mo/Si samples ($d_{\mathrm{Si}}=34$ Å: ●—$H_{c\parallel}(t)$; ▼—$H_{c\perp}(t)$, $d_{\mathrm{Si}}=18$ Å; ■—$H_{c\parallel}(t)$; ▲—$H_{c\perp}(t)$). Inset: $d_{\mathrm{Si}}=18$ Å, $H_{c\parallel}(t)$.

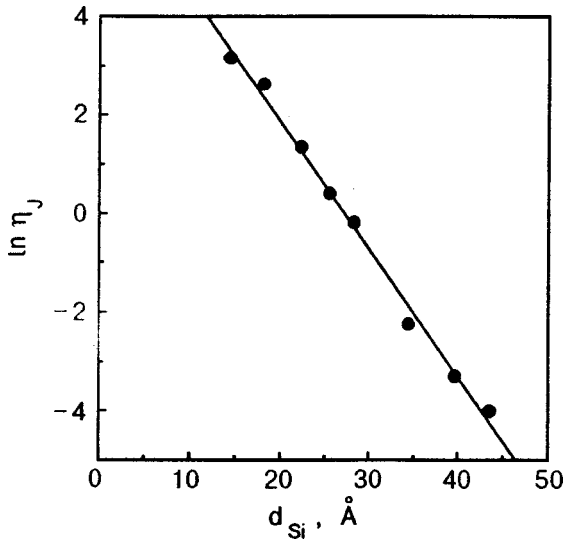

FIG. 5. Josephson coupling energy η_J as a function of d_{Si} for the Mo/Si sample series investigated.

$$\eta_J=\eta_{J0}\exp(-d_{\mathrm{Si}}/d_0). \tag{2}$$

As it was mentioned in the Introduction, Ruggiero, Barbee and Beasley [1] have found the same type of relationship between the interlayer coupling energy and the spacer thickness on Nb/Ge superlattices. From the observed exponential relationship between η_J and d_{Si} (Fig. 5) we obtain the d_0 value of 3.9 Å which may be considered as a characteristic tunnel length for amorphous silicon. For amorphous Ge the value $d_0=8$ Å was derived.[1] In the latter case, the accuracy of d_0 evaluation was not very high because, of large spread of the data points. This spread in the experiments mentioned was, probably, inevitable because, as d_{Ge} varied, the thickness of Nb layers did not remain constant as in our experiments (d_{Nb} was varied in a range 30–65 Å). It is possible that the variation of γ with d_m at a constant d_s value, observed on Mo/Si superlattices, cannot be excluded for S/I multilayers having different constituent materials. It may be the reason for large spread of the points.

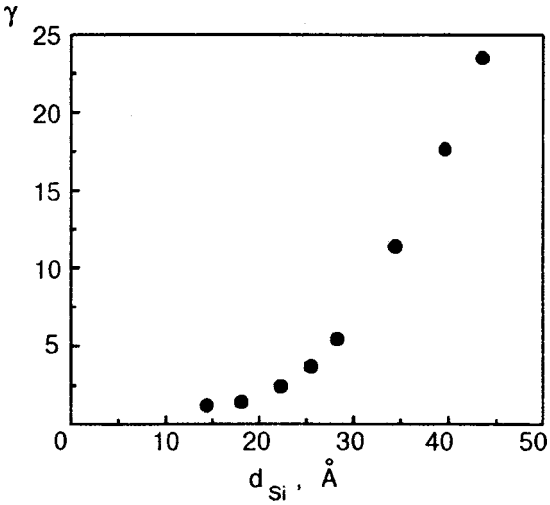

FIG. 4. The anisotropy parameter $\gamma=(M/m)^{1/2}$ as a function of d_{Si} for multilayers investigated.

All the above results provide a clear answer to the important issue arising in the context of the observation of the oscillation effects found on a series of Mo/Si samples with variable d_m. The issue is whether the semiconductor interlayer thickness variation leads to the appearance of the oscillation effects, just as it occurs when d_m varies at constant d_s. All dependencies of kinetic and superconducting parameters on d_s, if any, appeared to be monotonic. Simultaneously fair evidence for the exponential dependence of coupling energy on the spacer thickness is obtained for the first time.

It should be mentioned that there are experiments on V/C layered system [20,21] where the oscillations of T_c, $dH_{c\perp}/dT$ and normal resistivity were observed with the variation of the carbon spacer thickness. These oscillation effects were explained by Kagan and Dubovskii,[22] who assumed that the oscillations in the metal-semiconductor system are mainly associated not with the quantization of transverse motion of electrons in metal films, but with a change in the boundary conditions at the interface between a metal and semiconductor layers. These conditions depend on a spacer thickness. Such an effect should be expected in the case of the crystalline semiconductor interlayer. Our experimental results indicate that such effects are absent in a case of Mo/Si layered system with amorphous silicon spacers.

Another interesting question that is widely discussed[23–28] concerns the nature of the superconducting phase transition in the layered superconductors with the Josephson-type coupling and the influence of the interlayer coupling on the transition temperature T_c. According to the mean field theory,[29] the T_c of S/I multilayers should coincide with that of the separate superconducting layers. When the fluctuations are taken into account the situation changes essentially. The most extensive study of this issue was performed in the works of Horovitz.[24–26] It was shown that at a finite coupling

the layered system should exhibit at the critical temperature the three-dimensional phase transition. The T_c value differs from that for noncoupled individual films. In the system of coupled layers the T_c is determined by the competing influence of two types of the topological excitations (the thermally excited vortices and antivortices piercing the superconducting layers which should appear in a two-dimensional superconductor in the vicinity of the Berezinsky–Kosterlitz–Thouless transition[30–32] and the vortex loops proliferating between superconducting layers [23]). It is predicted that increased coupling should lead to the enhancement of T_c. As the data of Figs. 2 and 5 show, namely, such a type of dependence of T_c on the interlayer coupling is observed in our experiments. The data on Mo/Si sample series with the variable d_m and $d_{\mathrm{Si}}=\mathrm{const}$[5] confirm such an observation as well. The minima on the oscillating T_c vs d_m dependence correspond to the d_m values where the anisotropy parameter is the largest (i.e., the coupling parameter has its minimum). As with the multilayer set investigated here, relatively small T_c variation is observed whereas the η_J changes almost by an order of magnitude.

The data, which are qualitatively similar to those reported in this work, were obtained on Nb/Ge multilayers.[1] There is the same trend to T_c enhancement when the Ge spacer thickness decreases. However, the latter data do not permit estimating the role of the interlayer coupling due to the interfering effect of inhomogeneities in the metal layers. The inner structure of Nb films consisting of layers with essentially different conductivity allows the authors to provide another explanation for the T_c vs d_{Ge} dependence in terms of the proximity effect. Nevertheless, according to the recent concepts of the layered superconductor physics the alternative interpretation of the experiments [1] cannot be excluded either.

The considerably stronger effect of coupling on T_c is observed on the multilayers including high-T_c materials.[33–35] When superconducting layers of $YBa_2Cu_3O_7$ are separated by the insulating layers of $PrBa_2Cu_3O_7$, the T_c of the superlattices diminishes drastically with the an increase in the insulating layer thickness, reaching the saturation at 10–20 K for the spacer thickness of 6–10 unit cells of $PrBa_2Cu_3O_7$.[33–35] There are other ways to control the anisotropy parameter γ in high temperature compounds: intercalation, variations of the oxygen concentration, doping with some specific impurities.[35–37] In all above mentioned cases the superconducting transition temperature decreases with the coupling weakening, but for $YBa_2Cu_3O_7$ the dependence of T_c on γ is not universal; it is different for chain doping and for the plane doping.[37] While the relative T_c change in $YBa_2Cu_3O_7$ is quite noticeable with the variation of the oxygen deficiency, its change at plane doping (the variation of Zn concentration) is far greater. All existing experimental data are in good qualitative agreement with the predictions of the theory,[24–26] but a more detailed comparison with theory will be interesting. For the present set of Mo/Si superlattices it is difficult to make such a comparison because the necessary conditions of the constant normal resistivity through all the set of the samples were not fulfilled.

CONCLUSIONS

1. The exponential dependence of the Josephson coupling energy on the silicon spacer thickness is found on Mo/Si superlattices with the constant thickness of molybdenum layers and variable d_{Si}. The characteristic electron tunneling length for amorphous silicon determined from the experimental data is equal to 3.9 Å.

2. All the dependencies of superconducting and kinetic parameters on the Si interlayer thickness (if any) are monotonic according to the expectations based on the theory.[13]

3. The diminishing of the Josephson coupling parameter leads to a decrease in the superconducting transition temperature, in agreement with the theory of Horovitz [24–26] and with the experimental data on high temperature materials.

ACKNOWLEDGEMENTS

One of the the authors (N.Ya.F.) is grateful to Prof. B. Horovitz for the valuable discussions, which partially inspired us to carry out these investigations. A.S.S. is grateful to Prof. R. Tidecks and Prof. K. Samwer for stimulating discussions. We are grateful to V. Langer and A. I. Erenburg for x-ray examination of the crystal structure of Mo/Si multilayers.

*Only in the dependence of $dH_{c\perp}/dT|T_c$ on d_{Mo} the slight hints on the oscillations with very small amplitude, may, appear, but a large spread of the experimental data does not allow us to state this positively.

[a]E-mail: fogel@ilt.kharkov.ua

[1] S. T. Ruggiero, T. W. Barbee, and M. R. Beasley, Phys. Rev. B **26**, 4894 (1982).
[2] L. I. Glazman, I. M. Dmitrenko, V. L. Tovazhnyanskii, N. Ya. Fogel, and V. G. Cherkasova, Zh. Éksp. Teor. Fiz **92**, 1461 (1987) [Sov. Phys. JETP **85**, 821 (1987)].
[3] E. I. Buchstab, V. Yu. Kashirin, N. Ya. Fogel, V. G. Cherkasova, V. V. Kondratenko, A. I. Fedorenko, and S. A. Yulin, Fiz. Nizk. Temp. **19**, 704 (1993) [Low Temp. Phys. **13**, 506 (1993)].
[4] V. Yu. Kashirin, N. Ya. Fogel, V. G. Cherkasova, E. I. Buchstab, and S. A. Yulin, Physica B **194–196**, 2381 (1994).
[5] N. Ya. Fogel, O. G. Turutanov, A. S. Sidorenko, and E. I. Buchstab, Phys. Rev. B **54**, 2372 (1997).
[6] N. Ya. Fogel, E. I. Buchstab, A. S. Pokhila, A. I. Erenburg, and V. Langer, Phys. Rev. B **53**, 71 (1996).
[7] Yu. F. Komnik and E. I. Buchstab, Pis'ma Zh. Éksp. Teor. Fiz. **6**, 536 (1967) [JETP Lett. **6**, 58 (1967)].
[8] Yu. F. Komnik, E. I. Buchstab, Yu. V. Nikitin, and F. I. Chuprinin, Thin Solid Films **11**, 43 (1972).
[9] Yu. F. Ogrin, V. N. Lutskii, and M. I. Elinson, Pis'ma Zh. Éksp. Teor. Fiz. **3**, 114 (1966) [JETP Lett. **8**, 71 (1966)].
[10] I. M. Lifshitz and A. M. Kosevich, Sov. Phys. Dokl. **91**, 277 (1953).
[11] Yu. F. Komnik, *Physics of Metal Films*, Atomizdat, Moscow (1978).
[12] N. Ya. Fogel, E. I. Buchstab, O. A. Koretzkaya, A. S. Pokhila, V. G. Cherkasova, and S. A. Yulin, Fiz. Nizk. Temp. **22**, 359 (1996) [Low Temp. Phys. **22**, 277 (1996)].
[13] N. Ya. Fogel, E. A. Kovtun, R. I. Shekhter, and A. A. Slutskin, Fiz. Nizk. Temp. **25**, 168 (1999) [Low Temp. Phys. **25**, 168 (1999)].
[14] E. I. Buchstab, A. V. Butenko, N. Ya. Fogel, V. G. Cherkasova, and R. L. Rosenbaum, Phys. Rev. B **50**, 10063 (1994).
[15] R. A. Klemm, A. Luther, and M. R. Bessley, Phys. Rev. B **B12**, 877 (1975).
[16] L. N. Bulaevskii, Usp. Fiz. Nauk. **116**, 449 (1975) [Sov. Phys. Usp. **18**, 514 (1976)].
[17] G. Deutscher and O. Entin-Wohlman, Phys. Rev. B **17**, 1249 (1978).
[18] V. M. Gvozdikov, Fiz. Nizk. Temp. **16**, 5 (1990) [Sov. J. Low Temp. Phys. **16**, 1 (1990)].

[19] W. E. Lawrence and S. Doniach, in *Proceedings of the XII International Conference on Low Temperature Physics*, E. Kanda (Ed.), Academic, Kyoub 1971, p. 361.
[20] V. M. Golyanov and M. N. Mikheeva, Zh. Éksp. Teor. Fiz. **70**, 2236 (1976) [Sov. Phys. JETP **43**, 1167 (1976)].
[21] V. M. Golyanov, A. A. Teplov, and M. B. Tsetlin, J. Low Temp. Phys. **28**, 29 (1977).
[22] Yu. Kagan and L. D. Dubovskii, Zh. Éksp. Teor. Fiz. **72**, 646 (1977) [Sov. Phys. JETP **5**, 339 (1977)].
[23] J. Friedel, J. Phys.: Condens. Matter **1**, 7757 (1989).
[24] B. Horovitz, Phys. Rev. Lett. **67**, 378 (1991).
[25] B. Horovitz, Phys. Rev. B **47**, 5947 (1993).
[26] B. Horovitz, Physica A **200**, 296 (1993).
[27] S. E. Korshunov, Europhys. Lett. **11**, 757 (1990).
[28] M. Dzierzawa, M. Zamora, D. Baeriswyl, and X. Bagnoud, Phys. Rev. Lett. **77**, 3897 (1996).
[29] V. M. Gvozdikov, Fiz. Nizk. Temp. **15**, 636 (1989) [Sov. J. Low Temp. Phys. **15**, 358 (1989)].
[30] J. M. Kosterlitz and D. J. Thouless, J. Phys. C **6**, 1181 (1973).
[31] V. L. Berezinskii, Zh. Éksp. Teor. Phys. **61**, 1144 (1971) [Sov. Phys. JETP **54**, 610 (1972)].
[32] B. I. Halperin and D. R. Nelson, J. Low Temp. Phys. **36**, 599 (1979).
[33] J. M. Triscone, O. Fisher, O. Brunner, L. Antognazza, A. D. Kent, and M. G. Karkur, Phys. Rev. Lett. **64**, 804 (1990).
[34] Q. Li, X. X. Xi, X. D. Wu, A. Inam, S. Vadlamannati, W. L. Mclean, T. Venkatasaran, R. Ramesh, D. M. Hwang, J. A. Martinez, and L. Nazar, Phys. Rev. Lett. **64**, 3086 (1990).
[35] D. H. Lowades, D. P. Norton, and J. D. Budai, Phys. Rev. Lett. **65**, 1160 (1990).
[36] X. D. Xiang, W. A. Vareka, A. Zetti, J. L. Corkill, M. L. Cohen, N. Kijima, and R. Gronsky, Phys. Rev. Lett. **68**, 530 (1992).
[37] Ö. Rapp, M. Andersson, J. Axnas, Yu. Eltsev, B. Lundqvist, and A. Rydh, in *Proceedings of the Conference on Symmetry and Pairing in High T_c Superconductors*, M. Ausloos (Ed.), World Scientific, Yalta (1998), p. 301.

This article was published in English in the original Russian journal. It was edited by R. T. Beyer.

LOW-TEMPERATURE MAGNETISM

Low-temperature magnetic properties and stress effects in glassy Fe-B alloys: the eutectic region

A. B. Beznosov, E. L. Fertman, V. V. Eremenko, V. A. Desnenko, and V. Z. Bengus

*B. Verkin Institute for Low Temperature Physics and Engineering, National Academy of Sciences of Ukraine, 47, Lenin Ave., 310164, Kharkov, Ukraine**

(Submitted May 26, 1999)
Fiz. Nizk. Temp. **25**, 857–860 (August–September 1999)

The magnetic properties of glassy $Fe_{100-x}B_x$ ($x=14,16,17,20$) alloys under a low mechanical stress (up to 68 MPa) at temperatures 10–300 K, in magnetic fields up to 40 Oe, have been studied. Low temperature anomalies of magnetic susceptibility, as well as substantial differences in the effects of stresses on the low field magnetic characteristics of alloys with various boron contents, have been revealed. The eutectic alloy $Fe_{83}B_{17}$ was found to be the least sensitive to applied stresses, magnetic fields, and temperature changes: it possesses the lowest magnetic induction in the reversibility fields region and the highest local anisotropy fluctuations. The hypoeutectic $Fe_{84}B_{16}$ alloy is the most sensitive to applied stresses at room temperature, but its sensitivity substantially reduces with increasing load, as well as with decreasing temperature. The results obtained reflect the special character of the alloys electronic structure at the eutectic point. © *1999 American Institute of Physics.* [S1063-777X(99)00908-1]

The amorphous alloys $Fe_{100-x}B_x$ are soft magnetic materials with a wide field of applications.[1–3] In particular, much attention has focused on the alloys in the region of $x=17$ (the eutectic composition), due to the possibility of special interatomic interactions in these alloys [4,5]. We have used the effect of stress on the magnetic properties to study the nature of differences of the alloys properties.

EXPERIMENTAL PROCEDURE

The studied samples $Fe_{100-x}B_x$ ($x=14,16,17,20$) were prepared from 30 μm thick and 6 mm wide amorphous ribbons, obtained by the planar flow casting technique.

The effect of tension as well as pressure on the magnetic induction B, was measured. The pulse-induction technique was used, with longitudinal magnetic fields $0 \leqslant H \leqslant 40$ Oe, temperatures 300 and 77 K, and tension stresses σ near 22 and 63 MPa in the 1st kind experiments, as well as the SQUID magnetometer, normal to the ribbon's surface external magnetic field 20 Oe (the effective field in the samples was substantially reduced by the demagnetization factor $N \sim 10$), temperatures $10\,\mathrm{K} \leqslant T \leqslant 230\,\mathrm{K}$, and the normal to the ribbons surface uniaxial pressure of about 20 MPa in the 2nd kind experiments.

RESULTS AND DISCUSSION

Magnetic characteristics

Longitudinal field. It was revealed that the eutectic alloy $Fe_{83}B_{17}$ possesses the lowest value of B in fields above 5 Oe at all studied temperatures and stresses. This is in agreement with the opinion that fluctuations of the local anisotropy field in this alloy are the highest in the considered system [6]. The $B(H)$ curves (Fig. 1) suggest that the $Fe_{83}B_{17}$ alloy has the smallest saturation induction. This result corresponds to the saturation magnetization measurements of Bengus *et al.*[4]

At 300 K the hypoeutectic alloy $Fe_{84}B_{16}$ possesses the highest magnetic permeability μ, and the lowest coercivity H_c and magnetic remanence B_r (Table I). At 77 K the difference between the μ of $Fe_{84}B_{16}$ and other alloys decreases.

Transverse field. The effective magnetic susceptibility of the samples χ_{eff} measured in the 2nd experiment slowly decreased with decreasing temperature over almost the whole temperature range. There was a steep slope at about 20 K, which was evidently connected with a magnetic phase transition to the disordered asperomagnetic phase.[7] The χ_{eff} curve of the eutectic alloy $Fe_{83}B_{17}$ was substantially lower than that of the other alloys. This may be considered as an evidence of the highest local magnetic anisotropy in the alloy.

Local anisotropy. The analysis of the field dependence of magnetization $\mathbf{M}=(\mathbf{B}-\mathbf{H})/4\pi$ in the region approaching saturation is carried out in the framework of the local anisotropy model. The parameters A_i of the equation

$$M=\sum_{i=0}^{6} A_i H^{-0.5i} \tag{1}$$

in the region of longitudinal magnetic fields $16\,\mathrm{Oe} \leqslant H \leqslant 40\,\mathrm{Oe}$ were evaluated by the least squares method. The validity was analyzed of the sum (1) as a whole, as well as of

 © 1999 American Institute of Physics

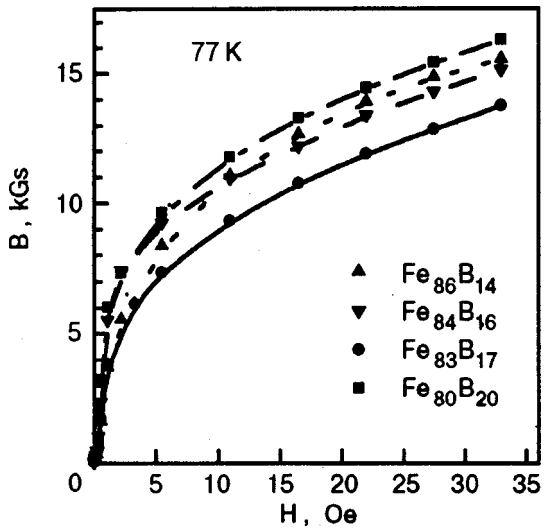

FIG. 1. The magnetic induction field dependences of $Fe_{100-x}B_x$ (x =14,16,17,20) amorphous alloys under zero load at 77 K.

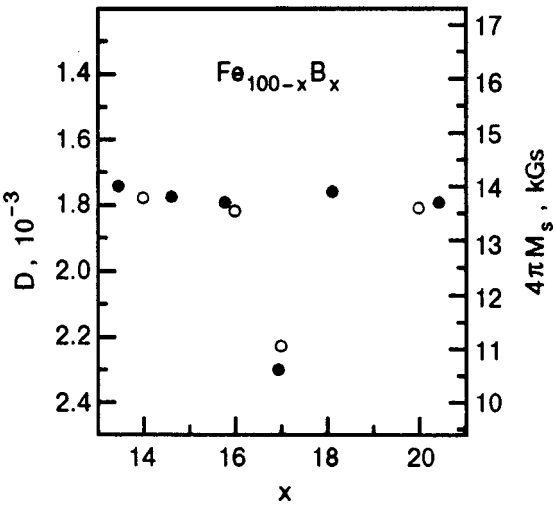

FIG. 2. The parameter D(○) from Eq. (2), reflecting the local magnetic anisotropy fluctuations in the amorphous alloys $Fe_{100-x}B_x$ under zero load at 77 K, and saturation magnetization (●) [4] at 4.2 K versus x.

its separate components. It was found that the best approximation of experimental data corresponds to the equation

$$M = M_\infty[1-(DM_\infty/H)^{0.5}], \quad (2)$$

describing the zero-dimensional violations of the translation symmetry [8] of the system. The parameter D in Eq. (2) characterizes the local magnetic anisotropy fluctuations value.

As one can see in Fig. 2, the concentration dependence of parameter D shows a singularity at the eutectic point x =17, which correlates well with the analogous singularity of the low temperature high field magnetization M_s from.[4]

The results obtained agree with work by Iskhakov *et al.*,[6] who reported that the eutectic alloy had the maximum value of mean square fluctuations of local magnetic anisotropy.

Tension effects

Applied tensile stress leads to a growth in magnetic induction B, magnetic permeability μ and remanence B_r, and to a decrease in H_c (but no H_c decrease for $Fe_{84}B_{16}$).

Permeability. The increase of magnetic induction is mainly seen in fields up to about 30 Oe. At both room and liquid nitrogen temperatures, the growth of the maximum value of magnetic permeability μ_{max} of all the studied alloys under load is very sharp and range up to 1.5–3 times at about 63 MPa. This can be seen at Fig. 3, where the load effect is shown for the alloy $Fe_{84}B_{16}$.

At 300 K the smallest value of $\Delta\mu_{max}/\Delta\sigma$ is exhibited by the eutectic alloy $Fe_{83}B_{17}$. When the temperature is lowered to 77 K, μ_{max} decreases about 2 times. The smallest value of $\Delta\mu_{max}/\Delta\sigma$ at 77 K is for the $Fe_{84}B_{16}$ alloy.

Magnetic remanence. The applied loads lead to 1.6–3.6 times growth in remanence; the change in remanence per unit stress $\Delta B_r/\Delta\sigma$, is nearly equal for all studied alloys and temperatures, except for the hypoeutectic alloy $Fe_{84}B_{16}$. This alloy exhibits the smallest remanence without load at both studied temperatures, the largest value of $\Delta B_r/\Delta\sigma$ at 300 K and the smallest at 77 K (Fig. 4).

Coercivity. The coercivity H_c of all the alloys decreased with increasing applied load, except for $Fe_{84}B_{16}$, which increased. But its coercivity remains the smallest at all

TABLE I. The maximum magnetic permeability μ_{max}, coercivity H_c, and magnetic remanence B_r of glassy Fe-B alloys at nitrogen (77 K) and room (300 K) temperatures.

	μ_{max}		B_r, Gs		H_c, Oe	
Alloy	77 K	300 K	77 K	300 K	77 K	300 K
$Fe_{86}B_{14}$	2957	7228	980	1358	0.495	0.231
$Fe_{84}B_{16}$	4600	12651	303	756	0.165	0.132
$Fe_{83}B_{17}$	3235	7478	419	1496	0.341	0.264
$Fe_{80}B_{20}$	3802	8357	1566	1804	0.418	0.308

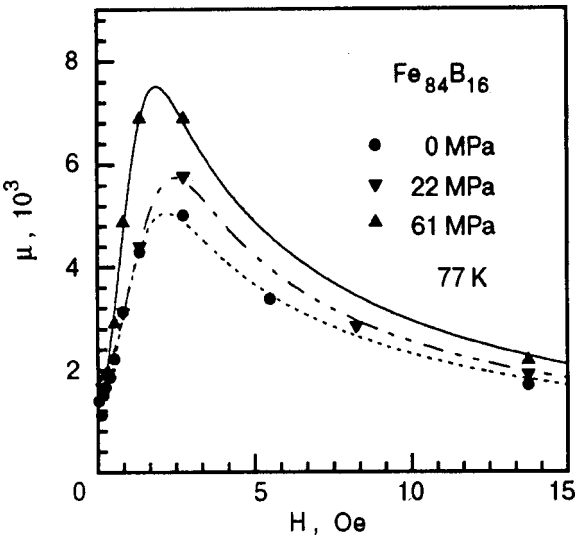

FIG. 3. Magnetic permeability μ of amorphous $Fe_{84}B_{16}$ alloy at liquid nitrogen temperature under the various tensile loads (22 and 61 MPa) versus magnetic field H.

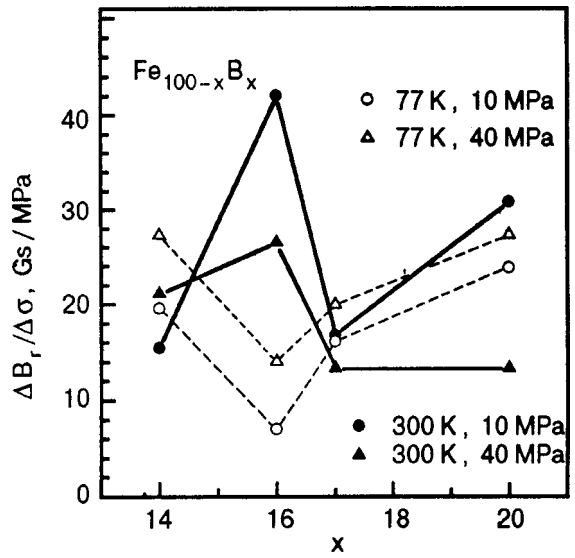

FIG. 4. The average derivative $\Delta B_r/\Delta\sigma$ of amorphous Fe-B alloys at temperatures 77 and 300 K under tension stresses of 10 and 40 MPa.

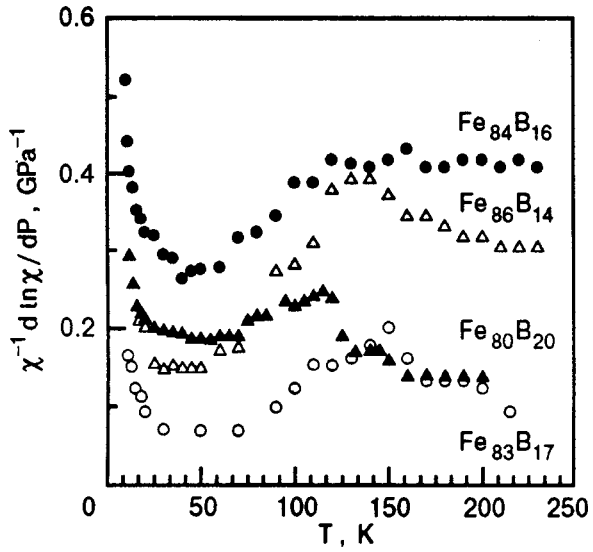

FIG. 5. The temperature dependence of the value $\chi^{-1}d\ln\chi/dP$ for amorphous Fe-B alloys under the normal to the ribbons surface uniaxial pressure of 20 MPa.

the studied temperatures and loads. At the same time the coercivity of the eutectic alloy $Fe_{83}B_{17}$ is nearly independent of the applied load, its $\Delta H_c/\Delta\sigma$ value is rather small.

The obtained data show that the eutectic alloy $Fe_{83}B_{17}$ is the least sensitive to changes in temperature and applied load: the changes per unit stress of its coercivity $\Delta H_c/\Delta\sigma$, remanence $\Delta B_r/\Delta\sigma$ and permeability $\Delta\mu_{max}/\Delta\sigma$ are comparatively small at both studied temperatures. The threshold (i.e. separating the unchanged and changed electronic structures) $Fe_{84}B_{16}$ alloy is the most sensitive to applied load at room temperature, and its properties are the most sensitive to temperature as well. When the temperature decreases its sensitiveness to the load drops sharply.

Uniaxial pressure effects

The data obtained in the uniaxial pressure and the tensile experiments are in a good agreement. The magnetic susceptibility drops under pressure at all the temperatures studied, but the temperature dependence is not monotonic.

When lowering the temperature all the alloys showed an increasing value of $\chi^{-1}d\ln\chi/dP$ in the range 230–150 K (for alloy $Fe_{84}B_{16}$ the increase was only small), a maximum at 110–140 K, a decrease at 110–30 K, and an abrupt growth at temperatures lower than 30 K (Fig. 5). The $\chi^{-1}d\ln\chi/dP$ value was chosen for the analysis, because it is independent of the demagnetization factor: $\chi^{-1}d\ln\chi/dP=\chi_{eff}^{-1}d\ln\chi_{eff}/dP$. The main features of the temperature behavior of this value are determined by the behavior of $d\chi_{eff}/dP$, because χ_{eff} depends comparatively slightly on the temperature.

Since the interatomic distances weakly change with temperature (the studied alloys possess invar-type properties [9]), the presence of $\chi^{-1}d\ln\chi/dP$ maxima means a change in electronic structure. The growth of $\chi^{-1}d\ln\chi/dP$ at temperatures lower than 30 K is evidently connected with the formation of an asperomagnetic structure in this temperature region.[7]

The smallest value of $\chi^{-1}d\ln\chi/dP$ corresponds to the eutectic composition ($x=17$). This is in a good agreement with the concentration dependence of the failure stress of the studied alloys,[4] as well as with our data on tension stress effects.

CONCLUSION

The results obtained confirm that the eutectic alloy $Fe_{83}B_{17}$ possesses a special and most stable atomic and electronic structure with the highest local anisotropy. It has the lowest magnetic induction and permeability, and it is the least sensitive to applied load and decreasing temperature. The results are in good agreement with the idea of an extremely disordered structure of intercluster boundaries of eutectic alloy $Fe_{83}B_{17}$, in which the clusters are supposed to have a quasicrystal structure.[4]

The hypoeutectic $Fe_{84}B_{16}$ alloy exhibits the highest value of magnetic permeability and the lowest remanence and coercivity. It is the most sensitive to the applied loads at room temperature, and its properties are also the most sensitive to changes in temperature. Therefore, it possesses the smallest local magnetic anisotropy and the least stable electronic structure.

ACKNOWLEDGMENT

The amorphous ribbons were lent for the research by P. Duhaj (Institute of Physics of Slovak Academy of Sciences, Bratislava). Authors are thankful to P. Duhaj, E. D. Tabachnikova and A. S. Panfilov for collaboration.

DEDICATION

Authors dedicate this paper to the memory of Boris Ieremievich Verkin, Scientist and Organizer of Science, who has founded and for thirty years directed the Institute for

Low Temperature Physics and Engineering of the Academy of Sciences of Ukraine, where authors have the good fortune to work.

*E-mail: beznosov@ilt.kharkov.ua

[1] F. E. Luborsky, *Amorphous Metallic Alloys*, Butterworths, London (1983).
[2] R. Hasegawa and R. Ray, J. Appl. Phys. **49**, 4174 (1978).
[3] R. Hasegawa, J. Magn. Magn. Mater. **100**, 1 (1991).
[4] V. Z. Bengus, P. Duhaj, E. B. Korol'kova, E. D. Tabachnikova, A. V. Golik, and S. I. Tarapov, Fiz. Nizk. Temp. **20**, 1082 (1994) [Low Temp. Phys. **20**, 853 (1994)].
[5] A. B. Beznosov, E. L. Fertman, V. A. Desnenko, V. Z. Bengus, and V. A. Ushakov, in Novye Magnitnye Materialy Mikroelectroniki, Pt. 1, 212, MGU, Moskva (1998).
[6] R. S. Iskhakov, M. M. Karpenko, G. V. Popov, and V. P. Ovcharov, Fiz. Met. Metalloved. **61**, 265 (1986).
[7] V. G. Bar'yakhtar, G. A. Takzei, A. B. Surzhenko, and M. V. Gavrilenko, Fiz. Tverd. Tela **34**, 245 (1992) [Sov. Phys. Solid State **34**, 129 (1992)].
[8] S. V. Vonsovsky, *Magnetism*, Wiley, New York, 1974.
[9] K. Fukamichi, M. Kikuchi, S. Arakawa, and T. Masumoto, Solid State Commun. **23**, 955 (1977).

This article was published in English in the original Russian journal. It was edited by R. T. Beyer.

Raman scattering and phase transitions in mixed crystals $K_{1-x}(NH_4)_xH_2PO_4$

Yu. A. Popkov, A. V. Van'kevich, I. A. Taranova, and E. M. Savchenko

*Kharkov State University, 310077 Kharkov, Ukraine**)*

L. A. Shuvalov

L. Shubnikov Institute of Crystallography, Russian Academy of Sciences, 117333 Moscow, Russia
(Submitted February 24, 1999)
Fiz. Nizk. Temp. **25** , 861–867 (August–September 1999)

Spectral parameters of the Raman scattering band corresponding to intrinsic vibration $\nu_2(A_1)$ of the PO_4 tetrahedron in mixed crystals of $K_{1-x}A_xDP$ with various ammonium concentrations are studied in the temperature range 4.2–300 K. Abrupt changes in frequency and half-width of the band are observed during transitions to ordered ferroelectric ($x=0.00, 0.02, 0.04, 0.08$) or antiferroelectric ($x=0.74$,0.82) phases. The decrease in the band half-width during ordering indicates the participation of excitations responsible for the corresponding states in relaxation processes. The transition to the structural glass phase ($x=0.22, 0.32, 0.53$) is not accompanied with sharp changes in the band parameters, but the band half-width at low temperatures is smaller than the expected value for totally disordered paraelectric phase.
© *1999 American Institute of Physics.* [S1063-777X(99)01008-7]

INTRODUCTION

Crystals belonging to the KDP family are classical objects for investigating phase transitions to the ferroelectric (FE) or antiferroelectric (AFE) state.[1] In actual practice, this large class includes crystals with the general formula AH_2BO_4 (and their deuterized analogs), where A=K, Rb, Cs, Tl, or NH_4 and B=P or As. Antiferroelectric properties are observed only for ammonium-based crystals, while the remaining compounds experience transition to the FE state upon cooling.

Most compounds at room temperature possess the same tetragonal symmetry D_{2d}^{12} with two structural units in a unit cell, and lattice parameters for different compounds have close values. For this reason, we can obtain mixed (including FE–AFE) crystals in the entire concentration range. Different types of ordering in initial pure compounds leads to frustration for mixed crystals at low temperatures. Thus, all premises for the formation of a new ''phase'' referred to as dipole, or structural, or proton (deuteron) glass are created. We write the word ''phase'' in inverted comas since the corresponding state is nonergodic and does not obey the laws of equilibrium thermodynamics.

However, we can introduce the order parameter for the glass state also, for example, the Edvards–Anderson parameter $q_{EA}=\langle\langle S_i\rangle_T^2\rangle_C$,[2] where the first averaging is of the thermodynamic type, while the second is the configuration averaging, and the role of spin S_i at a lattice site of mixed crystals belonging to the KDP family can be played by the ''up'' or ''down'' displacement of protons from the central position. The glass state is studied best of all for magnetic systems (see, for example, the review by Korenblit and Shender[3] and the literature cited therein), but it remains unclear even for spin glasses whether the state is a phase in the conventional sense and whether a phase transition to this state exists. For this reason, any new result obtained for the glass phase is of considerable interest.

In the case of mixed crystals belonging to the KDP family, the glass state was observed for several systems.[1)] The system $K_{1-x}(NH_4)_xH_2PO_4$ (KADP) has been studied most intensely in recent years.[10–12] The phase diagram of this system includes the ferroelectric phase existing in the ammonium concentration range $x=0$–0.2 as well as the antiferroelectric phase ($x=0.72$–1.00) and the glass phase formed in the intermediate concentration range. Raman scattering spectra proved that a transition to the glass state occurs in two stages: at first the position of ammonium ions is fixed at $T_m\approx 120$ K, and the formation of the phase is completed with ordering of protons at $T_g\approx 70$ K.[12–15]

Here we report on new data for the $K_{1-x}(NH_4)_xH_2PO_4$, which convincingly illustrate the presence of transitions to the FE and AFE phases and the structural glass (SG) phase.

DISCUSSION OF EXPERIMENTAL RESULTS

Experimental Technique

Experiments were made by using the Raman scattering technique, involving the excitation by 4880 Å line emitted by a 100-mW argon laser in the 90° scattering geometry. We used a refined spectrometer DFS-24, photon counting technique, and automated system of control, data recording and processing. Details of sample preparation and classification and the features of the experimental setup were reported earlier.[12] Measurements were made in the temperature range 4.2–300 K.

In our experiments, we studied in detail the behavior of the $\nu_2(A_1)$ vibrational mode of the PO_4 group (according to the Shur classification),[16] belonging to the frequency range of the order of 350 cm^{-1}. The corresponding line is quite intense and is observed, in accordance with the selection

 © 1999 American Institute of Physics

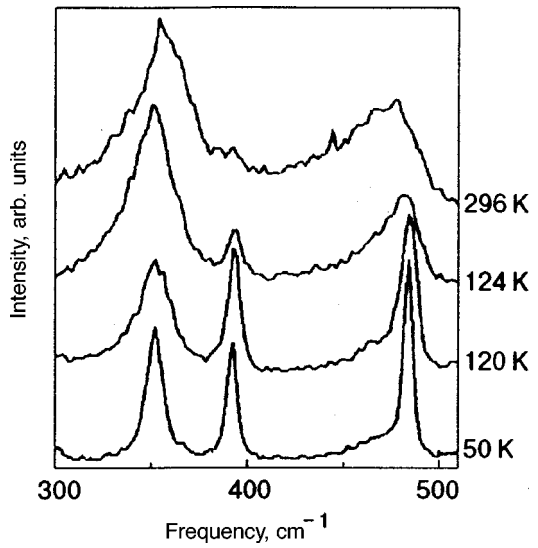

FIG. 1. Raman spectra for a pure KDP crystal in the $y(xx)z$ polarization at several temperatures. $T_C = 122$ K. Spectral resolution is 2.5 cm^{-1}.

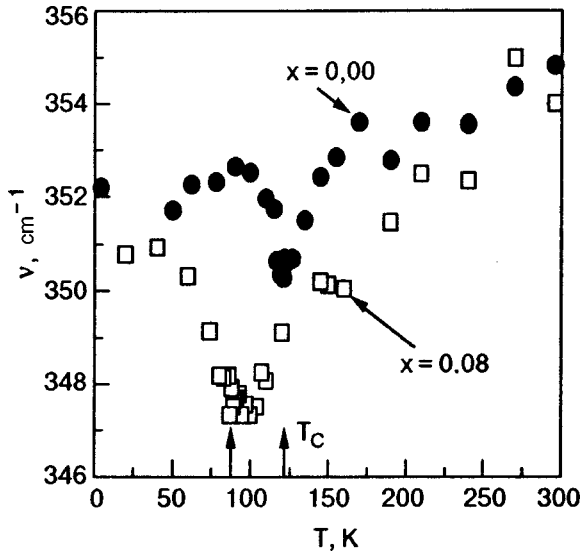

FIG. 2. Temperature dependence of frequency (position of the peak) for the $\nu_2(A_1)$ Raman band for samples undergoing a phase transition to the ferroelectric state. Arrows indicate the corresponding Curie temperatures.

rules, in the polarizations xx, yy, and zz. We shall describe here only the results obtained in the $y(xx)z$ geometry.

Transition to Ferroelectric Phase

After the transition to the ferroelectric phase, the crystal symmetry is lowered from the tetragonal symmetry D_{2d}^{12} to the orthorhombic symmetry C_{2v}^{19}, and the x- and y-axes are rotated approximately through 45°. In our experiments, we studied samples with four concentrations ($x = 0.00$, 0.02, 0.04, and 0.08) in which a transition to the FE state takes place. The results are perfectly identical for all the samples, the only difference being that the temperature T_c of the transition to the FE phase decreases with increasing ammonium concentration, and the temperature range in which strong changes in spectral parameters occur becomes more extended.

Figure 1 shows the Raman spectra for a pure KDP crystal in the range of low- frequency vibrational modes of the PO_4 group at several temperatures. The temperature T_c for KDP is 122 K. Bands with frequencies near 350, 385, and 480 cm^{-1} correspond to the vibrational modes $\nu_2(A_1), \nu_2(B_2)$, and $\nu_4(B_1)$ of the PO_4 tetrahedron.[16,17] The emergence of the mode $\nu_2(B_2)$ (which must be observed in the spectra with the xy polarization) upon cooling and its enhancement below T_c is associated with the rotation of the x- and y- axes (see above).

The temperature dependence of the spectral position of the $\nu_2(A_1)$ band, which is presented in Fig. 2 for samples with two concentrations, is quite interesting and peculiar. A similar λ-shaped dependence was also obtained for samples with other concentrations, the temperature T_c corresponding to the minimum on these curves in all cases. To our knowledge, no such dependences have been detected earlier for any band in the Raman spectra of crystals of the KDP family, although a similar behavior was observed for other compounds. For example, the spectral position of a number of low-frequency bands in the Raman spectrum of the ammonium fluoroberyllate crystal $(NH_4)_2BeF_4$ also has a minimum at the ferroelectric phase transition.[18]

The ''softening'' of the $\nu_2(A_1)$ mode observed by us during the FE transition cannot be attributed to electrostriction since other modes [e.g., $\nu_1(A_1)$] should also exhibit a similar dependence, but the change in its frequency upon the transition is step-wise (see Fig. 4 in Ref. 12).

Hattori *et al.*,[19] who also investigated the $\nu_2(A_1)$ line in the $x(zz)y$ polarization in the RADP system (which is very close to KADP in its properties), observed a complex variation of the shape of the line in the phase-transition region. They explained some of the obtained results by the coexistence of FE, AFE, and paraelectric modes with different spectral positions and different temperature dependences. Using such a decomposition of the $\nu_2(A_1)$ line, we can explain the formation of a doublet during the AFE phase transition, which was observed by us (see below). However, we did not observe any change in the shape of the line for crystals undergoing a transition to the FE phase. While analyzing the spectra, we assumed that the line has a symmetric Lorentzian shape (see Fig. 1).

The temperature dependence of the half-width of the line under investigation for a pure KDP crystal is shown in Fig. 3. Similar temperature dependences were also observed for samples with ammonium concentration $x = 0.02$,0.04, and 0.08: the half-width of the line decreases abruptly during a transition to the ferroelectric phase. This points to a contribution to the linewidth from excitations responsible for the ordered FE state. In our case, these are soft phonon modes. It should be noted that a similar strong increase in the line half-width was observed, for example, in optical absorption spectra of antiferromagnetic compounds during ordering (see Fig. 3 in Ref. 20) and served as a proof of the participation of magnons in the formation of the spectra. In magnetically ordered crystals, the role of ''soft'' excitations condensed during a transition is played just by magnons.

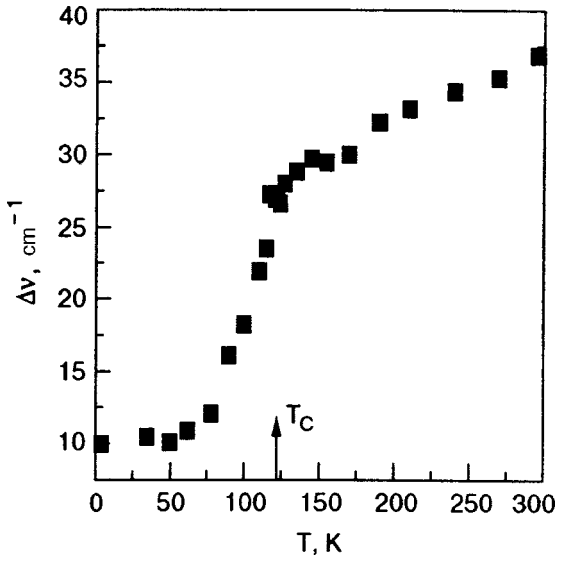

FIG. 3. Temperature dependence of half-width (width at half-height) of the $\nu_2(A_1)$ band for a pure KDP crystal.

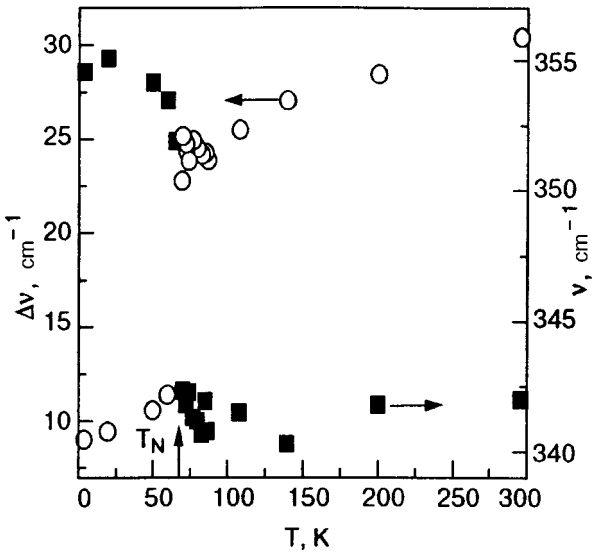

FIG. 5. Temperature dependence of frequency (■) and half-width (○) of the $\nu_2(A_1)$ line for a $K_{0.26}A_{0.74}DP$ crystal.

Transition to Antiferroelectric Phase

A transition to the AFE state in pure $NH_4H_2PO_4$ (ADP) crystals occurs at $T_N = 148$ K. This first-order phase transition is accompanied by strong electrostriction, and below T_N the monocrystalline samples disintegrate into a powder, which makes it impossible to carry out high-quality polarization studies of Raman spectra in the AFE phase. Addition of 15–25% of potassium preserves the AFE transition, while electrostriction is suppressed significantly, and the samples are not destroyed down to helium temperatures. In our experiments, we studied two such samples with the ammonium concentration 0.74 and 0.82.

Figure 4 shows Raman spectra of the crystal with $x = 0.74$ in the region of the vibrational mode ν_2 of the PO_4 tetrahedron. It can be seen that the $\nu_2(A_1)$ line has the doublet structure in the immediate vicinity of the transition ($T_N = 68.5$ K in this sample), although it is correctly described by a solitary line of the Lorentzian shape away from the transition (on the high and low temperature sides). It was mentioned above that the doublet structure is probably associated with the coexistence of two (paraelectric and antiferroelectric) modes with several differing frequencies in a narrow temperature range (3–4 K). The temperature dependence of frequency and half-width of this mode is shown in Fig. 5. It can be seen that the band parameters change jump-wise as a result of the transition. As in the case of transition to the FE state, an abrupt change of the half-width from 25 to 10 cm^{-1} is observed in a narrow temperature interval during the transition to the AFE phase.

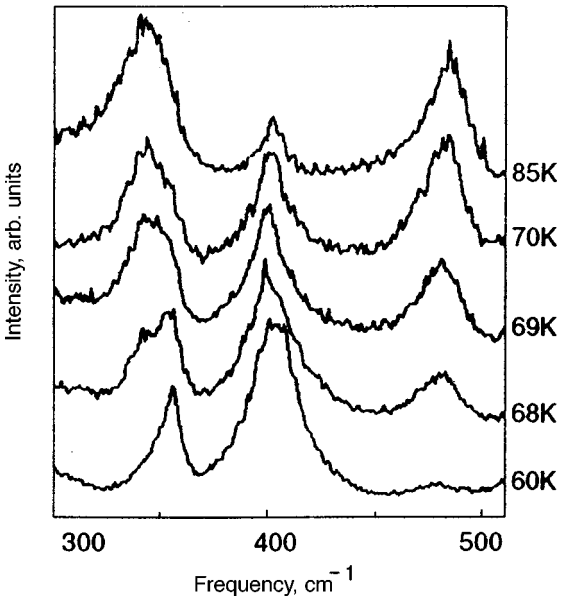

FIG. 4. Raman spectra for a $K_{0.26}A_{0.74}DP$ crystal in the $y(xx)z$ polarization at several temperatures. $T_N = 68.5$ K. Spectral resolution is 2.5 cm^{-1}.

Transition to the Structural Glass Phase

In the intermediate concentration range ($0.2 < x < 0.72$ for KADP) in which the structural glass (SG) phase is formed, the lattice symmetry apparently remains tetragonal (D_{2d}^{12}) even at helium temperatures. Quite reliable x-ray diffraction data for such crystals were obtained for the RADP system.[21] Sketchy information obtained for KADP only indicate the anomalies in the behavior of the lattice parameters.[22]

An analysis of Raman spectra (for samples of three concentrations $x = 0.22, 0.32$ and 0.53 from the intermediate range) shows that the general form of the spectra does not change in the temperature range 300-4.2 K. Three lines with frequencies of the order of 350, 395, and 480 cm^{-1}, which are preserved down to 4.2 K, can be observed in the frequency range under investigation even at room temperature (Fig. 6). The intensity ratio for these lines does not change upon cooling. The emergence of the $\nu_2(A_2)$ band with frequency 395 cm^{-1} is apparently associated with breaking of translational invariance in impurity crystals.

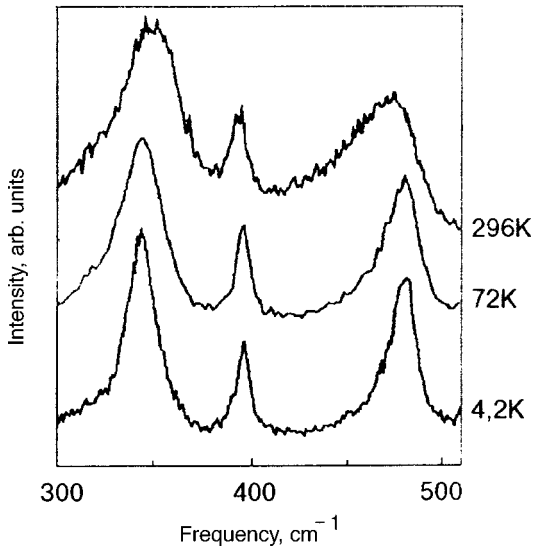

FIG. 6. Raman spectra for a $K_{0.68}A_{0.32}DP$ crystal in the $y(xx)z$ polarization at several temperatures. $T_m=120$ K, $T_g=70$ K. Spectral resolution is 2.5 cm^{-1}.

The temperature dependences of frequency and half-width of the $\nu_2(A_1)$ line for the $K_{0.68}A_{0.32}DP$ crystal are shown in Fig. 7. It can be seen that there are no features of a phase transition at T_m or at T_g, although a considerable decrease in the half-width of the line is observed upon cooling.

The existence of the glass phase is visually illustrated in Fig. 8 showing the concentration dependences of frequency and half-width of the $\nu_2(A_1)$ band at room temperature and at liquid helium temperature. The clearly manifested linear change in the spectral position of the band at $T=296$ K can serve as a test for a control of the component concentrations in the crystal (a similar behavior was also observed for the $\nu_1(A_1)$ band with a frequency close to 920 cm^{-1} (see Fig. 3 in Ref. 12). The half-width of the band at room temperature

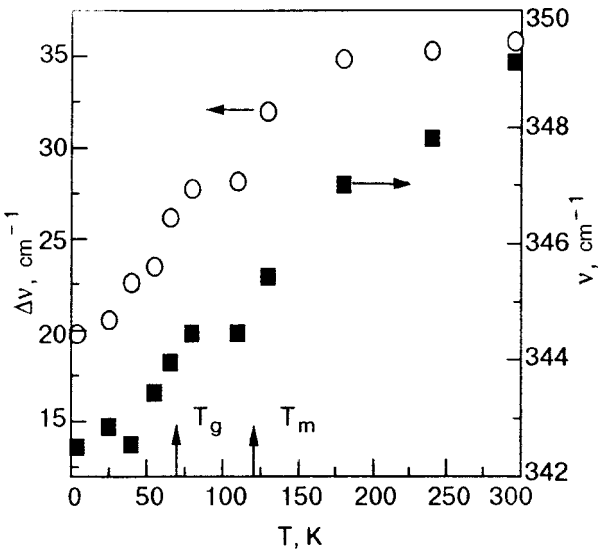

FIG. 7. Temperature dependence of frequency (■) and half-width (○) of the $\nu_2(A_1)$ band for a $K_{0.68}A_{0.32}DP$ crystal.

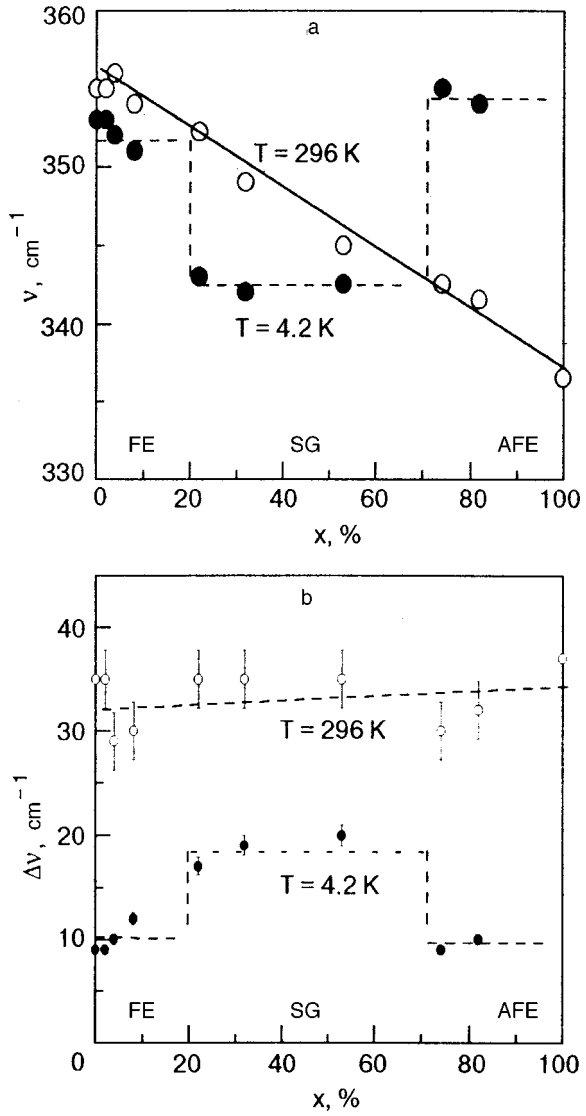

FIG. 8. Concentration dependence of frequency (a) and half-width (b) of the $\nu_2(A_1)$ band for mixed $K_{0.68}A_{0.32}DP$ crystals at two temperatures.

is also almost independent of concentration and amounts approximately to 30–35 cm^{-1}.

A different situation takes place at $T=4.2$ K. It can be seen that the frequencies of the bands and their half-widths have ''jumps'' at the interfaces between ferroelectric and structural glass and antiferroelectric–structural glass. The fact that a phase other than the paraelectric phase is formed in the intermediate range of concentrations follows from the values of half-widths of the bands. Indeed, for a completely disordered phase like the paraelectric phase, we could expect the value obtained from the extrapolation of half-widths of the bands from the high-temperature range for samples undergoing FE and AFE phase transitions. It can be seen from Figs. 3 and 5 (light circles) that such an extrapolation gives $\Delta\nu\approx 24\pm 1.5$ cm^{-1} (the same result was obtained for samples with other ammonium concentrations: $x=0.02$,0.04, and 0.08 for FE and $x=0.82$ for AFE), while the value of half-width for the samples with intermediate values of $x=0.22$,0.32, and 0.53 does not exceed 20 cm^{-1} at $T=4.2$ K. This difference is much larger than the error in

determining the half-width (this error is $\sim 1\ \mathrm{cm}^{-1}$ at 4.2 K), which points to the existence of ordering in the glass phase.

CONCLUSION

We studied the temperature dependence of the spectral position and half-width of the Raman scattering line corresponding to the $\nu_2(A_1)$ vibrational mode of PO_4 tetrahedron with a frequency near $350\ \mathrm{cm}^{-1}$ in the $y(xx)z$ scattering geometry. Experiments were made of samples belonging to the $K_{1-x}(NH_4)_xH_2PO_4$ system with ammonium concentrations $x=0.00, 0.02, 0.04$, and 0.08 in which the ferroelectric phase is formed at low temperatures. Samples with $x=0.74$ and 0.82 undergoing the antiferroelectric phase transition, and three samples with intermediate concentrations $x=0.22, 0.32$, and 0.53 in which the structural glass phase is formed. Strong changes in frequencies and half-widths of the lines are observed in transitions to the FE and AFE phases. As we approach the phase-transition temperatures from below, an abrupt broadening of the lines by $15-20\ \mathrm{cm}^{-1}$ is observed, indicating the emergence of additional scattering mechanisms associated just with structural disordering. The ''soft'' phonon mode whose frequency tends to zero in the transition region is responsible for the PT in ferroelectric crystals. Thus, the soft phonon mode is a parameter of the transition and must be completely symmetric in the low-temperature phase.[23] Consequently, its interaction with the mode under investigation having the A_1 symmetry is justified. A similar temperature dependence of the line half-width was also observed for the $\nu_1(A_1)$ band with a frequency close to $920\ \mathrm{cm}^{-1}$ in the spectrum of KADP crystals undergoing the ferroelectric phase transition (see curves *1* and *2* in Fig. 7 in Ref. 12). It should be noted that a strongly overdamped soft mode is present in samples of mixed KADP crystals in the entire concentration range,[13] its frequency having the minimum value in the region of temperatures corresponding to transitions to the low-temperature phases.

No sharp anomalies in the spectral parameters of the $\nu_2(A_1)$ band as well as the entire Raman spectrum are observed for samples with concentrations from the intermediate region, which confirms the invariability of the tetragonal symmetry of mixed crystals down to helium temperatures. However, temperature dependences of frequency and especially the half-width of the $\nu_2(A_1)$ band show that the phase formed at low temperatures differs from the paraelectric phase. This follows from the half-width of the band at 4.2 K, which is smaller than should be expected from the extrapolation of the corresponding curves to zero temperature for samples in the entire concentration range. Our earlier experiments[13–15] proved that the structural glass phase is heterogeneous and includes FE as well as AFE clusters. The results obtained by us here show that the size of these clusters is not large, otherwise the half-width of the band under investigation would be much larger that observed in experiments even at low temperatures (especially in the intermediate concentration range). The last statement is confirmed by the concentration dependences of the spectral positions of the band.

This paper is dedicated to the blessed memory of B. I. Verkin, who was a remarkable scientist and organizer. One of the authors (Yu. A. Popkov) was among first postgraduate students of Boris Ieremievich at the Institute for Low Temperature Physics and Engineering and was fortunate to take first lessons of science from this outstanding teacher.

*)E-mail: yury.a.popkov@univer.kharkov.ua

1) $Rb_{1-x}(NH_4)_xH_2PO_4$ (RADP),[4] $Rb_{1-x}(ND_4)_xD_2PO_4$ (DRADP),[5] $Rb_{1-x}(NH_4)_xH_2AsO_4$ (RADA),[6] $Rb_{1-x}(ND_4)_xD_2AsO_4$ (DRADA),[7] $K_{1-x}(NH_4)_xH_2AsO_4$ (KADA),[8] and $Cs_{1-x}(NH_4)_xH_2AsO_4$ (CADA)[9] and some other systems.

[1] G. A. Smolenskii, V. A. Bokov, V. A. Isupov *et al.*, *Physics of Ferroelectric Phenomena* [in Russian], Nauka, Moscow (1985).
[2] S. F. Edvards and P. V. Anderson, J. Phys. F **5**, 965 (1975).
[3] I. Ya. Korenblit and E. F. Shender, Usp. Fiz. Nauk **157**, 267 (1989) [Sov. Phys. Usp. **32**, 139 (1989)].
[4] E. Courtens, J. Phys. Lett. **43**, 199 (1982).
[5] Z. Kutnjak, P. Pirc, A. Levstik *et al.*, Phys. Rev. B **50**, 12421 (1994).
[6] F. L. Howell, N. J. Pinto, and V. H. Schmidt, Phys. Rev. B **46**, 13762 (1992).
[7] Z. Trybula, J. Stankowski, L. Szczepanska *et al.*, Physica B **153**, 143L (1988).
[8] Z. Trybula, V. H. Schmidt, and S. E. Drumheller, Phys. Rev. B **43**, 1287 (1991).
[9] T. K. Song, S. E. Moon, K. H. Noh, and S. I. Kwun, Phys. Rev. B **50**, 6637 (1994).
[10] Y. Ono, T. Hikita, and T. Ikeda, J. Phys. Soc. Jpn. **56**, 577 (1987).
[11] S. F. Gridnev, L. N. Korotkov, L. A. Shuvalov, and R. M. Fedosyuk, Kristallografiya **36**, 931 (1991).
[12] Yu. A. Popkov, A. V. Van'kevich, L. A. Shuvalov, and R. M. Fedosyuk, Fiz. Nizk. Temp. **19**, 195 (1993) [Low Temp. Phys. **19**, 138 (1993)].
[13] Yu. A. Popkov and A. V. Van'kevich, Fiz. Nizk. Temp. **21**, 1217 (1995) [Low Temp. Phys. **21**, 930 (1995)].
[14] A. V. Van'kevich, Yu. A. Popkov, E. M. Savchenko, and I. A. Taranova, Fiz. Nizk. Temp. **22**, 1216 (1996) [Low Temp. Phys. **22**, 959 (1996)].
[15] Yu. A. Popkov, I. A. Taranova, A. V. Van'kevich, and E. M. Savchenko, J. Korean Phys. Soc. **32**, 613 (1998).
[16] M. S. Shur, Kristallografiya **12**, 215 (1967).
[17] E. Courtens and H. Vogt, J. Chim. Phys. (Paris) **82**, 317 (1985).
[18] Yu. A. Popkov, V. F. Shabanov, V. V. Eremenko, and K. S. Aleksandrov, Fiz. Nizk. Temp. **1**, 936 (1975) [Sov. J. Low Temp. Phys. **1**, 448 (1975)].
[19] T. Hattori, H. Araki, S.-J. Nakashima, *et al.*, J. Phys. Soc. Jpn. **57**, 1127 (1988).
[20] V. V. Eremenko, *Introduction to Optical Spectroscopy of Magnets* [in Russian], Naukova Dumka, Kiev (1975).
[21] S. Iida and H. Terauchi, J. Phys. Soc. Jpn. **52**, 4044 (1983).
[22] Y. Ono, N. Yumada, and T. Hikita, J. Phys. Soc. Jpn. **60**, 2673 (1991).
[23] G. Z. Cummins and A. P. Levanyuk, *Light Scattering near Phase Transition Points* [in Russian], Nauka, Moscow (1990).

Translated by R. S. Wadhwa

ELECTRONIC PROPERTIES OF METALS AND ALLOYS

Nonquantum oscillations associated with the dynamics of an electron in superlattice

A. M. Kosevich

B. Verkin Institute for Low Temperature Physics and Engineering, National Academy of Sciences of the Ukraine, 310164 Kharkov, Ukraine[*)]

I. D. Wagner

Grenoble High Magnetic Field Laboratory, MPI-FRF and CNRS, Grenoble Cedex 09, France
(Submitted March 1, 1999)
Fiz. Nizk. Temp. **25**, 868–875 (August–September 1999)

Oscillations associated with the classical motion of a Bloch electron in a spatially periodic structure whose period considerably exceeds the atomic spacing are discussed. Such phenomena include the so-called Bloch oscillations, i.e., the vibrational motion of an electron in a constant uniform magnetic field, and the oscillatory dependence of magnetoresistance on a constant magnetic field, associated with the geometrical resonance at which the electron orbit diameter in the magnetic field is commensurate with the superlattice period. © *1999 American Institute of Physics.* [S1063-777X(99)01108-1]

INTRODUCTION

Experimental investigations of the de Haas–van Alphen effect carried out by B. I. Verkin laid the foundation of the modern theory of quantum oscillations in metals. His works are widely cited in scientific publications and are highly acclaimed in the monograph by Shoenberg.[1] One of the remarkable results of his investigations concerns the dependence of the quantum oscillations periods on the shape of the Fermi surface. It is well known that the shape of the Fermi surface is determined by the dispersion relation of an electron in a metal and reflects the periodicity of the crystal lattice.[2] On the other hand, since quantum magnetic oscillations in metals are usually described in the semiclassical longwave approximation, the spatial periodicity of the crystal lattice is not manifested strongly in the motion of electrons in the coordinate space.

However, periodic semiconducting structures have been created recently with a period considerably exceeding the crystal lattice period (atomic spacing). Such conducting superlattices serve as a platform for studying the peculiarities of the classical motion of electrons in the coordinate space of periodic structures.[3] Hence the problem of electron dynamics acquires significance under conditions when the cyclotron orbit diameter becomes commensurate with the superlattice period. This also imparted a new look to the seemingly abstract and old academic problem of Bloch oscillations of an electron in a constant uniform magnetic field.

We shall discuss these two different problems which are connected only through the common term ''oscillations.''

The paper begins with a discussion of the latter problem as the simplest one in formal notation of mathematical relations illustrating the laws governing the Bloch oscillations of an electron, as well as the less thoroughly studied oscillatory dependence of thermodynamic and kinetic characteristics of an electron gas on magnetic field, which come to mind at the mention of magnetic oscillations. The phenomenon of Bloch oscillations is associated with the dynamics of an individual electron and is due entirely to the specific nature of the dispersion relation for an electron in a metal or semiconductor, i.e., the periodic dependence of the energy and velocity of an electron on its quasimomentum. If the electron momentum increases monotonically with time under the action of an external electric field (this may happen over an interval of time much shorter than the relaxation time for an electron moving in the crystal), its velocity changes sign periodically and the ''classical'' motion of the electron (disregarding interband transitions) becomes oscillatory.[2] In the absence of a magnetic field, the vibrational frequency, which must be much larger than the reciprocal of the relaxation time, is proportional to the electric field and spatial period of the conducting structure under consideration.

Although the frequency of Bloch oscillations depends on the spatial period, the periodicity of layered structures is taken into account only implicitly in calculations, i.e., through the formulation of the specific dispersion relation. Since the nonmonotonicity of the electron energy dependence on momentum is the principal factor in the description of the effect under consideration, we would like to take it into account not only in estimates, but also in actual computations and in the form of final formulas. In this connection, we shall confine ourselves to the simplest but frequently encountered form of the periodic dependence, viz., the sinusoidal dependence of energy on quasimomentum.

In crossed electric and magnetic fields, Bloch oscillations may compete with the cyclotron motion of an electron in a uniform magnetic field. The ''competition'' between two types of oscillatory motion is described by an equation equivalent to the equation for the oscillations of a math-

 © 1999 American Institute of Physics

ematical pendulum which can be analyzed easily in the limiting cases. In particular, it is found that in quite strong magnetic fields and weak electric fields, the Bloch oscillations of an electron are practically not observed against the background of its cyclotron motion.

In the second part of this communication, we shall consider only the cyclotron motion of electrons in a strong magnetic field under the assumption that the conducting medium has a layered periodic structure with a macroscopic period. Under conditions corresponding to the experimental realization of such a situation, the periodic perturbation with a macroscopic period is superimposed on the periodic crystal field with atomic period. In this case, the unperturbed motion of an electron is governed as a rule by some complex dispersion relation in the general case. In the dynamics of an electron with an arbitrary dispersion relation, it is a complicated task to take perturbation into account, and we shall not tackle this problem here. We shall proceed from the fact that if the macroscopic period is much larger than the atomic spacing, we can separately deal with the problems of determining the role of the peculiarities of the ''initial'' arbitrary dispersion relation and the additional macroscopic spatial periodicity. Hence we assume that the unperturbed motion of an electron obeys an isotropic quadratic dispersion relation, and pay special attention to the effect of periodic potential with a macroscopic period on the properties of the electron gas. In order to obtain the results in an explicit form, we again confined our analysis to the motion of an electron in a spatially periodic potential with a small amplitude, where the use of the perturbation theory leads to the derivation of simple formulas.

We determined the energy spectrum of an electron with a quadratic dispersion relation in the presence of a uniform magnetic field and a weak periodic potential with a one-dimensional periodicity in the direction perpendicular to the applied magnetic field. In other words, we have derived the semiclassical dispersion relation for an electron in a periodic structure with a one-dimensional periodicity in a uniform magnetic field.

In the concluding section of this paper, we calculate the electric conductivity of an electron gas with the obtained dispersion relation in the relaxation time approximation and describe the classical oscillations of magnetoresistance in a varying magnetic field. As in Shubnikov–de Haas effect, these oscillations can be observed only at low temperatures. However, the parameter defining the amplitude decrease with temperature in the ratio d/a in the obtained formulas (d is the lattice period and a is the atomic spacing) is smaller than in the Shubnikov–de Haas effect, and hence the phenomenon described here can be observed at higher temperatures.

1. BLOCH OSCILLATIONS OF AN ELECTRON IN A SUPERLATTICE

The peculiarities of the dynamics of an electron in a superlattice are associated with the specific energy features during its motion in a periodic field. The state of an electron in a periodic structure is determined by its quasimomentum $\mathbf{p}$, and its energy $\varepsilon(\mathbf{p})$ is a periodic function of the quasimomentum (for brevity, we shall use the term ''momentum'' in the following). Such a dependence of the electron energy is essentially quantum-mechanical.[2] Without going into details concerning the justification of the procedure and confining ourselves to the semiclassical approximation, we shall follow the effective Hamiltonian technique and treat $\varepsilon(\mathbf{p})$ as the kinetic energy of a free particle to formulate the electron mechanics in analogy with classical mechanics. According to classical mechanics, the Hamiltonian of an electron in applied electric and magnetic fields has the form

$$\mathcal{H}=\varepsilon\left(\boldsymbol{p}-\frac{e}{c}\,\mathbf{A}(\mathbf{r})\right)-e\varphi(\mathbf{r}), \tag{1}$$

where $\boldsymbol{p}$ is the canonical momentum of the electron, $\mathbf{p}=\boldsymbol{p}-(e/c)\mathbf{A}$ its kinematic momentum, $\mathbf{A}$ and φ are the vector and scalar potentials of the applied fields. The equation for free electron motion has the conventional form

$$\frac{d\mathbf{p}}{dt}=e\mathbf{E}+\frac{e}{c}\,[\mathbf{v}\times\mathbf{H}], \tag{2}$$

where $\mathbf{E}$ and $\mathbf{H}$ are the electric and magnetic field strengths.

We shall confine ourselves to the most interesting case of a layered structure, assuming its superlattice properties to be one-dimensional. Let the x-axis be directed at right angles to the layers. In the simplest (strong bond) approximation, the dispersion relation for the electron in the absence of a magnetic field has the form

$$\varepsilon(\mathbf{p})=\frac{p_\perp^2}{2m_0}+\Delta\,\sin^2\frac{p_x d}{2\hbar}, \tag{3}$$

where $p_\perp^2=p_y^2+p_z^2$; m_0 is the effective mass in the plane of the superlattice layers, d the superlattice period, and Δ the width of the energy band associated with the motion along the x-axis.

According to Eq. (3), we have

$$v_\perp=\frac{P_\perp}{m_0};\quad v_x=A\,\sin\frac{p_x d}{\hbar};A=\frac{1}{2}\,\frac{\Delta}{\hbar}\,d=\text{const}. \tag{4}$$

Suppose that a constant electric field E is applied along the x-axis and that no magnetic field is applied. In this case, taking into account the dissipative processes (caused by the collisions of the electron with other quasiparticles or impurities in the metal), the effective equation for the electron motion, which describes the situation qualitatively, can be presented in the form

$$\frac{d\mathbf{p}_\perp}{dt}=-\frac{1}{\tau_0}\,\mathbf{p}_\perp,\quad \frac{dp_x}{dt}=eE-\frac{p_x}{\tau}, \tag{5}$$

where τ is the relaxation time. It follows from Eq. (5) that, for the initial condition $p_x=0(t=0)$, we have $\mathbf{p}_\perp=0$, while p_x can be defined by the equation

$$\frac{dp_x}{dt}+\frac{p_x}{\tau}=eE. \tag{6}$$

In conventional conductors (without a superstructure, for $d\sim a$), as well as in superlattices with small d, $eEd\tau<\hbar$ in electric fields below the breakdown value, and hence Eq. (6)

has a steady-state solution $p_x = p_0 = eE\tau$ for $t \gg \tau$ corresponding to the motion of an electron at a constant velocity $v_x = A \sin(eEd\tau/\hbar)$.

For $eEd\tau \ll \hbar$, such a solution defines the conventional electron mobility in a semiconductor

$$\frac{v_x}{E} = eA\tau d = \frac{e\tau}{m^*}. \tag{7}$$

For $eEd\tau \gg \hbar$, however, we obtain for small values of $\tau \ll t$

$$p_x = eEt, \tag{8}$$

and the electron velocity is defined in the main approximation in the small parameter $\hbar/(eE\tau d)$ as follows:

$$v_x = A \sin \omega_b t, \tag{9}$$

where $\omega_b = eEd/\hbar$ is the Bloch frequency (also known as the Stark frequency) characterizing the electron oscillations in a superlattice in a constant electric field. These oscillations are called the Bloch oscillations.

For an electron moving in crossed electric and magnetic fields, the Bloch oscillations compete with the cyclotron oscillatory motion of the electron. Although this question has been discussed in the literature (see, for example, Ref. 3), we shall consider it here in the simplest form, assuming that the cyclotron and Bloch oscillations periods are much smaller than the relaxation time (i.e. formally put $\tau = \infty$). Assuming that the magnetic field B is directed along the z-axis, we can write Eqs. (4)–(6) in the form

$$\frac{dp_x}{dt} = \frac{eB}{c} v_y + eE; \quad v_x = A \sin \frac{p_x d}{\hbar};$$

$$\frac{dp_y}{dt} = -\frac{eB}{c} v_x; \quad v_y = \frac{p_y}{m}. \tag{10}$$

This system of equations can be reduced to a single second-order differential equation

$$\frac{d^2 p_x}{dt^2} + mA\omega_c^2 \sin \frac{dp_x}{\hbar} = 0 \tag{11}$$

with the initial condition (for $t = 0$)

$$p_x = 0, \ \frac{dp_x}{dt} = eE + m\omega_c V_0, \tag{12}$$

where $\omega_c = eB/mc$, and V_0 is the initial velocity of the electron along the y-axis. The constant A is associated with the effective mass m^* of an electron moving with a small momentum along the x-axis: $m^* = \hbar/(Ad)$.

We introduce the dimensionless variable $z = p_x d/\hbar$. In this case,

$$\frac{d^2 z}{dt^2} + \Omega_0^2 \sin z = 0, \tag{13}$$

where

$$\Omega_0^2 = \left(\frac{mAd}{\hbar}\right)\omega_c^2 = \frac{m}{m^*}\,\omega_c^2 = \frac{1}{mm^*}\left(\frac{eB}{c}\right)^2. \tag{14}$$

The solution of Eq. (13) for a mathematical pendulum has a form that depends on the magnitude of the first integral

$$\mathcal{J} = \frac{1}{2}\left(\frac{dz}{dt}\right)^2 + \Omega_0^2(1 - \cos z). \tag{15}$$

The critical boundary value $\mathcal{J} = \mathcal{J}_0 \equiv 2\Omega_0^2$ divides the electron trajectories into two groups:

(1) For $\mathcal{J} < \mathcal{J}_0$, the electron oscillates along the x-axis with a frequency $\omega = \pi\Omega_0/[2\mathcal{K}(k)]$, where $\mathcal{K}(k)$ is the total elliptic integral of the first kind and the parameter $k = \sqrt{\mathcal{J}/\mathcal{J}_0}$. In the limit $\mathcal{J} \ll \mathcal{J}_0$, the electron performs cyclotron oscillations with a frequency $\omega = \Omega_0$.

(2) For $\mathcal{J} > \mathcal{J}_0$, the motion of the electron along the x-axis remains finite, but it oscillates with a frequency $\omega = \pi\Omega_0/[k\mathcal{K}(k)]$, where $k = \sqrt{\mathcal{J}_0/\mathcal{J}}$. In the limit $\mathcal{J} \gg \mathcal{J}_0$, the electron performs Bloch oscillations with a frequency $\omega = \omega_B \equiv eEd/\hbar$.

2. CLASSICAL MAGNETORESISTANCE OSCILLATIONS IN A PERIODIC POTENTIAL

The new spurt of interest towards magnetic oscillations in metals can be attributed to the emergence of new objects in experimental physics, i.e., two-dimensional electron systems. These systems display a new type of oscillatory effect that is typical of a two-dimensional electron gas modulated periodically in space.[4,5] The observed phenomenon differs from the Shubnikov–de Haas effect and has the form of a geometric resonance, reflecting the commensurability of the diameter of the cyclotron orbit of an electron in a magnetic field with the period of spatial modulation of the crystal field. In this connection, it is expedient to speak of the analogy between the observed effect and the geometric resonance during absorption of ultrasound in metals in a magnetic field. An acoustic wave in the sample creates spatial modulation whose period is commensurate with the electron orbit diameter, and this leads to resonance effects (see, for example, Ref. 6).

We shall present below a theory for such an effect in a three-dimensional electron gas modulated by a periodic potential that depends only on one coordinate at right angles to the applied magnetic field. Such a modulation may be achieved by creating a superlattice with a submicrometer period. This kind of magnetic oscillations in a superlattice were apparently observed for the first time by Chang *et al.*[7] as per observations made by Shekhter *et al.*[8]

Let us consider an ideal electron gas in an external periodic potential field that depends on only one spatial coordinate. For example, this may be a superlattice of the layered structure type with a period d much larger than the atomic spacing a. If the external magnetic field B is parallel to the layers, the unperturbed electron motion occurs along a trajectory whose projection on a plane perpendicular to B has the form of a closed orbit (a circle in the simplest case). It is assumed that the diameter D of the cyclotron orbit corresponding to the Fermi energy may be larger than d. Since the diameter of the electron orbit is inversely proportional to the magnetic field ($D \sim 1/B$), a variation in the value of $1/B$ by an amount corresponding to the increment $\delta D = d$ must lead to a resonant variation of the kinetic characteristics of the electron gas. Naturally, oscillations with a variation of $1/B$

will be observed under the condition that the electron mean free path l exceeds the length of the cyclotron orbit ($l > \pi D$). Moreover, the temperature must be quite low as in the Shubnikov–de Haas effect. It turns out, however, that the temperature dependence is determined in this case by the parameter $(T/\hbar\omega_c)(\hbar p_F d)$ which is smaller than the corresponding parameter in the Shubnikov–de Haas effect by the factor $\hbar p_F d$ (here, ω_c is the cyclotron frequency and p_F the Fermi momentum of the electron gas).

Since the oscillations attenuate upon an increase in the value of the above parameter, the effect is observed at comparatively higher temperatures. This is due to the fact that it is a classical effect and has nothing to do with the quantization of energy levels in a magnetic field.

2.1. Electron Energy Spectrum

In order to obtain explicit quantitative relations and simple dependences, we consider the simplest form of the periodic potential:

$$V(x) = V_0 \cos\left(2x\,\frac{x}{d}\right) \tag{16}$$

and assume that the period d is much larger than the atomic spacing, i.e., $d \gg a_0$.

Let the magnetic field vector be parallel to the superlattice layers and directed along the z- axis. We use an appropriate calibration for the vector-potential $\mathbf{A}(0,Bx,0)$ and write the Hamiltonian function for an electron in magnetic field B and in the field of the periodic potential (16):

$$\mathscr{H} = \frac{p_x^2}{2m} + \frac{p_z^2}{2m} + \frac{1}{2}\,m\omega_c^2(x-x_0)^2 + V(x), \tag{17}$$

where $\omega_c = eB/mc$ is the cyclotron frequency, and $x_0 = -cp_y/eB$ is the center of the electron orbit for $p_y = \text{const}$. Obviously, the electron moves under the condition $p_z = \text{const}$ and is described by the equations

$$\frac{d^2x}{dt^2} + \omega_c^2(x-x_0) = -\frac{1}{m}\,\frac{dV}{dx} \equiv \frac{2\pi V_0}{md}\,\sin 2\pi\,\frac{x}{d}, \tag{18}$$

$$\frac{dy}{dt} = \omega_c(x-x_0). \tag{19}$$

The solution of these equations in the absence of a periodic potential ($V(x) \equiv 0$) can be presented in the form

$$x = x_0 + R\,\sin\,\omega_c(t-t_0), \tag{20}$$

$$x_0 = \text{const}, \quad t_0 = \text{const},$$

where R is the cyclotron radius of the electron orbit which is connected with the energy E_0 of an electron moving in the xy plane through the relation

$$E_0 \equiv \frac{p_x^2}{2m} + \frac{1}{2}\,m\omega_c^2(x-x_0)^2 = \frac{1}{2}\,m\omega_c^2R^2. \tag{21}$$

Expression (20) can be used to make the limiting transition to the electron dynamics in the absence of a magnetic field ($B \to 0$), when

$$x = x_0 + R_0\,\sin\,\omega_c(t-t_0) \to x_1 + v_0 t,$$

where $v_0 = \sqrt{2E_0/m} = \text{const}$, $x_1 = x_0 - v_0 t_0 = \text{const}$. Assuming the periodic potential to be small, we use the perturbation theory, defining the order of approximation by the power of the amplitude of potential V_0. In this case, the total electron energy in the first order of the perturbation theory can be written in the form

$$E = \frac{p_x^2}{2m} + E_0 + \langle V(x_0 + R\,\sin\,\phi)\rangle, \tag{22}$$

where the phase $\phi = \omega_c(t-t_0)$, and the angle brackets $\langle \ldots \rangle$ indicate time averaging over the period $2\pi/\omega_c$.

Simple calculations described in detail in Ref. (9) lead to the following final expression for the energy of an electron moving in the xy-plane:

$$E_\perp \equiv E - \frac{p_z^2}{2m} = E_0 + V_0\mathcal{J}_0\left(2\pi\,\frac{R}{d}\right)\cos\left(2\pi\,\frac{x_0}{d}\right), \tag{23}$$

where $\mathcal{J}_n(x)$ is an nth order Bessel function of the first kind, and the expression (21), viz., $R = (2E_0/m\omega_c^2)^{1/2}$, should be used on the right-hand side.

Note that the notation of the last term in (23) differs from the quantum expression of Gerhardts *et al.*[5] for the energy of two-dimensional motion of an electron in a magnetic field and in one-dimensional periodic potential, although both expressions should describe the same electron energy spectrum under the condition $2\pi R \gg d$. The apparent discrepancy vanishes if we consider that the asymptotic forms for large arguments can be written as

$$\mathscr{L}_n(x) = e^{x/2}\mathcal{J}_0(\sqrt{2\nu x}), \quad x \to \infty, \tag{24}$$

where $\mathscr{L}_n(x)$ is a Laguerre polynomial of degree **n**. It is also obvious that semiclassical quantization of the energy of a harmonic oscillator leads to the expression

$$E_0 \equiv \frac{1}{2}\,m\omega^2R^2 = n\hbar\omega, \quad n \gg 1.$$

Thus, the degeneracy in the position of the center of the orbit is removed for an electron moving in a periodic field:

$$E = \frac{p_z^2}{2m} + E_\perp(E_0, x_0). \tag{25}$$

It is quite significant that, in the state with fixed values of E_0, p_z and x_0, the electron in an external periodic potential field has a velocity component

$$v_y = \frac{\partial E}{\partial p_y} = -\frac{1}{m\omega_c}\,\frac{\partial E}{\partial x_0}$$

$$= \frac{2\pi V_0}{m\omega_c d}\,\mathcal{J}_0\left(2\pi\,\frac{R}{d}\right)\sin\left(2\pi\,\frac{x_0}{d}\right). \tag{26}$$

Since the periodic potential $V(x)$ depends on the x-coordinate, it generates a force acting on the electron along the y-axis. Hence the velocity (26) is an analog of the Hall drift velocity in crossed electric and magnetic fields.

Let us calculate the density of states corresponding to the spectrum (22) and (23). The number of electron states per unit volume corresponding to energies lower than E is given by

$$N(E)=\frac{2}{(2\pi\hbar)^3}\int dxdp_xdp_ydp_z$$
$$=\frac{2(2m)^{3/2}}{(2\pi\hbar)^2\hbar d}\int\sqrt{E-E_\perp}\,dE_0dx_0, \tag{27}$$

where integration with respect to x_0 must be carried out over the period d of the external potential. Taking formula (23) into consideration and separating the term linear in V_0 in the integrand of (27), we obtain

$$N(E)=\frac{2(2m)^{3/2}}{(2\pi\hbar)^2\hbar d}\left\{\int_{-V_0}^{E}\sqrt{E-E_0}\,dE_0\int dx_0 - \frac{1}{2}V_0\int_0^E\frac{\mathcal{J}_0(2\pi R/d)}{\sqrt{E-E_0}}\,dE_0\int_0^d\cos(2\pi x_0/d)dx_0\right\}. \tag{28}$$

It can be seen that the last term on the right-hand side of this expression vanishes on account of the cosine integral over a complete period. Thus, the approximation used by us does not contain any dependence of the number of states $N(E)$ on the periodic potential, and hence on the magnetic field:

$$N(E)=N_0(E)=\frac{8\pi(2mE)^{3/2}}{3(2\pi\hbar)^3}, \tag{29}$$

where $N_0(E)$ is the number of electron states of a free electron gas.

It follows hence that thermodynamic properties of an electron gas in the superlattice under investigation are also independent of the magnetic field. It should be emphasized that we have analyzed the classical motion of an electron in a periodic potential in the presence of a magnetic field. Hence the obtained results naturally in accord with the general physical conclusion that the dependence of thermodynamic properties of matter on magnetic field is a purely quantum effect.

However, the magnetic field dependence emerges during calculation of the kinetic characteristics of the electron gas, which involves the probability of transition between various electron states (in particular, between states with different x_0).

2.2. Transverse Magnetoresistance Oscillations of an Electron Gas in a Superlattice

Let us now calculate the low-temperature electric conductivity of an ideal gas of electrons with dispersion relation (25) which are scattered by impurities. Since our aim is to find qualitative features of the magnetic field dependence of electric conductivity, we confine ourselves to the relaxation time approximation (known as the τ-approximation). Disregarding the weak periodic potential $V(x)$, we obtain in this approximation the following transverse components of the electric conductivity tensor:

$$\sigma^0_{xx}=\sigma^0_{yy}=\sigma_0/[1+(\omega_c\tau)^2],$$
$$\sigma^0_{xy}=\sigma^0_{yx}=\tau\omega_c\sigma^0_{xx},\quad \sigma_0=e^2\tau N_0/m,$$

where N_0 is the total number of conduction electrons per unit volume.

Let us now take into consideration the weak periodic potential $V(x)$. The existence of the steady-state velocity (26) leads to the following additional contribution to the electric conductivity component for $\omega_c\tau\gg1$:

$$\partial\sigma_{yy}=-2e\int\tau v_y^2\frac{df}{dE}\frac{dxd^3p}{d(2\pi\hbar)^3} - \frac{e^2(2m)^{3/2}}{(2\pi\hbar)^2\hbar d}\int\tau v_y^2\frac{df}{dE}\frac{dEdE_0dx_0}{\sqrt{E-E_0}}, \tag{30}$$

where $f(E)$ is the Fermi distribution function, and integration with respect to x_0 is carried out over a single period d.

It should be observed in the first place that since $df/dE<0$, the correction to electric conductivity is always positive.

Assuming that the relaxation time depends on the total electron energy ($\tau=\tau(E)$) and taking formula (26) into consideration, we can present Eq. (30) in the form

$$d\sigma_{yy}=-\frac{\pi e^2(2m)^{3/2}}{(2\pi\hbar)^3}\left(\frac{2\pi cV_0}{edB}\right)^2\int_0^\infty\tau(E)\Phi(E)\frac{df}{dE}\,dE, \tag{31}$$

where

$$\Phi(E)=\int_0^E\mathcal{J}_0^2\left(2\pi\frac{R(E)}{d}\right)\frac{dE_0}{\sqrt{E-E_0}}. \tag{32}$$

Let us analyze properties of the function (32) separately by taking formula (21) into consideration. A trivial change of variables gives

$$\Phi(E)=\sqrt{E}\int_0^1\mathcal{J}_0^2\left(2\pi\frac{R(E)}{d}\sqrt{\xi}\right)\frac{d\xi}{\sqrt{1-\xi}}. \tag{33}$$

It can be seen that for $2\pi R\ll d$,

$$\Phi(E)=\sqrt{E}\int_0^1\frac{d\xi}{\sqrt{1-\xi}}=\sqrt{2E},\quad E\to0. \tag{34}$$

However, the most interesting process for us is the opposite limiting case $2\pi R\gg d$ for which the following relations are automatically satisfied:

$$\Phi(E)\sim\frac{2d\sqrt{E}}{\pi^2R(E)}\int_0^1\frac{dx}{\sqrt{1-x^2}}\cos^2\left(2\pi\frac{R(E)}{d}x-\frac{x}{4}\right) \sim\frac{d\sqrt{E}}{\pi^2R(E)}\left[1+\frac{1}{2}\sqrt{d/D}\sin\left(2\pi\frac{D}{d}-\frac{x}{4}\right)\right], \tag{35}$$

where $D=2R(E)$.

Let us now turn to formula (31). At low temperatures, the derivative of the Fermi function does not differ much from the delta function. Hence in the main approximation, we can write for $2\pi R\gg d$

$$\delta\sigma_{yy}=\frac{e^2n(\zeta)\tau(\zeta)}{m^2\omega_c^2R(\zeta)d}\,V_0\left[1-\frac{1}{2}\left(\frac{d}{D(\zeta)}\right)^{1/2}\int_0^\infty\frac{df}{dE}\times\sin\left(2\pi\,\frac{D(E)}{d}-\frac{x}{4}\right)dE\right], \tag{36}$$

where ζ is the Fermi energy that does not differ from the chemical potential of the electron gas at low temperatures, and $n(\zeta)$ is the density of electron states with the Fermi energy:

$$n(\zeta)=\frac{4\pi(2m)^{3/2}}{(2\pi\hbar)^3}\,\sqrt{\zeta}.$$

Finally let us verify that for $D(\zeta)\gg d$, the last term in (36) describes the oscillatory dependence of σ_{yy} on magnetic field. Indeed,

$$-\int_0^\infty\frac{df}{dE}\sin\left(2\pi\,\frac{D(E)}{d}-\frac{\pi}{4}\right)dE\approx\sin\left(2\pi\,\frac{D(\xi)}{d}-\frac{\pi}{4}\right)\Psi\left(\pi^2T\,\frac{D(\zeta)}{d\zeta}\right), \tag{37}$$

where T is the electron gas temperature, and $\Psi(z)=z/\sinh z$. Thus,

$$\delta\sigma_{yy}\approx\frac{e^2n(\zeta)\tau(\zeta)}{m^2\omega_c^2R(\zeta)d}\,V_0^2\left[1+\frac{1}{2}\left(\frac{d}{D(\zeta)}\right)^{1/2}\Psi\left(\pi^2T\,\frac{D(\zeta)}{d\zeta}\right)\times\sin\left(2\pi\,\frac{D(\zeta)}{d}\right)\right]. \tag{38}$$

Since $D(\zeta)=2c\sqrt{2m\zeta}/(eB)$, Eq. (38) describes the oscillatory dependence of electric conductivity on magnetic field. Like Shubnikov–de Haas oscillations, these oscillations have a constant period in $1/B$ corresponding to a magnetic field variation for which the electron orbit diameter $D(\zeta)$ changes by an amount equal to the period of the external potential $V(x)$. Hence the oscillations under consideration are not associated with the quantum motion of an electron in a magnetic field and can be treated as the manifestation of the geometrical resonance of the same type that lead to Pippard's effect during absorption of ultrasound in a metal in the presence of a magnetic field (see, for example, Ref. 6). The temperature dependence of the classical oscillations (38) is defined by the same function $\Psi(z)$ as in the Shubnikov–de Haas effect (see Ref. 10). However, while this dependence is determined in the Shubnikov–de Haas effect by the dimensionless parameter $T/(\hbar\omega_c)$ whose increase leads to an attenuation of oscillations, this parameter in formula (38) has the form

$$(T/\hbar\omega_c)(\hbar dp_F)\sim(T/\hbar\omega_c)(a/d), \tag{39}$$

where p_F is the Fermi momentum and a the mean separation between electrons in the gas. Since the separation a is a microscopic parameter and the parameter d a macroscopic parameter, we should put $a\ll d$. In this case, the classical oscillations (38) attenuate to a smaller extent with increasing temperature than the Shubnikov–de Haas oscillations (and can be treated as a relatively ''high-temperature'' effect). However, the situation may alter in semiconductors or semimetals, where $a\sim d$. The experiments described by Chang *et al.*[7] were carried out for $\hbar/dp_F\simeq10^{-6}$ cm.

The amplitude of oscillations is small and is determined by the smallness of the ratio $(V_0/\zeta)^2$:

$$\delta\sigma_{yy}/\sigma_0\sim(V_0/\zeta)^2.$$

The value of the parameter (39) depends significantly on the samples used. For example, Chang *et al.*[7] used the value $V_0\simeq0.1\zeta$.

One of the authors (AMK) would like to thank the management of the Grenoble High Magnetic Fields Laboratory for hospitality during his stay in Grenoble where the idea behind this work was born.

*)E-mail: kosevich@ilt.kharkov.ua

[1] D. Shoenberg, *Magnetic Oscillations in Metals*, Cambridge University Press, Cambridge (1984).
[2] I. M. Lifshits, M. Ya. Azbel', and M. I. Kaganov, *Electron Theory of Metals*, Consultants Bureau, New York, 1973.
[3] F. G. Bass and A. A. Buldakov, *Kinetic and Electrodynamic Phenomena in Classical and Quantum Semiconductor Superlattices*, Nova Science Publishers Inc., New York (1998).
[4] D. Weiss, K. V. Klitzing, K. Plood, and G. Weitmann, Europhys. Lett. **8**, 179 (1989).
[5] R. R. Gerhardts, D. Weiss, and K. V. Klitzing, Phys. Rev. Lett. **62**, 1173 (1989).
[6] A. A. Abrikosov, *Introduction to the Theory of Normal Metals* [in Russian], Nauka, Moscow (1972).
[7] L. L. Chang, H. Sakaki, C. A. Chang, and L. Esali, Phys. Rev. Lett. **38**, 1489 (1977).
[8] R. I. Shekhter, E. N. Bogachek, and I. O. Kulik, Fiz. Tverd. Tela (Leningrad) **20**, 1433 (1978) [Sov Phys. Solid State **20**, 824 (1978).
[9] A. M. Kosevich, in *Problems in Theoretical Physics* [in Russian] Naukova Dumka (1991).
[10] L. D. Landau and E. M. Lifshitz, *Physical Kinetics* [in Russian], Nauka, Moscow (1979).

Translated by R. S. Wadhwa

Coupling of electromagnetic and acoustic modes in metals

L. T. Tsymbal, A. N. Cherkasov, and O. F. Panchenko

A. Galkin Institute of Physics and Technology, National Academy of Sciences of the Ukraine, 340114 Donetsk, Ukraine)*

(Submitted March 3, 1999)
Fiz. Nizk. Temp. **25**, 876–888 (August–September 1999)

The results of a detailed theoretical analysis of coupling of weakly damped electromagnetic and acoustic waves in metals are presented. The main difference between the natures of coupling of modes propagating in the same (helicon–phonon resonance) or opposite (doppleron–phonon resonance) directions is established. The dispersion curves are split in the former case and bound in the latter case. As a result, a gap appears in the spectrum of coupled modes in the collisionless limit, both modes being soundlike. It is shown that in the case of doppleron–phonon resonance, inductive as well as deformative interaction of electrons with the lattice must be taken into account. © *1999 American Institute of Physics.* [S1063-777X(99)01208-6]

INTRODUCTION

The problem of propagation and coupling of collective excitations in condensed media, including metals, is one of the most important and interesting problems in solid state physics. Two typical cases can be singled out in an exhaustive analysis of this problem. The first case involves the coupling of collective modes, viz., excitations of various subsystems in the metal. It should be observed, however, that the system of coupled modes is common for all coupled subsystems in a metal. Hence the appurtenance of any mode to a particular subsystem is, in general, arbitrary. The identification of modes may become quite impossible in the vicinity of the points of their degeneracy. By the term ''mode'' we mean a certain excitation characterized by a wave vector **k**. The effects considered in this publications can serve as an example of such a coupling. The specific aim of our investigations is to study the nature of the interaction of ultrasonic and propagating electromagnetic modes in normal metals subjected to an applied magnetic field **H**. Although the term ''mode interaction'' is used frequently, it is obvious that it is not the modes that interact, but rather the subsystems of the metal, like the ionic and electron subsystems in the present case. This can be illustrated graphically by exciting oscillations in one of the subsystems of the metal. As a result of interaction, oscillations are generated inevitably in the coupled subsystem also. In this work, we shall not discuss this aspect of the problem, but confine ourselves to an analysis of the dispersion relation for coupled ultrasonic and electromagnetic waves, without going into the aspects concerning the excitation of these waves in the metal. The second case concerns coupling of modes which are collective excitations of the same subsystem in the metal. Naturally, it is meaningless to speak of any interaction in this case. However, irrespective of the type of coupled modes, both cases are covered by the same laws governing the coupling problem as a whole. This can be seen clearly from a comparative analysis carried out by us for the system of modes formed as a result of coupling of electromagnetic and acoustic modes, or of electromagnetic modes with one another.

For the range of frequencies and fields in which we are interested and which are confined by the inequalities

$$\omega \leqslant \nu \ll \omega_c , \tag{1}$$

two types of weakly attenuating electromagnetic waves can propagate in metals, viz, helicons which exist only in noncompensated metals,[1–3] and dopplerons which have been detected in many compensated and noncompensated metals.[4–8] In (1), ω is the frequency of the wave, ν the electron relaxation frequency, and $\omega_c = eH/mc$ the cyclotron frequency.

Helicons and dopplerons are relatively ''slow'' waves, and their spectra may intersect the spectra of transverse acoustic modes in fields and frequency intervals attainable in real experiments. The helicon–phonon resonance (HPhR) predicted in Refs. 9 and 10 (see also Ref. 11) and observed experimentally in Ref. 12 was analyzed subsequently by various groups (see, for example, Refs. 13 and 14), as well as the reviews by Kaner and (Skobov[15] and Mertsching[16]). Naturally, one and the same dispersion equation describes the spectrum and damping of coupled modes in the case of HPhR as well as doppleron–phonon resonance (DPhR). However, this equation can be simplified considerably for the case of HPhR. This is due to the fact that the helicon–phonon interaction is described quite correctly in the local limit. As a result, the nature of helicon–phonon coupling is practically independent of details of electron energy spectrum and is determined mainly by inductive interaction of electrons with the lattice.[14] In view of the simplicity of the HPhR theory, it is hard to obtain from the experiment any basically new information except that it confirms the validity of the theory. Apparently, this is one of the reasons behind the small number of publications devoted to the experimental investigation of the effect. Apart from the work of Grimes and Buchsbaum,[12] we can mention the magnetoacoustic

 © 1999 American Institute of Physics

studies of HPhR in potassium[17,18] and indium.[19] The second reason is associated with the imposition of a lower limit on resonance fields associated with Doppler-shifted cyclotron resonance (DSCR). As a result, this region is found to be unattainable in real experiments. This is especially true for metals with relatively large velocities of sound and difference in electron and hole concentrations.[20]

The existence of dopplerons is associated with the Fermi degeneracy of conduction electrons in metals and DSCR, which leads to a strong spatial dispersion of the metal conductivity. Nonlocal effects cannot be disregarded any longer, and hence the deformation interaction of electrons with the lattice cannot be neglected either. All this complicates the coupling analysis in the case of DPhR.

Doppleron–phonon resonance, which was predicted and detected for the first time in cadmium,[21] was later observed in other metals also (see, for example, Ref 22 and the literature cited therein). However, the obtained experimental results were used mainly for constructing doppleron spectra and for calculating nonlocal conductivity of metals. However, the peculiarities of the interaction itself have not been studied extensively. Mention can be made only of the publication by Medvedev *et al.*[23] who attempted to analyze DPhR in cadmium theoretically, and of our publication[20] in which we studied the amplitude–frequency dependence of DPhR in tungsten. However, the results obtained in these works are not of general nature. For example, the authors of Ref. 23 used a highly simplified model of the metal and confined their analysis of the interaction to just a strong coupling of dopplerons with sound. As a result of such a simplification, the calculated magnetic field dependence of the acoustic absorption coefficient is not even in qualitative agreement with the results obtained in experiments.[21,22] In Ref. 20, the dispersion equation was solved only for a weak coupling of dopplerons with sound, although a justification was provided for such an approach.

According to their properties, dopplerons can be divided into two basically different groups. The first group contains dopplerons whose phase velocity $\mathbf{v}_{\rm ph}$ and group velocity $\mathbf{v}_{\rm gr}$ are collinear. Dopplerons belonging to the second group have opposite directions of velocities $\mathbf{v}_{\rm ph}$ and $\mathbf{v}_{\rm gr}$. We studied[24] the coupling of the second type of doppleron mode with a helicon and found that the spectrum of coupled modes in such a case differs radically from the spectrum obtained, e.g., for HPhR. In the present work, we shall also consider the coupling of a doppleron mode and an acoustic mode propagating towards each other. The main aim of our research is to establish the general laws governing this type of coupling and to carry out a comparative qualitative and quantitative analysis of the spectra of coupled modes for DPhR and HPhR. We used a simple but realistic model of an uncompensated metal. The dispersion equation for coupled modes was solved numerically with the help of Muller's method (generalized secant method) with deflation.[25] In order to find the physical meaning of the obtained results, we used an approximate but quite precise solution of this equation.

DISPERSION EQUATION AND THE MODEL OF A METAL

1. The equations in the theory of elasticity and Maxwell's equations, together with material relations, form a complete system of equations describing elastic and electromagnetic oscillations in metals (see, for example, Refs. 14, 26 as well as the review articles in Refs. 15, 16, and 27). For monochromatic plane waves ($\mathbf{u}$, $\mathbf{E}\propto\exp(i\mathbf{k}\cdot\mathbf{r}-i\omega t)$; $\mathbf{u}$ is the lattice displacement vector and $\mathbf{E}$ the electric field), these equations have the form

$$\sum_{\beta,\gamma,\delta}\lambda_{\alpha\beta\gamma\delta}k_\beta k_\gamma u_\delta-\rho\omega^2u_\alpha=f_\alpha, \tag{2}$$

$$-\mathbf{k}\times\mathbf{k}\times\mathbf{E}=(4\pi i\omega/c^2)\mathbf{j}, \tag{3}$$

$$\mathbf{f}=\hat{G}\mathbf{E}+\hat{L}\mathbf{u},\quad \mathbf{j}=\hat{\sigma}\mathbf{E}+\hat{g}\mathbf{u}. \tag{4}$$

Here $\mathbf{k}$ is the wave vector, ρ the density of the material, $\hat{\lambda}_{\alpha\beta\gamma\delta}$ the elastic constant tensor, and $\mathbf{f}$ the volume density of the force exerted by electrons on the lattice, $\mathbf{j}$ the total current density, $\hat{G}$, $\hat{L}$, $\hat{\sigma}$ and $\hat{g}$ are material tensors, while α,β,γ, and δ correspond to x, y, and z. Equations (2)–(4) have been written without taking into consideration the Stewart–Tolman effect whose role in a strong magnetic field H is negligible.

We shall confine our analysis to coupling in the geometry $\mathbf{k}\|\mathbf{H}\|\hat{z}$, where $\hat{z}$ is the symmetry axis of at least third order. In this case, we can separate longitudinal and transverse oscillations in Eqs. (2)–(4). For circularly polarized transverse components, $\psi_\pm=\psi_x\pm i\psi_y$ (here, $\pm$ is the polarization and $\psi=u,E$), and the dispersion relation for coupled ultrasonic and electromagnetic waves has the form

$$(k^2c^2-4\pi i\omega\sigma_\pm)(k^2v_s^2-\omega^2-L_\pm/\rho)=(4\pi i\omega/\rho)g_\pm G_\pm. \tag{5}$$

For $\varphi=\sigma,L,g,G$; $\varphi_\pm=\varphi_{xx}\pm i\varphi_{yx}$; $v_s=(\lambda_{xzzx}/\rho)^{1/2}$ is the velocity of the transverse acoustic wave. It can be seen from Eqs. (2)–(5) that the nature of interaction of electromagnetic and acoustic waves is determined by tensors $\hat{g}$ and $\hat{G}$. If the interaction is excluded, i.e., for $g_\pm G_\pm\to0$, we obtain from (5) the familiar equations

$$k^2c^2=4\pi i\omega\sigma_\pm(k), \tag{6}$$

$$k^2v_s^2=\omega^2+L_\pm(k)/\rho, \tag{7}$$

describing the spectrum of electromagnetic waves and the acoustic spectrum normalized by the electron–phonon interaction.

Material tensors $\hat{g}$, $\hat{G}$ and $\hat{L}$ are linear combinations of eletroacoustic coefficients whose exact expressions were obtained by Kontorovich.[27,28] In the following, we shall assume that the Fermi surface (FM) of the metal is axially symmetric relative to the $\hat{z}$-axis. Neglecting the Stewart–Tolman effect, we obtain in this case

$$\sigma_\pm=e^2\langle v_\pm v_\pm^*\rangle, \tag{8}$$

$$g_\pm=\mp\frac{\omega e^2H}{c}\left\langle v_\pm^*\left(v_\pm\pm\frac{ck}{eH}\Lambda_\pm\right)\right\rangle, \tag{9}$$

$$G_{\pm}=\mp_i \frac{e^2H}{c}\left\langle\left(v_{\pm}\pm\frac{ck}{eH}\Lambda_{\pm}\right)^{*}v_{\pm}\right\rangle, \tag{10}$$

$$L_{\pm}=i\omega\left[\frac{eH}{c}\right]^2\left\langle\left|v_{\pm}\pm\frac{ck}{eH}\Lambda_{\pm}\right|^2\right\rangle. \tag{11}$$

Here **v** is the electron velocity ($v_{\pm}=v_x\pm iv_y$), $\hat{\mathbf{\Lambda}}$ is the deformation potential tensor ($\Lambda_{\pm}=\Lambda_{xz}\pm i\Lambda_{yz}$), the asterisk (*) indicates complex conjugation, and the angle brackets indicate integration over the Fermi surface (FS):

$$\langle\psi\rangle=i\frac{2\pi}{(2\pi\hbar)^3}\int_{FS}\frac{\psi|m|dp_z}{\omega+i\nu\pm\omega_c-kv_z}. \tag{12}$$

2. Let us specify the form of the deformation potential tensor. In contrast to the unperturbed dispersion relation which has been studied in detail for most metals, precious little is known at present about this characteristic of electrons. This is mainly due to the complexity of the microscopic theory of deformation interaction. Hence the most acceptable solution consists of the approximation of the tensor by models which can describe the experimental results quite correctly. Such a model must be ''physical'' on the one hand and relatively simple on the other hand since the main aim of our analysis is to compute the integrals (8)–(11) and to solve Eq. (5). To a certain extent, these requirements are met by a tensor corresponding to isotropic dispersion relation:

$$\Lambda_{\alpha\beta}=\lambda_0 m\left(\frac{1}{3}v^2\delta_{\alpha\beta}-v_{\alpha}v_{\beta}\right). \tag{13}$$

For free electrons, $\lambda_0=1$. Hence λ_0 is a parameter whose magnitude determines the departure from the quadratic dispersion relation.

Substituting (13) into Eqs. (9)–(11), we obtain

$$g_{\pm}(k)-i\omega G_{\pm}(k)=\mp\frac{\omega H}{c}[(1-\lambda)\sigma_{\pm}(k)+\lambda\sigma_{\pm}(0)], \tag{14}$$

$$L_{\pm}(k)=i\omega\left[\frac{H}{c}\right]^2[(1-\lambda)^2\sigma_{\pm}(k)+\lambda(2-\lambda)\sigma_{\pm}(0)]. \tag{15}$$

Here $\lambda=\lambda_0(1\pm i\gamma)$, where $\gamma=(\nu-i\omega)/\omega_c$. Formulas (14) and (15) were derived under the assumption that the cyclotron mass m and its sign, as well as ν and λ_0 are constant for all carriers.

3. Let us approximate the FS of a one-sheet electron surface of the type ''corrugated cylinder,'' [6,20,24] which is axially symmetric relative to the $\hat{z}$-axis:

$$S(p_z)=S_0+S_1\cos(\pi p_z/p_0),\quad |p_z|\leqslant p_0, \tag{16}$$

where $S(p_z)$ is the area of cross-section of the FS by the plane $p_z=\text{const}$, S_0, $S_1\leqslant S_0$, and $p_0>0$ are the parameters of the model. In view of $v_{\pm}v_{\pm}^{*}=S(p_z)/\pi m^2$ and $v_z=-(\partial S/\partial p_z)/2\pi m$ we obtain from (8)

$$\sigma_{\pm}=\pm i(Nec/H)[(1\pm i\gamma)^2-(kv_m/\omega_c)^2]^{-1/2}. \tag{17}$$

Here $v_m=|\partial S/\partial p_z|_m/2\pi m$, where $|\partial S/\partial p_z|_m$ is the maximum value of the derivative $\partial S/\partial p_z$, and N is the electron concentration defined by the relation

$$N=\frac{2}{(2\pi\hbar)^3}\int_{FS}S(p_z)dp_z. \tag{18}$$

For convenience of analysis, w introduce the dimensionless parameters

$$q=kv_m/\omega_c,\quad \xi^3=\omega_c^3c^2/\omega_p^2\omega v_m^2, \tag{19}$$

where $\omega_p=(4\pi Ne^2/m)^{1/2}$ is the plasma frequency. Let us now transform Eq. (5) with coefficients (14) and (15), and present it with the help of parameters (17) in the form

$$[q^2\xi^3\pm F_{\pm}(q)][q^2-q_s^2+\alpha_2(q)]=\alpha_1(q), \tag{20}$$

where

$$\alpha_1(q)=\alpha_0 q_s[(1-\lambda)q^2\xi^3\mp\lambda_0]^2, \tag{21}$$

$$\alpha_2(q)=\alpha_0 q_s[(1-\lambda)^2q^2\xi^3\pm\lambda\lambda_0], \tag{22}$$

$\alpha_0=(Nm/\rho)(v_m/v_s)$, $F_{\pm}(q)$ is a nonlocal factor in the conductivity ($\sigma_{\pm}=\pm i(Nec/H)F_{\pm}$) and $q_s=q|_{k=k_s}$ ($k_s=\omega/v_s$).

APPROXIMATE SOLUTION OF THE DISPERSION EQUATION FOR COUPLED MODES

1. Let us first consider briefly the spectrum of electromagnetic modes in the absence of interaction between the electrons and the lattice. We present Eq. (6) in the form

$$\mp q^2\xi^3=F_{\pm}(q). \tag{23}$$

The analytic and graphic solutions of this equation in the polarization ''$-$,'' obtained in the limit $\gamma\to 0$ ($F_0=F_{\pm}|_{\gamma=0}$ are presented in Fig. 1. The spectrum of electromagnetic modes is defined in universal coordinates $z\propto k/\omega^{1/3}$ ($z\equiv q\xi$), $\xi\propto H/\omega^{1/3}$ In this case, these coordinates are preferable to other universal coordinates $q\propto k/\omega_c$, $\xi^{-3}\propto\omega/\omega_c^3$. For $\xi>\xi_m$ ($\xi_m=(27/4)^{1/6}$) the solutions of Eq. (23) are purely real since the function F_0 is also real-valued for $q^2<1$. For $q^2>1$, the function $F_0(q)$ is imaginary due to collisionless attenuation of electromagnetic modes as a result of DSCR. Collisions lead to a blurring of the edge of collisionless attenuation, the function $F_{\pm}(q)$ becomes complex for $q^2<1$, and hence helicon and doppleron modes will attenuate. Suppose that the inequalities $|\gamma|\ll 1$, $|q''/q'|\ll 1$ ($q=q'+iq''$) are satisfied. In this case, using the expression for conductivity, we obtain as a result of simple transformations of (23) the following approximate equations describing the spectrum and damping of weakly attenuating electromagnetic modes for $\nu\neq 0$[20]:

$$q'^2\xi^3\cong F_0(q'), \tag{24}$$

$$2q'q''\cong F_{-}''(q')/[\xi^3-\partial F_0/\partial(q'^2)], \tag{25}$$

where

$$F_{-}''(q')\cong\frac{\nu}{\omega_c}[F_0(q')+2q'^2\partial F_0/\partial(q'^2)].$$

It can be seen from the inset to Fig. 1 and from formula (25) that $\partial F_0/\partial(q^2)>\xi^3$ for the doppleron mode and the quantity $q'q''$ is negative. The minus sign appears due to the fact that for such a model of the FS, the doppleron group

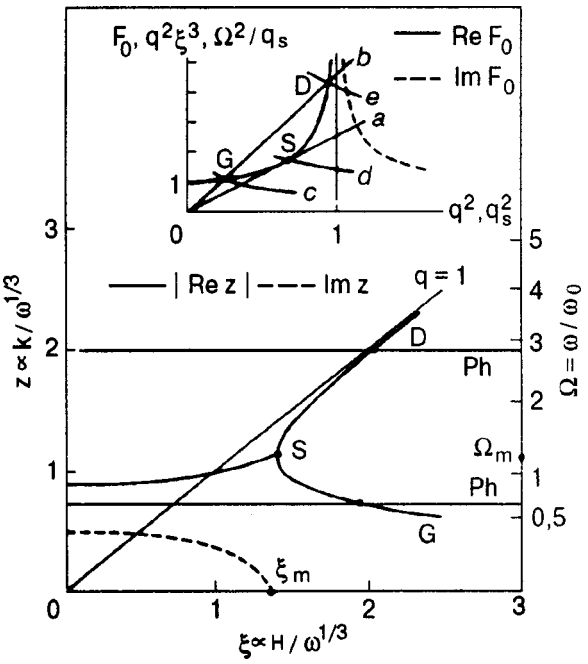

FIG. 1. Spectrum of electromagnetic modes in polarization ''$-$'' in metals with conductivity (17), $z=q\xi$. The horizontal straight lines Ph ($z=z_s$; $z_s=z|_{k=k_s}$) describe the spectrum of sound in the absence of interaction of electrons with the lattice. The points of interaction of the spectra correspond to the helicon–phonon ($z_s=0.75$) and doppleron–phonon ($z_s=2$) resonances. The Ω-axis ($\Omega^2=z_s^3$) defines the acoustic frequency. The inset shows the graphic solution of (23) and (28), $F_0=F_\pm|_{\gamma=0}$. The straight lines *a* and *b* correspond to the left-hand side of (23) in the polarization ''$-$'' for successively increasing values of ξ. Curves *c*,*d* and *e* reflect the left-hand side of (28) for successively large values of Ω. The straight line *a* corresponds to the value $\xi=\xi_m$ ($\xi_m=(27/4)^{1/6}$). and curve *d* to the value $\Omega=\Omega_m(\Omega_m^4=2)$. *G* and *D* are the helicon and doppleron solutions respectively.

velocity $v_{gr}=d\omega/dk$ and the phase velocity $v_{ph}=\omega/k$ are directed opposite to each other. Indeed, in the limit $\gamma\to 0$, we can easily obtain from (23) a relation connecting these quantities:

$$v_{gr}/v_{ph}=2[\xi^3-\partial F_0/\partial(q^2)]/\xi^3. \tag{26}$$

As in Eq. (25), the sign of the right-hand side of (26) and hence the mutual orientation of the vectors $\mathbf{v}_{gr}$ and $\mathbf{v}_{ph}$ is determined by the difference $[\xi^3-\partial F_0/\partial(q^2)]$. Note that Eq. (26) is an exact equality unlike (25).

2. Under conditions of weak coupling of both (ionic and electron) subsystems of the metal, the ''acoustic'' solution of Eq. (20) can be presented in the form

$$q^2\simeq q_s^2+\left[-\alpha_2(q_s)+\frac{\alpha_1(q_s)}{q_s^2\xi^3\pm F_\pm(q_s)}\right]. \tag{27}$$

Resonant interaction of electromagnetic modes with sound is associated with the denominator of the last term on the right-hand side of (27): resonance occurs as $\mathrm{Re}[q_s^2\xi^3-F_-(q_s)]\to 0$. However, the resonance condition is no longer satisfied at quite high frequencies since in this case, unlike relations (24) and (25) written for electromagnetic modes, we must take into account the finite value of the function $|F_\pm|$ as a result of collisions. This question was studied in greater details in Ref. 20. For $q_s^2\xi^3\gg|F_\pm|$, the interaction of collective electromagnetic modes with sound can be disregarded completely. If, however, the inequality $|(1-\lambda)q_s^2\xi^3|\gg\lambda_0$ is also satisfied, formula (27) is transformed into (7) with $k=k_s$ on the right-hand side. Equation (7) describes the one-particle resonance interaction of electrons with sound due to DSCR. Such an interaction (magnetoacoustic resonance), which is of deformation type, was considered earlier by Kaner *et al.*[29] For our model of FS in a relatively clean metal ($\nu\sim 10^9\ \mathrm{s}^{-1}$) with typical parameters, the inequality $q_s^2\xi^3\gg|F_\pm|$ is valid at frequencies in the hypersonic range ($\omega>10^{10}-10^{11}\ \mathrm{s}^{-1}$). As the frequency decreases, vortex fields begin to play a significant role,[30,31] and the inductive mechanism of electron interaction with sound will dominate over the deformation mechanism (the expression ''screening of electron–phonon interaction by vortex fields'' was used by Grishin *et al.*[30]). Naturally, we shall be interested in this frequency range in the present work.

3. Renormalization of the acoustic spectrum caused by electron–phonon interaction is rather insignificant. Hence the position of resonance (helicon–phonon or doppleron–phonon) is defined with a fairly high degree of precision by the point of intersection of the spectrum of propagating electromagnetic modes with the straight line $z=z_s$ (Fig. 1). The position of this point on the plane (ω,H) is defined by Eq. (24) which assumes the following form for $q'=q_s$:

$$\Omega^2/q_s=F_0(q_s). \tag{28}$$

Here $\Omega^2\equiv z_s^3$; $\Omega=\omega/\omega_0(\omega_0^2=\omega_p^2v_s^3/c^2v_m)$. The plane $\Omega\propto\omega$, $\Omega/q_s\propto H$ corresponds to the plane (ω,H).[20] For the model considered by us, we obtain from Eq. (28) $q_s^2\simeq\Omega^4/(1+\Omega^4)$. The graphic solution of this equation is presented in the inset to Fig. 1. The values $\xi=\xi_m$ and $q^2=2/3$ correspond to the straight line *a* and curve *d*. Hence, in accordance with (28), HPhR will be observed at frequencies satisfying the inequality $\Omega^4<\Omega_m^4=2$, while DPhR will be observed at frequencies $\Omega>\Omega_m$.

For typical values of parameters of a metal

$$N=10^{22}\ \mathrm{cm}^{-3};$$

$$v_s=3\times 10^5\ \mathrm{cm/s};$$

$$|\partial S/\partial p_z|_m/2\pi\hbar=1.1\ \text{Å}^{-1} \tag{29}$$

the quantity $\omega_0/2\pi$, which determines the scale along the Ω axis in Fig. 1, is $\sim$460 MHz.

The solution (27), obtained in the weak coupling limit, is used frequently for analyzing magnetoacoustic resonance (see, for example, Refs. 11 and 30 as well as the review by Mertsching[16]). However, the correctness of the solution for resonance of the interaction of collective electromagnetic modes with sound must be justified. Hence we shall derive a more precise solution of the dispersion equation. Let us first approximate Eq. (20) to a simpler one. We shall seek the solution in the ''$-$'' polarization in the form $q=q_s+\Delta q$, where $|\Delta q|\ll q_s$. Using the expansion of the function $F_-(q)$ in the small parameter $(q^2-q_s^2)$ and confining the expansion to the first two terms, we put $q=q_s$ in the expressions for α_1 and α_2. In this case. Eq. (20) assumes the following form

$$[q^2-q_s^2+\alpha_3(q_s)][q^2-q_s^2+\alpha_2(q_s)]=q_s^4\eta(q_s), \tag{30}$$

where

$$\alpha_3=[q_s^2\xi^3-F_-(q_s)]/[\xi^3-\partial F_0/\partial(q_s^2)];$$

$$\eta=\alpha_1(q_s)/q_s^4[\xi^3-\partial F_0/\partial(q_s^2)].$$

The quantity η is called the constant of coupling of electromagnetic modes with sound. Substituting into (30) the approximate relation $q^2-q_s^2\cong 2q_s\Delta q$ and solving it for Δq, we obtain

$$\Delta q_{1,2}\cong\frac{1}{4q_s}\{-[\alpha_3(q_s)+\alpha_2(q_s)] \pm\sqrt{[\alpha_3(q_s)-\alpha_2(q_s)]^2+4q_s^4\eta(q_s)}\}. \tag{31}$$

This is the approximate form of the solution (20) with external parameters z_s (i.e., Ω, $q_s=z_s/\xi$) and ξ. In the limit

$$|\alpha_3-\alpha_2|^2\gg 4q_s^4|\eta| \tag{32}$$

the solution (31) can be presented in the form of the approximate relations

$$\Delta q_1\cong\frac{1}{2q_s}\left(-\alpha_2(q_s)+\frac{q_s^4\eta(q_s)}{\alpha_3(q_s)-\alpha_2(q_s)}\right), \tag{33}$$

$$\Delta q_2\cong\frac{1}{2q_s}\left(-\alpha_3(q_s)-\frac{q_s^4\eta(q_s)}{\alpha_3(q_s)-\alpha_2(q_s)}\right). \tag{34}$$

For reasonable values of the frequency and model parameters for the metal, $|\alpha_2|^2\ll 4q_s^4|\eta|$. In this case, if the condition (32) is satisfied, the inequality $|\alpha_3|\gg|\alpha_2|$ holds. It can be seen now that the relation (33) is an ''acoustic'' solution of the dispersion equation, which practically coincides with (27). Hence the inequality (32) is the condition for verifying the correctness of the weak coupling approximation. Depending on the magnitude of z_s, solution (34) is a ''helicon'' or ''doppleron'' solution. However, unlike (33), this solution is valid only in the vicinity of the resonance since the initial inequality $|\Delta q_2|\ll q_s$ is violated away from resonance.

It can be seen from (34) that inequality (32) is equivalent to the condition of smallness (in magnitude) of the second term on the right-hand side of (34) in comparison with the first term. At resonance, $q_s^2\xi^3=F'_-(q_s)$, and this condition can be presented in the form $|k''_{G,D}|\gg|k''_{\rm coupl}|$. Here, $k''_{G,D}$ is the damping coefficient for electromagnetic modes (helicons and dopplerons) in the absence of coupling (see the expression for α_3 and (25)), $k''_{\rm coupl}$ is the damping coefficient for these modes associated with coupling. The value of $k''_{\rm coupl}$ is determined by the second term on the right-hand sides of (33) and (34). The following distinguishing feature of the resonant interactions is worth noting: $\xi^3>\partial F_0/\partial(q_s^2)$ in the case of HPhR and the helicon–phonon coupling increases the sound attenuation coefficient by $k''_{\rm coupl}$, while the helicon attenuation coefficient k''_G decreases by the same amount. In the case of DPhR, the attenuation of both coupled modes increases.

In the case of strong coupling of electromagnetic modes with sound, i.e., in the limit opposite to the limit (32), formula (31) can be presented in the form

$$\Delta q_{1,2}\cong\frac{1}{2q_s}\left(-\frac{\alpha_3(q_s)+\alpha_2(q_s)}{2}\pm q_s^2\sqrt{\eta(q_s)} \pm\frac{[\alpha_3(q_s)-\alpha_2(q_s)]^2}{8q_s^2\sqrt{\eta(q_s)}}\right). \tag{35}$$

Away from resonance, the strong coupling condition is violated due to an increase in the quantity $|\alpha_3|$. Hence the solutions (35) are valid only in the immediate vicinity of the resonance.

ANALYSIS OF THE SPECTRA OF COUPLED ELECTROMAGNETIC AND ULTRASONIC MODES

In this section, we shall present graphically the numerical solutions of the dispersion equation (20) in the vicinity of HPhR and DPhR. Estimates for the values of frequencies, resonance fields H_r and damping coefficients k'' of coupled modes were obtained for the model of a metal with parameters (29), $\rho=10\,\mathrm{cm}^{-3}$ and $m=0.9\times10^{-27}$ g. Frequencies, i.e., the values of z_s, were chosen in such a way that the inequality $\xi^3\gg\partial F_0/\partial(q_s^2)$ is satisfied in the case of HPhR ($z_s=0.75$) and the opposite inequality holds for DPhR ($z_s=2$). For the chosen values of z_s, we obtain $\omega/2\pi\cong 346$ MHz, $H_r\cong 160$ kOe($\xi_r\cong 2.016$) and $\omega/2\pi\cong 920$ MHz, $H_r\cong 180$ kOe($\xi_r\cong 1.916$), respectively. The large value of resonance fields is due to the specific nature-coupling of electromagnetic and ultrasonic modes in uncompensated metals.[20] Moreover, we studied the dependence of the damping coefficient k'' for coupled modes on frequency ω and the deformation potential constant λ_0.

1. Let us consider an interesting limiting case $\gamma\to 0$. In the absence of coupling and in the vicinity of resonance, the attenuation of all three (helicon, doppleron and acoustic) modes is equal to zero in this case, and hence the strong coupling condition is satisfied.

The solutions of (20) in the vicinity of HPhR are shown in Fig. 2. It can be seen from Fig. 2 and Eq. (31) that, in the collisionless limit, both coupled modes are nonattenuating, and the dispersion curves do not intersect at the point of degeneration of modes, but are split by an amount $\Delta(\mathrm{Re}\,z)$. According to (35), the relative splitting $\Delta(\mathrm{Re}\,z)/z_s\cong\eta^{1/2}$. At very low frequencies like the ones considered in the present case, $\xi^3\gg\partial F_0/\partial(q_s^2)$, $q_s^2\xi^3=F_0\cong 1$ (local limit), the value of η is practically independent of λ_0 ($\alpha_1\cong\alpha_0 q_s$) and $\eta\cong\eta_0$, where $\eta_0\equiv\alpha_0 q_s\xi^3=H_r^2/4\pi\rho v_s^2$ is the known helicon–phonon coupling constant. Obviously, this constant describes the coupling only in the local limit. At higher frequencies, we must take into consideration nonlocal effects which lead, among other things, to a dependence of η on λ_0.

Figure 3 shows the solutions of (20) in the vicinity of DPhR. It can be seen from Figs. 2 and 3 that the spectra for HPhR and DPhR differ radically from one another. The doppleron and acoustic modes are hybridized, and hence both solutions of the dispersion equation become complex in a certain range of the values of ξ in the vicinity of resonance. The main features of the spectrum of coupled modes (see Fig. 3) are described in the limit $\gamma\to 0$ by the relation

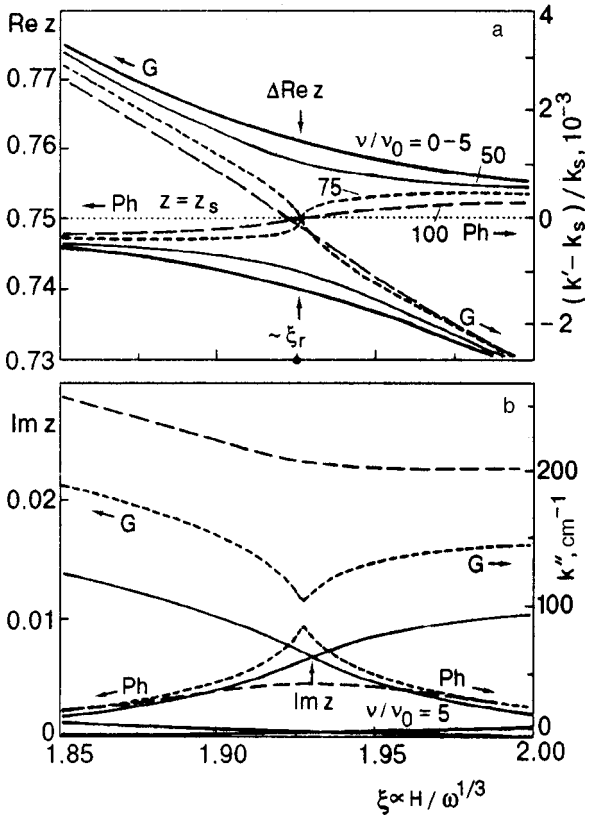

FIG. 2. Helicon–phonon resonance: spectrum of coupled helicon (G) and acoustic (Ph) modes ($z_s=q\xi$; see Fig. 1) in the vicinity of resonance, obtained for different values of ν/ν_0 (numerical solution of (20), $z_s=0.75$, $\lambda_0=1$, $\nu_0=10^9\ \mathrm{s}^{-1}$); for $\nu/\nu_0=0-5$, the dispersion curves almost coincide (a) for $\nu=0$, the damping of both modes is equal to zero (b).

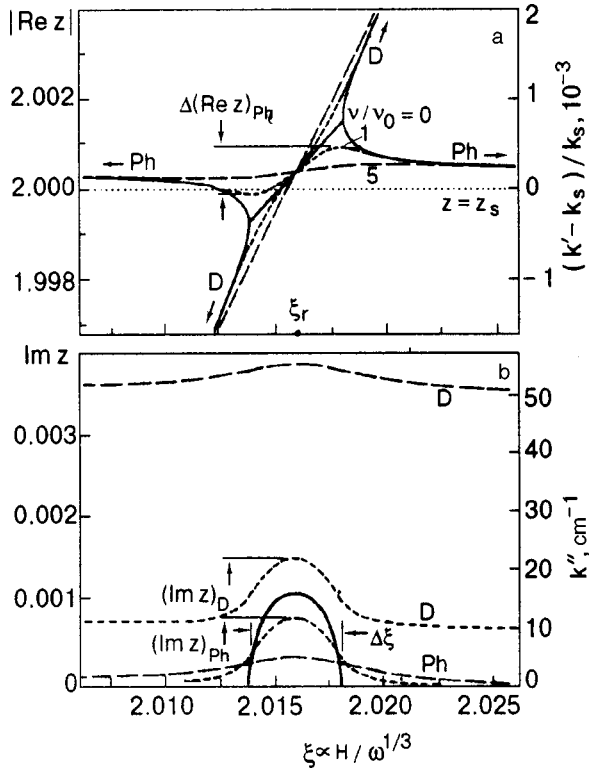

FIG. 3. Doppleron–phonon resonance: spectrum of coupled doppleron (D) and acoustic (Ph) modes ($z_s=q\xi$; see Fig. 1) in the vicinity of resonance, obtained for different values of ν/ν_0 (numerical solution of (20), $z_s=2$, $\lambda_0=1$, $\nu_0=10^9\ \mathrm{s}^{-1}$) (a); for $\nu=0$, the damping coefficients of both modes are equal (solid curve) (b).

$$\frac{\Delta(\mathrm{Re}\ z)_{\mathrm{Ph}}}{z_s}\cong 2\,\frac{(\mathrm{Im}\ z)_{\mathrm{Ph}}}{z_s}\cong\frac{1}{2}\,\frac{\Delta\xi}{\xi_r}\cong|\eta|^{1/2}. \tag{36}$$

In the case of DPhR at relatively high frequencies, $q_s\cong 1, z_s^3\cong\xi^3$ (see (28)) at resonance, and the expression for the coupling constant can be presented in the form

$$\eta\cong-\eta_0\,\frac{[(1-\lambda)z_s^3+\lambda_0]^2}{z_s^3\partial F_0/\partial(q_s^2)}. \tag{37}$$

It can be seen that in contrast to the HPhR, the value of η in DPhR depends on the shape of the FS as well as the deformation potential constant, and may turn out to be much smaller than η_0 in magnitude. In particular, for our model of FS, $\partial F_0/\partial(q_s^2)\cong z_s^9/2$ and $\eta\cong-0.5\times10^{-3}\eta_0$ for $z_s=2$ and $\lambda_0=1$. at resonance. Hence in the cases considered by us, DPhR is manifested ''more weakly'' than HPhR, although the value of H_r (and hence of η_0) was larger in the former case. In order to verify this it is sufficient to compare the scales of the coordinate axes in Figs. 2 and 3.

Another peculiarity of the obtained results is worth noting. It can be seen from Fig. 3(a) that the dispersion dependences for ''acoustic'' modes are displaced upwards relative to the straight line $z=z_s$ which is the sound spectrum in the absence of interaction between electrons and the lattice. This displacement is due to renormalization of the acoustic spectrum as a result of one-particle electron–phonon interaction which is described by the coefficient α_2 in (20). For DPhR $(z_s=2,\lambda_0=1)$, $\alpha_2\xi_r/2q_s\cong3\times10^{-4}$ in formula (33). This value is in good accord with the position of the ''resonance'' point relative to the straight line $z=z_s$.

2. The most distinguishing feature of the doppleron–phonon coupling is the emergence of a ''gap,'' i.e., region of values of ξ in which the solutions of the dispersion equation become complex even in the collisionless limit (see Fig. 3). The gap emerges both in field H (for $\omega=$const) and in frequency ω (for $H=$const). It can be seen from relations (31) and (35) that the emergence of the gap is associated with negative values of the coupling constant η in the case of DPhR. The sign of Re η as well as that of the right-hand sides of (25) and (26) is determined by the sign of the difference $\xi^3-\partial F_0/\partial(q_s^2)$ which is negative for the doppleron mode considered by us. Hence the emergence of a gap is basically due to coupling of the acoustic and doppleron modes which propagate towards each other. In the case of HPhR, both modes propagate in the same direction and Re $\eta>0$. Note that doppleron modes can exist with collinear $\mathbf{v}_{\mathrm{gr}}$ and $\mathbf{v}_{\mathrm{ph}}$ (see, for example, Ref. 32).

Earlier, we studied the coupling of a doppleron mode with a helicon,[24] which also leads to the emergence of a gap in the spectrum of electromagnetic modes. Indeed, it can be seen from Fig. 1 that the helicon mode is hybridized with the doppleron mode in the vicinity of $\xi=\xi_m$. As a result, the solutions of the dispersion equation become essentially complex for $\xi<\xi_m$ and describe the anomalous skin-effect in a magnetic field. In another classical example, such a coupling

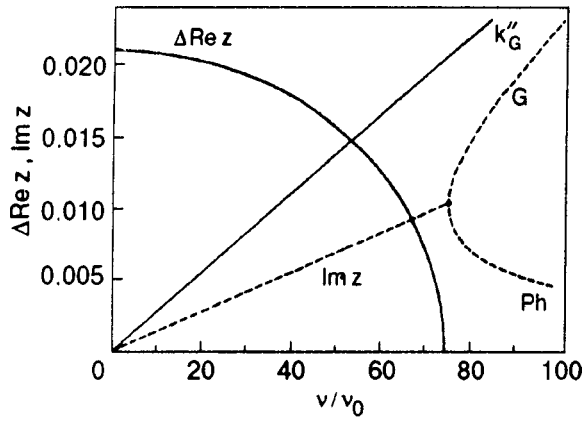

FIG. 4. Helicon–phonon resonance: dependence of the splitting $\Delta(\mathrm{Re}\, z)$ and damping $\mathrm{Im}\, z$ (see Fig. 2) of coupled modes at resonance on electron relaxation frequency ($z_s=0.75, \lambda_0=1, \nu_0=10^9\ \mathrm{s}^{-1}$); for $\nu/\nu_0 \geqslant 74.7$, the value of $\mathrm{Im}\, z$ corresponds to the maximum value for acoustic (Ph) and minimum for helicon (G) modes. The straight line k''_G is the damping coefficient for a helicon in the absence of coupling.

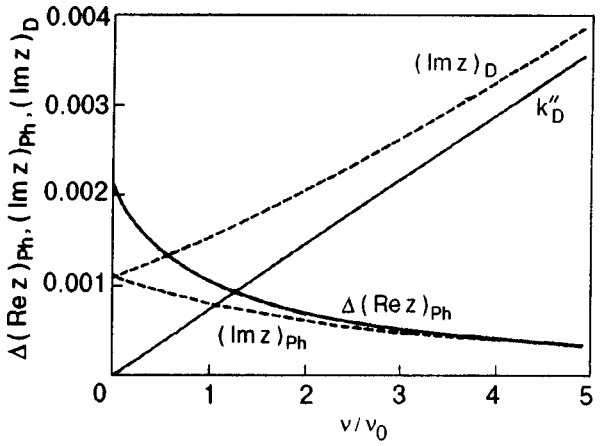

FIG. 5. Doppleron–phonon resonance: dependence of $\Delta(\mathrm{Re}\, z)_{\mathrm{Ph}}$ and damping $(\mathrm{Im}\, z)_{\mathrm{Ph}}$ and $(\mathrm{Im}\, z)_D$ (see Fig. 3) of coupled modes at resonance on electron relaxation frequency ($z_s=2, \lambda_0=1, \nu_0=10^9\ \mathrm{s}^{-1}$); the straight line k''_D is the damping coefficient for a doppleron in the absence of coupling.

occurs in a linear chain of atoms with two different alternating masses (see, for example, Ref. 33). Such a chain can be presented in the form of two strongly coupled (''light'' and ''heavy'') atomic subsystems. As a result, a gap in frequency ω separating the acoustic and optical branches appears in the vibrational spectrum of atoms. This example is interesting in the sense that, like the doppleron mode considered by us, the group and phase velocities of the optical phonons in this region are directed against each other. Hence it can be assumed that the formation of a gap in frequency ω is generally a characteristic feature of coupling of modes propagating against each other.

3. An inequality opposite to the inequality (32) is the condition for strong coupling of electromagnetic modes with sound. Since $|\alpha_2|^2 \ll 4q_s^4|\eta|$, the necessary and sufficient condition for the validity of this inequality is $|\alpha_3|^2 \ll 4q_s^4|\eta|$, According to (25), this inequality at resonance can be presented in the form

$$(k''_{G,D}/k_s)^2 \ll |\eta|. \tag{38}$$

Here, as before, $k''_{G,D}$ is the damping coefficient for electromagnetic modes in the absence of coupling [see (25)].

In the collisionless limit, the condition (39) is satisfied automatically ($k''_{G,D}=0$). It can be seen from (31) and Fig. (2) that a consideration of HPhR in collisions leads to a decrease in the splitting $\Delta\,\mathrm{Re}\, z$ of coupled modes as well as to their attenuation. The damping coefficient of both modes at resonance is $k'' \cong k''_G/2$. This is illustrated in Fig. 4. A comparison of (38) and the dependences presented in Fig. 4 shows that the condition (38) is satisfied quite well in the frequency range $\nu \leqslant 2\times 10^{10}\ \mathrm{s}^{-1}$. This estimate can be obtained directly by substituting into (38) the values of the metal parameters used by us: $z_s^6(\nu/\nu_0)^2 \ll 10^3$ ($\nu_0 = 10^9\ \mathrm{s}^{-1}$). The opposite inequality, i.e., the condition of weak coupling of helicons with sound, is satisfied for $z_s = 0.75$ only in very ''dirty'' metals ($\nu \geqslant 2\times 10^{11}\ \mathrm{s}^{-1}$). Hence, in typical metals with a quite high degree of purity ($\nu \leqslant 10^{10}\ \mathrm{s}^{-1}$), the approximation of strong coupling of helicons with sound is quite correct at HPhR.

In the case of DPhR, the electron relaxation leads to a blurring of the gap which is manifested clearly for $\nu=0$. With increasing ν, the damping of ''acoustic'' and ''doppleron'' modes resulting from their coupling decreases (Fig. 3). The nonresonance contribution to the doppleron damping increases in this case (straight line in Fig. 5). For the model of the metal considered by us and for $\lambda=1$, the strong coupling condition (38) in the case of DPhR can be presented in the form $z_s^6(\nu/\nu_0)^2 \ll 500$. For $z_s=2$, this condition is satisfied only in quite pure metals ($\nu \leqslant 10^9\ \mathrm{s}^{-1}$). The approximation of weak coupling of dopplerons with sound is valid in dirtier, but still adequately clean metals with $\nu \geqslant 5\times 10^9\ \mathrm{s}^{-1}$. Hence, in the case of DPhR in metals with typical values of $\nu \sim 10^9 - 10^{10}\ \mathrm{s}^{-1}$), we cannot prefer one coupling mode over the other.

4. It can be seen from Fig. 2(a) that while the dispersion curves do not intersect in the case of HPhR, the helicon and acoustic branches of the spectrum combine into a single system at resonance and are smoothly transformed into each other. Hence in the vicinity of resonance we cannot identify any coupled mode as a ''helicon'' or ''acoustic'' mode. Such a situation persists as long as the dispersion curves are split. For the case considered by us, splitting vanishes at $\nu = 74.7 \times 10^9\ \mathrm{s}^{-1}$. For higher values of ν, the coupled modes can be identified as ''helicon'' or ''acoustic'' modes (Fig. 4). However, we continue to use inverted commas since the mode identification in the vicinity of resonance remains conditional.

The appurtenance of any coupled mode to a metal subsystem is determined by the ratio of the intensities of ultrasonic and electromagnetic oscillation energies:

$$\frac{I_u}{I_E} = \frac{1}{\eta_0}\left|\frac{Hu_-}{cE_-}\right|^2 = \frac{1}{\eta_0}\left|\frac{q^2\xi^3 - F_-(q)}{(1-\lambda)F_-(q)+\lambda_0}\right|^2, \tag{39}$$

where q is the solution of the dispersion equation (20). Figure 6 shows the dependence of I_u/I_E obtained in the vicinity

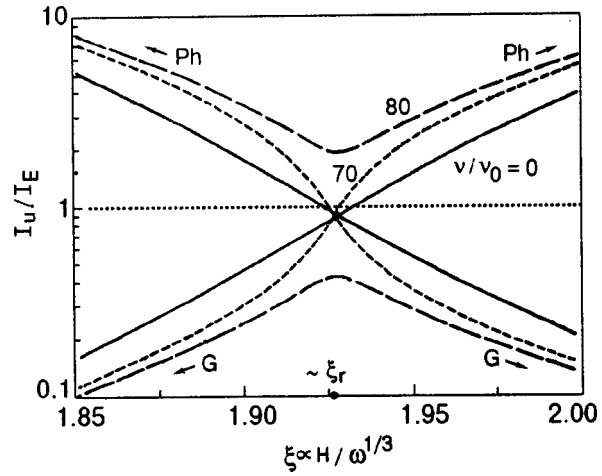

FIG. 6. Helicon–phonon resonance: the ratio of intensities of ultrasonic and electromagnetic oscillations in the vicinity of resonance, obtained for different values of ν/ν_0 ($z_s=0.75, \lambda_0=1, \nu_0=10^9\ \mathrm{s}^{-1}$).

of HPhR for different values of ν. It can be seen that for $\nu < 74.7\cdot 10^9\ \mathrm{s}^{-1}$, $I_u/I_E \cong 1$ for both modes in the vicinity of resonance. Hence in this range of frequencies ν, the coupled modes belong almost equally to both subsystems of the metal and none of them can be defined as heliconlike or soundlike mode. Such a definition becomes possible only for relatively large values of ν, to be more precise, upon a transition to the regime of weak coupling between helicons and sound.

It can be seen from Figs. 3 and 5 that, in contrast to helicon–phonon coupling, the coupled modes in DPhR can be identified as ''doppleron'' and ''acoustic'' modes for indefinitely small values of ν (for doppleron mode, $\mathrm{Re}\, z<0$ for $\mathrm{Im}\, z>0$). Hence the nature of the obtained I_u/I_E dependences (Fig. 7) may appear at first glance as quite unexpected and in contradiction to such a unique definiteness of mode identification. Astonishingly, both modes in the vicinity of resonance are found to be soundlike modes in the vicinity of resonance in a quite pure metal. Even for $\nu=5\times 10^9\ \mathrm{s}^{-1}$, when the approximation of weak coupling of

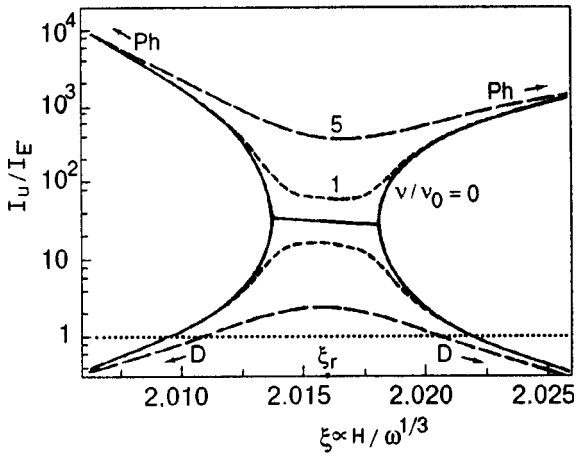

FIG. 7. Doppleron–phonon resonance: the ratio of intensities of ultrasonic and electromagnetic oscillations in the vicinity of resonance, obtained for different values of ν/ν_0 ($z_s=2, \lambda_0=1, \nu_0=10^9\ \mathrm{s}^{-1}$).

dopplerons with sound is valid, $I_u/I_E \approx 3$ and the ''doppleron'' mode still cannot be called doppleronlike.

In order to understand the origin of such a ''phenomenon,'' let us analyze in greater detail formula (39). We shall confine our analysis to the most interesting case $\gamma \to 0$ (strong coupling regime). Substituting the approximate relations $q^2 \cong q^2 + 2q_s\Delta q$ and $F_-(q) \cong F_-(q_s) + 2q_s\delta q \times [\partial F_0/\partial(q_s^2)]$ [where $2q_s\Delta q \cong \pm q_s^2\eta^{1/2}(35)$] into (39), we obtain at resonance

$$\frac{I_u}{I_E} \cong \frac{|\xi^3 - \partial F_0/\partial(q_s^2)|}{\xi^3}\left|1 \pm (1-\lambda_0)\,\frac{\partial F_0}{\partial(q_s^2)} \times \left(\frac{\eta_0}{\xi^3[\xi^3 - \partial F_0/\partial(q_s^2)]}\right)^{1/2}\right|^{-2}. \tag{40}$$

In the case of HPhR, $\xi^3 \gg \partial F_0/\partial(q_s^2)$ and $I_u/I_E \cong 1$ for $\lambda_0=1$ at relatively low frequencies. In turn, $\partial F_0/\partial(q_s^2) \gg \xi^3$ at relatively high frequencies in the case of DPhR, and hence the quantity I_u/I_E will be much larger than unity ($I_u/I_E \cong [\partial F_0/\partial(q_s^2)]/\xi^3$ for $\lambda_0=1$) and both modes are soundlike. For our model of FS, $\partial F_0/\partial(q_s^2) \cong z_s^9/2 (q_s \cong 1, \xi^3 \cong z_s^3)$ and $I_u/I_E \cong z_s^6/2.$ at resonance. For $z_s=2$, the ratio $I_u/I_E \cong 32$. This value is in good agreement with that obtained from a numerical solution of the dispersion equation, i.e., $I_u/I_E=31.3$ (Fig. 7, $\nu=0$). Finally, it should be observed that since the coefficient η_0 is small ($\eta_0 \sim 10^{-3}$ for $H \sim 10^5$ Oe), the ratio I_u/I_E (40) for reasonable values of the parameters ω and λ_0 depends weakly on the value of the constant λ_0.

5. We have considered two cases, viz., HPhR and DPhR, without taking into consideration the dependence of these effects on frequency ω and the deformation potential constant λ_0. Naturally, this dependence is determined to a considerable extent by the dependence of the coupling constant η on ω and λ_0. It can be seen from the expression for η that the frequency dependence of η is considerably influenced by the quantity λ_0, the direction in which λ_0 deviates from the value $\lambda_0=1$ being quite important. We shall consider this question in greater detail by taking the frequency dependence of the damping coefficient for coupled modes as an example.

For the model of FS considered by us, $q_s^2\xi^3 = F_0 \cong 1 - q_s^2/2$ (see the graphic solution of Eq. (28) in Fig. 1) at the resonance at quite low frequencies $\Omega < \Omega_m$ (HPhR). Since the value of q_s^2 is relatively small in this case, we can write $\eta \propto 1 - \lambda_0 q_s^2$ except for negligibly small terms. If the constant λ_0 is not too large, the dependence of η on λ_0 will be weak. In particular, $q_s^2 \simeq 0.15$ in the case considered by us ($z_s=0.75$). Upon a transition to the local limit ($F_0 \to 1$) at lower frequencies, this dependence can be disregarded completely. Consequently, in quite strong magnetic fields (the magnitude of resonance field increases with decreasing frequency), the coupling of helicons with sound is mainly due to inductive interaction of electrons with the lattice.[14] Such a conclusion can also be drawn without specifying the exact form of FS and deformation potential tensor, and by using only the symmetry properties of electroacoustic coefficients. These coefficients are even functions[27,28] and can be written

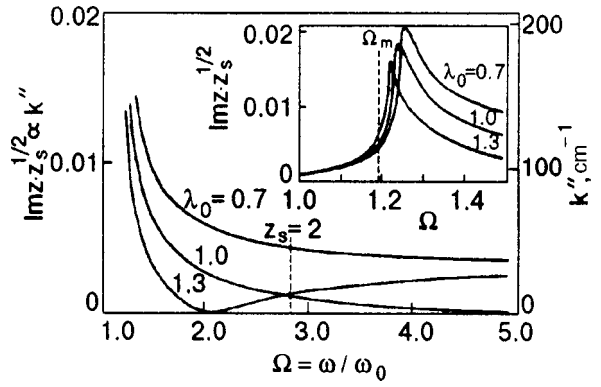

FIG. 8. Frequency dependence of the damping coefficient of ''acoustic'' ($\mathrm{Im}\, z = (\mathrm{Im}\, z)_{\mathrm{Ph}}$ for $\Omega \geqslant \Omega_m$; see Fig. 3) and coupled modes (for $\Omega \leqslant \Omega_m$; see Fig. 2) at resonance, obtained for different values of λ_0 ($\nu = 10^9\ \mathrm{s}^{-1}$). The point $z_s = 2, \lambda_0 = 1$ corresponds to the DPhR case considered above (Fig. 3).

in the form of expansions in even powers of q^2 for $q^2 < 1$. However, in contrast to the conductivity $e^2 < \nu\nu^* >$, the coefficients containing components of the tensor $\hat{\Lambda}$ are equal to zero for $q = 0$. For small values of q^2, it is sufficient to retain only the first terms in the expansions. Consequently the ratio of the ''inductive'' and ''deformation'' forces will be determined by the square of nonlocalization parameter, i.e., by the quantity q^2 (and not q as mentioned in Ref. 14).

According to Eq. (28), $q_s^2 \xi^3 = 1 + \Omega^4$ at resonance. Hence $q_s^2 \xi^3 > 3$ for DPhR ($\Omega \gg \Omega_m$), and the coupling constant η will depend strongly on λ_0. Figure 8 shows the frequency dependences of the damping constant for the ''acoustic'' mode ($\Omega \geqslant \Omega_m$) and coupled modes ($\Omega \leqslant \Omega_m$) at resonance for different values of the constant λ_0. Since coupling of various branches of the spectrum leads to its renormalization, the frequency Ω_m indicated in the figure tentatively separates the frequency regions corresponding to HPhR and DPhR. It can be seen that for $\Omega < \Omega_m$, the damping coefficient of coupled modes depends significantly on λ_0 only in a narrow frequency interval. This is due to the fact that in the case of HPhR, the damping of coupled modes under strong coupling conditions is determined mainly by the coefficient α_3 on the right-hand side of (35), which does not depend on λ_0 at all. The contribution dependent on λ_0 becomes significant only in the vicinity of Ω_m. The situation is quite different for $\Omega > \Omega_m$, when even a slight departure of the quantity λ_0 on either side of the value $\lambda_0 = 1$ leads to a quantitative as well as qualitative variation of the frequency dependence of damping coefficient for the ''acoustic'' mode. This points towards the significant role of the deformation interaction in the case of DPhR. Finally, let us consider an interesting peculiarity of the dependences shown in Fig. 8. For $\lambda_0 = 1.3$, the damping coefficient of the ''acoustic'' mode is very small in a certain frequency interval in the vicinity of $\Omega \cong 2$. This is due to the fact that for $q_s^2 \xi^3 = \lambda_0/(1-\lambda_0)$ ($\lambda_0 > 1$) the coupling constant $|\eta|$ in the polarization ''$-$'' is also very small on account of mutual suppression of the inductive and deformation interactions of dopplerons with sound.

6. Note that parameter β or, to be more precise, the difference $[\xi^3 - \partial F_0/\partial(q_s^2)]$, appears in the expression for η upon a transition from Eq. (20) to (30) as a result of transformation of the expression in the first brackets on the right-hand side of (20). Hence the above-mentioned properties of this parameter are determined only by the functional dependence $F_0(q)$ (i.e., conductivity of the metal) and peculiarities of solutions of the dispersion equation for electromagnetic modes. It may seem that the coupling constant η is independent of peculiarities of the acoustic spectrum associated with the electron–phonon interaction. However, such a dependence exists, even though it is quite weak. Indeed, while going over from Eq. (20) to (30), we need not put $q = q_s$ in the expression for the coefficient $\alpha_2(q)$, but expand this expression (as well as $F(q)$) in small parameter $q^2 - q_s^2$. Consequently, the denominator of the expression for η acquires a factor $1 + \partial\alpha_2/\partial(q_s^2)$ which can be neglected since it is always positive and practically does not differ from unity for reasonable values of ω and λ_0. It should also be observed that the limit $g_{\pm} G_{\pm} \to 0$ in Eq. (5) is not equivalent to the limit $\alpha_1 \to 0$ in (20), since the coefficient α_1 is a complex combination of the coefficients $\sigma_{\pm}$, $q_{\pm}$, $G_{\pm}$ and $L_{\pm}$. Hence the expression for η takes into account to a certain extent the interaction of collective electromagnetic modes with sound, as well as the electron–phonon interaction.

CONCLUSION

In this work, we have analyzed the peculiarities of coupling of propagating electromagnetic modes of helicons and dopplerons with ultrasonic waves. Although helicon–phonon interaction has been studied in detail by now, our analysis of this effect here is quite relevant as it allows a comparative analysis of two basically different cases of coupling, viz., coupling of modes propagating towards each other (DPhR) and modes propagating in the same direction (HPhR).

We have shown that the cardinal difference in the spectra of coupled modes in the cases under consideration is associated with the ratio of the quantities $\partial F_0/\partial(q_s^2)$ and ξ^3. This ratio has the form $\beta = q^2[\partial F_0/\partial(q_s^2)]/F_0(q_s)$. For $\beta > 1$, a doppleron mode is associated with the acoustic wave, its phase and group velocities being directed against each other, its spectrum acquiring a ''gap'' in the limit $\gamma \to 0$. The value of the parameter β is also significant. At quite high frequencies, $\beta \gg 1$ (DPhR) and both coupled modes in pure metals are soundlike in the vicinity of resonance. At low frequencies, $\beta \ll 1$ (HPhR) and $I_u/I_E \cong 1$ for both modes. Such properties of the parameter β are associated with the nature of roots of the dispersion equation (23). Nonlocal effects in conductivity lead to a resonant increase in conductivity for $q^2 \to 1$ (see inset to Fig. 1) and to the emergence of a doppleron solution of the dispersion equation. The derivative $\partial F_0/\partial(q_s^2)$ increases even more sharply. Consequently, $\beta \to \infty$ for $q^2 \to 1$. In the region of helicon solutions of Eq. (23), nonlocal effects are manifested less sharply, the derivative $\partial F_0/\partial(q_s^2)$ is finite, and $\beta \to 0$ ($F_0 \to 1$) for $q^2 \to 0$. This conclusion is practically independent of the specific form of FS.

This research was supported by the Ukrainian State Foundation for Fundamental Investigations (Project No. 2.4/

211). Dedicated to the indefatigable trailblazer Boris Ieremievich Verkin.

*)E-mail: tsymbal@host.dipt.donetsk.ua

[1] O. V. Konstantinov and V. I. Perel', Zh. Éksp. Teor. Fiz. **38**, 161 (1960) [Sov. Phys. JETP **11**, 117 (1960)].
[2] P. Agrain, in *Proceedings Int. Conf. on Semicond. Phys.*, Prague 1960.
[3] R. Bowers, C. Legendy, and F. Rose, Phys. Rev. Lett. **7**, 339 (1961).
[4] P. B. Miller and R. R. Haering, Phys. Rev. **128**, 126 (1962).
[5] E. A. Stern, Phys. Rev. Lett. **10**, 91 (1963).
[6] D. S. Falk, B. Gerson, and J. F. Carolan, Phys. Rev. B **1**, 406 (1970).
[7] O. V. Konstantinov and V. G. Skobov, Fiz. Tverd. Tela (Leningrad) **12**, 2768 (1970) [Sov. Phys. Solid State **12**, 2237 (1970)].
[8] L. M. Fisher, V. V. Lavrova, V. A. Yudin *et al.*, Zh. Éksp. Teor. Fiz. **60**, 759 (1971) [Sov. Phys. JETP **33**, 410 (1971)].
[9] G. Akramov, Fiz. Tverd. Tela (Leningrad) **5**, 1310 (1963) [Sov. Phys. Solid State **5**, 955 (1963)].
[10] D. N. Langenberg and J. Bok, Phys. Rev. Lett. **11**, 549 (1963).
[11] T. Kjeldaas, Phys. Rev. **113**, 1473 (1959). The helicon–phonon resonance was predicted for the first time in this work (see footnote on p. 1475), and hence the existence of electromagnetic waves (helicons) in metals was indicated here. Paradoxically, though, this fact has been ignored to this date.
[12] C. C. Grimes and S. J. Buchsbaum, Phys. Rev. Lett. **12**, 357 (1964).
[13] J. J. Quinn and S. Rodrigues, Phys. Rev. Lett. **11**, 552 (1963).
[14] V. G. Skobov and E. A. Kaner, Zh. Éksp. Teor. Fiz. **46**, 273 (1964) [Sov. Phys. JETP **19**, 189 (1964)].
[15] E. A. Kaner and V. G. Skobov, Adv. Phys. **17**, 605 (1968).
[16] J. Mertsching, Phys. Status Solidi B **37**, 465 (1970).
[17] T. G. Blaney, Philos. Mag. **15**, 707 (1967).
[18] T. G. Blaney, Philos. Mag. **17**, 404 (1968).
[19] V. V. Gudkov, Solid State Commun. **44**, 229 (1982).
[20] L. T. Tsymbal and A. N. Cherkasov, Fiz. Nizk. Temp. **24**, 250 (1998) [Low Temp. Phys. **24**, 189 (1998)].
[21] L. T. Tsymbal and T. F. Butenko, Solid State Commun. **13**, 633 (1973).
[22] L. P. Volkova, L. T. Tsymbal and A. N. Cherkasov, Fiz. Nizk. Temp. **9**, 1262 (1983) [Sov. J. Low Temp. Phys. **9**, 649 (1983)].
[23] S. V. Medvedev, V. G. Skobov L. M. Fisher, and V. A. Yudin, Zh. Éksp. Teor. Fiz. **69**, 2267 (1975) [Sov. Phys. JETP **42**, 1152 (1975)].
[24] L. T. Tsymbal, A. N. Cherkasov, and O. F. Panchenko, Fiz. Nizk. Temp. **24**, 1157 (1998) [Low Temp. Phys. **24**, 868 (1998)].
[25] D. E. Muller, Math. Tables and Other Aids to Comput. **10**, 208 (1956).
[26] V. M. Kontorovich, Zh. Éksp. Teor. Fiz. **45**, 1638 (1963) [Sov. Phys. JETP **18**, 1125 (1963)].
[27] V. M. Kontorovich, Usp. Fiz. Nauk **142**, 265 (1984) [Sov. Phys. Uspekhi **27**, 134 (1984)].
[28] V. M. Kontorovich, Zh. Éksp. Teor. Fiz. **59**, 2116 (1970) [Sov. Phys. JETP **32**, 1146 (1970)].
[29] E. A. Kaner, V. G. Peschanskii, and I. A. Privorotskii, Zh. Éksp. Teor. Fiz. **40**, 214 (1961) [Sov. Phys. JETP **13**, 147 (1961)].
[30] A. M. Grishin, V. G. Skobov, L. M. Fisher, and A. S. Chernov, Pis'ma Zh. Éksp. Teor. Fiz. **35**, 370 (1982) [JETP Lett. **35**, 455 (1982)].
[31] V. L. Gurevich, I. G. Lang, and S. T. Pavlov, Zh. Éksp. Teor. Fiz. **59**, 1679 (1970) [Sov. Phys. JETP **32**, 914 (1970)].
[32] V. V. Lavrov, S. V. Medvedev, V. G. Skobov *et al.*, Zh. Éksp. Teor. Fiz. **66**, 700 (1974) [Sov. Phys. JETP **39**, 338 (1974)].
[33] J. M. Ziman, *Principles of the Theory of Solids*, Cambridge Univ. Press, Cambridge (1972).

Translated by R. S. Wadhwa

Electromagnetic waves in organic conductors under strong magnetism of conduction electrons

V. G. Peschansky

B. Verkin Institute for Low Temperature Physics and Engineering, National Academy of Sciences of the Ukraine, 310164 Kharkov, Ukraine[*)]

D. I. Stepanenko

Kharkov State University, 310077 Kharkov, Ukraine

(Submitted March 22, 1999)
Fiz. Nizk. Temp. **25**, 889–893 (August–September 1999)

Wave processes in layered organic conductors in strong magnetic fields are investigated theoretically at low temperatures when the de Haas–van Alphen effect is manifested strongly. The spectrum and amplitude of weakly attenuating waves are determined in the vicinity of the electron phase transition where the formation of diamagnetic domains takes place. © *1999 American Institute of Physics.* [S1063-777X(99)01308-0]

The class of conductors having metal-type conductivity has been considerably broadened in recent years following the synthesis of organic layered structures. Their electric conductivity is strongly anisotropic, i.e., the conductivity along layers is much higher than its value at right angles to the layers.

The energy of charge carriers in layered conductors

$$\varepsilon(\mathbf{p})=\sum_{n=0}^{\infty}\varepsilon_n(p_x,p_y)\cos\left(\frac{anp_z}{\hbar}\right) \tag{1}$$

depends weakly on the momentum component $p_z=\mathbf{p}\cdot\mathbf{n}$ along the normal $\mathbf{n}$ to the layers, while the functions $\varepsilon(p_x,p_y)$ decrease sharply with increasing n. Formula (1) corresponds to the strong-coupling approximation in which overlapping of the wave functions of electrons belonging to different layers is small, and the separation a between them is much larger than the intralayer atomic separation.

The low-dimensional electron energy spectrum of such conductors, which are frequently called synthetic metals, facilitates the manifestation of Shubnikov–de Haas[1] and de Haas– van Alphen[2] quantum oscillations in them in a magnetic field H.

The oscillatory dependences of magnetoresistance[1] and magnetization of bismuth[2] discovered in Leiden were treated for a long time as anomalies in bismuth along with its other unusual properties, until the investigations carried out by Verkin *et al.*[3] in Kharkov and Shoenberg *et al.*[4] in Cambridge led to the conclusion that the oscillatory dependence of the physical characteristics of metals on inverse magnetic field at low temperatures is a common feature of metals. These oscillations can be observed only in quite strong magnetic fields, such that the separation $\Delta\varepsilon=\hbar\Omega$ between Landau levels exceeds their width $\hbar/\tau$ and the temperature blurring of the Fermi distribution function $f_0(\varepsilon)$ of charge carriers.[5–8] While these quantum oscillations in metals are caused only by a small fraction of charge carriers of the order of $(\hbar\Omega/\varepsilon_F)^{1/2}$ for which the area S of cross section of the Fermi surface $\varepsilon(\mathbf{p})=\varepsilon_F$ by the plane $p_H=\mathbf{p}\cdot\mathbf{H}/H$ is close to the extremal cross-sectional area S_{ext}, nearly all conduction electrons with Fermi energy ε_F are involved in the formation of oscillatory effects in layered quasi-two-dimensional conductors. As a result, the amplitude of oscillations of magnetization $\mathbf{M}$ is found to be quite large, and the magnetic susceptibility components $\chi_{ij}=\partial M_i/\partial B_j$ may become comparable with unity. In this case, we cannot disregard the difference between the magnetic induction $\mathbf{B}=\mathbf{B_0}+\mathbf{B}(\mathbf{r},t)$ and the magnetic field $\mathbf{H}=\mathbf{B}-4\pi\mathbf{M}(\mathbf{B})$. If one of the diagonal components of the magnetic susceptibility χ exceeds $1/4\pi$, the homogeneous state becomes unstable[9–11] and is replaced by an inhomogeneous state with alternating domains having different values of magnetic induction.[9,10] If the dissipative effects are insignificant, i.e. $\Omega\tau$ is quite large, the formation of a stationary domain structure may be accompanied by weakly attenuating oscillations of the electromagnetic field.[12,13] We shall use the following standard notation: $\mathbf{B}_0$ is the homogeneous part of magnetic induction, $\mathbf{B}(\mathbf{r},t)$ the magnetic field of the wave, $\Omega=eB_0/m^*c$ the rotational frequency of an electron in the magnetic field, e,m^*, and τ are its charge, effective cyclotron mass, and mean free time respectively, c is the velocity of light in vacuum, and $\hbar$ the Planck's constant.

The experimental observation of Shubnikov–de Haas quantum oscillations of magnetoresistance of organic metals $(\text{BEDT-TTF})_2\text{X}$ with different elements or complexes X at liquid helium temperatures in magnetic fields of the order of 10 T (see Refs. 14 and 15 and the literature cited in the review article Ref. 16) allows us to assume that the condition $\Omega\tau\gg1$ is clearly satisfied in the investigated samples, and the formation of a domain structure in layered organic conductors is quite possible.

1. Let us consider wave processes in layered conductors for the case when $\chi<1/4\pi$, and the homogeneous part $\mathbf{B}_0$ of the magnetic induction is directed along the normal to the layers, i.e., $\mathbf{B}_0=(0,0,B_0)$, and has a quite large value so that

 © 1999 American Institute of Physics

$\Omega\tau \gg 1$. Without any loss of generality during the solution of the problem, we confine ourselves to just the first two terms in expression (1) for $\varepsilon(\mathbf{p})$, assuming that $\varepsilon_1(p_x,p_y)$ is a constant quantity equal to $\eta v_0 \hbar/a$, where v_0 is the characteristic Fermi velocity of charge carriers along the layers, and the parameter of quasi-two-dimensionality of the electron energy spectrum $\eta \ll 1$.

In the vicinity of the electron phase transition with the formation of diamagnetic domains for $\kappa^2 = |1-4\pi\chi| \ll 1$ in the Maxwell equations

$$c\,\mathrm{curl}\,\mathbf{H} = 4\pi\mathbf{j} + \partial\mathbf{E}/\partial t;\quad c\,\mathrm{curl}\,\mathbf{E} = -\partial\mathbf{B}/\partial t;\quad \mathrm{div}\ \mathbf{B} = 0 \tag{2}$$

the linear term $(1-4\pi\chi)B_z(\mathbf{r},t)$ in the expansion of the function $\mathbf{H}(\mathbf{r},t)$ in the magnetic field $B_z(\mathbf{r},t)$ of the wave turns out to be of the same order as the nonlinear terms, and the wave process becomes essentially nonlinear even for small amplitudes of $\mathbf{B}(\mathbf{r},t)$ and of the electric field $\mathbf{E}(\mathbf{r},t)$ of the wave.[12,13]

If the magnetic susceptibility $\chi = \chi_{zz}$ is not too close to $1/4\pi$, i.e., $\kappa^2 B_z(\mathbf{r},t)$ is much larger than the nonlinear terms in the expansion of $\mathbf{H}(\mathbf{r},t)$ for quite small wave amplitudes, we can confine ourselves to the linear approximation while solving Maxwell's equations.

The current density $\mathbf{j}$ is connected with the electric field of a wave through an integral relation in the case of a strong spatial dispersion:

$$j_i(\mathbf{r},t) = \int dt'\,d^3\mathbf{r}'\,\sigma_{ij}(t'-t,\mathbf{r}'-\mathbf{r})E_j(t',\mathbf{r}') = \hat{\sigma}_{ij}E_j. \tag{3}$$

Using the Fourier representations for the electric and magnetic fields of the wave

$$\mathbf{E}(\mathbf{r},t) = \int d^3k\,\mathbf{E}(\mathbf{k})\exp[i(\mathbf{k}\cdot\mathbf{r}-\omega t)], \tag{4}$$

$$\mathbf{B}(\mathbf{r},t) = \int d^3k\,\mathbf{B}(\mathbf{k})\exp[i(\mathbf{k}\cdot\mathbf{r}-\omega t)], \tag{5}$$

we arrive at the following dispersion equation for determining the spectrum $\omega(\mathbf{k})$ of intrinsic vibrational modes:

$$\mathrm{Det}\begin{vmatrix} \sigma_{xx}-\xi(k_y^2\kappa^2+k_z^2) & \sigma_{xy} & \sigma_{xz} \\ \sigma_{yx} & \sigma_{yy}-\xi k_z^2 & \sigma_{yz}+\xi k_y k_z \\ \sigma_{zx} & \sigma_{zy}-\xi k_y k_z & \sigma_{zz}-\xi k_y^2 \end{vmatrix} = 0, \tag{6}$$

where the Fourier components of the electric conductivity tensor have the following form in the semiclassical approximation ($\hbar\Omega \ll \varepsilon_F\eta$):

$$\sigma_{ij}(\mathbf{k}) = \int \frac{2e^2}{(2\pi\hbar)^3}\,d\varepsilon\,\delta(\varepsilon(\mathbf{p})-\varepsilon_F)\int 2\pi m^*\Omega^{-1}dp_z \times \int_0^{2\pi} d\varphi\, v_i(\varphi)\int_{-\infty}^{0} d\varphi'\, v_j(\varphi') \times \exp\{\gamma\varphi' + \mathbf{k}\cdot[\mathbf{r}(\varphi'+\varphi)-\mathbf{r}(\varphi)]\}. \tag{7}$$

Here $\gamma = 1/\Omega\tau - i\omega/\Omega$; $\mathbf{r}(\varphi) = \Omega^{-1}\int_0^{\varphi}\mathbf{v}(\varphi')d\varphi'$; $\xi = c^2/(4\pi i\omega)$ the x-axis is directed at right angles to the wave vector $\mathbf{k}$ and to the vector $\mathbf{B}_0$ so that $\mathbf{k} = (0,\ k\sin\theta,\ k\cos\theta)$, and the dependence of the electron velocity on the dimensionless variable φ should be found with the help of the equation of motion for the charge

$$\frac{\partial\mathbf{p}}{\partial\varphi} = (m^*\mathbf{v}\times\mathbf{e}_3);\quad \mathbf{e}_3 = (0,0,1). \tag{8}$$

For $\theta = 0$, the exponent in formula (7) depends linearly on φ'. Integrating with respect to φ and φ', we obtain the following expression for $\sigma_{ij}(\mathbf{k})$:

$$\sigma_{ij}(k) = \int \frac{2e^2}{(2\pi\hbar)^3}\,d\varepsilon\,\delta[\varepsilon(\mathbf{p})-\varepsilon_F] \times \sum_n \frac{\hbar}{a}\int_0^{2\pi} 2\pi m^* d\alpha\,\frac{v_i^{-n}(\alpha)v_j^{n}(\alpha)}{\gamma_n\Omega + ikv_0\eta\sin\alpha}, \tag{9}$$

where $\gamma_n = \gamma + in, \alpha = ap_z/\hbar$, and

$$v_j''(\alpha) = \frac{1}{2\pi}\int_0^{\pi} d\varphi\ \ v_j(\varphi,\alpha)\exp\{-in\varphi\}. \tag{10}$$

As a result of simple computations, we arrive at the following expression for $\sigma_{ij}(\mathbf{k})$:

$$\sigma_{ij}(\mathbf{k}) = \omega_p^2 \sum_n C_{ij}^{(n)}[(kv_0\eta)^2 + (\gamma_n\Omega)^2]^{-1/2}, \tag{11}$$

where ω_p is the frequency of plasma oscillations in the system of conduction electrons, and $C_{ij}^{(n)}$ are numerical factors of the order of unity. For $i=j$, all of them are real and positive, while in nondissipative Hall components they are imaginary as a rule and change sign upon inversion of i and j, and hence a helicoidal wave is generated in a quite strong magnetic field for $\Omega \gg kv_0\eta$ and attenuates at distances $l_{\mathrm{hel}} = \delta_0(\Omega\tau)^{3/2}$, where $\delta_0 = c/[\omega_p(\omega\tau)^{1/2}]$.

If the wave vector deviates from the normal to the layers by an angle $\theta \geqslant \arctan\eta$, the spectrum of weakly attenuating waves is transformed considerably. A helicoidal wave can be generated only for $\tan^2\theta \leqslant \eta^2/\gamma_0 = \eta^2\Omega\tau$, when the dissipative part $\rho_{zz}\sin^2\theta$ of resistivity in the plane orthogonal to the vector $\mathbf{k}$ is much smaller than the Hall components.

For $\gamma_0 \geqslant \eta^2\kappa^2$ and $\eta^2 \ll \tan^2\theta \ll \eta^2/\gamma_0$ the attenuation wavelength is $\eta^2/\gamma_0\tan^2\theta$ times larger than the wavelength and is equal to

$$l_{\mathrm{hel}} = \delta_0(\Omega\tau)^{3/2}\eta^2\cos\theta\cot^{1/2}\theta. \tag{12}$$

In extremely strong magnetic fields, when $\gamma_0 \ll \eta^2\kappa^2$, the attenuation length of the helicoidal wave has the form

$$l_{\mathrm{hel}} = \delta_0(\Omega\tau)^{3/2}\eta^2(\kappa^2+\tan^2\theta)^{3/4}\cos\theta\cot^2\theta. \tag{13}$$

For $\tan^2\theta \geqslant \eta^2/\gamma_0$, the imaginary part of k is larger than, or comparable with, the real part and the wave process does not occur. Numerical factors of the order of unity, which depend on the specific form of the function $\varepsilon_0(p_x,p_y)$, have been omitted in formulas (12) and (13).

2. Analysis of the transient processes under conditions of the existence of the domain structure, when $\chi > 1/4\pi$, is much more complicated. We shall consider only the case of weak time and space dispersion of electromagnetic waves:

$$\omega\tau \ll 1,\quad kr_0 \ll 1,\quad \eta k_z v_0\tau \ll 1, \tag{14}$$

where r_0 is the radius of curvature of the electron orbit in the field $\mathbf{B}_0=(0,0,B_0)$. This enables us to present the integral expression (3) for conduction current and magnetization current $\mathbf{j}'=c\,\mathrm{curl}\,\mathbf{M}$ induced by an external magnetic field in a localized form, i.e., in the form of an expansion in powers of **E**, **B** and their derivatives. Eliminating the electric field **E** from the Maxwell equations (2), we obtain the following equation for the transient field $\mathbf{B}(y,z,t)$:

$$4\pi\frac{\partial\mathbf{B}}{\partial t}=-c^2\mathrm{curl}[\hat{\rho}\ \ \mathrm{curl}(\mathbf{B}-4\pi\mathbf{M})], \tag{15}$$

where $[\hat{\rho}\,\mathrm{curl}(\mathbf{B}-4\pi\mathbf{M})]_i=\rho_{ij}[\mathrm{curl}(\mathbf{B}-4\pi\mathbf{M})]_j$ and the components of the static resistivity tensor $\rho_{ij}=(\hat{\sigma}^{-1})_{ij}$ also contain, in addition to the semiclassical expression, small quantum corrections in parameter $(\hbar\Omega/\eta\varepsilon_F)^{1/2}$. Introduction of these corrections does not lead to a qualitative variation of the spectrum of weakly attenuating waves, and it is sufficient to consider the classical expression (9) for σ_{ij} for $k=0$.

The induced current density $\mathbf{j}'$ is defined mainly by the magnetization component M_z

$$j_x'=c\partial M_z/\partial y=c\chi(B_0)\partial B_z\partial y+\alpha\ \ c\ \ r_0^2\partial^3B_z/\partial y^3 - c\zeta\partial B_z^3/\partial y, \tag{16}$$

where $\zeta=(\beta/B_0^2)(\varepsilon_F/\hbar\Omega)^2$; α and β are numerical factors of the order of unity.

In the case of an isotropic dispersion relation for charge carriers in the layer plane, when $\rho_{xx}=\rho_{yy}=\rho_{zz}\eta^2=\rho_0=4\pi/\omega_p^2\tau$ we obtain after simple transformations the following expression for $B_z(y,z,t)$:

$$\left(\frac{\omega_p^2}{c^2\Omega}\right)^2\frac{\partial^2B_z}{\partial t^2}+\frac{\partial^2}{\partial z^2}\left(\frac{\partial^2H_z}{\partial y^2}+\frac{\partial^2B_z}{\partial z^2}\right) =\frac{\omega_p^2}{c^2\Omega^2\tau}\Delta_1\frac{\partial B_z}{\partial t}+\left(\frac{\omega_p^2}{c^2\Omega^2\tau}\frac{\partial}{\partial t}-\frac{1}{(\Omega\tau)^2}\Delta_1\right) \times\left(\frac{\partial^2H_z}{\partial y^2}+\frac{\partial^2B_z}{\partial z^2}\right), \tag{17}$$

where the operator Δ_1 has the form

$$\Delta_1=\frac{\partial^2}{\eta^2\partial y^2}+\frac{\partial^2}{\partial z^2}. \tag{18}$$

The time-independent solution of Eq. (17), i.e.,

$$B_1(y)=b_0\mu(1+\mu^2)^{-1/2}\,\mathrm{sn}\left(\frac{y}{\delta(1+\mu^2)^{1/2}},\mu\right) \tag{19}$$

defines a periodic domain structure with a period $D=4\delta(1+\mu^2)^{1/2}K(\mu)$ and domain wall thickness $\delta=(4\pi\alpha)^{1/2}r_0/\chi$.

Here $b_0=(\kappa^2/2\pi\zeta)^{1/2}=\kappa B_0(\hbar\Omega/\varepsilon_F)$, the modulus μ of the elliptic function *sn* is defined uniquely by the integration constant, and $K(\mu)=\int_0^{\pi/2}d\varphi(1-\mu^2\sin^2\varphi)^{-1/2}$ is a total elliptic integral of the first kind.

We shall seek the time-dependent solution of Eq. (17) in the form

$$B_z(y,z,t)=B_1(y)+b(y)\exp(-i\omega t+ik_zz). \tag{20}$$

Linearizing Eq. (17) in $b(y)$ and disregarding small terms proportional to γ_0^2, we arrive at the following linear equation in $b(y)$:

$$\left[k_z^2-i\gamma_0\omega\left(\frac{\omega_p^2}{c^2\Omega}\right)\right]\left[\kappa^2\frac{\partial b(y)}{\partial y^2}-12\pi\zeta\frac{\partial^2}{\partial y^2}[b(y)B_1^2(y)] +4\pi\alpha r_0^2\frac{\partial^4b(y)}{\partial y^4}\right]+i\frac{\gamma_0^\omega}{\eta^2}\left(\frac{\omega_p^2}{c^2\Omega}\right)\frac{\partial^2b(y)}{\partial y^2}=\lambda b(y), \tag{21}$$

where

$$\lambda=\left[\left(\frac{\omega_p^2}{c^2\Omega}\right)^2\omega^2-k_z^4+2i\gamma_0\omega k_z^2\left(\frac{\omega_p^2}{c^2\Omega}\right)\right].$$

Admissible values of the parameter λ for which the function $b(y)$ does not contain secular terms determine the possible wave spectrum. The case $\lambda=0$ corresponds to a wave propagating along the normal to the layers, and its frequency is defined as follows with an error not exceeding terms proportional to γ_0^2:

$$\omega=\frac{k^2c^2\Omega}{\omega_p^2}(1-i\gamma_0). \tag{22}$$

For $\lambda=0$, Eq. (21) is transformed into a Lamé equation which can be integrated in known transcendental functions. In the limiting case $\gamma\ll\kappa^2\eta^2$, the amplitude of $b(y)$ is expressed in terms of Jacobi's elliptic functions

$$b(y_1)=A\,\mathrm{cn}(y_1,\mu)\,\mathrm{dn}(y_1,\mu), \tag{23}$$

where A is a constant and $y_1=y/[\delta(1+\mu^2)^{1/2}]$.

Knowing $B_z(y,z,t)$, we can easily obtain the remaining components of the electromagnetic field. In zeroth approximation in γ_0, i.e., without taking dissipation into consideration, we obtain

$$B_x(y,z,t)=-k_z\delta(1+\mu^2)^{1/2}A\,\mathrm{sn}(y_1,\mu)\times\exp(-i\omega t+ik_zz);$$

$$B_y(y,z,t)=-ik_z\delta(1+\mu^2)^{1/2}A\,\mathrm{sn}(y_1,\mu)\times\exp(-i\omega t+ik_zz);$$

$$\mathbf{E}=-\frac{c\Omega}{\omega_p^2}[\mathbf{e}_3\times\mathrm{curl}\,\mathbf{H}(\mathbf{B})]. \tag{24}$$

If the domain size is large in comparison with δ, the function $b(y)$ differs considerably from zero only near the transient layer, i.e., in the vicinity of the points $y_1=2nK(\mu)$, where n is an integer.

Thus, in the case of a periodic domain structure, the amplitude of a helicoidal wave depends considerably on the size of the domains and the thickness δ of the periodic layer.

*)E-mail: vpeschansky@ilt.kharkov.ua

[1] L. V. Schubnikov and W. J. de Haas, Leiden Commun. **19**, 207f (1930).
[2] W. J. de Haas and P. M. van Alphen, Leiden Commun. **19**, 208d (1930).

[3] B. I. Verkin, D. Sc. Thesis, Kharkov (1956).
[4] D. Shoenberg, Magnetic Oscillations in Metals, Cambridge Univ. Press, Cambridge (1984).
[5] L. D. Landau, Proc. Roy. Soc. **170**, 341 (1939).
[6] A. I. Akhiezer, Zh. Éksp. Teor. Fiz. **9**, 197 (1939).
[7] L. Onsager, Philos. Mag. **43**, 1006 (1952).
[8] I. M. Lifshits and A. M. Kosevich, Zh. Éksp. Teor. Fiz. **29**, 730 (1955) [Sov. Phys. JETP **2**, 636 (1955)].
[9] J. H. Condon, Phys. Rev. **145**, 526 (1966).
[10] I. A. Privorotskii, Zh. Éksp. Teor. Fiz. **52** 1755 (1967) [Sov. Phys. JETP **25**, 1167 (1967)].
[11] I. A. Privorotskii and M. Ya. Azbel', Zh. Éksp. Teor. Fiz. **56**, 388 (1969) [Sov. Phys. JETP **29**, 214 (1969)].
[12] V. G. Peschansky and D. I. Stepanenko, Zh. Éksp. Teor. Fiz. **112**, 1841 (1997) [Sov. Phys. JETP **85**, 1007 (1997)].
[13] V. G. Peschansky and D. I. Stepanenko, Fiz. Nizk. Temp. **25**, 277 (1999) [Low Temp. Phys. **25**, 203 (1999)].
[14] M. V. Kartsovnik, V. N. Laukhin, V. N. Nizhankovskii, and A. A. Ignat'ev, Pis'ma Zh. Éksp. Teor. Fiz. **47**, 302 (1988) [JETP Lett. **47**, 363 (1988)].
[15] M. V. Kartsovnik, P. A. Kononovich, V. N. Laukhin, and I. F. Shchegolev, Pis'ma Zh. Éksp. Teor. Fiz. **48**, 498 (1988) [JETP Lett. **48**, 541 (1988)].
[16] O. V. Kirichenko, Ju. A. Kolesnichenko, and V. G. Peschansky, Phys. Revs. **18**, 1 (1998).

Translated by R. S. Wadhwa

Effect of pressure on the Fermi surface and electronic structure of $ErGa_3$

V. B. Pluzhnikov

International Laboratory of High Magnetic Fields and Low Temperatures, Gajowicka 95, 53-529 Wroclaw, Poland; B. Verkin Institute for Low Temperature Physics and Engineering, National Academy of Sciences of Ukraine, 47 Lenin Ave., Khar'kov 310164, Ukraine

A. Czopnik

W. Trzebiatowski Institute of Low Temperature and Structure Research, P.O. Box 1410, 50-950 Wroclaw, Poland

O. Eriksson

Condensed Matter Theory Group, Department of Physics, University of Uppsala, Box 530, S-751 21 Uppsala, Sweden

G. E. Grechnev and Yu. V. Fomenko

*B. Verkin Institute for Low Temperature Physics and Engineering, National Academy of Sciences of Ukraine, 47 Lenin Ave., Kharkov 310164, Ukraine**)

(Submitted March 9, 1999)
Fiz. Nizk. Temp. **25**, 894–902 (August–September 1999)

The Fermi surface and cyclotron masses of the $ErGa_3$ compound are studied by means of the de Haas–van Alphen technique under pressure. Concurrently, the electronic structure is calculated *ab initio* for the ferromagnetic phase of $ErGa_3$. The experimental data have been analyzed on the basis of the calculated volume-dependent band structure and compared with available results for isostructural $TmGa_3$ and $LuGa_3$ compounds. © *1999 American Institute of Physics.* [S1063-777X(99)01408-5]

1. INTRODUCTION

The objective of the present work is a study of the pressure effect on the Fermi surface (FS) and cyclotron masses of the $ErGa_3$ compound by means of the de Haas–van Alphen (dHvA) effect. The pressure derivatives of dHvA frequencies and cyclotron masses are of particular interest due to their assumed sensitivity to details of the exchange interaction and many-body effects. Therefore, the present investigation can provide a critical test for recently developed methods of *ab initio* calculations of electronic and magnetic structures, and to stimulate the formulation of improved theories for rare-earths (RE).

This work represents an extension of our recent studies[1–3] of the FS and electronic structure in the cubic $REGa_3$ compounds at ambient pressure. There are very little data available on the physical properties of $ErGa_3$. The compound crystallizes in the $AuCu_3$-type cubic structure and orders antiferromagnetically at $T_N = 2.8$ K by means of a continuous transition, and the corresponding magnetic structure is presumably the incommensurate modulated one.[4] It can be expected that at low temperatures $ErGa_3$ reveals large and field-dependent magnetization, in the same manner as is the case of $TmGa_3$.[2] This provides a number of complications in the Fourier analysis of dHvA oscillations. Specifically, the dHvA effect has to be studied in sufficiently strong magnetic fields where magnetization is almost saturated. These fields are expected to be higher than the critical field destroying the antiferromagnetic order. By this means the dHvA effect can be investigated in a paramagnetic phase of $ErGa_3$, in which magnetic field leads to a quasi-ferromagnetic configuration of magnetic moments.

In the present work the experimental study of the dHvA effect under pressure is complemented by *ab initio* calculations of the spin-polarized electronic structure of $ErGa_3$ when the atomic volume is varied through a small range around the equilibrium value. Basically, the dHvA data supplemented by results of the calculations provide a possibility to estimate the volume dependencies of the FS and exchange interaction parameters, as well as the many-body enhancement of band cyclotron masses. A comparison of the data of the pressure effect and the calculated volume dependent band structure can be especially useful in testing the adequacy of theoretical models employed for rare-earth compounds. The evaluated parameters of the electronic structure of $ErGa_3$ are also compared with corresponding results obtained for the isostructural compounds $TmGa_3$ and $LuGa_3$ at ambient pressure.[1,2]

2. EXPERIMENTAL TECHNIQUES

Single crystals of $ErGa_3$ were grown by the flux method from the melt of the nominal composition 90% at. Ga and 10% at. Er. The purity of starting metals was 6N for Ga and 4N for Er. The feed placed in a alumina crucible and sealed in a quartz tube in argon atmosphere under pressure of 150 Torr at room temperature, was heated in a resistance furnace up to 920 °C, held at this temperature for 48 h and

 © 1999 American Institute of Physics

then slowly cooled down at the rate 0.8 K/h. The synthesis was stopped at about 350 °C and then sample was cooled rapidly down to room temperature for avoiding the formation of $ErGa_6$ in peritetic reaction.[5] The resulting crystals of $ErGa_3$ were immersed in an excess of Ga which is easy to remove. The obtained crystals had the form of cubes with maximum dimensions $5\times5\times5$ mm. According to the *x*-ray examination the quality of single crystals was very good.

The dHvA effect measurements were performed on a spherical sample (diameter 2.5 mm) by using a standard field modulation technique at temperatures down to 1.5 K and in magnetic fields up to 15 T applied along principal crystallographic axes. Large amplitudes of the observed dHvA oscillations can be considered as another prove of the high quality of $ErGa_3$ single crystals. A standard Cu–Be clamp was used for the pressure effect study with an extracted benzine solvent as the medium transmitting pressure to the sample. The maximum pressure employed was 6.4 kbar at 4.2 K. A small manganin coil with resistance about 60 Ω was placed near the sample to measure the applied pressure. Preliminary this coil has been trained to cooling-pressure and then calibrated by measuring the superconducting transition temperature of Sn.[6] A deviation of the manganin coil resistance due to the residual magnetic field of the superconducting magnet has been also taken into account. The sample, the pick-up coil, and the manganin coil, all were placed in a teflon cell, filled with the extracted benzine solvent, and then the cell was put in the pressure clamp. A deviation from hydrostatic pressure and its effect on the measurements are estimated to be negligible by observing that the superconducting transition width of Sn does not change noticeably and amplitudes of the dHvA oscillations do not decrease substantially under pressures used in this work.

Since the pressure clamp is heated with the modulation field, there is a difference in temperatures between the helium bath and the sample in the pressure clamp. The modulation amplitude and frequency used in measurements were 40 G and 38.5 Hz, respectively. These amplitude and frequency were chosen to produce a large enough dHvA signal, and, at the same time, to reduce the heating power, which leads to a temperature difference not exceeding 0.02 K.

In a magnetic material, the dHvA oscillations are periodic in B^{-1}, where B is the magnetic induction. For a spherical sample as we have used $\mathbf{B}=\mathbf{H}_{\text{appl}}+(8\pi/3)\mathbf{M}$, where $\mathbf{H}_{\text{appl}}$ is the applied field and $\mathbf{M}$ is the magnetization. Complementary magnetization measurements were performed by a home made vibrating sample magnetometer. The field dependence of the magnetization along the principal crystallographic axes is shown in Fig. 1. This dependence can be reproduced by a fitting calculation in the molecular-field approximation. The Hamiltonian employed contains the crystal field (CF), the exchange and Zeeman terms. The molecular-field exchange parameter was estimated, based on the value of the paramagnetic Curie temperature, $\Theta_p = -10$ K. Then the best fit to the experimental data was obtained for the CF parameters x and W (in the usual notations of Ref. 7) equal to 0.22 and 0.25 K, respectively. This gives the Γ_7 doublet as the CF ground state, and the first excited state appeared to be the $\Gamma_8^{(1)}$ quartet at about 30 K.

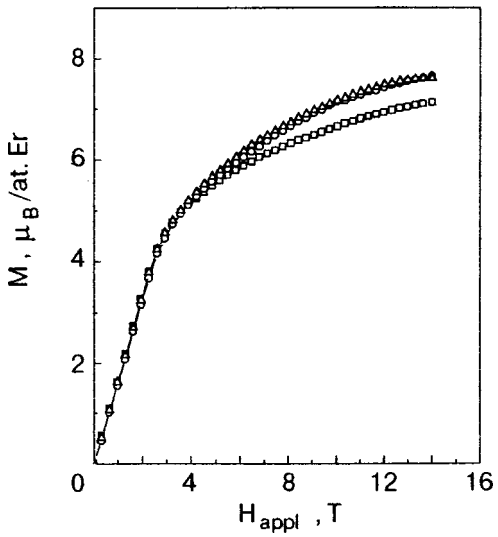

FIG. 1. Magnetization of $ErGa_3$ at 1.7 K in the magnetic field applied along ⟨100⟩ (□), ⟨110⟩ (○), and ⟨111⟩ (△) axes.

The total CF splitting is about 120 K. These parameters provided a possibility for evaluating the angular dependence of the magnetization.[3]

The applied pressure modifies a magnitude and field dependence of the magnetization due to a pressure influence on the CF splitting, as well as on the exchange interaction. It is well known, that CF of metallic rare-earth compounds contains contributions from charges of surrounding ligands as well as from the direct Coulomb and exchange interactions of the rare-earth ion with conduction electrons. In order to estimate the influence of the pressure on the CF we have restricted ourselves to the contribution from surrounding ligands within the point charge model. The applied pressure P brings about the volume dilatation $\delta V/V=-P/c_B$, were c_B-bulk modulus. Under pressure of 10 kbar $\delta V/V$ is estimated to be -0.013, when we assume for $ErGa_3$ the bulk modulus of $TmGa_3$, equal to $c_B=765$ kbar.[8] The change of CF due to this dilatation causes a variation of the magnetic induction at 1.7 K in the applied field of 15 T not larger than 20 G. One can estimate also a change of the magnetization in $ErGa_3$ due to a variation of the exchange interaction parameter under pressure by making use of appropriate data obtained for the isostructural $REIn_3$ compounds.[9,10] The corresponding variation of the magnetic induction with the applied pressure of 10 kbar is about -10 G at 1.7 K in the field of 15 T. Therefore, the total change of the magnetic induction reaches only 10 G, giving the relative variation of the dHvA frequency $\delta F/F\simeq 2.10^{-4}\,\text{kbar}^{-1}$, which may be neglected in the Fourier analysis of the dHvA oscillations.

The dHvA effect measurements were carried out in magnetic fields higher than 8 T where the magnetization does not change appreciably and the Fourier analysis of the dHvA oscillations can be performed. In another case a dHvA frequency would change its value following the strength of external magnetic field. It turns out that for this intensity range $ErGa_3$ is in the paramagnetic state, and the measurements were carried out in this phase well above the antiferro-paramagnetic transition. Actually, along all principal crystal-

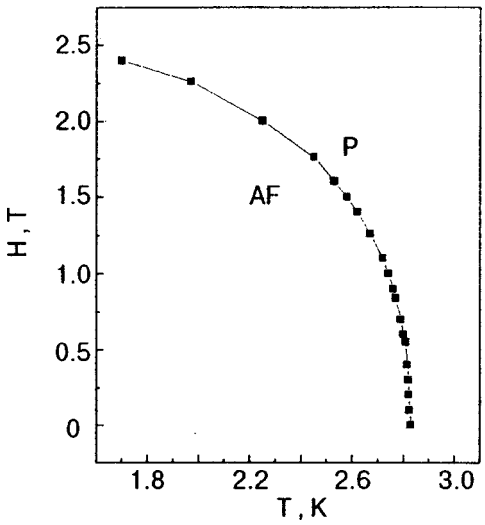

FIG. 2. Sketch of the magnetic phase diagram of $ErGa_3$ in the magnetic field applied along the ⟨100⟩-axis. The curve is a line of phase transitions between an antiferromagnetic state and the paramagnetic one.

lographic axes, ⟨001⟩, ⟨011⟩, and ⟨111⟩ the critical field of the antiferromagnetic-paramagnetic transition does not exceed 3 T. This is evident from a sketch of the magnetic phase diagram in Fig. 2, where the curve represents a transition between an antiferromagnetic state and the paramagnetic one for the fields applied along ⟨100⟩ axes. Actually, the magnetic phase diagram of $ErGa_3$ is more complex, and its full description, together with neutron diffraction data and the CF scheme examination, will be published elsewhere.[11]

The magnetization in magnetic fields higher than 8 T tends to saturate and magnetic moments settle into a quasi-ferromagnetic configuration. Moreover, the magnetization along all directions in a magnetic field higher than 8 T appeared to be almost temperature independent in the range 1.7–4.2 K. Therefore, the evaluated values of the magnetization along the principal crystallographic axes were used in the Fourier analysis of dHvA oscillations. It should be pointed out that for the field induced quasi-ferromagnetic configuration the dHvA spectrum of $ErGa_3$ can be compared with results of band structure calculations for the corresponding spin-polarized state.

3. DETAILS OF CALCULATIONS

At present it is commonly believed[12–14] that, within the local spin-density, approximation (LSDA), a strict band treatment of the $4f$ states is inadequate for heavy rare earths. In the corresponding spin-polarized calculations the *f*-shell is not filled and the $4f$ bands, which act as a sink for electrons, always cut the Fermi level (E_F) leading to absurd values of specific heat coefficients[12] and wrong $4f$ occupancies, close to the divalent (i.e., atomic) configuration.[15]

According to the photoemission data,[15–17] the $4f$ spectral density for Er and Er-based compounds was observed about 5 eV below E_F. Therefore, for the present purpose, which is mainly to describe the band structure for the ground state near E_F, it seems reasonable to treat $4f$ states in $ErGa_3$ as semilocalized core states, in line with Refs. 10, 13, 14 and 18.

In fact, the standard rare-earth model[12] is employed in this work in the limit of the large Hubbard repulsion U within the *ab initio* LSDA scheme[19] for the exchange-correlation effects. The localized *f*-states of Er were treated as spin-polarized outer-core wave functions, contributing to the total spin density. Consequently, the spin occupation numbers were fixed by applying the Russel–Saunders coupling scheme to the $4f$ shell, which was not allowed to hybridize with conduction electrons.

The self-consistent band structure calculations were carried out for the paramagnetic configuration phase of $ErGa_3$ by using the linear muffin-tin orbital method (LMTO) in the atomic sphere approximation (ASA) with combined corrections to ASA included.[20,21] In the framework of the LSDA, the spin density of the $4f$ states polarizes the ''spin-up'' and ''spin-down'' conduction electron states through the local exchange interaction. The exchange split conduction electron states interact with the localized f states at other sites, appearing as the medium for the indirect f-f interaction.[10,18]

In order to calculate FS orbits, the charge densities were obtained by including spin-orbit coupling at each variational step, as suggested in Refs. 12 and 13. In this case the spin is no longer a good quantum number, and it is not possible to evaluate the electronic structure for ''spin-up'' and ''spin-down'' bands separately. Also, we have employed the approximation, which has been extremely successful for rare-earths,[12] namely, to omit spin-orbit coupling in spin-polarized band structure calculations for $ErGa_3$. It gives the possibility of elucidating the role of the spin-orbit coupling, and also of presenting ''spin-up'' and ''spin-down'' bands for field-induced ferromagnetic phase of $ErGa_3$, where the exchange splitting is much larger than the spin-orbit coupling.

The band structure calculations were performed self-consistently on a uniform mesh of 455 points in the irreducible wedge of the cubic Brillouin zone for a number of lattice parameters close to the experimental one. The individual atomic radii of the components were chosen following the method outlined in Ref. 22.

The results obtained with the LMTO-ASA method were verified and supplemented by carrying out *ab initio* relativistic full-potential LMTO calculations of the electronic structure of $ErGa_3$ in an external magnetic field with the Zeeman term included (details of this method have been described elsewhere[23]). The calculated density of states (DOS) and band structure along selected high symmetry lines appeared to be similar in the two types of calculations.

The calculated partial densities of states for the ferromagnetic phase of $ErGa_3$ are presented in Fig. 3. Two fairly broad peaks, associated with bonding and antibonding states, originate due to hybridization of $5d$-states of Er and $4p$-states of Ga. As can be seen in Fig. 3, these *p*-states give substantial contribution to the total DOS at the Fermi energy. On the other hand, the exchange splitting is more pronounced for the $5d$-states of Er (about 20 mRy) due to the local exchange interaction. For hybridized electronic states at

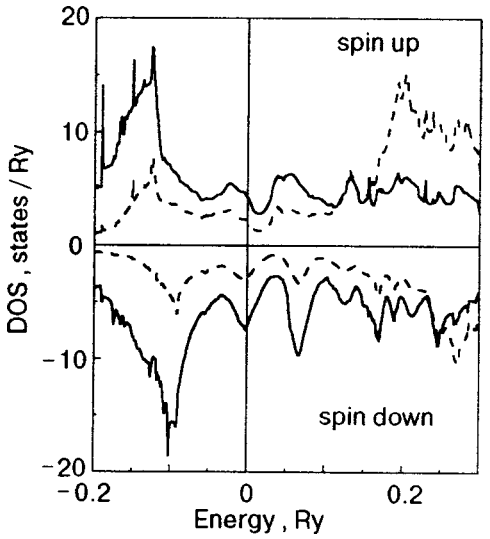

FIG. 3. Partial densities of states as a function of energy (relative to the Fermi energy E_F) for the ferromagnetic phase of $ErGa_3$. Solid lines stand for *p*-states of Ga, and dashed lines represent *d*-states of Er.

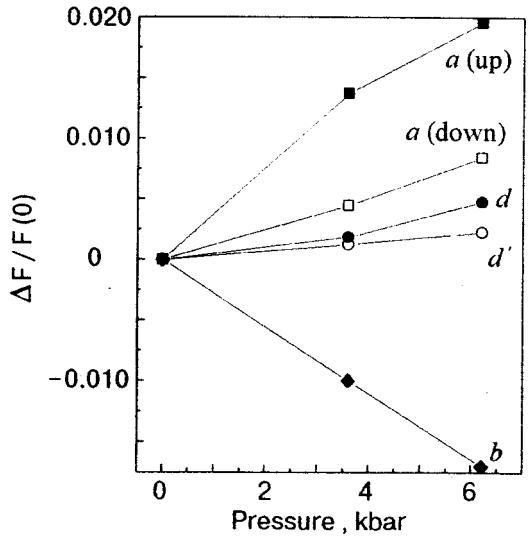

FIG. 5. Fractional changes of the dHvA frequencies, $\Delta F/F(0)$, as a function of pressure for the [100] magnetic field direction at 2.1 K. The frequencies are labeled according to Ref. 3 and Fig. 6. The *a*(up) and *a*(down) refer to the oscillations originating from the ''spin-up'' and ''spin-down'' subbands of the *a* branch, respectively. The solid lines are guides for the eye.

E_F the exchange splitting takes smaller values, reducing to about 1 mRy for the pure *p*-states.

4. RESULTS AND DISCUSSION

The Fourier spectra of dHvA oscillations in $ErGa_3$ observed along ⟨100⟩ axis at different pressures are presented in Fig. 4, and the pressure effect on the corresponding dHvA frequencies is exhibited in Fig. 5. For all the principal crystallographic axes, ⟨100⟩, ⟨110⟩, and ⟨111⟩, the dHvA frequencies at ambient pressure and their pressure derivatives $d \ln F/dP$ are listed in Table I.

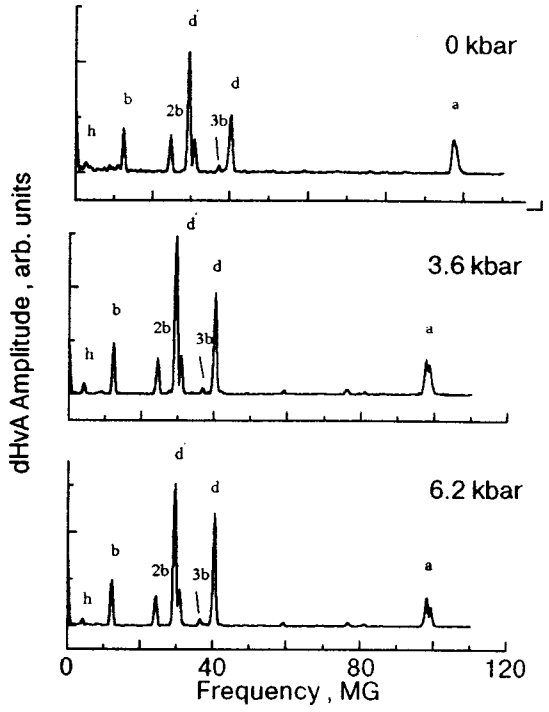

FIG. 4. Fourier spectra of dHvA oscillations observed at 2.1 K for magnetic fields directed along [100] axis at ambient pressure, 3.6 kbar, and 6.2 kbar.

For reference, the angular dependence of dHvA frequencies in the (100) and (110) planes, obtained at ambient pressure in Ref. 3, is shown in Fig. 6. The intersections of the calculated FS of $ErGa_3$ with planes of the cubic Brillouin zone (Fig. 7) reveal the ''spin-split'' almost spherical electron FS centered at *R*-point and the complicated multiply connected hole FS centered at Γ-and *X*-points. As can be seen in Fig. 6, the agreement between the calculated FS and the experimental data is quite good in the range of the high dHvA frequencies (branch *a* which arise from the FS sheet at *R*-point, and branch *d*, associated with the largest sheet of the hole FS centered at Γ-point), as well as the medium ones (branch *b*, related to the hole FS sheet at *X*-point). Instead of the calculated branch *j*, which arise from a ''neck'' at the symmetry line Γ*R*, a branch with a different angular field dependence has been observed in the range of low dHvA frequencies. It is analogous to the branch previously found in $LuGa_3$,[1] and labeled *h* in Fig. 6.

Basically, the dHvA spectrum of $ErGa_3$ in the field-induced ferromagnetic configuration appeared to be close to the spectrum of $LuGa_3$,[1] except for the presence of additional branch *d′* that is just below the *d* branch and located in the vicinity of the ⟨100⟩ axis. It should be pointed out that in a ferromagnetic configuration phase of the isostructural $TmGa_3$ compound the dHvA spectrum contains several *h*-like branches in the low frequency range and no *d′*-branch.[2]

The dHvA oscillations originating from the ''spin-split'' subbands were observed only for the *a* branch. This splitting is seen in Fig. 4 and Fig. 5, but not resolved in Fig. 6 owing to the scale chosen. Based upon the calculated partial DOS in Fig. 3, one can expect the more easily observed dHvA oscillations related to the majority states, having lower DOS and, correspondingly, lower band masses. In fact, the frequencies calculated for ''spin-up'' bands (which are actually

TABLE I. DHvA frequencies at ambient pressure, their pressure derivatives, and cyclotron effective masses at ambient pressure $ErGa_3$.

Field direction	F, MG	$d \ln F/dp$, 10^3 kbar^{-1}		m_c^*, m_0
	experiment	experiment	theory	experiment
⟨100⟩	98.71	2.3±0.3	1.3	0.96±0.02
	97.81	1.4±0.4	1.1	-
	41.07	1.7±0.2	2.0	0.91±0.02
	30.27	0.36±0.02	-	0.92±0.03
	12.66	−2.7±0.1	−2.8	0.44±0.02
	4.35	-	-	0.55±0.02
⟨110⟩	96.03	1.2±0.2	1.2	0.89±0.02
	95.17	1.0±0.3	1.1	-
	15.80	−1.2±0.1	-	-
	15.14	−1.1±0.1	-	0.57±0.02
	11.95	−2.4±0.2	−2.0	0.84±0.04
	3.37	−4.5±0.3	-	0.28±0.02
⟨111⟩	88.30	2.5±0.3	1.4	0.80±0.02
	87.58	1.7±0.1	1.2	-
	35.47	2.3±0.2	1.9	0.70±0.02
	4.21	-	-	0.51±0.02

presented in Fig. 6) appeared to be in better agreement with the experimentally observed ones.

The experimental pressure derivatives $d \ln F/dP$, presented in Table I, are rather large in comparison with free-electron scaling prediction, which gives two-thirds the volume compressibility or 0.87×10^{-3} kbar^{-1}, provided the available bulk modulus of $TmGa_3$[8] is accepted for $ErGa_3$. Basically, there is a qualitative agreement between the experimental and calculated $d \ln F/dP$ derivatives (again, the bulk modulus of $TmGa_3$ was used to convert the calculated volume derivatives to the pressure ones, listed in Table I). The main discrepancy between these derivatives can be seen for the *a* branch, where the average exchange splitting is given by

$$\Delta E = 2\mu_B \Delta F (m_0/m_c^b),$$

where m_c^b is the calculated band cyclotron mass and m_0 is the free-electron mass. Taking into account the small value of this exchange splitting for the *a* branch (about 1 mRy), the difference between experimental pressure derivatives for the corresponding ''spin-split'' subbands can be considered as surprisingly large.

It was originally suggested in Ref. 24, that there are two contributions in ferromagnetic metals to the pressure derivative of dHvA frequency. The first ''potential'' contribution comes from an atomic volume effect on the crystal potential, and also from a scaling effect due to the change of the Brillouin zone size. It can be approximated by the corresponding derivative for a non-magnetic reference compound with a close value of the compressibility (in our case it can be $LuGa_3$). The second ''magnetic'' contribution originates from the redistribution of conduction electrons between spin-split subbands with pressure and the corresponding changes of volume enclosed by FS sheets. Within the Stoner–Wohlfarth model this contribution for ferromagnetic 3*d*-metals was described qualitatively by considering a

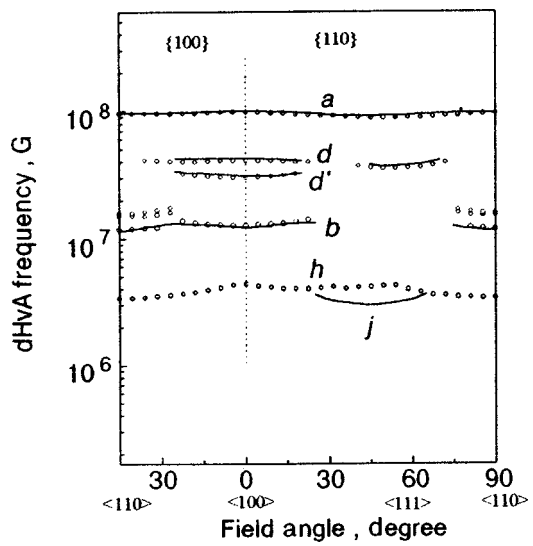

FIG. 6. Angular dependence of the dHvA frequencies in $ErGa_3$, taken from Ref. 3. Circles stand for the experimental data, solid lines show calculated results.

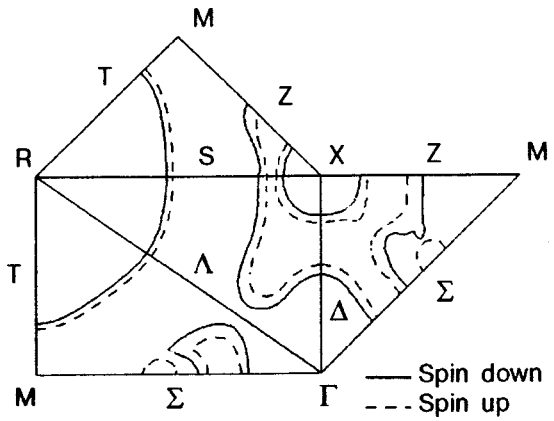

FIG. 7. Intersection of the Fermi surface for $ErGa_3$ with the Brillouin zone planes.

TABLE II. Cyclotron masses (experimental, m_c^*, and calculated, m_c^b, in units of free-electron mass) and the corresponding mass enhancement factor λ in $REGa_3$ compounds at ambient pressure. For $ErGa_3$, two effective masses measured at 4 kbar are also presented.

Branch and orientation	$ErGa_3$				$TmGa_3$[a]			$LuGa_3$[a]		
	m_c^*	m_c^*, 4 kbar	m_c^b	λ	m_c^*	m_c^b	λ	m_c^*	m_c^b	λ
a, ⟨100⟩	0.96±0.02	-	0.40	1.4	1.20±0.02	0.41	1.93	0.74±0.02	0.38	0.95
a, ⟨110⟩	0.89±0.02	-	0.37	1.4	1.02±0.03	0.38	1.68	0.73±0.02	0.36	1.03
a, ⟨111⟩	0.80±0.02	0.94±0.03	0.37	1.16	0.77±0.02	0.38	1.03	0.57±0.02	0.36	0.58
d, ⟨100⟩	0.91±0.02	-	0.46	0.98	1.30±0.02	0.46	1.83	0.63±0.02	0.48	0.31
d, ⟨111⟩	0.70±0.02	0.92±0.03	0.40	0.75	0.90±0.02	0.42	1.14	0.53±0.02	0.39	0.36

[a]Taken from Ref. 2

pressure effect on the exchange splitting Δ.[24] According to the present calculations, Fermi surfaces of $ErGa_3$ do not change uniformly because of a strong **k**-dependent *p*-*d* mixing effect on the exchange-split conduction band. As a result, the difference between pressure derivatives of the spin-split FS cross-sectional areas is inconsistent with prediction based on the Stoner–Wohlfarth model.

At this point, it is difficult to explain the discrepancy between the experimental and calculated derivatives of dHvA frequencies for the spin-split *a* branch in $ErGa_3$. A detailed consideration of this problem should obtain further arguments in future planned experiments, which are aimed to reveal exchange-splitting for other FS sheets, as well as their pressure dependence. Also, a study of the dHvA effect under pressure in the reference nonmagnetic compound $LuGa_3$ will provide a possibility to evaluate the ''potential'' contributions to the pressure derivatives for corresponding FS cross-sections of $ErGa_3$. In addition, spin-polarized calculations of the volume-dependent FS with full-potential LMTO method will be helpful to clarify this problem. Compared to the LMTO-ASA method used for this purpose, a full-potential technique provides better description of electronic density in the interstitial region and, accordingly, more realistic *p*-like and *p*-*d* hybridized conduction electron states.

Cyclotron masses m_c^* have been determined at ambient pressure for all dHvA frequencies in the field applied along the ⟨100⟩, ⟨110⟩ and ⟨111⟩ axes, and appeared to be smaller than free electron mass (see Table I). Also, the cyclotron masses measured at a pressure of 4 kbar for branches *a* and *d* in the field applied along the ⟨111⟩ axis are presented in Table II. Band cyclotron masses m_c^b have been calculated for *a* and *d* branches, and are also given in Table II.

The mass enhancement factor λ, which is defined by relation $m_c^* = m_c^b(1+\lambda)$, presents a measure of interaction strength of conduction electrons with low energy excitations. The λ-factors for electrons on *a* and *d* orbits in $ErGa_3$, $TmGa_3$,[2] and $LuGa_3$[1,2] are listed in Table II. In non-magnetic $LuGa_3$ the λ-factor is presumably a measure of electron-phonon interactions, whereas in $ErGa_3$ and $TmGa_3$ this factor also contains contribution(s) coming from magnetic excitations. As seen in Table II in $LuGa_3$ the λ factor ranges from 0.3 (*d* branch) to about 1 (*a* branch). Assuming that values of λ_{e-ph} in $REGa_3$ are close to the corresponding ones in $LuGa_3$, one can estimate magnetic contributions λ_{mag} in $ErGa_3$ to be 0.4–0.6 and 0.4–0.7 for *a* and *d* orbits, respectively. In $TmGa_3$ the corresponding values of λ_{mag} are larger and more anisotropic, namely 0.5–1 and 0.8–1.5.

The hybridization of conduction electrons with $4f$ states could contribute to the large cyclotron masses observed in $ErGa_3$ (and $TmGa_3$), and affect the shape of FS as well. For heavy rare-earths these hybridization effects are commonly overestimated within LSDA, and corresponding calculations would lead to substantial reduction of the conduction band width in $REGa_3$ and, therefore, to remarkably different bulk properties in comparison to $LuGa_3$. In accord with the lattice parameters behavior, which decrease slightly in a linear fashion in the series $ErGa_3$, $TmGa_3$, and $LuGa_3$ due to the lanthanide contraction, it can be expected, however, that conduction band widths are close in $REGa_3$, and band cyclotron masses should be also close. At the present stage even calculations performed within LSDA+U or a Hubbard-like scheme would not be of decisive importance,[14] and more elaborated analysis is necessary to estimate a scale of the hybridization effects.

One may assume that the distinctions between effective masses of $TmGa_3$ and $ErGa_3$ are most likely due to the different ground states $^3H_6$ and $^4I_{15/2}$ multiplets of Tm^{3+} and Er^{3+} ions in the CF of $TmGa_3$ and $ErGa_3$, respectively. The CF scheme of $TmGa_3$ provides the triplet $\Gamma_5^{(1)}$ as the ground state with intrinsic magnetic and quadrupolar moments.[8] Therefore, in $TmGa_3$ the enhancement factor λ presumably contains a contribution from coupled magnetic-quadrupolar excitations. Also, in the quasi-ferromagnetic configuration of magnetic moments, the exchange splitting of conduction bands can vary in $ErGa_3$ and $TmGa_3$ due to the difference in corresponding $4f$-shell spin occupation numbers. At the moment one cannot attribute the differences in cyclotron masses (and angular dependencies of dHvA frequencies as well) in an unambiguous way in $ErGa_3$ and $TmGa_3$ either to the conduction band splitting or the magnetostriction.

In addition, one more mechanism can govern these differences. Namely, it was shown in Ref. 25 that virtual magnetic excitations can contribute substantially to the effective mass of the conduction electrons in rare-earth systems. These excitations are magnetic excitons in a paramagnetic system

(e.g., praseodymium), and spin waves in magnetically ordered rare-earths. The mass enhancement appeared to be large, magnetic field dependent and proportional to the static susceptibility of magnetic system. According to estimations of the electronic specific-heat coefficients, performed in Ref. 25, the corresponding effective masses increase in the series of heavy rare-earth metals. This trend correlates with the observed cyclotron masses in $ErGa_3$ and $TmGa_3$, but considerable work is needed to employ the theory developed in Ref. 25 for a quantitative description of cyclotron masses in magnetic $REGa_3$ compounds. In this connection the results[26] of the dHvA effect studies at ambient pressure in isostructural $REIn_3$ compounds, which possess similar FS's, should be taken into consideration as well.

SUMMARY

As a whole, the calculated pressure derivatives of the dHvA frequencies in $ErGa_3$ appeared to be in agreement with the experimental ones although the nature of some discrepancies is not clear. In particular, the difference between pressure derivatives of the spin-split FS cross-sectional areas is inconsistent with estimations based on the Stoner–Wohlfarth model, as well as with the results of *ab initio* LSDA calculations. Also, a surprisingly large and intriguing pressure effect on cyclotron masses has been observed in $ErGa_3$, which cannot be explained within the standard rare-earth model employed. It has to be emphasized that different interactions (exchange splitting, CF and magnetic-quadrupolar excitations, spin waves) have to be taken into account in a further theoretical analysis of the revealed pressure effects on the FS and cyclotron masses. In addition, more experimental data on the pressure dependence of the dHvA frequencies and cyclotron masses in $REGa_3$ and $REIn_3$ compounds are much needed to elucidate the nature of these effects.

The authors dedicate this work to the 80th anniversary of B. I. Verkin, who was a pioneer of the dHvA effect studies under pressure.[27]

We are grateful to J. Klamut, I. V. Svechkarev and B. Johansson for their kind support.

This work has been partly supported by the Royal Swedish Academy of Sciences.

*)E-mail: grechnev@ilt.kharkov.ua

[1] V. B. Pluzhnikov, A. Czopnik, and I. V. Svechkarev, Physica **212**, 375 (1995).
[2] V. B. Pluzhnikov, A. Czopnik, G. E. Grechnev, N. V. Savchenko, and W. Suski, Phys. Rev. B **B59**, 7893 (1999).
[3] V. B. Pluzhnikov, A. Czopnik, and G. E. Grechnev, J. Phys.: Condens. Matter **11**, 4507 (1999).
[4] P. Morin, M. Giraud, P. L. Regnault, E. Roudaut, and A. Czopnik, J. Magn. Magn. Mater. **66**, 345 (1987).
[5] J. Pelleg, G. Kimmel, and D. Dayan, J. Less-Common Met. **81**, 33 (1981).
[6] T. F. Smith, C. W. Chu, and M. B. Maple, Cryogenics **9**, 53 (1969).
[7] K. R. Lea, M. J. M. Leask, and W. P. Wolf, J. Phys. Chem. Solids **23**, 1381 (1962).
[8] P. Morin, J. Rouchy, M. Giraud, and A. Czopnik, J. Magn. Magn. Mater. **67**, 95 (1987).
[9] A. Czopnik, A. S. Panfilov, and I. V. Svechkarev, Fiz. Nizk. Temp. **20**, 48 (1994) [Low Temp. Phys. **20**, 39 (1994)].
[10] G. E. Grechnev, A. S. Panfilov, I. V. Svechkarev, K. H. J. Buschow, and A. Caopnik, J. Alloys Compd. **226**, 107 (1995).
[11] A. Murasik, A. Czopnik, L. Keller, and P. Fischer, J. Magn. Magn. Mater. (1999), in press.
[12] M. S. S. Brooks and B. Johansson, in *Ferromagnetic Materials*, Vol. 7, K. H. J. Buschow (Ed.), North-Holland, Amsterdam (1993) p. 139.
[13] R. Ahuja, S. Auluck, B. Johansson, and M. S. S. Brooks, Phys. Rev. B **B50**, 5147 (1994).
[14] A. G. Petukhov, W. R. L. Lambrecht, and B. Segall, Phys. Rev. B **B53**, 4324 (1996).
[15] B. I. Min, H. J. F. Jansen, T. Oguchi, and A. J. Freeman, J. Magn. Magn. Mater. **61**, 139 (1986).
[16] J. F. Herbst and J. W. Wilkins, in *Handbook on the Physics and Chemistry of Rare Earths*, Vol. 10, K. A. Gschneidner, Jr., L. Eyring, and S. Hufner (Eds.), North-Holland, Amsterdam (1987), p. 321.
[17] A. J. Freeman, B. I. Min, and M. R. Norman, in *Handbook on the Physics and Chemistry of Rare Earths*, Vol. 10, K. A. Gschneidner, Jr., L. Eyring, and S. Hufner (Eds.), North-Holland, Amsterdam (1987), p. 165.
[18] M. S. S. Brooks, L. Nordstrom, and B. Johansson, Physica B **B172**, 95 (1991).
[19] U. von Barth and L. Hedin, J. Phys. C **C5**, 1629 (1972).
[20] O. K. Andersen, Phys. Rev. B **B12**, 3060 (1975).
[21] H. L. Skriver, *The LMTO Method*, Springer, Berlin (1984).
[22] O. K. Andersen, O. Jepsen, and M. Sob, in *Electronic Band Structure and its Applications*, M. Yussouff (Ed.), Springer, Berlin (1987) p. 1.
[23] G. E. Grechnev, A. S. Panfilov, I. V. Svechkarev, A. Delin, B. Johansson, J. M. Wills, and O. Eriksson, J. Magn. Magn. Mater. **492**, 137 (1999).
[24] G. Lonzarich and A. V. Gold, Can. J. Phys. **52**, 694 (1974).
[25] P. Fulde and J. Jensen, Phys. Rev. B **B27**, 4085 (1983).
[26] N. Nagai, I. Umehara, T. Ebihara, A. K. Albessard, H. Sugawara, T. Yamazaki, K. Satoh, and Y. Onuki, Physica B **B186–188**, 139 (1993).
[27] B. I. Verkin, I. M. Dmitrenko, and B. G. Lazarev, Zh. Éksp. Teor. Fiz. **31**, 538 (1956) [Sov. Phys. JETP **4**, 432 (1957)]; I. M. Dmitrenko, B. I. Verkin, and B. G. Lazarev, Zh. Éksp. Teor. Fiz. **33**, 287 (1957) [Sov. Phys. JETP **6**, 223 (1958)]; I. M. Dmitrenko, B. I. Verkin, and B. G. Lazarev, Zh. Éksp. Teor. Fiz. **35**, 328 (1958) [Sov. Phys. JETP **8**, 229 (1956)].

This article was published in English in the original Russian journal. It was edited by R. T. Beyer.

''High-temperature'' oscillations of bismuth conductivity in the ultra-quantum limit

Vit. B. Krasovitsky and V. V. Khotkevich

*B. Verkin Institute for Low Temperature Physics and Engineering, National Academy of Sciences of the Ukraine, 310164 Kharkov, Ukraine**

A. G. M. Jansen and P. Wyder

Grenoble High Magnetic Field Laboratory, Max Planck Institut and Centre National de la Recherche Scientifique, F-38042 Grenoble Cedex 9, France

(Submitted March 30, 1999)
Fiz. Nizk. Temp. **25**, 903–909 (August–September 1999)

The results of joint studies of Shubnikov–de Haas oscillations and ''high-temperature'' oscillations (HTO) of diagonal and nondiagonal components of the magnetoresistance tensor for pure bismuth in magnetic fields up to 20 T are presented. The oscillations are measured for magnetic field directions close to trigonal and binary crystallographic axes at temperatures 4–43 K. A comparison of the variation of energy spectrum parameters for bismuth in ultra-quantum limit with peculiarities of ''high-temperature'' oscillations leads to the conclusion confirming the correspondence between HTO periods to the width of the energy band overlapping region. In the case when light electrons in two ellipsoids are in the ultra-quantum limit, a correlation between the exit of the last Landau level of heavy electrons (i.e., complete closure of the third electron ellipsoid) and the vanishing of HTO periods is observed in high magnetic fields. This experimental fact can play a key role in the theoretical description of the nature of HTO. © *1999 American Institute of Physics.* [S1063-777X(99)01508-X]

INTRODUCTION

A new type of quantum oscillations of static conductivity of bismuth in a magnetic field was discovered by one of the authors (VBK) and Yu. A. Bogod in 1973.[1,2] The new oscillations are periodic in reciprocal magnetic field and are characterized by a frequency higher than that of Shubnikov–de Haas (SdH) oscillations. In contrast to SdH oscillations observed at $T \leqslant 4$ K, the new oscillations were detected in the temperature range 8–65 K and were referred to as ''high-temperature'' oscillations (HTO).[3,4] At high temperatures, HTO are observed for $T > \hbar\Omega_c$ (Ω_c is the characteristic cyclotron frequency), when SdH oscillations are exponentially small. HTO differ basically from SdH oscillations in a peculiar temperature dependence: The HTO amplitude $\tilde{\rho}$ rapidly attains its peak value at $T \approx 10$ K and then decreases slowly upon heating.[4] At $T > 10$ K, the derivative $(\partial/\partial T)\ln\tilde{\rho}$ is independent of cyclotron frequency. It was found[5] that the HTO amplitude in bismuth and semi-metallic bismuth–antimony alloys is correctly described by the function $[(\tau_l^m)^{-1} + (\tau_{ep}^m)^{-1}]\exp(-\alpha T)$, where $(\tau_{ep}^m)^{-1} \propto \times[\exp(\theta_m/T) - 1]^{-1}$; $\theta_m = \hbar s q_m / k_B = 37$ K; s is the velocity of sound, $\alpha = 0.22\,\mathrm{deg}^{-1}$, $\mathbf{q}_m$ is the wave vector of phonons, that corresponds to the separation between the characteristic points[6] of the electron and hole spectral branches, and $(\tau_i^m)^{-1}$ and $(\tau_{ep}^m)^{-1}$ are the probabilities of elastic and inelastic interband scattering of charge carriers.

The correlation between the HTO frequency F and the concentration n of charge carriers ($F \propto n^{2/3}$) was established in experiments carried out with bismuth and compensated semi-metallic bismuth-based alloys.[7] In the more general case of semimetallic alloys of bismuth with different numbers of electrons and holes, it was found[8] that $F \propto \varepsilon_F^e + \varepsilon_F^h = E_0$ (ε_F^e and ε_F^h are the Fermi energies of electrons and holes and E_0 is the width of the energy band overlapping region). Thus, the characteristic feature of HTO distinguishing them from other quantum oscillations in a magnetic field is the independence of the HTO frequency of the Fermi energy. This formed the basis of the hypothesis[6] according to which the HTO of kinetic coefficients in semimetals are associated with quantum oscillations of the probability of intervalley quasi-elastic scattering of charge carriers at the band edges. In other words, HTO are due to ''deep'' states of the electron (hole) spectral branches of a semimetal with energies close to the boundary energy for the hole (electron) branch. Subsequently, the idea put forth in Ref. 6 was considered theoretically by Bogod *et al.*,[9] and a general approach to the HTO problem was developed.

It turned out, however, that while the oscillation mechanism described above explains a number of properties of HTO, it does not lead to a complete solution of the problem.[9]

In Refs. 10–12, a model alternative to that in Refs. 6 and 9 was proposed for explaining the HTO origin. According to this model, conductivity oscillations are results of electron–hole transitions near the Fermi level rather than at the energy band boundaries. The necessary condition for generation of HTO in such a model is the multiplicity of effective masses of electrons and holes. Unfortunately, the analysis carried out in Ref. 5 revealed fundamental contradictions between the model[10–12] and experimental results, that cannot be eliminated simply by improving the model.

The facts described above lead to the conclusion that the

 © 1999 American Institute of Physics

origin of HTO can probably be determined with the help of experiments in which the energy spectrum parameters (Fermi energy, the energy width E_0 of overlapping of the conduction and valence bands, and charge carrier concentration) can be varied over a wide range. Such experiments for bismuth should be carried out in strong (up to 20 T and higher) magnetic field, in which energy parameters depend on the magnetic field considerably. The information concerning the variations in the energy spectrum can be obtained from oscillatory effects of the de Haas–van Alphen or Shubnikov–de Haas type with the help of an appropriate theoretical model of energy spectrum. It should be recalled that bismuth is a semimetal in which the relative energy difference E_0 between the top of the hole band (T_{45}) at the T-point and the bottom of the electron band (L_s) at the L-point of the Brillouin band is quite small ($\sim$30–40 meV). Since the gap E_g between the conduction band L_s and the valence band L_a lying below it is also small ($\sim$15 meV), the effective masses of electrons in three equivalent valleys are small. As a result, the values of E_g and E_0 change radically in high magnetic field, which in turn leads to a strong dependence of the charge carrier concentration and the Fermi energy on the magnetic field.

In this paper, we report on the results of joint measurements of SdH oscillations and HTO of the nondiagonal (ρ_{yx} and ρ_{zx}) and diagonal (ρ_{xx}) components of the magnetoresistance tensor, which were made on a monocrystalline bismuth sample at temperatures 4–43 K in magnetic fields up to 20 T. These experiments were aimed at obtaining new information on the HTO origin from a comparison of changes in the energy spectrum of Bi in the ultra-quantum limit with peculiarities of HTO.

EXPERIMENTAL RESULTS

The measurements of SdH oscillations and HTO were made in stationary magnetic fields up to 20 T on a pure bismuth sample under the conditions when $\mathbf{I}\|\mathbf{X}\|C_1$, $\mathbf{H}\perp C_1$ ($C_3\|\mathbf{Z}$, $C_2\|\mathbf{Y}$ and C_1 are the trigonal, binary, and bisector crystallographic axes, respectively and $\mathbf{I}$ is the current density vector). Since the HTO amplitude does not normally exceed 0.1–1% of the monotonic magnetoresistance component, we used in our measurements the following peculiar property of the nondiagonal component ρ_{yx} of the magnetoresistance tensor,[13] which allowed us to improve considerably the sensitivity, and hence the resolution of measurements: the monotonic component of the even part of ρ_{yx} vanishes in view of symmetry for exact orientation $\mathbf{H}\|C_3$, while the oscillating component remains unchanged. The nondiagonal magnetoresistance tensor component ρ_{zx} was measured for the orientation $\mathbf{H}\|C_2$. In this case, the monotonic component of the even part of ρ_{zx} does not vanish, but during the recording of ρ_{zx}, the ratio of the oscillating and monotonic components increases significantly in contrast to the diagonal component ρ_{xx}. For this reason, SdH and HTO oscillations were measured in the angular interval $\pm 10°$ relative to the direction $\mathbf{H}\|C_3$ and in the vicinity of the direction $\mathbf{H}\|C_2$. In the temperature range 4–15 K, SdH oscillations prevail in the dependences $\rho_{ik}(H)$, while HTO, which were detected in our experiments starting from 4 K up to 43 K, dominate above 15 K.

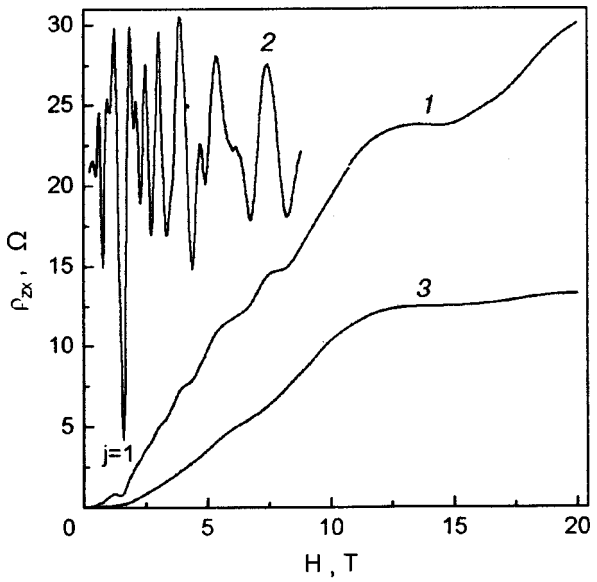

FIG. 1. Dependences of ρ_{zx} and ρ''_{zx} on magnetic field $\mathbf{H}\|C_2$: curves *1* and *3* correspond to ρ_{zx} at $T=4$ and 20 K, respectively, and curve *2* to ρ''_{zx} (in arbitrary units) at $T=4$ K.

Figure 1 shows the dependence $\rho_{zx}(H)$ (curve *1*) measured at 4 K in a magnetic field parallel to the binary axis C_2 and the second derivative $\rho''_{zx}=\partial^2\rho_{zx}/dH^2$ (curve *2*) obtained as a result of computer processing of the $\rho_{zx}(H)$ signal. The values of magnetic fields corresponding to minima of SdH oscillations obtained by us are close to those obtained in Refs. 14–17. For the given orientation of the magnetic field, oscillations from two electron ellipsoids with equal small cyclotron masses, an electron ellipsoid with heavy masses, and a hole ellipsoid with heavy masses are observed. The form of the $\rho_{zx}(H)$ dependence in weak magnetic field is determined by the passage of the Landau levels of light electrons through the Fermi level (the resonance number is determined by the value of the quantum number $j=0,1,2,\ldots$) for which the quantum limit takes place near $H\approx 1.5$ T, i.e., when the level $j=1$ intersects the Fermi level. The structure of oscillations in magnetic fields stronger than 1.5 T is determined by the Landau levels of heavy holes (quantum number $k=0,1,2,\ldots$) and heavy electrons.

The experimental dependence $\rho_{zx}(H)$ measured at 20 K for $\mathbf{H}\|C_2$ is shown by curve *3* in Fig. 1. ''High-temperature'' oscillations can be detected reliably on the second derivative ρ''_{zx} obtained as a result of computer processing of the corresponding curve $\rho_{zx}(H)$. A fragment of the dependence $\rho''_{zx}(H^{-1})$ is shown in Fig. 2 (curve *1*). Fourier analysis of oscillations on curve *1* indicates the presence of HTO periods corresponding to holes and equal to $0.165\times 10^{-1}\,\mathrm{T}^{-1}$ and $0.205\times 10^{-1}\,\mathrm{T}^{-1}$. As is usually the case with bismuth, HTO are observed as a superposition of two frequencies differing by a factor of 1.22.[4] The frequency spectrum of oscillation (inset to Fig. 2) also displays second harmonics of fundamental frequencies.

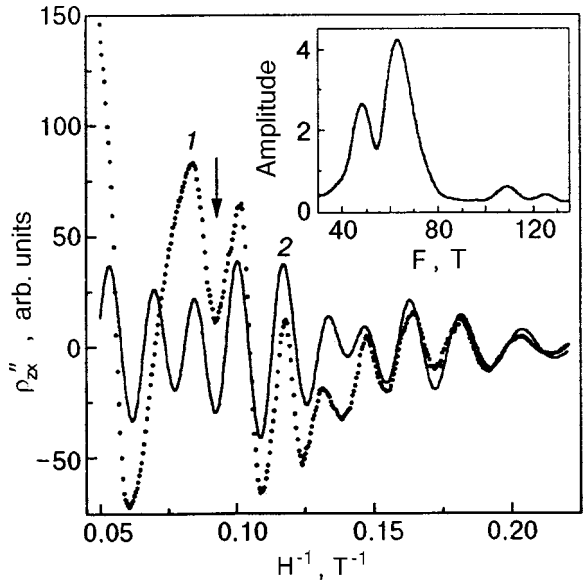

FIG. 2. ''High-temperature'' oscillations of resistivity ρ''_{zx} in bismuth for $\mathbf{H}\|C_2$, $T=20$ K. Curve *1* corresponds to the experiment, and curve *2* is the result of computer simulation. The inset shows the frequency spectrum of oscillations.

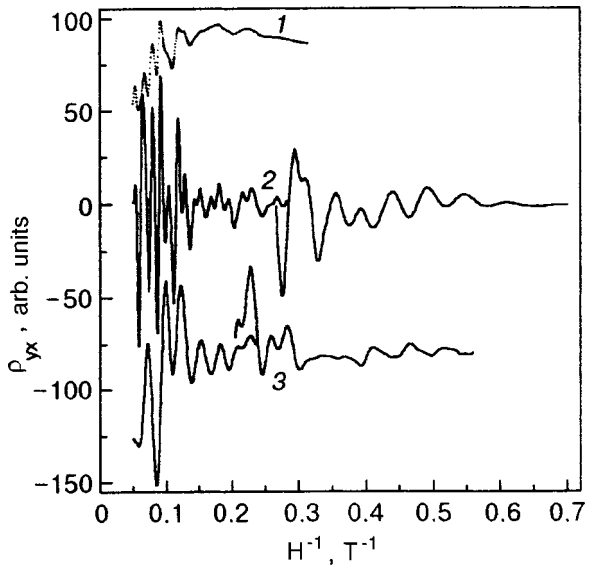

FIG. 4. Dependences of ρ_{yx} and ρ''_{yx} on the reciprocal magnetic field, $T=20$ K: $\rho_{yx}, \angle\mathbf{H},C_3=7°$ (curve *1*), and ρ''_{yx}, $\angle\mathbf{H},C_3=7°$ and 4.5° (curves *2* and *3*, respectively).

Figure 3 shows by way of an example the dependence $\rho_{yx}(H^{-1})$ (curve *1*) measured at 4 K for a direction of $\mathbf{H}$ close to the trigonal axis C_3 ($\angle\mathbf{H},C_3\approx 9°$). The second derivative $\rho''_{yx}(H^{-1})$ (curve *2*) was obtained as a result of computer processing of the dependence $\rho_{yx}(H^{-1})$. Fourier analysis of these curves reveals the presence of periods of SdH oscillations for electrons $P_1^e=2.6\times10^{-1}\,\mathrm{T}^{-1}$ and $P_2^e=0.95\times10^{-1}\,\mathrm{T}^{-1}$ and holes ($P^h=1.52\times10^{-1}\,\mathrm{T}^{-1}$) as well as HTO periods $P_1^{HTO}=0.48\times10^{-1}\,\mathrm{T}^{-1}$ and $P_2^{HTO}=0.6\times10^{-1}\,\mathrm{T}^{-1}$ attributed to holes (see the frequency spectrum in the inset to Fig. 3). Simultaneous observation of SdH oscillations and HTO in pure Bi at 4 K was carried out for the first time and has become possible owing to the application of strong magnetic fields, measurements of nondiagonal magnetoresistance tensor component ρ_{yx} (signal recording with a high-sensitivity amplifier), and high accuracy of measurements of the voltage drop across the sample. The form of the $\rho_{yx}(H)$ dependence in magnetic fields up to ≈ 5 T (see Fig. 3) is determined by the passage through the Fermi level of the Landau levels for electrons with the cyclotron mass $m_c^e\approx 0.03m_0$, which attain quantum limit (emergence of the level 0^+) near $H\approx 5$ T. Starting from fields ~ 4 T, oscillations of holes ($m_c^h\approx 0.06m_0$) are observed, which attain quantum limit near $H\approx 10$ T (emergence of the level 1^-), while oscillations of heavy electrons ($m_c^e\approx 0.1m_0$) take place above $H\approx 12$ T.

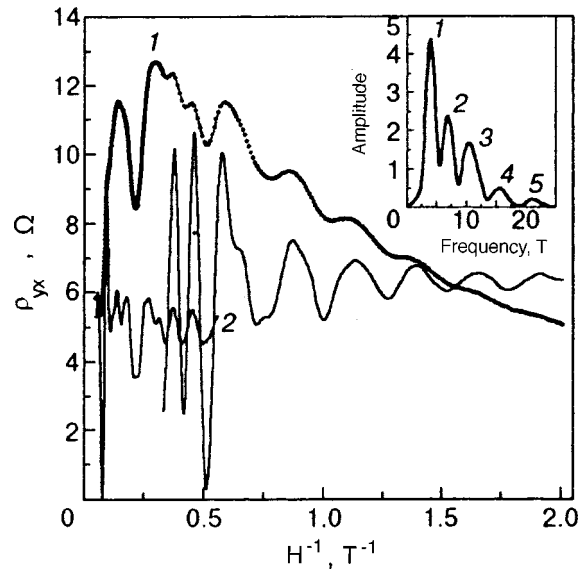

FIG. 3. Dependences of ρ_{yx} and ρ''_{yx} on the reciprocal magnetic field, $\mathbf{H}\|C_3$, $T=4$ K: curve *1* corresponds to ρ_{yx} and curve *2* to ρ''_{yx} (in arbitrary units). The inset shows the frequency spectrum of oscillations. SdH frequencies: F_1^e (*1*),F^h (*2*), and F_2^e (*3*); HTO frequencies: F_2^{HTO} (*4*) and F_1^{HTO} (*5*).

Figure 4 shows the $\rho_{yx}(H^{-1})$ dependence measured at 20 K in a magnetic field whose direction is close to the trigonal axis ($\angle\mathbf{H},C_3=7°$) and second derivatives $\rho''_{yx}(H^{-1})$ ($\angle\mathbf{H},C_3=4.5$ and 7°. In fields up to ~ 4 T, the HTO fundamental frequencies $F_1^{\mathrm{HTO}}=20.83$ T and $F_2^{\mathrm{HTO}}=16.66$ T are observed (the corresponding periods are $P_1^{HTO}=0.48\times10^{-1}\,\mathrm{T}^{-1}$ and $P_2^{HTO}=0.6\times10^{-1}\,\mathrm{T}^{-1}$), which increase in proportion to 2^r ($r=1,2,3,4,\ldots$) upon a further increase in H, the multiplicity being determined by $\angle\mathbf{H},C_3$. For example, the HTO frequency is doubled and increases four-fold for $\angle\mathbf{H},C_3=4.5$ and 7° respectively in high magnetic fields (see Fig. 4). At the same time, the main periods of HTO for $\angle\mathbf{H},C_3=1°$ are observed up to 20 T, the form of oscillations differing strongly from the sinusoid. On the whole the HTO pattern is quite complex. Fourier analysis of the frequency spectrum of oscillations reveals primarily the fundamental HTO frequencies which are usually manifested as a superposition of two frequencies differing by a factor of 1.22,[4] as well as combination and multiple frequencies. Low-frequency components of the signal can be suppressed and a high frequency multiple to one of the fundamental frequen-

cies can be singled out with the help of the derivatives of the signal with respect to magnetic field of an order higher than the second. For example, the eighth derivative of the dependence $\rho_{yx}(H^{-1})$ for $\angle \mathbf{H}, C_3 = 3°$ corresponds to the frequency 333.28 T which is higher than the fundamental frequency 20.83 T by a factor of 16.

DISCUSSION OF RESULTS

We analyzed the experimental data pertaining to the SdH effect by using the results obtained in Refs. 14–17, in which the variation of the position of the Fermi level and charge carrier concentration in bismuth in strong magnetic fields were calculated from the resonance values of magnetic fields for which the energies of Landau levels are equal to the energy of the Fermi level. The position of the Fermi level is determined by the conditions $n_l + n_h = p$, where n_l, n_h, and p are the concentrations of light electrons, heavy electrons, and holes, respectively. When the magnetic field is oriented along the binary axis C_2 and its magnitude $H > 1.5$ T, all light electrons lie at the level $j = 0$. The concentration of charge carriers in this case increases with magnetic field for two reasons: (1) due to linear dependence of the density of states at the level $j = 0$ on the magnetic field, and (2) due to the downward displacement of this level on the energy scale since the spin mass of light electrons is smaller than the orbital mass (the ratio of spin and orbital splitting is $\gamma = (H^{-1})^s/(H^{-1})^{\text{orb}} = 1.1$ for light electrons).[18] Experiments on magnetic reflection[15] proved that after convergence to the minimum distance for a certain $H_c \approx 10$ T, the bands L_s and L_a diverge due to interband interaction. Consequently, the dispersion relation for the lower ($j = 0$) Landau level for light electrons plays an important role in determining the theoretical values of the fields corresponding to oscillation minima. The corresponding theoretical model, which was proposed for the first time by Smith *et al.*[14] and modified later by Vecchi *et al.*,[15] has made it possible to interpret results on magnetooptical reflection in high magnetic fields[15] as well as on the SdH effect.[16,17] The position of the Fermi level in strong magnetic field depends only on n_l and p since n_l is much larger than n_h, i.e., $n_l \approx p$. Spin splitting for heavy electrons is stronger than the orbital splitting ($\gamma = 0.25$),[18] and the corresponding lower Landau level moves upwards along the energy scale upon an increase in H, intersecting the Fermi level at $H \approx 12$ T. After the disappearance of heavy electrons, the equality $n_l = p$ holds. According to Hiruma and Miura,[17] the value of Fermi level ε_F^e for electrons decreases from 26.5 meV ($H = 0$) to ~ 12 meV ($H = 20$ T), while the Fermi level ε_F^h for holes increases from 11 meV ($H = 0$) to ~ 25 meV ($H = 20$ T). The charge carrier concentration increases by a factor larger than three and is equal to 3×10^{17} cm^{-3} ($H = 0$) and 13×10^{17} cm^{-3} ($H = 20$ T). Spin splitting for heavy holes ($\mathbf{H} \| C_2$) is small ($\gamma = 0.05$),[18] and the upper Landau level $k = 0$ for holes moves downwards on the energy scale upon an increase in H, which leads together with a similar displacement of the lower energy level $j = 0$ for light electrons (in the case $H \leqslant 20$ T we are interested in) to a quite small change in the energy of band overlapping: $E_0 = 37.5$ meV ($H = 0$) and $E_0 \approx 35$ meV ($H = 20$ T).[15] It should be noted that the last result ($E_0(H) \approx E_0(0)$) is quite justified: since the electron energy associated with cyclotron motion, say, in a magnetic field of 20 T amounts to less than 0.2 eV, the additional energy is also low ($\sim 2 \times 10^{-6}$ eV/atom), i.e., the changes in the band structure are insignificant.

The period of SdH oscillations for holes for the direction of $\mathbf{H} \| C_2$ in fields $H > 1.5$ T is 0.72×10^{-1} T^{-1} and is twice as large as the corresponding value in the preultraquantum range of magnetic fields, which is due to monotonic increase in the value of ε_F^h with H. At $T = 20$ K, the amplitude of the SdH oscillations for holes is suppressed considerably, but these oscillations are still observed in fields exceeding ~ 3 T, for which the condition $\hbar \Omega_c^h > kT$ holds (the cyclotron mass for heavy holes is $m_c^h = 0.21 m_0$).[18] Peculiarities associated with the variation of the spectrum, e.g., transition to ultraquantum limit for light electrons for ~ 1.5 T and the emergence of the level $j = 0$ for heavy electrons for ~ 12 T, are clearly pronounced on the dependence $\rho_{zx}(H)$ measured at 20 K against the background of small amplitude of SdH oscillations for holes (curve *3* in Fig. 1). On the other hand, the HTO periods do not experience changes and remain the same in the preultraquantum and the ultraquantum ranges of magnetic fields in spite of considerable changes in the values of ε_F^e, ε_F^h, and charge carrier concentration. It is naturally hence to put HTO in correspondence with the spectral parameter remaining unchanged in the given experimental situation, i.e., the width E_0 of the region of band overlapping.

One more singularity of HTO presented in Fig. 2 is worth noting. This singularity becomes more visual if we compare the experimental dependence $\rho''_{zx}(H^{-1})$ with a similar oscillatory curve simulated on a computer with the help of a band frequency filter whose limits are determined by measured HTO frequencies. It can be clearly seen that the experimental curve *1* coincides with the calculated curve *2* only to the value $H^{-1} \approx 0.09$ T^{-1} at which the last oscillation minimum (marked by the arrow in the figure) is observed for HTO, since the next maximum and minimum belong to SdH oscillations for holes and accordingly are characterized by a larger period. It is natural to put in correspondence the vanishing of HTO in the given field with the exit of the last energy level $j = 0$ for heavy electrons for $H \sim 12$ T. This experiment can play basically a key role in the theoretical description of the HTO origin. In our opinion, however, additional measurements in strong magnetic fields or in alloys BiSb and BiTe with an appropriate direction of $\mathbf{H}$ are required for a reliable confirmation of this fact.

In the case when the magnetic field is oriented close to the trigonal crystallographic axis, the magnetic field dependence of energy parameters is more complicated than for $\mathbf{H} \| C_2$. For $\mathbf{H} \| C_3$, the spin mass for electrons is larger than the orbital mass ($\gamma = 0.53$),[18] and hence E_g increases with the magnetic field, i.e., the Landau level 0^- for electrons moves upwards on the energy scale. Similarly, the energy corresponding to the edge of the hole band (level 0^-) increases with H since the spin mass of holes is more than twice as large as the orbital mass ($\gamma = 2.15$).[18] As a result, the quantity E_0 depending on the velocities of relative mo-

tion of the bottom of the conduction band and the top of the valence band remains almost unchanged for $H \leqslant 20$ T. On the other hand, the Fermi energy ε_F^e for electrons in fields $H > 5$ T starts increasing and becomes higher by 30% for $H \approx 20$ T.[14,16] A comparison of changes occurring in the energy spectrum of bismuth in strong magnetic fields with HTO singularities does not reveal any obvious correlations. However, the very fact of observation of fundamental HTO periods for some directions of **H** near C_3, which remain unchanged up to 20 T, can be naturally put in correspondence with the invariability of E_0. At the present time, it is difficult to explain why the fundamental frequencies of HTO are suppressed by their harmonics (or new multiple frequencies) for certain directions of the magnetic field close to the trigonal axis in strong magnetic fields.

The conclusion that HTO frequencies are determined by the energy interval E_0 coincides with the results obtained in Refs. 3, 7, 8, and 19, where the value of E_0 was varied by one way or another. An analysis of the results of our experiments together with those obtained in Refs. 3, 7, 8, and 19, leads to the following conclusion. HTO periods vary in all experiments in which the energy parameters of the spectrum and E_0 change simultaneously (BiSb alloys,[7] axial compression of crystals,[19] and temperature deformation of the lattice[3]) and remain unchanged in experiments in which the energy parameters of the spectrum change for an invariable value of E_0 (uncompensated alloys BiTe, BiSbTe, and BiSbSn,[8] and measurements in the ultraquantum limit as in our experiments).

Thus, we have analyzed the experimental results of joint studies of SdH oscillations and HTO in bismuth in magnetic fields up to 20 T. Oscillations were measured in the temperature range 4–43 K in magnetic field directions close to the trigonal and binary crystallographic axes. It was found that for certain directions of strong magnetic field close to the trigonal axis the fundamental frequencies of HTO are suppressed by their harmonics or, probably, by new frequencies multiple to the fundamental frequencies. The fact that HTO disappear for $H \approx 12$ T for the direction $\mathbf{H} \| C_2$ is attributed to the exit of the last Landau level for heavy electrons. The general pattern of variation of the structure of the energy spectrum for bismuth in the ultraquantum limit determined from the results of measurements of SdH oscillations is compared with peculiarities of HTO. It is concluded that HTO periods are related to the width of the regions of energy band overlapping for bismuth.

This research was supported by and carried out at the Grenoble High Magnetic Field Laboratory.

*E-mail: krasovitsky@ilt.kharkov.ua

[1] Yu. A. Bogod and Vit. B. Krasovitsky, Preprint of Inst. for Low Temp. Physics and Engineering, Kharkov (1973).
[2] Yu. A. Bogod, Vit. B. Krasovitsky, and V. G. Gerasimechko, Preprint of Inst. for Low Temp. Physics and Engineering, Kharkov (1973); Zh. Éksp. Teor. Fiz. **66**, 1362 (1974) [Sov. Phys. JETP **39**, 667 (1974)].
[3] Yu. A. Bogod, V. G. Gerasimechko, and Vit. B. Krasovitsky, Fiz. Nizk. Temp. **1**, 1472 (1975) [Sov. J. Low Temp. Phys. **1**, 707 (1975)].
[4] Yu. A. Bogod, Vit. B. Krasovitsky, and S. A. Mironov, Zh. Éksp. Teor. Fiz. **78**, 1099 (1980) [Sov. Phys. JETP **51**, 554 (1980)].
[5] Yu. A. Bogod and Vit. B. Krasovitsky, Fiz. Nizk. Temp. **16**, 900 (1990) [Sov. J. Low Temp. Phys. **16**, 527 (1990)].
[6] Yu. A. Bogod, Fiz. Nizk. Temp. **12**, 1004 (1986) [Sov. J. Low Temp. Phys. **12**, 569 (1986)].
[7] Yu. A. Bogod, Vit. B. Krasovitsky, and E. T. Lemeshevskaya, Fiz. Nizk. Temp. **9**, 832 (1983) [Sov. J. Low Temp. Phys. **9**, 431 (1983)].
[8] Yu. A. Bogod, Vit. B. Krasovitsky, and E. T. Lemeshevskaya, Fiz. Nizk. Temp. **12**, 610 (1986) [Sov. J. Low Temp. Phys. **12**, 345 (1986)].
[9] Yu. A. Bogod, L. Yu. Gorelik, and A. A. Slutskin, Fiz. Nizk. Temp. **13**, 626 (1987) [Sov. J. Low Temp. Phys. **13**, 353 (1987)].
[10] V. M. Polyanovskii, Pis'ma Zh. Éksp. Teor. Fiz. **46**, 108 (1987) [JETP Lett. **46**, 132 (1987)].
[11] V. M. Polyanovskii, Ukr. Fiz. Zh. **33**, 1575 (1988).
[12] V. M. Polyanovskii, Ukr. Fiz. Zh. **34**, 459 (1989).
[13] Yu. A. Bogod and V. B. Krasovitsky, Phys. Status Solidi B **65**, 847 (1974).
[14] G. E. Smith, G. A. Baraff, and J. M. Rowell, Phys. Rev. **135**, A1118 (1964).
[15] M. P. Vecchi, J. R. Pereira, and M. S. Dresselhaus, Phys. Rev. B **14**, 298 (1976).
[16] K. Hiruma, G. Kido, and N. Miura, Solid State Commun. **31**, 1019 (1979).
[17] K. Hiruma and N. Miura, Tech. Rep. ISSP, Ser. A, No. 1292 (1983).
[18] V. S. Edelman, Usp. Fiz. Nauk **123**, 257 (1977) [Sov. Phys. Usp. **20**, 819 (1977)].
[19] Vit. B. Krasovitsky and V. V. Khotkevich, Fiz. Nizk. Temp. **17**, 710 (1991) [Sov. J. Low Temp. Phys. **17**, 374 (1991)].

Translated by R. S. Wadhwa

Effects of alloying and pressure on magnetic properties of itinerant intermetallic compound UFe_2

A. S. Panfilov and I. V. Svechkarev

*B. Verkin Institute for Low Temperature Physics and Engineering, National Academy of Sciences of Ukraine, 47 Lenin ave., 310164, Kharkov, Ukraine**

P. Diko, M. Mihalik, and A. Zentko

Institute of Experimental Physics, Slovak Academy of Sciences, 043 53 Košice, Slovak Republic
(Submitted April 7, 1999)
Fiz. Nizk. Temp. **25**, 910–919 (August–September 1999)

The ferromagnetic state of the itinerant compound UFe_2 correlated with a peak in the density of states at the Fermi level is well known to be strongly suppressed by replacing Fe with other $3d$ elements. To separate the effect of change in filling of the band from that of its deformation under alloying, the magnetic susceptibility of both quasi-binary alloys $U(Fe_{1-x}Me_x)_2$ (Me=Mn, Co) with a varying number of valence electrons and isoelectronic quasi-ternary alloys $U(Fe_{1-x}T_x)_2$, $U(Fe_{0.9-x}Mn_{0.1}T_x)_2$ and $U(Fe_{0.9-x}Co_{0.1}T_x)_2$ ($T=Mn_{0.5}Co_{0.5}$) was studied in the temperature range $4.2\,K \leqslant T \leqslant 300\,K$. Both effects were found to play important roles in suppression of the ferromagnetic state in UFe_2-based alloys. In addition, the magnetic susceptibility of $U(Fe_{1-x}Mn_x)_2$ and $U(Fe_{1-x}T_x)_2$ alloys and UCo_2 compound have been studied under pressure up to 4 kbar at $T=78$ and 293 K. The volume dependence of the exchange enhancement in spin paramagnetism of the UFe_2 compound and its alloys has been derived from analysis of the pressure effects in the framework of the Stoner model. © *1999 American Institute of Physics.* [S1063-777X(99)01608-4]

1. INTRODUCTION

In the series of the cubic C15-type Laves phase compounds UMe_2 (Me=Mn, Fe, Co, Ni) only UFe_2 is known to be ferromagnetic with $T_C=160\,K$ (see for example[1]) in which the magnetic moment resides mainly on the Fe sites.[2] The extensive magnetization studies of UFe_2[3] show that the temperature dependence of the spontaneous moment can be fitted well by the sum of spin-wave and Stoner-excitation contributions. The resulted spin-wave and Stoner parameters and the critical exponents near the magnetic phase transition as well are close to values reported for pure $3d$ ferromagnetics. These facts, along with the large electronic specific heat value,[4] strongly suggest the itinerant character of magnetism in the UFe_2 compound.

To explain tentatively the origin of magnetism in the UMe_2 compounds the simple band approach has been suggested[5] which assumes the transfer of $5f(6d)$ valence electron of uranium into the $3d$ states of transition metal. Then the magnetism of UNi_2 is mainly due to the partially occupied states of $5f$ band, whereas the magnetic moment on Fe atom in UFe_2 is caused by the unfilled $3d$ band. In this context, a rather weak spin paramagnetism of UCo_2 can easily be explained by the minimum in the density of states between $3d$ and $5f$ bands. Self-consistent band structure studies of the UMn_2-UNi_2 cubic Laves phase systems[6–8] have shown that the situation is more complicated due to a strong hybridization between $3d$ and $5f(6d)$ bands. The calculated density of states (DOS) contains the partial contribution of $3d$ state which to some extent reminds one of a rigid band and becomes progressively filled as we go from UMn_2 to UNi_2. In addition, there is the uranium $5f$ band which is also relatively rigid but stays pinned at the Fermi level in such a way that its occupation number is kept almost constant ($n_f \sim 2.7$ electrons per U atom[7,8]). As a consequence, the $5f$ contribution to the density of states (DOS) at the Fermi level appears to be rather high and roughly constant in magnitude for all mentioned compounds.

For UFe_2, the calculated ground state was found to be ferromagnetic with iron spin moment of $0{:}7\,\mu_B$.[7] This value is in quite good agreement with the experimental one ($0.59\,\mu_B{}^2$). However, the spin moment on uranium appears to be $-0.5\,\mu_B$ and antiparallel to the iron moment, which contradicts the experimentally observed small value ($0.06\,\mu_B{}^2$). The reason for this discrepancy is a substantial cancellation of the $5f$ spin moment by the orbital contribution which is due to spin-orbit coupling.[9–11]

As can be seen from the example of UFe_2, the available band structure calculations are in reasonable agreement with experiments, therefore, supporting an itinerant description for both $3d$ and $5f$ electrons in the mentioned systems. However, many of the details of quantitative agreement between theory and experimental data have yet to be worked out. Thus, for UMn_2 the calculated Stoner criterion for ferromagnetism was found to be just fulfilled,[6,7] that is in rather poor agreement with the experiments in which the only moderately enhanced paramagnetic state and no evidence for magnetic ordering have been observed.[12,13] In addition, the inherent fine structure of calculated DOS at the Fermi level

 © 1999 American Institute of Physics

along with large enhancement factor favors the strong temperature dependence of the magnetic susceptibility (as in the case of strongly enhanced paramagnetics such as Pd, $TiBe_2$, Ni_3Ga, and so on). In fact, this dependence for UMn_2 was found to be weak.[12,14]

The experimental studies of the magnetic properties of pseudobinary $U(Fe_{1-x}Me_x)_2$ alloys show that the ferromagnetic state of UFe_2 is strongly suppressed by substitution of iron with other $3d$ elements.[1] In order to estimate a critical concentration for disappearance of the ferromagnetic state in $U(Fe_{1-x}Me_x)_2$ alloys the calculation were made[8] using simulation of the electronic structure of selected disordered alloys by that of ordered stoichiometric compounds with the same number of valence electrons, namely U_2Fe_3Mn and UFeMn. Based on a quite reasonable agreement of calculation with experimental data, the authors of[8] concluded that influence of a disorder in the $3d$ metal sublattice is of relatively minor importance. In addition, for these systems the validity of the rigid-band was found to be good which is favored by a very similar shape and extension of the $3d$ wave function of iron and manganese in these types of pseudobinary alloys. On the other hand, the experimental data for $U(Mn_{1-x}Co_x)_2$ alloys[14] exhibit a well-defined maximum of the magnetic susceptibility at $x=0.5$ that corresponds to the same number of valence electrons as for UFe_2 compound. However, some difference in the magnetic properties of $U(Mn_{0.5}Co_{0.5})_2$ alloy and UFe_2 reveals that the simple rigid-band model fails to some extent to describe these properties.

The high pressure experimental[4,15] and theoretical[7,9] studies of the magnetic properties of UFe_2 show that its ferromagnetic state is strongly pressure dependent. Thus, the calculated spin magnetism disappears for a pressure between 400 and 500 kbar. With a linear extrapolation of the experimental value of pressure derivative for the Curie temperature, $dT_C/dP=-0.52$ K/kbar,[4] the critical pressure appears to be of about 300 kbar that is somewhat below the theoretical estimate. There is the same degree of agreement between the calculated pressure dependence of the magnetic moment, $d\ln m/dP=-3.0$ Mbar,[9] and the experimental one, $d\ln m/dP=-4.8$ Mbar.[4] In addition, the rhombohedrical distortion of UFe_2 is reported to occur just below the Curie temperature[1] that supports a large magnetoelastic effects in this compound.

As is evident from the foregoing, the electronic structure and magnetic properties of UFe_2 and related compounds are rather complicated and in order to gain a better understanding these properties further theoretical and experimental studies are required.

In the present work we give results of the magnetic susceptibility measurements for quasi-ternary $U(Fe_{1-x}T_x)_2$, $U(Fe_{0.9-x}Mn_{0.1}T_x)_2$ and $U(Fe_{0.9-x}Co_{0.1}T_x)_2$ ($T=Mn_{0.5}Co_{0.5}$) alloys and quasi-binary $U(Fe_{1-x}Me_x)_2$ (Me=Mn, Co) alloys in the temperature range $4.2\,\text{K}\leqslant T\leqslant 300\,\text{K}$. The experimental data on the concentration dependence of the magnetic properties for both isoelectronic quasi-ternary alloys and quasi-binary alloys with a varying number of valence electrons were used to separate the effect of the change in occupation of the band from that of its deformation under alloying. To estimate the role of the chemical pressure caused by a change in a lattice parameter, the pressure effects on the magnetic susceptibility of $U(Fe_{1-x}Mn_x)_2$ and $U(Fe_{1-x}T_x)_2$ alloys and UCo_2 compound have been studied at $T=78$ and 293 K and pressure up to 4 kbar. From analysis of the experimental data in the framework of the Stoner model, volume dependence of the exchange enhancement in spin paramagnetism of the UFe_2 compound and its alloys has been derived.

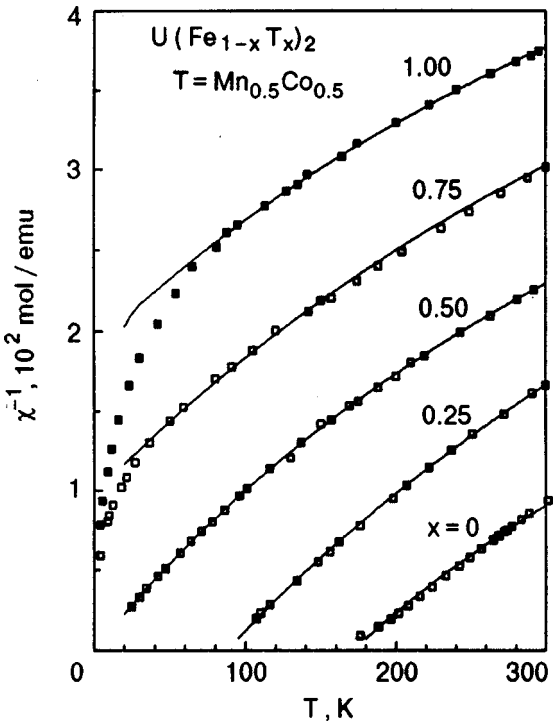

FIG. 1. Temperature dependences of the magnetic susceptibility for ternary isoelectronic alloys $U(Fe_{1-x}T_x)_2$ ($T=Mn_{0.5}Co_{0.5}$). Full lines correspond to fitting by Eq. (1).

2. EXPERIMENTAL TECHNIQUE AND RESULTS

The polycrystalline samples were prepared by melting high purity metals in an induction furnace under an argon atmosphere. The cubic Laves phase structure was confirmed by x-ray study. The composition of the samples was determined by chemical analysis.

A Faraday microbalance was used for susceptibility measurements in the temperature range 4.2–300 K in magnetic fields up to 10 kG. To eliminate small ferromagnetic contributions, which are probably due to the presence of some phases with higher T_C or unreacted transition metals, the corrected values of the magnetic susceptibility χ were determined by extrapolation of the measured $\chi(H^{-1})$ dependence to $H^{-1}=0$. The examples of the temperature dependence of reciprocal susceptibility for quasi-ternary alloys $U(Fe_{1-x}T_x)_2$ ($T=Mn_{0.5}Co_{0.5}$) are shown in Fig. 1. It can be seen that for $T\geqslant 50\,\text{K}$ the $\chi(T)$ values obey the modified Curie–Weiss law

$$\chi(T)=\chi_0+C/(T-\Theta), \tag{1}$$

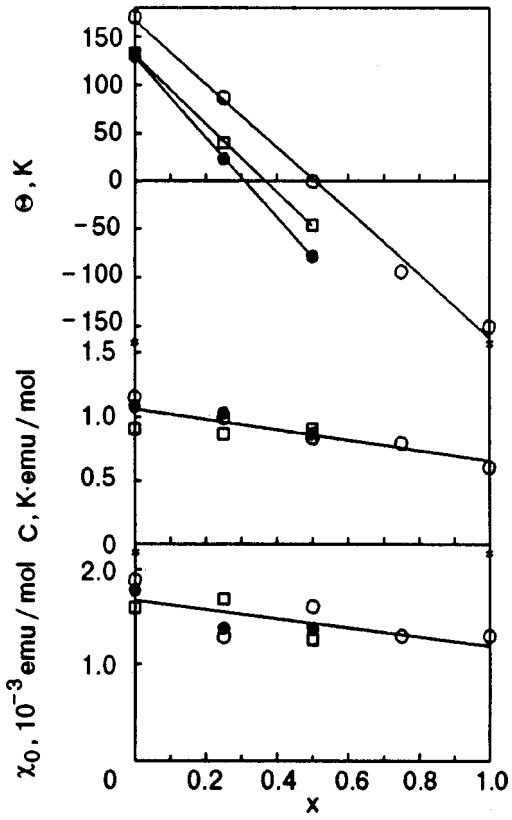

FIG. 2. Concentration dependences of the Curie–Weiss parameters for ternary UFe_2-based alloys: $U(Fe_{1-x}T_x)_2$ (T=$Mn_{0.5}Co_{0.5}$) (○); $U(Fe_{0.9-x}Mn_{0.1}T_x)_2$ (●): $U(Fe_{0.9-x}Co_{0.1}T_x)_2$ (□).

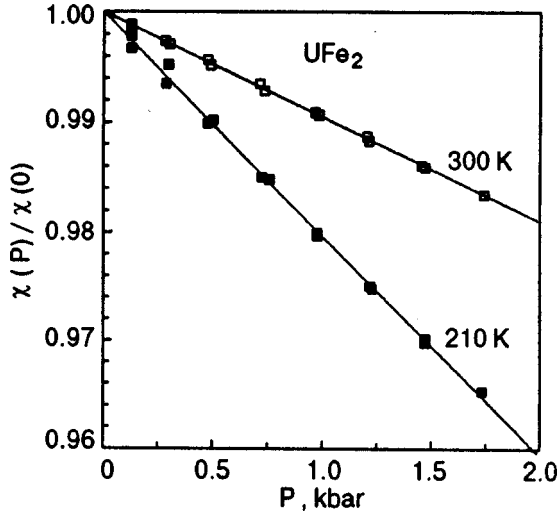

FIG. 3. Pressure dependence of the magnetic susceptibility for UFe_2 at two different temperatures normalized to its value at $P=0$.

where χ_0 is the temperature independent contribution (at $T<50$ K for some alloys the $1/T$ contribution, which is presumably of parasitic superparamagnetism nature, manifests itself). In Fig. 2 we plotted the Curie–Weiss parameters vs. concentration, obtained from experimental data at $T\geqslant 50$ K for $U(Fe_{1-x}T_x)_2$, $U(Fe_{0.9-x}Mn_{0.1}T_x)_2$ and $U(Fe_{0.9-x}Co_{0.1}T_x)_2$ alloys. It is evident from Fig. 2 that only the Curie temperature Θ is strongly affected by alloying whereas the Curie constant C and contribution χ_0 vary only slightly. It should be noted that the observed essential suppression of the ferromagnetic state in isoelectronic alloys cannot be explained by the simple rigid-band model.

For binary alloys studied, $U(Fe_{1-x}Mn_x)_2$ ($x=0.1, 0.25, 0.5, 1.0$) and $U(Fe_{1-x}Co_x)_2$ ($x=0.1, 0.2$), the $\chi(T)$ dependences are similar to those of Refs. 12, 14, 16 and Refs. 17 and 18, respectively, and are not shown here.

The study of the magnetic susceptibility under uniform pressures up to 4 kbar at liquid nitrogen and room temperatures was carried out by two methods: the Faraday method with the pendulum magnetometer placed directly into the high-pressure chamber,[19] and the levitation method.[20] The relative error did not exceed 0.05% in either case. As an example, the $\chi(P)$ dependence for UFe_2 at different temperatures is given in Fig. 3. It shows the magnitude of the pressure effect and its linear behavior, yielding values for $d\ln\chi/dP$. The $d\ln\chi/dP$ data for $U(Fe_{1-x}Mn_x)_2$ and $U(Fe_{1-x}T_x)_2$ (T=$Mn_{0.5}Co_{0.5}$) alloys and UCo_2 compound are summarized in Table I. Preliminary report on part of the results obtained was given in Ref. 21.

3. DISCUSSION

In the Stoner theory of itinerant electron magnetism, electron-electron interactions manifest themselves through the enhancement of the Pauli spin susceptibility χ_P by the Stoner factor S:

TABLE I. Experimental values of the pressure derivative $d\ln\chi/dP$ and the magnetic susceptibility χ itself at different temperatures for $U(Fe_{1-x}Me_x)_2$ alloys (Me=Mn, Co and $Mn_{0.5}Co_{0.5}$).

Compound	$-d\ln\chi/dP$, $Mbar^{-1}$	χ, 10^{-3} emu/mol	T, K
$U(Fe_{1-x}Mn_x)_2$			
$x=0.1$	8.3±0.5	8.32	293
0.25	7.5±0.5	5.97	,,
0.3	7.1±0.4	5.45	,,
0.5	5.2±0.4	4.05	,,
0.75	4.0±0.3	2.96	,,
1.0	3.6±0.3	2.38	,,
0.25	26.0±1.0	37.9	78
0.3	17.2±0.5	20.8	,,
0.5	7.1±0.5	6.8	,,
$U[Fe_{1-x}(Mn_{0.5}Co_{0.5})_x]_2$			
$x=0.25$	6.7±0.5	6.16	293
0.5	6.2±0.4	4.53	,,
0.75	4.9±0.4	3.48	,,
1.0	4.6±0.3	2.74	,,
UFe_2	10.1±0.5	10.7	300
	10.5±0.5	11.3	293
	21.2±1.0	33.1	210
UCo_2	2.25±0.3	1.11	300
	2.1±0.3	1.18	78

$$\chi = S\chi_P = \frac{\chi_P}{1-\alpha\chi_P}, \tag{2}$$

where $\chi_P = 2\mu_B^2 N(E_F)$, $N(E_F)$ is the density of states at the Fermi level; the molecular field constant $\alpha = (1/2\mu_B^2)I$, I is a parameter of the exchange-correlation interaction between the conduction electrons. For finite temperature, $\chi_P(T)$ is determined by the effective density of states at the Fermi level, $N(\mu,T) \equiv N$, given by

$$N(\mu,T) = \int_0^\infty N(E)[-\partial f(E,\mu,T)/\partial E]dE. \tag{3}$$

Here $f(E,\mu,T)$ is the Fermi–Dirac distribution function, wherein the chemical potential $\mu(T)$ is determined by assuming the number of band electrons in the system to be constant. In the case $IN \simeq 1$ (for strong itinerant paramagnets or weak ferromagnets at $T \geqslant T_C$) the enhanced spin paramagnetism is a dominant contribution to the magnetic susceptibility. Equation (2) will be considered to be appropriate for UFe_2 and its alloys studied to analyze the changes of their magnetic properties on alloying and under pressure.

3.1. Effects of alloying

In order to discuss the concentration dependence of the magnetic susceptibility, Eq. (2) is conveniently represented by

$$1/\chi(T) = 1/\chi_P(T) - \alpha. \tag{4}$$

Then the experimental values of $1/\chi$ for $U(Fe_{1-x}T_x)_2$ (see Fig. 1) plotted against concentration x appear to be an almost linear function of x with $\partial(1/\chi)/\partial x$ being roughly temperature independent. From Eq. (4) it follows that

$$\partial(1/\chi)/\partial x = \partial(1/\chi_P)/\partial x - \partial\alpha/\partial x \tag{5}$$

and the effect of alloying is evidently due to changes in both the density of states at the Fermi level and the molecular field constant α. There are no strong grounds for believing that α has a detectable concentration dependence. Its magnitude resulted from calculated values of I (9.3, 9.5 and 11.3 mRy ·cell for UMn_2, UFe_2 and UCo_2, respectively[9,22]) shows only a weak growing as we go from UMn_2 to UCo_2. Thus, as a preliminary, we can neglect this effect by assuming α to be constant. It should also be noted that the α value averaged over composition is unchanged with substitution of $Mn_{0.5}Co_{0.5}$ for Fe atoms in UFe_2 and related alloys provided that we admit α to be changing linearly along the UMn_2–UCo_2 series. Hence, the change in the magnetic properties of the isoelectronic alloys is assumed to be mainly caused by a change in the density of states N under alloying.

One mechanism of this change is the electron scattering on the disorder in the $3d$ sublattice due to the random occupation by impurity of the B sites in the AB_2 Laves system. The simplified description of the scattering effect can be given in terms of the effective temperature T^*[23,24]

$$T^* = \beta x, \tag{6}$$

where, in the general case, the coefficient β depends on the type of doping impurity. This assumption is demonstrated in Fig. 1 where the most pronounced effect of alloying can be imagined as the temperature shift in $1/\chi(T)$ dependences according to

$$1/\chi(T) \simeq (1/C)(T + T^* - \Theta). \tag{7}$$

Then the coefficient β in Eq. (6) can be estimated from the experimental data at any particular temperature as the ratio

$$\beta = \frac{\partial(1/\chi)/\partial x}{\partial(1/\chi)/\partial T}. \tag{8}$$

With the data at room temperature we obtain $\beta = 4.3 \pm 0.5$ K per at. % of $Mn_{0.5}Co_{0.5}$ which is the average of the results for $U(Fe_{1-x}T_x)_2$, $U(Fe_{0.9-x}Mn_{0.1}T_x)_2$ and $U(Fe_{0.9-x}Co_{0.1}T_x)_2$ alloys. The similar estimate follows directly from the concentration dependence of the paramagnetic Curie temperature (Fig. 2), namely, $\beta = 3.7 \pm 0.5$ K per at. % of $Mn_{0.5}Co_{0.5}$. Thus the value of β may be considered to be temperature independent and equal to

$$\beta = 4.0 \pm 0.5 \text{ K/at.\% Mn or Co} \tag{9}$$

assuming a similarity in the scattering properties of Mn and Co dopants in UFe_2 and related alloys.

As evident from the estimate obtained, the scattering effect plays an important role in suppression of the ferromagnetic state in UFe_2 based alloys. Thus, for the experimental value of the critical concentration $x \simeq 0.3$ for disappearance of ferromagnetism in $U(Fe_{1-x}Mn_x)_2$ and $U(Fe_{1-x}Co_x)_2$ alloys,[1] the reduction in the Curie temperature $T_C = 160$ K resulted only from the scattering is estimated to be close to 120 K. Therefore the rigid band model for UFe_2-based alloys has to be modified to account for this effect.

With the simplified description of scattering effect in terms of the effective temperature, the magnetic susceptibility as a function of the electron number can be derived from the experimental data on $\chi(T,x)$ in $U(Fe_{1-x}Mn_x)_2$ and $U(Fe_{1-x}Co_x)_2$ alloys by introducing a corresponding substitution of $(T - T^*)$ for argument T in the $\chi(T)$ dependence where for concentrated alloys $T^* = \beta x(1-x)$ is used instead of (6).

In Fig. 4 is shown the resulting dependence χ vs. number of valence electrons per $3d$ atom, n, measured from that for UFe_2 at $T = 250$ K which points to the essential effect of scattering in the magnetic susceptibility of the alloys studied.

Notice that the temperature and concentration independent contribution χ_0 in Eq. (1) becomes the dominant part of the magnetic susceptibility outside the range of $-0.7 \leqslant n \leqslant 0.6$. Its value in UFe_2 and UFe_2-based alloys (see Fig. 2) is close to the magnetic susceptibility of UCo_2 at $T = 4.2$ K which equals 1.35×10^{-3} emu/mol.[4] A comparison of this value with the estimate of the exchange-enhanced spin susceptibility in UCo_2, 1.28×10^{-3} emu/mol,[9] shows that it is reasonable to suggest the contribution χ_0 to be also of the spin nature. Therefore, for all alloys under consideration the magnetic susceptibility as a whole may be treated as being enhanced spin paramagnetism, that proves the use of the susceptibility data to recover the DOS curve for UFe_2 through the estimation of the Pauli spin susceptibility, $\chi_P(T) \propto N(E_F,T)$, in framework of Eq. (2).

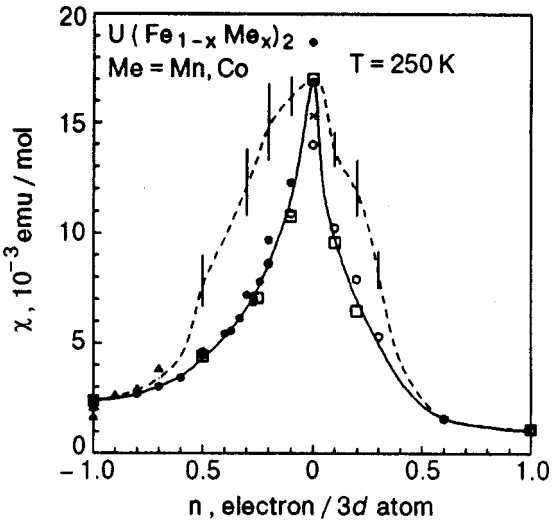

FIG. 4. Magnetic susceptibility of binary alloys $U(Fe_{1-x}Me_x)_2$ (Me=Mn, Co) at $T=250$ K as a function of the electron number measured from that of UFe_2 (full line): our data (□); Refs. 3 (×); 12 (●); 14 (△); 17, 18 (○). The dashed curve is the same dependence obtained by taking into account the scattering effect in terms of the effective temperature. Bars on the curve correspond to errors in estimation of the magnitude of β [see Eq. (9)].

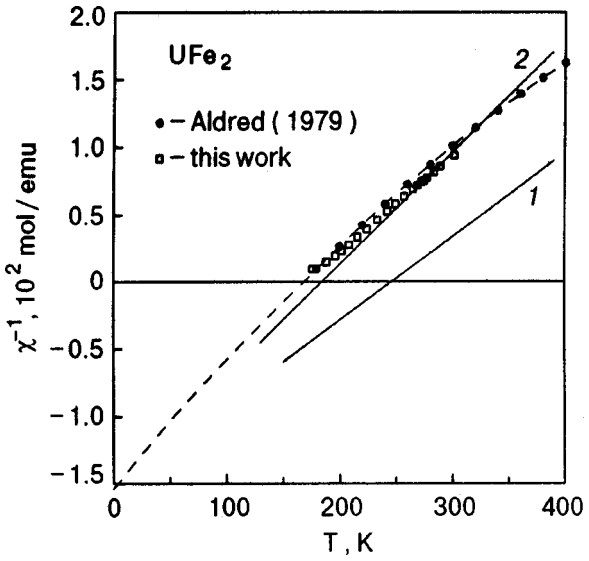

FIG. 6. Temperature dependence of the reciprocal magnetic susceptibility for UFe_2. The model descriptions of Eq. (12) (curve *1*) and Eq. (16) with $\lambda=0.2$ (K·emu/mol)$^{-1}$ (curve *2*).

Figure 5 shows the $\chi_P(n)$ dependence for the range $-1.0\leqslant n\leqslant 1.0$ and $T=250$ K which has been obtained from the $\chi(n)$ data of Fig. 4 by using Eq. (2) with calculated for UFe_2 value $\alpha=4.0\times10^3$ mol/emu ($I=0.0095$ Ry[9]). As seen, this dependence, and hence the dependence $N(n)$, takes the form of a peak and its maximum corresponds to the UFe_2 compound. In addition, some asymmetry in $\chi_P(n)$ about $n=0$ decreases noticeably after applying the corrections for the volume changes on alloying obtained with the experimental data for pressure dependence of the magnetic susceptibility (see Table I and discussion of the magnetovolume effects) and for the lattice parameters in alloys.[17,18] As is clear from Fig. 5, the corrections of $\chi_P(n)$ for both scattering and volume change in alloys are rather small in themselves. Nevertheless, their effects on the magnetic properties of UFe_2 based alloys appear to be important because of large exchange enhancement resulted from condition $\alpha\chi_P\sim1$.

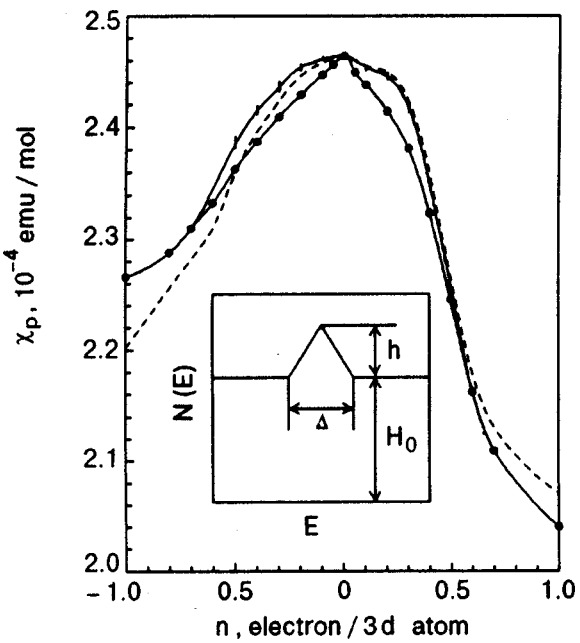

FIG. 5. The Pauli susceptibility at $T=250$ K as a function of the electron number measured from that of UFe_2: the curve marked by (●) corresponds to the experimental data in binary alloys, the solid line includes corrections for the scattering and the dashed line is the same for the constant volume conditions. Inset: a sketch of the model density of state curve.

Following Fig. 5, the density of states curve for UFe_2 at the vicinity of the Fermi level can be imagined as a peak h in height and Δ in width which is placed on the background of height N_0 with $h/N_0\ll1$ (see the insert in Fig. 5). The estimate $N_0\simeq92$ (spin·Ry·cell)$^{-1}$ follows from the value $\chi_P^0\simeq2.2\times10^{-4}$ emu/mol, corresponding approximately to the peak pedestal. The value $h\simeq18$ (spin·Ry·cell)$^{-1}$ results from the estimate of the total density of state at the Fermi level for UFe_2, $N\equiv N_0+h\simeq110$ (spin·Ry·cell)$^{-1}$, obtained from Eq. (4) by extrapolation of the experimental $1/\chi(T)$ dependence for UFe_2 in the paramagnetic region to $T=0$ K (see Fig. 6, dashed line) that yields $\chi_P(0)\simeq2.6\times10^{-4}$ emu/mol. As is evident from Fig. 5, the $\chi_P(n)$ peak for $T=250$ K has $\delta n\simeq1.5$ electrons per $3d$ atom in width and contains of about

$$S\sim\delta n(\chi_P^{\max}-\chi_p^0)/(\chi_P^0+\chi_P^{\max})\simeq0.15 \text{ states/cell.} \quad (10)$$

With the S and h values mentioned above the estimate $\Delta\simeq0.017$ Ry can be obtained if for simplicity the peak form is taken to be a triangle. Thus, the set of the model parameters is

$$N_0\simeq92\,(\text{spin}\cdot\text{Ry}\cdot\text{cell})^{-1},$$
$$h\simeq18\,(\text{spin}\cdot\text{Ry}\cdot\text{cell})^{-1},\quad \Delta\simeq0.017\text{ Ry}. \quad (11)$$

To check the validity of the model parameters estimated (11) we have applied them to describe the temperature dependence of the magnetic susceptibility for UFe_2 by using

Eqs. (2) and (3). With a linearized approximation for the Fermi–Dirac distribution function[25] the $\chi(T)$ is given by

$$\frac{1}{\chi(T)} \simeq \frac{1}{\chi_P(0)} + \gamma T - \alpha \tag{12}$$

with

$$\gamma = \frac{5.55 h k_B}{4\mu_B^2 (N_0+h)^2 \Delta} = \frac{5.55 k_B}{4\mu_B^2 S}\left(\frac{h}{N_0+h}\right)^2. \tag{13}$$

As a consequence, the temperature dependence of the magnetic susceptibility obeys the Curie–Weiss law (see Fig. 6) with parameters

$$C = \gamma^{-1}, \quad \Theta = \frac{C}{\chi_P(0)}[\alpha \chi_P(0) - 1]. \tag{14}$$

The resulted estimates, $C \simeq 1.6\,\mathrm{K\cdot emu/mol}$ and $\Theta \simeq 250\,\mathrm{K}$, are in reasonable agreement with the experimental values $C = 1.2\text{–}1.4\,\mathrm{K\cdot emu/mol}$ and $\Theta \simeq 170\,\mathrm{K}$[3,12,17] if we keep in mind the simplified character of the $\chi(T)$ description.

The approach used gives only the general features of the electronic structure and its relation to the magnetic properties in UFe_2. To get a more rigorous treatment of the experimental data some refinements of the analysis would be introduced. Thus, along with the electron scattering, the changes in the density of states for isoelectronic UFe_2 based alloys may be due to deviation from the rigid band behavior caused by formation under alloying of the impurity subbands. In this case the DOS of alloy is represented as a superposition of the DOS for individual compounds in the ratio determined by their concentration. For $U(Fe_{1-x}T_x)_2$ alloys, a rough estimate of this effect gives $\Delta N/N \sim -0.07$ for $x=1$ provided that we neglect the scattering. A moderate $\Delta N/N$ value obtained suggests that DOS of UMn_2 and UCo_2 are not different essentially from that of UFe_2. So, the rigid band model is rather good approximation for these systems (see also[8]).

It should be noted that estimated value for the density of states at the Fermi level in UFe_2, $N(E_F) \simeq 110\,(\mathrm{spin\cdot Ry\cdot cell})^{-1}$, is found to be somewhat less than the calculated one, 143 $(\mathrm{spin\cdot Ry\cdot cell})^{-1}$ [Refs. 7 and 9]. To eliminate this discrepancy a more appropriate value of α in Eq. (4) should be chosen.

Furthermore, on closer examination of the magnetic susceptibility, we have to take into account for a substantial cancellation of the $5f$ spin moments on the uranium atoms by the orbital contribution.[9–11] As a result, the magnitude of N derived from the measured susceptibility appears to be underestimated.

In addition, the refined version of the Stoner model (4) is required as well. In particular, the spin-fluctuation mechanism (SF) could be taken into account. In the simplified form SF leads to an additional term in the molecular field parameter α[26,27]

$$\alpha(T) \simeq \alpha(0) - \lambda T, \tag{15}$$

where λ is a constant determined by the band structure parameters.[26] Substitution of Eq. (15) into Eq. (12) gives

$$\frac{1}{\chi(T)} \simeq \frac{1}{\chi_P(0)} - \alpha(0) + (\gamma+\lambda)T. \tag{16}$$

As a result, the modified Curie–Weiss parameters are defined as

$$C^* = \frac{1}{\gamma+\lambda}, \quad \Theta^* = \frac{C^*}{\chi_P(0)}[\alpha(0)\chi_P(0) - 1]. \tag{17}$$

For UFe_2, the upper limit $\lambda \simeq 0.8\,(\mathrm{K\cdot emu/mol})^{-1}$ follows from the experimental value of the Curie constant provided the latter is completely determined by SF mechanism. Unfortunately, at present we have no direct quantitative estimate of the real role of SF in the magnetic properties in UFe_2 and related alloys. It is notable that the better agreement between the model description (12) and experimental $\chi(T)$ dependence in UFe_2 (Fig. 6) can be obtained by taking SF into account. In addition, because C is approximately constant in UFe_2-based alloys (see, for example,[12]), the SF parameter λ can be assumed not to be critically dependent on concentration. From this fact combined with a small value λT in itself $[(\lambda T/\alpha) \ll 1$ for the temperature range under consideration] one may speculate that SF does not play an important role in the behavior of the magnetic susceptibility of UFe_2 system under alloying.

3.2. Pressure effects

A phenomenological treatment of the experimental values of $d\ln\chi/dP$ can be given in the framework of the Curie–Weiss law (1) as

$$\frac{d\ln\chi}{dP} = \frac{\chi_0}{\chi}\frac{d\ln\chi_0}{dP} + \frac{\chi-\chi_0}{\chi}\left(\frac{d\ln C}{dP} + \frac{1}{T-\Theta}\frac{d\Theta}{dP}\right). \tag{18}$$

Since for UFe_2-based alloys $\chi_0/\chi \ll 1$, a rough estimate $d\ln\chi_0/dP \approx d\ln\chi(UCo_2)/dP \simeq -2\ \mathrm{Mbar}^{-1}$ is assumed to be reasonable. Thus, the derivatives $d\ln C/dP$ and $d\Theta/dP$ can be evaluated from Eq. (18) by using the available experimental data for $d\ln\chi/dP$ at two different temperatures (Table I). For UFe_2 and $U(Fe_{1-x}Mn_x)_2$ alloys with $x=0.1$, 0.25 and 0.3, these values appear to be weakly dependent on the concentration and equal to

$$d\ln C/dP = -6 \pm 1\ \mathrm{Mbar}^{-1},$$
$$d\Theta/dP = -620 \mp 100\,\mathrm{K\cdot Mbar}^{-1}. \tag{19}$$

Notice that the estimate for $d\Theta/dP$ agrees closely with value $dT_C/dP \simeq -0.5\,\mathrm{K/kbar}$ resulted for UFe_2[4,15] and $U(Fe_{1-x}Mn_x)_2$[28] alloys. As to the pressure derivative of the Curie constant, its magnitude appears to be surprisely large. At least such value is not resulted from simple band approach (13), (14) which predicts $d\ln C/dP \sim 0$ provided the uniform deformation of the band is assumed. It seems likely that large pressure dependence of C is a peculiar feature of UFe_2-based alloys. The origin of this peculiarity is not clear.

In the context of the Stoner model, Eq. (4), the pressure effect, $d\ln\chi/dP$, is given by

$$\frac{d\ln\chi}{dP} = \frac{d\ln\chi_P}{dP} + \alpha\chi\left(\frac{d\ln\chi_P}{dP} + \frac{d\ln\alpha}{dP}\right)$$
$$\equiv \frac{d\ln N}{dP} + \alpha\chi\left(\frac{d\ln N}{dP} + \frac{d\ln I}{dP}\right). \tag{20}$$

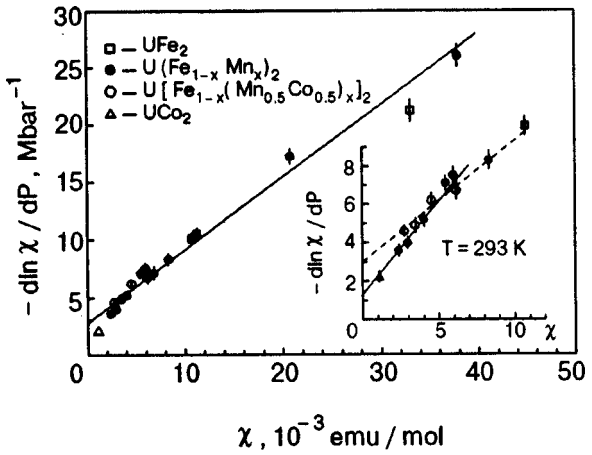

FIG. 7. Dependence of $d\ln\chi/dP$ on χ in $U(Fe_{1-x}Me_x)_2$ alloys. Me=Mn, $(Mn_{0.5}Co_{0.5})$, Co. Inset: the data at $T=293$ K, the initial slope of the dependence is given by dashed line.

It follows from Eq. (20) that the value of $d\ln\chi/dP$ for different temperatures and/or compositions of alloys can be approximated by a linear function of the magnetic susceptibility provided that the parameters $d\ln N/dP$, $d\ln I/dP$ and α $(\propto I)$ are weakly dependent on temperature and composition. The experimental values of $d\ln\chi/dP$ for $U(Fe_{1-x}Mn_x)_2$ and $U(Fe_{1-x}T_x)_2$ alloys are plotted against susceptibility in Fig. 7. In accordance with Eq. (20), this dependence is close to a linear one, described by the following relation between the parameters:

$$\frac{d\ln N}{dP}+\frac{d\ln I}{dP}=-0.16\pm0.03\ \text{Mbar}^{-1}, \tag{21}$$

$$\frac{d\ln N}{dP}\approx-3\ \text{Mbar}^{-1}. \tag{22}$$

As seen from Eq. (21), a nearly full compensation for the pressure effects in the density of states N and interaction parameter I is found. In such a situation, the total effect $d\ln N/dP+d\ln I/dP$ appears to be strongly dependent on the details of the behavior of both components under alloying and with the temperature change. Probably, the latter is a reason for a stronger $d\ln\chi/dP$ vs. χ dependence at the origin of the coordinates (see inset in Fig. 7) which contains the room temperature data. The inclusion of the terms $(\gamma+\lambda)T$ of Eq. (16) into consideration leads to an additional contribution into the initial sum $d\ln N/dP+d\ln I/dP$ in Eq. (20):

$$-\frac{(\gamma+\lambda)T}{\alpha}\left(\frac{d\ln(\gamma+\lambda)}{dP}+\frac{d\ln N}{dP}\right). \tag{23}$$

A rough evaluation of this term for $T=293$ K can be made by using the experimental data for $\gamma+\lambda\simeq C^{-1}\simeq0.8(\text{K}\cdot\text{emu/mol})^{-1}$ [see Eq. (17)], $d\ln(\gamma+\lambda)/dP\simeq-d\ln C/dP\sim6\ \text{Mbar}^{-1}$ and $d\ln N/dP\sim-3\ \text{Mbar}^{-1}$ which gives

$$-\frac{(\gamma+\lambda)T}{\alpha}\left(\frac{d\ln(\gamma+\lambda)}{dP}+\frac{d\ln N}{dP}\right)\simeq-0.15\ \text{Mbar}^{-1}. \tag{24}$$

With estimate obtained the resulted slope of $d\ln\chi/dP$ vs. χ dependence appears to be nearly twice as large as the initial one that is in a reasonable agreement with experimental data (inset in Fig. 7).

It should be noted that the corrections (24) do not depend obviously on a specific mechanism for the temperature dependence of the magnetic susceptibility and can be quantitatively included in an extended analysis of the pressure effects. In any case such inclusion remains the conclusion about a nearly complete compensation of pressure effects in N and I unchanged. Thus, on account of their small magnitude, the corrections mentioned above can be incorporated into the error bar for the total effect:

$$d\ln N/dP+d\ln I/dP=-0.16\pm0.15\ \text{Mbar}^{-1}. \tag{25}$$

Substitution of the bulk modulus value $B\simeq1.4$ Mbar, obtained from the sound velocity study in a UFe_2 single crystal,[29] into Eq. (25) gives

$$d\ln N/d\ln V+d\ln I/d\ln V=0.22\pm0.2. \tag{26}$$

It should be noted that the $d\ln\chi/dP$ data in Fig. 7 correspond to alloys with different derivative of χ with respect to a number of conduction electrons per atom n (see Fig. 4). Thus the lack of noticeable deviations of these data from the general linear run indicates that for UFe_2 and its alloys effects of electron transfer under pressure are likely to be small. The conclusion obtained is confirmed by theoretical estimate for this effect.[7]

In order to extract the change of I with volume from Eq. (26), the value $d\ln N/d\ln V$ have to be known. As a first step, the estimate $d\ln N/d\ln V\simeq2$ obtained from the experimental data in the inset of Fig. 7 can be appropriate, which agrees closely with value calculated for UFe_2 in paramagnetic state[22]

$$d\ln N/d\ln V=1.85. \tag{27}$$

The latter is assumed to be more realistic and has been used to obtain

$$d\ln I/d\ln V=-1.6\pm0.2. \tag{28}$$

This evaluated derivative is close to that obtained for strong itinerant paramagnets-vanadium,[20] palladium alloys[30] (Fe-Co)Si alloys,[31] Ni_3Al and TlCo compounds,[32] for which the $d\ln I/d\ln V$ values fall in the range from -0.7 to -1.3. On the other hand, these values differ essentially from the results of the LSDA calculations for UFe_2 (-0.1[7,22]) and for a number of d-metals and their compounds (from 0 to -0.2[33]). Thus, it may be suggested that the LSDA method, employing the exchange-correlation potential of a uniform electron gas, is not well suited for an explanation of the volume dependence of I in the systems with narrow bands such as d- and f-metals. For these systems, the Hubbard approach, which takes into account the energy of the intra-atomic Coulomb repulsion U, is more appropriate description. In the context of this approach[34,35] the relation between interaction parameter I and the band width W is given by

$$\frac{d\ln I}{d\ln V}=\frac{d\ln W}{d\ln V}f(W/U,n). \tag{29}$$

Here, the coefficient $f \leqslant 1$ depending on the ratio W/U, the band filling n and the crystal structure type. For $U=\infty$, f appears to be unity and the band width becomes the only energy parameter yielding $|d \ln I/d \ln V| \leqslant |d \ln W/d \ln V|$. Typical estimates of $d \ln I/d \ln V$ for d-metals within the Hubbard model[33,36] are in agreement with the experiment confirming the predominant role of short-range correlations in electron interaction for d-metals and their compounds, including UFe_2.

4. SUMMARY

The study performed makes it possible to conclude:

—Effects of deformation of the band under alloying caused by i) the electron scattering, ii) the assumed nonrigidity resulted from formation of the impurity subbands and iii) chemical pressure are comparable in their influence on the magnetic phase diagram with the band filling change.

—The Fermi level of UFe_2 is found to be located just at the top of a small and narrow $N(E)$ peak. This peak is the only peculiarity in the density of states detected in the $U(Mn–Fe–Co)_2$ system. The quantitative estimates for the peak parameters are obtained.

—The temperature and pressure dependence of the magnetic susceptibility in the $U(Mn–Fe–Co)_2$ system is satisfactorily described by the enhanced Pauli spin contribution within the band model. Probably, the uranium spin and orbital contributions are roughly canceled at all these conditions considering their functional dependence on the band structure parameters to be the same.

—There is no noticeable pressure effect on the Fermi level caused by the relative shift of bands with different symmetry and the corresponding electron transfer between them.

—Nearly full compensation for the pressure effects in the density of states N and interaction parameter I is found.

—Value for volume derivative $d \ln I/d \ln V$ confirms the predominant role of the short-range correlations in the electron interaction in the compounds considered.

Some numerical discrepancy between the band model used and the experimental data for the magnetic susceptibility can be attributed to neglecting of the orbital contribution as well as the spin fluctuations effect.

ACKNOWLEDGMENTS

The present paper is closely connected with the name of Academician B. I. Verkin, outstanding physicist, and organizer of science. His pioneer works on the pressure effect on the band structure of metals have stimulated a search for methods to study weak magnetism under pressure as an effective tool for investigation of the electron states in alloys. B. I. Verkin not only took an active interest in these studies but he also directly contributed to the development of cooperation between the institutes represented by the authors of the paper. We consider it a great honor for us to devote gratefully our paper to the memory of B. I. Verkin.

The authors would like to thank Dr. O. Eriksson for supplying the detailed results of the band structure calculation[7] at different atomic volumes and Dr. A. B. Beznosov for valuable discussions. The experimental assistance of L. S. Litinskaya is gratefully acknowledged.

*E-mail: panfilov@ilt.kharkov.ua

[1] G. Hilscher, J. Magn. Magn. Mater. **27**, 1 (1982); *ibid.* **25**, 229 (1982).
[2] G. H. Lander, A. T. Aldred, B. D. Dunlap, and G. K. Shenoy, Physica B & C **86–88B**, 152 (1977).
[3] A. T. Aldred, J. Magn. Magn. Mater. **10**, 42 (1979).
[4] J. J. M. Franse, P. H. Frings, F. R. de Boer, and A. Menovsky, *Physics of Solids under High Pressure*, J. S. Schilling and R. N. Shelton (Eds.), North-Holland, Amsterdam, p. 181 (1981).
[5] V. Sechovsky, Z. Smetana, G. Hilscher, E. Gratz, and H. Sassik, Physica B & C **102B**, 277 (1980).
[6] A. M. Boring, R. C. Albers, G. H. Schadler, A. C. Lawson, P. Weinberger, and N. E. Christensen, Phys. Rev. B **36**, 5507 (1987).
[7] O. Eriksson, B. Johansson, H. L. Skriver, and M. S. S. Brooks, Physica B & C **144B**, 32 (1986).
[8] O. Eriksson, B. Johansson, M. S. S. Brooks, and H. L. Skriver, Phys. Rev. B **40**, 32 (1989) 9519.
[9] M. S. S. Brooks, O. Eriksson, B. Johansson, J. J. M. Franse, and P. H. Frings, J. Phys. F **18**, L33 (1988).
[10] O. Eriksson, M. S. S. Brooks and B. Johansson, Phys. Rev. B **41**, 9087 (1990).
[11] B. Johansson, O. Eriksson, L. Nordström, L. Severin, and M. S. S. Brooks, Physica B **172**, 101 (1991).
[12] R. Grössinger, G. Hilscher, J. Kamesberger, H. Sassik, G. Wlesinger, V. Sechovsky, and J. Toul, J. Magn. Magn. Mater. **29**, 305 (1982).
[13] G. R. Marpoe, Jr. and G. H. Lander, Solid State Commun. **26**, 599 (1978).
[14] A. I. Meskhishvill, V. A. Pletyushkin, V. K. Slovyanskikh, V. I. Chechernikov, and T. M. Shavishvili, Fiz. Met. Metalloved. **45**, 935 (1978) (in Russian).
[15] P. H. Frings, J. J. M. Franse, and P. E. Brommer, J. Phys. C **18**, 1955 (1985).
[16] J. Toul, V. Sechovsky, and G. Hilscher, Acta Phys. Slov. **31**, 269 (1985).
[17] E. Burzo and M. Văleanu, Rev. Roum. Phys. **29**, 375 (1984).
[18] E. Burzo and M. Văleanu, J. Phys. F **12**, 3105 (1982).
[19] A. S. Panfilov, Phys. Tech. High Pressure **2**, 61 (1992) (in Russian).
[20] A. S. Panfilov, Yu. Ya. Pushkar, and I. V. Svechkarev, Fiz. Nizk. Temp. **14**, 532 (1988) [Sov. J. Low Temp. Phys. **14**, 293 (1988)].
[21] L. S. Litiaskaya, A. S. Panfilov, A. Zentko, P. Diko, and J. Miskuf, *Proceeding Int. Conf. Physics of Transition Metals*, Naukova Dumka Klev. 1989 Pt. 1, 211.
[22] Unpublished data of Ref. 7.
[23] A. Hahn and W. Treutmann, Z. Angew. Phys. **26**, 129 (1969).
[24] V. N. Manchenko, A. S. Panfilov, and I. V. Svechkarev, Zh. Éksp. Teor. Fiz. **71**, 2126 (1976) [Sov. Phys. JETP **44**, 1118 (1976)].
[25] C. J. Kriesman and H. B. Callen, Phys. Rev. **94**, 837 (1954).
[26] M. Shimizu, Physica B **159**, 26 (1989).
[27] T. Moriya and A. Kawabata, J. Phys. Soc. Jpn. **34**, 63 (1973); *ibid.* **35**, 669 (1973).
[28] L. R. Edwards and C. E. Olsen, Bull. Am. Phys. Soc. **18**, 360 (1973).
[29] T. P. Sorokina, G. M. Kvashnin, and A. M. Kapitonov, Fiz. Met. Metalloved. **66**, 1220 (1988).
[30] A. S. Panfilov, Yu. Ya. Pushkar, and I. V. Svechkarev, Zh. Éksp. Teor. Fiz. **95**, 751 (1989) [Sov. Phys. JETP **68**, 426 (1989)].
[31] A. S. Panfilov, I. V. Svechkarev, and L. F. Romasheva, Fiz. Nizk. Temp. **19**, 284 (1993) [Low Temp. Phys. **19**, 200 (1993)].
[32] P. E. Brommer, G. E. Grechnev, J. J. M. Franse, A. S. Panfilov, Yu. Ya. Pushkar, and I. V. Svechkarev, J. Phys.: Condens. Matter **7**, 3173 (1995).
[33] A. B. Kaiser, A. M. Oleś, and G. Stollhoff, Phys. Scr. **37**, 935 (1988).
[34] J. Kanamori, Prog. Theor. Phys. **30**, 275 (1963).
[35] N. D. Lang and H. Ehrenreich, Phys. Rev. **168**, 605 (1968).
[36] G. Stollhoff, A. M. Oleś, and V. Heine, Phys. Rev. B **41**, 7028 (1990).

This article was published in English in the original Russian journal. It was edited by R. T. Beyer.

LOW-DIMENSIONAL AND DISORDERED SYSTEMS

Cooper pairing of two-dimensional electrons in a quantizing magnetic field and the fractional quantum Hall effect

E. A. Pashitskiĭ

*Institute of Physics, National Academy of Sciences of the Ukraine, 252650 Kiev, Ukraine**
(Submitted March 2, 1999)
Fiz. Nizk. Temp. **25**, 920–935 (August–September 1999)

A brief review of the current state of the theory of fractional quantum Hall effect (FQHE) is given along with the assumption of possible connection between the experimentally observed features of the Hall resistance R_H of a two-dimensional ($2D$) electron system in a strong quantizing magnetic field for a fractional filling factor of the lowest Landau level $\nu=q/(2n+1)$ with $q\geqslant 2$, which cannot be described by the Laughlin wave function antisymmetric relative to pair transpositions, and the Cooper pairing of $2D$ electrons. It is assumed that the electron–electron attraction essential for Cooper pairing can be due to the interaction of $2D$ electrons with the surface acoustic waves ($2D$ phonons) and the surface $2D$ plasmons localized near the crystal interfaces (heterojunctions) in the vicinity of inversion layers in the metal–insulator–semiconductor (MIS) structures and heterostructures. The coexistence of coupled electron pairs and unpaired electrons under the FQHE conditions must lead to peculiarities of R_H for values of ν described by the Halperin relation following from the symmetry properties of the ''mixed'' wave function of pairs (bosons) and electrons (fermions). This relation makes it possible in principle to describe all experimental data on FQHE. The summation of ''ladder'' diagrams diverging according to a power law for $T\to 0$ leads to a Bethe–Salpeter-type equation for the vertex part of the electron–electron interaction for a $2D$ system in a quantizing magnetic field taking into account electron–electron and electron–hole pairing in the Cooper and zero-sound channels. This equation is used to calculate the critical temperature T_c of the phase transition to the state with coupled Cooper pairs and to prove that the value of T_c in the ultra-quantum limit is independent of the effective mass of electrons, i.e., on the $2D$ density of states. The phase diagram of the $2D$ system is constructed for the variable electron concentration and magnetic field. It is shown that the region of Cooper pairing of $2D$ electrons in the case of strong attraction almost coincides with the FQHE region for $\nu<1$, while the region of electron-hole pairing with the formation of charge-density waves (CDW) is expelled to the region with $\nu>1$, which is in accord with the experimental data concerning the CDW-induced features of the longitudinal resistance R_{xx} for $\nu=(2n+1)/2$ with $n\geqslant 2$. © *1999 American Institute of Physics.* [S1063-777X(99)01708-9]

1. INTRODUCTION

In 1998, the Nobel prize in physics was awarded to Tsui and Störmer[1] for experimental observation of the fractional quantum Hall effect (FQHE) in two-dimensional ($2D$) electron systems in a quantizing magnetic field (QMF) and to Laughlin[2] for the theoretical explanation of this effect. Laughlin's theory[2] based on the Justrow-type[3] variational wave function antisymmetric relative to pair transposition of particles (fermions) explained the existence of singularities (plateau) in the Hall resistance R_H in the case when the filling factor $\nu=N_S/N_L$ (where N_S is the number of $2D$ electrons and N_L the degeneracy of the Landau level (LL) per unit area) of the Lowest LL assumes fractional values $\nu=1/m$ with odd denominators $m=2n+1$ ($n=1,2,3,\ldots$) or $\nu=(1-1/m)$ in view of the electron–hole symmetry of the excitation spectrum.

It should be noted that the multielectron wave function Ψ of the ground state of a $2D$ system in the ultra-quantum limit, containing products of uniform m-degree polynomials of differences of complex $2D$ coordinates z_j and z_k for electrons, which was used by Laughlin[2] had been constructed for the first time by Bychkov, Iordanskii, and Eliashberg[4] before the FQHE was discovered.

Laughlin's contribution was not only that he constructed independently the polynomial variational function $\Psi\sim\Pi_{j<k}(z_j-z_k)^m$ for describing an ''incompressible'' quantum fluid of $2D$ electrons in a QMF, but primarily that he noted a remarkable analogy between the square of the modulus of Ψ and the partition function of a classical charged $2D$ plasma against a uniform compensating background with a logarithmic law describing the Coulomb interaction of particles with a ''charge'' $Q=m$. Proceeding from this formal analogy, Laughlin[2] proved that the adiabatic in-

 © 1999 American Institute of Physics

clusion of an additional magnetic flux quantum $\varphi_0 = hc/e$ is equivalent to the emergence of a fictitious unit ''charge'' that must be screened completely due to a redistribution of plasma particles with ''charge'' m. However, since real particles (electrons) in a $2D$ system possess the charge e, this means that each flux quantum is ''screened'' by a quasiparticles (quasi-hole) with the fractional effective charge $e^* = e/m$. The size of quasiparticles is determined by the screening radius which has the same order of magnitude as the magnetic quantum length $l_H = \sqrt{\hbar c/eH}$ in the ultraquantum limit, while their effective charge e^* is connected with the Hall conductivity $\sigma_H \equiv \sigma_{xy}$ through the gauge invariance condition[2] leading to fractional values of $\sigma_H = e^* e/h = e^2/hm$ in the plateau region, where the longitudinal components of the conductivity and resistance tensors σ_{xx} and R_{xx} vanish.[1]

Laughlin's wave function[2] describes the ground state of a system of strongly interacting $2D$ electrons, in which each electron corresponds to m magnetic flux quanta. This follows directly from the expression for the filling factor of the lowest LL if we assume that $N_L = 1/2\pi l_H^2 = H/\varphi_0$ so that $\nu = N_S \varphi_0 / H \equiv N_e / N_\Phi$, where $N_e = N_S S$ is the total number of electrons and $N_\Phi = HS/\varphi_0$ the total number of flux quanta in a $2D$ system of area S.

However, subsequent experiments[5–7] proved that singularities in σ_H and R_H are also observed for filling factors $\nu = q/m$ with $q \geqslant 2$. In this connection, Halperin[8] proposed that the fractions $\nu = 2/m$ and $\nu = (1 - 2/m)$ can be a result of formation of quite compact coupled electron pairs in the $2D$ system and constructed a Laughlin-type wave function $\tilde{\Psi}$ symmetric relative to transpositions of such pairs (bosons), but preserved its antisymmetry to transpositions of electrons within each pair. If all the electrons in the $2D$ system are coupled into pairs, singularities in R_H and σ_H must be manifested for $\nu = 4/p$, where p is an arbitrary even number, $p = 2(2n+1)$ or $p = 4(n+1)$. Along with fractional values of the filling factor $\nu = 2/(2n+1)$ with odd denominators, prime fractions $\nu = 1/(n+1)$ appear in this case with arbitrary (including even) denominators. In subsequent publications,[9,10] a more detailed analysis of the structure and energy of the ground state of a $2D$ system was carried out for the values of $\nu = 2/3, 2/5$, and $2/7$ as well as for a half-integral value of the filling factor for the lowest LL for $\nu = 1/2$.

Halperin[8] also proved that singularities in R_H and σ_H of a $2D$ system containing simultaneously coupled electron pairs and uncoupled electrons must be manifested for filling factors

$$\nu = \frac{4m + p - 4r}{mp - r^2}. \tag{1}$$

Here, as in Ref. 2, the exponent m of the polynomial $(z_k - z_j)^m$ determining exchange correlations between unpaired electrons is odd, while the index p responsible for correlation between coupled electron pairs is even, and the index r responsible for correlations of the electron–pair type can have any parity. Expression (1) contains a wide range of rational fractions and provides in principle a description for all the experimentally observed features of R_H under the FQHE conditions as well as the singularities of R_H such as fractions with even denominators $2n$ which have not been observed as yet.

Moreover, it was noted[8] that if $2D$ electrons form coupled many-particle complexes (n-multiplets), the wave function of the Laughlin type leads to singularities of R_H for filling factors $\nu = n^2/k$, where the numbers n and k must have the same parity, which corresponds to any rational fraction in the general case. However, a specific dynamic mechanism of formation of coupled pairs or n-multiplets in $2D$ systems in QMF was not considered in Refs. 8 and 9.

The FQHE theory was developed subsequently in several different directions associated with fundamental topological properties of $2D$ space and electron–electron interactions in $2D$ systems. These trends include, for example, the anyon FQHE model based on the permutation relations $P_{jk}\Psi = \exp(i\pi\alpha)\Psi$ with an arbitrary fractional statistical parameter α (instead of the integral values $\alpha = 0$ for bosons and $\alpha = 1$ for fermions). This corresponds to the so-called intermediate statistics for special $2D$ quasiparticles (anyons),[11,12] the values of $\alpha = 1/m$ leading directly to fractional filling factors $\nu = 1/m$. However, the fractions $\nu = q/m$ with $q > 1$ can be explained only by introducing a special ''hierarchic'' theory which presumes that excitations with another fractional value of α are formed over the gas of excitations (anyons) with one fractional statistical parameter.

It should be noted that the anyon model is also treated as a version of the theory of high-temperature superconductivity (HTSC),[11] but the extent of two-dimensionality of the electron spectrum in layered crystals of cuprate metal oxide compounds (MOC) exhibiting HTSC[13,14] is apparently insufficient for the existence of anyons. Besides, the FQHE was also explained on the basis of field-theoretical $2D$ models of compound fermions[15] and skirmions.[16] However, all these theories are characterized by a somewhat formal approach and rather complicated mathematical apparatus masking the physical meaning of the FQHE.

At the same time, a number of features of the FQHE (such as the emergence of fractional values of $\nu = q/m$ with $q > 1$) can be explained on the basis of comparatively simple concepts similar to those used in the standard theory of superconductivity (e.g., Cooper pairing of electrons, magnetic flux quantization, and dynamics of Abrikosov vortices in type II superconductors).

In this connection, let us consider briefly the superconductivity in strong magnetic fields. The problem on Cooper pairing of electrons in layered metals and $2D$ electron systems due to the electron–phonon interaction (EPI) in strong QMF was analyzed by us[18] even before the FQHE[1] and the integral quantum Hall effect (IQHE)[18] had been discovered. It was proved[18] that in the self-consistent field approximation, the superconducting transition temperature T_c as a function of the magnetic field strength H must experience giant oscillations with the period $\Delta H = H/N$, where N is the number of the upper filled LL, and with sharp drops in T_c almost to zero at the points of intersection of the Fermi level with the next LL. A similar result was obtained by Maniv *et al.*[19] in the semi-classical approximation in the range of ultra-

strong QMF ($H>120$ T) for the magnitude of the superconducting order parameter $\Delta_0(H)$ for layered crystals of high-temperature superconductors. This type of $T_c(H)$ oscillations, which are similar to de Haas–Van Alphen oscillations in normal metals, were considered theoretically earlier[20–22] for isotropic three-dimensional ($3D$) type II superconductors near the upper critical field H_{c2} and later[23–25] for strongly anisotropic quasi-one-dimensional superconductors with an open Fermi surface. Graber and Robins[26] observed the de Haas–Van Alphen effect experimentally in the layered superconductor $NbSe_2$ above and below $H_{c2}(T)$. After the discovery of IQHE and FQHE, the Cooper pairing of electrons in $2D$ systems was considered by Haldane and Rezayi.[27]

Simonyan *et al.*[28] reported recently on possible observation of superconductivity at $T<1$ K in Si-based metal–insulator–semiconductor (MIS) structure with an anomalously high mobility of $2D$ electrons. Phillips *et al.*[29] proposed a plasmon mechanism of such a superconductivity based on Cooper pairing of $2D$ electrons due to their interaction with intrinsic $2D$ plasmons which have an acoustic-type dispersion relation[30] $\omega_q \sim q$ for $q\to 0$ and have the root spectrum $\omega_q=(2\pi e^2 N_S q/m_e^* \varepsilon_0)^{1/2}$ for $q\neq 0$ (where m_e^* is the effective electron mass and ε_0 the permittivity of the lattice). However, such a mechanism is hardly probable since the phase velocity of $2D$ plasmons is anomalously high for $q\to 0$, $\omega_q/q=c/\sqrt{\varepsilon_0}$ (where c is the velocity of light in vacuum) and exceeds considerably the Fermi velocity for electrons $v_F=\hbar k_F/m_e$ (where $k_F=\sqrt{2\pi N_S}$). Moreover, a wide region of strong quantum Landau damping exists for $q\geqslant k_F$ and $\omega\leqslant\omega_q$ due to the decomposition of plasmons into electron–hole pairs in which electron–electron Coulomb repulsion prevails.

On the other hand, it was proved by us earlier[31] that weakly damped surface $2D$ plasmons with a root dispersion relation and a relatively low frequency can exist near the interface (heterojunction) between semiconductors with ''light'' electrons and ''heavy'' holes (as, for example, in GaAs/AlGaAs heterostructure). The interaction between such plasmons can lead to Cooper pairing of degenerate $2D$ electrons. In addition, in layered semiconducting systems we must take into account the existence of surface $2D$ phonons localized at the interfaces between crystals (see below).

In this paper, we consider the possible effect of Cooper pairing of $2D$ electrons in a strong QMF on the peculiarities of the FQHE. Since the EPI between degenerate $2D$ electrons in the surface inversion layers and the bulk acoustic and optical phonons in semiconducting crystals is weaker than the Coulomb repulsion, we assume here that the strong electron– electron attraction required for Cooper pairing of $2D$ electrons can be due to the effective EPI with surface $2D$ phonons at the interface between the semiconducting (Si) crystals and the insulator (SiO_2) in a MIS structure or at the heterojunction between pure and doped semiconducting crystals in heterostructures of the $GaAs/Al_xGa_{1-x}As$ type. In the latter case, an additional mechanism of attraction can be the interaction of ''light'' $2D$ electrons in the GaAs crystal with surface $2D$ plasmons[31] whose existence is associated with collective (plasma) oscillations of ''heavy'' holes in AlGaAs.

We shall use the equation for the vertex component (four-pole) Γ_{ee} of the electron–electron interaction, which is similar to the Bethe-Salpeter equation and was obtained by the summation of ''ladder'' diagrams diverging according to a power law for $T\to 0$ taking into account the processes of electron–electron and electron–hole pairing in the Cooper and zero-sound channels to calculate the critical temperature T_c of the transition of the $2D$ system to a state with coupled triplet Cooper pairs of electrons with parallel spins at the lowest LL. It will be proved that in the ultra-quantum limit, the value of T_c is independent of the effective mass of $2D$ electrons (i.e., the $2D$ density of states (DS) in the parabolic region $g_{2D}=m_e^*/2\pi\hbar^2$) so that Cooper pairing is possible in principle even for $m_e^*\ll m_0$ (where m_0 is the mass of a free electron), and the size of Cooper pairs is of the order of the magnetic length l_H and is smaller than the average distance between particles for $\nu=k_F^2 l_H^2<1$.

We shall construct the phase diagram of a $2D$ system for varying concentration N_S of $2D$ electrons and magnetic field strength H and prove that the region of Cooper pairing of electrons with a strong attraction virtually coincides with the region of the FQHE for $\nu<1$, while the region of electron–hole pairing with the formation of charge-density waves (CDW)[32] is expelled to the sector of the FQHE with $\nu>1$, which is in qualitative agreement with experimental data[33] on observation of R_{xx} singularities due to CDW[34–36] for $\nu=(2n+1)/2$ with $n\geqslant 2$.

According to Halperin,[8] the coexistence of coupled Cooper pairs and unpaired electrons below T_c must lead to R_H and σ_H singularities for the values of the filling factor ν determined by the Halperin equation (1). This relation allows us to explain the features of the FQHE for $\nu=q/(2n+1)$ with $q\geqslant 2$[5–7] that cannot be explained on the basis of the Laughlin theory.[2] We shall discuss a significant difference between a state with local Cooper pairs in $2D$ systems in a QMF for $\nu<1$ and the superconducting state of traditional superconductors with strongly overlapping Cooper pairs.[37]

2. COOPER PAIRING OF ELECTRONS IN $2D$ SUPERCONDUCTORS IN A QUANTIZING MAGNETIC FIELD

It was noted in Introduction that the problem on Cooper pairing of electrons in two-dimensional superconductors of the type of layered dichalcogenides of transition metals and in $2D$ electron systems (MIS structures) due to the EPI in strong QMF was considered earlier[18] under the condition that the cyclotron frequency $\omega_c=eH/m_e^* c$ of electrons satisfies the conditions

$$k_B T_c \ll \hbar\omega_c \ll \hbar\overline{\omega}_{\rm ph}, \tag{2}$$

where $\overline{\omega}_{\rm ph}$ is the average (Debye) frequency of the phonon spectrum and k_B the Boltzmann's constant. Since the Fermi energy for metals is $E_F\gg\hbar\overline{\omega}_{\rm ph}$, the number of filled quantum LL is large, $N\approx E_F/\hbar\omega_c\gg 1$. For this reason, we used in Ref. 18 the self-consistent field approximation in which the

integral equation linearized for the spatially nonuniform superconducting order parameter $\Delta(r)$ for $T\to T_c$ has the form[37]

$$\Delta(\mathbf{r})=\int d^2r' K(\mathbf{r},\mathbf{r}')\Delta(\mathbf{r}'). \tag{3}$$

Here $\mathbf{r},\mathbf{r}'$ are the longitudinal coordinates in the plane of the layers (x,y), and K is the kernel of the nonlocalized electron–electron interaction:

$$K(\mathbf{r},\ \mathbf{r}')=\frac{1}{2}(\overline{V}_{\rm ph}-\overline{V}_C)\times\sum_{n,n'}\frac{\tanh(\xi_n/2k_BT_c)+\tanh(\xi_{n'}/2k_BT_c)}{\xi_n+\xi_{n'}}\times\sum_{k_y,k_y'}\Psi^*_{nk_y}(\mathbf{r})\Psi^*_{n'k_y'}(\mathbf{r})\Psi_{nk_y}(\mathbf{r}')\Psi_{n'k_y'}(\mathbf{r}'), \tag{4}$$

where $\overline{V}_{\rm ph}$ and $\overline{V}_C$ are the matrix electrons of the electron–electron interaction (due to the EPI) and the screened Coulomb repulsion averaged over the transverse momentum q_z being transferred, ξ_n is the energy of an electron at the nth LL measured from the Fermi level, and $\Psi_{nk_y}(r)$ the wave function of a $2D$ electron in the Landau calibration:[38]

$$\Psi_{nk_y}(\mathbf{r})=\frac{1}{\sqrt{L_y}}\exp(ik_yy)\Phi_n(x-k_yl_H^2), \tag{5}$$

which corresponds to the LL with the energy

$$E_n^{(\pm)}=(n+1/2)\hbar\omega_c\pm 1/2g\mu_BH.$$

Here L_y is the size of the $2D$ system along the y-axis, g the gyromagnetic ratio, μ_B Bohr's magneton, and Φ_n are the eigenfunctions of the linear oscillator.

For $k_BT_c\ll\hbar\omega_c$, the main contribution to the sum over n and n' in (4) comes from the upper LL, i.e. from the term with $n=n'=N$. Consequently, we can assume to within small terms of the order of $k_BT_c/\hbar\omega_c$ that $\xi_n=\xi_{n'}=\delta\mu(T_c)$ in (4), where $\delta\mu(T)$ is the shift of the level of chemical potential $\mu(T)$ relative to the upper LL for $T\neq 0$. The quantity $\delta\mu(T)$ is determined to an exponential accuracy by the relation

$$\delta N_S=N_L[\exp\{\delta\mu(T)/k_BT\}+1]^{-1}. \tag{6}$$

Here δN_S is the number of $2D$ electrons at the upper LL. Introducing the filling factor for the upper level in the form $\nu_N=\delta N_S/N_L$, we obtain from (6) the relation

$$\delta\mu(T)=-k_BT\ln\left(\frac{1-\nu_N}{\nu_N}\right), \tag{7}$$

which is valid for $|\delta\mu|<\hbar\omega_c/2$ in the region $0<\nu_N<1$. As a result, taking into account (4) and (7) for $L_y\to\infty$, we can write Eq. (3) in the form[18]

$$\Delta(x)=N_L(\overline{V}_{\rm ph}-\overline{V}_C)\frac{\tanh\left(\frac{1}{2}\ln|1-1/\nu_N|\right)}{k_BT_c\ln|1-1/\nu_N|}\times\int_{-L_{x/2}}^{L_{x/2}}dx'\Delta(x')f_N(x,x'), \tag{8}$$

where

$$f_N(x,x')=\int_{-\infty}^{\infty}dx_0\Phi_N(x'+x_0)\Phi_N(x'-x_0)\times\Phi_N(x+x_0)\times\Phi_N(x-x_0)\Phi_N(x-x_0); \tag{9}$$

$x_0=k_yl_H^2$, and L_x is the size of the $2D$ system along the x-axis ($L_x\gg l_H$). Since the filling factor ν_N changes periodically (from 0 to 1) with the period

$$\Delta H=H/N=H\hbar\omega_c/E_F(N\gg 1). \tag{10}$$

with the filling (or depletion) of the succeeding LL upon a change in H, the value of T_c, in accordance with (8), is also an oscillating function of H and exhibits deep depressions almost to zero at the points $\nu_N=0$ and $\nu_N=1$ at which the Fermi level intersects LL, while the quantity T_c as a function of ν_N had broad peaks at the points $\nu_N=1/2$, when the upper LL is half-filled. The width of the peaks depends on the number N of the upper filled LL and increases with decreasing N, i.e., upon an increase in H.

A similar result was obtained by Maniv *et al.*[19] in the semi-classical approximation for the modulus of the superconducting order parameter $\Delta_0(H)$ in the region of ultrastrong QMF ($H>120$ T) for layered HTSC crystals. Oscillations of $T_c(H)$ and $\Delta_0(H)$ in $2D$ superconductors in QMF are similar to de Haas–Van Alphen oscillations observed experimentally in layered crystals of $NbSe_2$[27] and in cuprate compounds YBaCuO.[39,40]

The following two important circumstance are worth noting. First, according to (8), the value of T_c for a $2D$ system in a QMF does not depend on the electron density of states (DS) in contrast to traditional superconductors.[37,41] This means that for $\overline{V}_{\rm ph}>\overline{V}_C$, Cooper pairing of $2D$ electrons in a QMF is possible even for $m_e^*\ll m_0$, when the ultra-quantum limit $\hbar\omega_c\geqslant E_F$ is reached in really attainable magnetic field $H\geqslant 10$ T, i.e., the conditions for the FQHE are realized for $\nu=2E_F/\hbar\omega_c<1$. Second, Eq. (8) implies that ''ladder'' diagrams in the Cooper channel of the electron–electron interaction in $2D$ systems in QMF for $T\to 0$ diverge according to a power law (in proportion to $1/T^n$) in contrast to the logarithmic divergence typical of isotropic $3D$ superconductors[41] (see below).

If we go over to the ultra-quantum limit, when $N=0$ and $\nu_0=\nu=N_S/N_L$, the integrals with respect to x_0 and x' in (9) for the electron wave functions $\Phi_0(x)=1/(\pi^{1/4}\sqrt{l_H})\exp(-x^2/2l_H^2)$ for the lowest LL can be evaluated explicitly, and the value of T_c is given by

$$T_c=N_L(\overline{V}_{\rm ph}-\overline{V}_C)/2k_B. \tag{11}$$

In this case, the nonuniform order parameter $\Delta(x)$ depends on x according to the exponential (Gaussian) law $\Delta(x)=\Delta_0\exp(-x^2/l_H^2)$. It follows hence that the typical size of

coupled electron pairs is equal to l_H and is smaller than the average distance between pairs $\overline{r} \geqslant (N_S/2)^{-1/2}$ for $\nu = k_F^2 l_H^2 < 1$. For this reason, a macroscopic coherent condensate of Cooper pairs existing in the superconducting state of traditional superconductors[41] is not formed in the $2D$ system for $T < T_c$ in the present case. If the Zeeman splitting $\Delta E = g\mu_B H \geqslant k_B T_c$, the triplet Cooper pairing of $2D$ electrons with parallel spins at the lowest LL is advantageous from the energy point of view.

It should be borne in mind, however, that the transition to the ultra-quantum limit is strictly speaking incorrect in the self-consistent field approximation since $2D$ electrons form a strongly correlated incompressible quantum liquid.[2] In this case, Cooper pairing can be described with the help of the Schrieffer variational function[41]

$$|\tilde{\Psi}_S\rangle \sim \prod_{\mathbf{k}} \exp\{g_{\mathbf{k}} B_{\mathbf{k}}^+\} |\Psi_L\rangle = \prod_{\mathbf{k}} (1 + g_{\mathbf{k}} B_{\mathbf{k}}^+) |\Psi_L\rangle,$$

where $B_{\mathbf{k}}^+$ is the creation operator for a Cooper pair, $g_{\mathbf{k}}$ the Fourier component of the wave function for virtual phonons, and $|\Psi_L\rangle$ the Laughlin wave function[2] describing the ground state of the $2D$ system.

3. CONDITIONS FOR COOPER PAIRING OF ELECTRONS IN SEMICONDUCTING 2*D* SYSTEMS

It is well known that the necessary condition for Cooper pairing of electrons due to the EPI is that the attraction associated with the exchange of virtual phonons must be stronger than the screened Coulomb repulsion. The fulfillment of this condition for metals with $E_F \gg \hbar\omega_{\rm ph}$ is facilitated due to additional suppression of repulsion in view of the emergence of a large Bogoliubov–Tolmachev logarithm $\ln E_F/\hbar\omega_{\rm ph}$ in the Morel–Anderson Coulomb ''pseudopotential.''[41] Semiconducting $2D$ systems with $E_F = \pi\hbar^2 N_S/m_e^* \leqslant \hbar\overline{\omega}_{\rm ph}$ do not exhibit such a suppression and the condition $\overline{V}_{\rm ph} > \overline{V}_C$ is rather stringent.

In the longwave limit (taking into account the smallness of the electron Fermi momentum $k_F \ll \pi/a$), the expression for the matrix element $\overline{V}_{\rm ph}$ describing the retarded attraction between $2D$ electrons due to the exchange of virtual bulk acoustic and optical phonons and averaged over the transverse momentum q_z being transferred can be written in the form (see Ref. 42)

$$\overline{V} \cong \frac{a^2 d}{2L}\left[D_a^2/M_a S^2 + \gamma_0^2/\overline{M}_a \omega_0^2\right], \tag{12}$$

where a is the lattice constant, d the average width of the region of localization of $2D$ electrons in the inversion layer, L the crystal thickness, M_a and $\overline{M}_a$ are the total and reduced masses of atoms in the unit cell, D_a is the deformation potential for acoustic phonons with the phase (acoustic) velocity s, and γ_0 the deformation constant for nonpolar optical phonons with frequency ω_0. Since the typical values of $d = (30-50)$ Å (see Ref. 43) is much smaller that $L \approx 3000-5000$ Å, the effective attraction between $2D$ electrons and bulk phonons due to the EPI is weak and cannot exceed the Coulomb repulsion whose averaged matrix element has the form

$$\overline{V}_C \cong 2\pi e^2/\varepsilon_0(\overline{q}_\parallel + \kappa_e), \tag{13}$$

where $\hbar\overline{q}_\parallel$ is the average longitudinal momentum being transferred ($\overline{q}_\parallel \approx k_F$), and κ_e the reciprocal electron screening length which is equal to $2/a_e^*$ for $H = 0$ (where $a_e^* = \varepsilon_0\hbar^2/m_e^* e^2$ is the effective Bohr radius of electron; see Ref. 30), while in the ultra-quantum limit $\kappa_e = L_H$ (see Ref. 2). Indeed, substituting into (12) the optical constant $\gamma_0 = D_0/2a$, where D_0 is the optical deformation potential which is abnormally large for GaAs crystals, $D_0 \approx (42-48)$ eV,[44,45] and using the values of longitudinal and transverse optical phonon frequencies $\omega_0 \approx (270-290)\ \text{cm}^{-1}$ as well as the masses of Ga and As atoms, for $\varepsilon_0 \approx 13$, $m_e^* \approx 0.068 m_0$, and $k_F \leqslant 2\cdot 10^6\ \text{cm}^{-1}$ under the assumption that the contributions of all optical and acoustic branches are approximately the same, and using (13), we obtain an estimate for the ratio $\overline{V}_{\rm ph}/\overline{V}_C \leqslant 10^{-2}$, which apparently rules out completely the Cooper pairing of $2D$ electrons due to the EPI.

However, we have disregarded the fact that a MIS structure must contain surface acoustic waves (SAW) and optical ''interfacial'' phonons of various types at the interface between media, including the heterojunction between a pure GaAs crystal and doped semiconductor $Al_xGa_{1-x}As$ or the interface between the semiconductor Si and the insulator SiO_2.[46,47] The interaction of $2D$ electrons with such SAW ($2D$ phonons) can be much more effective than with bulk phonons. Indeed, if the depth λ of SAW penetration to the bulk of the crystal is of the order of or larger than the width d of localization of $2D$ electrons in the surface inversion layers and the phase velocity $\tilde{s}$ of SAW along the surface is much smaller than the velocity of sound s in the bulk of the crystal, the order of magnitude of the matrix element of the EPI due to the exchange of virtual SAW can be estimated as

$$\tilde{V}_S \cong \frac{a^2 D_a^2}{2M_a \tilde{s}^2} \tag{14}$$

and can be much higher than $\overline{V}_{\rm ph}$ in (12) if $D_a \cong D_0$, $d \gg a$, and $s^2 \gg \tilde{s}^2$. For example, the phase velocity and the reciprocal penetration depth of a shear SAW at the interface between two crystals with different shear moduli $\mu_1 > \mu_2$ and densities $\rho_1 > \rho_2$ are given by

$$\tilde{s} = \sqrt{(\mu_1^2 - \mu_2^2)/(\mu_1\rho_1 - \mu_2\rho_2)};$$
$$\lambda_i^{-1} = q_1\sqrt{1 - \tilde{s}^2/s_{ti}^2}, \tag{15}$$

where $s_{ti} = \sqrt{\mu_i/\rho_i}$ is the transverse sound velocity in the ith crystal ($i = 1,2$). It follows hence that $\tilde{s}^2 \ll s_{ti}^2$ if the quantities $\Delta\mu = (\mu_1 - \mu_2)$ and $\Delta\rho = (\rho_1 - \rho_2)$ satisfy the conditions

$$\Delta\mu \ll \mu_i;\ \ \Delta\mu/\Delta\rho \ll \mu_i/\rho_i\ \ (i = 1,2), \tag{16}$$

and $\lambda_i \geqslant d$ if $q_\parallel \cong k_F \leqslant 2\cdot 10^6\ \text{cm}^{-1}$. Thus, the conditions $\overline{V}_S \gg \overline{V}_{\rm ph}$ and $\overline{V}_S > \overline{V}_C$ can be satisfied in principle.

An indirect evidence of the existence of a strong EPI in Si–MIS structure can be the observation[28] of superconduc-

tivity suppressed by a longitudinal magnetic field. An additional mechanism of electron–electron attraction (besides SAW) in GaAs/$Al_xGa_{1-x}As$ heterostructure can be the exchange of virtual surface plasmons which can exist due to the difference in the effective masses of electrons ($m_e^*=0.068m_0$) and holes ($m_h^*=0.6m_0$) localized on different sides of the heterojunction. It was proved in Ref. 31 that the frequency of such plasmons for the same permittivity of the crystals is given by

$$\omega_q=\Omega_h(1+\sqrt{1+\kappa_e^2/q_\parallel^2})^{-1/2}, \tag{17}$$

where Ω_h is the plasma frequency of ''heavy'' holes, so that for $q_\parallel<\kappa_e$ we obtain $\tilde{\omega}_q=\Omega_h\sqrt{q_\parallel/\kappa_e}$. The exchange of surface plasmons together with slow SAW can ensure in principle the condition $(\tilde{V}_S+\tilde{V}_{\rm pl})>\tilde{V}_C$, where $\tilde{V}_{\rm pl}$ is the matrix element of the electron–plasmon interaction, required for Cooper pairing of ''light'' electrons.

However, the abnormally small effective mass of degenerate $2D$ electrons in GaAs, and hence the low DS $g_{2D}=m_e^*/2\pi\hbar$ practically rules out the superconductivity for $H=0$ in a GaAs/AlGaAs heterostructure in contrast to a Si–MIS structure in which the effective electron mass in Si is much larger ($m_e^*\approx(0.19–0.96)m_0$). Besides, the silicon crystal has a multivalley band structure, which also facilitates the enhancement of the mechanism of Cooper pairing due to an effective increase in the DS and an increase in the coupling constant.[48,49]

The situation changes radically in a strong QMF since in this case (see above and Ref. 18) the superconducting transition temperature is determined by a combination of parameters which is independent of m_e^*: $T_c\sim N_L\equiv g_{2D}\hbar\omega_e$. For this reason, Cooper pairing is possible in principle even for ''light'' $2D$ electrons with $m_e^*\ll m_0$ in GaAs (see below).

4. COMPETITION BETWEEN COOPER AND ELECTRON–HOLE PAIRING IN $2D$ SYSTEMS IN A QUANTIZING MAGNETIC FIELD

It was proved in Ref. 18 in the self-consistent field approximation[37] which in fact corresponds to summation of ''ladder'' diagrams in the Cooper channel[50] that the high superconducting transition temperature T_c in $2D$ systems in QMF is a linear function of the electron–electron interaction constant and does not depend on the density of states and effective mass of $2D$ electrons [see (8) and (11)].

A similar result was obtained by Fukuyama *et al.*[32] in the Hartree–Fock approximation for the electron–hole pairing under the action of the Coulomb attraction in a $2D$ system in the ultra-quantum limit. The critical temperature for type II phase transition in a state with coupled electron–hole pairs (excitons) and with a quantum CDW with the wave vector $Q_0=1.568/l_H$ (i.e., with the spatial period $L_0=2\pi/Q_0\approx 4l_H$) is independent of the electron DS and is given by

$$T_{CDW}=0{,}557\nu(1-\nu)e^2/\varepsilon_0 l_H k_B. \tag{18}$$

In an arbitrary QMF, this problem can be solved by summing up the ''ladder'' diagrams in the zero-sound channel,[50]

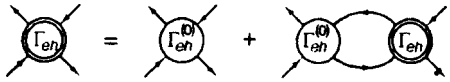

FIG. 1. Bethe–Salpeter equation for the vertex part of the electron–electron interaction.

whose simplest element is the polarization operator for $2D$ electrons, which is defined in the random-phase approximation as[18]

$$\Pi_e(x,x';q_y,\omega)=2\sum_{n,n'}\frac{f(E_{n'})-f(E_n)}{\hbar\omega-E_n+E_{n'}} \times\int_{-\infty}^{+\infty}\frac{dk_y}{2\pi}\Phi_n(x-x_0)\Phi_n(x'-x_0) \times\Phi_{n'}(x'-x_0+y_0)\Phi_{n'}(x-x_0+y_0) \times e^{i(2x_0-y_0)(x-x')/l_H^2}, \tag{19}$$

where $f(E_n)$ is the Fermi distribution function and $y_0=q_y l_H^2$. In the statistical limit ($\omega\to 0$) for the upper LL ($n=n'=N$), expression (19) assumes the form

$$\Pi_e(x,x';q_y,0)=-2N_L\frac{\nu_N(1-\nu_N)}{k_BT}F_N(x,x',y_0), \tag{20}$$

where

$$F_N(x,x',y_0)=\int_{-\infty}^{+\infty}dx_0\Phi_N(x-x_0)\Phi_N(x'-x_0) \times\Phi_N(x'-x_0+y_0)\Phi_N(x-x_0+y_0) \times\cos[(2x_0-y_0)(x-x')/l_H^2]. \tag{21}$$

It follows from (20) that the ''ladder'' diagrams from the perturbation theory for the vertex component Γ_{eh} of the electron–hole interaction diverge according to a power law ($\sim 1/T^n$) for $T\to 0$ as in the Cooper channel. The summation of these diagrams leads to a Bethe–Salpeter equation[51] for Γ_{eh} (Fig. 1), whole pole component determines the critical temperature $T_{\rm CDW}$ of the transition to a spatially inhomogeneous state with a quantum CDW. Such an equation was analyzed by Moessner and Chalker[35] for a large number of filled LL ($N\gg 1$). In the ultra-quantum limit, all the integrals with respect to x, x_0, and x' in (20) and (21) can be evaluated explicitly. Taking into account the Coulomb interaction as well as the EPI, we ultimately obtain

$$T_{CDW}\cong 0.681N_L(\overline{V}_C+\overline{V}_{\rm ph})\frac{\nu(1-\nu)}{k_B}\exp\left(-\frac{Q_1^2l_H^2}{2}\right). \tag{22}$$

where the wave vector Q_1 and the period $L_1=2\pi/Q_1$ for a quadratic quantum CDW are determined from the condition $L_1^2=2\pi l_H^2$ (see Ref. 52).

It follows from (18), (20), and (22) that the maximum value of T_{CDW} as a function of the total filling factor $\nu=N_S/N_L$ is attained at the points $\nu=(2n+1)/2$. This is in good accord with the predictions of singularities of the transport resistance R_{xx} (and probably the Hall resistance

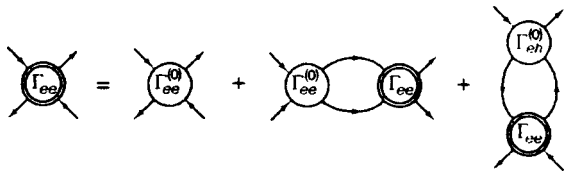

FIG. 2. Equation for the vertex part of the electron–electron interaction in a $2D$ system in QMF with a discrete electron spectrum, obtained by independent summation of ladder diagrams in the Cooper and zero-sound channels.

$R_{xy}=R_H$) at these points[34–36] (see also Ref. 53), which were observed recently.[33] It should be noted that a singularity in R_H for $\nu=5/2$ was observed earlier for a GaSb–InAs–GaSb quantum well.[54]

It should be emphasized that expression (18) leads to a too high estimate of $T_{CDW}\approx 20\,\mathrm{K}$ for $H\approx 10\,\mathrm{T}$ and $N_S\sim 10^{11}\,\mathrm{cm}^{-2}$,[31] while the R_{xx} singularities associated with CDW were actually observed by Lilly *et al.*[33] at $T<0.15\,\mathrm{K}$. This also refers to expression (22) and is apparently due to the fact that strong many-particle correlations between electrons and holes in a Laughlin[2] $2D$ ''incompressible'' quantum liquid are disregarded in the Hartree–Fock and self-consistent field approximations. These correlations lead to breaking of electron-hole pairs (excitons) at higher values of T (it will be proved below that this concerns the Cooper pairing also).

Electron–hole pairing in $2D$ systems in QMF takes place only when the screened Coulomb interaction is stronger than the EPI ($\overline{V}_C>\overline{V}_{\mathrm{ph}}$). If, however, the resultant attraction between electrons ($\widetilde{V}_S+\widetilde{V}_{\mathrm{pl}}$) considered in Sec. 3 is stronger than the screened Coulomb repulsion $\overline{V}_C$ (which decreases with increasing magnetic field since $\kappa_e\approx l_H^{-1}\sim H$) due to the interaction of $2D$ electrons with slow SAW and/or with the surface $2D$ plasmons, we must simultaneously take into account the Cooper and electron–hole pairing. In this respect, the situation for $2D$ systems in QMF, for which the ''ladder'' diagrams in the Cooper and zero-sound interaction channels have the same (power-type) divergence for $T\to 0$, strongly resembles the situation in quasi-one-dimensional (chain) metals in which the corresponding diagrams display the same (logarithmic) divergence. It is well known that this necessitates the application of the so-called ''parquet'' approximation.[55–58]

However, we can use here (in view of the discreetness of the electrons spectrum of a $2D$ system in a QMF) a simpler approach based on a Bethe–Salpeter type equation[51] for the vertex component (four-pole) Γ_{ee} of the electron–electron interaction, in which independent summation of ''ladder'' diagrams in the Cooper and zero-sound channels is carried out (Fig. 2). The pole component of this equation determines the critical temperature T_c of the transition to a state with coupled Cooper pairs taking into account the competition between electron–electron and electron–hole pairing mechanisms. Confining our analysis to the point-like instantaneous interaction independent of spins for the sake of simplicity, in which the expression

$$\Gamma^{(0)}(x_1,x_2,x_3,x_4)=V\delta(x_1-x_2)\,\delta(x_1-x_3)\,\delta(x_1-x_4), \quad (23)$$

holds[50] for the initial vortices $\Gamma_{ee}^{(0)}$ and $\Gamma_{eh}^{(0)}$, we can write the equation shown graphically in Fig. 2 (in the mixed coordinate–momentum representation) and taking into account only the pole component Γ_{ee} in the following form:

$$\int_{-\infty}^{+\infty}dx\Gamma_{ee}(q_y,x)=\frac{N_L}{k_BT_c}\int_{-\infty}^{+\infty}dx'\Gamma_{ee}(q_y,x')\Bigg\{\widetilde{f}_N(x')\times[\widetilde{W}_{ee}-\widetilde{V}_C(0)]\frac{\tanh\left(\frac{1}{2}\ln|1-1/\nu_N|\right)}{\ln|1-1/\nu_N|}-\nu_N(1-\nu_N)\widetilde{F}_N(x',y_0)\times[\widetilde{W}_{ee}+\widetilde{V}_C(q_y)]\Bigg\}. \quad (24)$$

Here, the functions $\widetilde{f}_N(x')$ and $\widetilde{F}_N(x',y_0)$ are defined as integrals with respect to x of expressions (9) and (21), while the quantity $\widetilde{W}_{ee}>0$ stands for the resultant electron–electron attraction due to the interaction with slow SAW and with surface $2D$ optical phonons and $2D$ plasmons (in the latter case, we should probably take into account the effect of the strong magnetic field on the plasma oscillation spectrum for ''heavy'' holes). It follows from (24) that T_c has a minimum at points $\nu_N=1/2$ as a function of ν_N, and is equal to zero for $\nu_N=0$ or 1. Going over to the ultra-quantum limit ($N=0$) and assuming that $\Gamma_{ee}(x)\sim \mathrm{e}^{-x^2/l_H^2}$ (in analogy with $\Delta(x)\sim \mathrm{e}^{-x^2/l_H^2}$), we obtain the following approximate expression for T_c:

$$T_c\cong T_0h\left[\left(\beta-\frac{1}{\sqrt{h}}\right)\frac{\tanh\left(\frac{1}{2}\ln|1-h|\right)}{\ln|1-h|}\sim\frac{0.681}{h}\left(1-\frac{1}{h}\right)\mathrm{e}^{-2/h}\left(\beta+\frac{1}{2+\sqrt{h}}\right)\right]. \quad (25)$$

where

$$T_0=e^2k_F/2\varepsilon_0k_B;\quad \beta=\varepsilon_0k_F\widetilde{W}_{ee}/2\pi e^2;$$

$$h=1/\nu=H/H_0,\quad H_0=\varphi_0N_S.$$

Hence, it follows that $T_c>0$ if $\beta>1/\sqrt{h}$ (the necessary condition) and if the first term in the square brackets on the right-hand side of (25), which described the contribution of the Cooper channel, is larger than the second term corresponding to the contribution of the zero-sound channel (sufficient condition).

Figure 3 shows the dependences of T_c/T_0 on the dimensionless magnetic field $h=H/H_0$, calculated by formula (25) for various values of the parameter β characterizing the relation between the effective attraction $\overline{W}_{ee}$ (due to the EPI) and the average unscreened Coulomb repulsion $2\pi e^2/\varepsilon_0k_F$ between degenerate $2D$ electrons.

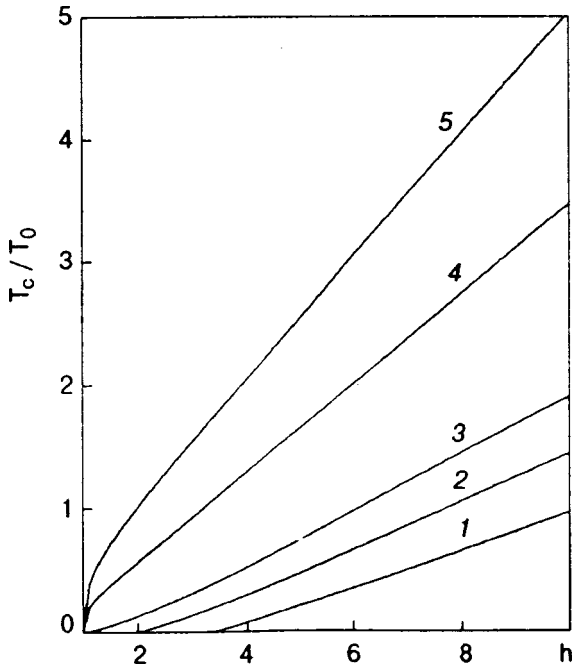

FIG. 3. Dependence of T_c on the magnetic field $h=H/H_0$ for various values of the parameter β: 0.7 (curve *1*), 0.85 (curve *2*), 1.0 (curve *3*), 1.5 (curve *4*), and 2.0 (curve *5*).

It can be seen that for $\beta \geqslant 1$, a transition to the state with Cooper pairing in a $2D$ system is possible for $H \geqslant H_0$ if $T<T_c$, while such a transition for $\beta<0.85$ is possible only in the region of fields $H \geqslant 2H_0 (h \geqslant 2)$.

It should be noted that $T_0 \geqslant 65\,\mathrm{K}$ and the field $H_0 \geqslant 4\,\mathrm{T}$ for a GaAs crystal with $\varepsilon \approx 13$ for $N_S \geqslant 10^{11}\,\mathrm{cm}^{-2}$ and $k_F=\sqrt{2\pi N_S} \geqslant 10^6\,\mathrm{cm}^{-1}$. This apparently corresponds to strongly exaggerated absolute values of $T_c \geqslant 20\,\mathrm{K}$ (for $h \geqslant 3$ and $\beta \geqslant 1$), which appear due to the fact that strong electron–electron correlations facilitating the breaking of Cooper pairs are not taken into account in the self-consistent field approximation. However, we can expect that the relative mutual effect of the Cooper and electron–hole pairing is take into account quite consistently since these processes are considered here in the same approximation.

The right-hand sides of Figs. 4(a), 4(b), and 4(c) show the regions of Cooper pairing ($T_c>0$) in coordinates magnetic field strength H vs. $2D$-electron concentration N_S (in the units of the field $H_0=N_S\varphi_0$) for various values of the dimensionless parameter α connected with β through the relation

$$\alpha=\beta\sqrt{H_{0\,\min}/H_0}; \quad H_{0\,\min}=N_{S\,\min}\varphi_0, \tag{26}$$

where $N_{S\,\min} \approx 10^{11}\,\mathrm{cm}^{-2}$ and $H_{0\,\min} \approx 4\,\mathrm{T}$. It can be seen that the region of Cooper pairing expands with increasing α and fills almost the entire sector $H>H_0$ for $\alpha \geqslant 0.75$, while for $\alpha \leqslant 0.38$ this region is expelled to the sector $H<H_0<2H$ for $H \leqslant 40\,\mathrm{T}$ (i.e., to the region $1<h<2$). This means that Cooper pairing of $2D$ electrons is possible only in the interval $1/2<\nu<1$, while the state with $\nu=1/2$ is not realized (states with $\nu<1/2$, however, can be realized in view of the electron–hole symmetry).

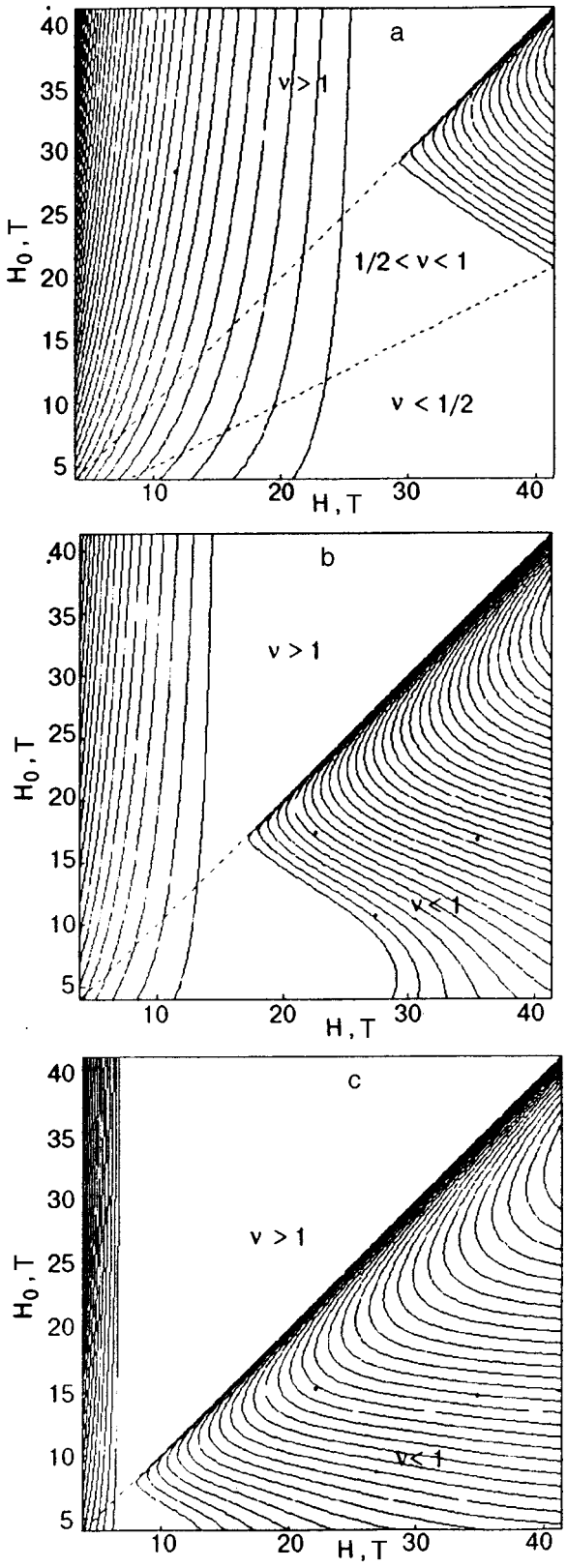

FIG. 4. Phase diagram on the $H-H_0$ plane for a $2D$ system in the ultraquantum limit for various values of the parameter α: 0.38 (a), 0.50 (b), and 0.75 (c). The state with $\nu=1/2$ for $\alpha \leqslant 3.8$ can be formed only due to the electron–hole pairing in the region $\beta<\sqrt{\nu}(H \leqslant 25\,\mathrm{T})$.

The left-hand sides in Figs. 4 (vertical hatching) also show the range of $\beta \leqslant 1/\sqrt{h}$ in which the electron–hole pairing involving the generation of CDW is possible for $T<T_{CDW}$. It can be seen that with increasing α this region shrinks rapidly and is expelled almost completely to the sector $H<H_0$ for $\alpha \geqslant 0.75$ [see Fig. 4(c)]. In view of the relation $h=1/\nu$, the latter is in qualitative agreement with the singularities of the transport resistance R_{xx} observed in $2D$ systems for $\nu=(2n+1)/2$ with $n \geqslant 2$,[32] which are attributed to a quantum CDW[34–36] having a T_{CDW} peak at half the filling of the upper LL.

5. COOPER PAIRING AND FQHE

The phase diagram in Fig. 4 shows that the region of Cooper pairing for $2D$ electrons virtually coincides with the FQHE region in the case of a strong electron–electron attraction, when the parameter $\alpha \sim 1$.

It should be emphasized, however, that the state of a $2D$ system below T_c in the ultra-quantum limit ($\nu<1$), when the average distance between Cooper pairs $\overline{R} > \sqrt{2/N_S}$ is much longer than the diameter l_H of a pair, differs significantly from a macroscopically coherent superconducting state in traditional superconductors with strongly overlapping wave functions of Cooper pairs[37,41] which display infinitely large conductivity ($\sigma \to \infty$) and undamped Meissner currents below the thermodynamic ($H_c(T)$) or the lower critical [$H_{c1}(T)$] magnetic fields for type I or type II superconductors, respectively.

Local triplet Cooper pairs in a $2D$ system at $T<T_c$ under the conditions of the FQHE do not overlap and behave in spin-independent transport phenomena almost in the same way as unpaired ''magnetized'' electrons. This explains zero values of the diagonal components of the magnetoresistance ($R_{xx}=0$) and conductivity ($\sigma_{xx}=0$) tensors in the absence of scattering at defects in the regions of H and N_S, where the Hall (nondiagonal) component of the resistance ($R_{xy}=R_H$) and conductivity ($\sigma_{xy}=\sigma_H$) have a plateau corresponding to discrete quantum values $\sigma_H=1/R_H=e^2\nu/2\pi\hbar$.

Thus, coupled Cooper pairs can coexist with uncoupled electrons in $2D$ systems at $T<T_c$ if the electron–electron attraction (due to the interaction with SAW and surface $2D$ plasmons) is strong enough ($\alpha \geqslant 1, \beta \geqslant 1$). For such a state, Halperin[8] constructed a mixed wave function Ψ of the Laughlin type,[2] which is antisymmetric relative to permutations of unpaired electrons and electron within each pair and symmetric relative to permutations of pairs. Such a multielectron wave function of the ground state leads to singularities in R_H and σ_H for filling factors ν satisfying the Halperin relation (1).

If a $2D$ system contains N_p coupled electron pairs and N_e uncoupled electrons (for the total number of electrons $N_S=2N_p+N_e$ per unit area), the requirement that the electrons and pairs must occupy the same region of $2D$ space leads to the following relation[8] between N_p and N_e:

$$\frac{N_p}{N_e}=\frac{2m-r}{p-2r}, \tag{27}$$

where m is odd and p is even, while the number r may have any parity.

For $T \to 0$, when all electrons are coupled into Cooper pairs and $N_e=0$, relation (27) implies that $p=2r$ so that $\nu=2/r$ if $r \neq 2m$ in accordance with (1). For odd values of $r=(2n+1)$, this corresponds to the results of numerous experiments on observation of the FQHE[5–7] for the following values of filling factor taking into account the electron–hole symmetry of the perturbation spectrum:

$$\nu=\frac{2}{2n+1}; \quad \nu=\frac{2n-1}{2n+1}\,(n=1,2,3,\ldots). \tag{28}$$

Even values of $r=4n$, which rule out the case when $r=2(2n+1)$, correspond to simple fractions $\nu=1/2n$ with even denominators that have not been observed as yet (see Ref. 10).

On the contrary, at $T \to T_c$, when the number of coupled Cooper pairs $N_p \to 0$, it follows from (27) that $r=2m \equiv 2(2n+1)$. In this case, the filling factor (1) for any (even) values of p is equal to $\nu=1/m \equiv 1/(2n+1)$, i.e., it is reduced to simple Laughlin fractions with odd denominators as expected.[2]

However, not all values of ν from (1) can be realized in the case of Cooper pairing of $2D$ electrons since the relative numbers of free and coupled electrons

$$\nu_e \equiv \frac{N_e}{N_e+2N_p}=\frac{p-2r}{4m+p-4r};$$

$$\nu_p \equiv \frac{2N_p}{N_e+2N_p}=\frac{2(2m-r)}{4m+p-4r} \tag{29}$$

in the temperature range $0 \leqslant T \leqslant T_c$ depend on T and vary from $\nu_e=0$ and $\nu_p=1$ at $T=0$ to $\nu_e=1$ and $\nu_p=0$ at $T=T_c$, the total number of particles being conserved ($\nu_e+\nu_p=1$), which imposes certain limitations on the indices m, p, and r.

For example, all values of $r=p/2$ (except $r=2m$) correspond to the values $\nu_e=0$ and $\nu_p=1$ which are realized only for $T \to 0$. According to Eq. (1), $\nu=2/r=4/p$ can contain in this case fractions with even denominators ($\nu=1/2$ for $p=2r=8$, $\nu=1/4$ for $p=2r=16$, and so on). On the contrary, the values of $r=2m$ (but $r \neq p/2$) correspond to $\nu_e=1$ and $\nu_p=0$ at $T \geqslant T_c$. But since the values of ν, ν_e, and ν_p must be positive at $T>$ (but $T<T_c$), we must confine our analysis, in accordance with (1) and (29), to the values of r and p (for a fixed m) which satisfy the inequalities

$$r<p/2; \quad r<2m; \quad r<m+p/4; \quad r<\sqrt{mp}. \tag{30}$$

For example, for $m=3$ at $T=0$, when $\nu_e=0$ and $\nu_p=1$, we find from (1) that $\nu=2/3$ for $p=2r=6$, $\nu=1/2$ for $p=2r=8$, and $\nu=2/5$ for $p=2r=10$, while at the point $T=T_c$, when $\nu_e=1$ and $\nu_p=0$, we obtain $\nu=1/3$ for $r=6$ for any p (except $p=12$). If we take into account the fact that the relative number ν_p of paired electrons, which can be regarded as an ''order parameter,'' decreases monotonically with increasing T (probably, according to a law close to the temperature dependence of the gap width in the BCS theory),[41] we can construct the following hierarchy of frac-

tional values of ν for $m=3$ for various values of T at which the relevant singularities in R_H must be observed, starting from low values of T:

$\nu_p=5/6$ ($\nu_e=1/6$): $\nu=2/11$ for $r=1$ and $p=4$;

$\nu_p=4/5$ ($\nu_e=1/5$): $\nu=5/7$ for $r=2$ and $p=6$;

$\nu_p=2/3$ ($\nu_e=1/3$): $\nu=3/5$ for $r=2$ and $p=8$ or $\nu=3/7$ for $r=4$ and $p=10$;

$\nu_p=1/2$ ($\nu_e=1/2$): $\nu=4/7$ for $r=1$ and $p=12$, $\nu=1/2$ for $r=2$ and $p=12$, $\nu=4/9$ for $r=3$ and $p=12$, $\nu=5/9$ for $r=4$ and $p=12$ or $\nu=4/11$ for $r=4$ and $p=20$ or for $r=5$ and $p=12$.

Similarly, we can obtain the sets of ν for different values of ν_p (i.e., different values of T) for other values of m also. For example, for $m=5$ at $T=0$, when $\nu_p=1(\nu_e=0)$ and $r=p/2$, we obtain, in addition to the fractions listed above ($\nu=2/3$, 1/2 and 2/5), the fractional values $\nu=1/3$ for $p=2r=12$, $\nu=2/7$ for $p=2r=14$, $\nu=1/4$ for $p=2r=16$, and $\nu=2/9$ for $p=2r=18$. At $T=T_c$, when $\nu_p=0$ ($\nu_e=1$), we obtain $\nu=1/5$ for $r=10$ for any p (except $p=20$).

For intermediate temperatures ($0<T<T_c$) for $m=5$, we obtain from (1) and (29) [together with (30)] the following hierarchy:

$\nu_p=4/5$ ($\nu_e=1/5$): $\nu=5/9$ for $r=2$ and $p=8$;

$\nu_p=3/4$ ($\nu_e=1/4$): $\nu=2/9$ for $r=2$ and $p=20$ or $\nu=4/11$ for $r=4$ and $p=12$;

$\nu_p=2/3$ ($\nu_e=1/3$): $\nu=3/5$ for $r=0$ and $p=10$ or $\nu=3/7$ for $r=2$ and $p=12$;

$\nu_p=1/2$ ($\nu_e=1/2$): $\nu=4/11$ for $r=1$ and $p=20$, $\nu=2/9$ for $r=8$ and $p=20$ or $\nu=2/5$ for $r=0$ and $p=20$.

For $m=7$ at $T=0$, when $\nu_p=1(\nu_e=0)$, we obtain the additional fractions $\nu=2/11$ for $p=2r=22$, $\nu=1/6$ for $p=2r=24$, and $\nu=2/13$ for $p=2r=26$, while at $T=T_c$, when $\nu_p=0$ ($\nu_e=1$), we obtain $\nu=1/7$ for $r=14$ and any p (except $p=28$).

In the temperature range $0<T<T_c$, for $m=7$ we obtain, in accordance with (1), (29), and (30),

$\nu_p=4/5$ ($\nu_e=1/5$): $\nu=5/11$ for $r=2$ and $p=10$;

$\nu_p=3/4$ ($\nu_e=1/4$): $\nu=2/7$ for $r=8$ and $p=20$;

$\nu_p=2/3$ ($\nu_e=1/3$): $\nu=2/5$ for $r=2$ and $p=12$, $\nu=1/3$ for $r=2$ and $p=16$, $\nu=3/11$ for $r=4$ and $p=18$ or $\nu=1/5$ for $r=8$ and $p=22$;

$\nu_p=1/2$ ($\nu_e=1/2$): $\nu=1/4$ for $r=2$ and $p=28$, $\nu=2/9$ for $r=4$ and $p=28$, $\nu=1/5$ for $r=6$ and $p=28$ or $\nu=1/6$ for $r=10$ and $p=28$.

If we carry out additional antisymmetrization of the Halperin wave function[8] for a system of coupled electron pairs relative to transpositions of electrons from different pairs and take into account the fact that transposition of electrons within a pair are immaterial in the calculation of the ground-state energy, we can exclude the fractional values of ν with even denominators, which are not observed in experiments. In this case, the index p determining the double number of flux quanta per pair is given by

$$p=2(2s+u+w), \tag{31}$$

where s and w are odd numbers corresponding to exchange correlations for all possible transpositions of electrons, u is an arbitrary integer ($u\geqslant 0$), and the even number $2u$ corresponds to the symmetric of the wave function under transpositions of the centers of mass of the pairs.

If we assume that the energy minimum corresponds to the minimum value of $u=0$ (see Ref. 8), so that transpositions of pairs are unimportant, the admissible value of the index p are

$$p=2[2(2l+1)+(2k+1)]; \quad l,k=0,1,2,3,..., \tag{32}$$

or $p=2(2n+1)=6,10,14,\ldots$ (for $n=1,2,3,\ldots$). In this case, relation (1) leads to fractional values of filling factor with odd denominators only: $\nu=q/(2n+1)$, $q\geqslant 1$.

6. CONCLUSION

Thus, the hypothesis on possible Cooper pairing of $2D$ electrons in strong QMF due to the EPI (which is independent of the effective mass m_c^* and the density of states), which was formulated in Ref. 18, allows us to explain virtually all experimentally observed singularities of the Hall resistance R_H in semiconducting heterostructures under the FQHE conditions[1,5–7,43,59] on the basis of the ''mixed'' wave function of coupled electron pairs and unpaired electrons in the ultra-quantum limit proposed by Halperin.[8]

The necessary condition for Cooper pairing is a strong attraction between electrons, that is capable of overcoming the screened Coulomb repulsion. Such an attraction cannot be ensured by deformation-type EPI with bulk acoustic and optical phonons in semiconducting GaAs and Si crystals.[44,45] For this reason, the effect of Cooper pairing was in fact disregarded and was not taken into account in an analysis of the properties of $2D$ semiconducting systems in QMF and of the new Laughlin quantum $2D$ liquid[2,60] (except in Refs. 27 and 61).

However, the fact that SAW ($2D$ phonons)[46,47] and surface plasmons[31] whose interaction with $2D$ electrons in surface layers can be much more effective than with bulk $3D$ phonons can exist at the interfaces (heterojunction) in

layered MIS systems and heterojuctions has not been taken into consideration by any author. The existence of such surface phonon modes in semiconducting $2D$ systems is confirmed in optical experiments on Raman scattering (see, for example, Refs. 62–64). Here we assumed that the interaction with these ''interfacial'' modes ensures a strong attraction and Cooper pairing of electrons in $2D$ systems; an indirect evidence of this effect is the superconductivity observed in a Si–MIS structure at $T<1$ K.[28]

The size of coupled Cooper pairs formed under the condition $\nu=k_F^2 l_H^2<1$ is of the order of the magnetic length l_H and is smaller than the average distance $\overline{r}>k_F^{-1}$ between pairs. As a result, a macroscopic coherent quantum superconducting condensate cannot be formed in a $2D$ system under the FQHE conditions in contrast to traditional superconductors with strongly overlapping wave functions of Cooper pairs.[41] Local pairs behave in transport processes like ''magnetized'' electrons with the wave functions $\Psi_0(x)\propto\exp(-x^2/2l_H^2)$, determining the zero values of the longitudinal conductivity components $\sigma_{xx}=\sigma_0/(1+\omega_c^2\tau^2)$, where $\sigma_0=e^2N_S\tau/m_e^*$, as well as of the resistivity $\rho_{xx}=\sigma_{xx}/(\sigma_{xx}^2+\sigma_H^2)$ for infinitely long relaxation time ($\tau\to\infty$) and for $\sigma_H=1/R_H=e^2\nu/2\pi\hbar$ in contrast to the superconducting state with $\sigma\to\infty$.

A transition to the superconducting state can occur in weaker magnetic fields when $\nu=k_F^2 l_H^2>4\pi$ so that each flux quantum corresponds to a large number of electrons, and the size of Cooper pairs ($\sim l_H$) becomes larger than the average distance between them ($\overline{r}\approx\sqrt{2/N_S}$ for $T\to0$), i.e., a coherent superconducting condensate of Cooper pairs can be formed.

Finally, the magnetic flux quanta screened by Meissner superconducting currents of a macroscopically large number of Cooper pairs in the limit $\nu\to\infty$ are transformed into $2D$ Abrikosov vortices carrying a half-integral magnetic flux quantum $\varphi_s=\varphi_0/2$.

Integral values of Hall conductivity $\sigma_H=c\alpha_0 n$ (where $\alpha_0=e^2/2\pi\hbar c\simeq1/137$ is the fine-structure constant) under the IQHE conditions[17] are due to a finite degeneracy of Landau levels in $2D$ systems ($N_L=(1/2)\pi l_H^2=H/\varphi_0$) so that the filling (depletion) of the succeeding LL upon a change in H or N_S starts for $T\to\infty$ only after the previous LL is filled (depleted) completely. Such almost ideal $R_H=1/\sigma_H$ steps were observed by Laughlin[65] at $T=8$ K.

On the other hand, fractional values of $\sigma_H=c\alpha_0/m$ under the FQHE conditions[1] are due to the ''rigidity'' of the Laughlin wave function[2] describing a strongly correlated incompressible $2D$ liquid. The number m is magnetic flux quanta in such a ''structurized'' liquid per electron in the ground state is strictly fixed and remains constant until the increasing (decreasing) magnetic field H attains a ''critical'' value for which the total magnetic flux $\Phi=HS$ through the $2D$ system corresponds to the number φ_0 of quanta per electron that has increased (decreased) by two. It can be stated that a ''potential barrier'' preventing a change in the number of flux quanta in the ground state exists in the region of intermediate fields. It was proved by Laughlin,[2] however, that excited states corresponding to the creation or annihilation of solitary quanta φ_0 can be formed, which is accompanied by a spatial redistribution of electron density corresponding to the emergence of an additional fractional charge $e^*=e/m$ (i.e., a quasiparticle or quasi-hole with the effective charge $\pm e^*$) in a region of size of the order of l_H. For example, dissipative Hall current (for zero transport current in the limit $\omega_c\tau\to\infty$) generates additional magnetic flux quanta (entering) at one end of the $2D$ system, which drift in the crossed electric **E** and magnetic **H** fields (together with ''screening'' quasiparticles having a fractional charge e^*) to the opposite end, where they are annihilated. It should be noted that Abrikosov quantum vortices in the resistive state of ideal type II superconductors in the absence of pinning centers in magnetic fields $H_{c1}<H<H_{c2}$ propagate in a similar way.[37]

Thus, there is no basic difference between fractional and integral quantum Hall effects in $2D$ systems and type II superconductors in view of the universal gauge invariance of quantum-mechanical systems which was pointed out by Laughlin[66] and Halperin[67] even prior to the discovery of the FQHE.

According to Halperin's relation (1), R_H singularities can be observed in principle at $T<T_c$ for values of the filling factor $\nu=1/2n$ and $\nu=1-1/2n$ ($n=1,2,3,\ldots$) along with singularities of R_H and σ_H for fractional values of $\nu=q/(2n+1)$ with odd denominators and with $q\geqslant1$ but with $q<(2n+1)$ under the conditions when Cooper pairing in the $2D$ system dominates over the exciton pairing, for example, due to the suppression of screened Coulomb repulsion upon an increase in the magnetic field H in the ultraquantum limit[5–7] (see Figs. 3 and 4). However, the condition of symmetrization of the wave function for Cooper pairs allows us to exclude fractions with even denominators. On the whole, the assumption on Cooper pairing of $2D$ electrons in combination with the superposition of coupled electron pairs and free electrons, which is described by the Halperin variational wave function,[8] makes it possible to obtain a richer set of quantum singularities of the Hall resistance R_H and conductivity σ_H than other models of the FQHE.[11,12,15,59,60]

The author expresses his sincere gratitude to M. Ya. Valakh for qualified consultations on the physical properties of semiconductors of the GaAs and Si type, to A. L. Kasatkin for a discussion of problems associated with applicability of the self-consistent field approximation and the Bethe–Salpeter equation for describing Cooper pairing in $2D$ metals in QMF, to V. M. Loktev, S. M. Ryabchenko, and V. B. Timofeev for fruitful and stimulating discussions, and to E. G. Galkina, A. E. Pashitskii, and V. I. Pentegov for computer calculations and assistance in preparing the manuscript.

This paper was written to commemorate the 80th anniversary of Boris Ieremievich Verkin, who was the creator and the first Director of a unique research center, viz., the Institute of Low Temperature Physics and Engineering of the National Academy of Sciences of the Ukraine. The work is devoted to problems which were objects of continued interest to B. I. Verkin, viz., phenomena in strong magnetic fields at low temperatures and the superconductivity mechanisms (Cooper pairing) in low-dimensional systems.

*E-mail: pashitsk@iop.kiev.ua

[1] D. C. Tsui, H. L. Störmer, and A. C. Gossard, Phys. Rev. Lett. **48**, 1559 (1982).
[2] R. B. Laughlin, Phys. Rev. Lett. **50**, 1395 (1983); Science **242**, 525 (1988).
[3] R. Justrow, Phys. Rev. **98**, 1479 (1955).
[4] Yu. A. Bychkov, S. V. Iordanskii, and G. M. Eliashberg, Pis'ma Zh. Éksp. Teor. Fiz. **33**, 152 (1981) [JETP Lett. **33**, 143 (1981)].
[5] H. L. Störmer, A. Chang, and D. C. Tsui *et al.*, Phys. Rev. Lett. **50**, 1953 (1983).
[6] E. F. Mendez, M. Heiblum, L. L. Chang, and L. Esaki, Phys. Rev. B **28**, 4886 (1983).
[7] A. M. Chang, P. Berglund, and D. C. Tsui *et al.*, Phys. Rev. Lett. **53**, 997 (1984).
[8] B. I. Halperin, Helv. Phys. Acta **56**, 75 (1983).
[9] R. Mort and B. I. Halperin, Phys. Rev. B **33**, 2221 (1986).
[10] B. I. Halperin, P. A. Lee, and N. Read, Phys. Rev. B **47**, 7312 (1993).
[11] F. Wilczek, *Fractional Statistics and Anyon Superconductivity*, World Scientific, Singapore (1990).
[12] A. Lerda, *Anyons*, Springer-Verlag (1992).
[13] J. G. Bednorz and K. A. Müller, Z. Phys. B: Condens. Matter **84**, 189 (1986).
[14] D. Nelson, M. Wittinham, and T. George (Eds.), *High-Temperature Superconductors* (Russian translation), MIR, Moscow (1988).
[15] J. K. Jain, Phys. Rev. Lett. **63**, 199 (1989).
[16] S. L. Sondhi, A. Karlhede, S. A. Kivelson, and E. H. Rezayi, Phys. Rev. B **47** (1993).
[17] K. von Klitzing, C. Dorda, and M. Pepper, Phys. Rev. Lett. **45**, 494 (1980).
[18] A. L. Kasatkin and E. A. Pashitskii, Ukr. Fiz. Zh. **22**, 467 (1977).
[19] T. Maniv, A. I. Rom, I. D. Vagner, and P. Wyder, Phys. Rev. B **46**, 8360 (1992).
[20] A. R. Rajagopal and R. Vasudevan, Phys. Lett. **20**, 585 (1966); **23**, 539 (1966).
[21] L. Gunter and L. W. Gruenberg, Solid State Commun. **4**, 329 (1966).
[22] L. W. Gruenberg and L. Gunter, Phys. Rev. **176**, 606 (1968).
[23] L. P. Gor'kov and A. G. Lebed', J. Phys. (Paris) **43**, L433 (1984).
[24] A. G. Lebed', Pis'ma Zh. Éksp. Teor. Fiz. **44**, 89 (1986) [JETP Lett. **44**, 114 (1986)].
[25] N. Dupuis, G. Montambaux, and C. A. R. Sa de Melo, Phys. Rev. Lett. **70**, 2613 (1993).
[26] J. E. Grabner and M. Robbins, Phys. Rev. Lett. **36**, 422 (1976).
[27] F. D. M. Haldane and E. Rezayi, Phys. Rev. Lett. **60**, 956 (1988); **61**, 1985 (1988).
[28] D. Simonyan, S. V. Kravchenko, M. P. Sarachik, and V. M. Pudalov, Phys. Rev. Lett. **79**, 2304 (1997).
[29] P. Phillips, S. Knysh, and D. Davidovich, Nature **395**, 253 (1998).
[30] T. Ando, A. Fowler, and F. Stern, *Electronic Properties of Two-dimensional Systems*, American Physical Society, New York (1982).
[31] E. A. Pashitskii, Éksp. Teor. Fiz. **56**, 662 (1969) [Sov. Phys. JETP **29**, 362 (1969)].
[32] H. Fukuyama, P. M. Platzman, and P. W. Anderson, Phys. Rev. B **19**, 5211 (1979).
[33] P. M. Lilly, K. B. Cooper, J. P. Eisenstein *et al.*, Preprint cond-mat/9808227.
[34] A. A. Koulakov, M. M. Fogler, and B. I. Shklovskii, Phys. Rev. Lett. **76**, 499 (1996).
[35] R. Moessner and J. T. Chalker, Phys. Rev. B **54**, 5006 (1996).
[36] M. M. Fogler and A. A. Koulakov, Phys. Rev. B **55**, 9326 (1997).
[37] P. de Gennes, *Superconductivity of Metals and Alloys*, New York (1966).
[38] L. D. Landau and E. M. Lifshitz, *Quantum Mechanics* [in Russian], Nauka, Moscow (1974).
[39] G. Kido, K. Komorita, H. Katayama-Yoshida, and T. Takahashi, J. Phys. Chem. Solids **52**, 465 (1991).
[40] C. M. Fowler, B. I. Freeman, W. L. Hults *et al.*, Phys. Rev. Lett. **68**, 534 (1992).
[41] J. R. Schrieffer, *The Theory of Superconductivity*, Benjamin, New York, 1964.
[42] V. F. Gantmakher and I. B. Levinson, *Scattering of Charge Carriers in Metals and Semiconductors* [in Russian], Nauka, Moscow (1984).
[43] E. I. Rashba and V. B. Timofeev, Fiz. Tekh. Poluprovodn. (St. Petersburg) **20**, 977 (1986) [Sov. Phys. Semiconductors **20**, 617 (1986)].
[44] M. Cardona, H. Grimsditsch, and D. Olego, in *Light Scattering in Solids* (edited by J. L. Birman, H. Z. Cummins, and K. K. Rebane), Plenum Press, New York (1979).
[45] P. Vogl and W. Potz, Phys. Rev. B **24**, 2025 (1981).
[46] L. D. Landau and E. M. Lifshitz, *Theory of Elasticity* [in Russian], Nauka, Moscow (1965).
[47] A. Oliner (Ed.), *Acoustic Surface Waves* Springer, Heidelberg (1978).
[48] M. Cohen, H. Gladstone, M. Jensen, and J. Schrieffer, in *Superconductivity of Semiconductors and Transition Metals*, (Ed. by R. Parks), Marcel–Dekker, New York (1969).
[49] E. A. Pashitskii and A. S. Shpigel, Ukr. Fiz. Zh. **23**, 669 (1978).
[50] A. A. Abrikosov, L. P. Gor'kov, and I. E. Dzyaloshinskii, *Methods of Quantum Field Theory in Statistical Physics* [in Russian], Fiz.-mat. Lit., Moscow (1962).
[51] E. M. Lifshitz and L. P. Pitaevskii, *Relativistic Quantum Theory* [in Russian], Part 2, Nauka, Moscow (1971).
[52] Yu. A. Bychkov and E. I. Rashba, Pis'ma Zh. Éskp. Teor. Fiz. **38**, 195 (1983) [JETP Lett. **38**, 229 (1983)].
[53] Y. Kuramoto, Phys. Rev. Lett. **50**, 866 (1983).
[54] E. E. Mendez, L. L. Chang, and C. A. Chang *et al.*, Surf. Sci. **142**, 215 (1984).
[55] Yu. A. Bychkov, L. P. Gor'kov, and I. E. Dzyaloshinskii, Zh. Éksp. Teor. Fiz. **50**, 738 (1966) [Sov. Phys. JETP **23**, 489 (1966)].
[56] I. E. Dzyaloshinskii and A. I. Larkin, Zh. Éksp. Teor. Fiz. **61**, 791 (1971) [Sov. Phys. JETP **34**, 422 (1971)].
[57] L. P. Gor'kov, and I. E. Dzyaloshinskii, Zh. Éksp. Teor. Fiz. **67**, 397 (1974) [Sov. Phys. JETP **40**, 198 (1974)].
[58] A. T. Zheleznyak, V. M. Yakovenko, and I. E. Dzyaloshinskii, Phys. Rev. B **55**, 3200 (1997).
[59] T. Chakraborty and P. Pietilainen, *The Quantum Hall Effects: Integral and Fractional*, Springer-Verlag (1995).
[60] S. Das Sarma and Aron Pinczuk (Eds), *Perspective in Quantum Hall Effects: Novel Quantum Liquids in Low-Dimensional Superconductor Structures*, J. Wiley and Sons (1996).
[61] G. Moore and N. Read, Nucl. Phys. B **360**, 362 (1991).
[62] M. Nakayama, M. Ishida, and N. Sano, Phys. Rev. B **38**, 6348 (1988).
[63] Z. V. Popovich, M. Cardona, E. Richter *et al.*, Phys. Rev. B **41**, 5904 (1990).
[64] C. Trallero-Ginev, F. Garcia-Moliner, V. R. Velasco, and M. Cardona, Phys. Rev. B **45**, 11944 (1992).
[65] G. Ebert, K. V. Klitzing, C. Probst, and K. Ploog, Solid State Commun. **44**, 95 (1982).
[66] R. B. Laughlin, Phys. Rev. B **23**, 5632 (1981).
[67] B. I. Halperin, Phys. Rev. B **25**, 2185 (1982).

Translated by R. S. Wadhwa

The ground state of the ''frozen'' electron phase in two-dimensional narrow-band conductors with a long-range interelectron repulsion. Stripe formation and effective lowering of dimension

A. A. Slutskin, V. V. Slavin, and H. A. Kovtun

*B. Verkin Institute for Low Temperature Physics and Engineering, National Academy of Sciences of Ukraine, 47, Lenin Ave., 310164, Kharkov, Ukraine**

(Submitted March 29, 1999)
Fiz. Nizk. Temp. **25**, 936–943 (August–September 1999)

In narrow-band conductors a weakly screened Coulomb interelectron repulsion can supress narrow-band electrons' hopping, resulting in formation of a ''frozen'' electron phase which differs principally from any known macroscopic self-localized electron state including the Wigner crystal. In a zero-band-width limit the ''frozen'' electron phase is a classical lattice system with a long-range interparticle repulsion. The ground state of such systems has been considered in the case of *two* dimensions for an *isotropic* pair potential of the mutual particle repulsion. It has been shown that particle ordering into stripes and effective lowering of dimension resides universally in the ground state for any physically reasonable pair potential and for any geometry of the conductor lattice. On the basis of this fact a rigorous general procedure for describing the ground state fully has been formulated. Arguments have been adduced that charge ordering into stripes in high-T_c superconductors testifies to the presence of a ''frozen'' electron phase in these systems. © *1999 American Institute of Physics.* [S1063-777X(99)01808-3]

1. INTRODUCTION

High-T_c superconductors studies have caused a surge of interest in the properties of narrow-band layered and two-dimensional (2D) conductors. An important consequence of the layerness is substantial weakening of the screening of a Coulomb interaction between the charge carriers. (The screening radius cannot, under any circumstances, be less than the interlayer distance). In addition, in layered conductors it is possible to well separate the charge carriers (for definiteness, we consider them electrons) from the donors, so that the mean energy, u_{ee}, of the long-range interelectron repulsion prevails over the energy of an electron attraction to the donors. Under these conditions it is the mutual repulsion of narrow-band electrons that can suppress their tunneling between the equivalent orbits of the conductor lattice, resulting in formation of a ''frozen'' electron phase (FEP) which differs principally from any known macroscopic self-localized electron state including the Wigner crystal.[1] The FEP occurs when the electron bandwidth, t, is less than $\delta u = (a/r_{ee})u_{ee}$, where δu is the typical change in the narrow-band electron Coulomb energy in electron hopping, a is the range of hopping, r_{ee} is the mean electron separation. The high-T_c cuprates, grain boundaries of polycrystal electroceramic materials,[2] as well as some art 2D conductors[3–5] appear to be most favorable for 2D FEP coming to existence.

The macroscopic behavior of the 2D FEP is rather unconventional. Its distinctive features are rooted in properties of its ground state (GS) at $t \ll \delta u$. In the limit $t/\delta u \to 0$ the GS of the 2D FEP is much the same as that of other 2D lattice systems with a long-range interparticle repulsion. (An example is an ensemble of adsorbed atoms strongly interacting with their substrate and mutually repelling each other[6]). As far as we know, neither the thermodynamics nor the GS of such systems have been studied adequately. Here we offer a unified approach to the description of the GS of the 2D zero-bandwidth FEP (and similar lattice systems) with an *isotropic* pair potential of the interelectron repulsion, $v(r)$ (r is the distance between interacting electrons). The key point of our consideration is a new phenomenon—a *zero-temperature effective lowering of dimension* (LOD)—which we have revealed to underlie (*despite the pair potential isotropy*) the main GS properties of the 2D FEP for: i) arbitrary arrangement of the sites which can be occupied by electrons provided that the sites constitute a primitive lattice (it is called the host lattice below); ii) any filling factor, $\rho = N/\mathcal{N}$ ($N \to \infty$ and $\mathcal{N} \to \infty$ are the total numbers of the electrons and the host-lattice sites, respectively); iii) any physically reasonable $v(r) > 0$. We take the term LOD to mean that the GS of the 2D FEP is a set of different effective 1D FEP whose ''particles'' are periodic stripes on the lattice of the 2D conductor. For each 1D system of the set there is its own ρ interval where this 1D FEP represents the 2D one, the whole range, $0 \leqslant \rho \leqslant 1$, comprising all the intervals. The LOD enables us to offer a rigorous analytical procedure for the 2D FEP GS description, using the exact results of the general theory of the 1D lattice systems with a long-range interparticle repulsion.[7–9]

2. HAMILTONIAN. SIMPLE CRYSTALS

The Hamiltonian, $\mathcal{H}$, of the system under consideration has the form

$$\mathcal{H}\{n(\mathbf{r})\} = \frac{1}{2}\sum_{\mathbf{r}\neq\mathbf{r}'} v(|\mathbf{r}-\mathbf{r}'|)n(\mathbf{r})n(\mathbf{r}'), \qquad (1)$$

 © 1999 American Institute of Physics

where $\mathbf{r}=m_1\mathbf{a}_1+m_2\mathbf{a}_2$ are radius vectors of the host-lattice sites, $m_{1,2}$ are integers, $\mathbf{a}_{1,2}$ are host-lattice primitive translation vectors (PTVs); the occupation numbers of the host-latice sites, $n(\mathbf{r})=0$ or 1, are microscopic variables;[1)] the sum is taken over the whole host lattice. The pair potential is assumed to be an everywhere convex function of the form $v(r)=\tilde{v}(r)/r$, where the function $\tilde{v}(r)$ depends on the character of the screening medium and its position with respect to the 2D FEP. In any case $\tilde{v}(r)$ tends to zero as r^{-2} or faster when $r\to\infty$; $\tilde{v}(0)=e^2/\kappa$ (e is the electron charge, κ is the dielectric permittivity). Otherwise, $\tilde{v}(r)$ can be reckoned as arbitrary: as will be shown below, its specific form is immaterial to our approach.

Among the GS configurations $\{n(\mathbf{r})\}$ with different ρ the *simplest* ones are 2D crystals with one electron per cell (''S-crystals'').[2)] Their inverse ρ values make up an infinite set of integers $Q_j=|\det\{m^j_{\kappa\lambda}(\mathbf{a}_1,\mathbf{a}_2)\}|$, where j indexes S-crystals, the integers $m^j_{\kappa\lambda}(\kappa,\lambda=1,2)$ are components of S-crystal PTVs in the $\mathbf{a}_\lambda$ basis; Q_j is the jth S-crystal elementary-cell area measured in units of that of the host lattice, $\sigma_0=|\mathbf{a}_1\times\mathbf{a}_2|$.

Our strategy is to derive the full description of the GS for any $\mathbf{a}_{1,2}$, starting with consideration of small vicinities of $\rho=1/Q_j$. Since specific $m^j_{\kappa\lambda}$ values are irrelevant to this reasoning, we drop the index j at Q and at other characteristics of the S-crystals for a while.

Due to the discreteness of the system with the Hamiltonian (1) a macroscopically small change, $\delta\rho$, in ρ ($\delta\rho\to 0$, $N^{1/2}|\delta\rho|\to\infty$ when $N\to\infty$) produces only *isolated defects* in an S-crystal, the space structure of the defects essentially depending on whether they result from an increase or a decrease in ρ. This fact is expressed by the identity

$$E_g(N\pm|\delta N|,\mathcal{N}\pm|\delta\mathcal{N}|)-E_g(N,\mathcal{N}) = \pm\mu_\pm|\delta N|\mp P_\pm|\delta\mathcal{N}|, \tag{2}$$

where E_g is the GS energy, δN and $\delta\mathcal{N}$ are changes in N and $\mathcal{N}$ producing $\delta\rho$. The proportionality coefficients, $\mu_-<\mu_+, P_-<P_+$, are the values of the chemical potential, μ, and the pressure, P, which are the endpoints of the μ and P intervals of S-crystal existence. They are determined by the energies of formation of corresponding defects. Thus, in a certain vicinity of $\rho=1/Q$ the GS is bound to be a superstructure of the defects. Our next step is to find them.

3. ZERO-DIMENSIONAL DEFECTS AND THEIR COALESCENCE

Adding one electron to or removing from an S-crystal results in the formation of a zero-dimensional defect, ''+defecton'' or ''−defecton'', respectively. One can be inclined to think that δN should be identified exactly with the total number of $\pm$defectons spatially separated, $\pm\mu_\pm$ being simply the energy of $\pm$defecton formation, $\epsilon_\pm$. However, this seemingly evident statement is actually incorrect due to a *coalescence* of defectons of the same ''sign''. In other words, if the number, $|\nu|$, of S-crystal electrons removed ($\nu<0$) or added ($\nu>0$) is more than 1, a *bound state* of $|\nu|$ $\pm$defectons arises whose energy is less than $|\nu|\epsilon_\pm$. We have revealed the coalescence by computation, using a ''dipole'' description of the GS with $\nu=\pm1,\pm2,...$, which we have specially worked out for this purpose. The dipole approach offers a clear view of how the defectons' bound state arises despite the fact that the defectons of the same sign repel each other, being widely spaced.

At $\nu\neq0$ a perturbed S-crystal is formed where, in addition to electrons, placed at host-lattice sites in the interstices of the S-crystal ($\nu>0$) or empty S-crystal sites, ''holes,'' ($\nu<0$), there are generally a certain number of S-crystal electrons shifted from their native S-crystal sites. The latter can be considered as ''antiparticles'' whose charge is equal to the electron one in magnitude but is opposite in sign, a pair ''an electron shifted by a vector $\xi+$, its antiparticle located at an S-crystal site $\mathbf{r}$'' being the ''$\mathbf{r}$, ξ-dipole.'' Thus, the perturbation of the *S*-crystal can be envisioned as an ensemble consisting of several dipoles and $|\nu|$ interstitial particles/holes (IP/Hs). The dipoles interact with the IP/Hs and with each other. The energy of interaction between an IP/H (at $\mathbf{r}=0$) and $\mathbf{r}$, ξ-dipole is $u_\xi(\mathbf{r})=\text{sign }\nu(v(|\mathbf{r}-\xi|)-v(|\mathbf{r}|))\equiv\text{sign }\nu\hat{\Delta}_\xi v(|\mathbf{r}|)$; the energy of interaction between $\mathbf{r}$, ξ, and $\mathbf{r}'$,ξ'-dipole is $u_{\xi,\xi'}(\mathbf{r}-\mathbf{r}')=\hat{\Delta}_\xi\hat{\Delta}_{\xi'}v(|\mathbf{r}-\mathbf{r}'|)$. The IP/Hs, in turn, undergo a mutual repulsion and are exposed to an ''external'' field, $u(\mathbf{r})$, which is equal to $-2u_0$ for holes (here and further on u_{ee} of the S-crystal is denoted by u_0), and for IPs it is the field produced at a point $\mathbf{r}$ by all electrons of the S-crystal. In these terms the change in the GS energy at a given ν, $U_{\rm GS}(\nu)$, takes the form

$$U_{\rm GS}(\nu)=\min(V_{\rm rep}+U_d+U_{\rm exc}+U). \tag{3}$$

Here $V_{\rm rep}=\sum_{\alpha<\beta}v(|\mathbf{r}_{\alpha\beta}|)$ is the energy of the mutual repulsion of the IP/Hs; $U_d=\sum_{\alpha,i}u_{\xi_i}(\mathbf{r}_{\alpha i})$ is the energy of their interaction with the dipoles; $U_{\rm exc}=\sum_i\delta u_{\xi_i}+\sum_{i<k}u_{\xi_i,\xi_k}(\mathbf{r}_{ik})>0$ is the excitation energy of an S-crystal with n_d dipoles at $\nu=0$; $\delta u_\xi\sim u_0|\xi|^2/r_{ee}^2>0$ is the energy of formation of one dipole; $U=\sum_\alpha u(\mathbf{r}_\alpha)$ is the energy of the IP/Hs in the external field mentioned; the indices $\alpha=1,...,|\nu|$ and $i=1,...,n_d$ enumerate the IP/H radius-vectors and dipoles, respectively, n_d is the total number of the dipoles; $\mathbf{r}_{ab}\equiv\mathbf{r}_a-\mathbf{r}_b$. The minimum is taken with respect to n_d, the dipole variables, $\mathbf{r}_i$, ξ_i, and $\mathbf{r}_\alpha$. Therefore, the dipole approach allows to work with only a few discrete variables. This facilitates considerably the Monte-Carlo computer simulation of the $\pm$defectons ($U_{\rm GS}(\pm1)=\pm\epsilon_\pm$) and their coalescence at $|\nu|>1$.

The mechanism of the coalescence can be elucidated by the following heuristic arguments. The GS total dipole energy, $E_d(\nu)=U_{\rm exc}(\nu)+U_d(\nu)$, is negative, so that for any $|\nu|$ the GS space structure is determined by an interplay between negative U_d and positive $U_{\rm exc}$, $V_{\rm rep}$. The IP/H-dipole interaction gives the maximal gain in energy when *each* IP/H is embedded in a shell of four dipoles that are attracted to it, the dipoles' antiparticles forming a parallelogram of a size $\sim r_{\rm ee}\sim Q^{1,2}$ (Fig. 1). The shells of neighboring IP/Hs are bound to share some of their dipoles for $U_{\rm exc}$ (and hence n_d) to be as small as possible. This requirement can be fulfilled only when all IP/Hs are *aligned in a row*, the near-neighbor IP/Hs being shifted relative to one another by the same S-crystal PTV with the modulus $\sim r_{ee}$ (Fig. 1). In such a case $|E_d(\nu)|$ is more than the magnitude of the dipole energy of

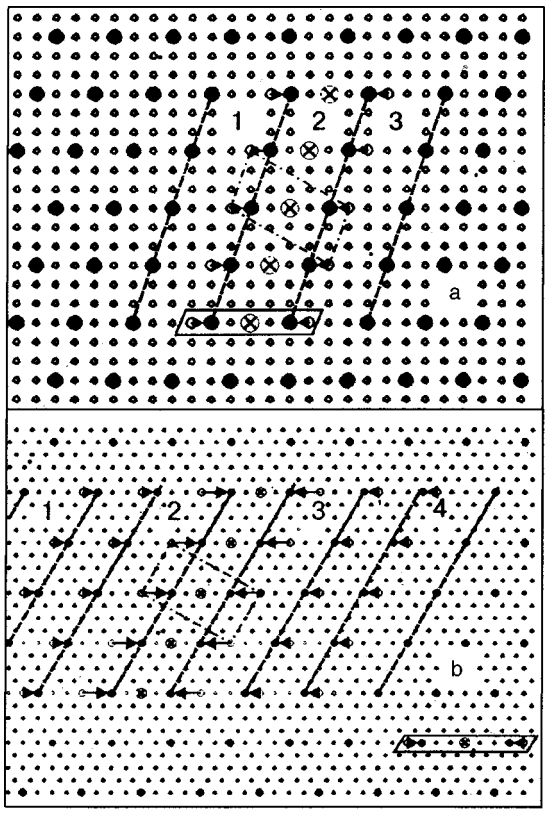

FIG. 1. The coalescence for square $(a, Q\approx 9)$ and triangular $(b, Q=16)$ host lattices $(\nu=-5)$. Here ○ denotes host-lattice sites, ●—particles; ○—antiparticles; ⊗—holes; →—dipoles; solid boxes mark off a single defecton. The shells of dipoles surrounding holes are marked off by the dash-dotted parallelograms. The dotted lines show nucleation of the elementary stripes enumerated by 1,2,... . In the case (a) boundary effects dominate the mutual repulsion of the unfinished −stripes; in the case (b) the tendency to −stripes divergence is seen. Both configurations refer to the pair potentials which meet the condition $\gamma\sim 1$.

$|\nu|$ infinitely separated defectons, $E_d^{\infty}=|\nu|E_d(\pm 1)$. The coalescence arises when the energy gain, $\Delta=|E_d(\nu)|-|E_d^{\infty}|$, exceeds $V_{\rm rep}$ of the IP/Hs aligned in the row. Since $\Delta \sim|\nu|\upsilon(r_{ee})$ this condition is met if $\upsilon(r)$ decreases not too slowly, or, more exactly, if

$$\gamma=\int_{r_{ee}}^{\infty}\upsilon(r)dr/r_{ee}\upsilon(r_{ee})\leqslant 1. \tag{4}$$

The computer simulation carried out with the model potential $\upsilon(r)\propto r^{-\beta}\exp(-r/R)$ over a wide range of the parameters, β, R, has confirmed that the condition (4) is really the criterion of the coalescence for any $|\nu|$ (and any $\mathbf{a}_{1,2}$).

Criterion (4) is for the most part fulfilled. It holds for any $\tilde{\upsilon}(r)$ (Sec. 2) such that $\tilde{\upsilon}(0)-\tilde{\upsilon}(r_{ee})\sim\tilde{\upsilon}(0)$. This case will be the focus of our attention from here on. The parameter γ becomes $\gg 1$ if $\tilde{\upsilon}(r)$ decreases substantially only for r which are exponentially large in γ. In this limit the mutual repulsion of the IP/Hs disrupts their row, and there is no coalescence, at least for sufficiently large $|\nu|$. However, in Sec. 8 it is outlined that the LOD governs the GS in this rather special case also.

4. THE LOWERING OF DIMENSION

The elementary stripes in the 2D *''frozen'' electron phase*

As follows from the aforesaid, the bound state of $|\nu|$ defectons is transformed into a periodic *stripe-like* structure with an infinite increase in $|\nu|$ (Fig. 1). It consists of elementary 1D defects which, as will be shown below, repel each other. Therefore, it is *the simplest* 1D *defects* that are expected to form the GS superstructure. An arbitrary 1D defect of such a type is a stripe of rarefaction or compression that arises when an S-crystal part adjacent to a line of electrons with some PTV, $\mathbf{d}$, is shifted as a whole relative to the other one by a host-lattice translation vector, ξ. Formation of one stripe of length L_s changes $\mathcal{N}$ by $\delta\mathcal{N}=\pm\sigma L_s$ $(\sigma=|\mathbf{d}\times\xi|$, L_s is measured in units of $|\mathbf{d}|)$. The corresponding change in energy, δE, is proportional to $\delta\mathcal{N}$:

$$\delta E/|\delta\mathcal{N}|=\varepsilon(\mathbf{d},\xi)=\sigma^{-1}\sum_{n=1}^{\infty}{\sum_{\mathbf{r}}}'\ u_{\xi}(\mathbf{r}-n\mathbf{f}). \tag{5}$$

Here $\sum_{\mathbf{r}}'$ means summation over the S-crystal semiplane $\mathbf{r}=k\mathbf{d}+l\mathbf{f}$ $(-\infty<k<\infty, -\infty<l\leqslant 0)$; $\mathbf{f}$ is any S-crystal PTV other than $\mathbf{d}$. The GS is realized by the stripes with $\mathbf{d}=\mathbf{d}_{\pm}$ and $\xi=\xi_{\pm}$ which minimize $\varepsilon(\mathbf{d},\xi)$ at a given sign of $-\delta\mathcal{N}$ ($-$ or $+$ symbolizes rarefaction or compression, respectively). We shall call these stripes ''−stripes'' or ''+stripes.''

The energies $\varepsilon_{\pm}=|\varepsilon(\mathbf{d}_{\pm},\xi_{\pm})|$ are the quantities $P_{\pm}$ [see (2)] associated with ±stripes formation. The corresponding $\mu_{\pm}$, as follows from general thermodynamic considerations, are

$$\tilde{\varepsilon}_{\pm}=u_0+Q\varepsilon_{\pm}. \tag{6}$$

Lest there be any contradiction with the fact of the coalescence, energies $\tilde{\varepsilon}_{\pm}$ and $\epsilon_{\pm}$ are bound to satisfy inequalities

$$\epsilon_{-}<\tilde{\varepsilon}_{-}<\tilde{\varepsilon}_{+}<\epsilon_{+}. \tag{7}$$

When $Q\gg 1$ and $\upsilon(\mathbf{r})$ goes to zero over distances $R\ll r_{ee}\sim Q^{1/2}$, they follow from simple estimates. Taking into account that $|\xi_{\pm}|\sim a_0$, and, correspondingly, $|\mathbf{d}_{\pm}\times\xi_{\pm}|\sim Q^{1/2}\sigma_0$, from Eq. (5) we obtain: $\varepsilon_{\pm}\sim(a_0Q^{1/2}/R)u_0$. On the other hand, $|\epsilon_{-}|\sim u_0\sim\upsilon(r_{ee})$, and hence, $\tilde{\varepsilon}_{-}\gg|\epsilon_{-}|$. In the case under consideration $\epsilon_{+}\sim\upsilon(r_{\rm min})$, where $r_{\rm min}$ is the least of the distances between the IP and the S-crystal sites. This energy is much more than ε_{+} as $R\ll r_{ee}$.

To make sure that the inequalities (7) hold for other $\upsilon(r)$ and R/r_{ee} we have computed $\varepsilon_{\pm}$ [basing ourselves on Eq. (5) and Eq. (6)] in parallel with Monte-Carlo computer studies of the coalescence. They have confirmed that the inequalities are really the case for all $\upsilon(r)$ under consideration and for all Q, maybe except $Q=2$.

Together with the mutual repulsion of ±stripes of the same sign the inequalities (7) lead to the conclusion that +stripes or −stripes do constitute the GS superstructure in the vicinity of $1/Q$. The position of each ± stripe—a constituent of the superstructure—is determined by the stripe ''coordinate,'' l, which is the total number of particle lines (with the PTV $\mathbf{d}_{\pm}$) between this stripe and some fixed one

($l=0$). A set of these coordinates uniquely determines the 2D FEP space structure. Therein lies the LOD.

The ground state superstructure of stripes

The GS arrangement of the $\pm$stripes is governed by the pair potential of the stripe-stripe interaction,

$$V_{ss}^{\pm}(l)=\sum_{n=l+1}^{\infty}\sum_{\mathbf{r}}{}'\, u_{\xi_{\pm},-\xi_{\pm}}(\mathbf{r}-n\mathbf{f}_{\pm}-\xi_{\pm}) \tag{8}$$

where inter-stripe ''distance'' $l=1,2,...$; $\mathbf{f}_{\pm}$ is an S-crystal PTV other than $\mathbf{d}_{\pm}$, $\Sigma_{\mathbf{r}}'$ means the same as in Eq. (5) ($\mathbf{d},\mathbf{f}=\mathbf{d}_{\pm},\mathbf{f}_{\pm}$). For all $v(r)$ under consideration $\Sigma_{\mathbf{r}}'(n)>0$, and $\Sigma_{\mathbf{r}}'(n)>\Sigma_{\mathbf{r}}'(n+1)$. Hence, $V_{ss}(l)>0$ is a convex function of l. This enables us to describe the $\pm$stripes superstructure at $\theta-Q\neq 0$ ($\theta=1/\rho$) on the basis of the universal 1D algorithm,[7–9] considering the stripes as the ''particles'' of an effective 1D FEP:

$$l_m=[m/c_{\pm}];\quad c_{\pm}=|\theta-Q|/\sigma_{\pm},\quad \sigma_{\pm}=|\mathbf{d}_{\pm}\times\xi_{\pm}| \tag{9}$$

where [...] is the integral part of a number, m enumerates the $\pm$stripes; integer l_m is the coordinate of mth stripe, which is a pair of neighboring lines of electrons $\mathbf{r}_{m,1}(k)=k\mathbf{d}_{\pm}+l_m\mathbf{f}_{\pm}+m\xi_{\pm}$ and $\mathbf{r}_{m,2}(k)=\mathbf{r}_{m,1}(k)+\mathbf{f}_{\pm}+\xi_{\pm}$ ($k=0,\pm 1,...$). The superstructure described by Eq. (9) is thus a mixture of $-$stripes ($\theta-Q>0$) or $+$stripes ($\theta-Q<0$) and unperturbed stripes of the S-crystal which are parallel to $\mathbf{d}_{\pm}$, so that $c_{\pm}=N_s/\mathcal{N}_s$ is the concentration of the $\pm$stripes; N_s is their number; $\mathcal{N}_s$ is the total number of the $\pm$stripes and the S-crystal ones. The number of unperturbed stripes between mth and $m+1$th $\pm$stripes equals $l_{m+1}-l_m-1$.

An algorithm for arrangement of electrons' lines

Simple crystals with $\mathbf{f}_{\pm}=q_{\pm}\xi_{\pm}$, where $q_{\pm}=Q/\sigma_{\pm}$ is an integer, are of frequent occurrence. Particularly, this occurs of necessity for a triangular host lattice (Sec. 7), and also for $\sigma_{\pm}=\sigma_0$, as is typical of S-crystals on a host lattice of a lower symmetry. In such a case the above-mentioned electron lines of both types, $\mathbf{r}_{m,1}(k)$ and $\mathbf{r}_{m,2}(k)$, fall into the class of electron lines $k\mathbf{d}_{\pm}+l\xi_{\pm}$ ($k=0,\pm 1,...$; l is an integer), which can be considered as 1D ''particles'' with ''coordinates'' l. Their arrangment, as follows from Eq. (9), obeys the algorithm:

$$l_m=[sm],\quad s=q_{\pm}\mp.c_{\pm},$$

where l_m is the ''coordinate'' of the mth line, s is the mean line separation measured in units of $|\xi_{\pm}|$.

5. DEVIL STAIRCASE

The dependence of $c_{\pm}$ (or ρ) on μ, much the same to the 1D FEP,[7–9] is a well-developed fractal structure, a devil staircase whose steps occur at all *rational* $c_{\pm}=M/L\leqslant 1$ (M, L are coprime integers). At given M, L the GS configuration of the 2D FEP is thus a ''FEP crystal'' with L electrons per cell and with PTV's $\mathbf{d}_{\pm}$, $L\mathbf{f}_{\pm}+M\xi_{\pm}$.

In the commonly occurring case that $\mathbf{f}_{\pm}$ is a multiple of $\xi_{\pm}$ (Sec. 4) the steps' widths, $\Delta\mu=\Delta\mu(M/L)$, can be found by direct application of the 1D theory,[8,9] considering the energy of the line-line repulsion,

$$\mathcal{V}(l)=\sum_{k=-\infty}^{\infty} v(|k\mathbf{d}_{\pm}+l\xi_{\pm}|)$$

(l is the distance between interacting lines), as the 1D pair potential. This produces

$$\Delta\mu=\mathcal{L}\sum_{m=1}^{\infty} m[\mathcal{V}(\mathcal{L}m-1)-2\mathcal{V}(\mathcal{L}m)+\mathcal{V}(\mathcal{L}m+1)],$$

where $\mathcal{L}=q_{\pm}L\mp M$ is the period of the lines' pattern. The expression in the brackets is positive, since $\mathcal{V}(l)$ is a convex function in the case under consideration. Generally, $\Delta\mu(M/L)$ are expressed in terms of $V_{ss}^{\pm}(l)$ by a slight modification of the 1D theory.

6. J-BRANCHES AND FIRST-ORDER TRANSITIONS IN THE GROUND STATE OF THE 2D ''FROZEN'' ELECTRON PHASE

The algorithm (9) can be extended over the whole $c_{\pm}$ range, $0<c_{\pm}<1$, provided the crystal with one particle per cell (''S′-crystal'' with PTVs $\mathbf{d}_{\pm}$, $\mathbf{f}_{\pm}+\xi_{\pm}$) which arises at $c_{\pm}=1$ ($\theta=Q\pm\sigma_{\pm}$) is stable (i.e., it is another S-crystal) or metastable. This follows from the fact that i/ owing to the coalscence of defectons macroscopically small variations in θ generate, at any $c_{\pm}$, 1D defects only; ii/ these 1D defects, according to our computer calculations, have the same PTV, $\mathbf{d}_{\pm}$, for all $c_{\pm}$.

Moreover, due to (meta)stability of the S′-crystal the algorithm (9) holds over a θ range adjacent to the interval $|Q-\sigma_{-},Q+\sigma_{+}|$. In such a case Eq. (9) determines a mixture of stripes of new geometry which are characterized by a new triple of vectors, $\mathbf{d}_{\pm}'$, $\mathbf{f}_{\pm}'$, $\xi_{\pm}'$, the analogues of $\mathbf{d}_{\pm}$, $\mathbf{f}_{\pm}$, $\xi_{\pm}$, and the $\pm$stripes concentration $c_{\pm}'=|\theta-Q\pm\sigma_{\pm}|/|\mathbf{d}_{\pm}'\times\xi_{\pm}'|$. Transition from one geometry to another is continuous in θ since $c_{\pm}'$ goes to zero when $\theta\to Q+\sigma_{\pm}$.

Continuously extending the algorithm (9) in the manner shown above, we obtain the ''j-branch'' (we introduce the index j again) which comprises all (meta)stable structures Eq. (9) connected in continuity with the starting S-crystal. The corresponding energy, $E_j(\theta)$, can easily be found in terms of $V_{ss}^{\pm}(l)$, using Eq. (9). As a rule, there exist different S-crystals belonging to the same j-branch. On the other hand, as we have computed, intersections of different $E_j(\theta)$, and hence, *zero-temperature first-order transitions in variables μ or P* (a type of polymorphism), are universally present in the 2D FEP. (See example in Sec. 7). The dependence of E_g on θ is the function which comprises all stable portions of all $E_j(\theta)$.

Thus, owing to the LOD described above the GS of the 2D FEP is fully determined by the S-crystals PTVs, $m_{\kappa\lambda}^{j}$, the ''directors'', $\mathbf{d}_{\pm}^{j}$, and the displacement vectors, $\xi_{\pm}^{j}$, together with the set of $E_j(\theta)$ intersection points which are the only GS characteristics changing on small variations in $v(r)$. All these quantities can be computed on the basis of Eq. (5) and Eq. (9) by a self-consistent procedure, finding the S-crystals together with the j-branches. We have found the GS for triangular and square host lattices as well as for a number of those with central symmetry only. The computation has not

revealed principal differences between GS properties of 2D FEP with different geometry of host lattices, at least for those which are not significantly anisotropic.

7. EXAMPLE

Here we illustrate the above general results with a triangular host lattice (THL). All triangular lattices on the THL are necessarily S-crystals. This follows from the fact that it is the triangular lattice that realizes the *absolute* energy minimum of the system whose electrons are free to move. Such S-crystals are ''p,q-crystals'' with PTVs $p\mathbf{a}_1+q\mathbf{a}_2$, $p\mathbf{a}_2+q\mathbf{a}_3$ and $\theta=p^2+q^2-pq$ (p,q are arbitrary integers, $\mathbf{a}_{1,2,3}$ is a triple of THL PTVs which are equal in the modulus and form an angle of 120° with each other). Using the procedure discussed in Sec. 6, we have found that all 0, q-crystals belong to the same j-branch (the main branch), which covers the range $4\leqslant\theta<\infty$. The S′-crystals of the 0, q-ones are S-crystals too. They occur at $\theta=q(q+1)(2\leqslant q<\infty)$ and have PTV's $q\mathbf{a}_\kappa$, $(q+1)\mathbf{a}_\lambda$ ($\kappa,\lambda=1,2,3;\ \kappa\neq\lambda$). The stripe structures (9) have the same PTV, $q\mathbf{a}_\kappa$, for all θ of the interval $[q(q-1), \dot{q}(q+1)]$, their $\xi_\pm$ being $\pm\mathbf{a}_\lambda(\kappa\neq\lambda)$.

When $p,q\neq 0$, j-branches of different p,q-crystals are distinct. They do not have mutual intersections, but all intersect the main branch, the intersections occurring at rather small concentrations of the p,q-crystals' $\pm$stripes. In other words, the intervals of p,q-crystals stability $(p,q\neq 0)$, and correspondingly main-branch metastability, turn out to be narrow.

8. THE LIMIT OF $\gamma\gg 1$

So far, the more frequent case of $\gamma\lesssim 1$ (Sec. 3) has been discussed. Here we outline the limiting case $\gamma\gg 1$. It is realized when the Coulomb interelectron forces are screened by conductors that are at distances $\gg r_{ee}$ from the 2D FEP. Modeling such a situation by the potential $v(r)\propto r^{-1}\exp(-r/R)$ with $R\gg r_{ee}$, we have computed that the energies $\epsilon_\pm,\varepsilon_\pm$ satisfy the inequalities $\varepsilon_-<\epsilon_-<\epsilon_+<\varepsilon_+$, which are opposite to those of Eq. (7). Due to this fact it should be expected that the GS for $\rho-1/Q\ll 1/Q$ is a superstructure of separated S-crystal *zero-dimensional* defects, but not one-dimensional ones (stripes). We have revealed that these zero-dimensional defects are ''bidefectons,'' which are complexes consisting of two bound defections. Well-separated bidefectons can be considered as new particles on the S-crystal as the host lattice, the mean bidefecton separation, r_d, being equal to $\sim|2(\rho-1/Q)|^{-1/2}$. The effective pair potential of a mutual bidefecton repulsion is characterized by the same space parameter, R, as $v(r)$. If $r_d\gtrsim R$, the bidefectons, according to the general results of Secs. 3 and 4, are bound to be ordered into stripes arranged by the algorithm (9). Extention of this reasoning to the case of $R\gg r_d$ leads to new stripe-like superstructures consisting of zero-dimensional defects of ''new'' S-crystals, and so on. Eventually a well-developed fractal arises. Though details of its structure are still to be determined, it is safe to say now that the LOD does take place for $\gamma\gg 1$, too.

9. SUMMARY

The above consideration shows that the electron ordering into stripes and the effective lowering of dimension reside universally in the 2D FEP. In essence, a combination of discreteness of electrons' positions with a long-ranged interelectron repulsion is the only factor which gives rise to this phenomenon. For this reason it is also bound to arise with an external disorder present, the stripes being fractured and pinned by the disorder. Thus, stripe formation in 2D and layered narrow-band conductors can be considered to be the principal signature of a 2D FEP.

The charge ordering in cuprates as a manifestation of a 2D *''frozen'' electron phase*

From the above standpoint the charge ordering in CuO_2 planes of *high-temperature superconductors* (cuprates)[11] (neutron scattering),[12] (channeling) is of especial interest. The fact that it takes place even with very low doping[12] suggests that a 2D FEP might be present in these systems primordially. One can envision that formation of ionized oxygen molecules, O_2^{2-}, in oxygen planes gives a certain energy gain even in cuprates of the *stoichiometric* composition.[3)] In consequence, a part of electrons leaves the oxygen planes for s-orbits of Cu^{2+} ions in CuO_2 planes, resulting in formation of a number of Cu^+ ions. Since the amplitude of electron hopping $Cu^+\leftrightarrow Cu^{2+}$ is relatively small, the Cu^+ ensemble should be expected to be a 2D FEP, the concentration of the Cu^+ and, correspondingly, of the O_2^{2-} being determined by thermodynamic equilibrium between the 2D FEP and the ensemble of the O_2^{2-}. It is evident that stripe formation in the 2D FEP of Cu^+ ions inevitably brings to existence O^- superstructures in CuO_2 planes. Their PTVs are likely to be the same as that of the Cu^+ FEP.

In the connection with the aforesaid it should be noted that a simple explanation of the high-temperature superconductivity can be offered in terms of the 2D FEP, taking into account the finiteness of the bandwidth.[1] It lies in the fact that a virtual exchange of 2D FEP elementary excitations between oxygen holes (which are known to be free charge carriers in the doped cuprates) leads inevitably to a mutual effective attraction of the holes and thereby to superconductivity (of purely Coulomb origin) with high T_c. Our preliminary studies have shown that the lowest-energy elementary excitations in the cuprate 2D FEP are kinks on the disorder-fractured stripes.

Some expectable features of the 2D *''frozen'' electron phase thermodynamics and conductivity as a consequence of the stripe formation*

Our preliminary studies have shown that the effective lowering of dimension in the ground state of the 2D FEP accounts for a fairly interesting and unusual low-temperature thermodynamics. It is characterized by first-order transitions in the T,μ-plane (T is the temperature) from the FEP crystals (Sec. 5) slightly perturbed by an ideal gas of separate defectons (they are zero-dimensional defects which arise due to thermal activation) to a strongly correlated liquid of thermally fractured stripes (''FEP liquid'') where there is no long-range order. The melting temperature as the function of μ turns out to be reduced to zero at the endpoints of the

intervals of the devil staircase. Therefore, at any $T \neq 0$ there is a set of alternating μ intervals which correspond to the FEP crystals or the FEP liquid.

Conduction in the 2D FEP liquid is expected to be by movement of kinks of the fractured stripes, each kink carrying a fractal charge (measured in units of e). That in the FEP crystals is of the common Drude type, the charge carriers being $\pm$defectons with the charge $\pm e$. With a change in μ (at a fixed T) these conduction mechanisms alternate, resulting in pronounced 2D FEP resistivity oscillations which reflect the ground-state devil-staircase dependence of ρ on μ: the oscillations' peaks are bound to occur close to the *rational* filling factors of the FEP crystals which survive at a given T. This phenomenon is yet another distinctive mark of the 2D FEP. We have found it to be very similar to the resistivity oscillations of a conductive sheet in a system metal–*n*-type semiconductor–*p*-type semiconductor,[3] which still remain to be explained. We are going to publish the results concerning this issue in the near future.

It is remarkable that an artificially created external perturbation localized within a small region can block up conduction over all FEP liquid, pinning only one stripe. The most appropriate systems to test this experimentally are perhaps granular thin films like those described in Ref. 4. A similar phenomenon was reported in Ref. 5. Yet granular films used in the experiments[5] were highly disordered, and it is unclear now whether the above theory works in such a situation.

ACKNOWLEDGMENTS

We gratefully acknowledge discussions with Prof. M. Pepper, Prof. B. Shklovskii, and Prof. P. Wiegmann.

*E-mail: slutskin@theor.kharkov.ua

[1)]The ρ values are assumed not to be too close to $\rho = 1$, so that we can neglect the configurations with $n(\mathbf{r}) = 2$ in (1) and take no account of the spin variables.

[2)]As was shown in Ref. 10, if $\nu(\mathbf{r})$ were box-like, it would not be the case due to a clusterization of the particles.

[3)]A point in favor of this fact is a noticeable disorder ($\sim$20%) in arrangement of O^- along c-axis of $La_{2-x}Sr_xCuO_4$ which was revealed (by channeling method[13]) even for low x.

[1] A. A. Slutskin and L. Yu. Gorelik, Fiz. Nizk. Temp. **19**, 1199 (1993) [Low Temp. Phys. **19**, 852 (1993)]; A. A. Slutskin, Usp. Fiz. Nauk **165**, 707 (1995) [Phys. Usp. **38**, 669 (1995)].
[2] W. Heywang, *Amorfe und Policrystalline Halbleiter*, Springer Verlag (1984); A. A. Slutskin and V. I. Makarov, in *Proceedings of Electroceramics* **5**, September, 1996 Aveiro Portugal, p. 267.
[3] M. Pepper, J. Phys. C **12**, L617 (1979).
[4] R. G. Osifchin, W. J. Mahoney, J. D. Bielefeld, R. P. Andres, J. I. Henderson, and C. P. Kybiak, Superlattices Microstruct. **18**, 283 (1995).
[5] H. Nejoh and M. Aono, Appl. Phys. Lett. **64**, 2803 (1994).
[6] V. L. Pokrovsky and A. L. Talapov, *Theory of Incommensurate Crystals*, N. Y., Harward Acad. (1984), I. F. Ljuksutov, A. G. Naumovets, and V. L. Pokrovsky, *Two-Dimensional Crystals*, Naukova Dumka, Kiev (1988).
[7] J. Hubbard, Phys. Rev. B **17**, 494 (1978).
[8] P. Bak and R. Bruinsma, Phys. Rev. Lett. **49**, 249 (1982).
[9] Ya. G. Sinal and S. Ye. Burkov, Usp. Mat. Nauk **38**, 205 (1983).
[10] M. M. Fogler, A. A. Koulakov, and B. I. Shklovskii, Phys. Rev. B **54**, 1853 (1996).
[11] J. M. Tranquada, B. J. Sternlieb, J. D. Axe, Y. Nakamura, and S. Uchida, Nature (London) **375**, 561 (1995).
[12] A. S. Borovik, E. A. Kovaleva, and V. I. Makarov, Phys. Lett. A **172**, 457 (1993).
[13] V. I. Makarov, R. P. Slabospitsky, N. A. Skakun, A. S. Borovik, A. P. Voronov, A. Yu. Grinchenko, V. S. Malishevscy, and V. A. Oleinik, Fiz. Nizk. Temp. **17**, 476 (1991) [Sov. J. Low Temp. Phys. **17**, 251 (1991)].

This article was published in English in the original Russian journal. It was edited by R. T. Beyer.

PHYSICAL PROPERTIES OF CRYOCRYSTALS

Influence of an orthodeuterium impurity on the thermal conductivity of solid parahydrogen

O. A. Korolyuk B. Ya. Gorodilov A. I. Krivchikov, and V. G. Manzhelii

*B. Verkin Institute for Low Temperature Physics and Engineering, National Academy of Sciences of Ukraine, 47, Lenin Ave., 310164, Kharkov, Ukraine**

(Submitted February 23, 1999)
Fiz. Nizk. Temp. **25**, 944–949 (August–September 1999)

The thermal conductivity of solid parahydrogen with orthodeuterium impurity at an impurity concentration from 0.01 to 1% has been studied in the temperature range from 1.8 to 9 K. The nonlinear concentration dependence of the thermal resistivity of the investigated samples is explained by the fact that the intensity of normal three-phonon scattering processes is comparable to that of resistive processes. The analysis of the experimental results has been made in the framework of the Callaway model by using different models for the impurity phonon scattering. It has been found that the intensity of phonon impurity scattering in parahydrogen with orthodeuterium impurity is essentially higher than classical theory predicts and it is close to analogous scattering in solutions of helium isotopes with the equal reduced molar volume given. It is considered that additional impurity scattering of phonons is connected with the change of force constants and lattice distortion in the vicinity of impurity molecules. The quantitative estimation of the mentioned effects has been made. © *1999 American Institute of Physics.*
[S1063-777X(99)01908-8]

INTRODUCTION

The mechanism of the influence of isotopic impurities on the thermal conductivity of quantum crystals should be more complicated than in a case of classical crystals. An isotopic impurity disturbs the zero vibrations of a quantum crystal, which leads to the appearance of lattice distortion and the change of force constants in the vicinity of an isotopic point defect.[1–3] Therefore, when describing phonon scattering by isotopic point defects in quantum crystals, one needs to take into account not only the difference in the masses of the impurity and matrix molecules but also the two other effects mentioned. If molecules of the solution have rotational degrees of freedom, then one has also to take account of scattering by excitations of rotational motion of molecules. Simultaneous action of several mechanisms of phonon scattering impedes the interpretation of results of thermal conductivity studies. To make easier the extraction of contributions of the distortion and the change of force constants to thermal resistivity it is appropriate to study solutions with central interaction; such molecules have no rotational degrees of freedom. To such solutions one can refer ^{3}He–^{4}He and solid solutions of spin-nuclear modifications of hydrogens, which molecules are in the ground rotational state with $J=0$ (parahydrogen and orthodeuterium). The thermal conductivity of solid solutions ^{3}He–^{4}He have been studied experimentally in.[4–9] Quantum effects in solid hydrogens are less defined than in solid helium isotopes. However, solid hydrogens have higher ratio of molecular weights of isotopes. As we know, the influence of isotopic impurities on thermal conductivity of solid hydrogen has not previously been studied experimentally. The influence of Ne impurity on the thermal conductivity of solid parahydrogen was studied in Ref. 10. The closeness of the Lennard-Jones potential parameters of hydrogen and neon permits one to consider neon impurities in parahydrogen as quasi-isotopic ones. However, the analysis of data on the thermal conductivity of solid p-H_2 with Ne impurity did not result in finding the effects due to distortion and the change of force constants in the background of a very high mass effect ($M_{Ne}/M_{H_2}=10$).

The given work represents a study of the thermal conductivity of solid parahydrogen with orthodeuterium impurities with the aim of finding and analyzing the contribution of distortion and the change of force constants to phonon scattering.

THEORETICAL MODELS

Phonon scattering by isotopic impurities was first studied theoretically by Pomeranchuk in 1942.[11] At present various versions of the Klemens model (review[12]), the resonance scattering model (review,[13]) and the Antsygina–Slyusarev model[14] are used to describe phonon scattering by point defects. In the longwave limit when an impurity molecule and its vicinity vibrate as a unit, all the scattering mechanisms are of a Rayleigh character.

The Klemens model is most widely used to describe phonon scattering by point defects. In addition to the mass defect, this model takes a local change of force constants and

 © 1999 American Institute of Physics

the field of lattice distortions around an impurity into account. Matrix and impurity atoms vibrate as a unit with the same vibration amplitudes. The rate of phonon relaxation is proportional to the fourth power of frequency and has the form

$$\tau_{\text{imp}}^{-1}=\frac{c\Gamma V}{4\pi s^3}\omega^4, \tag{1}$$

where c is the impurity concentration; V is the molar volume of matrix; s is the sound velocity in the matrix; ω is the phonon frequency; and Γ is a parameter characterizing the intensity of impurity scattering. The parameter Γ expressed through the mass defect $\varepsilon=\Delta M/M$, the local change of force constants $\Delta\varphi/\varphi$, and the relative radial distortion $\Delta\delta/\delta$ has the form[15]

$$\Gamma=\varepsilon^2+2(\Delta\varphi/\varphi-6.4\gamma\Delta\delta/\delta)^2, \tag{2}$$

where γ is the Grüneisen constant. The Klemens model is used only in the case of longwave acoustic phonons. This condition is fulfilled for quantum crystals whose melting temperatures are essentially lower than the Debye temperature Θ_D. So, $T_m=13.81$ K, $\Theta_D(T\to 0)=118.5$ K[16] for solid parahydrogen in equilibrium with vapor.

Another approach is used in the model by Antsygina and Slyusarev (hereafter AS). It is based on the successive solution of kinetic equation for scattering by a heavy impurity in a rigid lattice taking account of local change of force constants. The rate of phonon relaxation is described by the expression

$$\begin{aligned}\tau_{\text{imp}}^{-1}=2c\omega&\left[\frac{g_1+g_2}{2}+g_1g_2P(\omega)\right]^2R_2(\omega)\\&\times\left\{\left[1+\frac{g_1+g_2}{2}-[P(\omega)-R_1(\omega)]\right.\right.\\&\left.-g_1g_2P(\omega)R_1(\omega)\right]^2\\&\left.+\left[\frac{g_1+g_2}{2}+g_1g_2P(\omega)\right]^2R_2^2(\omega)\right\}^{-1},\end{aligned} \tag{3}$$

where g_1 and g_2 are the parameters of the model; the functions $P(\omega)$, $R_1(\omega)$ and $R_2(\omega)$ are determined by the phonon spectrum of the matrix. The parameters $g_1=-\varepsilon/(\varepsilon+1)$, where ε is the mass defect $\Delta M/M=(M_i-M)/M$, M_i and M are the masses of impurity and matrix molecules, respectively. The local changes of force constants are taken into account by the parameter $g_2=M_is_i^2/Ms^2-1$, where s_i and s are the sound velocities for pure components. In the Debye approximation the functions $P(\omega)$, $R_1(\omega)$ and $R_2(\omega)$ have a form

$$\begin{aligned}P(\omega)&=1-1.5\omega/\omega_D+3(\omega/\omega_D)^2-3(\omega/\omega_D)^3\\&\quad\times\ln(1+\omega_D/\omega),\\R_1(\omega)&=-1-1.5\omega/\omega_D-3(\omega/\omega_D)^2-3(\omega/\omega_D)^3\\&\quad\times\ln|1-\omega_D/\omega|,\\R_2(\omega)&=3\pi(\omega/\omega_D)^3,\end{aligned}$$

where ω_D is the Debye frequency.

At $g_2=0$ the expression (3) transforms into an expression characteristic of resonance phonon scattering by an isotopic impurity. According to (3), the frequency dependence of the phonon relaxation rate is rather complicated and its form depends on the relationship between g_1 and g_2. In the general case the relaxation rate decreases sharply and tends to zero near the Debye frequency.

In Ref. 17 it has been shown that impurity scattering of phonons in solid solution of Ar in parahydrogen is much better described by the AS model than by the models of Klemens and resonance scattering of phonons.

EXPERIMENTAL TECHNIQUE

The thermal conductivity of solid solutions of orthodeuterium in parahydrogen was measured by the steady-state method. The sample was grown in a stainless steel tube with an inner diameter of 4.5 mm and length of 38.5 mm. Two carbon resistance thermometers TRC-2 (VINIIFTRI) were fixed on the external surface of the tube. One of the thermometers served as a gauge for temperature stabilization, the second served for measuring a temperature difference along the sample.

Hydrogen preliminarily purified by a palladium filter with the content of chemical impurities not more than 10^{-7} and deuterium of chemical purity 99.67% were used to prepare solutions. Parahydrogen with 0.21% of orthohydrogen and orthodeuterium with 2% of paradeuterium were obtained by conversion of liquid hydrogen and deuterium as a result of contact with $Fe(OH)_3$ at $T=20$ K. Gaseous mixtures were prepared in a glass vessel at room temperature. An error in the measurement of deuterium concentration in the mixture was less than 15% of the indication.

The crystals were grown from a gaseous mixture under a pressure of 50 Torr (somewhat lower than pressure at the triple point of pure parahydrogen) with the rate 0.13 mm/min. During the growth of the crystals the temperature of bottom of the cell decreased linearly with time and the difference in temperatures between the top and bottom of the cell was kept up equal to 7 K. After crystallization the sample was annealed. The temperature along the sample was equalized over a period of two hours, fixed equal to 12.5 K and kept constant for two hours as well. Further, when passing from one measurement to another the sample temperature changed so that the maximum temperature difference along the crystal should not exceed 0.3 K. The procedure described above made it possible to obtain good-quality samples and avoid the influence of anisotropy of *hcp* lattice of parahydrogen on thermal conductivity of samples.[18]

EXPERIMENTAL RESULTS AND DISCUSSION

Thermal conductivity of three samples of p-H_2 and five solutions $(p\text{-}H_2)_{1-c}(o\text{-}D_2)_c$ at deuterium concentrations (c) 0.01%; 0.05%; 0.1%; 0.5%; 1% were measured.

Thermal conductivity of pure p-H_2 agrees well with the literature data obtained for polycrystals with grain sizes about 1 mm. The data on the thermal conductivity of p-H_2

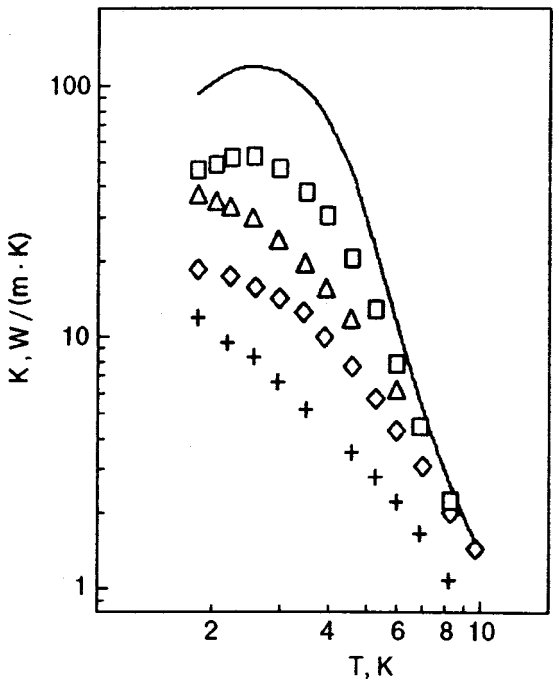

FIG. 1. Temperature dependence of thermal conductivity of $(p\text{-}H_2)_{1-c}(o\text{-}D_2)_c$ for different concentrations of $o\text{-}D_2$ c, %: 0 (solid line, pure $p\text{-}H_2$); 0.01 (□); 0.05 (△); 0.1 (◇); 1 (+).

crystals made it possible to conclude that the samples prepared by the technique described above are polycrystals without a selected crystallographic direction.

Figure 1 presents the experimental data obtained in the given work for pure parahydrogen and $p\text{-}H_2$-$o\text{-}D_2$ solutions. The thermal resistivity of the samples depends nonlinearly on the concentration. As shown in [19], the nonlinear concentration dependence of thermal resistivity arises due to interference of normal three-phonon scattering processes and impurity scattering. In the temperature range below 4 K the thermal conductivity curves for different concentrations have various slopes. This shows that in addition to impurity scattering it is also necessary in this temperature range to take into account the scattering on the boundaries of crystalline grains, which intensity changes from sample to sample. The form of temperature dependences of thermal conductivity corresponds to the analogous dependences obtained for ^{3}He with ^{4}He.[9]

The analysis of the experimental data was made in the framework of the Callaway model, taking account of normal phonon-phonon scattering processes (N processes) in the approximation of a Debye phonon spectrum. The thermal conductivity was calculated by the formula

$$K(T)=GT^3(I_1+I_2^2/I_3), \tag{4}$$

where

$$I_1=\int_0^{\Theta/T}\tau_C(x,T)f(x)dx; \quad I_2=\int_0^{\Theta/T}\frac{\tau_C(x,T)}{\tau_N(x,T)}f(x)dx;$$

$$I_3=\int_0^{\Theta/T}\frac{\tau_C(x,T)}{\tau_N(x,T)\tau_R(x,T)}f(x)dx;$$

$$G=k_B^2/(2\pi^2\hbar^3 s); \quad f(x)=x^4e^x/(e^x-1)^2;$$

$$x=\hbar\omega/k_BT;$$

Θ is the Debye temperature, $\tau_R(x,T)$ is the relaxation time of resistive scattering processes; $\tau_N(x,T)$ is the relaxation time of normal phonon-phonon processes, and $\tau_C(x,T)$ is the combined relaxation time:

$$\tau_C^{-1}(x,T)=\tau_R^{-1}(x,T)+\tau_N^{-1}(x,T).$$

In the solutions $(p\text{-}H_2)_{1-c}(o\text{-}D_2)_c$ the resistive processes are formed by phonon-phonon processes (U processes) $[\tau_U(x,T)]$, scattering by the boundaries of crystalline grains $[\tau_B(x,T)]$, scattering by molecules of $o\text{-}D_2[\tau_I(x,T)]$:

$$\tau_R^{-1}(x,T)=\tau_U^{-1}(x,T)+\tau_B^{-1}(x,T)+\tau_I^{-1}(x,T). \tag{5}$$

The characteristics of three-phonon U and N processes are determined only by the properties of the crystalline *hcp* lattice of hydrogen and practically do not depend on the presence of impurity molecules at a small impurity concentration:

$$\tau_U^{-1}(x,T)=A_Ux^2T^3e^{-E/T}, \quad \tau_N^{-1}(x,T)=A_Nx^2T^5.$$

The boundary scattering depends on an average size of crystalline grains L and sound velocity s:

$$\tau_B^{-1}=s/L.$$

The intensity of N processes is taken from the data of Ref. 19 ($A_N=6.7\times10^4\,s^{-1}\cdot K^{-5}$), and the parameters of U processes are obtained from the data on thermal conductivity of pure parahydrogen ($A_U=5.69\cdot10^7\,s^{-1}\cdot K^{-3}$, $E=36.57\,K$).[18] It is worth noting that to describe the thermal conductivity of samples without impurities it was necessary to introduce an additional mechanism corresponding to impurity scattering at the deuterium concentration $c=0.01\%$. Later it was taken into account when analyzing thermal conductivity of impurity crystals. Note that the natural content of deuterium atoms in hydrogen changes within $(1.39–1.56)\times10^{-4}$.[20]

The analysis of the experimental data was made separately for the impurity scattering models of Klemens and Antsygina-Slyusarev by using dependences (1) or (3), respectively.

To fit the calculated curves to the experimental data we used a mean free path of phonons at boundary scattering (L) and the parameters characterizing the intensity of impurity scattering (ε_{eff},Γ) as the fitting parameters. A parameter g_2 in the AS model was calculated using the average sound velocities for pure $p\text{-}H_2$ and $o\text{-}D_2$ obtained from the data on Debye temperatures of these substances. For $p\text{-}H_2$ $\Theta=118.5\,K$[16] and $s_{H_2}=1342.34$ m/s, for $o\text{-}D_2$ $\Theta=111.5\,K$[16] and $s_{D_2}=1202.8$ m/s, and $g_2=0.606$. For each of the impurity scattering versions the calculated thermal conductivity curves agree satisfactorily with the experimental ones. Figure 2 gives the experimental data for deuterium concentration $c=0.1\%$ and the calculated dependences of thermal conductivity versus temperature for two models of impurity scattering. The table presents the optimal fitting parameters as a function of the deuterium concentration.

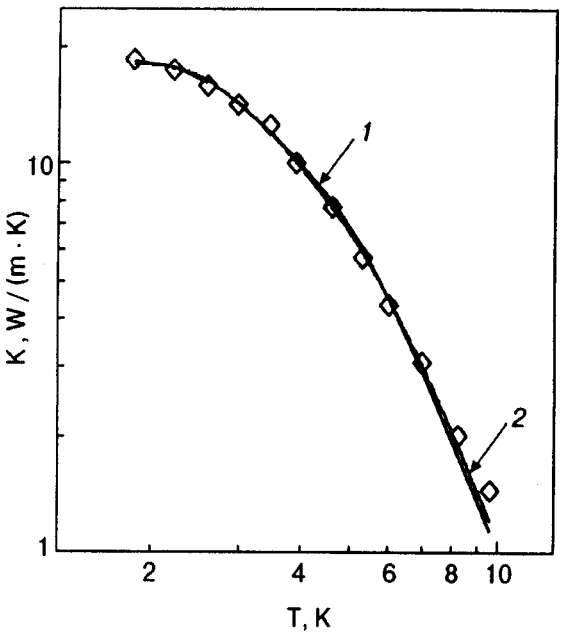

FIG. 2. Temperature dependence of thermal conductivity of solid solution at $c=0.1\%$: the experimental data ($\diamond$), according to the Klemens model (*1*) and to the AS model (*2*).

At deuterium concentration $c \leqslant 0.1\%$ the parameters Γ and ε_{eff} do not depend on concentration within the limits of the experimental error. This means that the deuterium molecules can be considered as independent scattering centers in this concentration range. At $c > 0.1\%$ Γ and ε_{eff} decrease with increasing concentration.

When treating the results of the thermal conductivity study of solid solutions ^{3}He–^{4}He,[4–9] the authors practically used only the Klemens model. This model makes it possible to compare the increase of intensity of phonon scattering by impurities ($\alpha=\Gamma/(\Delta M/M)^2$) due to the quantum effects for the cases of solid isotopic solutions of helium and hydrogen. In our opinion, the most accurate thermal conductivity measurements of solutions ^{3}He–^{4}He were made in Refs. 8,9. According to Ref. 9, at molar volume $V=20.56\,\text{cm}^3$/mole and ^{3}He concentration from 0.05 to 0.5% the values of α changed within 3–3.4. According to Table I, for solutions at equilibrium pressure of vapor and low deuterium concentrations $\alpha=1.64$ ($\alpha=\Gamma$, as $\Delta M/M=1$). Thus, at low pressures the quantum isotopic effect in helium is twice as great, though the mass defect is four times less. It should be noted, however, that the magnitude α characterizing the quantum effect decreases from 3 to 1, approaching the classical value with decreasing molar volume from 21.56 to 11.5 cm^3/mole. It is interesting to compare α of crystalline hydrogen and helium at equal reduced volumes $V^*=V/(N\sigma^3)$, where σ is the gas-kinetic diameter of molecules, N is Avogadro's number. If one takes $\sigma=2.62$ Å for ^{4}He and 2.96 Å for H_2 and D_2,[16] then the molar volume of helium $V_{(^4\text{He})}=15.95\,\text{cm}^3$/mole corresponds to the molar volume of hydrogen at equilibrium vapor pressure and helium temperatures ($V=23.16\,\text{cm}^3$/mole). On the basis of the dependence of α on molar volume of solid helium,[5,7] we have obtained $\alpha=1.5$ for solid ^{3}He–^{4}He solutions at $V=15.95\,\text{cm}^3$/mole that is somewhat less than the value $\alpha=1.64$ for solutions D_2–H_2 at equal reduced volume.

Let us now estimate the relative change of the force constant $\Delta\varphi/\varphi$ and the relative radial distortion of a lattice $\Delta\delta/\delta$ in the vicinity of the impurity molecule D_2 in solid H_2. In the framework of Klemens model [see formula (2)] these effects cannot be determined independently. The magnitude $\Delta\varphi/\varphi$ can be calculated independently from the data on heat capacity of solutions of orthodeuterium in parahydrogen.[21] According to Ref. 21, $\Delta\varphi/\varphi=0.3$. If one uses this value and formula (2), then we obtain the value $\Delta\delta/\delta$ given in Table I. The last value can be compared with $\Delta\delta/\delta$ evaluated by the formula

$$\frac{\Delta\delta}{\delta}=\frac{(V_{o-\text{D}_2})^{1/3}-(V_{p-\text{H}_2})^{1/3}}{(V_{p-\text{H}_2})^{1/3}}.$$

Using the following values of molar volumes $V_{o\text{-D}_2}=19.9\,\text{cm}^3$/mole and $V_{p\text{-H}_2}=23.16\,\text{cm}^3$/mole we obtain $\Delta\delta/\delta=-0.049$. Since both methods of determining the relative radial distortion are rough approximations, the agreement of the values $\Delta\delta/\delta$ obtained by these methods can be considered as satisfactory.

The analysis of the experimental results has shown that the deviations from classical scattering of phonons by an isotopic impurity are observed in crystals of parahydrogen with orthodeuterium impurity. At the same time both the simple and physically rather clear Klemens model and the more consistent AS model describe satisfactorily the impurity contribution to thermal resistivity of a crystal. Both models show the deviation in the behavior of impurity scattering from the classical case. However, the Klemens model (unlike the AS model) permits one to estimate the distortion and the change of force constants in the vicinity of an impurity molecule. The main result of the present work is the discovery

TABLE I. Fitting parameters of impurity scattering Γ, ε_{eff} and averaged mean free path of phonon at boundary scattering L, obtained from the experimental data on $K(T)$ for $(p-\text{H}_2)_{1-c}(o\text{-D}_2)_c$.

	Klemens model			AS model	
c, %	Γ	$\Delta\delta/\delta$	L, m m	ε_{eff}	L, m m
0.01	1.64	−0.021	0.879	2.14	1.08
0.05	1.64	−0.021	2.50	1.98	2.68
0.10	1.69	−0.022	0.464	2.03	0.698
0.50	1.49	−0.015	0.276	1.95	0.436
1.00	1.19	−0.001	2.18	1.72	2.68

and the quantitative estimation of the influence of quantum effects on impurity scattering of phonons in solid hydrogen.

The observed concentration dependences for impurity and boundary scattering give grounds for assuming that experiments with analogous objects made in the lower temperatures range (where the thermal conductivity is mainly determined by a defect structure of crystal) will make it possible to study not only the behavior of isotopic impurity but finer effects as well, related to the influence of impurity on the defect structure of crystal. Note that it is impossible to draw conclusions on the influence of impurities on a defect structure in a sample on the basis of data on the temperature dependence of thermal conductivity in a phonon maximum region. No dependence of boundary scattering parameter on concentration of D_2 is observed in the solution. To obtain extra information on the influence of macroscopic defects on thermal resistance in H_2 it is necessary to widen the region of studying to the side of temperatures lower than 1.7 K.

The authors are indebted to T. N. Antsygina and K. A. Chishko for useful consultations and fruitful discussions of the experimental results.

The authors dedicate this paper to academician B. I. Verkin on the occasion of his 80th birthday. Owing to his perspicacity and initiative the studies of cryocrystals became possible in our Institute.

*E-mail: korolyuk@ilt.kharkov.ua

[1] J. Callaway, Phys. Rev. **122**, 787 (1961).
[2] P. G. Klemens and A. A. Maradudin, Phys. Rev. **123**, 804 (1961).
[3] P. G. Klemens, R. De Bruya Ouboter, and C. Le Pair, Physica, **30**, 1863 (1964).
[4] E. J. Walker and H. A. Fairbank, Phys. Rev. **118**, 913 (1960).
[5] R. Berman, C. L. Bounds, and S. J. Rogers, in Proceedings Roy. Soc. (London) **A289**, 66 (1965).
[6] B. Bertman, H. A. Fairbank, Clark W. White, and Michael J. Crooks, Phys. Rev. **142**, 74 (1966).
[7] R. Berman, C. L. Bounds, C. R. Day, and H. H. Sample, Phys. Lett. **A26**, 185 (1968).
[8] D. T. Lawson and H. A. Fairbank, J. Low Temp. Phys. **11**, 363 (1973).
[9] A. A. Golub and S. V. Svatko, Fiz. Nizk. Temp. **6**, 1112 (1980) Sov. J. Low Temp. Phys. **6**, 540 (1980).
[10] V. G. Manzhelii, B. Ya. Gorodilov, and A. I. Krivchikov, Fiz. Nizk. Temp. **22**, 174 (1996) Low Temp. Phys. **22**, 131 (1996).
[11] I. Pomeranchuk, J. Phys. USSR **6**, 237 (1942).
[12] R. Berman, *Thermal Conductivity in Solids*, Clarendon Press, Oxford (1976).
[13] C. W. Mccombie and I. Slater, in Proceedings Phys. Soc. **84**, 499 (1964).
[14] T. N. Antsygina and V. A. Slyusarev, Fiz. Nizk. Temp. **19**, 494 (1993) Low Temp. Phys. **19**, 348 (1993).
[15] G. P. Srivastava, *The Physics of Phonons*, Adam Hilger, Bristol, Philadelphia and New York (1990).
[16] Physics of Cryocrystals, V. G. Manzhelii, Yu. A. Freiman, M. L. Klein, and A. A. Maradudin (Eds.) [Part 1, Quantum Molecular Crystals, authored by Vadim G. Manzhelii, Mikhail A. Strzhemechny], AIP Press, Woodbury, New York (1996).
[17] B. Ya. Gorodilov, A. I. Krivchikov, V. G. Manzhelii, and N. N. Zholonko, Fiz. Nizk. Temp. **20**, 78 (1994) Low Temp. Phys. **20**, 66 (1994).
[18] O. A. Korolyuk, B. Ya. Gorodilov, A. I. Krivchikov, A. S. Pirogov, and V. V. Dudkin, J. Low Temp. Phys. **111**, 515 (1998).
[19] T. N. Antsygina, B. Ya. Gorodilov, N. N. Zholonko, A. I. Krivchikov, V. G. Manzhelii, and V. A. Slyusarev, Fiz. Nizk. Temp. **18**, 417 (1992) Sov. J. Low Temp. Phys. **18**, 263 (1992).
[20] M. P. Malkov, Handbook on *Physical Technical Basis of Cryogenics*, Nauka, Moscow (1985).
[21] M. I. Bagatskii, I. Ya. Minchina, V. G. Manzhelii, and A. I. Krivchikov, Fiz. Nizk. Temp. **12**, 343 (1986) Sov. J. Low Temp. Phys. **12**, 194 (1986).

This article was published in English in the original Russian journal. It was edited by R. T. Beyer.

Formation and trapping of electron excitations in neon cryocrystals

I. Ya. Fugol, A. G. Belov, E. I. Tarasova, and E. M. Yurtaeva

*B. Verkin Institute for Low Temperature Physics and Engineering, National Academy of Sciences of the Ukraine, 310164 Kharkov, Ukraine**

(Submitted March 9, 1999)
Fiz. Nizk. Temp. **25**, 950–963 (August–September 1999)

Specific features of exciton states in neon are analyzed in the approximation of a rigid lattice, taking into account its easy deformability. Regular alteration of atomic and molecular states upon a transition from heavy inert elements to light elements leading to the emergence of a number of typical distinctions of band excitations in neon is considered. Dynamic parameters of electrons, holes, and excitons associated with resonant energy transfer in the crystal and with self-trapping of quasiparticles are specified. It is shown that the strong coupling of the lowest exciton state with local vibrations of the surrounding lattice results in mixing of free and self-trapped excitations and in a considerable decrease in the mobility of excitons. A comparison of experimental and theoretical absorption spectra of mixed states makes it possible to refine the parameters of the exciton–phonon interaction for the singlet and triplet components of the exciton. © *1999 American Institute of Physics.* [S1063-777X(99)02008-3]

INTRODUCTION

The physics and spectroscopy of cryocrystals of inert element or rare gas solids (RGS) were chosen as a basic trend from the very outset of investigations in the low temperature physics in Kharkov. At the beginning of the thirties, I. V. Obreimov, the founder of the first physicotechnical institute in the Ukraine, was interested in the problem of light absorption in the condensed phase and attracted attention of Ya. I. Frenkel to the astonishing (at that time) emergence of discrete (narrow) absorption bands and luminescence in the spectrum of solids during their cooling to low temperatures. This formed the basis of the concept of excitons in the crystal lattice. The basic model in the Frenkel theory of excitons was the atomic argon crystal.[1] However, experiments on RGS spectroscopy were impossible at that time since they required the development of special technique for far vacuum ultraviolet region in the energy range $E \geqslant 10$ eV containing the lowest excited states of Ne, Ar, Kr, and Xe atomic cryocrystals.

Thirty years later, outstanding theoretical, experimental, and technical achievements of scientists in the field of low-temperature physics stimulated the creation of a new special Institute of Low Temperature Physics and Engineering in Kharkov. The organizer and inspirer of behind the foundation of this institute was Boris Ierimievich Verkin. At that time, one of the author of this paper (I. Ya. Fugol) put forth the idea of low-temperature experiments aimed at studying excitons in atomic cryocrystals. Boris Ierimievich showed his interest in this idea and supported it since it naturally matched with his plans for the development of cryocrystal physics at the Institute for Low temperature Physics and Engineering. During all subsequent periods of time, B. I. Verkin facilitated the establishment and evolution of this trend which has become a leading direction in the department of spectroscopy of condensed media at the Institute. After another 20 years, the results of scientific achievements in this field were summarized in the monograph ''Cryocrystals.''[2] Three of the four parts of this book are devoted to the physics of cryocrystals grown at the Institute. This trend was recognized all over the world and still retains its scientific priority.

Since the 1970's, when it became possible to study experimentally the excited states of RGS cryocrystals, rich scientific information has been accumulated, which is reflected in the well- known books and reviews.[3–8] Nevertheless, the experimental results do not agree with the theoretical models used for describing excited electron states of solid neon (as well as solid helium) and various approaches exist for their description. This paper is the first of two articles devoted by the authors to the memory of respected Boris Ierimievich Verkin. In the present paper, we touch upon the central problems of the structure and dynamics of excitons and electrons in the Ne lattice on the basis of new concepts developed on the basis of experimental results and theoretical investigations carried out at B. Verkin Institute for Low Temperature Physics and Engineering in recent years.

If we consider a series of classical cryocrystals of rare gases (with the exception of the Ne quantum crystal), solid Ne occupies the extreme position in view of the simplicity of its structure and the smallness of the forces of interaction between atoms in the crystal lattice. Neon behaves as a marginal crystal in some aspects of lattice dynamics (for example, as regards the applicability of the theory of elasticity) and band structure (for example, the correctness of exciton model is doubtful in view of the smallness of the dielectric constant).

It is still unclear whether the energy structure of excited exciton states of the Ne crystal can be connected with those for an individual atom or molecule). The answer to this ques-

 © 1999 American Institute of Physics

tion for the ground state of the crystal is almost obvious. It is well known that the approximation of paired molecular potentials of Ne_2, taking into account small corrections for a many-particle system, can serve as the basis crystal potential and provides a correct description for most effects in lattice dynamics. Generally speaking, the approximation of atomic or molecular excitations is not indisputable for the band and exciton states of Ne cryocrystals. On the one hand, it is generally accepted that the effective mass approximation (EMA) presuming a weak coupling between an excited electron and a hole (exciton) in a medium with dielectric screening is valid for describing excitons in the liquid and solid phases of heavy inert elements such as Xe, Kr, and Ar. On the other hand, it was proposed recently that the exciton model is not applicable altogether for describing excitations in condensed helium, and that the best agreement with experimental results is attained in terms of trapped excitations of the molecular type.[9] For this reason, a detailed analysis of situation in Ne cryocrystals is undoubtedly essential. In addition, recent experimental investigations of relaxation of excitations and energy transfer to impurity centers and crystal boundaries[10,11] necessitate a more exact determination of the dynamic parameters of electrons, holes, and excitons (such as the position of band and local energy levels and band width) as well their transport properties associated with the electron–phonon interaction for a correct interpretation of experimental data.

In Sec. 1, the relation of atomic and molecular excitations with crystal excitations is established on the basis of their description with the help of Rydberg series with a quantum defect. New estimates of exciton band widths as well as effective masses of electrons, holes, and excitons are obtained. The effect of mixing of the lowest states of free and self-trapped excitations due to strong coupling between excitons and the local deformation of the neon lattice is investigated in Sec. 2. The theoretical absorption spectrum and the experimental spectrum are compared to obtain the values of the exciton–phonon coupling parameters for the singlet and triplet components of the exciton transition.

1. MOLECULAR POTENTIALS, BAND MODEL, AND STRUCTURE OF EXCITON STATES

Let us analyze the evolution of electron excitations in the transition of Ne from atom and molecule to the solid state and consider possible alternative approaches to the description of the energy structure. We shall first consider an idealized model in a rigid lattice without taking into account the electron–phonon interaction and easy deformability of Ne cryocrystals. We start from atomic and molecular electron excitations in Ne in the free state.

A Ne atom in the ground state $^1S_0$ has a closed configuration of 10 electrons: $1s^2 2s^2 2p^6$. The lowest excitations transfer one of $2p$-electrons to the next $(2+n)s$-orbitals ($n=1,2,3,\ldots$) forming a defective Rydberg s-series whose each term splits into two components due to the spin–orbit (SO) interaction with the total angular momenta $j=3/2$ and $j=1/2$ of the hole core of the atom. The series $(2+n)s_{3/2,1/2}$ are limited by the ionization potentials $I(3/2)=21.56\,\text{eV}$ and $I(1/2)=21.657\,\text{eV}$ so that their SO splitting amounts to $\Delta_{SO}=0.097\,\text{eV}$. The lowermost excitation of $2p^5 3s$ corresponds to the terms $^3P_{0,1,2}(j=3/2)$ and $^1P_1(j=1/2)$, the oscillator force of $(^1P_1-{}^1S_0)$ transition ($F=0.16$) for free atoms being an order of magnitude higher than for $(^3P_{0,1,2}-{}^1S_0)$ transitions; from the latter three transitions, we will be interested only in the observable transition $^3P_1-{}^1S_0$. The energy position of energy levels with $n\geqslant 1$ in the gas is determined by the interaction of an electron located at a large distance from the atomic core with the effective charge of the nucleus Z^*. If the radius r_0 of the atomic core is much smaller than the radius r_n of the excited state, we can assume that the charge is point-like and that the problem is similar to that for a hydrogen atom. In other words, we assume that the quantization of energy levels $E_n(n)$ occurs in accordance with the quantization of the radius $r_n=n^2 a_0$ of the electron orbit (a_0 is the Bohr radius). The influence of Z^* differing from unity can be effectively taken into account by introducing the correction to the quantum number (quantum defect δ) in the expression for energy terms as well as in the expression for radii. If the radius of the atomic core cannot be neglected, the familiar simple dependence $E_n(n)$ and/or $r_n(n)$ is violated. Bearing in mind that we subsequently compare the result with the exciton series (the index n labels excited states), we describe the defective Rydberg atomic series as follows:

$$E_n = I - \frac{R(Z^*)^2}{(n+1)^2} \equiv I - \frac{R}{(n+1-\delta_n)^2}, \quad n=1,2,3,\ldots, \quad (1)$$

where I is the ionization potential, $R=m_0 e^4/2\hbar^2=13.6\,\text{eV}$ the Rydberg constant, m_0 and e are the mass and charge of a free electron, and δ_n is the correction to the quantum number $n'=n+1$ ($\delta_n<0.33$ for inert atoms), which has a tendency to a noticeable decrease with increasing atomic number of the inert element and to a slight decrease with increasing n for each inert atom. For the singlet series of the Ne atom, $\delta_1=0.32$ and $\delta_5=0.31$, the former value describing the position of absorption band of the entire series to within 0.01 eV. The parameters δ_n for the triplet series virtually coincide with those for the singlet series. The first terms of atomic series correspond to $E_1(3/2)=16.67\,\text{eV}$ and $E_1(1/2)=16.84\,\text{eV}$. For calculating the series, we used the data for atomic spectra from Ref. 12. In order to outline the peculiarities in the structure of the Ne atom leading to inapplicability of the Wannier model for the lowest excitons in the crystal, we compare them with the corresponding excitations in Xe for which the model mentioned above was used successfully. For example, $\delta_1=0.08$ and $\delta_4=0.01$ for the triplet series of the Xe atom. The application of description (1) for electron transitions together with corresponding quantization of the orbit radius is substantiated by the requirement of weak coupling between an excited electron with the atomic core, i.e.,

$$W_n = \frac{R}{(n+1-\delta)^2} \ll R; \quad r_0 \ll r_n. \quad (2)$$

The terms with $n>1$ for all inert atoms undoubtedly satisfy this requirement, and the radii of electron states can be determined from the formula

$$r_n=(n+1-\delta_n)^2 a_0, \quad a_0=0.53\,\text{Å}, \tag{3}$$

Let us now consider the lowermost excitations for which condition (2) is not satisfied exactly. We have $W_1=R/2.8=4.85\,\text{eV}$ for the neon atom and $W_1=R/3.7=3.67\,\text{eV}$ for the xenon atom. Estimating the radii by using formula (3), we obtain ($r_0=\langle r\rangle$ from Ref. 13: calculations are made in accordance with values of I):

$$\text{Ne:}\quad r_0\cong 0.51\,\text{Å},\quad r_1\cong 1.49\,\text{Å},\quad r_2\cong 3.85\,\text{Å},\quad \frac{r_1}{r_0}=2.92;$$

$$\text{Xe:}\quad r_0\cong 1.24\,\text{Å},\quad r_1\cong 1.95\,\text{Å},\quad r_2\cong 4.51\,\text{Å},\quad \frac{r_1}{r_0}=1.57. \tag{4}$$

The ratio r_1/r_0 is small and is larger significantly in the case of Ne. The mechanism of the influence of the atomic core on excited states typical of light atoms (He and Ne) is associated with a considerable part of the nuclear charge uncompensated by shells lying deeper than the valence shell (there are four electrons in all), which is manifested in the Coulomb potential through an increase in the effective nuclear charge Z^* (the potential is pulled downwards). In the case of Ne, this leads to a very large potential I and a relatively large defect δ_n in the terms of excited states. The first requirement in (2) is not satisfied exactly. On the contrary, condition (2) for radii holds much better since uncompensated charge compresses the valence shell to the size of the hydrogen atom (by the way, He has the same radius r_0 and exhibits a similar effect for an even larger potential I), and the estimate (3) taking into account the quantum defect can be regarded as reliable to a certain extent. The mechanism typical of heavy atoms (Kr and Xe) is associated with the presence of a large number of electrons in deeper shells of the atom. On the one hand, they create a very high electron density around the nucleus ($Z^+=54e$ for Xe) and screen it to the value of $Z^*\sim 1$ even for electrons of the valence shell. The ionization potential $I(3/2)=12.13\,\text{eV}$ for the Xe atom is close to R (we can formally compare it with the case $n'=1$), while the first excited state is close to the position of the electron energy level in the hydrogen atom with the principal quantum number $n'=2$, i.e., we obtain a small δ in the positions of terms and better fulfillment of the energy requirement in (2). On the other hand, five electron shells of the atom occupy a large volume in view of orthogonality of wave functions with different quantum numbers. A correction to the potential appearing in the form of repulsion from the atomic core shifts the peak of the density of the excited electron to the region of large $r_1>r_0$. In this case, $r_0>2a_0$ (which contradicts the value of I), and the estimate of the radius r_1 obtained by formula (3) is very rough. Thus, the ''non-Rydberg'' nature of the lowermost excitations is manifested in one way or another for all rare gases; for these reasons, such excitations should be classified as states of intermediate coupling with the atomic core. In the formation of the condensed phase, this peculiarity is manifested in the obvious genetic relation between excited and atomic states and in unconditional predominance of the contribution from nearest neighbors to the interaction of an excitation with the lattice.

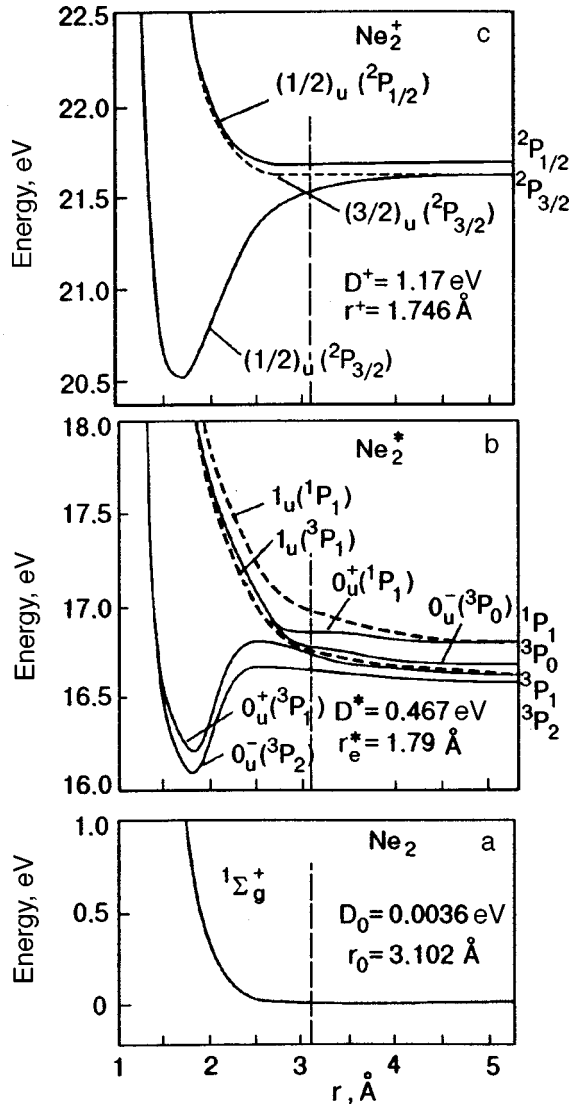

FIG. 1. Potential of the neon molecule in the ground state (a), for lowermost excited levels (b) and for a positive ion (c). Only antisymmetric state (u) making contributions to the band states in the crystal are presented. Dashed curves denote doubly degenerate energy levels.

In the case of spherically symmetric excited states, the effect of the environment can be taken into account in the first approximation by using pair potentials for an isolated excited molecule. In Fig. 1, the potential curves of the Ne_2 molecule are shown in three fragments: in the ground state [Fig. 1(a)], lower states of excited Ne_2^* molecule [Fig. 1(b)], and potential curves for the molecular ion Ne_2^+ [Fig. 1(c)]. The curves in Fig. 1 are plotted according to the results of *ab initio* calculations[14] which were subsequently confirmed in experiments. The vertical straight line crossing all the potentials is drawn at the atomic spacing $d=3.15$ Å in the crystal. It should be noted that the curves contain no contribution from long-range forces, viz., dipole–dipole interaction and polarization attraction, that give a relatively small contribution to potentials. In the framework of our analysis, these results demonstrate the effect of the most short-range component of atomic interaction due to the overlapping of the electron wave functions of two atoms approaching each

other. According to calculations,[15] the potential curve of the ground $^1\Sigma_g^+$ state of Ne_2 has a shallow well with the dissociation energy $D_0=0.0036$ eV for $r_0=3.102$ Å. Much more stable molecules can be formed as a result of interaction of a normal and an excited atom.

Figure 1(b) shows the part of lowest molecular states which dissociate to the atomic energy levels $Ne(^1S_0)+Ne(3s;^{1,3}P)$ and correlate with the fcc symmetry of the Ne crystal lattice with a single atom in the unit cell. This condition preserves only odd u terms (nondegenerate 0_u^+ and doubly degenerate 1_u) which form together the F_{1u} crystalline states with the weight contribution $F_{1u}=(1/3)0_u+(2/3)1_u$. It can be seen from [Fig. 1(b)] that along with a large number of repulsive terms (all the π-terms), there exist strongly coupled states with the dissociation limit to the triplet $^3P_{1,2}$ states and a deep well $D^*\approx 0.5$ eV for $r_e^*=1.79$ Å. For the singlet terms 0_u^+, a shallow well is formed for $r_e^*=2.7$ Å. A distinguishing feature of the lowest molecular states of Ne_2^* as compared to heavy rare gases is the presence of potential maxima (humps) at distances $r_H=2.9$ Å$>r_e$. According to estimates,[14] the height of these humps in Ne_2^* is of the order of 0.07 eV for r_H, while the repulsion whose magnitude at 0_u^+ and 1_u is $+0.04$ eV still dominates in the region $r\approx d$. The long-range repulsion peaks of this type emerge as a result of quantum symmetry effects in view of the Pauli exclusion principle. The origin and the height of far-lying humps on the interaction potentials of the normal and excited helium atoms were discussed in Ref. 16. It was found that the height of the hump for helium is ~ 0.14 eV for $r_H=2.65$ Å, and its origin is connected with the predominance of the positive contribution to energy in the case of simultaneous exchange of an excited electron and the nucleus in antisymmetric states.

According to Cohen and Schneider,[14] the resonant attraction cannot compete with repulsion having a longer range when two neon atoms approach each other to a distance $r\approx d$. In this case, the excitation preserves the spherical symmetry relative to the ion, although the resonant coupling between valence electrons at shorter distances leads to the formation of a deep molecular state with the symmetry $D_{\infty h}$. Generally speaking, the magnitude of resonant attraction is an important parameter determining one of the contributions to the exciton band width (it determines the nondiagonal matrix element T_{nm} of excitation transfer between neighboring sites n and m in the lattice). Unfortunately, Cohen and Schneider[14] did not separate this contribution for the excited state. Its magnitude can be estimated indirectly from the molecular ion potentials responsible for the formation of the hole band of the crystal.

Figure 1(c) shows the potential curves for the Ne_2^+ molecular ion formed as a result of interaction of a normal Ne atom ($^1S_0$) and an atomic ion taking into account its SO splitting Ne^+ ($2p^5$; $^2P_{3/2}$, and $^2P_{1/2}$). The ion with $j=3/2$ corresponds to a deep well with $D^+\approx 1.2$ eV for $r^+\approx 1.75$ Å, whose depth is twice as large as that for an excited Ne_2^* molecule. The ion with $j=1/2$ has a weakly coupled state for $r_e=2.7$ Å. Since all interactions are constructed only with the participation of valence electrons, the upper repulsion potentials are of the same type as for the ground

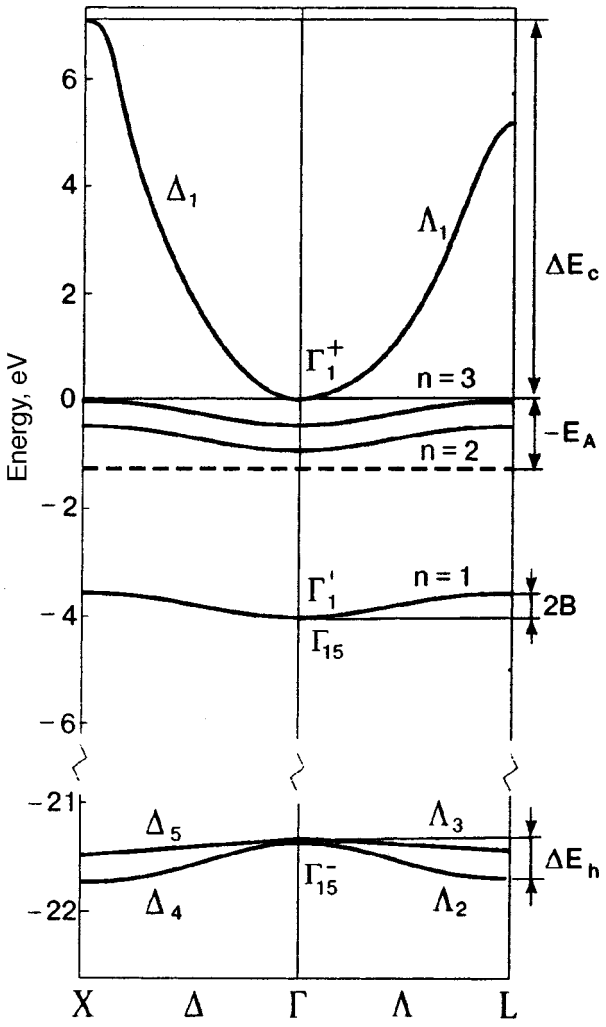

FIG. 2. Energy band diagram for Ne cryocrystals: hole bands (bottom), conduction bands (top), and exciton bands (below, in the region of dielectric gap).

state, and a very weak attraction dominates for the long-range ($r\approx d$) interactions (repulsion humps are absent). It should be noted that the potential curves for $Ne_2^+(1/2)$ for $r\approx d$ almost coincide with the ionization limit $I(1/2)$ of the atom, indicating a small width of the hole band for the singlet.

The long-range polarization interaction plays a leading role in the formation of energy structure of RGS. In the series of inert elements, Ne has the smallest polarizability (it is an order of magnitude smaller than for Xe in the ground state), and hence a small permittivity $\varepsilon=1.24$. For this reason, the Coulomb potential for electron excitations in the crystal is slightly ''compressed.'' This effect, in turn, is compensated by the above-mentioned increase in the excitation energy due to repulsion from nearest atoms, and as a result the dielectric gap E_g in Ne almost coincides with the ionization potential of the atom. At the same time, the ionization energy in Xe crystal ($\varepsilon=2.18$) decreases significantly ($E_g=9.33$ eV), as a result of which the excitations become weakly coupled. Figure 2 shows the band diagram of states in the k-space for the high-symmetry points Γ, L, and X in the Brillouin zone. The dispersion along (Δ) or (Λ) direc-

tions determines the width ΔE_h of the hole band including the SO splitting which changes in the crystal insignificantly as compared to the gas ($\Delta_{SO} \approx 0.1$ eV). The series of exciton bands ($n=1,2,3,\ldots$) lying above the hole band converges to the bottom of the conduction band at the point Γ_1. The lowest conduction band is plotted on s-wave orbitals and has an isotropic dispersion relation in the lower part. The available results of calculations of the band structure of Ne exhibit a spread of a few electron-volts in the value of conduction band width,[17–19] but most of authors admit that the dispersion in a considerable part of the band resembles astonishingly the dispersion of a free electron with a purely parabolic dispersion relation, i.e., the electron mass m_e in the band is close to the mass m_0 of a free electron. It is well known that electrons in Ne relax rapidly to the upper part of the band, and only low-energy particles are observed in experiments on photoemission during the scanning of the entire conduction band even for quite thin samples.[4] For this reason, it is sufficient to estimate the transport properties of electrons in the region of quadratic dispersion relation in order to analyze the recombination of charges and their trapping. The midpoint of the band in the Γ—X direction corresponds to the value of $k=\pi/a$ for which we obtain $E_c(\pi/a) \approx 2$ eV from the data obtained by Rossler.[17] In this case, in the effective mass approximation (EMA) we can equate

$$\frac{1}{2}\Delta E_c^X = \frac{\hbar^2 \pi^2}{2 m_e a^2} \approx 2 \text{ eV}, \tag{5}$$

which gives $m_e \approx m_0$.

The hole band width ΔE_h also exhibits a considerable spread in the values obtained by using different theoretical models. According to the results obtained in Refs. 17–20, the total width of the overall hole band in the absence of SO splitting amounts to 0.5 eV, while the value calculated taking into account the SO splitting for subbands with $j=3/2$ and $j=1/2$ does not exceed 0.4 eV. On the other hand, the experiments on energy distribution of electrons in Ne in extrinsic photoeffect make it possible to determine the density of states in the hole bands and give the value ~ 1 eV for the total width of both $2P$ bands in Ne.[4] On the basis of experimental data, we find that the maximum half-width of an individual subband is $\Delta E_h/2 \simeq 0.4$ eV, which is twice as large as the corresponding half-width obtained from theoretical analysis. The corresponding effective mass of a hole (calculated in analogy with (5)) is found to be $m_h = 4.7 m_0$.

A discrepancy also exists between theoretical and experimental results concerning the exciton bands in Ne. Exciton states are classified according to the parameter $\xi = r_n/d$ into cases of strong and weak coupling, i.e., we have twice as stringent criterion as criterion (2) for atoms. As a rough estimate, we use the radii of atomic excitations in Ne given by (3) and (4). The first excited state corresponds to $\xi_1 = 1.49/3.15 \approx 0.5$, the second to $\xi_2 \approx 1.2$, and the condition $\xi_n \gg 1$ of weak coupling is satisfied rigorously only starting from the third term in series (1). It can be seen that the approximation of weak coupling describes correctly the high excited states ($n \geqslant 2$) and is naturally valid for an analysis of the conduction band itself.

The weak coupling approximation is based on Bloch functions describing an additional electron in the conduction band and a hole in the valence band, which are separated by the gap E_g and interact with the effective charge $e_{\text{eff}} = e/\sqrt{\varepsilon_0}$. The remaining valence electron and atomic cores are taken into account by introducing the crystal potential determining effective masses of an electron m_e and a hole m_h in corresponding bands. In this effective mass approximation, the motion of an electron and a hole relative to their common center of mass is characterized by the reduced mass μ, while the motion of their center of mass is characterized by the sum of effective masses ($m_e + m_h$). The expression for exciton band energy $E_n(k)$ (Wannier–Mott exciton series) and general relations between parameters can be written in the form typical of rare-radius excitons:

$$E_n(k) = E_g - \frac{G}{n^2} + \frac{\hbar^2 k^2}{2(m_h + m_e)}, \quad n = 1,2,3,..., \tag{6}$$

$$G = R\frac{\mu}{\varepsilon_0^2} \cdot = \frac{m_0 e^4}{2\hbar^2}\frac{\mu}{\varepsilon_0^2}, \quad \frac{1}{\mu} = \frac{1}{m_e} + \frac{1}{m_h}, \tag{7}$$

were n is the number of the exciton band and G the binding energy for exciton (an analog of the Rydberg energy in the solid phase), and μ is expressed in the units of m_0. The second term in (6) determines the position of the bottom of the nth exciton band with the width described by the third term in (6). The binding energy can be determined in accordance with the values of masses obtained above for Ne:

$$G = R\frac{\mu}{\varepsilon_0^2} = 8.83\mu = 7.24 \text{ eV} \tag{8}$$

for $m_e \approx m_0$, $m_h = 4.7\ m_0$, and $\mu = 0.82\ m_0$.

The absorption spectrum for solid Ne indeed contains two series of bands with a blue matrix shift relative to the gas, which converge virtually to the ionization limit for atom. All exciton bands are in one-to-one correspondence with atomic lines. Figure 3 shows absorption bands for a Ne cryocrystals at $T=8$ K according to Saile and Koch,[21] while the top of the figure shows the energy levels for gas and the ionization limits $I(3/2)$ and $I(1/2)$. We tried to select a hydrogen-like series for the series $\Gamma(1/2)$ which would describe the experimental positions of bands with $n=2,3,4$, have the binding energy $G=7.25$ eV, and converge to the limit $E_g(1/2) \approx I(1/2)$. These requirements are met only for a series with a quantum defect (correction to an integral value of n) having the form

$$E_n(k) = E_g - \frac{G}{(n+\delta_n)^2}, \quad \delta_n \equiv \delta = 0.32, \ n = 1,2,3,... \tag{9}$$

In Fig. 4, we choose the denominator of (9) as the abscissa in order to demonstrate the coincidence of the dependence (9) (dashed curve) with experimental positions of exciton bands (solid curve). A similar series can be also proposed for describing $\Gamma(3/2)$ excitons taking into account the fact that the series must converge to the limit $E_g(3/2)$. The corresponding exciton radii can be estimated from the formulas

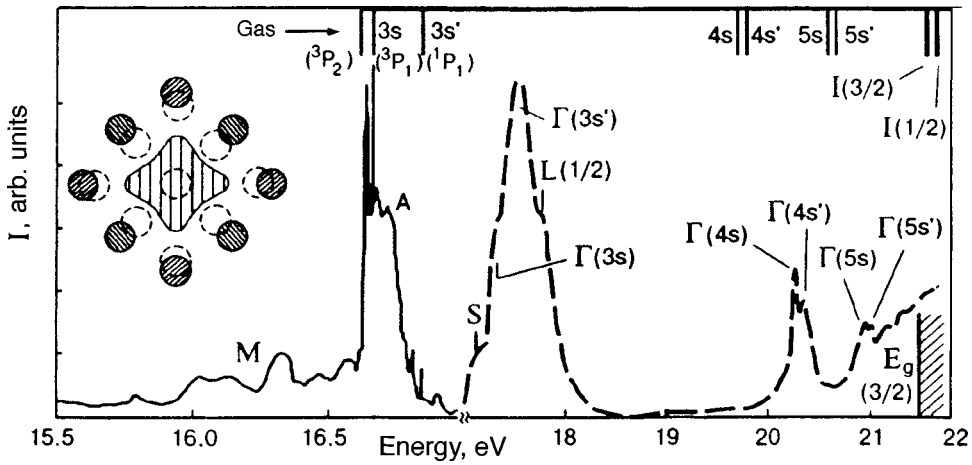

FIG. 3. Absorption (dashed curve) and luminescence (solid curve) spectra for solid Ne; absorption bands for isolated atoms in the gas are shown on the top. The inset shows the repulsion of the nearest neighbors in the lattice by an excited atom for one-center self-trapping.

$$r_n=\frac{\varepsilon_0}{\mu}(n+\delta)^2 a_0, \tag{10}$$

$r_1=1.39\,\text{Å}, \quad r_2=4.30\,\text{Å}, \quad r_3=8.82\,\text{Å}, \quad r_4=14.92\,\text{Å}.$

The use of a defective hydrogen-like series of the type (9) naturally makes the descriptions of solid-state and atomic absorption alike [cf. formulas (1) and (9) as well as the lower dot-and-dash curve in Fig. 4 corresponding to experimental energies of atomic absorption bands and the upper straight line]. It should be noted that using the reliable theoretical and experimental estimates of effective masses of electron and hole, we had to write the exciton series in the form (9) with a positive correction to the quantum number $(n+\delta)$. The necessity of introduction of a quantum correction to the Wannier–Mott exciton series for cryocrystals was considered by some authors[22,23] from a general point of view, but the pragmatic argumentation (choice of parameters) required for its unambiguous application was missing. A few series with a quantum defect were proposed[4,22,23] for solid Ne with different initial approximations. It should be noted that according to Resta *et al.*,[23] one of these series was characterized by the same parameters μ, G, and E_g which were unambiguously chosen by us in (8) as the most reliable parameters.

In the weak coupling approximation, the kinetic energy of exciton is determined by its mass $m_{\text{ex}}=(m_e+m_h)$, and hence the half-width of the exciton band along the Γ-direction for excitons with $n\geqslant 2$ can be estimated as

$$m_{\text{ex}}=m_0+4.7m_0=5.7m_0,$$

$$B_{\text{ex}}^{EMA}=\frac{\hbar^2\pi^2}{2m_{\text{ex}}a^2}=0.3\,\text{eV}. \tag{11}$$

The described model of excitons disregards their lowest excitation state with $n=1$. A rigorous criterion for the applicability of the EMA involves the estimation of the ratio of the Fourier transform of the wave function $A(k)$ for exciton at the center of the Brillouin zone (with $k=0$) and at its boundary $(k=q_D)$, where q_D is the radius of the Debye sphere in the k-space, whose volume is equal to the volume of the Brillouin zone ($q_D=6.2/a$ for an fcc lattice[2]). The ratio of these functions is defined as[24]

$$\frac{A(q_D)}{A(0)}=\frac{1}{[1+(q_D r_{\text{ex}})^2]^2}. \tag{12}$$

Its smallness determines the accuracy of the EMA. For the exciton with $n=1$ in Ne [r_1 is given by (10)], we have

$$\frac{A(q_D)}{A(0)}=0.04 \quad \text{for} \quad q_D=1.4\,\text{Å}^{-1}. \tag{13}$$

For comparison, we note that the ratio (12) for typical semiconductors has the smallness 10^{-4}. According to (13), excitons with $n=1$ in Ne correspond to the intermediate case.

The fact that the state with $n=1$ is correctly described by relation (9) (see Fig. 4) can be explained by the abovementioned effect, when the repulsion of an excited electron from the nearest surroundings plays the same role as a decrease in the effective charge of the nucleus, and this effect is taken into account just by permittivity. At the same time, for $\delta=0.32$ we obtain a good agreement for the exciton radii with the lowest atomic excitation for $n=1$ [cf. formula (3)], which is natural to expect for $r_1<d$. In other words, it appears that the model with a quantum defect is applicable in a certain sense for the lowermost exciton state also. It should

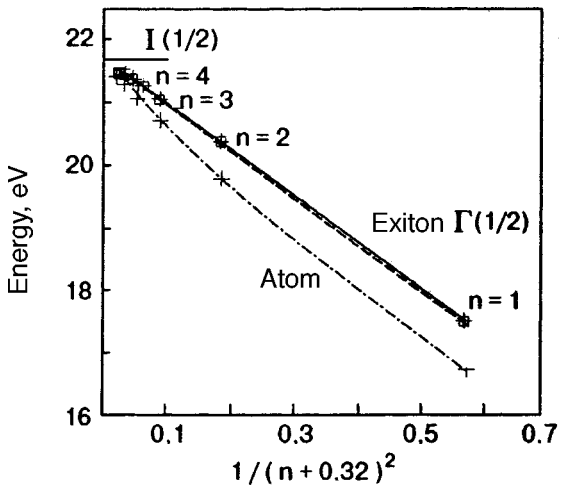

FIG. 4. Rydberg series for $\Gamma(1/2)$ excitons (solid line) and for an atom in the singlet state (dot-and-dash curve). The dashed line corresponds to dependence (9).

be noted that Andreoni *et al.*[25] managed to obtain a satisfactory coincidence of the theoretical position of the lowest exciton band with experimental data for a certain modification of the EMA; however, they did not analyze the dispersion of exciton states.

In accordance with the general principles formulated by Knox,[26] a number of theoretical calculations of the width and position of the exciton with $n=1$ in Ne were made in the strong coupling approximation.[27,28] Using orthogonalized atomic wave functions as the basis, Sribnaya *et al.*[28] estimated the width of the lowest exciton band as $2B=0.4$ eV. However, difficulties were encountered in explaining the position of the bottom of the exciton band with $n=1$. In this respect, *a priori* calculations made by Boursey *et al.*[29] who used potential curves of excited Ne_2^* molecules for interatomic distances $r=d$ proved to be more successful. The energy of transition to the exciton state with $n=1$ was calculated according to the algorithm typical of Frenkel (small-radius) exciton in the form

$$E_f(k)=E_{0f}+D_f+L_f(k), \tag{14}$$

where E_{0f} is the energy of the $0-f$ transition in a free atom, D_f is the displacement of the transition energy due to the interaction of the excited atom with all the surrounding atoms in the crystal (matrix shift), and $L_f(k)$ is the resonant contribution due to dipole–dipole translation of the excitation over the lattice. The value of D_f was calculated from the data on repulsive molecular potentials for $r=d$ according to Cohen and Schneider[14] [see Fig. 1(b)] and using the theoretical crystal potential of polarization attraction taking into account the Van der Waals terms R^{-6} and R^{-8}. Using the results obtained in Ref. 29, we can estimate the matrix shifts and positions of matrix levels (i.e., the midpoints of exciton bands $E_{\mathrm{mid}}=E_{0f}+D_f$) for the lowest atomic transitions with $j=3/2(^3P_1)$ and $j=1/2(^1P_1)$:

$$D_f(^3P_1-{}^1S_0)=0.916\ \mathrm{eV};\quad D_f(^1P_1-{}^1S_0)=0.881\ \mathrm{eV}; \tag{15}$$

$$(E_{0f}+D_f)_{3/2}=17.587\ \mathrm{eV};\quad (E_{0f}+D_f)_{1/2}=17.729\ \mathrm{eV}. \tag{16}$$

It should be recalled that the resonant contribution which was not separated in potentials was included by us in (15). The exciton band width was estimated in Ref. 29 taking into account only the contribution from the long-range dipole–dipole interaction. In this case, the oscillator force F in solid Ne was assumed to be equal to $F=0.11$ for the two exciton transitions $\Gamma(3/2)$ and $\Gamma(1/2)$, which corresponds to complete mixing of singlet and triplet states in the solid phase. It is well known that exciton states experience crystal splitting in the cubic lattice into transverse and longitudinal excitons depending on the mutual orientation of the exciton wave vector **k** and the dipole moment **p** of the optical transition. Transverse excitons ($\mathbf{p}\perp\mathbf{k}$) lying below the matrix level and having a dispersion relation with a positive effective mass are manifested in absorption. The decrease in energy of transverse excitons to the bottom of the band as a result of dipole– dipole energy transfer is given by[26]

$$L^{\perp}=\frac{4\pi}{3}\frac{P^2}{V_0}=\frac{8\pi}{3}\frac{e^2\hbar^2F}{a^3m_0E_T\varepsilon_0},\quad p^2=\frac{e^2\hbar^2F}{a^3m_0E_T\varepsilon_0}, \tag{17}$$

where $V_0=a^3/4$ is the volume of a unit lattice and E_T is the energy of the transition. The energy (17) corresponds to the band width of transverse excitons to within the coefficient of the order of 0.5 depending on the crystallographic direction.[26] According to the estimated obtained in Ref. 29, this value for solid Ne amounts to

$$L^{\perp}(3/2)=0.087\ \mathrm{eV}\ \text{ and }\ L^{\perp}(1/2)=0.097\ \mathrm{eV}. \tag{18}$$

The position of excitons $\Gamma(3/2)$ and (1/2) was determined for $E_T(3/2)=17.5$ eV and $E_T(1/2)=17.63$ eV taking into account (14) and (16). The discrepancy between these data and experimental results[21] (with a blue sift) amounts to 0.15 and 0.13 eV, respectively.

It should be recalled that the matrix element T_{nm} (and hence the exciton band width) contains the contribution not only from the long-range dipole-dipole interaction, but also from the exchange energy responsible for the formation of the hole band, which is not negligibly small. In this connection, we shall mention one more version of the modified strong coupling approximation developed by Ratner and Tarasova,[30] in which the band width must be determined by the sum of the contribution due to the dipole–dipole interaction and the contribution from the hole band (under the assumption that $\Delta E_h \ll I$). The result can be written in the form

$$B=L^{\perp}+\gamma\Delta E_h/2,\quad \gamma\sim\exp[-0.48(d/r_n)^{3/2}]. \tag{19}$$

If we use in this formulas the values of r_1 and ΔE_h determined above, we obtain the following expression for estimation the half-width of the exciton band with $n=1$ in Ne:

$$\gamma=0.23,\quad \gamma\Delta E_h/2=0.09\ \mathrm{eV}\ \text{ and }\ B\approx 0.2\ \mathrm{eV}. \tag{20}$$

Thus, the contribution to the total half-width of the band from the dipole–dipole and exchange interactions are almost identical, which sharply distinguishes the situation with Ne from that for heavier RGS in which the first contribution is negligibly small.

2. MIXING OF STATES OF FREE AND SELF-TRAPPED EXCITONS IN EASILY DEFORMABLE Ne LATTICE

Since the lowest states of excitons with $n=1$ in Ne are characterized by an intermediate radius, they can be described taking into account the interaction of an excited atom only with the nearest neighbors in the lattice. This peculiarity also determined the choice of the approach to the description of the exciton–phonon interaction which is put in correspondence in this case to the potentials of interaction of the excited atom with the surrounding atoms in the ground state in the lattice [see Fig. 1(b)] and is mainly determined by the electron– electron repulsion. The exciton–phonon interaction is manifested in the exciton–phonon scattering ensuring the energy relaxation of excitons in the band as well as in the intensity of interaction between excitons with a local deformation of the lattice, leading to self-trapping of an exciton. Self-trapping of excitons is a very important factor determining the dynamics of excited states, the distribution of relaxation channels among intrinsic, impurity, and defective states, as well as the transport of excitation energy in the crystal.

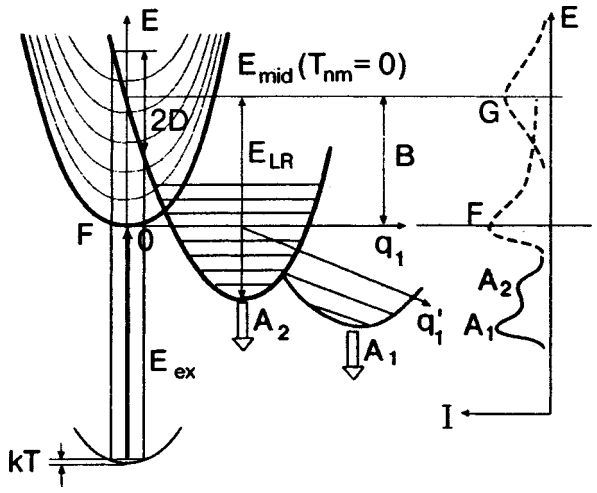

FIG. 5. Diagram of coupling of the states of free and self-trapped excitons in the space of configurational coordinates. The corresponding absorption and luminescence spectra are shown schematically on the right.

It should be recalled that Ne displays intense luminescence of one-center self-trapped excitons (of the quasi-atomic type, denoted by A in Fig. 3),[11] and much weaker luminescence of two-center excitons (of the quasi-molecule type, denoted by M).[31] The formation of quasi-atomic centers is accompanied by the repulsion of nearest neighbors in the lattice by the excited atom (see the inset to Fig. 3). Figure 5 shows schematically the process of self-trapping accompanied with the formation of a quasi-atomic center in the model of configuration coordinates. The state of an excited atom in the crystal corresponds to the local crystal excitation level E_{mid} in the undeformed lattice in the absence of excitation energy transfer to a neighboring atom ($T_{nm}=0$). The resonant coupling lowers the energy of band quasiparticles relative to the local energy level by $B=0.2$ eV. Self-trapping is a competing process lowering the energy of a local excitation. The ground-state potential determines the amplitude of atomic vibrations in the lattice, and the quantity D characterizes the corresponding fluctuation of electron energy during the time $\hbar/\overline{\omega}$ of lattice vibration and determines the width of absorption spectrum of a local center.[2–7] The depth E_{LR} of the potential of the self-trapped state in the approximation linear in deformation and in the elastic approximation for the lattice is connected with the exciton-phonon coupling parameter D through the relation

$$D=(\omega E_{LR})^{1/2}, \tag{21}$$

where ω is the characteristic energy of phonons in the lattice. A band exciton stays at a lattice site for a short time $\hbar/B \ll \hbar/\omega$ (adiabaticity condition), and the extent of its scattering at the local potential is determined by the nonadiabaticity parameter

$$\lambda=D^2/B^2. \tag{22}$$

It should be recalled that the fulfillment of the condition $\lambda \ll 1$ corresponds to a weak exciton–phonon scattering $\Gamma(E)/E \ll 1$, where $\Gamma(E)$ is the probability of one-phonon scattering for an exciton with the kinetic energy E. In this case, coherent nature of notion of a band exciton is manifested in dynamic narrowing of the absorption line (as compared to the local center) and its displacement to the region of the bottom of the band, $E_T=E_{\mathrm{mid}}-B(E=0)$. If $E_{LR}>B$ (condition of strong coupling), we must also take into account simultaneously the probability of exciton transition to the self-trapped state, $G_{ST}(E)$. In this case, the coherence condition for the exciton has the form $[\Gamma(E)+G_{ST}(E)]/E \ll 1$.

In order to characterize the intensity of the exciton–phonon interaction, the experimentally observed Stokes luminescence shift $S=E_{LR}-B$ is normally used. Knowing the value B, we can determine the value of E_{LR} and then find the value of D using formula (21). The probability of a transition to the self-trapped state can be estimated on the basis of the formula

$$G_{ST}(E)=\sqrt{2\pi}\frac{(E-E_{\mathrm{mid}})^2}{D}\exp\left[-\frac{(E-E_{\mathrm{mid}})^2}{2D^2}\right], \tag{23}$$

which is valid for $|E-E_{\mathrm{mid}}| \gg D$.[32]

For a one-center self-trapping of an exciton with $n=1$ in Ne, we have the following parameters: $S=0.65$ eV, $E_{LR}=0.85$ eV, $\omega=0.0075$ eV, $D=0.08$ eV, and $\lambda=0.21$. Thus, in accordance with the chosen approximation, we observe in Ne the situation with a relatively weak exciton–phonon scattering and strong coupling with a local deformation:

$$\omega \ll D \lesssim B < E_{LR}. \tag{24}$$

The calculations of $G_{ST}(E)$ made in Ref. 33 proved that the following relation holds for any values of exciton energy in the band with $n=1$ in Ne:

$$G_{ST}(E) \gg E > \Gamma(E) \sim \lambda E, \tag{25}$$

and hence the situation in Ne can be classified according to the intensity of the exciton– phonon interaction as an exceptionally strong coupling (as compared to heavier cryocrystals of inert elements) leading to a considerable mixing of the states of free and self-trapped excitons.[34] In this connection, several problems appear simultaneously in the description of properties of excitations with $n=1$: (1) the problem of the energy spectrum for quasiparticles; (2) the description of the absorption spectrum and analysis of its peculiarities as compared to the spectrum of conventional excitons, and (3) the applicability of the approximation linear in deformation for determining the constant D.

The only source of information on exciton states in Ne prior to relaxation to the self-trapped state is the absorption spectrum since luminescence spectrum does not display such states. The absorption spectrum (dashed curve in Fig. 3) has a very large width $\Delta E \sim 0.3$ eV and an asymmetric shape with a long blue tail. Such a shape can be described neither by a Lorentzian with a typical one-phonon damping Γ (which corresponds to the spectra of free excitons), nor by a Gaussian with the characteristic damping D (which is used for local centers). The description based on an asymmetric Lorentzian with the overall damping $G_{ST}(E)+\Gamma(E)$ used by us in Ref. 33 can be regarded only as an estimate since it is applicable only when the band properties of excitons are preserved. Thus, it remains for us only to analyze the the pos-

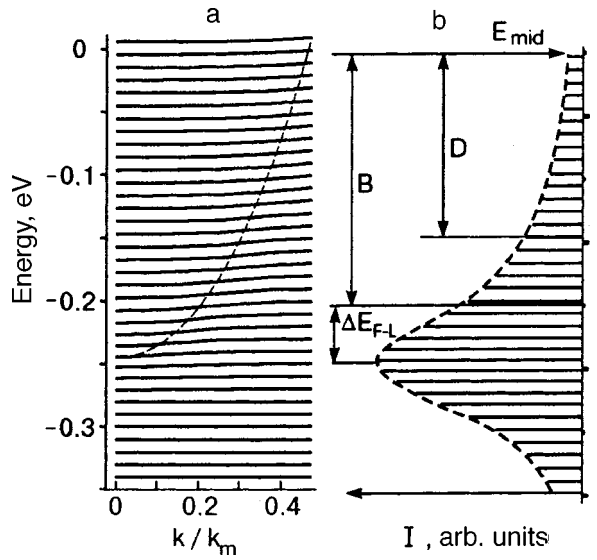

FIG. 6. Dispersion curves for mixed states of free excitons and high-energy vibrons of self-trapped excitations (a). The absorption spectrum corresponding to mixed states is shown in (b).

sibility of describing the absorption spectrum by calculating the dispersion relation for mixed states of free (F) and self-trapped (ST) excitations.

The idea of configurational mixing is based on the quantum-mechanical analysis of motion of atoms in the lattice. The states of free excitons as well as the energy levels of vibrational excitations of a self-trapped type (see Fig. 5), which differ in the configuration of nuclear wave functions the more significantly, the stronger the lattice deformation around a local excitation, lie above the bottom of the band. The process of self-trapping in the nonadiabatic approximation can be regarded as the transformation of the kinetic energy of a band exciton to the kinetic energy of local vibrations of atoms around the excitation. The application of such an approach leads to a renormalization of one-site exciton–vibrational (for brevity, vibron) energy levels of ST states (which are equidistant in accordance with the linear approximation for the exciton–phonon interaction and the harmonic approximation for the lattice) to a set of narrow bands with a peculiar dispersion relation. The equation describing the dispersion relation $E(k)$ for mixed exciton–vibron narrow-band states has the form[34]

$$\sum_s \frac{j_k}{E(k)-e_s}=\frac{1}{\varepsilon(k)}, \tag{26}$$

$$j_s=\frac{\hbar\overline{\omega}}{2\pi}\exp\left[-\frac{(e_s-e_{\mathrm{mid}})^2}{2D^2}\right].$$

Here e_s is the energy of the s vibrational level of the self-trapped state, $\varepsilon(k)$ corresponds to the dispersion branch for an exciton in a rigid lattice, measured from the lattice-site level e_{mid} (e_s and e_{mid} are measured from the bottom of the self-trapped state), and j_s corresponds to the Frank–Condon factor for a local center.

Here we calculate the energy spectrum corresponding to Eq. (26) with $D=0.145$ eV. The results of calculation are presented in [Fig. 6(a)]. At the middle of the band $E=E_{\mathrm{mid}}$, the parameter j_s has the maximum value $\sim\hbar\overline{\omega}/D$, and the effect of mixing of states is manifested most strongly. The width of the energy region with a relatively strong mixing in the band is of the order of D (see Fig. 5), which embraces almost the entire band in the case under investigation. As a result, the branches of exciton–vibron states in Ne have a gentler slope than in Ar.[33] The dashed curve marks the region of strongest variation of the shape of the curves, which corresponds to the dispersion relation $\varepsilon(k)$ for F excitons, which is stretched in the downward direction. The absorption spectrum calculated taking into account the contribution from each branch for $k=0$ by the formula

$$A(E_i)=\frac{1}{B^2}\left[\sum_s \frac{j_s}{(E_i-e_s)^2}\right]^{-1} \tag{27}$$

is shown in Fig 6(b). The envelope of the spectrum is characterized by a large width, long blue tail, and the shift of the peak to the red part of the spectrum by ΔE_{F-L} relative to the position of the bottom E_T of the band for F excitons in a rigid lattice.

Naturally, it is important to describe numerically the actual absorption spectrum (see dashed curve in Fig. 4). An analysis of the spectrum carried out using the value of D estimated by formula (21) led to an inadequately narrow absorption band. In this connection, we must consider a peculiar feature of the Ne lattice, viz., its easy deformability associated with a small value of binding energy per atom, $E_b=0.02$ eV. At the initial stage of self-trapping, the deformation (i.e., expansion of the cavity around an excitation) occurs with preserved point symmetry of the crystal (coordinate q_1 in Fig. 5). The metastable state corresponding to the elastic limit of the lattice emits radiation in the form of the A_2 band. As a result of a high probability that the value of energy decreases with a change in the coordination number of the surrounding (configurational coordinate q_1' in Fig. 5),[6] a state is formed which emits radiation in the form of the A_1 band shifted to the red region by 0.1 eV ($\ll E_{LR}=0.85$ eV). In view of the small value of E_b, the two bands are close to the emission line from an isolated atom.[11] Returning to the potentials of an excited molecule [see Fig. 1(b)], we see that the energy of the electron–electron repulsion decreases nonlinearly with increasing distance to the position of isolated atoms. The value of E_{LR} used by us for determining the value of D has a contribution from the averaged value of deformation potential, while the contribution to the absorption spectrum comes from the maximum value of the deformation potential, which can be noticeably higher than its average value.

Thus, in order to describe the experimental absorption spectrum, we must vary the value of D. Figure 7 shows the spectra corresponding to the position of E_{mid} of the exciton singlet $\Gamma(1/2)$ with the different values of the parameter D. The asymmetric broadening of the absorption band and a noticeable increase in the shift ΔE_{F-L} with increasing D is observed. Each spectrum is normalized to unity in the sum of the contributions from narrow bands.

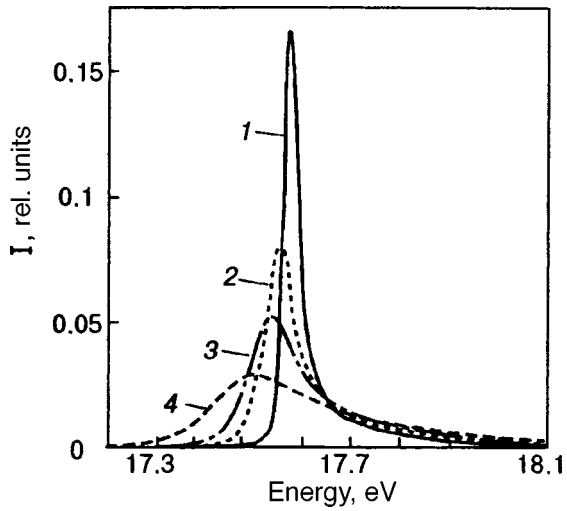

FIG. 7. Calculated absorption spectra for the singlet with $n=1$ in Ne for different values of the exciton–phonon coupling parameter D, eV: 0.09 (curve *1*), 0.12 (curve *2*), 0.15 (curve *3*), and 0.20 (curve *4*); $B=0.2$ eV and $E_{\text{mid}}=17.82$ eV.

In Fig. 8, the experimental absorption spectrum (solid curve) is compared with the sum of two theoretical spectra (dashed curve) for the triplet with the parameter $D=0.145$ eV and the singlet with the parameter $D=0.2$ eV (the individual contributions from these states are shown by dot-and-dash curves). The coincidence can be regarded as satisfactory except two singularities. A low-intensity line (S) observed on the red side of the triplet peak (denoted by ''3'') is reliably identified as absorption of surface excitons (this line is not considered by us here). Another (L) band observed on the blue side is separated approximately by 0.3 eV from the singlet peak (''1'') is attributed by some authors to the emergence of longitudinal excitons.[4–6,21] It should be recalled that polariton effects in active optical transitions in the presence of a considerable spatial dispersion (the criteria of this effect can be found, for example, in Ref. 6) are manifested in the broadening of transmission and reflection spectra to the magnitude Δ_{LT} of transverse–longitudinal splitting.

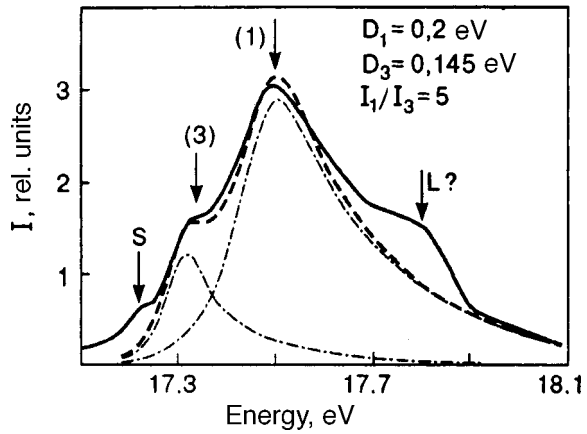

FIG. 8. Comparison of the experimental (solid curve) and theoretical (dashed curve) absorption spectra for excitons with $n=1$ in Ne. Dot-and-dash curves describe the contributions from the triplet (3) and singlet (1) states.

These effects were used to explain not only the width of spectra for xenon, but also the doublet structure of absorption spectra for Kr and Ar with a clearly manifested additional peak at the frequency corresponding to longitudinal excitons just for the singlet transition. For this reason, it was natural to propose a similar interpretation for a high-intensity exciton singlet transition in Ne also. Calculations made by different authors[35] lead to values of $\Delta_{LT}\sim 0.25-03$ eV, which formed the basis of such an interpretation.

Here we propose an alternative explanation of the abnormally large width of the absorption band, which appears as more logical in the case of exceptionally strong exciton–phonon interaction. It was proved above that the effective masses of exciton–vibron states of all narrow bands in this case are very large, and the spectrum is quasi-linear. Consequently, the possibility of observation of polariton effects on the basis of spatial dispersion becomes problematic in this situation and obviously requires additional detailed analysis.

In order to explain the fact that the singlet transition corresponds to the larger value of D, we recall that the singlet $^1P_1$ forms only repulsive terms with a normal atom, but the triplet $^3P_1$ forms a very deep bound state 0_u^- due to resonant coupling, which modifies the shape of the potential curve for the crystal.

In accordance with the decomposition of the absorption band into the contributions from the triplet and singlet states (see Fig. 8), a comparison of the corresponding integral intensities leads to the following ratio of oscillator forces for excitations in solid Ne:

$$I_1:I_3=F_1:F_3=5:1. \tag{28}$$

It should be recalled that the corresponding ratio for a gas is 10:1, and its value for a solid according to experimentally-based estimates[35] must vary from 5 to 10 (the contributions of the bands in the spectrum cannot be separated accurately). We obtained the minimum ratio due to the fact that the blue tail of the triplet band calculated by us makes a significant contribution to the observed peak of the singlet band. A leveling out of band intensities due to the mixing of states in the solid phase is typical for cryocrystals of inert elements (mostly for heavier atoms).[35] Theoretical estimates obtained for Ne differ by an order of magnitude in publications which appear most realistic as regards the positions of the bands (from the ratio 1:1 in Ref. 29 to 50:1 in Refs. 24 and 25).

The values of transition energies corresponding to the local energy level E_{mid} were also determined by fitting the theoretical spectrum to the experimental one (cf. the values given in (16)): $(E_{0f}+D_f)_{3/2}=17.60$ eV; $(E_{0f}+D_f)_{1/2}=17.82$ eV. The following values were obtained for additional shifts of the bands ΔE_{FL} (see Figs. 6 and 7): $\Delta E_{F-L}(3/2)=0.05$ eV, $\Delta E_{F-L}(1/2)=0.12$ eV.

Thus, the effect of the exciton–phonon interaction on the position of the peak of the absorption band is comparable with the values of both contributions to the exciton band width, which were considered in the previous section [see formulas (18)–(20)].

*E-mail: fugol@ilt.kharkov.ua

[1] J. I. Frenkel, Phys. Rev. **37**, 1276 (1931).
[2] A. F. Prikhot'ko, V. G. Manzhelii, I. Ya. Fugol *et al.*, in *Cryocrystals* (ed. by B. I. Verkin and A. F. Prikhot'ko) [in Russian], Naukova Dumka, Kiev (1983).
[3] I. Ya. Fugol', Adv. Phys. **27**, 1 (1978).
[4] N. Schwentner, E. E. Koch, and J. Jortner, *Electronic Excitations in Condensed Rare Gases*, Springer-Verlag, Berlin (1985).
[5] G. Zimmerer, in *Excited State Spectroscopy in Solids*, XCVI Corso Societa Italiana di Fisica, Bologna (1987).
[6] I. Ya. Fugol', Adv. Phys. **37**, 1 (1988).
[7] M. Ueta, H. Kanzaki, K. Kobayashi *et al.*, in *Excitonic Processes in Solids*, Springer-Verlag, Berlin–Heidelberg–New York–Tokyo (1986).
[8] I. Fugol, Pure Appl. Chem. **69**, 1219 (1997).
[9] M. Joppien, D. Varding, G. Zimmerer, and T. Muller, Proceedings Reprint, SPIE **2362**, 334 (1995).
[10] A. G. Belov, I. Ya. Fugol, and E. M. Yurtaeva, Fiz. Nizk. Temp. **19**, 600 (1993) [Low Temp. Phys. **19**, 427 (1993)].
[11] A. G. Belov, G. M. Gorbulin, I. Ya. Fugol, and E. M. Yurtaeva, Fiz. Nizk. Temp. **23**, 439 (1997) [Low Temp. Phys. **23**, 322 (1997)].
[12] C. E. Moore, *Atomic Energy Levels*, Natl. Bur. Circ. No. 467, U.S. GPO, Washington, D.C. (1958).
[13] A. A. Radtsig and B. M. Smirnov, *Reference Data on Atomic and Molecular Physics*, Springer-Verlag, Berlin, 1985.
[14] J. S. Cohen and B. Schneider, J. Chem. Phys. **61**, 3230 (1974).
[15] I. A. Barker, in *Rare Gas Solids* (ed. by M. K. Klein and J. A. Venables), vol. 1, Academic Press, London (1976).
[16] I. Ya. Fugol, Usp. Fiz. Nauk **97**, 429 (1969) [Sov. Phys. Usp. **12**, 182 (1969)].
[17] U. Rossler, in *Rare Gas Solids* (ed. by M. K. Klein and J. A. Venables), Vol. 1, Academic Press, London (1976).
[18] L. Dagens and F. Perrot, Phys. Rev. B **5**, 641 (1972).
[19] A. B. Kunz and D. J. Mikish, Phys. Rev. B **8**, 779 (1973).
[20] E. V. Zarochintsev, E. P. Troitskaya, and E. Ya. Fain, Fiz. Tverd. Tela (Leningrad) **21**, 438 (1979) [Sov. Phys. Solid State **21**, 259 (1979)].
[21] V. Saile and E. E. Koch, Phys. Rev. B **20**, 784 (1979).
[22] R. Resta, Phys. Status Solidi B **86**, 627 (1978).
[23] L. Resca, R. Resta, and S. Rodriguez, Phys. Rev. B **B18**, 696 (1978).
[24] F. Bassani and G. Pastori Parravicini, *Electronic States and Optical Transitions in Solids* Pergamon Press, Toronto (1975).
[25] W. Andreoni, F. Perrot, and F. Bassani, Phys. Rev. B **B14**, 3589 (1977).
[26] R. S. Knox, *Theory of Excitons*, Academic Press, New York, London (1963).
[27] A. Gold, Phys. Rev. **124**, 1740 (1961).
[28] V. K. Sribnaya, K. B. Tolpygo, and E. P. Troitskaya, Fiz. Tverd. Tela (Leningrad) **20**, 1668 (1978) [Sov. Phys. Solid State **20**, 966 (1978)].
[29] E. Boursey, M.-C. Castex, and V. Chandrasekharan, Phys. Rev. B **16**, 2858 (1977).
[30] A. M. Ratner and E. I. Tarasova, Fiz. Nizk. Temp. **4**, 1180 (1978) [Sov. J. Low Temp. Phys. **4**, 556 (1978)].
[31] O. N. Grigorashchenko, Yu. I. Rybalko, E. V. Savchenko, and I. Ya. Fugol, Fiz. Nizk. Temp. **8**, 886 (1982) [Sov. J. Low Temp. Phys. **8**, 447 (1982)].
[32] A. Sumi, J. Phys. Soc. Jpn. **47**, 1538 (1979).
[33] I. Ya. Fugol and E. I. Tarasova, Fiz. Nizk. Temp. **23**, 767 (1997) [Low Temp. Phys. **23**, 578 (1997)].
[34] K. Cho and Y. Toyozawa, J. Phys. Soc. Jpn. **30**, 1555 (1971).
[35] V. Saile, Appl. Opt. **19**, 4115 (1980).

Translated by R. S. Wadhwa

LATTICE DYNAMICS

Analysis of thermodynamic properties of fullerite C_{60}

N. A. Aksenova, A. P. Isakina, A. I. Prokhvatilov, and M. A. Strzhemechny

*B. Verkin Institute for Low Temperature Physics and Engineering, National Academy of Sciences of the Ukraine, 310164 Kharkov, Ukraine**

(Submitted March 2, 1999; revised April 21, 1999)
Fiz. Nizk. Temp. **25**, 964–975 (August–September 1999)

The thermal expansion coefficients of pure fullerite are determined on the basis of powder x-ray studies in the temperature range 30–293 K. The obtained results are in good agreement with dilatometric and neutron-scattering data. The data on thermal expansion are used to analyze the heat capacity at constant volume C_V. The intramolecular component of C_V is analyzed consistently and accurately taking into account the complete set of temperature-dependent intramolecular eigenfrequencies. The rotational component of heat capacity is obtained by subtracting the intramolecular and phonon contributions from the total C_V. The phonon component is evaluated on the basis of the Debye model using the Debye temperature ($\Theta_D^{(0)}=55.4\,\mathrm{K}$) calculated from the known sound velocities. The general and partial Grüneisen parameters are calculated as functions of temperature. The results obtained for the high-temperature phase indicate that rotations of C_{60} molecules are strongly hindered and intercorrelated. © *1999 American Institute of Physics.* [S1063-777X(99)02108-8]

INTRODUCTION

The peculiarities observed in the physical properties of fullerite C_{60} are determined to a considerable extent by variations in the orientational subsystem. A deeper understanding of the origin of these peculiarities necessitates a detailed analysis of the structural and thermodynamic properties of fullerite crystals and requires information on its rotational and vibrational spectra. Peculiarities in the physical properties of C_{60} appearing as a result of variation of the rotational state of the molecules in the order–disorder phase transition region ($T_c=260\,\mathrm{K}$) and at lower temperatures were studied in detail by many authors who used various methods including x-ray[1–9] and neutron diffraction,[10–12] nuclear magnetic resonance,[13–17] calorimetry[18–30] Raman and infrared spectroscopy,[30–33] inelastic neutron scattering,[34–38] electron diffraction,[39–41] and dilatometry.[42–44]

It was found that in the high-temperature phase C_{60} molecules are orientationally disordered. A decrease in temperature leads to consecutive freezing of rotations and to the formation of a number of phase states differing in the type of rotational motion of molecules. At 260 K, a phase transition to the orientationally ordered phase takes place, in which the molecules with the third-order axes are oriented along four spatial diagonals ($\langle 111\rangle$ directions) of the cubic lattice. During their rotation about $\langle 111\rangle$ axes, molecules consecutively occupy six orientational wells which are quite deep (the height of the barrier separating them is approximately 250 meV) and differ in depth approximately by 10 meV.[44] These states correspond to two different energy minima for the mutual orientation of neighboring molecules: the global minimum when one of the fifth-order axes of a molecule is directed to the midpoint of one of the double bonds of a neighboring molecule (pentagon molecular configurations) and the local minimum when the third-order axis of a molecule is directed to the midpoint of the double bond of a neighboring molecule (hexagonal configurations). As the temperature decreases, the frequency of molecular rotations becomes lower, and the concentration ratio for these two orientational states changes in favor of the former state. The retardation of rotational motion of molecules affecting significantly the form of temperature dependences of a number of physical parameters (lattice constants, intensity of reflections, thermal expansion coefficients, and so on) starts being manifested even at $T\leqslant 160\,\mathrm{K}$. Below 90 K, molecular rotations are frozen completely, and the orientational glass state is formed.

A number of aspects, however, remained not quite clear. For example, is was not proved completely whether molecular rotation above 260 K is noticeably retarded or completely free. It has not been established unambiguously whether phenomena observed near 90 K correspond to a thermodynamically equilibrium structural phase transition, or the observed peculiarities reflect kinetic phenomena, or are features of a ''glass'' transition. In addition, the data on thermal expansion, which are often used for an analysis of the physical properties of crystals, were obtained in a wide temperature range only by the scanning dilatometry method,[42] and it was interesting to compare them with the results obtained by other methods.

In this paper, we present the thermal expansion coefficients obtained by x-ray dilatometry and carry out an analysis of thermodynamic properties (heat capacity and the Grüneisen parameter) of fullerite C_{60} in the temperature range 30–300 K. We used the experimental data on the crystal structure of fullerite C_{60}, temperature dependence of lattice

 © 1999 American Institute of Physics

parameters, molar volumes, and density which were obtained by us earlier[45–48] as well as the available data on the measurements of heat capacity at constant pressure, compressibility, sound velocities, and other thermodynamic parameters. As a result of our calculations, we singled out and analyzed the contributions to thermodynamic properties of C_{60} due to thermal excitations of the translational and rotational subsystems. Our conclusions are compared with the conclusions drawn by other authors from independent considerations.

THERMAL EXPANSION

In our previous publications,[45–48] we reported on x-ray studies of polycrystalline samples of pure (99.98%) fullerite C_{60} in the temperature range 5–293 K. We obtained a detailed (with a step 2–5 K) temperature dependence of the cubic lattice parameter a (shown graphically in Fig. 2 in Ref. 45) for the low-temperature orientationally ordered ($T<260$ K, symmetry $Pa3$) and high-temperature orientationally disordered ($T>260$ K, symmetry $Fm3m$) phases. The error in determining the lattice parameters was $\pm 0.02\%$. The temperature dependence $a(T)$ was plotted on the basis of experimental data obtained for several samples subjected to heating and cooling. The large body of experimental data obtained for lattice parameters enabled us to carry out a reliable statistical processing by the least squares method (LSM) and to reconstruct the temperature dependence of a from the average values in the entire temperature range under investigation. The absolute value of the lattice parameter at room temperature and its temperature variation[45] within the above-mentioned error are in good agreement with the available data obtained by x-ray and neutron diffraction methods on polycrystalline samples[1,10,11,49] and single crystals[2,8,50] of fullerite C_{60}. Here we report on the numerical values of lattice parameters, molar volumes, density, and thermal expansion coefficients (Table I). The latter were determined by differentiating the averaged temperature dependence of lattice parameters with an error $\pm 5\%$ for the major part of the temperature interval, and up to $\pm 10\%$ in the immediate vicinity of phase transitions due to an increase in the spread in lattice parameters in these regions. Figure 1 shows the x-ray linear thermal expansion coefficients $\alpha = (\Delta a/a)\Delta T$ obtained by us for polycrystalline samples together with dilatometric values of α obtained by Gugenberger *et al.*[42] for single crystals. It can be seen that out results are in good agreement with dilatometric values in the major part of the temperature interval. Some discrepancy is observed only in the immediate vicinity of the temperatures T_c corresponding to the orientational phase transition, T_g corresponding to the end of formation of glass state, and at low temperatures $T<50$ K. The difference in the thermal expansion coefficients in these regions can be attributed to different microstructural states of the samples (polycrystals and single crystals) as well as to experimental difficulties in the study of anomalous behavior of thermodynamic quantities near critical points and different sensitivities of the x-ray and dilatometric methods to crystal lattice defects.

We also analyzed the results of neutron diffraction studies[10] of the temperature dependence of the lattice parameter for a polycrystalline sample of fullerite C_{60}. The obtained values of linear thermal expansion coefficient of C_{60} are in accord (to within possible error in their determination) with our results and with the results of dilatometric measurements (see Fig. 1).

It follows from Refs. 10, 45, 46, and 51 that the temperature dependence of lattice parameters near 155 K has a typical kink corresponding to an insignificant singularity on the temperature dependence of the temperature dependence of the linear thermal expansion coefficient (see Fig. 1). It is

TABLE I. Lattice parameter a, molar volume V, X-ray density ρ, volume coefficients of thermal expansion β, velocities of longitudinal v_l and transverse v_t sound of ultrapure fullerite C_{60}.

T, K	a, Å	V, cm^3/mole	ρ, g/cm^3	β, 10^{-5} K^{-1}	v_l, 10^5 cm/s	v_t, 10^5 cm/s
30	14.043	416.93	1.7285	-	3.04	1.46
40	14.044	416.98	1.7283	1.50	3.03	1.46
50	14.045	417.07	1.7279	2.16	3.02	1.45
60	14.046	417.13	1.7277	2.88	3.01	1.45
70	14.047	417.32	1.7269	3.69	3.01	1.44
80	14.050	417.55	1.7259	5.10	3.00	1.44
90	14.053	417.85	1.7247	-	2.99	1.44
100	14.058	418.30	1.7229	1.05	2.98	1.43
110	14.059	418.34	1.7228	1.29	2.98	1.43
120	14.060	418.40	1.7224	1.65	2.97	1.43
130	14.061	418.49	1.7221	2.10	2.96	1.42
140	14.062	418.61	1.7216	2.85	2.94	1.41
150	14.063	418.74	1.7210	3.45	2.90	1.39
160	14.065	418.94	1.7203	4.22	2.86	1.37
170	14.068	419.12	1.7195	4.50	2.82	1.36
180	14.070	419.34	1.7186	5.31	2.81	1.35
190	14.073	419.59	1.7176	6.09	2.80	1.34
200	14.076	419.87	1.7164	6.84	2.78	1.33
210	14.079	420.17	1.7152	7.51	2.76	1.33
220	14.083	420.51	1.7138	8.25	2.74	1.32
230	14.087	420.88	1.7123	9.00	2.72	1.31
240	14.092	421.28	1.7107	9.75	2.70	1.30
250	14.097	421.71	1.7089	10.50	2.68	1.29
255	14.099	421.95	1.7079	-	2.68	1.28
265	14.154	426.92	1.6881	4.56	2.55	1.22
270	14.155	427.02	1.6877	4.65	2.55	1.22
280	14.158	427.24	1.6868	5.22	2.54	1.22
290	14.161	427.49	1.6858	5.76	2.50	1.20

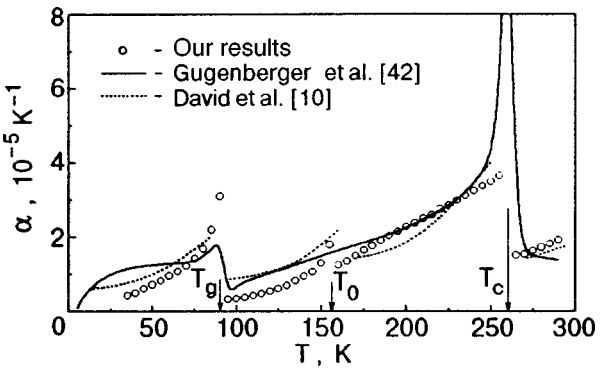

FIG. 1. Temperature dependence of x-ray linear thermal expansion coefficients for pure fullerite C_{60} in comparison with the dilatometric data[42] and the results of processing of neutron diffraction data[10] for lattice parameters.

assumed[16,26,51] that the anomaly at $T_0 \approx 155$ K is associated with freezing of molecular rotations, leading to the formation of glass state in C_{60}. It should be noted that the beginning of glass formation is manifested more clearly on the temperature dependences of elastic properties and sound absorption[52] as well as in photoconductivity.[53] Besides, superstructural reflexes forbidden for the $Pa3$ symmetry are observed at $T < 160$ K.[6] It was proved by us earlier[45] that structural diffraction lines are broadened in this temperature region, indicating the emergence of a nonuniform local deformation of the lattice.

In addition to x-ray thermal expansion coefficients obtained by us here and the results of dilatometric measurements on single crystals,[42] thermal expansion of thin films of fullerite C_{60} was studied recently by the electron-diffraction method,[39] while high-sensitivity dilatometry was applied for powder samples compacted under a pressure up to 1 GPa.[43] The average value $2.5\times10^{-5}\,K^{-1}$ of the linear thermal expansion coefficient obtained for films having a thickness of 6 nm in the temperature range 80–273 K was found to be higher than for bulk poly- and monocrystalline samples. The measurements of linear thermal expansion of compacted samples[43] were made in the temperature range 2–9 K. The results obtained at 5–9 K are in good agreement with the data obtained for single crystals.[42] It should be noted that even before the experimental data[43] were reported, the assumption concerning the presence of anomaly in the thermal expansion of C_{60} near 0 K and probably the emergence of negative coefficient could be made on the basis of an analysis of the low-temperature part of the $\alpha(T)$ dependence obtained in Ref. 42 (strong tendency of the value of α to zero in Fig. 1 of Ref. 42 away from $T=0$ K). Indeed, Aleksandrovskii *et al.*[43] subsequently proved experimentally that thermal expansion coefficients become negative even at $T < 3.4$ K. The negative volume expansion of crystals is a rare phenomenon which can be due[43] to tunnel transitions in the rotational subsystem of the crystal.[54–57]

HEAT CAPACITY

An analysis of thermodynamic parameters of fullerite C_{60} (including its heat capacity) was carried out earlier by many authors (see Refs. 23,26,33,58–63). In view of the absence of sufficient experimental data, various theoretical models[23,26,33,60,63] were often used to single out heat capacity components corresponding to different degrees of freedom. The most comprehensive analysis of heat capacity components was carried out recently by Tewari *et al.*[23] on the basis of models containing cubic and planar collective and localized modes that reflect correctly the dynamics of the diamond and graphite lattices. However, none of these authors took into account extensively the anharmonism and correlations of rotations and vibrations of molecules near the phase-transition temperatures, consist or separated the heat capacity component associated with pure rotation of molecules in orientationally ordered and disordered phases on the basis of experimental data, which is an important problem in an analysis of lattice dynamics and phase transitions.

TABLE II. Temperature dependence of heat capacities at constant pressure C_P and constant volume C_V, intramolecular heat capacity C_{in}, adiabatic compressibility χ_S, characteristic Debye temperature $\Theta_D^{(0)}$ heat capacity C_{rot} of the rotational subsystem, and Grüneisen parameter γ_{lat}.

T, K	C_P	C_V	C_{in}	χ_S, 10^{-11} cm^2/dyne	$\Theta_D^{(0)}$, K	C_{rot}, cal/(mol·k)	γ_{lat}
	cal/(mol·k)						
30	9.55	-	0.4	0.90_4	55.2	-	-
40	10.75	10.7_3	1.6	0.90_9	55.1	3.4_7	1.8_1
50	11.70	11.2_2	2.2	0.91_4	54.9	3.4_2	2.4_7
60	12.18	12.1_3	3.3	0.92_1	54.7	3.3_4	3.5_1
70	13.37	13.3_6	4.4	0.92_4	54.6	3.2_6	4.4_3
80	16.48	16.2_6	7.3	0.92_9	54.5	3.2_0	5.9_7
90	19.91	19.1_2	10.3	0.93_5	54.3	3.0_6	-
100	20.30	20.2_9	12.2	0.94_1	54.1	2.1_8	1.3_8
110	23.88	23.8_6	16.1	0.94_6	54.0	2.0_1	1.7_3
120	28.66	28.6_3	20.0	0.95_1	53.9	2.7_4	2.0_0
130	32.48	32.4_3	23.7	0.95_7	53.7	2.8_1	2.5_1
140	37.02	36.9_0	27.9	0.97_1	53.3	3.0_5	3.2_3
150	41.80	41.6_2	32.3	0.99_6	52.6	3.4_0	3.7_2
160	46.58	46.3_0	36.8	1.02_9	51.8	3.5_7	3.8_6
170	52.55	52.2_2	41.6	1.05_3	51.2	4.6_9	4.0_3
180	58.04	57.5_6	46.3	1.06_3	50.9	5.2_9	4.2_8
190	65.68	65.0_3	51.5	1.07_4	50.7	7.5_6	4.0_2
200	71.65	70.8_0	55.7	1.08_8	50.4	9.1_6	4.1_7
210	78.82	77.7_9	60.8	1.10_4	50.0	11.0_1	3.7_9
220	89.09	87.7_6	65.2	1.12_0	49.7	16.5_6	3.1_0
230	101.51	99.8_9	70.4	1.13_7	49.3	23.5_4	2.7_0
240	132.56	130.6_0	75.5	1.15_5	48.9	49.1_5	1.5_4
250	179.13	177.3_0	80.8	1.17_7	48.5	90.5_5	-
265	105.57	105.1_5	89.0	1.32_0	45.9	10.2_0	2.3_4
270	107.48	107.0_4	90.9	1.32_3	45.8	10.1_9	2.2_3
280	112.26	111.8_0	96.4	1.32_5	45.7	9.4_5	2.6_1
290	117.03	116.3_2	101.3	1.37_0	45.0	9.0_7	2.8_6

Remark: χ_S is calculated for polycrystalline samples.

In order to analyze heat capacity and separate contributions of various types, we shall require the values of adiabatic χ_S and isothermal χ_T compressibilities. Low-disperse samples can be regarded as isotropic, and hence we can use the following relation:

$$\chi_S = \rho(v_l^2 - 4/3v_t^2)^{-1}. \quad (1)$$

We calculated the value of χ_S on the basis of our results on the density ρ of fullerite C_{60} as well as the results of measurements of the longitudinal v_l and transverse v_t sound velocities,[52,64–66] The absolute values of the velocities of sound were determined in Refs. 64 and 66 for polycrystalline samples and are given only for one temperature (290 K) where $v_l = (2.49 \pm 0.02)\cdot 10^5$ cm/s and $v_t = (1.20 \pm 0.01)\cdot 10^5$ cm/s. The relative variation of the sound velocities with temperature $v(T)/v(300\,\text{K})$ at $T < 290$ K was measured by the ultrasound method on polycrystals in Refs. 52,65–68, the results of measurements being very close. Using the above values of sound velocities at room temperature and their variation upon cooling from Refs. 52, 67, 68, we reconstructed the absolute values of v_l and v_t in the temperature range 30–300 K (see Table I). The values of compressibilities χ_S calculated on the basis of Eq. (1) (with an error not exceeding $\pm 5\%$) for polycrystalline samples are given in Table II. Recently, the sound velocities for single crystals were determined by Soifer and Kobelev.[69] The estimates of

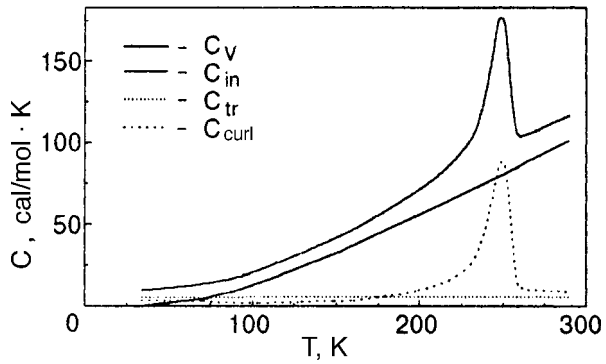

FIG. 2. Temperature variation of intramolecular C_{in}, rotational C_{rot}, and translational C_{tr} contributions to heat capacity at constant volume C_V for fullerite C_{60}.

the macroscopic bulk compression modulus given in Ref. 69 for polycrystal proved to be 25% higher than the values obtained from measurements of sound velocities on polycrystalline samples. It should also be noted that the values of the bulk compression modulus are in good agreement with direct measurements of compressibility of polycrystals.[70,71] Since the data for single crystals[69] were obtained only at room temperature, we could not use them for an analysis of the temperature dependence of thermodynamic parameters. We are aware of the fact that the absolute values of χ_S given in Table II for polycrystals can differ significantly from true values. However, this does not affect considerably the estimates that will be obtained by us below.

An extensive analysis of heat capacity and separation of different types of contributions to thermodynamic properties were carried out by us on the basis of the most reliable data[17,18] on heat capacity at constant pressure C_P, which were used to calculate the heat capacity at constant volume C_V:

$$C_V = C_P - \beta^2 VT/\chi_T, \tag{2}$$

where β is volume thermal expansion coefficient, V the molar volume, and χ_T the isothermal compressibility defined as

$$\chi_T = \chi_S + \beta^2 VT/C_P. \tag{3}$$

It can be easily verified that $\Delta\chi = \chi_T - \chi_S$ varies in the entire temperature range form 0.8% (at 40 K) to 0.6% (at 290 K), which allow us to use in (2) any compressibility almost without increasing the error in the calculation of C_V. The values of constant-volume heat capacity calculated according to formula (2) are presented in Table II and in Fig. 2. It can be seen that the difference $\Delta C = C_P - C_V$ is comparable to the error in the calculation of C_V and is much smaller than the absolute values of heat capacity C_P (or C_V) and hence does not affect the results of separation of the contributions to heat capacity. It should be noted that in contrast to classical simplest molecular crystals, the difference $(C_P - C_V)$ obtained for fullerite C_{60} is small even at high temperatures, but exceeds the error of its determination by a factor of several units. The main reason behind the smallness of $(C_P - C_V)$ is the value of thermal expansion coefficients which are at least an order of magnitude smaller than the values typical of molecular cryocrystals.[72]

In the temperature range under investigation, the heat capacity at constant volume under the assumption that the contributions are additive can be presented in the form

$$C_V = C_{\text{rot}} + C_{\text{tr}} + C_{\text{in}}, \tag{4}$$

where the individual terms on the right-hand side correspond to rotational, translational, and intramolecular degrees of freedom respectively. The rotational heat capacity C_{rot} was obtained by separating the well-defined translational C_{tr} and intramolecular C_{in} contributions from the total heat capacity C_V. According to the results obtained by Yu *et al.*,[60] the lattice and intramolecular modes are separated by a large gap (of the order of 22 meV), which enabled them to use the approximation of rigid molecules for calculating the low-temperature thermodynamic parameters of C_{60} crystals.

A detailed analysis of heat capacity of C_{60} at low temperatures was carried out for the first time by Beyermann *et al.*[20] who proved that the heat capacity in the temperature range 1.4–20 K can be described correctly by the sum of three types of contributions associated with translational (Debye model) and librational (Einstein model) vibrations of C_{60} molecules as well as the linear contribution emerging due to the presence of two-level states in the crystals, which are similar to those observed in glasses. The phonon component of the heat capacity of C_{60} was described in different versions using two ($\Theta_{D1} = 49$ K and $\Theta_{D2} = 67$ K) or one characteristic Debye temperature ($\Theta_D = 74$ K).[20] The value of $\Theta_D = 50$ K was obtained by Atake *et al.*[18,19] from an analysis of heat capacity. However, some other authors report on much higher values of the characteristic Debye temperature. For example, according to Olson *et al.*,[21] $\Theta_D = 80$ K. The estimates obtained on the basis of the results of investigation of elastic properties of single crystals by the ultrasound method at room temperature give $\Theta_D = 66$ K[69] and 100 K[73].[1)] Such a large spread in the data on the characteristic phonon temperature is primarily not due to errors in the measurements of heat capacity, but due to indeterminacy in the choice of the temperature interval for separating the dependence AT^3 from the total heat capacity C_P, and hence considerable errors in the separation of the ''glass'' and phonon contributions. Besides, a possible reason behind the large spread in the values of Θ_D can be the difference in the purity of experimental samples. It is well known[74] that admixtures of C_{70} molecules considerably affect the phase-transition temperature T_c in C_{60}, decreasing it linearly with an intensity of 5 K per percent of impurity. In our opinion, the high values of Θ_D obtained by Grevei *et al.*[25] are due to the presence of C_{70} impurity in the samples. According to Olson *et al.*,[21] the cubic temperature dependence of heat capacity for pure fullerite C_{60} is manifested most clearly at $T < 1$ K, while an analysis of the phonon heat capacity was carried out by many authors at temperatures above 4.2 K.

In order to separate the phonon heat capacity of fullerite C_{60}, we calculated the Debye temperature from the data on longitudinal and transverse sound velocities and molar volumes by using the well-known relation for the zero-point Debye temperature[75]:

$$\Theta_D^{(0)} = \frac{h}{k}(9N/4\pi V)^{1/3}(v_l^{-3} + 2v_t^{-3})^{-1/3}, \quad (5)$$

where h and k are the Planck and Boltzmann constants and N is the Avogadro constant. In our calculations, we used the values of sound velocities and molar volume given in Table I. The limiting value of the zero-point Debye temperature (at $T = 0$ K) was found to be $\Theta_D^{(0)} = 55.4$ K.

The variation of $\Theta_D^{(0)}$ with temperature (Table I) was taken into account for calculating the lattice contribution $C_{\rm tr}$ to heat capacity, associated with translational vibrations of C_{60} molecules. The obtained results show that the phonon component of heat capacity at $T > 30$ K varies with temperature only slightly and amount to 5.62 cal/(mole·K) at 30 K and 5.94 cal/(mole·K) at room temperature. Consequently, the lattice heat capacity of fullerite C_{60} attains its high-temperature limit $C_{\rm tr} = 3R$ (R is the gas constant) even at quite low temperatures.

In the temperature range under investigation (especially in its high-temperature part), the contribution $C_{\rm in}$ of intramolecular vibrations to heat capacity can be significant for substances formed by large molecules of the fullerene type. The spectrum of intramolecular vibrations of C_{60} contains a large number (174) of optical frequencies.[76–78] In an analysis of $C_{\rm in}$, we used the values of the lowermost frequencies (in $\rm cm^{-1}$) experimentally observed in the Raman and infrared spectra at 40 K (the degeneracy is indicated in the parentheses): 272 (5), 433 (5), 496 (1), 533 (3), 567 (3), 709 (5), 772 (5), 1099 (5), 1252 (5), 1425 (5) and 1575 (5). These values make a noticeable contribution (at least 0.5 cal/(mole·K) to the heat capacity $C_{\rm in}$. The temperature variation of the frequencies and the jumps observed for some of their values during the phase transition at 260 K were taken into account using the data obtained in Ref. 78, while for the remaining frequencies we used the average statistical values of the temperature gradient and the jump at the transition. It is worth noting that intramolecular modes are characterized by high harmonicity (Raman frequencies coincide to a high degree of accuracy with the sum of corresponding fundamental frequencies) and a weak coupling with the lattice (weak temperature dependence). The values of $C_{\rm in}$ were calculated in the Einstein approximation taking into account the degeneracy for each of the optical modes listed above. The results of calculations are presented in Table II and in Fig. 2. As expected, the temperature dependence of the heat capacity component $C_{\rm in}$ does not experience noticeable changes in the region of orientation phase transition. Pay attention to the fact that intramolecular vibrations make a noticeable contribution to the total heat capacity, which increases almost linearly above 100 K and becomes predominant in the high-temperature phase. At the same time, the rotational component $C_{\rm rot}$ of heat capacity increases noticeably as we approach the phase-transition point, and then decreases abruptly in the high-temperature phase. The rapid increase in $C_{\rm rot}$ at temperatures above ~ 200 K is associated with intensification of orientational disordering of molecules. Other molecular crystals also display a similar behavior of the rotations heat capacity in the region of orientational phase transitions.[72,79]

Most of the authors investigating the lattice dynamics of fullerite C_{60} emphasize that above the high-temperature phase transition point, C_{60} molecules become orientationally disordered and rotate freely. In such a situation, we should expect that $C_{\rm rot}$, must be smaller than or equal to $3R/2$ (~ 3 cal/(mole·K)), which is the classical limit for a three-dimensional rotator. However, the results of our analysis of heat capacity indicate that the rotational motion of fullerene C_{60} molecules in the fcc phase is retarded considerably. The rotational heat capacity at $T > T_c$ is noticeably smaller than $3R$ and decreases from 10.2 to 8.9 cal/(mole·K) in the temperature range 260–300 K. These results indicate the presence of collective pre-transition phenomena and considerable correlation of molecular rotations in fullerite. It should be noted in this connection that a similar results (without a detailed analysis) was actually obtained by Akate *et al.*[19] who described the temperature dependence of $(C_P - C_{\rm in})$. The values obtained for the high-temperature phase correspond to our values of $(C_{\rm tr} + C_{\rm rot})$ to within the error of their measurements. The conclusion about strong retardation of rotational motion of molecules in the high-temperature phase of C_{60} is also supported by the results of investigation of IR spectra,[33] indicating that some of low-frequency librational modes are preserved in samples heated above the orientation phase-transition temperature T_c up to 300 K. Evidences of strong correlation of rotational motion of C_{60} molecules in the fcc phase were also obtained in experiments on inelastic scattering of x-rays.[5]

GRÜNEISEN PARAMETERS

An analysis of the lattice dynamics in the harmonic approximation shows that vibrations of particles at the bottom of a parabolic potential well do not affect the values of force constants of the crystal and the vibration frequency ω_i of the particles. In this case, thermal expansion of the solid must be equal to zero. In actual practice, however, vibrations are anharmonic. The anharmonism of lattice vibrations and its enhancement with increasing temperature lead to a noticeable dependence of force constants (and vibrational frequencies) on the separation between particles (crystal volume). A measure of anharmonicity of lattice vibrations can be the Grüneisen parameter defined as

$$\gamma_i = -d \ln \omega_i / d \ln V, \quad (6)$$

where ω_i is the frequency of the ith mode.

In thermodynamics, the Grüneisen parameter connects the basic thermodynamic characteristics of a substance and can be calculated on the basis of experimental data from the formula

$$\gamma = \beta V / \chi_T C_V. \quad (7)$$

For atomic cryocrystals (crystals of inert gases) whose lattice dynamics is determined only by phonon vibrations, the value of the Grüneisen parameter γ is constant in a wide temperature range and is equal to 2.7 ± 0.3 on the average.[80] Close values of $\gamma = 2.2$–2.9 are also observed for most simple molecular cryocrystals[72,79] at low temperatures and away from phase transitions, where the influence of the librational sub-

system and correlation effects is weak. The values of γ_{libr} characterizing the anharmonism of librational vibrations are slightly lower for simplest molecular crystals like nitrogen than γ_{trans} and vary from 1.6 to 1.9 for different substances. The determination of γ_{libr} is normally based on relation (6) using direct experimental data on the temperature dependence of librational frequencies.

The Grüneisen parameter for fullerite C_{60} crystals was determined earlier in Refs. 43,70,81, and 82. Further, the values of γ for intramolecular vibrations were estimated on the basis of Raman and IR investigations[83,84] leading to quite small values of the order of 0.04–0.09 indicating a high harmonicity of intramolecular vibrations of C_{60} molecules during the excitation of first levels for all low-lying frequencies.

The most detailed analysis of Grüneisen parameters and their temperature dependences was carried out by White *et al.*[82] who calculated consistently the total Grüneisen parameter γ characterizing all the three types of vibrations (translational, librational, and intramolecular), the parameter γ_{lat} corresponding to translational and librational modes, and finally γ_{tr}. The calculations made in Ref. 82 were based on a not quite correct assumption concerning the smallness of the contribution of the librational subsystem to thermal expansion of C_{60}. Such an assumption is completely correct only for low temperatures ($T<30$ K) but not at all for high temperatures, when this contribution can constitute a noticeable part of the contribution from the translational subsystem or even exceed it. For this reason, we shall disregard in the subsequent analysis the results obtained by White *et al.*[82] the data on the temperature dependence of the total coefficient γ were also obtained by us for fullerite C_{60} samples with different purity.[85] It should be noted, however, that the values of γ obtained in Refs. 82 and 85 do not correspond to the Grüneisen parameter characterizing the anharmonism of lattice vibrations especially in the temperature range where the contribution of intramolecular vibrations to heat capacity C_V becomes significant (the heat capacity component C_{in}, see Fig. 2). In this temperature range, the values of γ calculated from the experimental data on β, V, C_V, and χ_T give values much lower than those typical of monatomic crystals since the contribution of intramolecular vibrations to the lattice volume and thermal expansion is practically equal to zero, while the contribution to heat capacity is quite large and increases with temperature. Consequently, purely lattice characteristics should be used for determining the Grüneisen parameter corresponding to translational vibrations alone.

In accordance with formula (7), we calculated the effective Grüneisen parameter γ_{lat} determined only by frequencies of phonon and rotational vibrations of molecules in the temperature range 30–300 K. We used the values of the thermal expansion coefficient β, x-ray density ρ, molar volumes V, isothermal compressibility χ_T, and heat capacity C_V for pure fullerite C_{60}, which are given in Tables I and II. While calculating γ_{lat}, we took into account only the component of heat capacity C_V associated with the phonon and rotational subsystems of fullerite C_{60} (see Table II and Fig. 2).

The results of calculation of the Grüneisen parameter γ_{lat} are presented in Table II and in Fig. 3, where these data are given together with the total parameter γ. The same figure

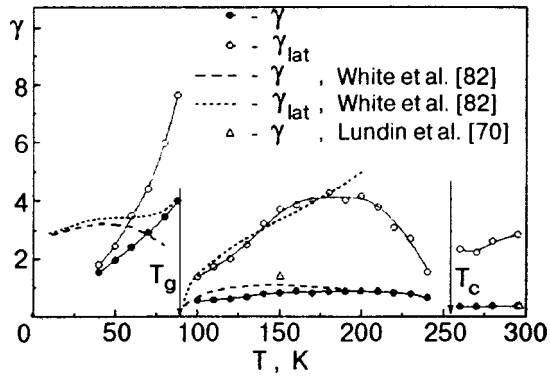

FIG. 3. Effect of temperature of the total (γ) and lattice (γ_{lat}) Grüneisen parameters for fullerite C_{60} according to our results and the results of analysis carried out in Refs. 70 and 82.

shows for comparison the results obtained in Refs. 70 and 82. It can be seen that the values of γ and γ_{lat} obtained by us are close in the temperature range $T<70$ K, where the contribution to heat capacity from intramolecular vibrations is still small, but in contrast to Ref. 82, the values of these parameters decrease almost linearly with temperature. This circumstance can be explained by the difference in the thermal expansion coefficients and the form of their temperature dependence obtained by us and by Gugenberger *et al.*[42] since White *et al.*[82] used in their calculations the results obtained in Ref. 42. For $T>100$ K, the difference between the values of γ and γ_{lat} is large in the wide temperature range 120–230 K. The values of the total parameter γ in this range are close to 1.0 and are almost independent of temperature, while γ_{lat} attains values ≈ 4.0. In the high-temperature phase, the total parameter γ is small (<0.5) and practically constant up to 300 K, while γ_{lat} exhibits a weak temperature dependence and is equal to 2.86 at room temperature. This value is close to the upper boundary of the values of γ typical of disordered phases of simple molecular crystals (the dispersion of γ is described above). Figure 3 shows that our results for γ and γ_{lat} in the temperature range 100–300 K are close to the values obtained in Refs. 70 and 82.

While calculating the values of γ_{lat} in the region of orientational ordered phase above the glass-formation temperature ($T_g<T<T_c$), we must bear in mind that the change in the volume of a fullerite C_{60} crystal is determined (see Ref. 82) not only by the anharmonism of translational and librational vibrations of molecules, but also by the variation of the composition of pentagonal and hexagonal configurations of molecules. An increase in the content of hexagonal component having a smaller volume upon heating of the crystal leads to lower values of actual thermal expansion coefficients, and hence lower values of γ_{lat}. White *et al.*[82] believe that this effect is responsible for noticeably higher values of the dilatometric thermal expansion coefficient[42] in the region of orientational glass with a ''frozen'' concentration of the hexagonal component than at temperatures above T_g (glass formation point). Knowing the temperature dependence of the composition of orientational configurations, we could try to separate the corresponding contribution to the volume and thermal expansion of fullerite. However, this does notcom-

plete the solution of the problem on determining the Grüneisen parameters since the variation of composition of orientational configurations in crystals apparently also affects the compressibility and heat capacity. This leads to the conclusion that the sign of the expected variation of γ_{lat} and its temperature behavior cannot be predicted even qualitatively without a detailed analysis and complete account of all the above-mentioned factors. In other words, we must take into consideration the thermodynamic parameters determined only by translational and rotational motion in calculations.

It should be noted that the temperature dependences of γ_{lat} obtained by White *et al.*[82] and by us in the temperature range $T_g < T < T_c$ are different (see Fig. 3). In our opinion, the continuous increase in γ_{lat} observed by White *et al.*[82] can be explained by the fact that they used the values of rotational heat capacity calculated on the basis of the Einstein model for a three-dimensional oscillator with the characteristic temperature $\Theta_E = 46$ K without taking into account disordering and correlation effects. The value of C_{lib} determined in this way attains its high-temperature constant value $3R$ in the temperature range under consideration, while the temperature variation of γ_{lat} is mainly determined by the continuous increase in the crystal volume and its thermal expansion coefficients. For this reason, the values of γ_{lat} obtained by us here appear as more realistic.

Dilatometric measurements of thermal expansion[43] have made it possible to trace the tendency in the variation of the Grüneisen parameter for $T \to 0$ K. It was proved on the basis of calculations that the parameter γ above the helium temperature have almost a constant value close to those obtained by White *et al.*[82] and equal to 3.4 on the average. For $T < 4.2$ K, a catastrophic drop in γ takes place, rending γ to the range of large negative values (of several tens) at temperatures below 3.4 K. Aleksandrovskii *et al.*[43] attribute this effect, as well as the negative thermal expansion of the crystal, to the presence of tunnel energy levels in the energy spectrum of the crystal, whose nature is not completely clear as yet.

CONCLUSION

Reliable experimental data on lattice parameters, density, and molar volumes obtained in a wide temperature range enabled us to determine the x-ray thermal expansion coefficients of pure fullerite C_{60} to a high degree of precision. The obtained results are in good agreement with the results of dilatometric[42] and neutron diffraction[10] measurements of thermal expansion of C_{60} single crystals in the major part of the investigated temperature interval except narrow regions adjoining phase-transition points. The thermal expansion data were used to analyze virtually the entire aggregate of thermodynamic parameters: heat capacity at constant volume C_V, compressibility χ_S, Debye temperature $\Theta_D^{(0)}$, and the total (γ) and lattice (γ_{lat}) Grüneisen parameters. A consistent and most comprehensive analysis of intramolecular heat capacity C_{in} is carried out for the first time taking into account the complete set of temperature-dependent intramolecular eigenfrequencies whose contribution to heat capacity at room temperature amounts to at least 0.5 cal/(mole·K). It is proved that intramolecular vibrations affect significantly the total heat capacity C_V even at $T \approx 100$ K, and their contribution is decisive in the high-temperature phase. Under the assumption of additive contributions to heat capacity C_V, we separated the phonon C_{tr} and rotational C_{rot} heat capacity components reliably. The phonon heat capacity was calculated in the Debye model using the zero-point Debye temperature determined from sound velocities and found to be $\Theta_D^{(0)} = 55.4$ K. It turned out that the value of C_{tr} is virtually constant in the entire temperature range under investigation (30–293 K) and corresponds to its high-temperature limit $3R$ (R being the gas constant). It should be noted that the total Grüneisen parameter γ in the high-temperature phase is constant, while its partial component γ_{lat} exhibits a weak temperature dependence and is equal to 2.86 at room temperature. This value is in good agreement with the values of Grüneisen parameter typical of completely disordered phases of simple molecular crystals.

The analysis of the rotational component of heat capacity clarified the origin of the orientationally disordered statistically, phase of fullerite C_{60}. The obtained results indicate that C_{60} molecules in the high-temperature phase are orientationally disordered statistically, but their rotation is considerably retarded (especially in the vicinity of the order–disorder phase transition). This conclusion is confirmed by the experimental observation of librational bands at room temperature.[33]

The possibility of describing the thermodynamic properties of orientationally ordered and disordered phases of C_{60} crystals on the basis of the model of additive contributions from translational and rotational subsystems demonstrated by us here indicates that the deformation of the lattice spectrum of fullerite due to the libron–phonon interaction is small below the room temperature (at least for thermodynamic parameters). This conclusion corresponds to the results of theoretical analysis of fullerite C_{60} spectra[60] and is also valid for most simple molecular crystals.

The authors are grateful to R. S. Ruoff who presented ultrapure fullerite for our experiments and to V.D. Natsik for fruitful discussions.

*E-mail:isakina@ilt.kharkov.ua

[1)] Grevey *et al.*,[25] who analyzed the results of their measurements of heat capacity of crystalline extracts C_{60}/C_{70} in the temperature range 4–10 K, obtained even a higher value of $\Theta_D = 188$ K.

[1] P. A. Heiney, J. Phys. Chem. Solids **53**, 1333 (1992).
[2] R. Moret, P. A. Albouy, V. Agafonov *et al.*, J. Phys. (Paris) **I2**, 511 (1992).
[3] R. Moret, S. Revy, and J. M. Godard, J. Phys. (Paris) **I2**, 1699 (1992).
[4] R. Moret, Phys. Rev. B **48**, 17619 (1993).
[5] P. Lounois, S. Revy, and R. Moret, Phys. Rev. B **52**, 5414 (1995).
[6] K. Sakaue, N. Toyoda, H. Kasatani *et al.*, J. Phys. Soc. Jpn. **63**, 1237 (1994).
[7] N. Toyoda, K. Sakaue, H. Terauchi *et al.*, J. Phys. Soc. Jpn. **63**, 2025 (1994).
[8] H. Kasatani, H. Terauchi, Y. Hamanaka, and S. Nakashima, Phys. Rev. B **47**, 4022 (1993).
[9] G. B. M. Vaughan, Y. Chambre, and D. Dubois, Europhys. Lett. **31**, 525 (1995).

[10] W. I. F. David, R. M. Ibberson, T. J. S. Dennis *et al.*, Europhys. Lett. **18**, 219 (1992).
[11] W. I. F. David, R. M. Ibberson, and T. Matsuo, Proc. R. Soc. London, Ser. A **A442**, 129 (1993).
[12] D. A. Neumann, I. R. D. Copley, R. L. Cappelletti *et al.*, Phys. Rev. Lett. **67**, 3808 (1991).
[13] R. Taylor, J. P. Hare, A. K. Abdul-Sada, and H. W. Kroto, J. Chem. Soc. Chem. Commun. **20**, 1423 (1990).
[14] R. D. Jonson, G. Meijer, and D. S. Bethune, J. Am. Chem. Soc. **112**, 8993 (1990).
[15] R. Tycko, G. Dabbagh, R. M. Fleming *et al.*, Phys. Rev. Lett. **67**, 1886 (1991).
[16] R. Blinc, J. Seliger, J. Dolinsek, and D. Arcon, Phys. Rev. B **49**, 4993 (1994).
[17] D. Johnson, C. S. Yannoni, H. C. Dorn *et al.*, Science **255**, 1235 (1992).
[18] T. Atake, T. Tanaka, H. K. Kikuchi *et al.*, Physica C **185–189**, 427 (1992).
[19] T. Atake, T. Tanaka, H. Kawaji *et al.*, Chem. Phys. Lett. **196**, 321 (1992).
[20] W. P. Beyermann, M. F. Hundley, and J. D. Thompson, Phys. Rev. Lett. **68**, 2046 (1992).
[21] J. R. Olson, K. A. Topp, and R. O. Pohl, Science **259**, 1145 (1993).
[22] K. V. Devadhasan, D. V. Natarajan, J. Janaki *et al.*, Solid State Commun. **92**, 715 (1994).
[23] S. P. Tewari, S. Silotia, and K. Bera, Solid State Commun. **107**, 129 (1998).
[24] T. Matsuo, H. Suga, W. I. F. David *et al.*, Solid State Commun. **83**, 711 (1992).
[25] E. Grevei, B. Nysten, M. Cassan *et al.*, Solid State Commun. **85**, 73 (1993).
[26] R. Satio, G. Dresselhaus, and M. S. Dresselhaus, Phys. Rev. B **49**, 2143 (1994).
[27] V. Sridharan, K. V. Devadhasan, D. V. Natarajan *et al.*, Solid State Commun. **108**, 393 (1998).
[28] M. A. Ivanov and V. M. Loktev, Fiz. Nizk. Temp. **19**, 618 (1993) [Low Temp. Phys. **19**, 442 (1993)].
[29] V. M. Egorov, V. V. Shpeizman, and I. N. Kremenskaya, Pis'ma Zh. Tekhn. Fiz. **19**, 49 (1993) [Tech. Phys. Lett. **19**, 621 (1993)].
[30] V. M. Egorov, I. N. Kremenskaya, B. I. Smirnov, and V. V. Shpeizman, Fiz. Tverd. Tela (St. Petersburg) **37**, 3493 (1995) [Sov. Phys. Solid State **37**, 1919 (1995)].
[31] P. M. H. van Loosdrecht, P. J. M. van Bentum, M. A. Verheijen, and G. Meijer, Chem. Phys. Lett. **198**, 578 (1992).
[32] M. Matus and H. Kuzmany, Appl. Phys. A **56**, 241 (1993).
[33] G. Kato, C. Yokomizo, H. Omata *et al.*, Solid State Commun. **93**, 801 (1995).
[34] W. I. F. David, R. M. Ibberson, J. C. Mattewman *et al.*, Nature **353**, 147 (1991).
[35] D. A. Neumann, J. R. D. Copley, W. A. Cappelletti *et al.*, Phys. Rev. Lett. **67**, 3808 (1991).
[36] L. Pintschovius, B. Renker, F. Gompf *et al.*, Phys. Rev. Lett. **69**, 2662 (1992).
[37] D. A. Neumann, J. R. D. Copley, W. A. Kamitakahara *et al.*, J. Chem. Phys. **96**, 8631 (1992).
[38] C. Coulombeau, H. Jobic, P. Bernier *et al.*, J. Phys. C **96**, 12731 (1992).
[39] V. P. Dravid, S. Liu, and M. M. Kappes, Chem. Phys. Lett. **185**, 75 (1991).
[40] G. van Tendeloo, S. Amelinckx, M. A. Verheijen *et al.*, Phys. Rev. Lett. **69**, 1065 (1992).
[41] A. T. Pugachev, N. P. Churakova, and N. I. Gorbenko, Fiz. Nizk. Temp. **23**, 854 (1997) [Low Temp. Phys. **23**, 642 (1997)].
[42] F. Gugenberger, R. Hedl, C. Meingast *et al.*, Phys. Rev. Lett. **69**, 3774 (1992).
[43] A. N. Aleksandrovskii, V. B. Esel'son, V. G. Manzhelii *et al.*, Fiz. Nizk. Temp. **23**, 1256 (1997) [Low Temp. Phys. **23**, 943 (1997)].
[44] C. Meingast and F. Gugenberger, Mod. Phys. Lett. B **7**, 1703 (1993).
[45] S. V. Lubenets, V. D. Natsik, L. S. Fomenko *et al.*, Fiz. Nizk. Temp. **23**, 338 (1997) [Low Temp. Phys. **23**, 251 (1997)].
[46] L. S. Fomenko, V. D. Natsik, S. V. Lubenets *et al.*, Fiz. Nizk. Temp. **21**, 465 (1995) [Low Temp. Phys. **21**, 364 (1995)].
[47] A. P. Isakina, A. I. Prokhvatilov, M. A. Strzhemechny, and N. A. Aksenova, Czech. J. Phys. **46**, 2713 (1996).
[48] A. P. Isakina, A. I. Prokhvatilov, M. A. Strzhemechny, and N. A. Aksenova, in *Recent Advances in the Chemistry and Physics of Fullerenes and Related Materials* (ed. by K. M. Kadish and R. S. Ruoff), The Electrochemical Society, Inc., Pennington (1997).
[49] J. E. Fisher and R. A. Heiney, J. Phys. C **54**, 1725 (1993).
[50] J. Li, S. Komiya, T. Tamura *et al.*, Physica C **195**, 205 (1992).
[51] J. D. Axe, S. C. Moss, and D. A. Neumann, in Solid State Phys. (ed. by H. Ehrenreich and F. Spaepen), Acad. Press, New York (1994).
[52] X. D. Shi, A. R. Kortan, J. M. Williams *et al.*, Phys. Rev. Lett. **68**, 827 (1992).
[53] H. Yamagushi, T. Yamagushi, S. Kagoshima *et al.*, J. Phys. Soc. Jpn. **64**, 527 (1995).
[54] D. C. Heberlein and E. D. Adams, J. Low Temp. Phys. **3**, 115 (1970).
[55] A. N. Aleksandrovskii, V. B. Kokshenev, V. G. Manzhelii, and A. M. Tolkachev, Fiz. Nizk. Temp. **4**, 915 (1978) [Sov. J. Low Temp. Phys. **4**, 435 (1978)].
[56] A. N. Aleksandrovskii, V. G. Manzhelii, V. B. Esel'son, and B. G. Udovichenko, J. Low Temp. Phys. **108**, 279 (1997).
[57] Yu. A. Freiman, Fiz. Nizk. Temp. **9**, 657 (1983) [Sov. J. Low Temp. Phys. **9**, 335 (1983)].
[58] X.-P. Li, J. P. Lu, and R. M. Martin, Phys. Rev. B **46**, 4301 (1992).
[59] L. N. Yakub, Fiz. Nizk. Temp. **19**, 726 (1993) [Low Temp. Phys. **19**, 522 (1993)].
[60] J. Yu, L. Bi, R. V. Kalia, and P. Vashishta, Phys. Rev. B **49**, 5008 (1994).
[61] T. Yildirim and A. B. Harris, Phys. Rev. B **46**, 7878 (1992).
[62] V. I. Zubov, N. P. Tretiakov, J. N. Teixeira Rabelo, and J. F. Sanchez Ortiz, Phys. Lett. A **194**, 223 (1994).
[63] V. D. Natsik and A. V. Podol'skii, Fiz. Nizk. Temp. **24**, 689 (1998) [Low Temp. Phys. **24**, 523 (1998)].
[64] I. O. Bashkin, N. P. Kobelev, A. P. Moravskii, and Ya. M. Soifer, in *Proceedings Int. Workshop: Fullerens and Atomic Clusters (IWFAC-93)*, St. Petersburg (1993).
[65] N. P. Kobelev, A. P. Moravskii, Ya. M. Soifer *et al.*, Fiz. Tverd. Tela (St. Petersburg) **36**, 2732 (1994) [Phys. Solid State **36**, 1491 (1994)].
[66] N. P. Kobelev, Ya. M. Soifer, I. O. Bashkin *et al.*, Phys. Status Solidi B **190**, 157 (1995).
[67] Ya. M. Soifer, N. P. Kobelev, I. O. Bashkin *et al.*, J. Phys. (Paris) **6**, Suppl. **C8**, 621 (1996).
[68] Ya. M. Soifer and N. P. Kobelev, Mol. Mater. **7**, 267 (1996).
[69] N. P. Kobelev, R. K. Nikolaev, Ya. M. Soifer, and S. S. Khasanov, Fiz. Tverd. Tela (St. Petersburg) **40**, 173 (1998) [Phys. Solid State **40**, 154 (1998)].
[70] A. Lundin, B. Sundqvist, P. Skoglund *et al.*, Solid State Commun. **84**, 879 (1992).
[71] A. Lundin and B. Sundqvist, Europhys. Lett. **27**, 463 (1994).
[72] *Cryocrystals* (ed. by B. I. Verkin and A. F. Prikhot'ko) [in Russian], Naukova Dumka, Kiev (1983).
[73] S. Hoen, N. G. Chopra, X.-D. Xiang *et al.*, Phys. Rev. B **46**, 12737 (1992).
[74] D. Havlik, W. Schranz, M. Haluska *et al.*, Solid State Commun. **104**, 775 (1997).
[75] G. Leibfrid, *Microscopic Theory of Mechanical and Thermal Properties of Crystals*, in Handbuch der Physik, Vol. 7, Pt. 1, S. Flügge, Ed., Springer-Verlag, Berlin, 1955.
[76] Z.-H. Dong, P. Zhou, J. M. Holden, and P. C. Eklund, Phys. Rev. B **48**, 2862 (1993).
[77] J. L. Feldman, J. Q. Broughton, L. L. Boyer *et al.*, Phys. Rev. B **46**, 12731 (1992).
[78] P. M. H. van Loosdrecht, P. J. M. van Bentum, and G. Meijer, Phys. Rev. Lett. **68**, 1176 (1992).
[79] *Physics of Cryocrystals* (ed. by V. G. Manzhelii and Yu. A. Freiman), AIP Press, Woodbury New York (1996).
[80] *Rare Gas Solids* (ed. by M. L. Klein and J. A. Venables), Acad. Press Inc., London (1997).
[81] L. A. Girifalco, J. Phys. C **96**, 858 (1992).
[82] M. A. White, C. Meingast, W. I. F. David, and T. Matsuo, Solid State Commun. **94**, 481 (1995).
[83] S. H. Tolbert, A. P. Alivisatos, and H. E. Lorenzana, Chem. Phys. Lett. **188**, 163 (1992).
[84] K. Aoki, H. Yamawaki, Y. Kakudata *et al.*, J. Phys. C **95**, 9037 (1991).
[85] N. A. Aksenova, A. P. Isakina, A. I. Prokhvatilov *et al.*, in *Recent Advances in the Chemistry and Physics of Fullerenes and Related Materials* (ed. by K. M. Kadish and R. S. Ruoff), The Electrochemical Society, Inc., Pennington (1994).

Translated by R. S. Wadhwa

Localization of vibrations near impurity atoms in semi-infinite and infinite linear chains

M. A. Mamalui, E. S. Syrkin, and S. B. Fedosev

*B. Verkin Institute for Low Temperature Physics and Engineering, National Academy of Sciences of the Ukraine, 310164 Kharkov, Ukraine**

(Submitted April 1, 1999)
Fiz. Nizk. Temp. **25**, 976–986 (August–September 1999)

Exact analytic expressions for local densities of atoms of the system as functions of the distance to a defect as well as defect parameters (variations of mass and force constants) are derived for an semi-infinite linear chain with an impurity at the end as well as for an infinite linear chain with an interstitial or substitutional impurity (a triatomic defect cluster in the general case). The dependences of the conditions of formation and frequencies of local vibrations and of the amplitudes of vibrations of these frequencies (i.e., the form of their damping) on defect parameters are determined for different atoms of the system. Exact analytic expressions determining the threshold values of the defect parameters as functions of the distance between and impurity atom and the end of the chain are derived and analyzed. © *1999 American Institute of Physics.* [S1063-777X(99)02208-2]

The most common method of obtaining compounds with preset thermodynamic, optical, and electron properties is the introduction of various impurities to the crystal matrix.[1–3] For this reason, the derivation of exact expressions describing analytically various aspects of the effect of impurities on quasiparticle spectra of excitations in the crystal lattice is an important problem even if the model used is extremely simple. The interest in quasi-one-dimensional systems (various chain, microscopic, and nanostructures, linear macromolecules, etc.) is due to advances in the technology of growing perfect low-dimensional single crystals.[4–6] The quasi-low-dimensional behavior of electron and phonon parameters is a distinguishing feature of HTSC systems as well as many traditional superconductors[7] due to the presence of chain elements in their structure. This necessitates the derivation of exact analytic expressions for vibrational parameters of one-dimensional chains with local violation of periodicity in the arrangement of atoms. A simple type of such a violation is the presence of local substitutional or interstitial impurities in the chain.

In this paper, we obtain exact analytic expressions for local densities of vibrations using the method of **J**-matrices[8–10] and the amplitudes of vibrations of impurity atoms as well as atoms located near a substitutional or interstitial impurity in a linear (semi-infinite or infinite) chain with a monatomic unit cell are analyzed. An impurity differs from an atom in the matrix lattice in the mass and force constants of interaction with nearest neighbors.

Among other things, situations are considered when the amplitude of vibrations of atoms adjacent to an impurity can be larger than the amplitude of vibrations of an impurity atom at the local frequency are considered. A more general case of an impurity separated from the end of a chain by an arbitrary number of atomic spacings is also analyzed, and the dependence of threshold values of defect parameters on the location of the impurity atoms is derived.

GREEN'S FUNCTION FOR A SEMI-INFINITE LINEAR CHAIN WITH AN IMPURITY AT THE END

Let us consider a semi-infinite monatomic chain whose extreme (''surface'') atom is replaced by an impurity differing from the matrix atoms in mass as well as constant of coupling with a neighboring atom (Fig. 1a). The operator of perturbations describing such a defect has the form

$$\Lambda^s(n,n') = -\mathbf{L}(n,n')\Theta(-n)\Theta(-n') + \frac{\lambda_m}{4}\frac{\eta+1}{\varepsilon+1}\delta_{n,0}\delta_{n',0} - \frac{\lambda_m}{4}\left[\frac{1+\eta}{\sqrt{2(1+\varepsilon)}}-1\right] \times (\delta_{n,0}\delta_{n',1}+\delta_{n',0}\delta_{n,1}). \quad (1)$$

Here $n=0,1,2,\ldots$, $\varepsilon=(m'-m)/m$ (mass defect, where m' and m are the mass of impurity and matrix atom, respectively), $\eta=(\alpha'-\alpha)/\alpha$ (defect of force interaction, where α' and α are constants of force interaction between an impurity atom and matrix atoms, and between matrix atoms), and $\mathbf{L}_0$ is the operator describing vibrations of atoms in a perfect chain:

$$\mathbf{L}_0(\mathbf{r},\mathbf{r}') = \mathbf{L}_0(\mathbf{r}-\mathbf{r}') = \frac{\lambda_m}{4}\begin{cases} -1, & |\mathbf{r}-\mathbf{r}'|=a; \\ 2, & |\mathbf{r}-\mathbf{r}'|=0; \\ 0, & |\mathbf{r}-\mathbf{r}'|>a \end{cases} \quad (2)$$

($\lambda_m=4\alpha/m$ is the square of maximum frequency of vibrations of the perfect linear chain).

The Green's function of such a system, i.e., the first diagonal element of the operator $\mathbf{G}\equiv(\lambda\mathbf{I}-\mathbf{L}-\mathbf{\Lambda}^s)^{-1}$ (λ is the square of the frequency) can be easily determined by the method of **J**-matrices (see, for example, Refs. 8–10). Similar calculations for one-dimensional systems are described in detail in Refs. 11–14).

The operators $\mathbf{L}$ and $\mathbf{\Lambda}^s$ are presented in the form of **J**-matrices of the form $a_i\delta_{ik}+b_i(\delta_{i,k+1}+\delta_{i,k-1})$ in the basis $\{\mathbf{h}_n\}_{n=0}^{\infty}=\{(-1)^n|n|1\rangle\}_{n=0}^{\infty}$, where the index n labels atoms starting from the surface. The rank of the matrix of the op-

 © 1999 American Institute of Physics

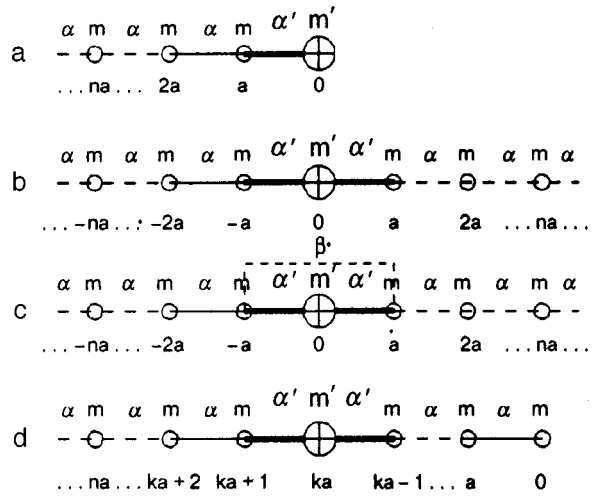

FIG. 1. Schematic diagram of the systems under investigation: semi-infinite chain with a substitutional impurity at the free end (a), infinite chain with substitutional (b) and interstitial (c) impurity, and semi-infinite chain with a substitutional impurity separated by k atomic spacings from the free end (d).

erator $\mathbf{\Lambda}^s$ is equal to two, and all the matrix elements of the **J**-matrix of the operator **L** (whose rank is equal to infinity) except a_0 are equal to the limiting values of matrix elements of the **J**-matrix of the operator, whose spectrum has no gaps and lies in the $[0,\lambda_m]$ band, i.e., $a=\lambda_m/2$ and $b=\lambda_m/4$.

If the matrix elements of the **J**-matrix starting from a certain number n are equal to their limiting values, the Green's function in Ref. 9 satisfies the following relation:

$$\mathcal{G}_{00}(\lambda)=(\mathbf{h}_0,\mathbf{G}\mathbf{h}_0)=\frac{Q_n(\lambda)-b_{n-1}Q_{n-1}(\lambda)K_\infty(\lambda)}{P_n(\lambda)-b_{n-1}P_{n-1}(\lambda)K_\infty(\lambda)}. \quad (3)$$

The orthogonal polynomials $\{P,Q\}_m(\lambda,\eta,\varepsilon)$ appearing in this expression under the initial conditions $P_{-1}(x)\equiv 0$; $P_0(x)\equiv 1$; $Q_0(x)\equiv 0$; $Q_1(x)=b_0^{-1}$ satisfy the following recurrence relations:

$$b_m\{P,Q\}_{m+1}(x)=(x-a_m)\{P,Q\}_m(x)-b_{m-1}\{P,Q\}_{m-1}(x) \quad (4)$$

while the function $K_\infty(\lambda)$ is determined by the form of limiting values of the elements of the **J**-matrix, i.e.,

$$K_\infty(\lambda)=4\lambda_m^{-2}[2\lambda-\lambda_m+2Z(\lambda)\sqrt{\lambda|\lambda-\lambda_m|}]; \quad (5)$$

$$Z(\lambda)=i\Theta(\lambda)\Theta(\lambda_m-\lambda)-\Theta(\lambda-\lambda_m), \quad (6)$$

in our case, and $\Theta(x)$ is the Heaviside Θ-function.

For the system under investigation, $n=2$ and

$$\mathcal{G}^s_{00}(\lambda,\eta,\varepsilon)=\frac{1}{R^s(\lambda,\eta,\varepsilon)}\left\{-\lambda\left[\lambda\eta-\frac{\lambda_m}{8}\frac{\eta+1}{\varepsilon+1}[\eta(2\epsilon+3)+(2\epsilon+1)]\right]+Z(\lambda)\frac{\lambda_m}{8}\frac{(\eta+1)^2}{\varepsilon+1}\sqrt{|\lambda(\lambda_m-\lambda)|}\right\}, \quad (7)$$

where

$$R^s(\lambda,\eta,\varepsilon)=\lambda\left\{-\lambda^2\eta+\lambda\frac{\lambda_m}{4}\frac{\eta+1}{\varepsilon+1}\times[(\eta+1)(\varepsilon+2)-2]+\frac{\lambda_m^2}{16}\left(\frac{\eta+1}{\varepsilon+1}\right)^2\right\}. \quad (8)$$

The function $G^s_{00}(\lambda,\eta,\varepsilon)$ has poles at the points

$$\lambda^s_{l1,l2}=\frac{\lambda_m}{8\eta}\left(\frac{\eta+1}{\varepsilon+1}\right)\{(\eta+1)(\varepsilon+2)-2\pm\sqrt{(\eta+1)[(\eta+1)(\varepsilon+2)^2-4(\varepsilon+1)]}. \quad (9)$$

The pole $\lambda^s_{l1}\equiv\lambda^s_l$ corresponding to the plus sign of the radical in (9) coincides with the upper boundary of the continuous spectrum band for $\eta^s_l=(2\varepsilon+1)/(2\varepsilon+3)$:

$$\lambda^s_l(\eta^s_l)=\lambda_m$$

and increases in proportion to the coupling constant α' and to the mass m' (i.e., ε and η) if the inequality $\eta\geqslant(2\varepsilon+1)/(2\varepsilon+3)$ holds. Consequently, λ^s_l defines the square of local frequency emerging in the given system. The intensity of this local vibration is determined by the residue at this pole and is given by

$$\mu^s_l=\left[1-\frac{(\eta+1)(\varepsilon+1)}{\sqrt{(\eta+1)[(\eta+1)(\varepsilon+2)^2-4(\varepsilon+1)]}}\right]\times\Theta\left(\eta-\frac{2\varepsilon+1}{2\varepsilon+3}\right). \quad (10)$$

The local phonon density of vibrations of an impurity atom at the end of the chain as a function of squared frequency and parameters of local distortion of coupling and mass has the form

$$g^s(\lambda,\eta,\varepsilon)=\frac{1}{\pi}\operatorname{Im}\mathcal{G}^s_{00}(\lambda,\eta,\varepsilon)+\mu_l\delta(\lambda-\lambda_l)=\frac{(\lambda_m/8)[(\eta+1)^2/(\varepsilon+1)]\sqrt{(\lambda_m-\lambda)/\lambda}}{-\lambda^2\eta+\lambda(\lambda_m/4)[(\eta+1)/(\varepsilon+1)][(\eta+1)(\varepsilon+2)-2]+(\lambda_m^2/16)[(\eta+1)/(\varepsilon+1)]^2}+\mu_l\delta(\lambda-\lambda_l). \quad (11)$$

It should be noted that $\eta=\eta_l$ corresponds to the emergence of root singularity in the local density $\rho^s(\lambda_m,\eta,\varepsilon)\propto(\lambda_m-\lambda)^{-1/2}\to\infty$ at the upper boundary of the continuous spectrum band.

The local density of vibrations of an atom in the chain separated by n atomic spacings from the free end is given by[12]

$$g_n^s(\lambda,\eta,\varepsilon)=g^s(\lambda,\eta,\varepsilon)\tilde{P}_n^2(\lambda,\eta,\varepsilon), \tag{12}$$

where $\tilde{P}_n(\lambda,\eta,\varepsilon)$ are orthogonal polynomials generated by the **J**-matrix of the operator $\mathbf{L}+\mathbf{\Lambda}^s$ (4).

A comparison of formulas (9), (10), and (11) with expressions for the square of frequency and intensity of a local vibration as well as the local density of vibrations of an impurity atom derived in Ref. 11 for an infinite linear chain with a substitutional impurity shows that they are transformed into one another under the substitution $2\varepsilon+1\to\varepsilon$ in formulas (9), (10), and (11), i.e., local parameters of vibrations of an impurity at the free end correspond to similar parameters of a substitutional impurity with a mass twice as large in an infinite chain. For this reason, we shall analyze these parameters for both these systems simultaneously.

LOCAL VIBRATIONS IN SEMI-INFINITE AND INFINITE CHAINS

We analyze the behavior of local vibrational densities of a monatomic linear chain with interactions between nearest neighbors, which contains a substitutional or interstitial impurity (the only difference between these types of impurities is that direct interaction between the nearest neighbors of an impurity atom is preserved in the case of interstitial impurity; Fig. 1b and c respectively). It can be easily seen that a semi-infinite chain can contain only a substitutional impurity. We shall assume that an impurity atom is located at the origin of coordinates.

Nearest neighbors of an impurity are also defect atoms and form with the impurity a defect cluster (triatomic in an infinite chain and diatomic in a semi-infinite one).

An impurity atom in an infinite chain is a symmetry center for the system under investigation, and the space H of atomic displacements can be presented as a direct sum of subspaces of symmetric and antisymmetric displacements invariant relative to the operators $\mathbf{L}$ and $\mathbf{L}+\mathbf{\Lambda}$.

The subspace of symmetric (antiphase) displacements is a linear envelope stretched aver the vectors

$$\mathbf{h}_n^{(\pm1)}=\frac{(-1)^n}{\sqrt{2}}\left|\begin{matrix}n+1\\-n-1\end{matrix}\right|\left.\begin{matrix}1\\-1\end{matrix}\right\rangle. \tag{13}$$

An impurity atom located at the symmetry center is at rest in the given subspace.

The subspace of antisymmetric (synphase) displacements is a linear envelope stretched over the vectors

$$\mathbf{h}_0^{(0)}=|0|1\rangle;\quad \mathbf{h}_n^{(0)}=\frac{(-1)}{\sqrt{2}}\left|\begin{matrix}n\\-n\end{matrix}\right|\left.\begin{matrix}1\\1\end{matrix}\right\rangle. \tag{14}$$

In each of these subspaces, the operator **L** induces the operators $\mathbf{L}^{(0)}$ and $\mathbf{L}^{(\pm1)}$ respectively, which have the form of **J**-matrices whose matrix elements can be calculated easily.[11]

The first diagonal matrix elements of operators induced by Green's operator in each of the invariant subspaces (Green's function) can be written in the form

$$\mathcal{G}_{00}^{(0)}(\lambda,\eta,\varepsilon)=\frac{-4\lambda\eta+\lambda_m[(1+\eta)/(1+\varepsilon)][(1+\eta)(2+\varepsilon)-2]}{R^{(0)}(\lambda,\eta,\varepsilon)}+\lambda_m\frac{(1+\eta)^2}{1+\varepsilon}\sqrt{|(\lambda-\lambda_m)/\lambda|}\frac{Z(\lambda)}{R^{(0)}(\lambda,\eta,\varepsilon)}, \tag{15}$$

where

$$R^{(0)}(\lambda,\eta,\varepsilon)=-4\lambda^2\eta+\lambda\lambda_m\left(\frac{1+\eta}{1+\varepsilon}\right)[(1+\eta)(3+\varepsilon)-4]+\lambda_m^2\left(\frac{1+\eta}{1+\varepsilon}\right)^2,$$

(after the substitution $\varepsilon\to2\varepsilon+1$, this expression is transformed into (7)), and

$$\mathcal{G}_{00}^{\pm}(\lambda,\eta)=\frac{4}{\lambda_m}\frac{[2\lambda-\lambda_m(1+\eta)+2Z(\lambda)\sqrt{\lambda|\lambda-\lambda_m|}]}{R^{(\pm1)}(\lambda,\eta)}, \tag{16}$$

where

$$R^{(\pm1)}(\lambda,\eta)=-4\lambda\eta+\lambda_m(1+\eta)^2.$$

The quantity $Z(\lambda)$ is defined in (6).

Proceeding from the form of basis vectors (13) and (14), we can easily verify that the Green's function $\mathcal{G}_{00}^{(0)}(\lambda,\eta,\varepsilon)$ is the same for substitutional and interstitial impurities, while the function $\mathcal{G}_{00}^{(\pm1)}(\lambda,\eta,\beta)$ for an interstitial impurity can be obtained from (16) through the substitution $\eta\to\eta+\beta/\alpha$.

The roots of the functions $R^{(0)}(\lambda,\eta,\varepsilon)$ and $R^{(\pm1)}(\lambda,\eta)$ ($\lambda_l^{(0)}$ and $\lambda_l^{(\pm1)}$, respectively) lie beyond the continuous spectrum band

$$\lambda_l^{(0)}=\frac{\lambda_m}{8}\left(\frac{1+\eta}{1+\varepsilon}\right)\left\{3+\varepsilon-\frac{1-\varepsilon}{\eta}+\frac{3+\varepsilon}{\eta}\left((1+\eta)\times\left[\left(\frac{1-\varepsilon}{3+\varepsilon}\right)^2+\eta\right]\right)^{1/2}\right\}>\lambda_m; \tag{17}$$

$$\lambda_l^{(\pm1)}=\lambda_m\frac{(1+\eta)^2}{4\eta}>\lambda_m. \tag{18}$$

These roots determine the squares of the frequencies of local vibrations, while residues at these points determine the intensity of these vibrations ($\mu_0^{(0)}$ and $\mu_0^{(\pm1)}$, respectively):

$$\text{rés}_{\lambda=\lambda_l^{(0)}}G_{00}^0(\lambda,\eta,\varepsilon)\equiv\mu_0^{(0)}\theta\left(\eta-\frac{\varepsilon}{2+\varepsilon}\right), \tag{19}$$

$$\mu_0^{(0)}=\mu_0^{(0)}(\eta,\varepsilon)=1-(1+\varepsilon)\left[\frac{1+\eta}{\eta(3+\varepsilon)^2+(1-\varepsilon)^2}\right]^{1/2},$$

$$\text{rés}_{\lambda=\lambda_l^{(\pm1)}}G_{00}^{(\pm1)}(\lambda,\eta)=\mu_0^{(\pm1)}\theta(\eta-1)=\frac{\eta^2-1}{\eta^2}\theta(\eta-1). \tag{20}$$

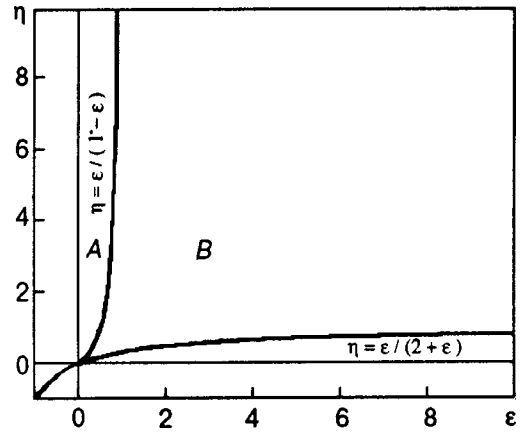

FIG. 2. Region of existence of local vibrations in the cyclic space $H^{(0)}$ generated by a displacement of an impurity atom ($\eta>\varepsilon/(2+\varepsilon)$) and its division into regions of predominant localization of these vibrations at the impurity itself (A) and at its nearest neighbors (B). The region with $\eta>1$ containing local vibrations in the cyclic subspace $H^{(\pm 1)}$ generated by antiphase displacement of nearest neighbors of the impurity atom is also shown (the impurity is at rest in this subspace).

The range of values of η and ε for which the intensity differs from zero is the range of local vibrations with the frequency $\sqrt{\lambda_l^{(i)}}$. In other words, local vibrations are formed in the subspace $H^{(\pm 1)}$ for

$$\eta>1; \tag{21}$$

and in the subspace $H^{(0)}$ for

$$\eta>\frac{\varepsilon}{2+\varepsilon} \tag{22}$$

(Fig. 2). It should be noted that for $\eta>1$, two mutually orthogonal local vibrations are formed in the system under investigation irrespective of the mass of impurity.

A root singularity emerges for $\lambda=\lambda_m$ at ''threshold'' values of parameters of the defect $\eta=1$ in the subspace $H^{(\pm 1)}$ and $\eta>\varepsilon/(2+\varepsilon)$ in the subspace $H^{(0)}$ for the corresponding values of spectral density (Fig. 3).

It was proved in Refs. 12–14 that the intensity of a local vibration varies with increasing atomic number n according to the law

$$\mu_n=\mu_0 P_n^2(\lambda,\eta,\varepsilon). \tag{23}$$

It is well known (see, for example, Ref. 8) that the contribution from local frequency to the root-mean-square displacement of an atom is proportional to the intensity of the local vibration, and hence the amplitude of the local vibration attenuates with increasing distance from the defect in proportion to $P_n(\lambda,\eta,\varepsilon)$.

An impurity atom does not participate in motion occurring the cycling subspace $H^{(\pm 1)}$, and hence the ratio of vibrational amplitudes at the local frequency $\sqrt{\lambda_l^{(\pm 1)}}$ of atoms with numbers m and n is

$$\frac{u_m}{u_n}=\left|\frac{P_{m-1}^{(\pm 1)}(\lambda_l^{(\pm 1)},\eta)}{P_{n-}^{(\pm 1)}(\lambda_l^{(\pm 1)},\eta)}\right|.$$

It can easily be verified that the values $P_n^{(\pm 1)}(\lambda_l^{(\pm 1)},\eta)=1/\eta^n$, i.e., form an infinite decreasing geometric progression in the region of existence of local vibrations for the cyclic subspace $H^{(\pm 1)}$ (for $\eta>1$), and the amplitude of local vibrations in this space attenuates exponentially with increasing distance from the defect. The sum of intensities of local vibrations at all atoms is given by

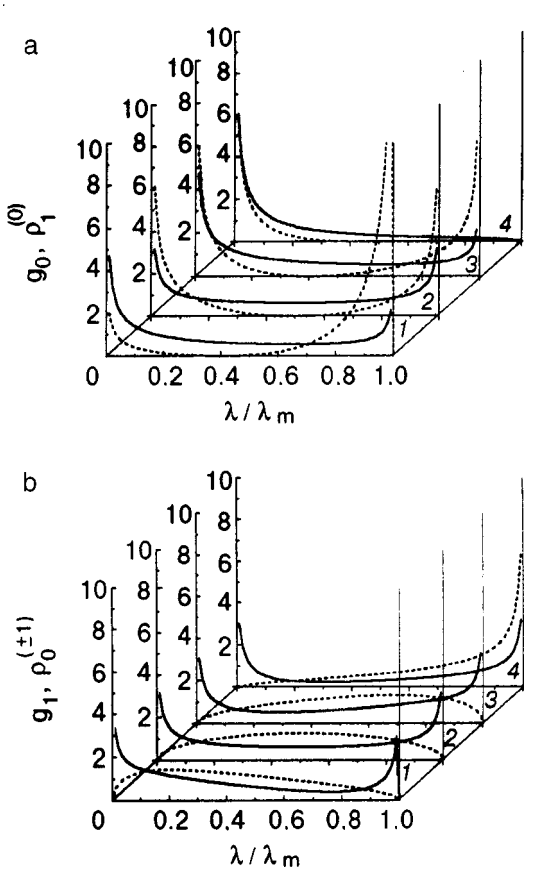

FIG. 3. Local and spectral densities characterizing vibrations of defect cluster atoms for values of defect parameters corresponding to the formation of local vibrations in various subspaces: the functions $g_0(\lambda)\equiv\rho_0^{(0)}(\lambda)$ (solid curves) and the functions $\rho_1^{(0)}(\lambda)$ (dashed curves) (a), the functions $g_1(\lambda)$ (solid curves) and the functions $\rho_0^{(\pm 1)}$ (dashed curves) (b). Curves *1–3* correspond to threshold values for the formation of a local vibration in the subspace $H^{(0)}[\eta=\varepsilon/(2+\varepsilon)]$: $\eta=-1/3$, $\varepsilon=-0.5$ (curves *1*), $\eta=\varepsilon=0$ (curves *2*), $\eta=0.2$, $\varepsilon=0.5$ (curves *3*) and $\eta=\varepsilon=1$ (curves *4*) correspond to the threshold value for the emergence of a local vibration in the subspace $H^{(\pm 1)}(\eta=1)$.

$$\sum_{n=0}^{\infty}\mu_n^{(\pm)}(\eta)=1, \tag{24}$$

which is in accord with the familiar formulas for the variation of the total phonon spectrum of the crystal due to an impurity in the presence of local vibrations (see, for example, Refs. 8,15–20).

Similarly, we can write the change in the amplitude of vibrations of atoms with $n\geqslant 0$ at the local frequency $\sqrt{\lambda_l^{(0)}}$ in the cyclic space $H^{(0)}$ generated by a displacement of the impurity atom itself in the form

$$\frac{u_m}{u_n}=\left|\frac{P_m^{(0)}(\lambda_l^{(0)},\eta)}{P_n^{(0)}(\lambda_l^{(0)},\eta)}\right|.$$

Using the method of mathematical induction, we can prove that starting from $n=1$, the values of the polynomials $[P_n^{(0)}(\lambda_l^{(0)},\eta,\varepsilon)]^2$ form a geometric progression. We shall prove that

$$\sum_{n=0}^{\infty}\mu_n^{(0)}(\eta,\varepsilon)\equiv\mu_0^{(0)}(\eta,\varepsilon)\sum_{n=0}^{\infty}[P_n^{(0)}(\lambda_l^{(0)},\eta,\varepsilon)]^2=1, \tag{25}$$

which gives, among other things, the common ratio of the progression $[P_2^{(0)}(\lambda_l^{(0)},\eta,\varepsilon)/P_1^{(0)}(\lambda_l^{(0)},\eta,\varepsilon)]^2<1$.

We transform the left-hand side of (25) as

$$\mu_0^{(0)}(\eta,\varepsilon)\left\{1+\sum_{n=1}^{\infty}[P_n^{(0)}(\lambda_l^{(0)},\eta,\varepsilon)]^2\right\}$$
$$=\mu_0^{(0)}(\eta,\varepsilon)\times\left\{1+\frac{[P_1^{(0)}(\lambda_l^{(0)},\eta,\varepsilon)]^4}{[P_1^{(0)}(\lambda_l^{(0)},\eta,\varepsilon)]^2-[P_2^{(0)}(\lambda_l^{(0)},\eta,\varepsilon)]^2}\right\},$$

use the identity

$$[P_1^{(0)}(\lambda_l^{(0)},\eta,\varepsilon)]^2\equiv\frac{P_1^{(0)}(\lambda_l^{(0)},\eta,\varepsilon)+P_2^{(0)}(\lambda_l^{(0)},\eta,\varepsilon)}{2}\sqrt{2(1+\varepsilon)},$$

whose validity can be verified easily by substituting (17) into the recurrence relations (4), and write (25) in the form

$$\mu_0^{(0)}(\mu,\varepsilon)[P_1^{(0)}(\lambda_l^{(0)},\eta,\varepsilon)]^2\sqrt{2(1+\varepsilon)}=2[1-\mu_0^{(0)}\times(\eta,\varepsilon)][P_1^{(0)}(\lambda_l^{(0)},\eta,\varepsilon)-P_2^{(0)}(\lambda_l^{(0)},\eta,\varepsilon)]. \tag{26}$$

The validity of this expression can be verified easily with the help of (4), (17), and (20).

Thus, the amplitudes of both local vibrations attenuate exponentially with increasing n beyond a defect cluster. Within this cluster, the ratio of the amplitudes $u_0(\lambda_l^{(0)},T)$ and $u_l(\lambda_l^{(0)},T)$ depends on the defect parameters. The amplitude of local vibrations of an impurity atom exceeds that of similar vibrations of its nearest neighbor if

$$[P_1^{(0)}(\lambda_l^{(0)},\eta,\varepsilon)]^2<\frac{2}{1+\varepsilon}, \tag{27}$$

i.e.,

$$-\frac{(1+\eta)(1-\varepsilon)-4\eta}{\eta}<\frac{1}{\eta}\sqrt{(1+\eta)[\eta(3+\varepsilon)^2+(1-\varepsilon)^2]}<\frac{(1+\eta)(1-\varepsilon)+4\eta}{\eta}.$$

The left part of this inequality holds identically, while its right part holds if the following two conditions

$$\begin{cases}\eta\geqslant\dfrac{\varepsilon-1}{5-\varepsilon}\quad,\\ \eta>\dfrac{\varepsilon}{1-\varepsilon}\quad,\end{cases}$$

are satisfied simultaneously, or for

$$\eta<\frac{\varepsilon-1}{5-\varepsilon}$$

(naturally, we speak only of the values of defect parameters for which the local vibration exists in the cyclic space $H^{(0)}$, i.e., $\eta>\varepsilon/(2+\varepsilon)$).

These conditions are satisfied for region A in Fig. 2.

In region B in the same figure, we have

$$0<\frac{\varepsilon}{2+\varepsilon}<\eta<\frac{\varepsilon}{1-\varepsilon},$$

i.e., the local vibration in the cyclic subspace $H^{(0)}$ generated by a displacement of the impurity is localized mainly at nearest neighbors.

It should be recalled that substituting $2\varepsilon+1$ for ε in the subspace $H^{(0)}$ leads to relevant results for a semi-infinite chain with an impurity at its free end, while the substitution of $\eta+\beta/\alpha$ for η in the space $H^{(\pm1)}$ leads to the results for an interstitial impurity.

IMPURITY RESONANT LEVELS IN CONTINUOUS SPECTRUM BAND FOR A LINEAR CHAIN

It is well known (see, for example Refs. 16 and 17) that an isotopic impurity cannot be responsible for the formation of a linear chain of sharp resonant peaks in the continuous spectrum band for the density of states (quasi-local vibrations). However, such states quasi-localized at an impurity atom can be formed in the presence of an impurity in the chain differing from the matrix atoms not only in mass, but also in the force interaction with nearest neighbors (light and weakly coupled impurity). The possibility of such a localization was pointed out, for example, by Skripnik,[21] while a detailed analysis of the evolution of local density for an impurity atom during the formation of such sharp resonant peaks was carried out in Ref. 11. However, the behavior of local densities and other spectral parameters of neighboring atoms, especially nearest neighbors forming a defect cluster together with the impurity, in the vicinity of such a quasi-local frequency is also of considerable interest.

Let us consider the frequency distribution of vibrations in the continuous spectrum band for the system under investigation. The spectral densities $\rho^{(0)}(\lambda,\eta,\varepsilon)$ and $\rho^{(\pm1)}(\lambda,\eta)$ are defined on the interval $[0,\lambda_m]$ and are given by

$$\rho^{(0)}(\lambda,\eta,\varepsilon)=\frac{\lambda_m}{4\pi}\frac{[(1+\eta)^2/(1+\varepsilon)]\sqrt{(\lambda_m-\lambda)/\lambda}}{R^{(0)}(\lambda,\eta,\varepsilon)}; \tag{28}$$

$$\rho^{(\pm1)}(\lambda,\eta)=\frac{8}{\pi\lambda_m}\frac{\sqrt{\lambda(\lambda_m-\lambda)}}{R^{(\pm1)}(\lambda,\eta)}. \tag{29}$$

Local densities $g_n(\lambda,\eta,\varepsilon)$ can now be obtained easily with the help of the formula

$$g_n(\lambda,\eta,\varepsilon)=\left[\rho^{(0)}(\lambda,\eta,\varepsilon)+\mu_0^{(0)}\theta\left(\eta-\frac{\varepsilon}{2+\varepsilon}\right)\delta(\lambda-\lambda_l^{(0)})\right]\pm[P_n^{(0)}]^2(\lambda,\eta,\varepsilon)+[\rho^{(\pm1)}(\lambda,\eta)+\mu_0^{(\pm1)}\theta\times(\eta-1)\delta(\lambda-\lambda_l^{(\pm1)})][P_{n-1}^{(\pm1)}]^2(\lambda,\eta). \tag{30}$$

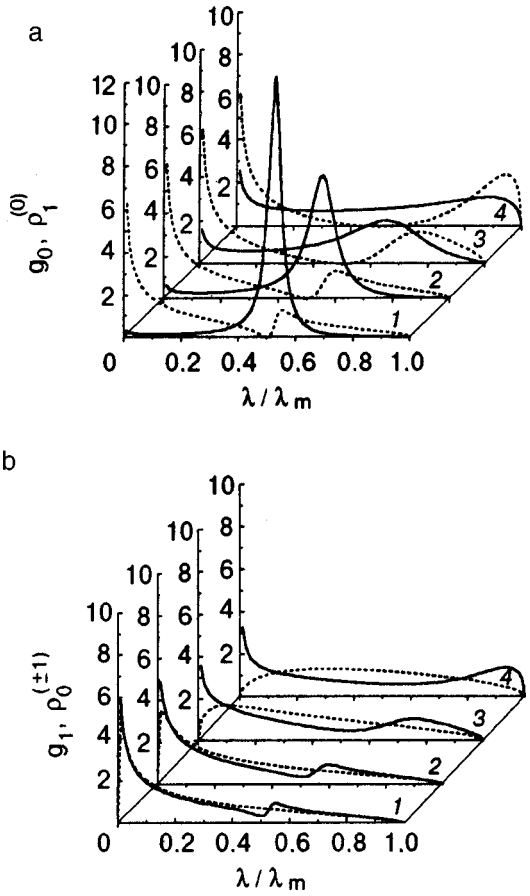

FIG. 4. Local and spectral densities characterizing vibrations of defect cluster atoms for values of defect parameters corresponding to the formation of vibrations localized at a light weakly coupled impurity with frequencies lying in the continuous spectrum band of a linear chain: the functions $g_0(\lambda)\equiv\rho_0^{(0)}(\lambda)$ (solid curves) and the functions $\rho_1^{(0)}(\lambda)$ (dashed curves) (a), the functions $g_1(\lambda)$ (solid curves) and the functions $\rho_0^{(\pm 1)}(\lambda)$ (dashed curves) (b); $\eta=\varepsilon=-0.9$ (curves *1*), $\eta=\varepsilon=-0.8$ (curves *2*), $\eta=\varepsilon=-0.5$ (curves *3*) and $\eta=\varepsilon=-0.2$ (curves *4*).

For example, we can easily verify and prove rigorously with the help of mathematical induction that for any n

$$g_n(\lambda,0,0)=\rho^{(0)}(\lambda,0,0)=\frac{\rho_n^{(0)}(\lambda,0,0,)+\rho_{n-1}^{(\pm 1)}(\lambda,0)}{2}$$

$$=\frac{1}{\pi}\frac{1}{\sqrt{\lambda(\lambda_m-\lambda)}},$$

i.e., is equal to the density of states for an perfect linear chain.

Figure 4 shows the evolution of local densities and the spectral densities for atoms in the impurity cluster appearing in them upon a change in the defect parameters. For all the curves, $\eta=\varepsilon<0$, and a localized vibration is gradually formed at the impurity atom. The squared frequency λ^* of this vibration is approximately at the midpoint of the band corresponding to allowed values of λ.

Figure 4a shows local densities $g_0(\lambda,\eta,\varepsilon)\equiv\rho_0^{(0)}\times(\lambda,\eta,\varepsilon)$ of an impurity atom (solid curves) and the spectral densities $\rho_1^{(0)}(\lambda,\eta,\varepsilon)$ (dashed curves). It can be seen that as a sharp resonant peak with a half-width $\Delta\lambda<\lambda^*$ is formed, the spectral density node $\rho_1^{(0)}(\lambda,\eta,\varepsilon)$ ($\lambda^*=a_0^{(0)}$ is the root of the polynomial $P_1^{(0)}(\lambda,\eta,\varepsilon)$ or, according to (4), the square of the Einstein frequency in the given cyclic subspace) falls in this half-width. This can be easily grasped since the quasi-local frequency approaches the Einstein frequency upon enhancement of localization. Consequently, vibrations of nearest neighbors of an impurity virtually do not interact with vibrations of the impurity atom for $\lambda\in[\lambda^*-\Delta\lambda,\lambda^*+\Delta\lambda]$. This leads to localization of vibrations at frequencies for which not only the total phonon density for an ideal system, but the spectral density in the corresponding invariant subspace is not small at all. The local densities $g_1(\lambda,\eta,\varepsilon)$ of nearest neighbors (solid curves in Fig. 4b) are mainly determined by vibrations from the cyclic space $H^{(\pm 1)}$ orthogonal to displacements of the impurity (the corresponding spectral densities $\rho_0^{(\pm 1)}(\lambda,\eta)$ are shown by dashed curves in the same figure).

DEPENDENCE OF THRESHOLD VALUES OF DEFECT PARAMETERS ON THE SEPARATION BETWEEN IMPURITY AND THE END ATOM IN THE CHAIN

It was proved in the previous sections that only a local frequency (9) can be formed in a semi-infinite chain with a substitutional impurity at the free end, while the presence of the same impurity ''in the bulk'' of the chain generates two local frequencies (17) and (18). This important fact reflects the difference in the number and types of independent vibrations which can involve an impurity atom under the surface and on it (in other words, we are speaking of the number of possible orthogonal displacements within a defect cluster, which generate different subspaces of displacement). For example, independent vibrations of atoms in an infinite chain, which are affected by the presence of an impurity, correspond to the general scheme of splitting into the subspaces (13) and (14). One of the subspaces corresponds to displacements of the impurity and subsequently to synphase displacements of its nearest neighbors, while the other subspace corresponds to antiphase displacements of the nearest neighbors of the fixed impurity atom. Obviously, the situation must not change radically until the impurity becomes a surface atom with only one neighbor. In this case, the number of independent (orthogonal) types of vibrations involving the impurity atom decreases to one. This type of vibrations is determined by the displacement of the impurity itself and corresponds to the generating vector $\mathbf{h}_0^s=|0|1\rangle$ in the subspace H^s.

The confirmation of these arguments by calculations and the derivation of exact analytic expressions for vibrational parameters in the model of a two-parametric substitutional impurity separated from the chain ''surface'' by an arbitrary number of atomic spacings (following the general algorithm of application of the method of **J**-matrices described in the previous section) generally encounters unsurmountable difficulties of computational nature. This is due to the need of taking into account the mutual arrangement of lattice defects separated by large distances, i.e., with an arbitrary large rank of the perturbation matrix. However, a certain modification of this algorithm allows us to derive analytically the exact

dependence of the threshold values of parameters describing the defect on the ''depth'' of the given impurity under the surface. It will be shown that the behavior of this dependence is in good agreement with the above conclusions.

Let us consider a semi-infinite monatomic chain with a substitutional impurity differing from the matrix atoms in mass and interaction with nearest neighbors. We assume that the impurity is separated from the surface by k matrix atoms (see Fig. 1d). We obtain the complete system of basis vectors in the only subspace for the semi-infinite chain by choosing the displacement of the end atom as a generating vector. The Jacobi matrix of the dynamic operator for the given system has the following elements:

$$(\mathbf{L}+\Lambda)_{ik}=\begin{bmatrix} a/2 & b & 0 & 0 & 0 & 0 & \dots \\ b & a & b & 0 & 0 & 0 & \dots \\ \dots & \dots & \dots & \dots & \dots & \dots & \dots \\ \dots & \dots & b & a & b & \dots & \dots \\ \dots & \dots & b & \tilde{D}_k^*(\eta,\varepsilon) & b & \dots & \dots \\ \dots & \dots & \dots & b & a & b & \dots \\ \dots & \dots & \dots & \dots & \dots & \dots & \dots \end{bmatrix}, \quad (31)$$

where a and b are the limiting values to which the elements a_n and b_n of the Jacobi matrix tend upon an increase in the number n (in our case, $a=\lambda_m/2$ and $b=\lambda_m/4$). The Jacobi matrix whose elements correspond to distortion of mass and force constants at the distance k from the end of the chain is denoted by

$$\tilde{D}_k(\eta,\varepsilon)=\begin{bmatrix} \tilde{a}_{k-1}(\eta) & \tilde{b}_k(\eta,\varepsilon) & 0 \\ \tilde{b}_k(\eta,\varepsilon) & \tilde{a}_k(\eta,\varepsilon) & \tilde{b}_{k+1}(\eta,\varepsilon) \\ 0 & \tilde{b}_{k+1}(\eta,\varepsilon) & \tilde{a}_{k+1}(\eta) \end{bmatrix}, \quad (32)$$

where

$$\tilde{a}_{k-1}(\eta)=\tilde{a}_{k+1}(\eta)=a\left(1+\frac{\eta}{2}\right),$$

$$\tilde{b}_{k-1}(\eta,\varepsilon)=\tilde{b}_k(\eta,\varepsilon)=b\,\frac{1+\eta}{\sqrt{1+\varepsilon}}, \quad (33)$$

$$\tilde{a}_k(\eta,\varepsilon)=a\left(\frac{1+\eta}{1+\varepsilon}\right).$$

Using the expression for Green's function of system (3) in accordance with the mechanism of detachment of discrete states from the continuous spectrum band, we can write the equation for the threshold combinations of the values of defect parameters $\{\eta,\varepsilon\}_d$:

$$\tilde{R}(\lambda_m)\equiv\tilde{P}_{k+1}(\lambda_m^*,\eta,\varepsilon)-\tilde{b}_k(\eta,\varepsilon)\tilde{P}_k(\lambda_m,\eta,\varepsilon)K_\infty(\lambda_m)=0. \quad (34)$$

In the lattice region unaffected by direct interaction with the defect, the polynomials $P_n(\lambda)$ at the upper boundary of the continuous spectrum of the chain have the simple form

$$P_n(\lambda_m)=2n+1,$$

where $n=0,1,\dots,k-1$. However, starting from $n=k$, the functions $P_n(\lambda_m)$ become dependent on the defect parameters and acquire a cumbersome form:

$$\tilde{P}_k(\lambda_m,\eta,\varepsilon)=\frac{\sqrt{\varepsilon+1}}{\eta+1}[2k(1-\eta)+(1+\eta)];$$

$$\tilde{P}_{k+1}(\lambda_m,\eta,\varepsilon)=\frac{2}{(\eta+1)^2}(2\varepsilon+1-\eta)[2k(1-\eta)+(1+\eta)]-(2k-1);$$

$$\tilde{P}_{k+2}(\lambda_m,\eta,\varepsilon)=\frac{2}{(\eta+1)^2}\{(2-\eta)(2\varepsilon+1-\eta)\times[2k(1-\eta)+(1+\eta)]\}-2k(3-2\eta)+(1-2\eta). \quad (35)$$

Consequently, expression (34) is simplified as follows:

$$\tilde{R}(\lambda_m)=\tilde{P}_{n+2}(\lambda_m)-\tilde{P}_{n+1}(\lambda_m). \quad (36)$$

Substituting (35) into (36), we can obtain the dependence of the threshold value of the coupling parameter of the defect on the separation between the impurity and the ''surface,'' i.e., the extreme atom of the chain corresponding to $n=0$, in the form of the solution of the equation

$$\eta^2[4k(\varepsilon+2)-(2\varepsilon+3)]-2\eta[4k(\varepsilon+1)+1]+[4k\varepsilon+(2\varepsilon+1)]=0. \quad (37)$$

Thus, we finally obtain

$$\eta_{1,2}(k,\varepsilon)=\frac{4k(\varepsilon+1)+1\pm2\sqrt{4k^2+(\varepsilon+1)^2}}{4k(\varepsilon+2)-(2\varepsilon+3)}. \quad (38)$$

Analyzing the limiting cases of the problem, i.e., an impurity in the form of a surface atom ($k\to0$) and an impurity in an infinite chain ($k\to\infty$), i.e.,

$$\lim_{k\to0}\eta_{1,2}(k,\varepsilon)=\begin{cases} -1 \\ \dfrac{1+2\varepsilon}{2\varepsilon+3} \end{cases} \quad (39)$$

and

$$\lim_{k\to\infty}\eta_{1,2}(k,\varepsilon)=\begin{cases} 1 \\ \dfrac{\varepsilon}{\varepsilon+2} \end{cases} \quad (40)$$

respectively, we can easily see that the replacement of the extreme atom of the chain by an impurity is the only case when only one local frequency exists in the entire range of variation of $\{\eta,\varepsilon\}$. The solution $\eta=-1$ corresponds to a nonphysical region of negative force coupling constant $\eta<-1(\alpha'<0)$, which allows us to disregard this value as a real ''threshold'' ensuring the formation of a discrete state.

Figure 5 shows the evolution of the threshold values of the parameter $\eta_{1,2}(k,\varepsilon)$ with increasing distance from the impurity atom to the ''surface.'' It turns out that in the limiting case (40), the threshold curves tend asymptotically to the dependences typical of an impurity in an infinite chain.

The coincidence between (39), (40) and analogous relations obtained for subspaces $H^{(0)}$,$H^{(\pm1)}$, and H^s confirms the correctness of the above analysis.

Thus, we have used the method of **J**-matrices to demonstrate that the exactly solvable model proposed here for in-

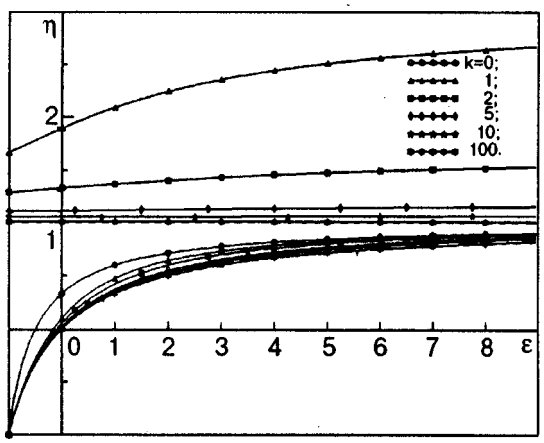

FIG. 5. Evolution of threshold values of the parameter $\eta_{1,2}(k,\varepsilon)$ with increasing separation of the impurity atom from the ''surface.''

terstitial (substitutional) impurities in a linear chain exhibits a variety of peculiarities (''threshold'' localization of vibrations beyond the continuous spectrum, formation of quasilocal resonant peaks of vibrational density in the range of allowed frequencies, the effect of ''redistribution'' of vibrational amplitude at discrete frequencies among the atoms of a defect cluster, etc.) typical of high-dimensional crystals. In the latter case, however, the computation of analogous characteristics involves considerable difficulties which can be overcome only through numerical count.

Theoretical and experimental analysis of low-dimensional systems as well as the effect of distortions in crystal regularity on the physical properties of solids always occupied an outstanding place among the topics of investigations at the Institute for Low Temperature Physics and Engineering. More than 30 years ago, V. I. Peresada of this *Institite* proposed the method of Jacobi matrices whose evolution demonstrated its exceptional efficiency for theoretical analysis of system with violated crystallographic regularities. These subjects formed the sphere of scientific interest of the B. I. Verkin, who headed the Institute and supported actively the creation and development of new methods of investigation. Many of such perfect and original methods were developed at the *Institute*.

For this reason, the authors are pleased to dedicate this research to the memory of Academician Boris Ieremievich Verkin, the founder of *ILTPE*.

*E-mail: syrkin@ilt.kharkov.ua

[1] M. Lanno and J. Bourgoin, *Point Defects in Semiconductors*, Springer-Verlag, Heidelberg (1981).
[2] *Structure of Metallic Solid Mixtures* (collected papers) [in Russian], Metallurgiya, Moscow (1966).
[3] G. Wertheim and A. Hausman, *Electron Structure of Point Defects*, Holland, Amsterdam, 1971.
[4] C. A. Melendres, V. A. Maroni, A. Naryanasami, and R. W. Siegel, J. Mater. Res. **4**, 1246 (1989).
[5] Y. Kanemitsu, K. Suzuki, Y. Nakayoshi, and Y. Masumoto, Phys. Rev. B **46**, 3916 (1992).
[6] P. Monceau (Ed.), *Electronic Properties of Inorganic Quasi-one-dimensional Compounds, Part I, Experiment*, Reidel Publ. Coompany, Dordrecht (1985).
[7] R. A. Klemm, in *Electronic Properties of Inorganic Quasi-one-dimensional Compounds, Part II, Experiment* (ed. by P. Monceau), Reidel Publ. Coompany, Dordrecht (1985).
[8] V. I. Peresada, in *Physics of Condensed State* [in Russian], ILTPE, Kharkov (1968).
[9] V. I. Peresada, V. N. Afanas'ev, and V. S. Borovikov, Fiz. Nizk. Temp. **1**, 461 (1975) [Sov. J. Low Temp. Phys. **1**, 227 (1975)].
[10] R. Haydock, in Solid State Phys. (ed. by H. Ehrenreich, F. Scitz, and D. Turnbull), Academic Press, New York (1980).
[11] E. S. Syrkin and S. B. Feodosyev, Fiz. Nizk. Temp. **20**, 586 (1994) [Low Temp. Phys. **20**, 463 (1994)].
[12] M. A. Mamalui, E. S. Syrkin, and S. B. Feodosyev, Fiz. Tverd. Tela (St. Petersburg) **38**, 3683 (1996) [Phys. Solid State **38**, 2006 (1996)].
[13] M. A. Mamalui, E. S. Syrkin, and S. B. Feodosyev, Fiz. Nizk. Temp. **24**, 773 (1998) [Low Temp. Phys. **24**, 583 (1998)].
[14] M. A. Mamalui, E. S. Syrkin, and S. B. Feodosyev, Fiz. Nizk. Temp. **25**, 72 (1999) [Low Temp. Phys. **25**, 55 (1999)].
[15] I. M. Lifshits, Nuovo Cimento Suppl. **3**, 716 (1956).
[16] A. A. Maradudin, E. Montroll, and J. Weiss, *Theory of Lattice Dynamics in the Harmonic Approximation*, Academic Press, New York (1963).
[17] A. M. Kosevich, *Theory of Crystal Lattice* [in Russian], Vishcha Shkola, Kharkov (1965).
[18] G. Leibfried and N. Brauer, *Point Defects in Metals. Introduction to the Theory*, Springer-Verlag, Heidelberg (1978).
[19] H. Böttger, *Principles of The Theory of Lattice Dynamics*, Physik-Verlag, Weinheim, 1983.
[20] A. P. Zhernov, N. A. Chernoplekov, and E. Morsan, *Metals with Nonmagnetic Impurity Atoms* [in Russian], Energoatomizdat, Moscow (1992).
[21] Yu. V. Skripnik, Ph. D. thesis, Kiev (1992).

Translated by R. S. Wadhwa

LOW-TEMPERATURE PHYSICS OF PLASTICITY AND STRENGTH

Empirical evaluation of electron and phonon drag coefficients for dislocations in Pb- and Al-based alloys

N. V. Isaev, V. D. Natsik, and V. S. Fomenko

*B. Verkin Institute for Low Temperature Physics and Engineering, National Academy of Sciences of the Ukraine, 310164 Kharkov, Ukraine**

(Submitted March 22, 1999)
Fiz. Nizk. Temp. **25**, 987–991 (August–September 1999)

The impurity concentration dependence of the temperature threshold of low-temperature anomalies of plasticity associated with the influence of inertial effects on the dislocation mobility is analyzed using the experimental data on the kinetics of plastic flow in five lead- and aluminum-based fcc solid solutions. It is shown that the results of such an analysis can be used for evaluating the electron and phonon drag coefficients for dislocations in these metals and to derive an empirical expression for the temperature dependence of phonon drag in the low-temperature range. © *1999 American Institute of Physics.* [S1063-777X(99)02308-7]

1. Experimentally detected regularities of plastic deformation in solid solutions in the range of moderately low temperatures are in good agreement with the ideas on thermoactivated motion of dislocations through impurity barriers (stoppers). However, peculiarities (anomalies) of plasticity observed in the range of hydrogen–helium temperatures could be explained only on the basis of several new hypotheses (see Refs. 1–3). It was proposed that one of the main reasons behind the anomalies is the effect of inertial properties of dislocations on the dynamics of their motion through impurity barriers.[4] As the temperature T is lowered, the average length L of a dislocation segment and the dynamic drag coefficient B decrease, and the dislocation segment becomes undamped. Under these conditions, collisions of dislocations with impurity atoms is accompanied by a dynamic increase in the average values of the angle of attack, leading to a sharp increase in the probability of overcoming of impurity barriers by a dislocation and to a considerable change in the kinetic of plastic flow of the alloy.

The most consistent analysis of the influence of inertial effects on the thermoactivated mobility of dislocations in an alloy was proposed in Ref. 5. The analysis is based on a statistical description of motion of dislocations through a random array of point barriers taking into account the dynamic increase in the angle of attack for a dislocation line approaching a barrier. This makes it possible to use the computer simulation method for calculating the average velocity of a dislocation over distance considerably longer than the mean distance between impurities and to describe typical features of manifestation of inertial effects, that can be observed in a macroscopic experiment. They include (1) the emergence of an anomaly on the temperature dependence of the yield stress $\tau_0(T)$ below a certain threshold temperature T_i depending on the impurity concentration C, (2) a sharp increase in the strain-rate sensitivity of deforming stress in the vicinity of the temperature $T_i(C)$, and (3) a jump in the deforming stress upon transition in a superconducting alloy, emerging due to inertial effects during plastic flow, whose magnitude exhibits a peculiar dependence on temperature and concentration.

A typical form of anomaly in $\tau_0(T)$ that can be obtained on the basis of the thermoinertial theory is a curve with a peak located below T_i, the value of T_i increasing with the impurity concentration. Other types of experimentally observed anomalies, e.g., the low-temperature plateau, are predicted by this theory only when special assumptions are made concerning the dependence of B on temperature and concentration of stoppers. The possibility of a transition from thermoinertial to quantum-inertial form of motion of dislocations through impurity barriers at low temperatures should also be taken into consideration.[2,3] In all cases, however, the conditions of undamped dislocation segment should be satisfied for manifestation of inertial effects. These conditions can be written in the form of two inequalities:

$$\tau^*(T,C)=\tau_0-\tau_i>0.5\tau_c,$$
$$B(T)L(\tau^*,C)<2\pi(ME_L)^{1/2}. \tag{1}$$

Here τ_0 is the deforming stress (yield stress), and τ^*, τ_i, and τ_c are the effective, internal, and critical stress of activationless motion of dislocations; E_L and M are the linear densities of intrinsic energy and mass of dislocations.

In order to prove that nondamping conditions can be satisfied for a specific crystal, we must determine the temperature and concentration dependences of quantities appearing in (1). For this purpose, we can use the rigorous procedure of thermoactivation analysis,[2,6,7] which makes it possible to determine the $\tau^*(T,C)$ dependence appearing in (1), to calculate the value of $\tau_c(C)$, to determine the type of statistics of the impurity barrier distribution along a dislocation, and to establish the dependence $L(\tau^*,C)$. A comparison of theoretical and experimental temperature dependences

 © 1999 American Institute of Physics

TABLE I. Plasticity parameters for some alloys.

Alloy	C	τ_c, MPa	κ, MPa	T_i, K	$\alpha\cdot 10^3$, Pa·s	$\eta\cdot 10^3$, Pa·s	$B\cdot 10^5$, Pa·s
	0.001	0.30		12			
	0.005	0.37		15			
Pb–Bi	0.01	0.57	5	17	0.7	9	1.6
	0.03	0.99		22			
	0.06	1.35		25			
	0.01	0.89		22			
Pb–Sn	0.02	1.26	11	26	0.8	3	4.4
	0.03	1.50		30			
	0.004	1.62		18			
Pb–Sb	0.007	1.87	16	20	1.0	3	4.2
	0.015	2.51		28			
Al–Li	0.038	12.70	90	34	0.9	200	2.8
	0.07	19.90		39			
Al–Mg	0.0062	8.70	110	21	1.0	280	1.8
	0.0152	15.40		27			
	0.0197	15.60		28			
	0.0380	18.10		31			

Notation: C is the impurity concentration, τ_c the critical stress of the activationless motion of dislocations, κ the proportionality factor in (6), T_i the threshold temperature of anomalous plasticity, α the coefficient defined by (7), η the constant in (4), and B the electron drag coefficient for dislocations.

of plasticity parameters makes it possible to determine to a fairly high degree of accuracy the value of the threshold temperature $T_i(C)$ below which inertial effects influence the motion of dislocations through impurity barriers considerably.

The main mechanisms of dynamic drag for dislocations in metals in the low-temperature region are electron and phonon viscosity:[8–10]

$$B(T)=B_{\rm ph}(T)+B_e\,. \tag{2}$$

The temperature dependence of the drag coefficient in this expression is determined by its phonon component $B_{\rm ph}(T)$, and B_e is the athermal contribution of conduction electrons to dislocation drag. Special experimental methods reviewed in Refs. 9 and 10 are used for measuring the phonon drag coefficient B. Two methods that are used more often are the recording of tracks of individual dislocations or slip lines under impact loading and the measurement of internal friction and separation of the contribution of dislocation segments trapped by impurities in it.

Reliable experimental data on the values of the electron and phonon components of the coefficient $B(T)$ have been obtained by the above-mentioned traditional methods only for a narrow range of crystals. In this connection, a new method for obtaining empirical estimates of low-temperature values of the phonon drag coefficient $B_{\rm ph}(T)$ and the electron drag coefficient B_e in solid solutions was proposed in Ref. 11. This method does not require special experimental techniques and is based only on the results of a detailed thermoactivation analysis of macroscopic parameters characterizing the plastic flow of alloys in the region where inertial effects are manifested.

It would be interesting to study the microscopic mechanism of motion of dislocations by using the scheme of empirical evaluation of $B(T)$ proposed in Ref. 11 in a wider range of alloys.

2. In this communication, we analyze the concentration dependence of the threshold temperature $T_i(C)$ of the low-temperature anomaly for a number of Pb- and Al-based fcc solid solutions. For this purpose, we use the data on the kinetics of low-temperature plasticity of polycrystals and single crystals of solid solutions, which were reported in earlier publications: Pb–Sn,[2,3] Pb–Sb,[3] Pb–Bi,[12] Al–Li,[13] and Al– Mg.[14] The empirical values of some plasticity parameters for these alloys that are required for subsequent calculations are given in Table I. Unfortunately, the error of measurements of these parameters for Al-based alloys was considerably larger than for Pb-based alloys: for Al–Li, these parameters were estimated on the basis of the data on low-temperature plasticity only for polycrystalline samples; for Al–Mg, we had no data sufficient for a rigorous thermoactivation analysis.

It can be seen from the table that the critical stress τ_c for activationless motion of dislocations and the threshold temperature T_i corresponding to the beginning of manifestation of anomalous plasticity increase with the impurity concentration. According to the results of thermoinertial theory, the $T_i(C)$ dependence for $\tau^*(T,C)>0.5\tau_c$ can be determined from the solution of the equation

$$[B_e+B_{\rm ph}(T)]L(\tau^*,C)=2\pi(ME_L)^{1/2}. \tag{3}$$

Theoretical analysis of phonon drag for dislocations proved[9,10] that at low temperatures $T\ll\Theta$ (Θ is the Debye temperature of the crystal), the $B_{\rm ph}(T)$ dependence is correctly approximated by a power function of the form

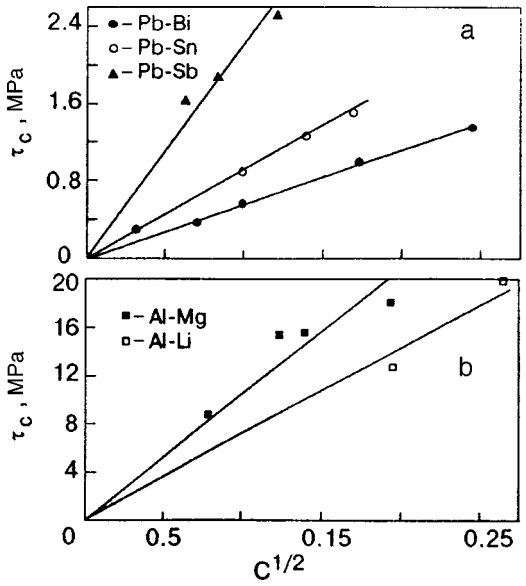

FIG. 1. Concentration dependences of critical stress τ_c for activationless motion of dislocations through impurity barriers in solid solutions: Pb-based alloys (a) and Al-based alloys (b).

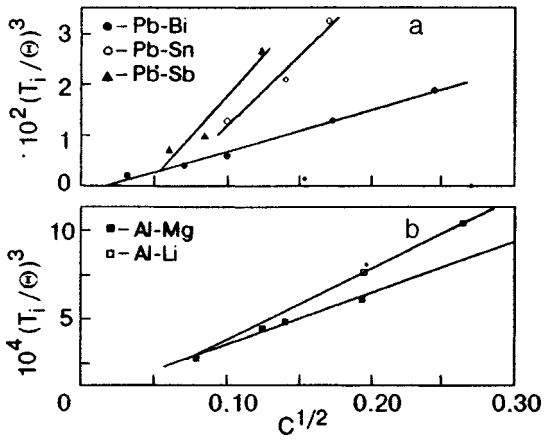

FIG. 2. Concentration dependences of the threshold temperature T_i of the anomaly, illustrating the validity of relation (7) for $\nu=3$: Pb-based alloys (a) and Al-based alloys (b).

$$B_{\rm ph}(T)\approx\eta(T/\Theta)^{\nu}. \tag{4}$$

Here η is a constant, and the value of the exponent ν is determined by the process of interaction of dislocations with phonons: if the dominating mechanism of dislocation drag is phonon wind (elastic scattering of phonons by the deformation field of dislocations), we have $\nu=5$, while in the case when the flutter effect (inelastic scattering of phonons by an elastic dislocation line) dominates, a weaker temperature dependence of the drag coefficient with $\nu=3$ is observed.

Thermoactivation analysis of the low-temperature plasticity parameters for fcc alloys proved that in the range of intermediate impurity concentrations $C\sim10^{-3}-10^{-1}$ and the effective stresses $\tau^*\simeq(0.1-0.5)\tau_c$, the impurity barrier distribution along a dislocation line is correctly described by the Friedel statistics.[15] In this statistics, the following relations hold:

$$L=(2E_Lb/\tau^*C)^{1/3}, \tag{5}$$

$$\tau_c=\kappa C^{1/2}. \tag{6}$$

The curves illustrating the validity of approximation (6) in the concentration range under investigation are given in Fig. 1, and the corresponding values of the constant κ depending on the strength of impurity barriers are given in Table I. Unfortunately, the error in determining the empirical values of the parameter κ in some cases is quite large in view of the absence of detailed information on the dependences $\tau_c(C)$ (as in the case of Al–Li alloys).

Assuming that the value of effective stress in the vicinity of the threshold temperature $\tau^*(T_i)\approx0.5\tau_c$ for all alloys and substituting (4) and (5) into (3), we obtain the following relations:

$$\eta(T_i/\Theta)^{\nu}=\alpha C^{1/2}-B_e,$$
$$\alpha=2\pi(ME_L)^{1/2}(\kappa/2E_Lb)^{1/3}. \tag{7}$$

In order to obtain numerical values of the parameter α, we used the values of the parameter κ from Table I, the estimates $M=0.5\rho b^2$ and $E_L=0.5Gb^2$ obtained on the basis of the continual theory of dislocations in the isotropic medium approximation, the values of shear modulus $G^{\rm Pb}=10^{10}$ Pa and $G^{\rm Al}=2.7\times10^{10}$ Pa typical of pure Pb and Al, the density $\rho^{\rm Pb}=10^4$ kg/m^3 and $\rho^{\rm Al}=0.27\times10^4$ kg/m^3, the magnitudes of the Burgers vector $b^{\rm Pb}=3.50\times10^{-10}$ m and $b^{\rm Al}=2.86\times10^{-10}$ m, and the Debye temperatures $\Theta^{\rm Pb}=98$ K and $\Theta^{\rm Al}=390$ K. The results of calculations are given in Table I.

The experimental values of $T_i(C)$ for all the alloys investigated by us indeed satisfy relation (7) if we choose the value of the parameter $\nu=3$. Figure 2 illustrates the linear approximation of relation (7) in appropriate coordinates, and the geometrical parameters of the straight lines in the figure allow us to obtain the values of the parameters η and B_e (see Table I). This result leads to the conclusion that the temperature dependence $B(T)$ for Pb and Al at $T\leqslant40$ K is determined by inelastic scattering of thermal phonons by dislocation lines (flutter effect).

The values of $B_{\rm ph}$ and B_e obtained by us are of the same order of magnitude as the empirical values of the dynamic drag coefficient for pure lead and aluminum obtained by other experimental methods (Fig. 3). A detailed analysis of the data presented in Refs. 9 and 10 indicates a wide spread of experimental estimates of B, which are as a rule one or two orders of magnitude higher than the theoretical estimates. The reasons behind such a discrepancy remain unclear. The spread in the values of B_e and the coefficient η obtained by us can be partially due to a large spread typical of the measured values of low-temperature plasticity parameters and a large error in determining the threshold temperature T_i.

3. The analysis of the parameters of low-temperature plasticity for five fcc solid solutions carried out by us here confirmed the efficiency of the method for empirical evaluation of the dynamic drag coefficient for dislocations in the low-temperature region proposed in Ref. 11. The method is based on macroscopic data on the kinetics of thermoacti-

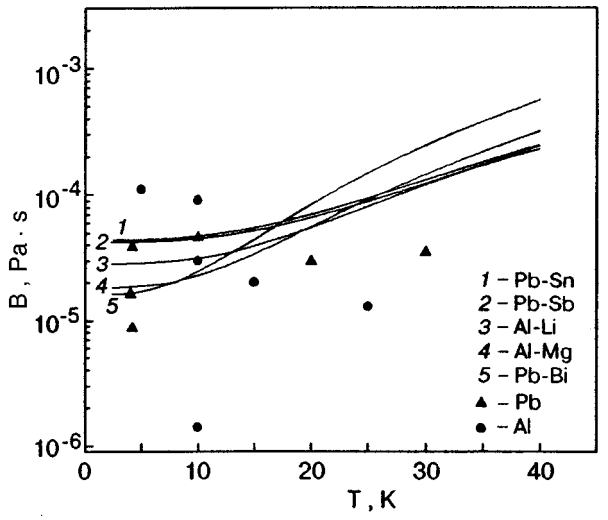

FIG. 3. Temperature dependences of the dynamic drag coefficient $B(T)$ for dislocations in $\log B$ vs. T coordinates: symbols correspond to low-temperature values of B for Pb and Al, obtained earlier by using special experimental methods,[9,10] solid curves describe the dependence $B(T) = \eta(T_i/\Theta)^3 + B_e$ for corresponding values of the parameters η and B_e from Table I.

vated plastic flow of alloys in a wide range of temperature and impurity concentration and on an analysis of the concentration dependence of the threshold temperature corresponding to manifestation of inertial properties of dislocations. The obtained values of the electron and phonon drag coefficients for dislocations are of the same order of magnitude as the estimates of these parameters obtained earlier on the basis of different methods.

This research was carried out under the support of the Ukrainian Foundation of Fundamental Studies (Project No. 2.4/156 ''Bion-2'').

We dedicate this work to the blessed memory of Boris Ieremievich Verkin. Owing to his prowess in organization and planning, the study of physical and mechanical properties of a wide class of materials under deep cooling has become one of the major topics of research in the Institute created by him. Permanent assistance and personal participation of Boris Ieremievich in these studies led to important scientific results in the field of fundamental physics of plasticity, superconductor and space material science, thus elevating B. Verkin Institute for Low Temperature Physics and Engineering to a leading position in the development of modern trends in low-temperature physical material science.

*E-mail: isaev@ilt.kharkov.ua

[1] V. I. Startsev, in *Dislocations in Solids*, Vol. 6 (ed. by F. R. N. Nabarro), North-Holland, Amsterdam (1983).
[2] I. A. Shepel, L. N. Zagoruiko, V. D. Natsik *et al.*, Fiz. Nizk. Temp. **17**, 390 (1991) [Sov. J. Low Temp. Phys. **17**, 202 (1991)].
[3] N. I. Isaev, V. D. Natsik, V. V. Pustovalov *et al.*, Fiz. Nizk. Temp. **18**, 911 (1992) [Sov. J. Low Temp. Phys. **18**, 641 (1992)].
[4] A. V. Granato, Phys. Rev. B **4**, 2196 (1971).
[5] A. I. Landau, Phys. Status Solidi A **61**, 355, 455 (1980); *ibid.* **65**, 119 (1981).
[6] U. F. Kocks, A. S. Argon, and M. F. Ashby, Prog. Mater. Sci. Oxford, Pergamon Press **19**, 288 (1975).
[7] V. N. Kovaleva, V. A. Moskalenko, and V. D. Natsik, Philos. Mag. A **70**, 423 (1994).
[8] M. I. Kaganov, V. Ya. Kravchenko, and V. D. Natsik, Usp. Fiz. Nauk **111**, 655 (1973) [Sov. Phys. Usp. **16**, 878 (1973)].
[9] V. I. Alshits and V. L. Indenbom, Usp. Fiz. Nauk **115**, 3 (1975) [Sov. Phys. Usp. **18**, 1 (1975)].
[10] V. I. Alshits and V. L. Indenbom, in *Dislocations in Solids*, vol. 7 (ed. by F. R. N. Nabarro), North-Holland, Amsterdam (1986).
[11] V. A. Moskalenko, V. N. Kovaleva, V. D. Natsik *et al.*, Fiz. Nizk. Temp. **22**, 1459 (1996) [Low Temp. Phys. **22**, 1108 (1996)].
[12] N. V. Isaev, V. D. Natsik, V. V. Pustovalov *et al.*, Fiz. Nizk. Temp. **24**, 786 (1998) [Low Temp. Phys. **24**, 593 (1998)].
[13] V. S. Fomenko, N. V. Isaev, and V. V. Pustovalov *et al.*, Fiz. Nizk. Temp. **19**, 429 (1993) [Low Temp. Phys. **19**, 301 (1993)].
[14] V. P. Podkujko and V. V. Pustovalov, Cryogenics **9**, 589 (1978).
[15] J. Friedel, *Dislocations*, Pergamon Press, London (1964).

Translated by R. S. Wadhwa

BRIEF COMMUNICATIONS

Visualization of the antiferromagnetic insulator–ferromagnetic metal phase transition in manganite $Nd_{0.5}Sr_{0.5}MnO_3$

S. L. Gnatchenko, A. B. Chizhik, I. O. Shklyarevskiĭ, and D. N. Merenkov

*B. Verkin Institute for Low Temperature Physics and Engineering, National Academy of Sciences of Ukraine, 310164 Kharkov, Ukraine**

V. I. Kamenev and Yu. G. Pashkevich

A. Galkin Physicotechnical Institute, National Academy of Sciences of Ukraine, 310114 Donetsk, Ukraine

K. V. Kamenev, G. Balakrishnan, and D. McK. Paul

Department of Physics, University of Warwick, Coventry CV4 7AL, England
(Submitted March 10, 1999)
Fiz. Nizk. Temp. **25**, 992–995 (August–September 1999)

It is found that the first-order phase transition from a nonmetallic antiferromagnetic (AFM) state to a metallic ferromagnetic (FM) state in manganite $Nd_{0.5}Sr_{0.5}MnO_3$ is accompanied by a significant change in the reflectivity of the visible light. This effect is used for visualizing the AFM–FM phase transition in $Nd_{0.5}Sr_{0.5}MnO_3$. The coexistence of AFM and FM phases was observed visually during spontaneous and field-induced AFM–FM transitions. In both cases, the transition occurs through nucleation and expansion of domains of the phase that is favorable from the energy point of view. However, the periodic domain structure of the intermediate magnetic state was not formed during the phase transition. A striped domain structure was formed in the AFM state while the FM phase had a uniform structure. © *1999 American Institute of Physics.* [S1063-777X(99)02408-1]

Over the last decade, manganites, viz., oxides of manganese with the perovskite structure $R_{1-x}A_xMnO_3$, where $R=La^{3+}$, Nd^{3+}, Pr^{3+}, Eu^{3+}…; $A=Ca^{2+}$, Sr^{2+}, Ba^{2+}, Pb^{2+},… have aroused considerable interest following the detection of giant magnetoresistance in these compounds.[1] This effect, which is observed in manganites in the vicinity of the Curie temperature T_C, is important not only for studying the origin of the phenomenon and its practical applications, but also because manganites are fascinating objects of investigation in view of a number of interesting properties, e.g., charge and orbital ordering, Jahn–Teller effect, as well as spontaneous and induced phase transitions (PT). Some manganites exhibit spontaneous and magnetic field-induced PT from nonmetallic AFM state to metallic FM state. Among others, the $Nd_{0.5}Sr_{0.5}MnO_3$ crystal undergoes this PT.[2–4] A decrease in temperature to $T_C \simeq 255$ K leads to FM ordering in $Nd_{0.5}Sr_{0.5}MnO_3$, while a spontaneous first-order PT metallic FM–insulating AFM is observed at a temperature T_{M-I} close to 160 K. The FM–AFM transition in this crystal coincides with charge ordering,[2] i.e., the emergence of a spatial ordering of holes, and hence of Mn^{3+} and Mn^{4+} ions. Note that the transition temperature T_{M-I} in manganites does not always coincide with the charge ordering temperature T_{co}. For example, $T_{M-I}<T_{co}$ in $Nd_{1-x}Ca_xMnO_3$ and $Pr_{1-x}Ca_xMnO_3$ $T_{M-I}<T_{c0}$.[5] At temperatures $T<T_{M-I}$, the magnetic field causes a dissolution of charge ordering in $Nd_{0.5}Sr_{0.5}MnO_3$ and induces a transition to the metallic FM state.

The metallic FM-insulating AFM transition in $Nd_{0.5}Sr_{0.5}MnO_3$ was studied earlier through conductivity and magnetization measurements,[2,3] radiographic methods,[2] and neutron diffraction technique.[4] It was found that the $Nd_{0.5}Sr_{0.5}MnO_3$ crystal in both states has an orthorhombic structure (space group $Pnma$).[1,4] The conductivity varies by more than two orders of magnitude upon PT while the magnetization changes by about $2.5\mu_B$/Mn.[2,3] The crystal lattice parameters also change significantly ($\sim 10^{-3}$–10^{-2}) during PT.[2,4] Upon a transition to the AFM state, the volume of the magnetic unit cell increases and a CE type AFM structure is established.[2,4,6] It is reported in the present work that the intensity of the visible light reflected from the $Nd_{0.5}Sr_{0.5}MnO_3$ crystal decreases considerably upon a PT from the metallic FM state to the insulating AFM state. This effect was used for visualizing and studying the two-phase state formed during the PT.

Crystals of $Nd_{0.5}Sr_{0.5}MnO_3$ were obtained by the zone melting technique and had cylindrical form. Samples were cut in the form of plates at right angles to the cylinder axis. The plates had an average size of about 3 mm and their thickness varied from 0.5 to 2 mm. X-ray investigations showed that the samples were not monocrystalline. However, they were highly textured with preferred orientations (100)

 © 1999 American Institute of Physics

and (010) of the crystallite axes in *Pnma* space group at an angle of 15° to the cylinder axis. The mutual disorientation of the crystallite axes did not exceed a few degrees. The lattice parameters measured at room temperature coincided with those obtained in Ref. 4 for $Nd_{0.5}Sr_{0.5}MnO_3$ up to third decimal place. The surface of the plates was polished mechanically to mirrorlike reflection state. The stresses emerging in the crystal as a result of mechanical polishing were removed by annealing the polished samples in air at a temperature of 950 °C for 20 hours. The metallic FM – insulating AFM transition in $Nd_{0.5}Sr_{0.5}MnO_3$ was studied by measuring the intensity of light reflected from the polished surface of the plate and visual observation of the two-phase state formed during PT. Samples were placed in an optical helium cryostat with a superconducting solenoid. The sample temperature could be varied in the interval $10\,K < T < 300\,K$ and was measured with the help of a copper–constantan thermocouple. The optical circuit for measuring the intensity of the reflected light consisted of a He–Ne laser, a light intensity modulator, and a photoelectric multiplier. The light from laser with $\lambda = 633$ nm was reflected from the plate, modulated in intensity, and supplied to the photoelectric multiplier. The angle of incidence of light on the sample was $\sim 10°$, and the signal from the PEM was detected by a synchronous amplifier. Visual observation of the domain structure was carried out in visible light with the help of a microscope. The image of the sample with a domain structure was observed and recorded by a video camera with a monitor and a VCR. The obtained image was also subjected to computer processing.

Figure 1 shows the temperature and field dependences $I(T)$ and $I(H)$ of the intensity of light reflected in the vicinity of the first-order phase transition metallic FM – insulating AFM. Figure 1a shows the dependence $I(T)$ measured in zero magnetic field. The phase transition corresponds to a jump in the intensity of the reflected light. In the insulating AFM state, the value of I is about half that in the metallic FM state. The transition occurred at $T \approx 154$ K during cooling and at $T \approx 162$ K during heating. In other words, it displayed a temperature hysteresis having a width of about 8 K. The intensity of the reflected light also changed abruptly in the field-induced phase transition metallic FM – insulating AFM at $T < 154$ K. The dependence $I(H)$ measured at $T = 144$ K is shown in Fig. 1b. It can be seen that the transition is accompanied by a variation of I by a factor of more than two, and a field hysteresis of width around 16 kOe. The inset to Fig. 1 shows a fragment of the $H-T$ phase diagram for $Nd_{0.5}Sr_{0.5}MnO_3$ reconstructed from optical measurements. Note that the results of investigation of the phase transition insulating AFM-metallic FM in $Nd_{0.5}Sr_{0.5}MnO_3$ obtained by measuring the reflected light are in good accord with the results of transport and magnetic measurements data obtained by Kuwahara *et al.*[2]

The observed effect of variation of the intensity of reflected light was used for visualizing first-order PT from insulating AFM state to metallic FM state in the manganite $Nd_{0.5}Sr_{0.5}MnO_3$. Visual observation of the two-phase state under phase transition was carried out in reflected white light with the help of a microscope. The first-order phase transition insulating AFM – metallic FM in $Nd_{0.5}Sr_{0.5}MnO_3$ occurred through nucleation and expansion of domains in the energetically advantageous phase. The expansion of such domains was accompanied by a decrease in the concentration of the energetically disadvantageous phase whose domains eventually disappeared and the sample was transformed completely into the energetically advantageous phase. Domains were formed in different parts of the sample, and the emerging two-phase domain structure was not reproduced completely during repeated observations of the transition under identical conditions. In other words, the domain structure was not defined uniquely by inhomogeneities of the sample, temperature or field. However, no periodic domain band structure of the magnetic intermediate state (IS) was observed during the transition. The existence of AFM and FM phases was observed at temperatures around 2 K in the field interval 5–7 kOe.

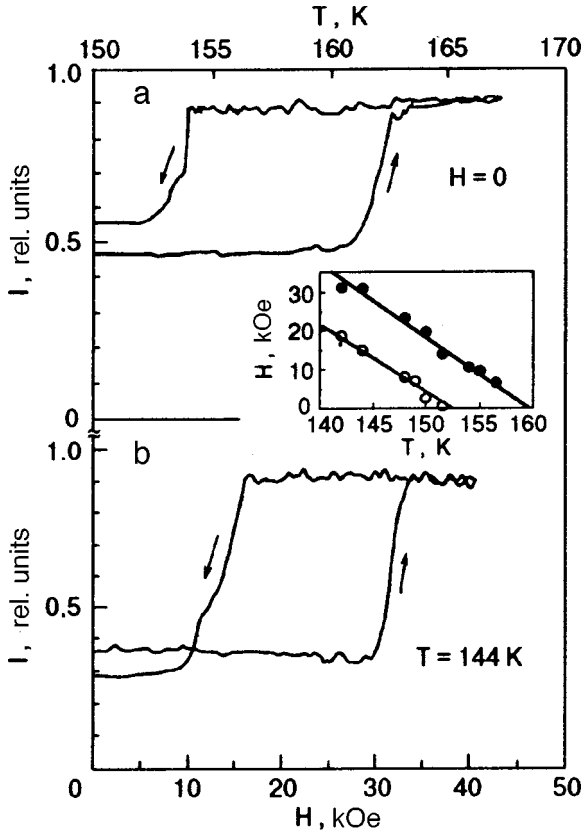

FIG. 1. Temperature ($H = 0$) and field ($T = 144$ K) dependences of the intensity of reflected light. Discontinuities on the dependences correspond to the insulating AFM–metallic FM phase transition. The inset shows a fragment of the $H-T$ phase diagram of $Nd_{0.5}Sr_{0.5}MnO_3$ obtained from optical measurements. Dark circles correspond to the transition induced by increasing field or temperature, and light circles to the same transition in decreasing field or temperature.

Visual observations also revealed that the insulating AFM phase is inhomogeneous. The band domain structure observed in the AFM state remained unchanged in a magnetic field right up to the field corresponding to the transition to the FM state. In the FM state, the sample was practically homogeneous but revealed in some cases weakly contrasted traces of the domain structure prevailing in the AFM phase before the onset of the transition to the FM state. The domain

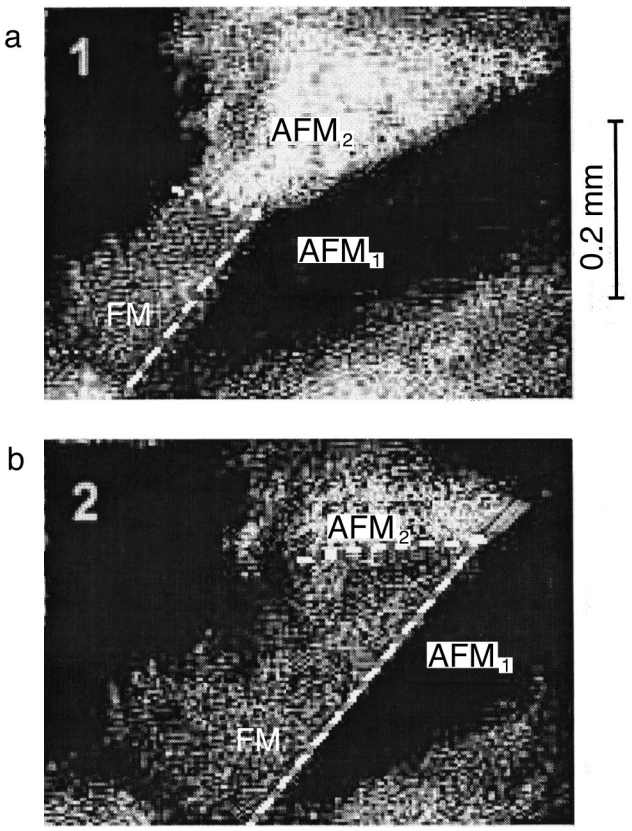

FIG. 2. Domain structure observed in $Nd_{0.5}Sr_{0.5}MnO_3$ during insulating AFM–metallic FM phase transition. The black and white domains correspond to the AFM phase and the gray one to the FM phase. The dashed line shows the interface between AFM and FM states, which is displaced in increasing field. The sample temperature $T=152$ K, and the applied magnetic field $H\approx 14$ kOe (a) and 16 kOe (b).

structure in the AFM state was not repeated in numerous observations of the transition from the FM to the AFM phase, but the orientation of domain walls in the sample was preserved. In some cases, the transition from the FM to AFM state was accompanied by the formation of a homogeneous AFM phase, i.e., the transition to one of the two possible AFM states was realized. Different values of I on the hysteresis loop for the AFM state (Fig. 1) are associated with different concentrations of two types of AFM domains.

Figure 2 shows a sample segment in which domains of the AFM (black and white) and FM (gray) phases can be seen. An increase in the magnetic field leads to an increase in the volume of the FM phase at the expense of the black and white domains of the AFM phase. The dashed line in the figure indicates the boundary region between the FM and AFM phases which is displaced upon an increase in the field.

The formation of a domain structure in the AFM state of $Pr_{0.5}Sr_{0.5}MnO_3$ was observed by electron microscopy technique.[7] In this manganite, the crystalline domain structure is formed as a result of structural phase transition with a decrease in symmetry from $I4/mcm$ to $Fmmm$ accompanying the PT from metallic FM state to insulating AFM state. However, a transition to the AFM state in $Nd_{0.5}Sr_{0.5}MnO_3$ is not accompanied by symmetry variations, although the parameters of the rhombic cell change significantly.[2] Moreover, the investigated samples are not monocrystalline. Hence the formation of a band domain structure in such samples with boundaries passing through the entire sample can be attributed to long-range interaction. There are no demagnetization fields in the AFM phase. The formation of the domain structure in the AFM phase is probably due to elastic stresses emerging in the crystal during PT as a result of strong variations in the crystal lattice parameters.

The absence of a magnetic intermediate state in $Nd_{0.5}Sr_{0.5}MnO_3$ during the FM–AFM phase transition in a magnetic field also requires an explanation. This transition is accompanied by a magnetization jump of about 400 G. Accordingly, the field interval corresponding to the intermediate state in thin films of $Nd_{0.5}Sr_{0.5}MnO_3$ must have a width of about 5 kOe. This value is comparable with the experimentally observed field interval corresponding to the existence of a two-phase state in the investigated samples. Hence the absence of the intermediate state cannot be attributed to sample inhomogeneities. In $Nd_{0.5}Sr_{0.5}MnO_3$, the intermediate state may not be formed during PT on account of an extremely large value of the interface walls energy associated with elastic stresses emerging at the boundary as a result of variations ($\sim 10^{-2}$) of the crystal lattice parameters during the phase transition.

Finally, it should be noted that the variation of the reflectivity observed by us during the metallic FM – insulating AFM phase transition in $Nd_{0.5}Sr_{0.5}MnO_3$ made it possible to visualize the two-phase state, determine the nature of the phase transition and the main properties of the two-phase domain structure. A domain structure was observed in the AFM phase. However, the origin of this domain structure and the reasons behind the absence of a magnetic intermediate state during phase transition remain unexplained and require further investigation.

*E-mail: gnatchenko@ilt.kharkov.ua

[1] A. P. Ramires, J. Phys.: Condens. Matter **9**, 8171 (1997).
[2] H. Kuwahara, Y. Tomioka, A. Asamitsu *et al.*, Science **270**, 961 (1995).
[3] Y. Tokura, H. Kuwahara, Y. Morimoto *et al.*, Phys. Rev. Lett. **76**, 3184 (1996).
[4] H. Kawano, R. Kajimoto, H. Yoshizawa *et al.*, Phys. Rev. Lett. **78**, 4253 (1997).
[5] M. Tokunaga, N. Miura, Y. Tomioka, and Y. Tokura, Phys. Rev. B **57**, 5259 (1996).
[6] E. O. Wollan and W. C. Koehler, Phys. Rev. **100**, 545 (1955).
[7] F. Damay, C. Martin, M. Hervieu *et al.*, J. Magn. Magn. Mater. **184**, 71 (1998).

Translated by R. S. Wadhwa